*NASA Conference Publication 3280*
*PREPRINT*

# 18th Space Simulation Conference Space Mission Success Through Testing



*Proceedings of a conference to be held at the Hyatt Regency Hotel Baltimore, Maryland October 31 to November 3, 1994*

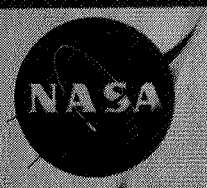

*NASA Conference Publication 3280*
***PREPRINT***

# 18th Space Simulation Conference Space Mission Success Through Testing

*Compiled by*
Joseph L. Stecher
*NASA Goddard Space Flight Center*
*Greenbelt, Maryland*

Sponsored by
National Aeronautics and Space Administration
Institute of Environmental Sciences
American Institute for Aeronautics and Astronautics
American Society for Testing and Materials
Canadian Space Agency


National Aeronautics
and Space Administration

**Goddard Space Flight Center**
Greenbelt, Maryland 20771

**1994**

This publication is available from the NASA Center for AeroSpace Information,
800 Elkridge Landing Road, Linthicum Heights, MD 21090-2934, (301) 621-0390.

## FOREWORD

The Eighteenth Space Simulation Conference, held at the Hyatt Regency Hotel in Baltimore, Maryland from October 31 through November 3, 1994, was hosted by the Institute of Environmental Sciences (IES) and was supported by the American Institute of Aeronautics and Astronautics (AIAA), the American Society for Testing and Materials (ASTM), the National Aeronautics and Space Administration (NASA), and the Canadian Space Agency (CSA).

These proceedings attest to the breadth of the conference; papers were presented on topics as diverse as materials degredation in low Earth orbit, the Martian environment and several aspects of the still commercially dominant geostationary orbit. A good cross section of the space flight community took advantage of the opportunity to get together, to share their experiences and to participate in the sessions addressed by three invited speakers. Frank Cepollina covered the Hubble Space Telescope (HST) Servicing Mission; Paul Regeon of Clementine Program fame- the role of testing in the Deep Space Program Science Experiment and Alexander Makarov of the Russian Space Agency- the facilities and capabilities of the NIICHIMMASH Organization. Tours of NASA Goddard Space Flight Center and Johns Hopkins University Applied Physics Laboratory and the preceding tutorial rounded out a comprehensive conference contributing to the knowledge of topics vital to the success of missions which have large commercial and scientific impacts.

Special thanks are due to the Technical Program Chair, Harold Fox and his Committee for their success in selecting the papers and planning the program. I wish to express my gratitude also to John Campbell (IES Meeting Manager), Russel T. Hollingsworth (Facilities Chair), and Joseph L. Stecher III (Publication Chair), for their effectiveness and professional performance. Our host society (the IES and its Executive Director, Janet A. Ehmann), and sponsoring agencies (AIAA, ASTM, NASA and CSA) are gratefully acknowledged. The Johns Hopkins University Applied Physics Laboratory provided the program and NASA published the Proceedings. Their kind generosity helped make this conference possible and the active participation of registrants made it a success.

Rolf Mamen
General Chair
18th Space Simulation Conference

## COMMITTEES FOR
## 18TH SPACE SIMULATION CONFERENCE

### MEETING MANAGEMENT COMMITTEE

| | |
|---|---|
| General Chairman: | Dr. Rolf Mamem, Canadian Space Agency |
| Technical Program: | Harold G. Fox<br>The Johns Hopkins University Applied Physics Laboratory |
| IES Meeting Manager: | John D. Campbell, Consultant |
| Publication Chairman: | Joseph L. Stecher, NASA Goddard Space Flight Center |
| IES Executive Director: | Janet A. Ehmann, Institute of Environmental Sciencs |

### TECHNICAL PROGRAM COMMITTEE

Greg Proulx, Hughes Aircraft Company
John W. Harrell, Jet Propulsion Laboratory
Albert R. Lunde, Boeing Aerospace
Robert G. Moss, Space Systems Loral
Peter W. Brinkmann, ESA/ESTEC
Patric F. Neary, TRW
Alda Simpson, NASA Goddard Space Flight Center
Michael Bietler, Martin Marietta Astro Space, East Windsor

### JOINT POLICY COMMITTEE

#### IES

John D. Campbell, Consultant
Joseph L. Stecher, NASA Goddard Space Flight Center

#### ASTM

Albert R. Lunde, Boeing Defense and Space Group
Robert G. Moss, Space Systems Loral

#### AIAA

John W. Harrell, Jet Propulsion Laboratory

# CONTENTS



† Abstracts only

# CONTENTS



† Abstracts only

# CONTENTS

## SESSION F (cont.)



## SESSION G: DYNAMICS TESTING



## SESSION H: LIFE SCIENCES AND SAFETY ISSUES



† Abstracts only

# CONTENTS

## SESSION I: NEW APPROACHES AND FACILITIES I



## SESSION J: NEW APPROACHES AND FACILITIES II



† Abstracts only

# EVALUATION OF REFORMULATED THERMAL CONTROL COATINGS IN A SIMULATED SPACE ENVIRONMENT PART I. - YB-71

**Clifford A. Cerbus**
**University of Dayton Research Institute**

**Patrick S. Carlin**
**USAF Wright Laboratory Materials Directorate**

## ABSTRACT

The Air Force Space and Missile Systems Center and Wright Laboratory Materials Directorate (WL/ML) have sponsored an effort to reformulate and qualify Illinois Institute of Technology Research Institute (IITRI) spacecraft thermal control coatings.

S13G/LO-1, Z93, and YB-71 coatings were reformulated because the potassium silicate binder, Sylvania PS-7, used in the coatings is no longer manufactured. Coatings utilizing the binder's replacement candidate, Kasil 2130, manufactured by The Philadelphia Quartz (PQ) Corporation, Baltimore, Maryland, are undergoing testing at the Materials Directorate's Space Combined Effects Primary Test and Research Equipment (SCEPTRE) Facility operated by the University of Dayton Research Institute (UDRI). The simulated space environment consists of combined ultraviolet (UV) and electron exposure with *in situ* specimen reflectance measurements. A brief description of the effort at IITRI, results and discussion from testing the reformulated YB-71 coating in SCEPTRE, and plans for further testing of reformulated Z93 and S13G/LO-1 are presented.

## INTRODUCTION AND BACKGROUND

The exterior surfaces of all spacecraft are covered with a combination of insulation and thermal control coatings to regulate the internal temperature of the spacecraft. This temperature depends on the internally generated heat of the spacecraft, the heat absorbed from the sun, and the heat radiated out to space. Insulation prevents heat from the sun from entering the spacecraft, but also prevents heat from escaping. Therefore, areas of the exterior surface must be exposed to space to allow radiation of excess heat. These areas, called radiators, are coated with thermal control coatings that allow radiation of thermal energy while reflecting most of the incident solar energy. The thermal balance of the spacecraft is determined by the solar absorptance ($\alpha_s$) and the thermal emittance ($\varepsilon$) of this surface coating. Usually, the thermal control coatings are chosen to provide the lowest possible absorptance and the highest possible emittance, for a minimum $\alpha_s/\varepsilon$ ratio. In addition, the coatings must be easy to apply, durable, low outgassing and stable in the space environment.

Zinc orthotitanate ($Zn_2TiO_4$, a.k.a., ZOT) and zinc oxide (ZnO) pigmented coatings are commonly utilized on spacecraft because of their optical properties and stability to the space environment. Three state of the art thermal control coatings, Z93, YB-71 and S13G/LO-1, supplied to the industry sole source by IITRI, incorporate potassium silicate as a major and vital component in their composition. Potassium silicate is manufactured using elevated temperatures and pressures to generate specific molar ratios of $K_2O$ and $SiO_2$ (ref. 1) and is purchased in solution form. Upon drying, the potassium silicate becomes a mixture of primarily $K_2O$ and $SiO_2$, with other various silicates of potassium ($K_2Si_2O_5$, $K_2SiO_3$, $K_2Si_4O_9 \cdot H_2O$, and $KHSi_2O_5$) theoretically present.

In the case of ZnO pigmented S13G/LO-1, which uses a silicone binder, the potassium silicate is used to reactively encapsulate the ZnO pigment particles. This allows for the formation of a barrier to photodeposition reactions on the surface of ZnO and enhances the space stability of the coating. In the case of the inorganic ZnO pigmented Z93 and ZOT pigmented YB-71, the potassium silicate constitutes the binder in the coatings. The potassium silicate used in the formulation of white spacecraft thermal control coatings, Z93, YB-71, and S13/GLO-1, was manufactured by Sylvania as PS-7 potassium silicate solution. Sylvania has discontinued the manufacture of PS-7, which has threatened the continued availability of these coatings to AF space systems. To ensure the continued supply of these thermal control coatings, WL/ML began a contracted effort with IITRI (points of contact: Yoshiro Harada and Mukund "Mike" Deshpande) in October of 1991 to reformulate and qualify new versions of Z93, YB-71, and S13G/LO-1 with an alternate and available binder system. The Air Force Space and Missiles Systems Center (SMC) sponsored this contractual effort and Jerry Bauer and Michael Meshishnek of The Aerospace Corporation provided technical guidance to the Materials Directorate.

IITRI identified The PQ Corporation's Kasil 2135 potassium silicate solution as an ideal replacement material for the Sylvania PS-7. The Kasil 2135 had better purity levels than the PS-7, but production of the Kasil 2135 is only performed on limited research levels, thus it was not considered a viable alternative. The PQ Corporation indicated that production of Kasil 2130 would be continued indefinitely. Since Kasil 2130 has identical $SiO_2$:$K_2O$ mole ratio of 3.3:1 as PS-7 and similar purity levels, viscosity, and other properties, IITRI chose it as the candidate replacement binder early in their effort. IITRI used Kasil 2130 to reformulate the coatings, performed various processing and properties evaluation studies, and demonstrated that Kasil 2130 is a suitable candidate material to replace PS-7 in the three thermal control coatings. ITTRI has designated the reformulated coating candidates as Z93P, YB-71P, and S13GP/LO-1. A Wright Laboratory technical report documenting the effort by IITRI will be available soon.

The final aspect of the program involves testing of the coatings in a simulated space environment and comparing the results to the original formulation coatings. Space simulation tests of these materials have been and are in the process of being conducted at various facilities. These include: UV & electron exposure testing at WL/ML's SCEPTRE facility and at The Aerospace Corporation, vacuum ultraviolet (VUV) & atomic oxygen exposure testing at both NASA Lewis and NASA Marshall, and planned UV & electron exposure testing at NASA Marshall. Additionally, the Canadian Space Agency flew samples of the candidate coatings in the "Materials Exposure in Low Earth Orbit (MELEO)" experiment on STS-52, where "all exposed samples showed no optical or physical degradation." IITRI has submitted coating samples to The Aerospace Corporation for flight testing on the upcoming Ballistic Missile Defense Organization (BMDO) sponsored Space Active Modular Materials Experiment (SAMMES).

The purpose of this study was to determine the performance of YB-71 and YB-71P in a multiple radiation environment consisting of high vacuum, low energy electron, and UV radiation. The results from the testing of Z93P and S13GP/LO-1 will be presented in the future.

## SCEPTRE DESCRIPTION

WL/ML's Space Combined Effects Primary Test Research Equipment (SCEPTRE) Facility is the only Air Force owned facility designed specifically for testing and qualification of spacecraft thermal control coating materials. Testing at the facility is performed in accordance with the guidelines established by the American Society for Testing and Materials (ASTM) *E 512-94 Standard Practice for Combined, Simulated Space Environment Testing of Thermal Control Materials with Electromagnetic and Particulate Radiation* (ref. 2). The system has the capability of providing synergistic UV and electron radiation environments similar to those experienced by satellites orbiting in mid-to -high earth orbits and is shown in figure 1. In addition, the system has the ability to perform *in situ* measurements of sample temperature and reflectance as a function of wavelength. The vacuum level is maintainable from approximately $6.7 \times 10^{-6}$ to $6.7 \times 10^{-5}$ Pa ($5 \times 10^{-8}$ to $5 \times 10^{-7}$ Torr), the

sample temperatures can range from room temperature to 100°C (212°F), the simultaneous multiple sun levels average between 1.0 to 3.0 equivalent ultraviolet suns (EUVS) (250-400 nm), and the electron flux is adjustable to a maximum of $10^{12}$ $e^-/cm^2/sec$ at energies adjustable to a maximum of 20 KeVs, for each of the two electron guns. This combination of specifically tailored parameters provides an accelerated testing environment with synergistic effects of vacuum, accelerated UV and electron radiation, and limited thermal cycling.

**Vacuum System**

The vacuum system is composed of a 45.72 cm (18 in) diameter belljar pumped by a Welch Vacuum Technology model 3106S turbomolecular pump, backed by a Welch Vacuum Technology model 1397 rotary pump. The chamber is monitored via two different ion gages, a Granville-Phillips 271 Series and a Fredricks-Televac model 3C5-2A2; and a Uthe Technology Inc. (UTI) model 100C residual gas analyzer. The chamber has the capability of exposing a maximum of five, 2.38 cm (15/16 in) diameter, specimens to the synergistic UV and electron radiation. Figure 2. shows the facility's sample wheel, containing five white thermal control coating specimens, positioned just below the Faraday cup. The specimens are indirectly cooled via a chilled water line. The temperature control system reduces the exposed specimens' temperatures by approximately 5.56°C (10°F).

**Solar Simulator**

The solar simulator consists of a moderately filtered 2500 Watt xenon arc lamp mounted in a modified Spectrolab X-25 solar simulator. The entire optical system of the Spectrolab X-25 has been replaced and redesigned by the University of Dayton Research Institute. The xenon arc lamp is nominally filtered and is capable of generating 6 EUVS and has a non-uniform intensity distribution across the beam's profile, with the center of the beam being more intense than the edges. The output of the solar simulator is measured with an EG&G model 580 spectroradiometer that is calibrated using an EG&G 1000 Watt quartz-tungsten-halogen FEL style lamp (250-1100 nm) traceable to the National Institute of Standards and Technology (NIST) data.

**Electron Guns**

The SCEPTRE Facility utilizes two Kimball Physics Inc. EFG-11 electron guns. These guns are designed to provide a flood of electrons with energies ranging up to 20 KeV. Their output are monitored by a Faraday cup situated 6.98 cm (2.75 in) above the center most sample position (see figure 2). A Keithley 617 programmable electrometer is used to measure the electron current generated by the Faraday cup. The electron beam is adjusted using a phosphor screen and assumed to be relatively uniform across the specimens.

**Spectrophotometer**

The spectrophotometer used to monitor the specimens' solar absorptance is a Perkin-Elmer Lambda 9 UV-Vis-NIR double beam spectrophotometer and is fiber-optically coupled to a Labsphere Inc. integrating sphere located inside the vacuum chamber. The spectrophotometer is designed to provide *in situ* NIST traceable reflectance measurements and is utilized periodically throughout the duration of a test.

**Data Acquisition**

The data acquisition is performed by a Digital Equipment Corp. (DEC) VAXstation III/GPX, in conjunction with hardware from a variety of other vendors, and utilizes IEEE-488, RS-232, analog-to-digital, and digital-to-analog interfaces. The system monitors the electron flux, vacuum level, specimen backside temperatures, and residual gases present in the vacuum chamber every 15 seconds and periodically records the data throughout the duration of a test. It also acquires data from the spectrophotometer and spectroradiometer and is used to analyze and graphically display the data.

## TEST DESCRIPTION

Testing of the YB-71 and YB-71P materials was intended to compare their relative performance in the SCEPTRE simulated space environment. Additionally, extra Z93 specimens were used as controls for direct comparisons between the three tests necessary for the reformulated IITRI materials. Each of the three tests was designed to have 1000 hours of exposure with accelerated UV and electron radiation. Due to the non-uniform distribution of the beam intensity described above, the level of UV acceleration varies with sample position in the SCEPTRE facility. The targeted UV levels for the five samples were: 3.0 EUVS for the Z93 control specimen and two specimens of each of the YB-71 and YB-71P materials each receiving 2.5 and 1.0 EUVS. The electron exposure is designed to provide accelerated low energy electron radiation compared to that experienced in geosynchronous orbits.

For the two electron guns that the facility has, energy levels of 1 KeV and 10 KeV were chosen. At the geosynchronous orbits there are both trapped and solar wind electrons. The AE8-MAX trapped electron model (ref. 3) and data originating from the SCATHA space flight experiment (ref. 4) were used in establishing the values of $3 \times 10^9$ $e^-/cm^2/sec$ for the 10 KeV electrons and $6 \times 10^9$ $e^-/cm^2/sec$ for the 1 KeV electrons. At 1000 hours of exposure this would generate a total fluence of $3.24 \times 10^{16}$ $e^-/cm^2$. Reference 4 indicates that the fluence of solar plasma electrons within the energy range of 0-10 KeV would be $5.8 \times 10^{15}$ $e^-/cm^2$ in a 1000 hour period, therefore the acceleration factor for the electron exposure is 5.5.

## SCEPTRE RESULTS

The first 600 hours of the YB-71 test, number 93QV01, proceeded very well. However, at 602 hours into the test, a power outage occurred that lasted approximately 40 minutes. This power outage caused a temporary loss in vacuum (estimated to be $1.0 \times 10^{-3}$ Pa ($7.5 \times 10^{-3}$ Torr)) and ultimately caused the electron gun filaments to burn out. The test was continued to 1000 hours of exposure with UV radiation only. The performance of the YB-71P material was very disappointing. Very early in the test it was obvious that the YB-71P material was not performing nearly as well as the YB-71. Figure 3. shows the results of the simulated space environment on all the Z93, YB-71, and YB-71P specimens' solar absorptance. All data in this graph were obtained by *in situ* reflectance measurements, except the last data points, which were measured within a few hours after exposure to air. These results were not satisfactory and created a lot of concern.

Synergistic atomic oxygen and VUV exposure testing performed at NASA Lewis (ref. 5), had showed Z93P to be a poor performer on one occasion. These results also generated a lot of concern, so the Z93P was re-tested with a specimen from a different batch of material. The re-test found the problem to be isolated to the batch of coating tested. For this reason it was thought that there might be a similar problem with a batch of the YB-71P. Since both the poor performing Z93P (tested at NASA Lewis) and the poor performing YB-71P (tested with SCEPTRE) were made with the same lot of Kasil 2130, it was decided to re-test the YB-71 and YB-71P in SCEPTRE. The second test, number 93QV02 exposed a YB-71 specimen, a YB-17P "bad batch" specimen (which was used as a reference in the 93QV01 test), two YB-71P specimens from a different batch, and a Z93 cross-reference specimen.

Performance of the second test was affected due to optical alignment problems within the solar simulator. The situation limited the unobscured UV exposure to three sample positions while the two outer-most positions were exposed to an unknown amount of gradient shading. Thus, the cross-reference Z93 specimen was not used in the same position as the 93QV01 test and only three specimens: the YB-71, YB-71P (suspected bad batch), and YB-71P (new batch), were exposed to known UV levels. The UV exposure of the second YB-71P (new batch) and the Z93 cross-reference specimens were not discernible, but were estimated to be about 1.0 EUVS.

The re-test of YB-71P showed that there was a difference in performance of the two different batches of YB-71P. Figure 4, shows the comparison of the YB-71 and YB-71P performance during the 93QV02 and 93QV01 tests. As previously mentioned for the 93QV01 data, all the 93QV02 data points were measured in vacuum, except the last 3 points which were measured in air over a period of 12 days. This figure shows that the new YB-71P can perform identically to the old YB-71 material and verifies the repeatability of results for like materials from different SCEPTRE tests. Histories for the 93QV01 and 93QV02 tests, including specimen backside temperature (figures 5-6), electron flux (figures 7-8), and specimen spectral reflectance data (figures 9-16) are included for reference. Note that in these figures, the suspected bad batch of YB-71P is labeled with an asterisk (YB-71P*). A summary of the test environments and solar absorptance data for each specimen, from both tests, is provided in table 1.

As mentioned above, there was a difference, between the tests, in the specimens' rates of solar absorptance "recovery" after exposure to air. The difference can only be attributed to the fact that after the second test, 93QV02, the specimens were not directly brought back to ambient conditions but the vacuum chamber was first purged with gaseous nitrogen prior to atmospheric exposure. This resulted in the specimens taking more than 12 days to recover only a fraction of their reflectance instead of essentially recovering instantaneously as they did in the 93QV01 test, without the nitrogen purge. It can be assumed that the gaseous nitrogen molecules, while not chemically reacting with the materials, did physically block access of the oxygen atoms to the material and restricted the rate and even extent of the oxygen recombination process that restores some of the material's reflectance properties.

Visual inspection of the specimens revealed that the old formulation of YB-71 tested in the 93QV02 test had a non-uniform, "blotchy" pattern of light and dark areas within the coupon. The poorer performing specimens from both tests exhibited more crazing (or micro-cracking) due to the shrinking associated with the loss of moisture from the materials than did the other specimens. The poorer performing specimens also exhibited a small amount of adhesion loss near the edges of the coupon.

| Material | EUVS (250-400 nm) | 1 KeV fluence (e-/cm2) | 10 KeV fluence (e-/cm2) | Pretest solar absorptance (in vacuum) | Posttest solar absorptance (in vacuum) | Change in solar absorptance (in vacuum) |
|---|---|---|---|---|---|---|
| **93QV01 (1000 hrs.)** | | | | | | |
| Z93 | 3.2 | 1.66E+16 | 8.32E+15 | 0.135 | 0.185 | 0.050 |
| YB-71 | 2.6 | 1.66E+16 | 8.32E+15 | 0.087 | 0.232 | 0.145 |
| YB-71 | 1.7 | 1.66E+16 | 8.32E+15 | 0.090 | 0.220 | 0.130 |
| YB-71P* | 2.1 | 1.66E+16 | 8.32E+15 | 0.089 | 0.282 | 0.193 |
| YB-71P* | 2.9 | 1.66E+16 | 8.32E+15 | 0.092 | 0.363 | 0.271 |
| **93QV02 (1265 hrs.)** | | | | | | |
| Z93 | 1.2 (est.) | 2.03E+16 | 1.01E+16 | 0.134 | 0.178 | 0.044 |
| YB-71 | 2.8 | 2.03E+16 | 1.01E+16 | 0.097 | 0.297 | 0.200 |
| YB-71P* | 2.7 | 2.03E+16 | 1.01E+16 | 0.106 | 0.419 | 0.313 |
| YB-71P | 2.5 | 2.03E+16 | 1.01E+16 | 0.093 | 0.266 | 0.173 |
| YB-71P | 1.1 (est.) | 2.03E+16 | 1.01E+16 | 0.097 | 0.233 | 0.136 |

*suspected bad batch

**Table 1. Summary of SCEPTRE Tests 93QV01 & 93QV02**

## XPS ANALYSIS

Several weeks after the completion of the 93QV01 test, surface analysis (X-ray Photoelectron Spectroscopy, XPS) was performed on the exposed YB-71P specimens, using a Surface Science Instruments apparatus which

utilizes a monochromatic X-ray source and charge neutralization, to determine if their poor performance was due to contamination. The XPS did reveal a slight amount of carbon but not enough to attribute to significant amounts of contamination.

Prior to the 93QV02 test, XPS was performed on a YB-71 specimen (which ended up being used as a reference in the 93QV02 test) and a YB-71P specimen from the suspected bad batch (which was exposed in the 93QV02 test) that showed a difference between the composition of the YB-71 and the YB-71P materials. The suspected bad batch YB-71P specimen contained more potassium than did the YB-71 specimen. The difference was measurable but initially not thought significant.

After the 93QV02 test, all three exposed YB-71 and YB-71P specimens and the exposed Z93 specimen were examined with the XPS analysis. This analysis showed that both the YB-71 and new batch of YB-71P contained about 12.5% potassium while the "bad batch" of YB-71P contained about 20% potassium. The Z93 specimen showed the smallest amount of potassium of any of the IITRI materials analyzed so far. This is interesting because, this material was shown to be the best performer in the 93QV01 test. Additionally, the light and dark areas of the "blotchy" areas previously discussed on the YB-71 used in the second test were separately examined with XPS. The results of this analysis are extremely interesting because it showed that in the old formulation of YB-71, with the Sylvania PS-7 binder, that the light areas contained 13.6% potassium and the darker areas contained 17.9% potassium. Thus, the XPS analysis suggests that there is direct link to the coating's performance and its potassium concentration at the surface. Table 2. summarizes the XPS results.

| Material | K | Si | K:Si Ratio | Change in solar absorptance (in vacuum) |
|---|---|---|---|---|
| **93QV01 (1000 hrs.)** | | | | |
| YB-71P* (2.85 EUVS) | 22.2% | 9.2% | 2.41 | 0.271 |
| YB-71P* (2.07 EUVS) | 21.0% | 9.8% | 2.14 | 0.193 |
| **93QV02 (1265 hrs.)** | | | | |
| YB-71P* | | | | |
| pretest | 20.3% | 9.9% | 2.05 | ***** |
| posttest (2.70 EUVS) | 20.4% | 9.9% | 2.06 | 0.313 |
| Z93 (1.2 EUVS, est.) | 12.3% | 22.1% | 0.56 | 0.044 |
| YB-71P (2.50 EUVS) | 12.6% | 16.0% | 0.79 | 0.173 |
| YB-71 (2.80 EUVS) (darker area) | 17.9% | 12.0% | 1.49 | ***** |
| YB-71 (2.80 EUVS) (lighter area) | 13.6% | 15.8% | 0.86 | ***** |

* suspected bad batch

**Table 2. Summary of XPS Results**

## RESULTS & DISCUSSION

As mentioned in the Introductory section, the $SiO_2$:$K_2O$ mole ratio of both PS-7 and Kasil 2130 is 3.3:1. This yields a theoretical K:Si ratio for the coatings of 0.6061. XPS analysis reveals that the YB-71P coating that performed well had a K:Si ratio close to the theoretical value. However, the poor performing coatings possessed significantly higher K:Si ratios. It is hypothesized that the excess potassium is the cause in the increased degradation of the coatings. Additional analysis needs to be performed to determine if the cause of the excess potassium is from the raw material itself (i.e., poor quality control of K/Si ratio) or from processing/ application parameters (humidity, moisture content, temperature, etc.) at IITRI. In order to help answer this, additional XPS

analysis is planned to determine if the excess potassium is found uniformly through the depth of the coating or only at the surface.

The reflectance spectra for all the poor performing YB-71P specimens (figures 9, 10, and 14), while showing total overall reduction in reflectance, also show a depression in the reflectance curve around 950 nm that is more pronounced than in the YB-71 specimens (figures 12, 13, and 15). This absorption band, which is characteristic of $Zn_2TiO_4$ , is discussed in detail in a 1971 American Institute of Aeronautics and Astronautics (AIAA) paper authored by Zerlaut, *et. al.* (ref. 6). This paper describes the $Ti^{+3}$ color center formation damage mechanism for $Zn_2TiO_4$ and presented findings which showed that reactively encapsulating the $Zn_2TiO_4$ with potassium silicate greatly reduces the extent of damage around 950 nm. The fact that the YB-71P coating is demonstrating a depression in the reflectance curve similar to that described in the paper is very interesting and presently unexplainable.

The inconsistency of the potassium silicate binder is a cause for concern. Similar testing of YB-71 and YB-71P materials from the same batches tested in SCEPTRE have been performed at The Aerospace Corporation, El Segundo, California. This testing has revealed similar results for the materials' performances. Currently, at the time of writing, testing is being performed at The Aerospace Corporation with 18 different samples of YB-71 and YB-71P materials to try to determine if the inconsistency is wide-spread or if this was just an isolated case.

Additional attempts at finding a replacement for the Sylvania PS-7 potassium silicate for use in other coatings, have been made by researchers at the Jet Propulsion Lab (JPL). They tried to identify a suitable conductive coating for use on the Cassini satellite's high gain antenna system and considered the NS43G coating (obtained from Space Control Coatings, Inc.), using both the PS-7 binder and the Kasil 2135 binder from The PQ Corporation as a possible candidate (ref. 7).

## FUTURE PLANS

Further investigation is currently on going, in cooperation with IITRI and The Aerospace Corporation, to determine the extent of the variation of YB-71P material. The results from SCEPTRE testing of Z93P and S13GP/LO-1 will be presented in the future.

## CONCLUSIONS & RECOMMENDATIONS

SCEPTRE testing of reformulated YB-71P was performed. Issues have risen concerning the reproducibility of the coating. Batch to batch variations in the stability of the coatings to the combined space environment were demonstrated. Some YB-71P specimens performed identically like the original YB-71 formulation. A different lot with a higher K:Si ratio performed very poorly. Additional testing of YB-71P is recommended to determine the cause of the batch to batch variations. It is suggested that lot testing of YB-71P coatings by the users be performed until the cause of the coating non uniformity can be determined.

## REFERENCES

1. Vail, J. G., *Soluble Silicates-There Properties and Uses, Vol. 1*, Reinhold Publishing Corp., New York, New York, 1952.
2. American Society for Testing and Materials, *E 512-94 Standard Practice for Combined, Simulated Space Environment Testing of Thermal Control Materials with Electromagnetic and Particulate Radiation*, 1993 Annual Book of ASTM Standards, Vol. 15.03, pp. 390-401,
3. Vette, J. I., *The AE-8 Trapped Electron Model Environment,* National Space Science Data Center, NSSDC/WDC-A-R&S 91-24, Greenbelt, MD, November, 1991.

4. Judeikis, H. S., *Space Radiation Effects of Teflon and Nomex Fibers*, The Aerospace Corporation, ATM-89(4945-01)-7, October, 1988.
5. Dever, J. A.; Bruckner, E. J.; Stidham, C. R.; Booth, R. E., *The Effects of Simulated Low Earth Orbit Environments on Spacecraft Thermal Control Coatings*, 38th International SAMPE Symposium, Vol. 38, Book 1, pp. 694-706, May, 1993.
6. Zerlaut, G. A.; Gilligan, J. E.; and Ashford, N. A., *Space Radiation Environmental Effects in Reactively Encapsulated Zinc Orthotitanates and Their Paints*, AIAA paper no. 71-449, AIAA 6th Thermophysics Conference, April 1971.
7. Hsieh, Cheng; Metzler, Ed; Forsberg, Gus; McHugh, Lisa; O'Donnell, Tim; and Cordaro, James, *Conductive White Thermal Control Paint for Spacecraft*, 38th International SAMPE Symposium, Vol. 38, Book 1, pp. 609-22, May, 1993.

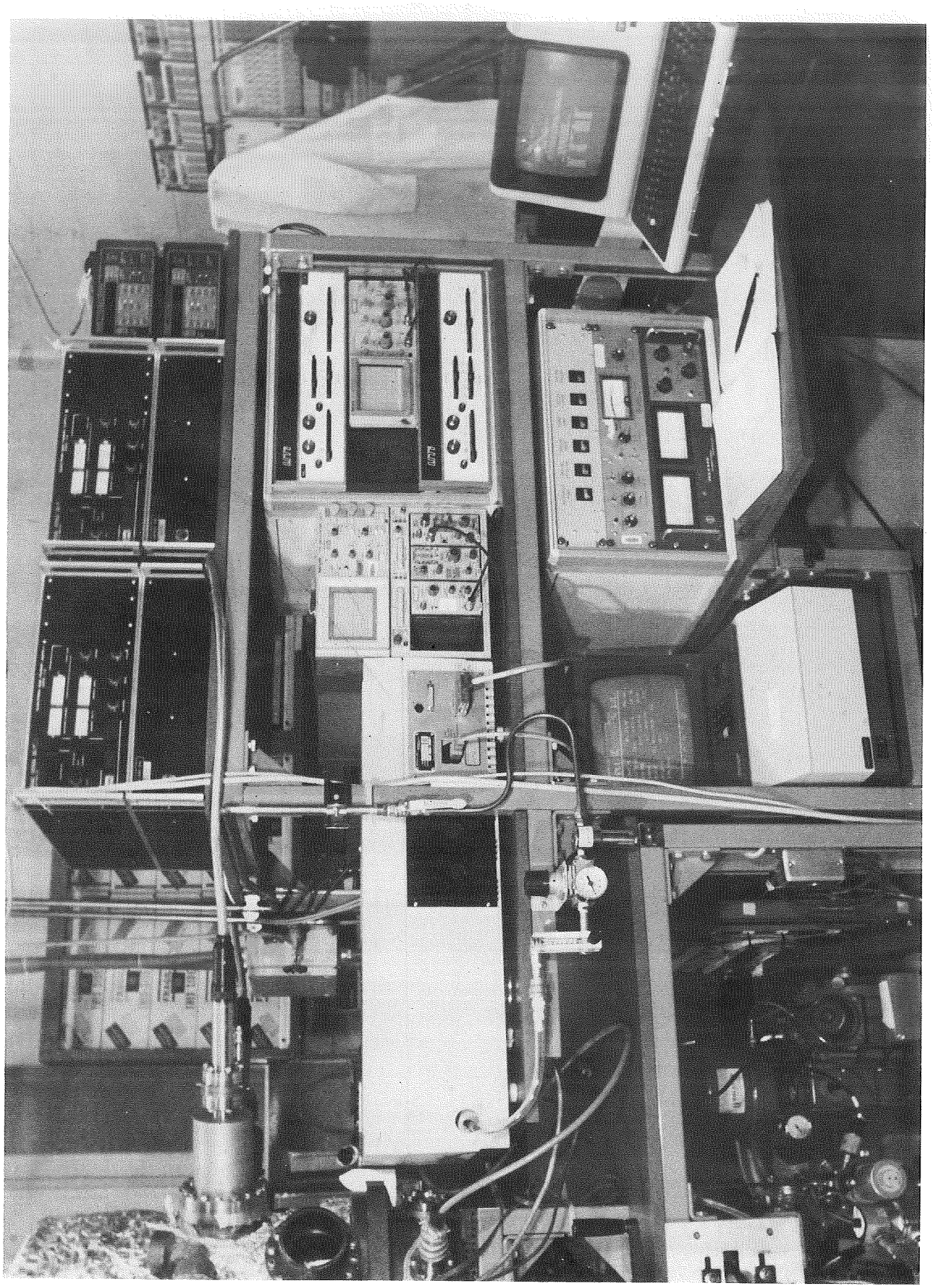

Figure 1. USAF WL/ML SCEPTRE Facility

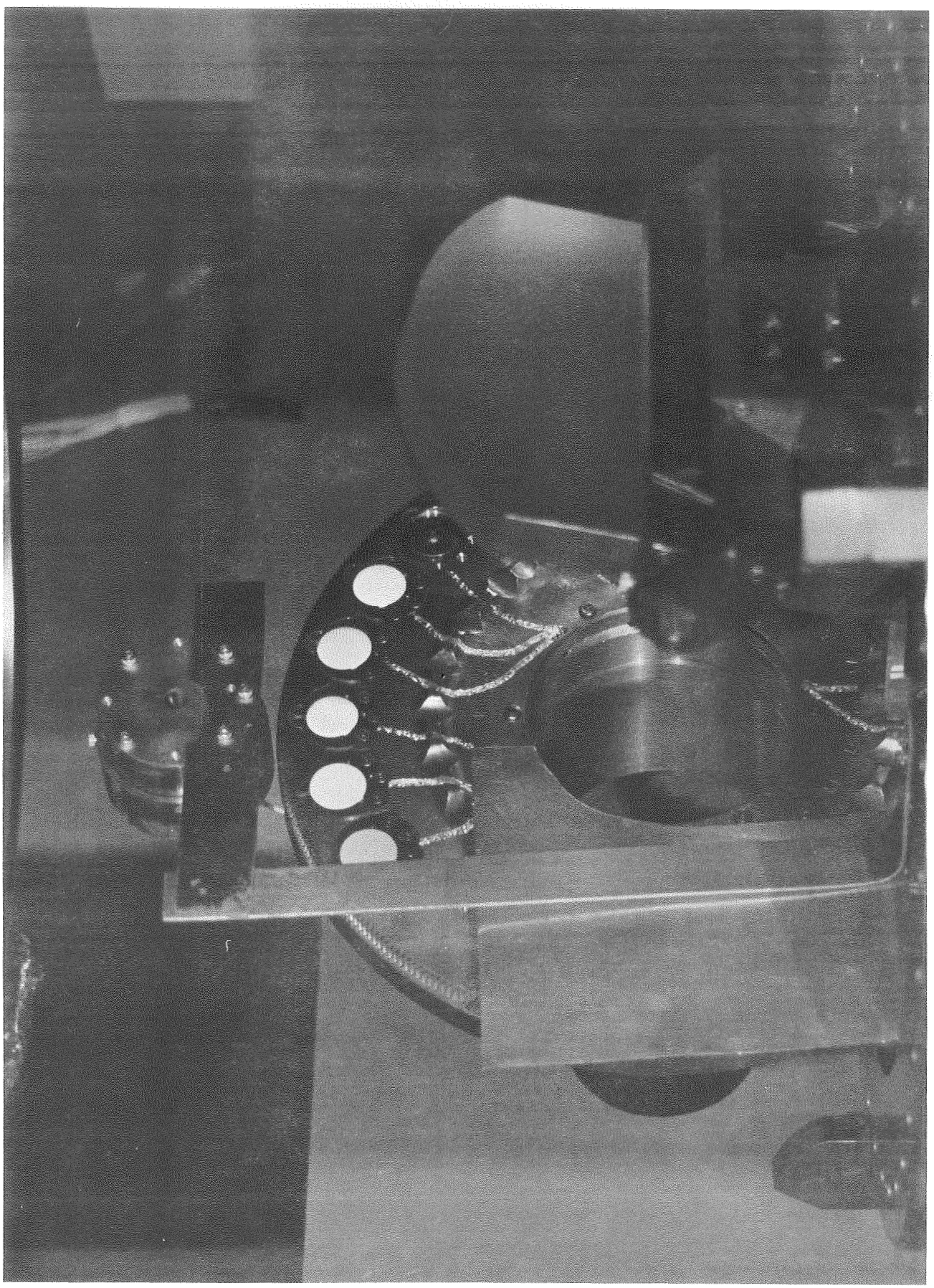

Figure 2. SCEPTRE Facility's Sample Wheel and Faraday Cup

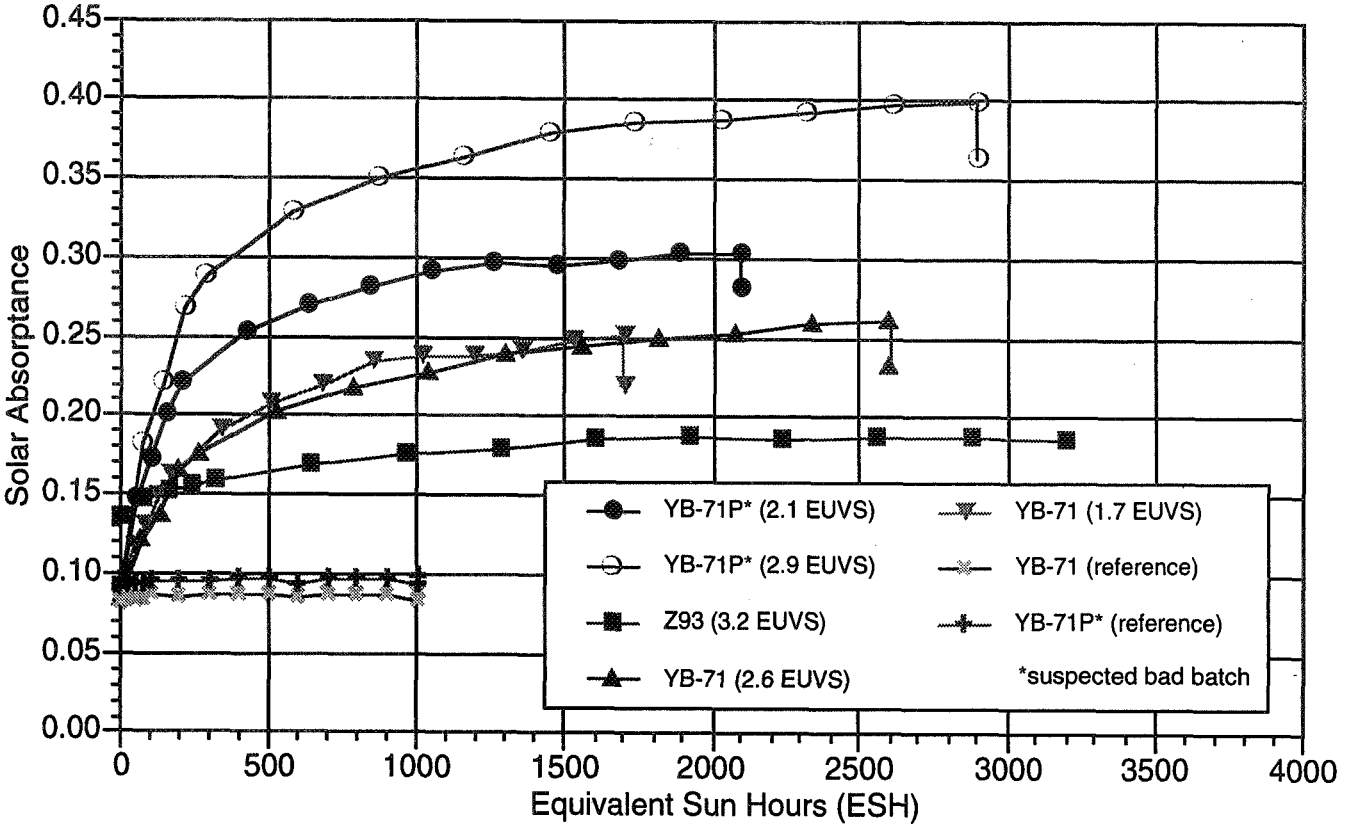


**Figure 3. USAF WL/ML SCEPTRE Test 93QV01 Solar Absorptance History**

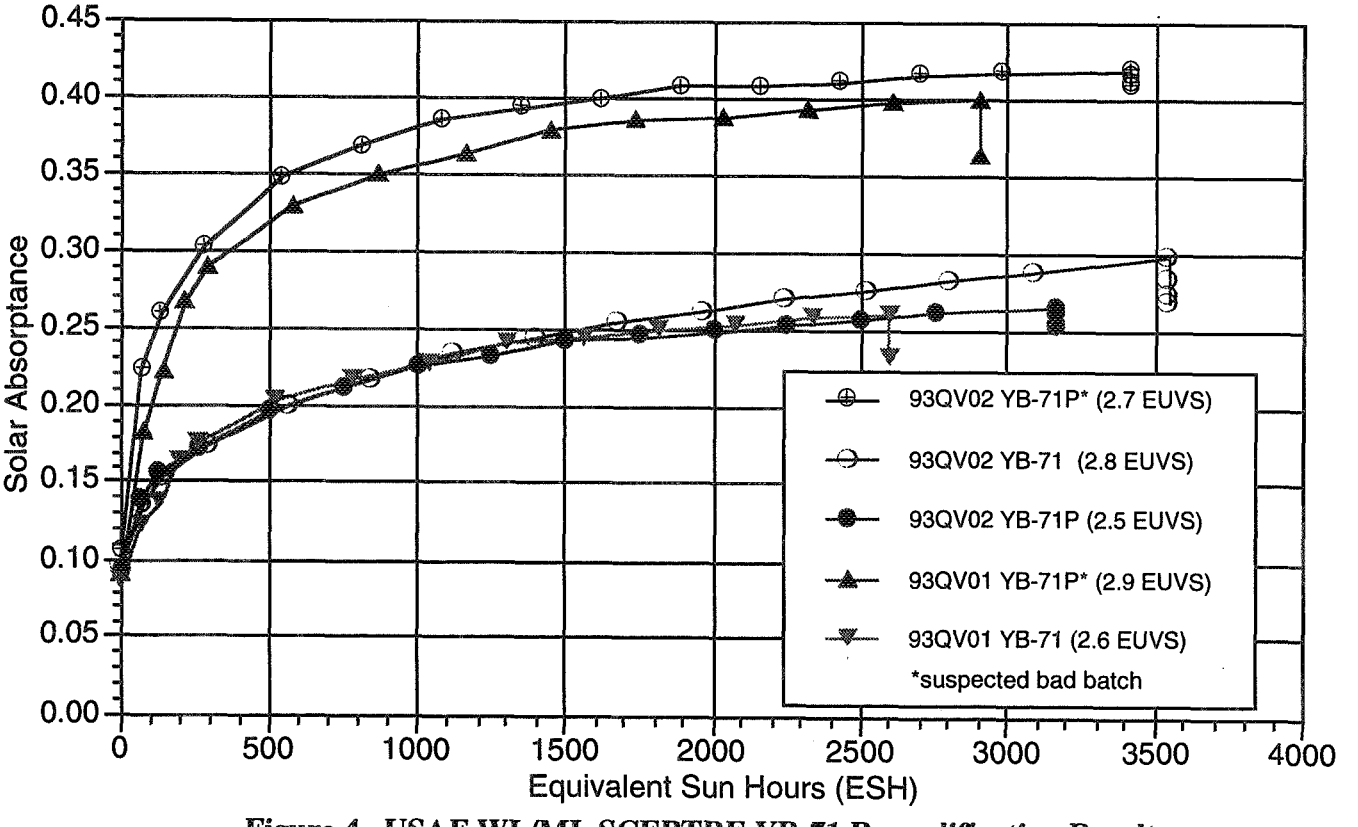


**Figure 4. USAF WL/ML SCEPTRE YB-71 Requalification Results**

Figure 5. SCEPTRE Test 93QV01 Specimen Temperature History

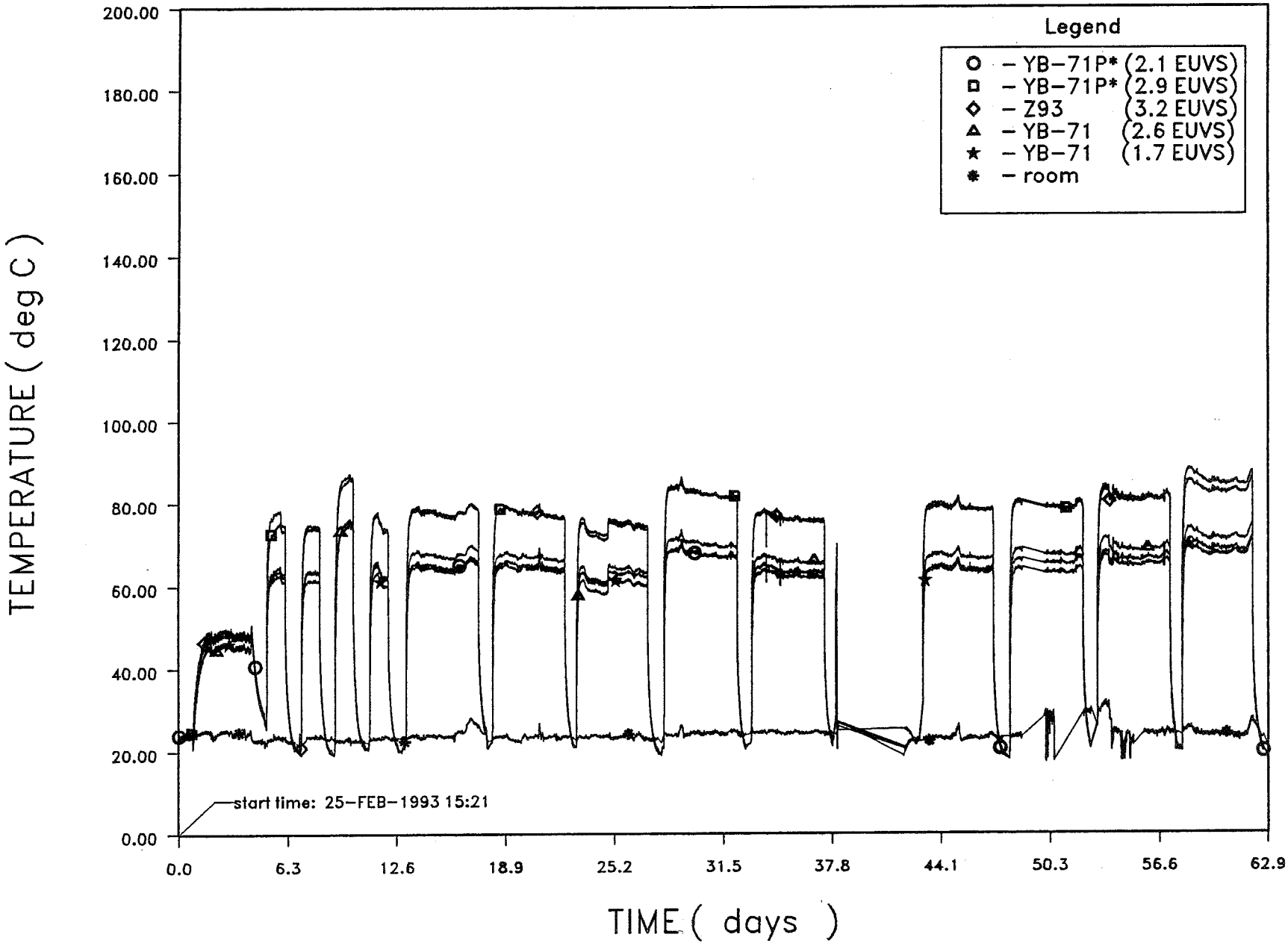

Figure 6. SCEPTRE Test 93QV02 Specimen Temperature History

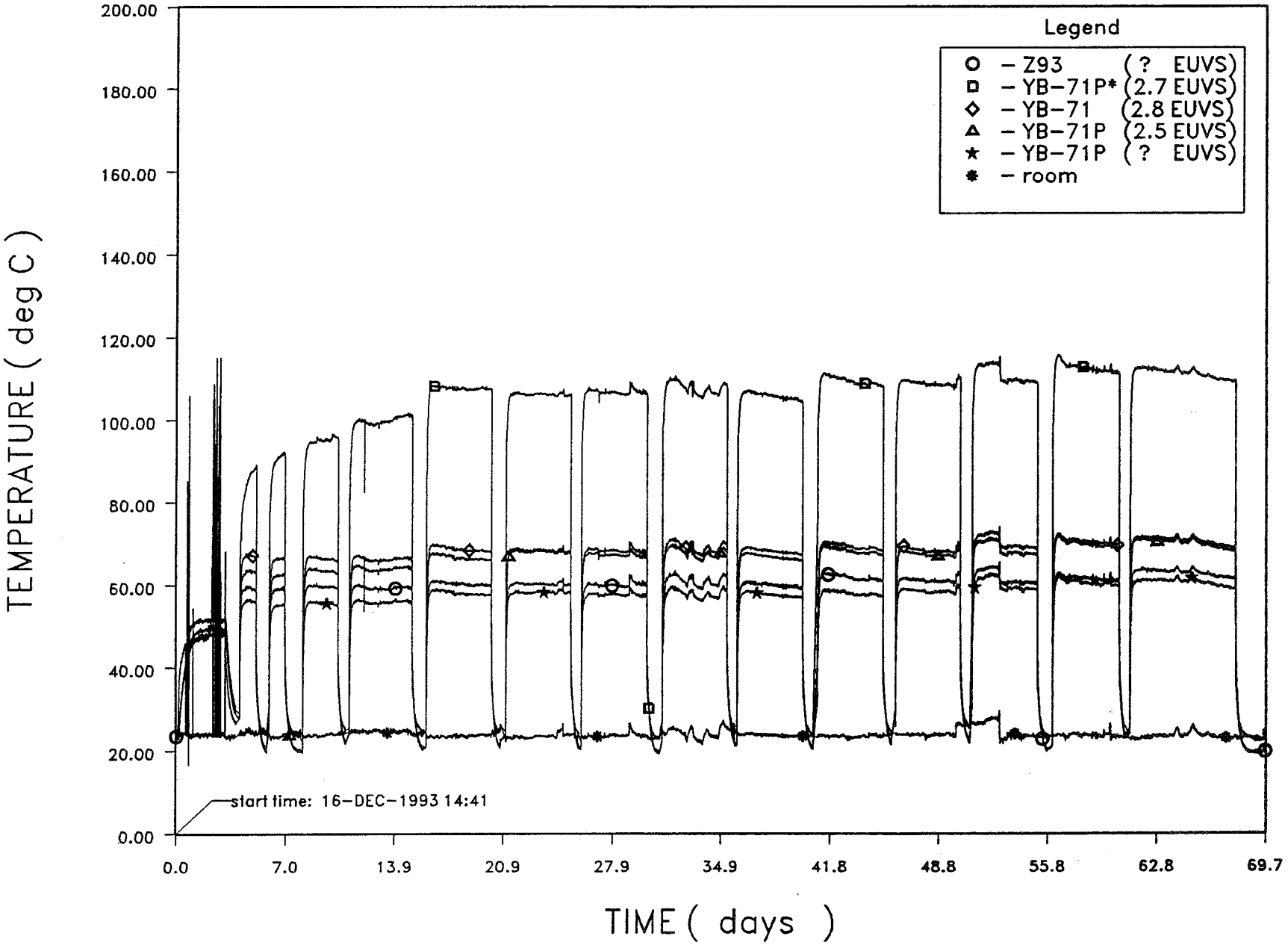

# Figure 7. SCEPTRE Test 93QV01 Electron Flux History

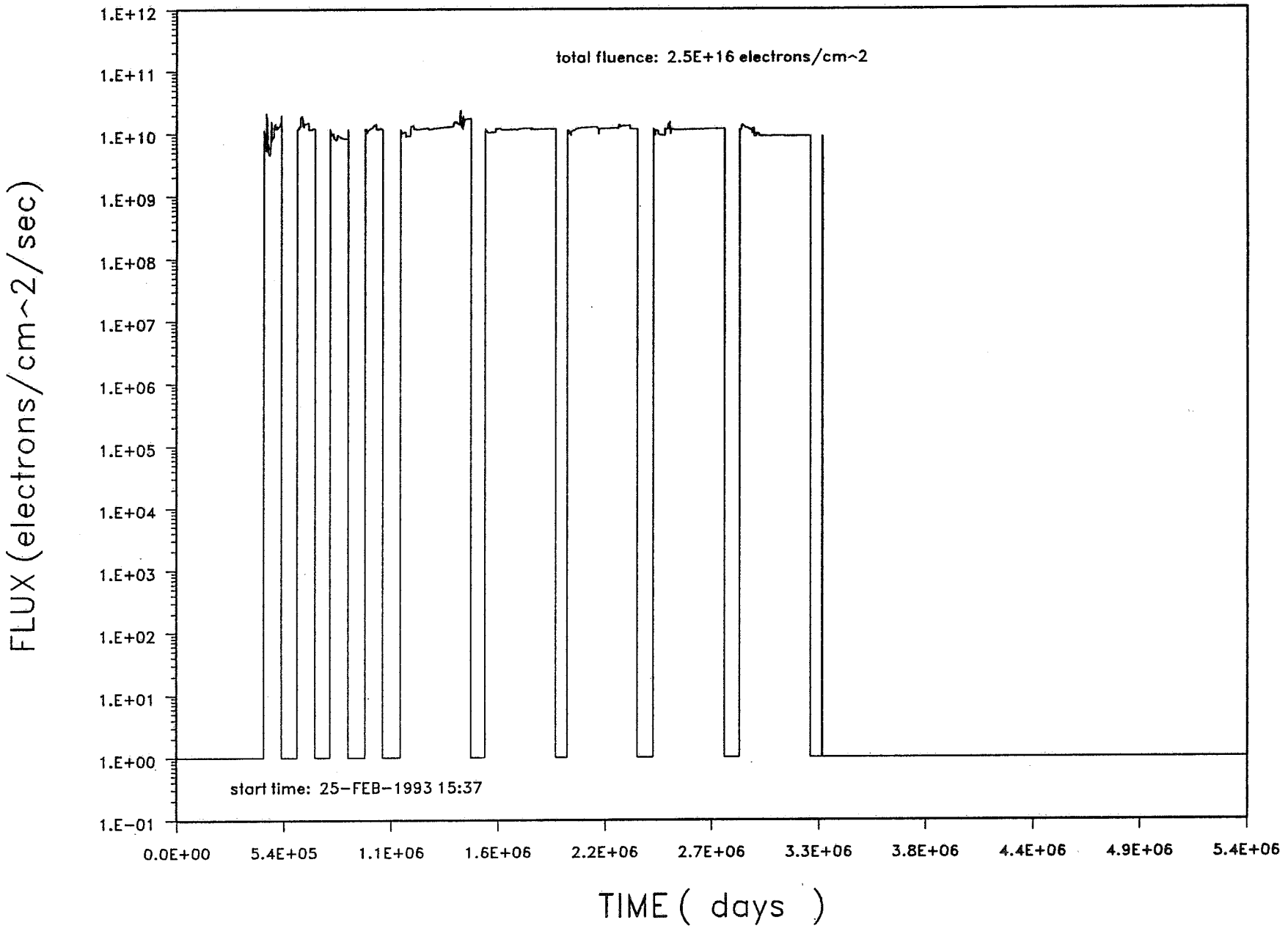

Figure 8. SCEPTRE Test 93QV02 Electron Flux History

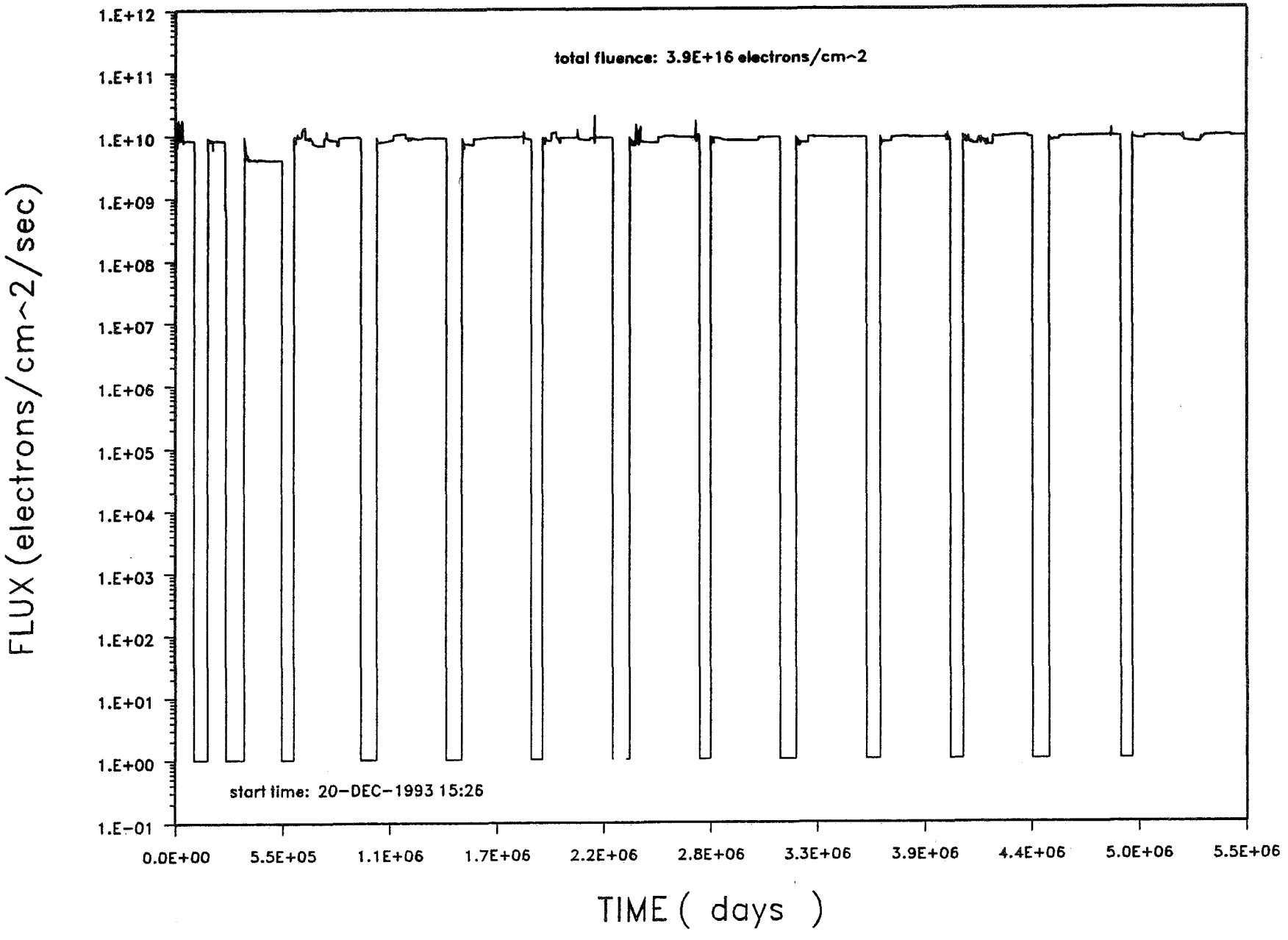

Figure 9. 93QV01 YB-71P* (2.1 EUVS) Reflectance History

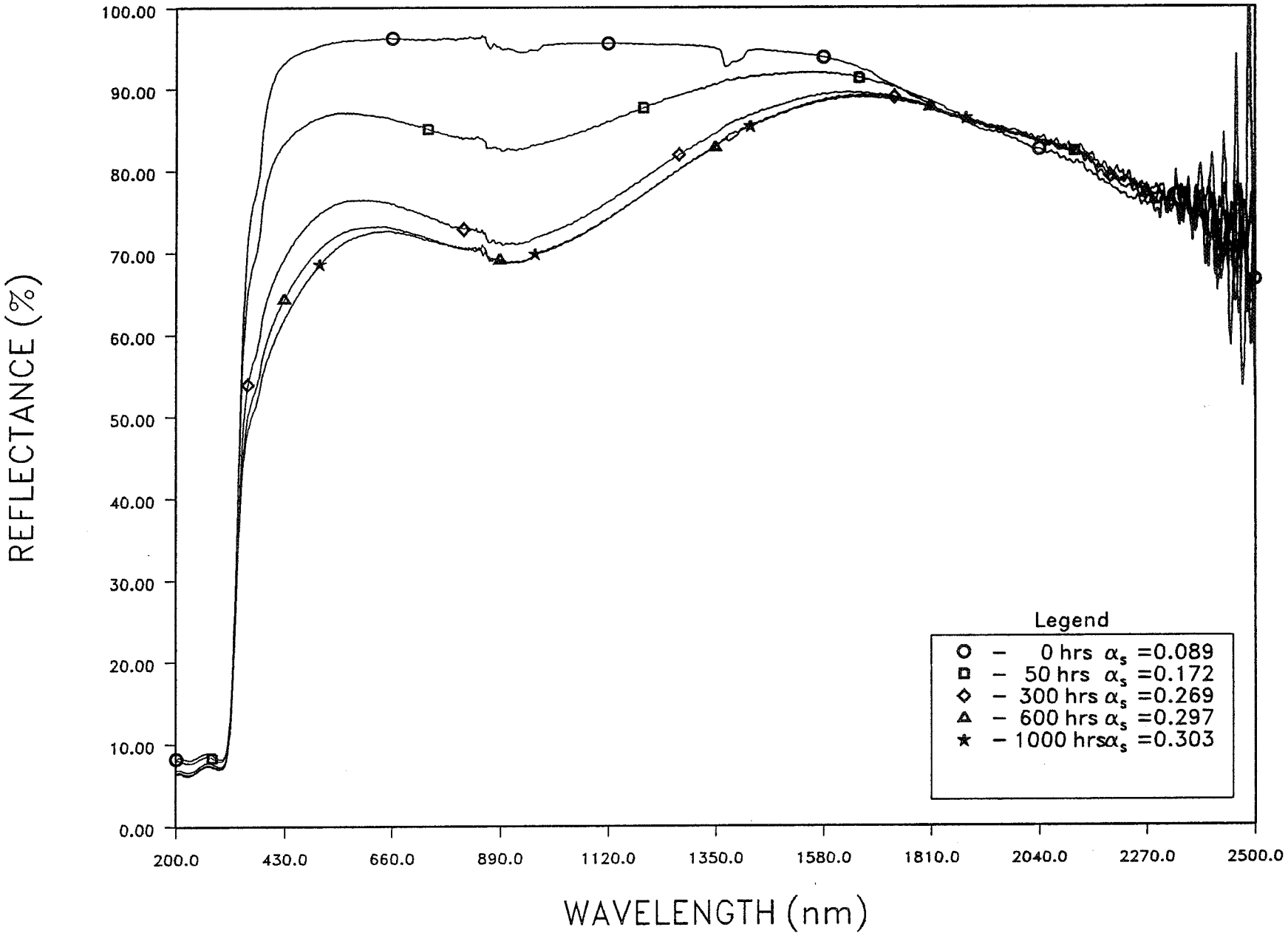

Figure 10. 93QV01 YB-71P* (2.9 EUVS) Reflectance History

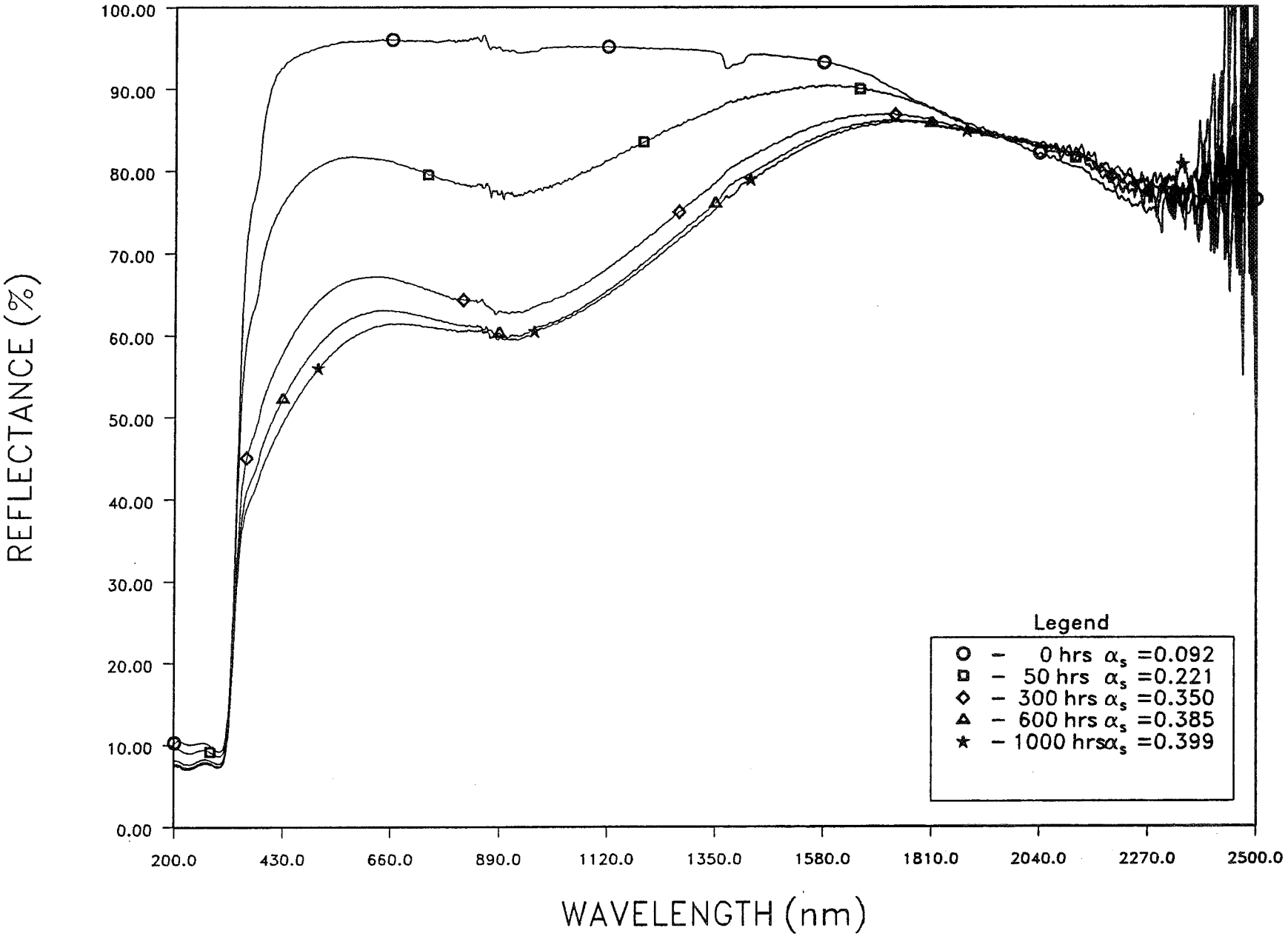

Figure 11. 93QV01 Z93 (3.2 EUVS) Reflectance History

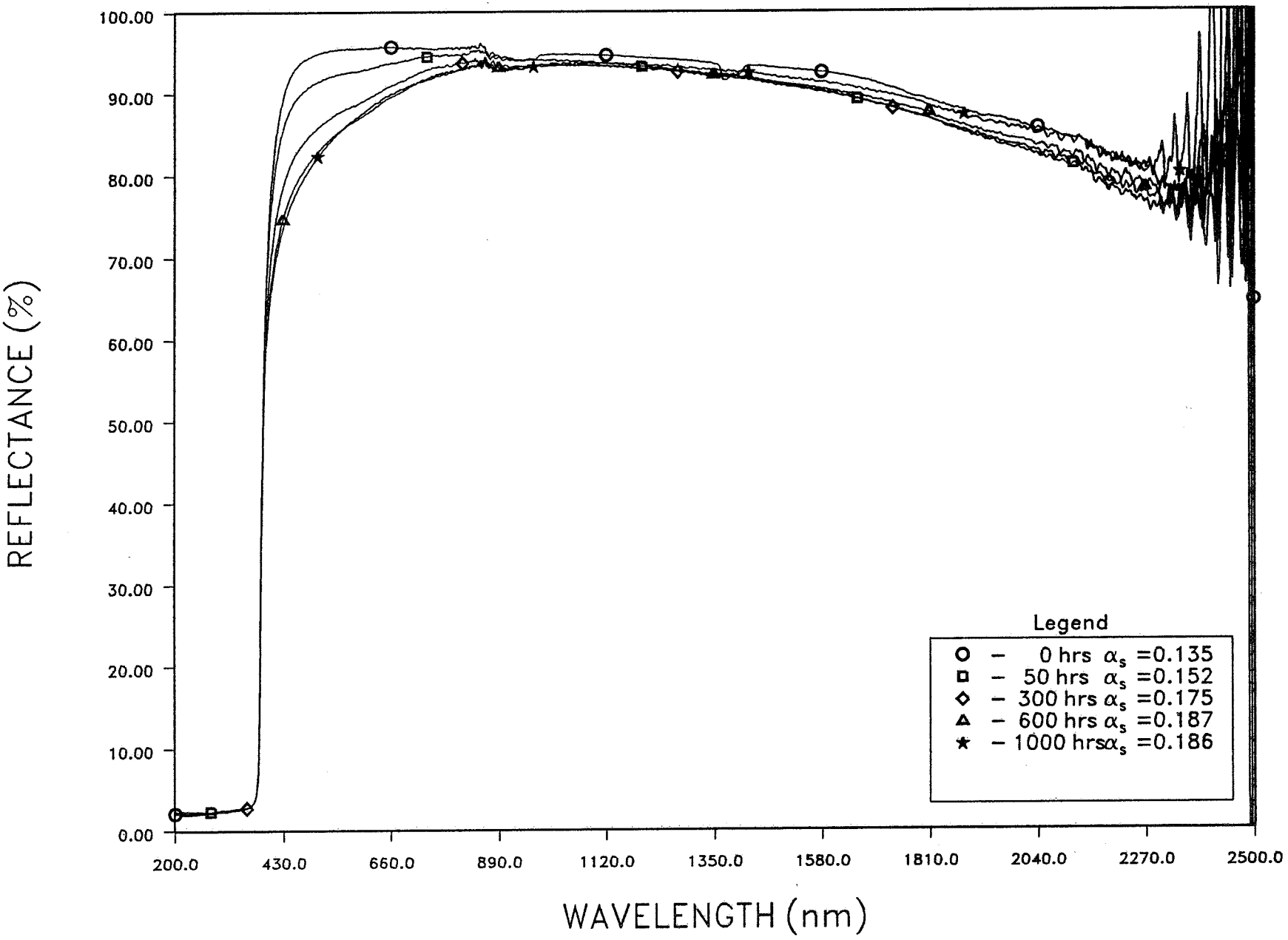

Figure 12. 93QV01 YB-71 (2.6 EUVS) Reflectance History

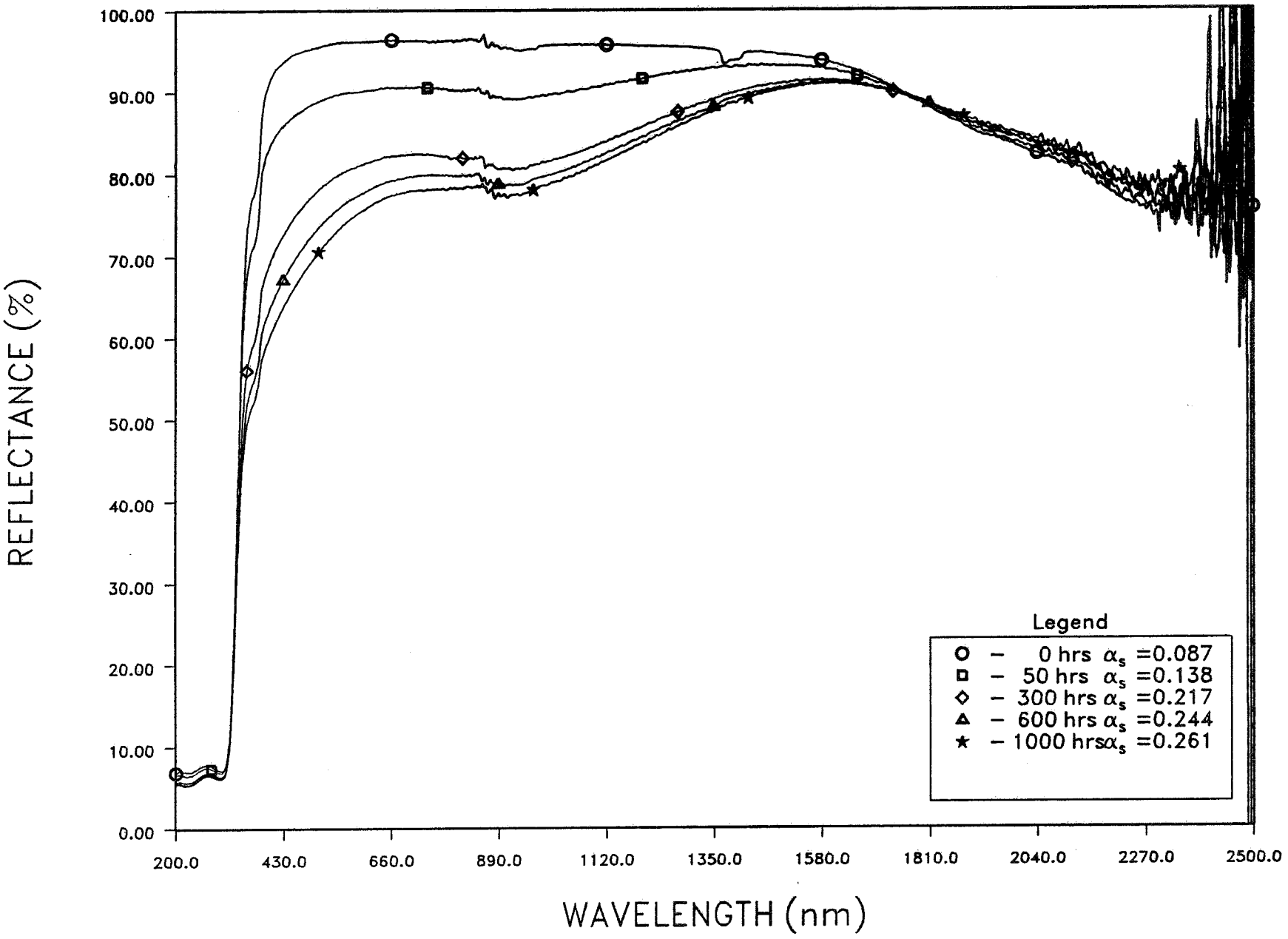

Figure 13. 93QV01 YB-71 (1.7 EUVS) Reflectance History

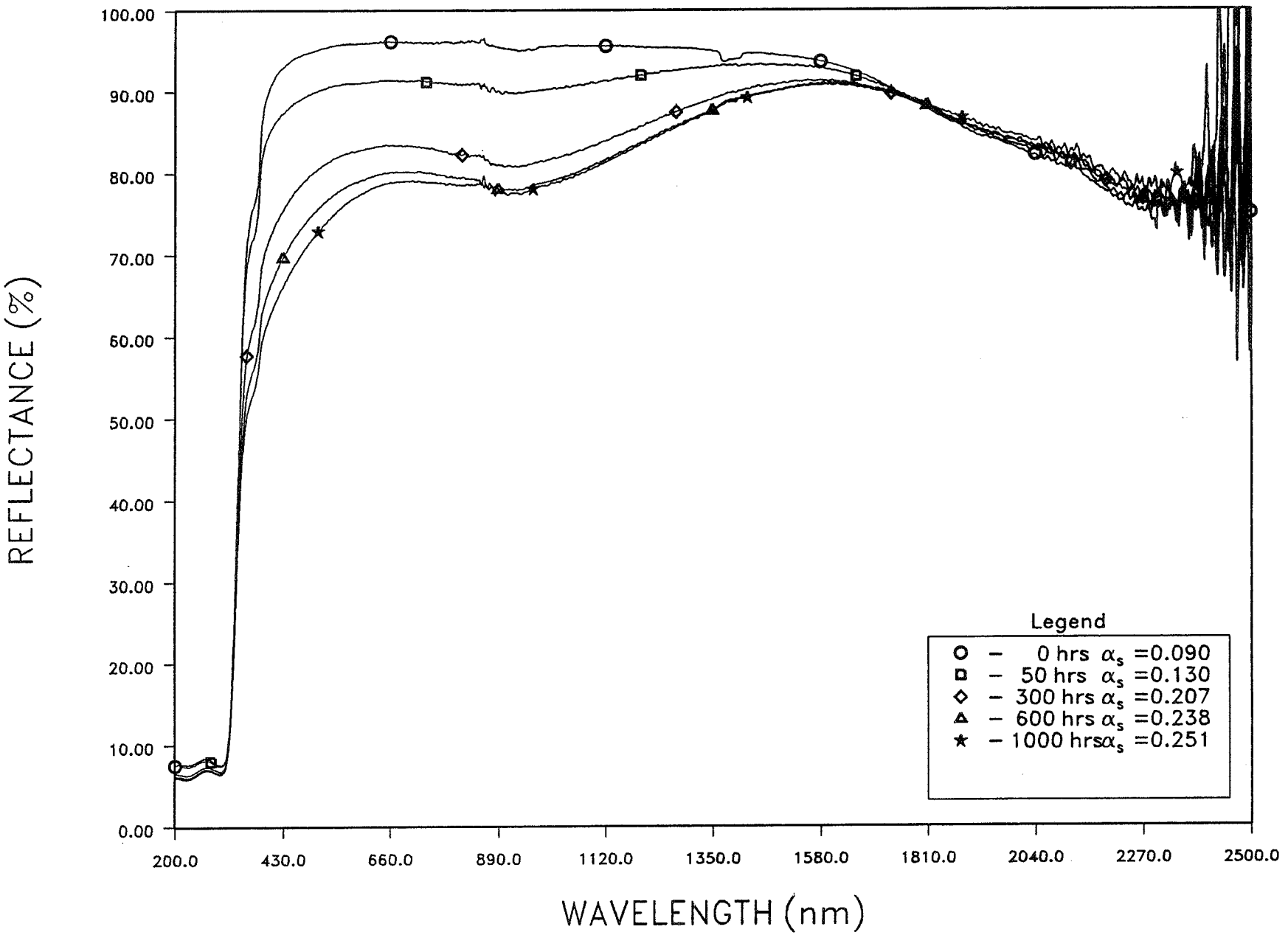

Figure 14. 93QV02 YB-71P* (2.7 EUVS) Reflectance History

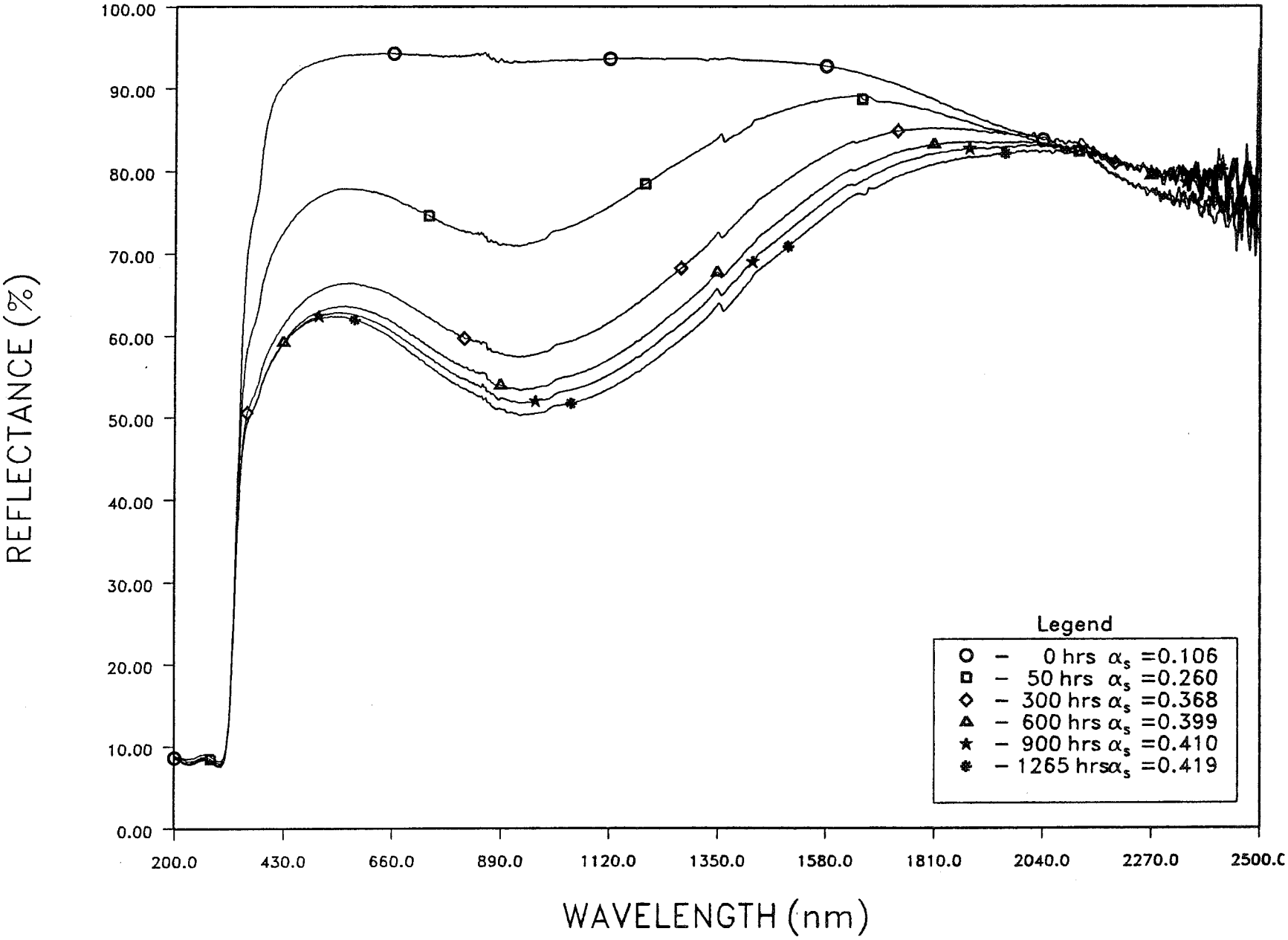

Figure 15. 93QV02 YB-71 (2.8 EUVS) Reflectance History

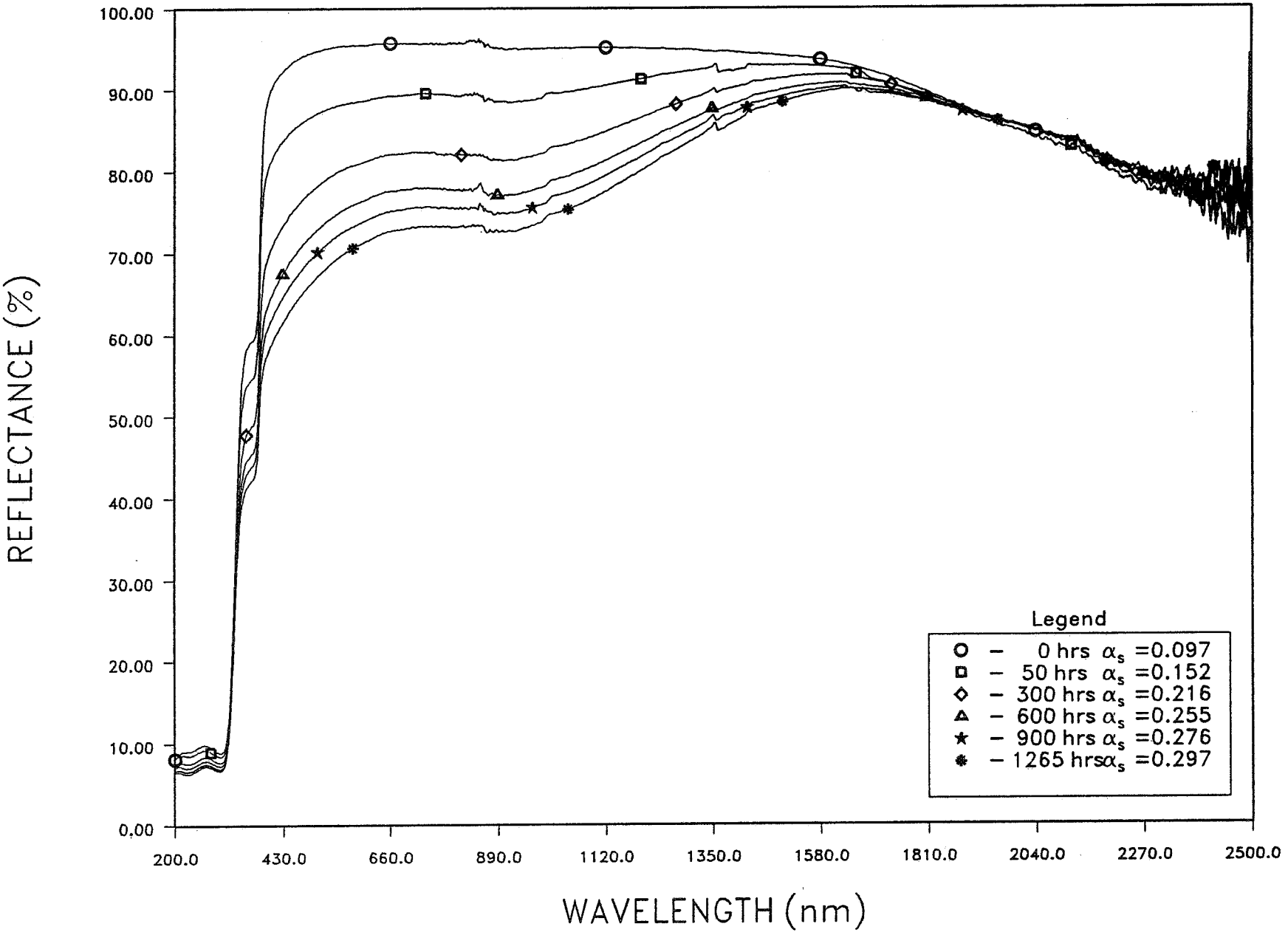

Figure 16. 93QV02 YB-71P (2.6 EUVS) Reflectance History

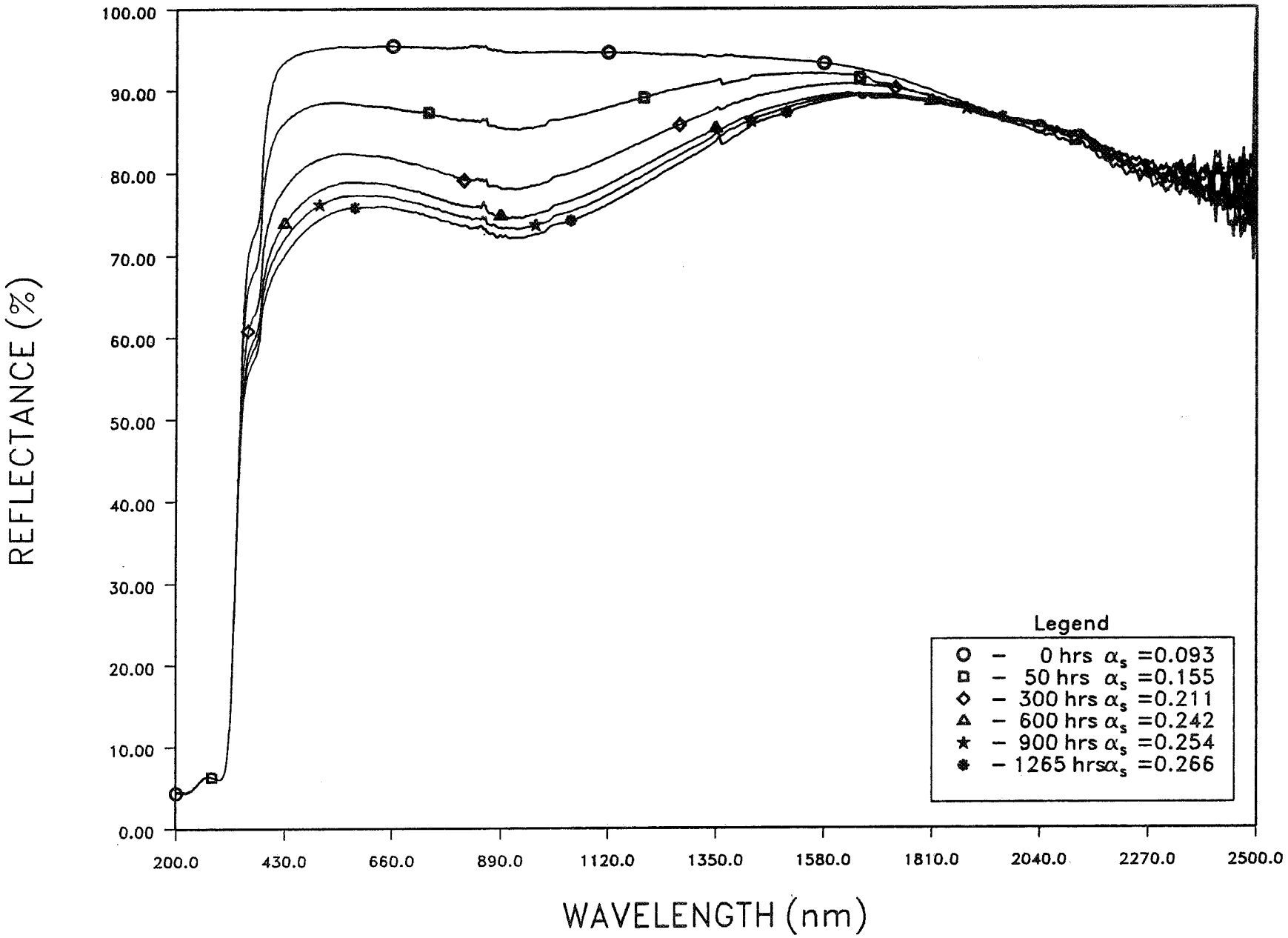

# PREDICTION OF PARTICULATE CONTAMINATION ON APERTURE WINDOW

Aleck L. Lee* and Michael C. Fong+
Space Systems Division
Lockheed Missiles & Space Company
Sunnyvale, CA 94086

## ABSTRACT

This paper presents an analysis to predict the effects of light scattering by surface particles on the sensor window of a missile during ascent flight. The particulate contaminant distribution on the window is calculated by tallying the number of particles in a set of size ranges. The particulate contamination at the end of the mission is predicted by adding the contributions from the events of ground and flight operations. The surface particle redistribution caused by vibroacoustically induced surface acceleration was found to contribute the most to the particulate surface contamination. The analytical surface obscuration calculation with a set of particle counts was compared to the results of image analyzer measurement. The analytical results, which were calculated with a given function of particle shape depending on the size, were more conservative than the measurement. A scattering calculation using a verified BSDF model showed that the scattering was less than 0.001 at 20° off the direction of the incident light in the mid IR wavelength when the surfaces were at Level 300 initially.

## INTRODUCTION

The aperture window of a tactical missile is highly contamination sensitive. The light scattering from the contaminant on the window surface contributes to the background stray light level that can be detrimental to the seeker operations. As the main effect of the contamination is light scattering when the window is exposed to the sunlight, the requirement can be also posed by the bidirectional scattering distribution function (BSDF). In this study the BSDF of the aperture window is calculated from the predicted surface particulate contamination distribution.

The service life of an aperture window starts from the delivery of the seeker hardware and ends with the impact of the target. The life span includes various phases of manufacturing and assembling process, storage, transportation, and ascent flight. This study presents a systematic approach to predict the level of particulate contamination of the aperture window in terms of obscuration increases on the aperture window during the manufacturing process and the ascent flight till the end of life.

The aperture window is located on the forecone of a tactical missile. The window has a field of view spanning from the forward direction to the side of the vehicle. A shroud, which has a smaller half-cone angle, is attached to the vehicle near the base of the forecone. The shroud protects the forecone from aeroheating during ascent, but proves to be a major contributor to the increase of particulate contamination on the aperture window.

The shroud consists of two halves with seam lines extending from the apex of the shroud to the base of the forecone assembly. One of the seam lines lies directly over the aperture window. There is a gap at the joining section of the body. The gap is sealed with an O-ring. The O-ring is sized for a 0.5 mm compression. Under load during ascent flight, the seam may open and ingest particles in the atmosphere to the interior of the shroud.

---

* Staff Engineer, IES Senior Member + Technical Consultant

At deployment, the shroud opens at the seam lines. The two halves of the shroud are pushed apart by inflating the gas bags above the forecone. As the shrouds are further apart, the hinge at the base will release the shroud from the launch vehicle. The particles generated from the surfaces of the gas bags and the seam lines will fall onto the forecone and the aperture window.

The sources and particulate contamination transport mechanisms are: particle redistribution caused by surface acceleration excited by the vibroacoustic field during ascent from the shroud, ingestion of exterior particulate materials through the seam line during ascent, particles generated from activation of separation air bags, and particles generated from shroud seam line during shroud separation. Each issue is discussed in this study, and the increase of surface obscuration due to each source is predicted. The effects of the final contamination level on the window are calculated with a BSDF model.

## SURFACE PARTICLES AND CLEANLINESS LEVEL

The correlation between surface particle obscuration and BRDF prediction has been investigated before (Refs. 1 and 2). For this analysis, the particle distribution data were obtained from four measurements for a sample with an image analyzer (IA). The samples were exposed to the environment of a typical optics laboratory for some time. The IA results showed the particle counts for given particle size ranges, i.e., the size bins, and the obscuration ratios under visible light and specific instrument setting conditions. The obscuration is expressed as percent area coverage (PAC). Table 1 summarizes the measured data.

Table 1 Measured data from an image analyzer.

| Case Number<br>Size bin, μm | 1 | 2 | 3 | 4 |
|---|---|---|---|---|
| < 10 | 492 | 477 | 367 | 350 |
| 10 - 25 | 861 | 852 | 501 | 518 |
| 25 - 50 | 305 | 311 | 138 | 140 |
| 50 - 100 | 43 | 38 | 20 | 21 |
| 100 - 150 | 4 | 4 | 2 | 2 |
| 150 - 250 | 1 | 0 | 0 | 0 |
| 250 - 500 | 1 | 1 | 0 | 0 |
| 500 - 750 | 0 | 0 | 0 | 0 |
| > 750 | 0 | 0 | 0 | 0 |
| Measured PAC, % | 0.0792 | 0.0781 | 0.1423 | 0.1426 |

The particle counts and the percent obscuration ratios (%OR) calculated with the PAC model are summarized in Table 2. Table 3 shows a comparison of the measured obscuration and the computed obscuration. The obscuration measured directly with the IA is approximately 63% of the computed obscuration made with the PAC model. The discrepancies in %OR results are attributed to the choice of particle geometry in the model and the settings of the IA scanning, such as the contrast threshold, pixel size, and so on. The last two columns of the table are the equivalent cleanliness levels calculated from the calculated %OR value and the IA measured value. The differences in the analytical results and the IA measurements show that the analytical results tend to be more conservative.

Table 2 Summary of measured data in numbers per sq ft.

| Case Number<br>Size bin, μm | 1<br>(#/ft$^2$) | 2<br>(#/ft$^2$) | 3<br>(#/ft$^2$) | 4<br>(#/ft$^2$) |
|---|---|---|---|---|
| < 10 | 126981 | 123109 | 376493 | 359053 |
| 10 - 25 | 222216 | 219894 | 513959 | 531398 |
| 25 - 50 | 78718 | 80266 | 141569 | 143621 |
| 50 - 100 | 11098 | 9807 | 20517 | 21543 |
| 100 - 150 | 1032 | 1032 | 2052 | 2052 |
| 150 - 250 | 258 | 0 | 0 | 0 |
| 250 - 500 | 258 | 258 | 0 | 0 |
| 500 - 750 | 0 | 0 | 0 | 0 |
| > 750 | 0 | 0 | 0 | 0 |
| Calculated %OR | 0.1243 | 0.1182 | 0.2257 | 0.2314 |

Table 3 Comparison of obscuration by IA and PAC.

| Case # | %OR, PAC Analytical | %OR, IA Measured | IA/PAC % | Equiv. Level based on Computed | IA |
|---|---|---|---|---|---|
| 1 | 0.1243 | 0.0792 | 63.72 | 448 | 408 |
| 2 | 0.1182 | 0.0781 | 66.07 | 444 | 407 |
| 3 | 0.2257 | 0.1423 | 63.05 | 505 | 461 |
| 4 | 0.2314 | 0.1426 | 61.62 | 508 | 461 |

## SURFACE PARTICULATE CONTAMINATION INCREASE

Particulate contamination on the aperture window increases during its service life. The sources of contamination are analyzed quantitatively in this section.

### Redistribution Caused by Vibroacoustic Environment

Particles on a surface can be resuspended if the surface acceleration overcomes the adhesion force between the particle and the surface. As a launch vehicle is ascending, the vibroacoustic field generated by the booster rockets and the boundary shearing noise excite the surfaces of the launch vehicle. The surface acceleration due to vibroacoustic excitation can be calculated with analytical models, such as VAPEPS (Ref. 3). When the surface acceleration is given in power spectral density (PSD), the root mean square surface acceleration can be calculated with an integration over the spectrum to obtain the results in g-rms. The fraction of resuspended particles can be correlated to g-rms with respect to particle sizes (Ref. 4).

Since the surface acceleration is not determined at the time of the analysis, a conservative value of 12 g-rms has been assumed. The particles resuspended from the inner side of the shroud are assumed to be uniformly distributed on the forecone. The effects of venting is not considered in this preliminary analysis. The particles on the aperture window are assumed originally to stay

on the outside surface. This assumption may be justified by the fact that the aperture window is facing the acceleration vector. Any particle resuspended by surface acceleration would settle back to the window surface. The initial particle distribution for both the shroud and the forecone surfaces is assumed to follow that described in MIL-STD 1246B with a slope of -0.926. This distribution represents a surface which has just been cleaned, in contrast to a surface collecting particles from fallout, where the slope would be smaller, ~-0.3. The effects of particle redistribution on the aperture window have been predicted and summarized in the table below.

Table 4 Particle redistribution from shroud to aperture window due to vibroacoustic excitation.

| Shroud Level | Original Level | Final Window Level | Final Obscuration (%) |
|---|---|---|---|
| 500 | 400 | 474 | 0.1852 |
| 400 | 400 | 431 | 0.1159 |
| 350 | 400 | 418 | 0.0993 |
| 300 | 400 | 409 | 0.0897 |
| 500 | 300 | 437 | 0.1243 |
| 400 | 300 | 370 | 0.0557 |
| 350 | 300 | 344 | 0.0394 |
| 300 | 300 | 325 | 0.0299 |

Table 4 shows that, if the aperture window was at Level 400 per Mil-Std 1246B initially, the surface obscuration will become 0.1852% if the shroud is at Level 500, 0.1159% if the shroud is at Level 400, and so on. The obscuration of a Level 400 surface is 0.0805% and a Level 300 surface is 0.0208%. If the budget of 0.25% obscuration is divided equally between the inside and outside surfaces, the obscuration allowance for each side is 0.125%. The particle redistribution from a Level 500 shroud would use up all of the budget. If the exterior surface of the aperture window is at Level 400, the cleanliness level of the shroud should be at Level 400 or better.

### Particulate Ingestion through Shroud Gap

As the vehicle ascends through the atmosphere, the aerodynamic loading and the stress may cause the shroud to deform and result in a gap in the seam lines. Assuming a maximum gap size of 10-mil, or 0.254 mm, the total area of the seam gap is calculated to be 123 $mm^2$. The projected area perpendicular to the flight direction is 21.4 $mm^2$ or 0.033 $in^2$.

The amount of particulate mass, M, flowing through the shroud gap area in each altitude range can be calculated by

$$M \cong (A)\,(DL)\,(LWC \text{ or } \rho)$$

where A is the projected area of the gap perpendicular to the flight direction and DL is the traveled distance in each altitude range. LWC is the liquid water content, and $\rho$ is the density of particles in the atmosphere. The number of particles contained in a given mass M can be calculated with the average mass of the particles.

The calculated results of mass and number of particles for each particle type ingested into the shroud in each altitude range are tabulated in Table 5. It is seen that relatively few rain, snow, or ice crystal particles are ingested into the shroud; but the total number of volcano dust particles can be as high as $2.9 \times 10^7$, based on a 10-mil gap size assumption.

Table 5 Mass and number of particles ingested into shroud through a 10-μm gap.

| Range No. | Altitude Range (km) | Particle Type | Particle Size (mm) | Density ($gm/cm^3$) | Distance Traveled (m) | Mass per Particle (gm) | No. of Particles Ingested |
|---|---|---|---|---|---|---|---|
| I | 0-2 | Rain | 1.5 | 0.03 | 4900 | $1.77 \times 10^{-3}$ | 2 |
| II | 0-2.44 | Dust | 0.0075 | $1 \times 10^{-5}$ | 6000 | $1.21 \times 10^{-10}$ | 5792 |
| III | 2-4 | Snow | 1.5 | 0.05 | 4800 | $1.77 \times 10^{-3}$ | 3 |
| IV | 4-7 | Snow | 0.5 | 0.03 | 7200 | $6.54 \times 10^{-5}$ | 71 |
| V | 7-10 | Ice Crystal | 0.3 | 0.02 | 7200 | $1.41 \times 10^{-5}$ | 218 |
| VI | 12.2-15.2 | Volc Dust | 0.001 | $1 \times 10^{-4}$ | 7200 | $5.24 \times 10^{-13}$ | $2.9 \times 10^7$ |

The ingested particles are assumed to deposit on the surface of forecone uniformly. Based on this assumption, the contribution to obscuration increase from each altitude range are computed. Table 6 summarizes the results. The range numbers in the table correspond to the particle types given in Table 5. The most significant contribution to surface PAC is that from volcano dusts (Range Number VI), which amounts to 0.0094%. The results show that the increases of surface contamination due to ingested particles from exterior sources may be negligible.

Table 6 Contribution to obscuration from exterior sources.

| Range Number | No of Particles | No. Particles per $ft^2$ | Average Size | Contribution to Obscuration (%) |
|---|---|---|---|---|
| I | 2 | 0.767 | 1.5 mm | 0.0014 |
| II | 5792 | 2222 | 7.5 μm | 0.0001 |
| III | 3 | 1.151 | 1.5 mm | 0.0022 |
| IV | 71 | 27.24 | 500 μm | 0.0057 |
| V | 218 | 83.64 | 300 μm | 0.0064 |
| VI | $2.9 \times 10^7$ | $1.113 \times 10^7$ | 1 μm | 0.0094 |

## Particulate Contamination due to Shroud Deployment

The shroud is deployed by inflating the gas bags in the forward part of the shroud. The enlarged bags open up the seam line and push the shrouds apart until the two halves are unlatched from their hinges at the base. There are two particulate sources during the deployment process: particles from the bag surface to the aperture window and particles generated due to ripping apart of the seam line. The issues are addressed as follows.

The problem of particle resuspension and redistribution from the gas bag surface is treated similar to what discussed in the preceding section. As the gas bags are inflated to the fully extended position, the mean surface vibration caused by the pyroshock has to be determined. An accurate calculation of the surface vibration level can be made with a gas bag model and the pyroshock analysis (Ref. 5). For the present analysis, a level of 20 g-rms is assumed.

The particles generated from the gas bag surfaces fall on the forecone. A uniform distribution of the particle over the forecone surface is again assumed. Because of the 15° half-cone angle, the contribution to surface particle density is multiplied by cos(75°). Table 7 summarizes the obscuration increases of the aperture surface from a range of gas bag surface cleanliness levels.

Table 7 Aperture window obscuration increase from gas bag operation.

| Gas bag surface Level | Obscuration increase, % |
|---|---|
| 750 | 0.1442 |
| 700 | 0.1000 |
| 600 | 0.0448 |
| 500 | 0.0178 |
| 400 | 0.0059 |
| 300 | 0.0015 |

A similar analysis is applied to calculate the obscuration increase of the aperture window due to seam line opening. The exact particle generation rate of the seam line opening is not available at the time of the analysis. However, the test result for the Centaur standard shroud separation system contamination was available (Ref. 6). In the longitudinal joint test the particle generation for the separation system using super-zip tube was measured. The test result is adopted here to show the potential effects of seam line opening during the shroud deployment. The predicted results are given in Table 8.

Table 8 Seam line opening induced aperture window obscuration increase.

| Particle size μm | Particle Count #/inch | Converted to #/sq ft | Percent Obscuration |
|---|---|---|---|
| 20 - 50 | 680 | 11050 | 0.00762 |
| 50 - 100 | 84 | 1365 | 0.00347 |
| 100 - 150 | 12 | 195 | 0.00109 |
| 150 - 250 | 6 | 98 | 0.00079 |
| 250 - 500 | 1 | 16 | 0.00011 |
| > 500 | 1 | 16 | 0.00017 |
| Total | | | 0.01325 % |

### Other Particulate Contamination Considerations

The contamination concerns from TLX line gas leakage was examined. Because the TLX line is located on the opposite side of the aperture window, and the shroud is deployed at zero angle of attack where there is no cross flow, the leakage, if any, will not cause any deposit on the aperture window. Therefore the TLX leakage is not a concern in the particulate contamination of the aperture window.

Questions were raised on the possibility that the particles on the aperture window will be scrubbed off by the shearing force after the protective shroud is jettisoned. An analysis was performed to address this problem (Ref. 7). The results show that at free stream Mach number equal to 6, the shearing force is still less than the adhesion force of a 10-μm particle on the surface at altitudes as low as 15 km. The larger particles, e.g. 30μm or larger, may be removed by the shearing force at this altitude. At higher altitudes, because of low ambient density, the shearing force decreases further with the altitude. At 100 km, the ambient density is five orders of magnitude lower than that at 15 km, and no particles will be removed at this and higher altitudes. It is concluded that the shearing cleaning of the window surface is possible, but not effective.

The particulate contamination caused by the charred particles from aeroheating on the aperture window seal was not pursued because of lack of proper data. This remains an open issue at this time, though its effects are expected to be small.

Operation of the divert jets near the terminal phase of the flight is a potential contamination concern. The plume interacts with the flowfield and induces boundary layer flow separation. The circulation of flow in the separated region may carry the combustion products and surface particles forward to deposit on the aperture window. This problem is out of the scope of this study and is not discussed here.

## SCATTERING FROM SURFACE PARTICLES

The LMSC Mie scattering/diffraction (RADSCA) model (Refs. 8 and 9) was used to compute the BSDF of the surface particles. The RADSCA code was verified by comparing its results to those generated with a published scattering model, PBHMIED (Refs. 10 and 11). Using the particle distribution of a Level 500 surface, the BSDF is computed with both codes.

Figure 1 shows a comparison between the BSDF calculated from PBHMIED, indicated with the solid line, using spherical particles and the results from the Mie scattering code for the Level 500 surface, noted with circles and squares. The coordinate is in $|\beta-\beta_0|$, where $\beta$ is $\sin\theta$ and $\theta$ is the scatter angle. $\beta_0$ is the sine of the incident angle $\theta_0$. The results using spherical particles from RADSCA agree well with the PBHMIED results. The results using cylindrical particles from RADSCA shows significant deviation at large scatter angles where $\theta$ is greater than 20°. Since the BSDF depends strongly on the wavelength and the particle shape, the deviation in BSDF caused by a different particle shape is not unexpected.

### BSDF Predictions

For a window with the cleanliness level specified on both sides, the number of surface particles is assumed to be the sum of the numbers of both sides. For a clean window, which is at Level 300 for both sides at the beginning of life, the particle counts are doubled that of a Level 300 surface. To see the effects of the added particles on the inside of the window, the BSDF for the window are computed. Figure 2 shows the BSDF of three window levels for 3μm wavelength.

The three BSDF curves correspond to the window of Level 300 on both sides, Level 300 on one side and Level 400 on the other side, and Level 400 on both sides. If the scattering limit is $10^{-3}$ at 20°, then only the window at Level 300 on both side will meet the requirement. The effects of window thickness and light refraction/transmission were not included in these calculations.

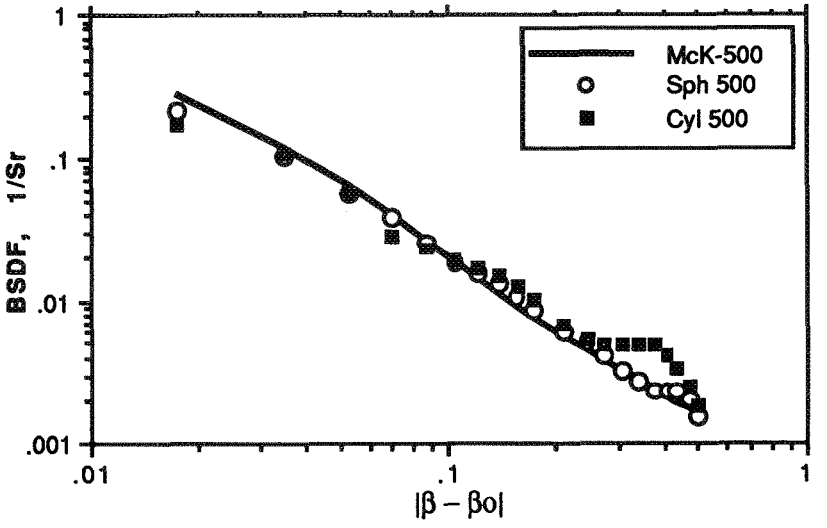


Fig. 1 Comparison of sphere-cylinder model for CL 500 ($\lambda$=3 μm, $\theta_O$ = 0° ). The solid line indicates the results from PBHMIED with spherical particles.

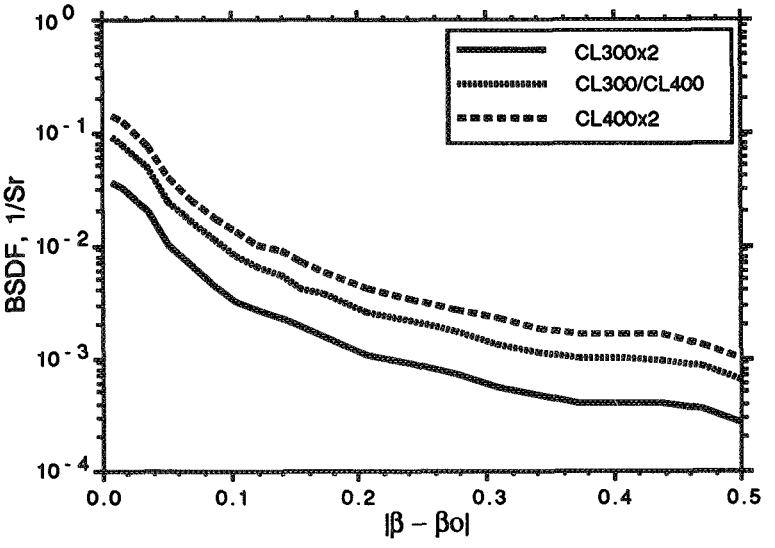


Fig. 2 The BSDF for the aperture window counted both sides.

For a practical analysis, let the window be at Level 300 on both sides initially. This level is attained by cleaning the window at the beginning of the manufacturing process to Level 100 and allowing for particle fallout during integration and tests.

As the vehicle goes through the events during ascent flight, additional particles will fall on the window due to vibroacoustic-induced redistribution, ingestion of foreign particles (of volcano

dusts, etc.), and deployment (which generates particles from unzipping the seam and popping of the gas bags). Taking these effects into consideration and assuming that the inside surface of the window is still at Level 300, the BSDF variation of the combined particle count is shown in Fig. 3 below. The solid line in the figure indicates the BSDF contributed from the outside window surface alone after accounting for the ascent flight effects. The dotted line shows the combined BSDF of the outside surface plus the inside surface at Level 300. The figure shows that the scattering level of the window is less than $10^{-3}$ at 20° and meets the straylight requirement.

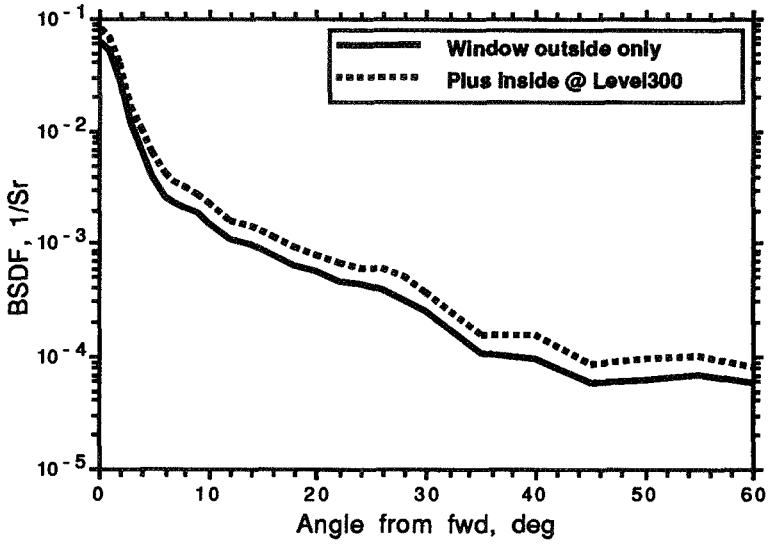


Fig. 3 The BSDF of the aperture window after going through ascent events and deployment for $\lambda = 3$ μm.

As the vehicle is subjected to the ascent vibroacoustic environment, the particles on the inside surface of the aperture window may also be resuspended. Because of the direction of acceleration vector, the resuspended particles are likely to be removed from the window without replenishment, thus leading to a cleaner inside surface than its initial cleanliness. Taking this effect into consideration, the resulting BSDF is shown in Fig. 4. In the figure, the BSDF of the aperture window for 3 to 5 μm wavelengths are shown. It is seen that the values of BSDF for a given set of wavelengths vary with scatter angle. At 0° the BSDF of the short wavelength (i.e. 3 μm) is the highest among the three, while at 25° the 4 μm value supersedes and so on. All three BSDF values at 20° scatter angle are less than $10^{-3}$, and meet the straylight requirement.

## Scattering Caused by Surface Roughness

The scattering caused by surface roughness is expressed in term of Total Integrated Scattering (TIS). The TIS can be measured with a simple instrument and correlated with the root mean square (rms) roughness of the surface (Ref. 12). The relation to convert the TIS to sample rms roughness is obtained from scalar scattering theory. The following formula can be used to calculate the TIS with given rms roughness d in Å and the wavelength λ in Å.

$$TIS = (4\pi d/\lambda)^2$$

If the window surface has a rms roughness of 6Å and the wavelength is assumed to be 4 μm, the TIS of the bare window is calculated as $3.6 \times 10^{-6}$, which is negligible comparing to the scattering contributed by the surface particles.

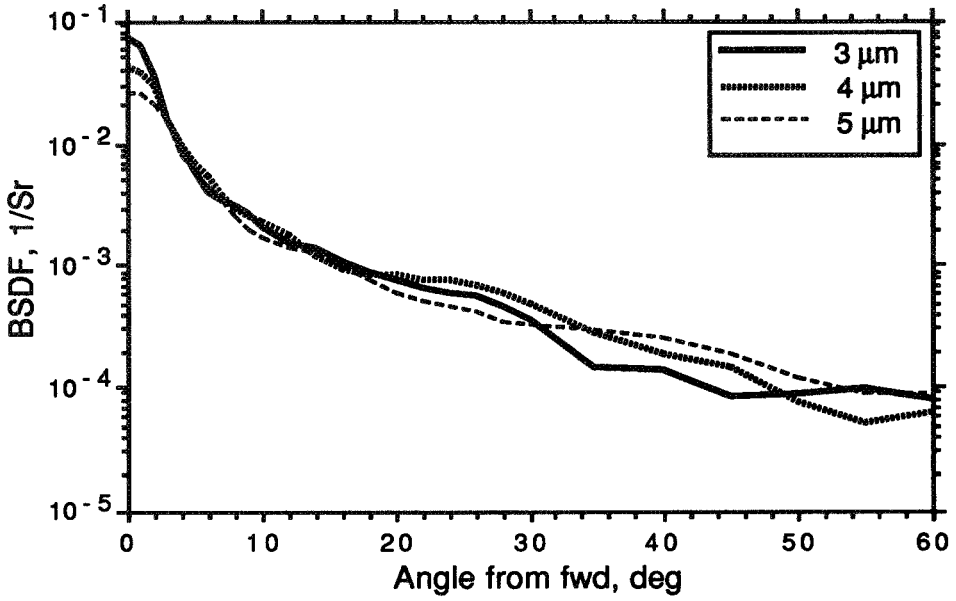


Fig. 4 The final BSDF for the aperture window for wavelengths of 3 μm, 4 μm, and 5 μm.

## CONCLUSIONS

A methodology to analyze the particulate contamination on the aperture window has been developed and presented in this paper. The analytical approach begins with a correlation between the specification of surface cleanliness level and the surface obscuration ratio to the surface particle densities in the size bins.

The particulate contamination increments contributed by the events during ascent and flight phases have been identified and predicted quantitatively in the analysis. The events include Vibroacoustic-induced particle redistribution, ingestion of particles during ascent, and the particles generated by shroud deployment.

The effects of particulate contamination on the aperture window are expressed in terms of BSDF. The software tool used to compute the BSDF was verified by comparison with the results from a published tool. The result shows the BSDF from the final particulate contamination on the aperture window at the end of mission. In the sample case used in the study, the predicted BSDF level meets the prescribed requirement.

## REFERENCES


1. P. T. Ma, M. C. Fong, and A. L. Lee, "Surface Particle Obscuration and BRDF Prediction," *Scattering from Optical Components*, SPIE Proceedings Vol. 1165, edited by J. C. Stover, SPIE Paper No. 1165-33, 1989.
2. P. T. Ma, "An Improved Particle Area Coverage Calculation Method," LMSC-SSD TSS-371, July 5, 1989.
3. Y. A. Lee, W. Hendricks, D. Park, et al., "Vibroacoustic Payload Environment Prediction System (VAPEPS)," NASA CR-166823, 1984.
4. A. Klavins and A. L. Lee, "Spacecraft Particulate Contaminant Redistribution," *Optical System Contamination: Effects, Measurement, Control,* SPIE Proceedings Vol. 777, edited by A. P. Glassford, Paper No. 777-27, 1987.
5. Y. A. Lee and W. Hendricks, "Pyroshock Analysis and Test of Composite Satellite Structure," DGLR/AIAA 92-02-167, 1992.
6. D. D. Smith, "Centaur Standard Shroud Separation System Contamination Test Report," LMSC-D466881, 10 September 1976.
7. C. Fan, "Shear Force Cleaning for Surface Particulate," LMSC-SSD TSS-478A, 3 June 1993.
8. E. C. Markovitz, "A Computer Code to Calculate the Straylight due to Particulate Contaminants on a Surface," LMSC-SSD TSS-301, May 19, 1986.
9. M. C. Fong, "Spacecraft Contamination Modeling Capability at LMSC - A Comprehensive Overview," LMSC-SSD TSS-473, November 18, 1992.
10. P. R. Spyak, "A Cryogenic Scatterometer and Scatter from Particulate Contaminants on Mirror," Univ. of Arizona Dissertation, 1990, also *Optical Engineering*, August 1992, Vol. 31, No. 8, pp.1746-1784.
11. P. R. Spyak and W. L. Wolfe, "Cryogenic Scattering Measurements," *Stray Light and Contamination in Optical System*, SPIE Vol. 967, 1988, pp.144-158.
12. J. C. Stover, *Optical Scattering - Measurement and Analysis*, McGraw-Hill, 1990, pp.87.

# EXPERIMENTAL STUDY OF SOLAR SIMULATOR MIRROR CRYOCONTAMINATION

V.L. Galjaev, A.A. Makarov, N.A. Afanassiev
NIICHIMMASH, Sergiev Posad, Moscow Russia
Russia

## ABSTRACT

• Key words: solar simulator, collimation mirror, cryocontamination

The background and tasks formulation of the study of Solar Simulator collimation mirror cryocontamination in Large Thermal Vacuum Facility are outlined, research methods and experiment procedures are described, experimental relationships obtained are analyzed and practical recommendations are given.

The accepted procedure of thermal vacuum tests as a rule defines the sequence of operations for verifying the spacecraft under test without taking into account measures for preventing Solar Simulator collimation mirror contamination and degradation. On the other hand, evacuation procedure is defined for conditions of achieving the required vacuum in the shortest possible time with using the available evacuation equipment at a regime close to the optimum one.

Similarly, cryopanel cooling down cyclogram and test object preparation process are not analyzed from the viewpoint of ways of reducing environmental detrimental effects on thermal vacuum facility contamination-sensitive systems. Solar Simulator mirror contamination and its reflective characteristics change results in degradation of solar flux parameters and reduction of simulator continuous operation time.

Methods of consideration of optical effects due to mirror surface contamination are actually missing. The effects themselves are not quite understood and data cited in literature as a rule, were obtained under conditions different from real thermal vacuum facility and therefore should be subjected to additional experimental verification. Only in the last few years contamination effect on optical surfaces degradation has been considered with using empirical relations.

Mirror reflective properties degradation leads to the increase of Solar Simulator errors. This ultimately has an adverse effect on S/C ground development, schedule and cost of thermal vacuum tests. Besides, the mirror maintenance in operable state becomes more expensive.

The present paper is dedicated to the study of Solar Simulator collimation mirror contamination and to the search of ways for improving the mirror design and thermal vacuum test procedure. On the basis of tests performed, recommendations are devised on reducing chamber inner-optical surfaces cryocontamination and degradation.

# ASTM E 1559 METHOD FOR MEASURING MATERIAL OUTGASSING/DEPOSITION KINETICS HAS APPLICATIONS TO AEROSPACE, ELECTRONICS, AND SEMICONDUCTOR INDUSTRIES

J. W. Garrett, A. P. M. Glassford, and J. M. Steakley
Lockheed Missiles & Space Company, Inc.

## ABSTRACT

The American Society for Testing and Materials has published a new standard test method for characterizing time and temperature-dependence of material outgassing kinetics and the deposition kinetics of outgassed species on surfaces at various temperatures. This new ASTM standard, E 1559[1], uses the quartz crystal microbalance (QCM) collection measurement approach. The test method was originally developed under a program sponsored by the United States Air Force Materials Laboratory (AFML) to create a standard test method for obtaining outgassing and deposition kinetics data for spacecraft materials. Standardization by ASTM recognizes that the method has applications beyond aerospace. In particular, the method will provide data of use to the electronics, semiconductor, and high vacuum industries.

In ASTM E 1559 the material sample is held in vacuum in a temperature-controlled effusion cell, while its outgassing flux impinges on several QCMs which view the orifice of the effusion cell. Sample isothermal total mass loss (TML) is measured as a function of time from the mass collected on one of the QCMs which is cooled by liquid nitrogen, and the view factor from this QCM to the cell. The amount of outgassed volatile condensable material (VCM) on surfaces at higher temperatures is measured as a function of time during the isothermal outgassing test by controlling the temperatures of the remaining QCMs to selected values. The VCM on surfaces at temperatures in between those of the collector QCMs is determined at the end of the isothermal test by heating the QCMs at a controlled rate and measuring the mass loss from the QCMs as a function of time and temperature. This reevaporation of the deposit collected on the QCMs is referred to as QCM thermogravimetric analysis. Isothermal outgassing and deposition rates can be determined by differentiating the isothermal TML and VCM data, respectively, while the evaporation rates of the species can be obtained as a function of temperature by differentiating the QCM thermogravimetric analysis data.

This paper describes the ASTM E 1559 test method and presents some typical data. The paper also describes the Lockheed ASTM E 1559 test apparatus.

## INTRODUCTION

Up to the present time two material screening techniques have been used by the aerospace and microelectronics industries, ASTM E 595[2] and ASTM F 1227[3], respectively, to measure total mass loss (TML) and collected volatile condensable materials (CVCM). These standards both specify single sample and deposition surface temperatures, and a single test duration, and provide integral rather than time-dependent TML and CVCM data. The vacuum/space compatibility of a material is determined by comparing its TML and CVCM data with arbitrary criteria. While the data measured by the ASTM E 595 and ASTM F 1227 tests are very valuable for material comparison and screening, they do not reflect the impact of a material on the performance of a specific component or system, with specific material and deposition surface temperatures.

In order to accurately predict the impact of contamination on space system performance, the aerospace community customarily models contamination generation, migration, and deposition using computer codes to represent the geometry and operational temperatures of the system of interest. This type of system modeling requires as input time- and temperature-dependent material outgassing/deposition kinetics data, which cannot be generated by the previous ASTM test methods. The Air Force Materials Laboratory Non-Metallic Materials Group recognized this situation and initiated a program with Lockheed Missiles & Space Company to develop a standardized method for characterizing materials outgassing rates and deposition kinetics. Between 1982 and 1989 Lockheed verified a test approach, designed a suitable test apparatus and developed the test procedure. This test method was demonstrated by establishing a twenty-material database for the Air Force, and by supporting numerous Lockheed and out-of-house programs with material outgassing measurements. A full description of the Air Force program and the test method developed is presented in the contract final report [4]. After the successful completion of this contract, the Air Force solicited the support of the ASTM Subcommittee E21.05 to pursue incorporation of the Lockheed developed method as a new ASTM standard test. The current edition of this standard was approved August 15, 1993 and is designated ASTM E 1559.

This paper describes the basic QCM collection measurement approach and reviews the major features of the ASTM E 1559 test method. The standard specifies certain apparatus minimum performance requirements and key dimensions, but much of the vacuum system and data acquisition system design can be chosen by the user. The paper therefore describes ASTM E 1559 apparatus requirements using the current Lockheed apparatus as an example. The paper also presents examples of the type of data provided by the test.

## TEST METHOD

### The QCM Collection Measurement Method

The QCM collection method for measuring outgassing and deposition kinetics is shown schematically in Figure 1. The material sample is placed in a temperature-controlled effusion cell in a vacuum chamber. Outgassing flux leaving the effusion cell orifice impinges on several QCMs which are controlled at selected temperatures. One of the QCMs is cryocooled, usually by liquid nitrogen for reasons of practicality, so as to collect essentially all the impinging species. The sample percent total mass loss (TML) and outgassing rate from the sample are determined as functions of time from the mass deposited on this QCM and the cell orifice-to-QCM view factor. The percent of outgassing species which are condensable on higher temperature surfaces is referred to as Volatile Condensable Material (VCM) and is measured as a function of time from the mass collected on the other QCMs, which are temperature-controlled appropriately. The QCMs and effusion cell are surrounded by a liquid nitrogen shroud to ensure that the molecular flux impinging on the QCMs is due only to the sample in the effusion cell.

After the isothermal outgassing test, a QCM thermogravimetric analysis (QTGA) is performed on the condensed outgassed species. The QCMs are individually heated at a controlled rate from their base temperatures to 398 K in order to volatilize the collected species, while the mass remaining on the QCMs is measured as a function of time and temperature. In general, the collected species have different evaporation characteristics and hence will leave the QCM surface at different temperatures. Therefore, QTGA data are characterized by temperature regimes in which the deposit mass remaining on the QCM decreases due to evaporation of a particular species, separated by temperature regimes in which no species evaporate. The number of temperature regimes in which the QCM deposit mass decreases indicates the number of major species present in the outgassing flux. The relative amount of a given species in the outgassing flux can be estimated from the ratio of the mass loss associated with the evaporation of that species to the total deposit mass on the QCM. QTGA also provides an effective means to clean the QCM surfaces before subsequent outgassing tests.

As shown in Figure 1, the QCM collection method allows for an optional mass spectrometer to be installed on the test chamber. By monitoring the mass spectra of the sample outgassing flux during the

isothermal test, and of the evaporation flux from the QCM during QTGA it is possible in many cases to identify the outgassed species, and to determine the relative outgassing rates of the different species.

The major advantages of the QCM collection method are ability to measure both outgassing and deposition data simultaneously; lack of constraints on sample size and shape (as long as it fits inside the effusion cell); and ability to thermally analyze the outgassed species by QTGA. The major possible disadvantages are the indirect nature of the mass measurement; non-condensability of some outgassed species at liquid nitrogen temperature; and possible influence of effusion cell pressure on outgassing rate. The error in mass measurement using calculated QCM/cell view factors has been shown to be no more than ±2 percent[4], and can be eliminated entirely by calibrating the apparatus using a material of known vapor pressure. Sample mass loss data obtained by QCM collection with pre- and post-test microbalance weighings have been found to agree within a few percent, confirming that most significant outgassed species are condensable at 90 K. Studies have shown[4] that effusion cell pressure can be kept low enough to have negligible effects on outgassing rates if the ratio of sample total outgassing rate to effusion cell orifice size is kept below easily maintainable limits.

### The ASTM E 1559 Test Method

ASTM E 1559 is based on the QCM collection method described above, with two types of test method constraints - Test Method A and Test Method B. Test Method A uses standard effusion cell temperatures, three QCMs with polished aluminum electrodes at standard temperatures, and apparatus dimensions and geometries in order to give standard view factors from the QCMs to the effusion cell orifice. Test Method B allows for deviations from these parameters in order for the user to perform custom tests using application-specific parameters or a modified apparatus.

Specifications for the ASTM E 1559 Test Standard are based on the design and performance of the vacuum outgassing/deposition kinetics apparatus and test procedure used at Lockheed. These specifications are summarized below. The apparatus in use at Lockheed performs tests under Test Method B in that an optional fourth QCM is used, the QCMs have gold electrodes, and an optional mass spectrometer is also installed.

## TEST APPARATUS

The major components of an ASTM E 1559 test apparatus are the vacuum system, the internal outgassing/ deposition measurement configuration, and the data acquisition system.

### Vacuum System

The principal components of the vacuum system are the main test chamber, the cryogenic cold shrouds, and the interlock chamber.

Lockheed's main test chamber is a stainless steel cylinder 50 cm high by 30 cm diameter and contains a liquid nitrogen-cooled shroud. This shroud minimizes molecular contamination from sources other than the effusion cell from reaching the QCMs and reduces the radiative heat load on the QCMs. A cryopump is used on the Lockheed chamber to maintain high-vacuum. The test apparatus in use at Lockheed is shown in Figure 2.

The ASTM standard requires that an interlock chamber be provided to permit the effusion cell to be placed in and removed from the main chamber without having to warm up the internal components and repressurize the main chamber. The interlock chamber is connected to the main chamber via a gate valve through which the effusion cell can be passed. Lockheed's interlock chamber uses a turbomolecular and direct-drive mechanical pump to perform the initial evacuation of the sample from atmospheric pressure.

## Internal Measurement Configuration

The outgassing/deposition measurement system includes the QCM assembly and the effusion cell. The QCM assembly consists of three QCMs, a cryogenic heat sink for the QCMs, and a system of cooled shrouds. An optional fourth QCM is utilized on the Lockheed system.

The ASTM E 1559 standard requires that the QCMs consist of two crystals (one for mass collection and one for reference) and that they have a sensitivity of at least 1 x $10^{-8}$ g/cm$^2$ Hz at 298 K. This is typically accomplished with crystals that have natural frequencies of 10 MHz to 15 MHz. The QCM crystals should have optically polished (i.e. specular) surfaces with uncoated aluminum electrodes. The Lockheed apparatus uses QCMs with 39°40' AT cut 10 MHz crystals that have a sensitivity of 4.49 x $10^{-9}$ g/cm$^2$ Hz. These crystals have optically polished surfaces with gold electrodes. Because of this electrode deviation from the standard, Lockheed stipulates that its apparatus is operating under Test Method B of the ASTM standard.

The QCMs are arranged symmetrically so that the sensing surface of each of the QCMs has the same view factor to the effusion cell orifice. The QCMs are angled at 10° from the vertical so that their axes intersect each other at a point 150 mm from the crystal surfaces. This intersection point is where the effusion cell orifice exit plane is positioned.

The QCM assembly has cryogenic heat sinks to thermally ground the QCMs to ≤ 90 K and cold shrouds to limit the impinging flux on the QCMs to the line-of-sight from the effusion cell orifice. The Lockheed apparatus utilizes a liquid nitrogen reservoir to obtain the necessary cryogenic temperatures conveniently and inexpensively. The QCMs are heat sunk to the bottom of the liquid nitrogen reservoir and are thermally shielded from each other by copper plates extending downwards between adjacent QCMs. The ASTM standard requires that each QCM have an independent temperature sensing and control system to allow the QCMs to be heated from their cryogenic heat sink temperature to 398 K. The temperature control system must be capable of controlling the QCM temperatures to a precision of ±0.5 K or better and also be capable of ramping the QCM temperatures at a constant rate of 1 K/minute.

The ASTM effusion cell is a cylindrical container approximately 65±5 mm inside diameter by 50±5 mm in deep, and is machine from copper or aluminum for high thermal conductivity. Lockheed utilizes a 63 mm diameter by 51 mm deep aluminum cell. The cell has a detachable cover plate which allows for insertion of material samples. This lid has a cylindrical orifice from which the outgassing flux from the sample exits. The orifice dimensions determine the flux distribution and are specified to be 3.0±0.1 mm diameter by 3.0±0.1 mm long. The cell has an integral temperature sensor and heater, and control system which permits operating the cell from ambient to 398 K with a precision of ±0.5 K or better. The effusion cell is positioned inside the main test chamber so that the center of the cell orifice exit plane coincides with the intersection point of the QCM axes. The cell orifice thus has the same view factor to the all four QCMs. The cell orifice is 150±1 mm from the surface of the sensing crystal in each QCM.

## Data Acquisition System

The ASTM standard test method does not specify a particular data acquisition technique. However, frequency and temperature data from the QCMs, temperature data from the effusion cell, and the time of data collection must be acquired at specified intervals over relatively long time periods (perhaps several days for an isothermal outgassing test). An automated computer-based data acquisition system is highly recommended to facilitate raw data recording and subsequent data processing and archiving. Lockheed utilizes a personal computer to control QCM and effusion cell operations and to acquire the necessary data. Data reduction is then readily accomplished by manipulating the data spreadsheet.

### Additional Supporting Equipment

An analytical laboratory balance is required for pre- and post-test weighing of material samples. The balance should have a 30 gram or greater tare (since this test method uses rather large samples) and it should have a readability of 10 μgram or better with a precision of ±10 μgram.

### Hardware Cleaning

The ASTM standard provides guidelines for vacuum chamber preparation and QCM handling and cleaning. These guidelines are consistent with common high vacuum practices and recommended instructions from QCM vendors.

## TEST SAMPLE REQUIREMENTS

ASTM E 1559 was developed to allow outgassing characterization of a wide variety of materials including adhesives, sealants, cable insulation, conformal coatings, electrical components, films and sheet materials, greases and liquids, pre-molded elastomer compounds, and tapes. In general, in order to perform an outgassing measurement, a representative sample of the material need only fit inside the effusion cell. Meaningful data interpretation requires that the material be well described in terms of its preparation, composition , and pre-conditioning. All sample material details pertinent to its heritage including batch or lot numbers should be noted.

Since outgassing of most space materials is diffusion-controlled, the test sample is prepared in either the geometry in which it is to be used, or in a geometry which permits the measured outgassing data to be related to a sample with another geometry using diffusion theory. Sample dimensions are, therefore, critical to data analysis and are measured to an accuracy of ±1 percent.

ASTM E 1559 specifies sample configurations, sample holders, and allowable geometries for a variety of different types of materials in order to constrain the internal diffusion flow to one dimension or to be representative of the materials application. Examples of the non-outgassing sample holders include 10 mm by 25 mm aluminum tubes for holding adhesives or sealants, and aluminum foil substrates for conformal coatings.

Initial sample mass is determined by the degree of sample outgassing and apparatus/QCM sensitivity limitations. Too small a sample may produce too small a deposit on the QCMs for accurate outgassing characterization and too large a sample may produce a deposit on a QCM large enough to damp the sensing crystal and thus saturate the output signal. Large deposits may also induce non-linear responses from the QCM particularly if the deposit is liquid rather than solid. Experience has shown that sample sizes of 0.5 to 10 gram (not including any substrate) consistently yield outgassing data within the dynamic range of the test apparatus. Sample mass is determined on a laboratory balance to an accuracy of ±10 μgram.

## TEST PROCEDURE

As mentioned previously, there are two versions of the test method. Test Method A prescribes specific QCM and sample temperatures and Test Method B allows for variances in these parameters to permit the user to customize a test to acquire application-specific data. Variations related to test operation under Test Method B must be noted in order to accurately interpret the data. Except for effusion cell and QCM setpoint temperatures the actual test procedure is the same for Test Method A or B.

### Test Chamber Preparation

In preparation for outgassing measurements the main test chamber is evacuated to less than $5 \times 10^{-5}$ torr and the cryogenic heat sinks for the QCMs and shrouds are then activated. The QCMs are heated to 398 K to remove any residual contaminants by evaporation and then allowed to cool to their operating

temperatures. The interlock chamber containing the effusion cell is also evacuated to less than $5 \times 10^{-5}$ torr at this time. These preceding steps are performed only when the apparatus is first turned on. For a series of outgassing measurements (i.e. normal operation) the chamber remains evacuated with the cryogenic heatsinks on and the QCMs at their operating temperatures. This is good practice for maintaining the cleanest apparatus with low background.

### Effusion Cell and Sample Preparation

Prior to a test the effusion cell is solvent cleaned and vacuum baked at 398 K for at least 12 hours in the interlock chamber. The cell is then cooled to ambient temperature, the interlock chamber is raised to one atmosphere using dry nitrogen, and the cell is removed for sample insertion. The interlock chamber is purged with dry nitrogen gas during the entire time it is at one atmosphere to minimize adsorption of water vapor. The sample is placed in the cleaned effusion cell, and the cell is placed on its holder in the interlock chamber. The interlock chamber is then closed to the atmosphere and the nitrogen gas purge is stopped.

### Isothermal Outgassing Test

At the beginning of a test the main chamber is at stable vacuum (about $1 \times 10^{-9}$ torr for the Lockheed apparatus) with heat sinks and shrouds cold, and the QCMs are at their operating temperatures with their output frequencies at equilibrium. For Test Method A the temperatures for the three QCMs are specified to be ≤90 K, 160 K and 298 K and each stable within ±0.5 K. The coldest QCM on the Lockheed apparatus is actually at about 80 K. The ASTM standard defines QCM frequency equilibrium as when the frequencies of each QCM vary by less than 0.2 Hz/minute when averaged over a 20 minute period.

Acquisition of QCM frequencies and temperatures, and effusion cell temperature is initiated about 20 minutes before the beginning of interlock chamber evacuation. This 20 minutes allows for verification of the stability of QCM frequencies and temperatures. Data is collected at 5 or 10 minute intervals with time zero being defined as the beginning of the interlock chamber evacuation.

The test begins with initiation of evacuation of the interlock chamber containing the effusion cell from atmospheric pressure. The ASTM procedure specifies that the interlock chamber containing an empty effusion cell should be capable of reaching $1 \times 10^{-5}$ torr in 5 minutes. After 5 minutes of pumping the isolation valve between the main chamber and the interlock chamber is opened for effusion cell insertion into the main chamber. Selection of the 5 minute initial evacuation is a compromise between the desire to reduce the interlock chamber pressure as much as possible before opening the isolation valve to minimize the ensuing rise in main chamber pressure, and the desire to obtain data as soon as possible after the sample has been first exposed to vacuum. During non-standard testing at Lockheed the interlock chamber evacuation period has been as short as 1 minute.

When the effusion cell has been positioned on its holder in the main test chamber the cell is heated to the specified test temperature. Test Method A specifies that each material sample shall be tested at three temperatures. The first test is at 398 K and the second test is at 348 K. A third test is conducted at 323 K or 373 K depending on the contaminant deposition on the ≤90 K QCM during the previous two tests. If the ≤90 K QCM deposition from the 348 K sample test is less than 5 percent of that from the 398 K sample test then the third test is conducted at 373 K. Effusion cell temperature is controlled to within ±0.5 K of the specified value. Sample temperature is probably the most application specific parameter involved in outgassing characterization tests and is therefore the most common test method variation. Outgassing measurements have been performed at Lockheed for sample temperatures ranging from 130 K to 450 K.

The isothermal outgassing test continues for up to 5 days for each sample. The test can be terminated before 5 days if the mass deposition rate on the ≤90 K QCM is less than twice that of the background deposition rate. The background deposition rate is determined by running a blank outgassing test on an empty effusion cell. ASTM E 1559 specifies that the background deposition rate on the ≤90 K QCM due to an empty effusion cell should be less than $5 \times 10^{-13}$ g/cm$^2$ s. For a 10 MHz QCM this

corresponds to a frequency shift of about 10 Hz/day. With careful apparatus design and construction, Lockheed has been able to achieve background deposition rates on its 80 K QCM of about 2 Hz/day.

An isothermal outgassing test also should be terminated if the deposit mass on a QCM gets large enough to cause inaccuracies in the output signal. Too large a deposit will damp out the oscillating crystal and large deposits (particularly liquids) may also not be coupled appropriately to the crystal. The point at which inaccuracies due to deposit size become significant may vary depending on the QCM and nature of the collected deposit. The ASTM standard specifies that if a QCM deposit exceeds $2 \times 10^{-4}$ g/cm$^2$ the test should be terminated. For a 10 MHz QCM this corresponds to a frequency shift of about 45 KHz.

At the end of the isothermal outgassing test period, the effusion cell is removed from the main chamber via the interlock, the interlock chamber is repressurized with dry nitrogen gas, and the effusion cell is allowed to re-equilibrate to ambient temperature. Once the cell is within 10 K of ambient room temperature it is removed from the interlock chamber, and the sample is removed from the cell and reweighed on the laboratory balance. Before starting another isothermal outgassing test, the effusion cell is thoroughly solvent cleaned and vacuum baked at 398 K for at least 12 hours. This effusion cell preparation for the next test is easily accomplished in the interlock chamber while the subsequent QCM thermogravimetric analysis test is being performed.

### QCM Thermogravimetric Analysis Test

At the end of the isothermal test the deposits collected on the QCMs are subjected, in turn, to QCM thermogravimetric analysis (QTGA). This test measures the QCM deposit mass as a function of temperature. Each QCM is heated from its base operating temperature to 398 K. Because the frequency of a QCM crystal is sensitive to heat flux through the crystal, the heating rate must be low enough to keep heat flux-induced frequency changes within acceptable limits. The heating rate selected for the ASTM procedure is 1 K/minute, based on published studies of heat flux effects on QCM frequency[5]. A maximum temperature of 398 K is selected for QTGA because this is equal to the maximum sample temperature and all deposited outgassed species should evaporate at temperatures below this unless they have changed chemically since deposition. It is also the maximum operating temperature of the QCMs.

After reaching 398 K, a QCM is maintained at this temperature until its frequency becomes stable i.e. until its collected deposit has completely reevaporated. The QCM is then cooled back to its operating temperature in preparation for the next isothermal outgassing test.

Because the reevaporation of collected species off a QCM can be a rather fast and eventful process compared to the outgassing test, the QCM temperature and frequency are recorded at one minute intervals during QCM thermogravimetric analysis .

## DATA PROCESSING

The ASTM E 1559 test method generates material data from *ex situ* and *in situ* measurements. The *ex situ* measurements consist of the pre- and post-test weighing of the sample on a laboratory balance. The *in situ* measurements consist of isothermal outgassing test data and QCM thermogravimetric analysis data. The *ex situ* laboratory balance measurements are reduced to yield an *ex situ* Total Mass Loss, $TML_{ex}$, value. The QCM frequency data from the isothermal outgassing test are reduced to give *in situ* Total Mass Loss, *TML*, and Volatile Condensable Material, *VCM*, as functions of test time. The QCM frequency and temperature data from the QCM thermogravimetric analysis are converted to mass remaining on the QCM, $m_Q$, as a function of QCM temperature.

In addition to this data processing specified by ASTM E 1559, the measured QCM data also can also analyzed to provide outgassing rates from the sample during the isothermal outgassing test and evaporation rates from the QCM during QCM thermogravimetric analysis. This data reduction will be discussed below in order to illustrate the scope of material characterization information that is generated by this test method.

## Ex Situ Measurements

The *ex situ* Total Mass Loss, $TML_{ex}$, in percent is calculated from pre- and post-test laboratory balance weighings by the following equation:

$$TML_{ex} = 100 * \left[ \frac{m_{s+h}(i) - m_{s+h}(f)}{m_{s+h}(i) - m_h} \right] \tag{1}$$

where $m$ indicates a measured mass, the subscripts $s$ and $h$ indicate the sample and holder, and $i$ and $f$ indicate initial and final weighings, respectively.

## Isothermal Outgassing Test

The pertinent data acquired during the isothermal outgassing test are the frequencies of the QCMs and the time since the start of the evacuation of the effusion cell in the interlock chamber. Isothermal outgassing data are calculated from QCM frequency data using the QCM mass sensitivity and the view factor from the QCM to the effusion cell orifice.

The QCM mass sensitivity is used to convert the QCMs output frequency into units of mass deposited on the QCM. The mass deposited on a QCM is calculated from the following equation:

$$m_d(T_q, T_s, t) = K_s \left[ f(T_q, T_s, t) - f(T_q, T_s, 0) \right] \tag{2}$$

where $m_d(T_q,T_s,t)$ is the mass deposit density (g/cm$^2$), $f(T_q,T_s,t)$ is the frequency (Hz) of the QCM at temperature $T_q$ with the sample at temperature $T_s$ at time $t$, and $K_s$ is the mass sensitivity factor (g/cm$^2$ Hz). Since the relationship between frequency shifts and mass deposited on the QCM crystal is linear well beyond the operating regime of the ASTM E 1559 measurements, the mass sensitivity factor, $K_s$, is constant for a given QCM type. The ASTM E 1559 standard provides $K_s$ values for typical QCMs. The QCMs used in the Lockheed apparatus have a sensitivity of, $K_s$ = 4.49 x 10$^{-9}$ g/cm$^2$ Hz. Further discussion on mass sensitivity of QCMs can be found in reference 5.

The second principal piece of information required for analyzing the isothermal outgassing test data is the view factor from the QCM to the effusion cell orifice. This view factor relates the mass deposit on the QCM to the mass lost from the sample and can be calculated from the following equation:

$$F_q = \frac{\pi r^2 W_{L/R}}{B(\phi_1)\cos(\phi_1)\cos(\phi_2)} \tag{3}$$

where
- $F_q$ = the view factor for QCM$_q$ to the effusion cell orifice (cm$^2$)
- $r$ = the distance from the cell orifice to the QCM$_q$ crystal (cm)
- $\phi_1$ = the angle between the QCM$_q$-to-orifice line of sight and the orifice normal
- $\phi_2$ = the angle between the QCM$_q$-to-orifice line of sight and the QCM$_q$ normal
- $L$ = the length of the effusion cell orifice (mm)
- $R$ = the radius of the effusion cell orifice (mm)
- $B(\phi_1)$ = the directivity of the angular flow from the effusion cell orifice
- $W_{L/R}$ = the transmission probability of the orifice

The $B(\phi_1)$ and $W_{L/R}$ functions account for the deviation from a cosine distribution for molecular flow leaving an orifice of finite length. The angular flow directivity, $B(\phi_1)$, can be calculated from the following equations[6]:

$$B(\phi_1) = 1 - \frac{2}{\pi}(1-\gamma)\left[\arcsin(p) + p\sqrt{1-p^2}\right]$$

$$+\frac{4}{3\pi}(1-2\gamma)\frac{1-(1-p^2)^{3/2}}{p} \qquad \text{for } p \le 1 \qquad (4)$$

and

$$B(\phi_1) = \gamma + \frac{4}{3\pi}\frac{(1-2\gamma)}{p} \qquad \text{for } p > 1 \qquad (5)$$

where

$$p = \frac{L\tan(\phi_1)}{2R} \qquad (6)$$

and

$$\gamma = \frac{\sqrt{L^2+4R^2} - L}{2R + \frac{4R^2}{\sqrt{L^2+4R^2}}} \qquad (7)$$

The other flux distribution related function in Equation 3 that needs to be established is the transmission probability, $W_{L/R}$. This factor represents the fraction of molecules entering the upstream face of the effusion cell orifice which exit the downstream face towards the QCMs. $W_{L/R}$ is a complex function of the geometry and dimensions of the orifice. Calculated values are available in literature[7,8] and are briefly summarized in the ASTM E 1559 standard.

The effusion cell orifice dimensions and geometries of the Lockheed apparatus are fully compliant with Test Method A. An effusion cell with an orifice that is 3.0 mm long by 3.0 mm diameter is positioned 15 cm from the face of the QCMs such that all the QCMs have the same view factor to the orifice and $\phi_1 = 10°$ and $\phi_2 = 0°$. Using Eqs. 4 through 7 and References 7 and 8 we find that these parameters result in a flux distribution where $B(\phi_1) = 0.8881$ and $W_{L/R} = 0.5136$. Substitution of these values into Equation 3 gives a value for the QCM-to-cell orifice view factor of $F_q = 415.08$ cm$^2$.

Total Mass Loss

The *in situ* Total Mass Loss (*TML*) expressed in percent of sample mass is calculated from the mass density deposited on the ≤90 K QCM and normalized with respect to the initial mass of the sample using the following equation:

$$TML(T_s,t) = 100 * \left[\frac{F_1 m_d(T_1,T_s,t)}{m_{s+h}(i) - m_h}\right] \qquad (8)$$

Equation 8 assumes that all of the outgassing flux impinging on this QCM is condensed. Some highly volatile outgassed species such as atmospheric gases will not deposit on the QCM but the error introduced by this assumption is acceptably small[4].

In some cases it is desirable to normalize the total mass loss to some other sample parameter. As an example, for coatings it is sometimes useful to normalize the data with respect to the surface area of the sample. That is, the total mass loss data could be expressed in terms of mass lost from the sample per unit area of sample (g/cm$^2$). ASTM E 1559 does not provide the specific equations for calculating total mass loss in these units, but the data can be easily reduced once $m_d$ and $F_1$ are established by substituting the sample surface area, $A_s$, for the initial sample mass in Equation 8.

Volatile Condensable Material

The Volatile Condensable Material (*VCM*) expressed in percent of sample mass is calculated from the mass density deposited on the higher temperature QCMs and normalized with respect to the initial mass of the sample using the following equation:

$$VCM(T_q,T_s,t) = 100 * \left[ \frac{F_q m_d(T_q,T_s,t)}{m_{s+h}(i) - m_h} \right] \tag{9}$$

where $q$ corresponds to the higher temperature QCMs. As with the total mass loss data reduction mentioned above, *VCM* can be expressed in alternative units by making the appropriate substitutions into Equation 9.

Outgassing Rate

A specific data reduction technique is not provided by ASTM E 1559 for calculating material outgassing rates. However, the test method does provide all the necessary raw data so that the end user can perform this analysis. The total outgassing rates from the sample are calculated from the data from the ≤90 K QCM. As with the TML calculations, this analysis assumes that essentially all of the outgassing flux impinging on the ≤90 K QCM is condensed. The mass deposit density on the ≤90 K QCM, $m_d(T_1,T_s,t)$, is differentiated as a function of time to give the deposition rate on this QCM. This deposition rate, $\dot{m}_d(T_1,T_s,t)$, is then used with the QCM-to-cell orifice view factor, $F_q$, and the sample surface area, $A_s$, in the following equation to calculate the total outgassing rate from the sample, $OGR(T_s,t)$, in units of g/cm$^2$ s:

$$OGR(T_s,t) = \frac{F_1 \dot{m}_d(T_1,T_s,t)}{A_s} \tag{10}$$

## QCM Thermogravimetric Analysis

The pertinent raw data acquired during the QCM thermogravimetric analysis consist of the frequencies and temperatures of the QCMs. The time between data measurements from the QCMs can be used for optional evaporation rate analysis.

Mass Loss from the QCM

As a QCM is heated up from its base operating temperature, the deposit collected during the isothermal outgassing test evaporates from the crystal. This causes a decrease in the QCMs output beat frequency. These frequency data are used with Equation 11 to calculate the mass loss (g/cm$^2$) from the QCM deposit during QTGA, $m_Q(T_q,t)$, as a function of temperature for each of the QCMs.

$$m_Q(T_q,t) = K_s\left[ f(T_q,0) - f(T_q,t) \right] \tag{11}$$

Although the types of QCMs specified for use in ASTM E 1559 utilize a reference crystal which helps compensate for thermal drift of the QCM frequency, some temperature effects on the output will still be present during the thermogravimetric analysis. Methods for correcting for this frequency-temperature response of a QCM have not been specified by ASTM E 1559. Lockheed, however, obtains a frequency-temperature response curve for a clean QCM by subjecting it to the QTGA heating profile of 1 K/minute. This clean QCM frequency-temperature profile (or a curve fit to it) can be then subtracted from the QCM thermogravimetric analysis test data as a correction.

Evaporation Rate from the QCM

More insight into the number of different species leaving the collected deposit during QCM thermogravimetric analysis and information about their vapor pressures can be obtained by examining the evaporation rates of the species from the QCMs. While, ASTM E 1559 does not specify a data reduction technique for calculating the evaporation rates from a QCM, the rates can be obtained by differentiating the QTGA mass loss data, $m_Q(T_q,t)$, from Equation 11 and taking into account the transmission probability of the aperture in the QCM case through which the evaporating flux leaves from the crystal. The evaporation rate from a QCM (g/cm$^2$ s)is calculated from the following equation:

$$Evaporation\ Rate\ from\ QCM = \frac{\dot{m}_Q(T_q,t)}{W_q} \tag{12}$$

where $W_q$ is the transmission probability for the aperture in the QCM case. This transmission probability is a function of the geometry of the aperture and can be obtained from references 7 and 8. $W_q = 0.89$ for the QCMs used in the Lockheed apparatus.

## DATA EXAMPLE

Results from a typical test are presented below to illustrate the material contamination characterization data provided by the ASTM E 1559 test. The test standard specifies a standard format of tabulated data which facilitates electronic transmittal and archiving of the data. For illustrative purposes all of the proceeding data is presented in a graphical format.

### Material Sample

The material used for this example is Chemglaze Z306 paint, a material commonly used in vacuum applications because of its optical properties. Because of its extensive use by industry, this paint has been tested in a variety of configurations. The data from this test was acquired in support of the evaluation of a new primer.

The material consists of a one-component, flat-black coating with carbon black pigment and polyurethane binder manufactured by Lord Corporation. The primer is produced by Deft Chemical Coatings. The sample consisted of two aluminum foil discs sprayed on one side with Deft primer and Chemglaze Z306. Sample dimensions and weights were obtained throughout the painting process. These data are summarized below in Table 1.

**Table 1 Chemglaze Z306/Deft Primer Samples**

| | Diameter (cm) | Primer Thickness (cm) | Topcoat Thickness (cm) | Substrate Mass (g) | Primer Mass (g) | Topcoat Mass (g) | Total Coating Mass (g) |
|---|---|---|---|---|---|---|---|
| Disc #1 | 4.12 | 0.0013 | 0.0081 | 0.16601 | 0.02392 | 0.10227 | 0.12619 |
| Disc #2 | 4.12 | 0.0013 | 0.0084 | 0.16623 | 0.02475 | 0.10566 | 0.13041 |
| | | | | **Totals** | 0.04867 | 0.20793 | 0.25660 |

The dimensions of the discs give a total sample area of 26.66 cm$^2$. The sample discs were positioned in the effusion cell so that outgassing from the painted faces was not impeded.

## Isothermal Outgassing Test

The isothermal outgassing test was performed per ASTM E 1559 Test Method B since four QCMs with gold electrodes were used. The QCMs were maintained at 80 K, 160 K, 220 K and 298 K. The material sample was at 125°C for a test duration of 24 hours. A post-test weighing of the sample was not made so an *ex situ* TML value was not obtained for this sample.

Figure 3 shows the actual frequency shift on the 80 K QCM and the corresponding mass deposit density (Equation 2) as functions of the test time. This is a typical curve for mass accumulation on a QCM showing a monotonically increasing deposit. At the start of the test (test time = 0) the clean QCM base frequency was about 2768 Hz. This increased by about 1759 Hz over the duration of the test, corresponding to a net deposit on the crystal of about $7.9 \times 10^{-6}$ g/cm$^2$.

Figure 4 gives the TML for the sample as a function of time. These data are obtained by applying Equation 8 to the 80 K QCM mass deposit density data of Figure 3. The $7.9 \times 10^{-6}$ g/cm$^2$ deposited on the QCM corresponds to a TML of 1.277 percent from the sample. Figure 4 also gives the TML data in units of g/cm$^2$ in which the mass loss is normalized with respect to the 26.66 cm$^2$ surface area of the sample. The TML for the sample in these units was $1.229 \times 10^{-4}$ g/cm$^2$.

In order to keep the data presentation concise, the frequency and mass deposit density data are not presented here for the warmer collector QCMs at 160 K, 220 K, and 298 K. However, these data were reduced using Equation 9 to obtain the VCM data shown in Figure 5. As with the TML data, this figure gives the VCM data in units of percent and g/cm$^2$. Figure 5 shows that as the collector QCM temperatures increase the VCM decreases, since the higher volatility species are not able to condense on the warmer QCMs. The VCM for the 298 K QCM shows a maximum after about 7 hours then a subsequent decrease. The deposition on a QCM is the kinetic balance between the total impingement flux and the reevaporation flux of higher volatility species. The constant evaporation rate of a species from the 298 K QCM is temporarily (for the first 7 hours) smaller than the impinging flux of this species from the sample and so a net deposition of the species on the QCM occurs. As this species is depleted from the sample its outgassing contribution to the impingement flux on the QCM is less and at 7 hours the kinetic balance is shifted such that the evaporation rate of the species is larger. This species continues to gradually evaporate from the 298 K QCM until it has been depleted from the QCM deposit. It appears that this point is reached at a test time of about 20 hours.

The total outgassing rate for the sample is shown in Figure 6. This is calculated from the mass deposition rate on the 80 K QCM using Equation 10. In this example, the deposition rate on the 80 K QCM was obtained by performing a point-by-point numerical differentiation of the mass deposit data shown in Figure 3. The outgassing rate for the Chemglaze Z306 sample decreases by three orders of magnitude from $10^{-7}$ to $10^{-10}$ g/cm$^2$ s over the 24 hour test.

## QCM Thermogravimetric Analysis

At the conclusion of the isothermal outgassing test, QTGA was performed per the ASTM standard. Each of the QCMs was heated from its base temperature to 398 K at 1 K/minute. Only the data from the 80 K QCM are presented here, since this QCM accumulates a deposit containing all the species representative of the outgassing flux.

As the QCM is heated the deposit evaporates from the crystal and the QCM frequency decreases. Figure 7 shows the frequency decrease as a function of QCM temperature for the QCM which was at 80 K during the isothermal outgassing test. As was mentioned previously, it is Lockheed practice to subtract the frequency-temperature response for the clean QCM from the measured output signal obtained during the QTGA of a collected deposit. Therefore, the QTGA data presented here show the QCM frequency decreasing to 0 Hz rather than to its original base frequency of several thousand Hz. Equation 11 is used to reduce the frequency data to obtain the mass loss from the QCM during the QTGA. The results of these

calculations are also presented in Figure 7. Inflection points in Figure 7 reveal when a different species is evaporating from the QCM. The relative amounts of the different species in the QCM deposit can be obtained by comparing the mass loss from the QCM due to each species.

The evaporation of a species from the QCM deposit during QTGA is made more apparent by examining the evaporation rate from the QCM. A point-by-point differentiation of the mass loss from the QCM during QTGA is performed at Lockheed to obtain the rate of mass loss from the QCM. These data are then used with Equation 12 to calculate the evaporation rate from the QCM as a function of QCM temperature. These data for the QTGA of the 80 K QCM are presented in Figure 8. As the temperature of the QCM increases the evaporation rate of a species also increases until it reaches a peak when the amount of that species on the QCM nears depletion. Therefore, the slope of the leading edge of a peak or shoulder in an evaporation rate curve is characteristic of the species being volatilized. The various peaks and different leading edge slopes in Figure 8 indicate at least seven distinct groups of species leaving the QCM. These data provide the basis for establishing additional information on the vapor pressures of these species.

## SUMMARY

Material outgassing measurement tests using ASTM E 1559 have been performed in support of various aerospace, electronic and semiconductor oriented companies. These industries are similar in that some of their products operate or are manufactured in a vacuum environment. As the sensitivity of these devices and processes to molecular contamination increases, more detailed characterization of the related construction materials must be obtained.

The ASTM E 1559 test standard is used to characterize the outgassing and deposition kinetics of virtually any material including adhesives, coatings, film and sheet materials, elastomers, composites, and components which can be cut to fit into the effusion cell. Lockheed has also used the test method to measure the vapor pressures of oils and greases. Outgassing rates from $10^{-14}$ to $10^{-5}$ g/cm$^2$ s and Total Mass Loss from samples of 0.0001 to 5 percent have been measured.

## REFERENCES


1. ASTM E 1559, "Standard Test Method for Contamination Outgassing Characteristics of Spacecraft Materials."

2. ASTM E 595, "Standard Test Method for Total Mass Loss and Collected Volatile Condensable Materials from Outgassing in a Vacuum Environment."

3. ASTM F 1227, "Standard Test Method for Total Mass Loss of Materials and Condensation of Outgassed Volatiles on Microelectronics-Related Substrates."

4. A.P.M. Glassford and J.W. Garrett, "Characterization of Contamination Generation Characteristics of Satellite Materials," USAF WRDC/MLBT Final Report WRDC-TR-89-4114, 22 November 1989.

5. A.P.M. Glassford, Lockheed Palo Alto Research Laboratory, "Analysis of the Accuracy of a Commercial Quartz Crystal Microbalance." Thermophysics of Spacecraft and Outer Planet Probes, AIAA Progress in Astronautics & Aeronautics, V. 56, A.M. Smith, Editor, 1977, pp. 175-196.

6. Y.N. Lyubitov, "Calculation of the Directivity Diagrams for Molecular Flow from a Cylinder," in *Molecular Flow In Vessels*, a special report translated from Russian by W.H. Furry & J.S. Woods, Consultants Bureau, New York, 1967, pp. 53-60.

7. P. Clausing, Z. Phys., Vol 66, 1930, pp. 471.

8. S. Dushman, Scientific Foundations of Vacuum Technique, 2nd edition, John Wiley and Sons, Inc., New York, 1962, pp. 94.

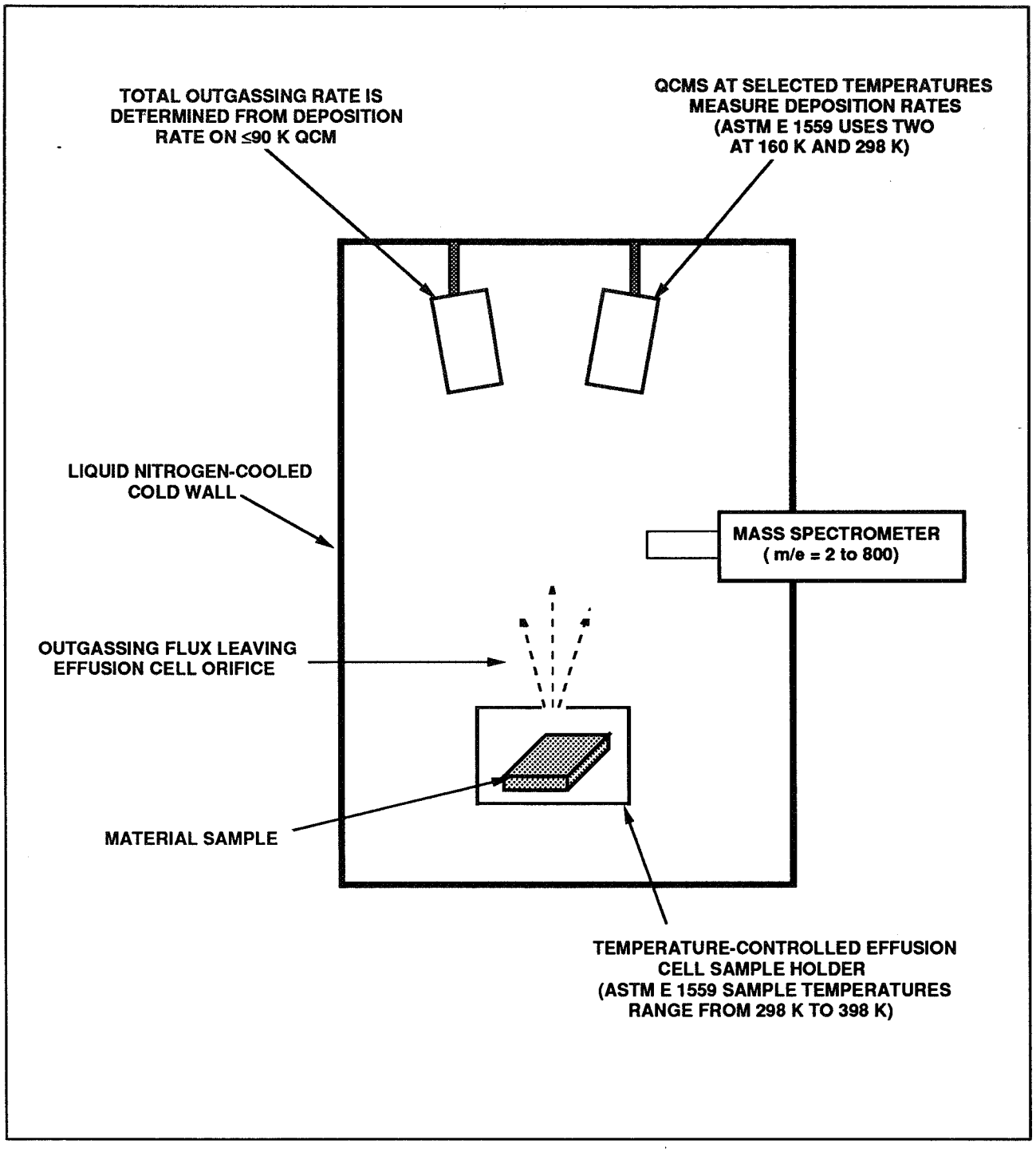


Figure 1. Schematic of the QCM Collection Measurement Method used for ASTM E 1559.

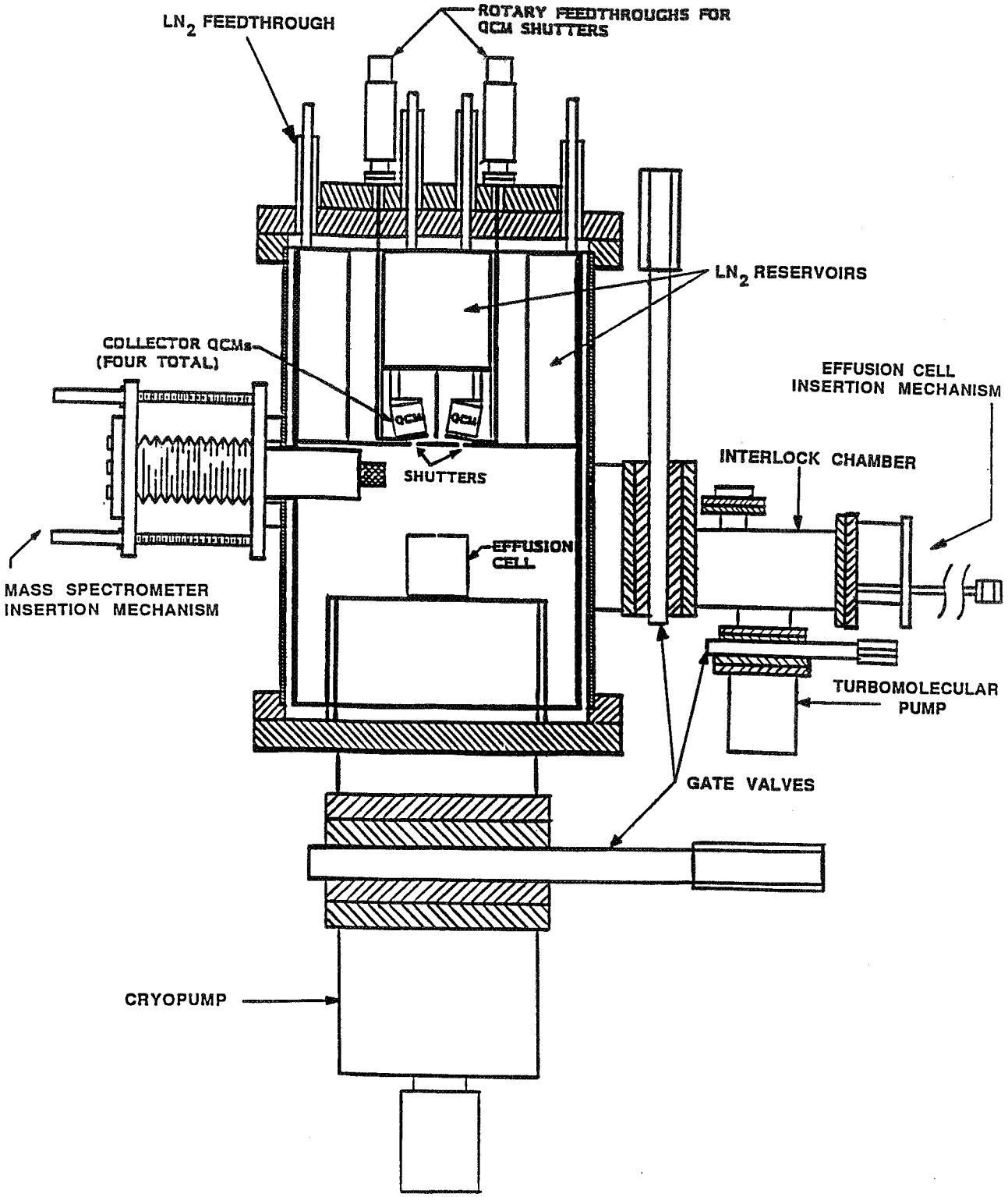


Figure 2. The Lockheed Vacuum Outgassing/Deposition Kinetics Apparatus.

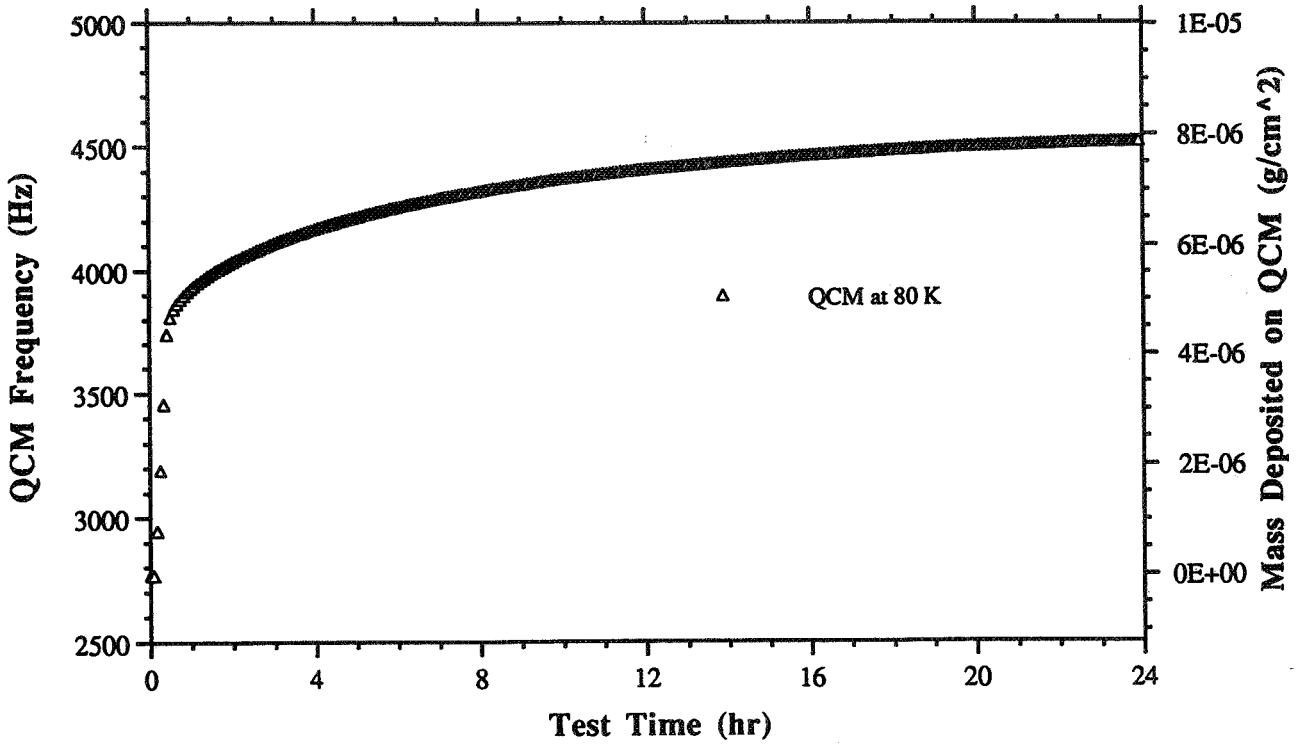


Figure 3. QCM Frequency and Mass Deposited on QCM as a Function of Time for the 80 K QCM during the Isothermal Outgassing Test on Chemglaze Z306/Deft Primer at 125°C.

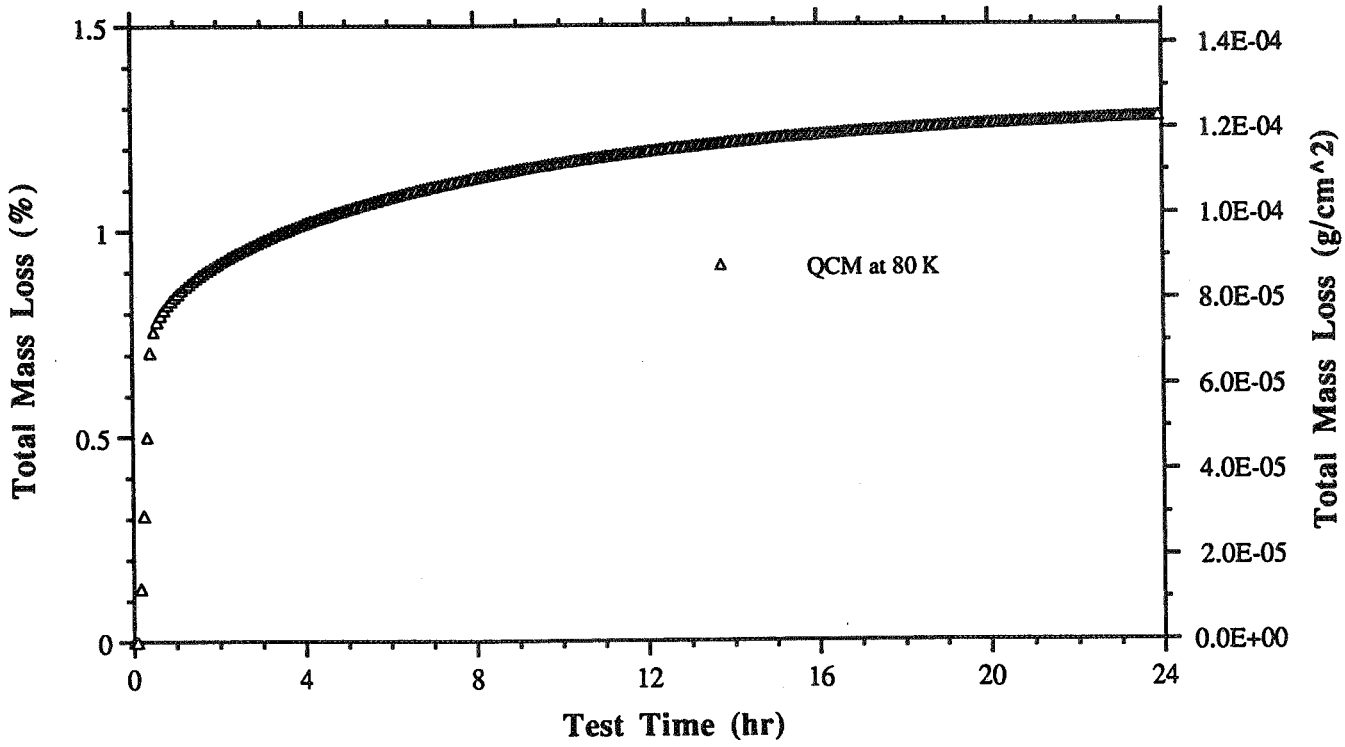


Figure 4. Total Mass Loss from the Sample as a Function of Time during the Isothermal Outgassing Test on Chemglaze Z306/Deft Primer at 125°C.

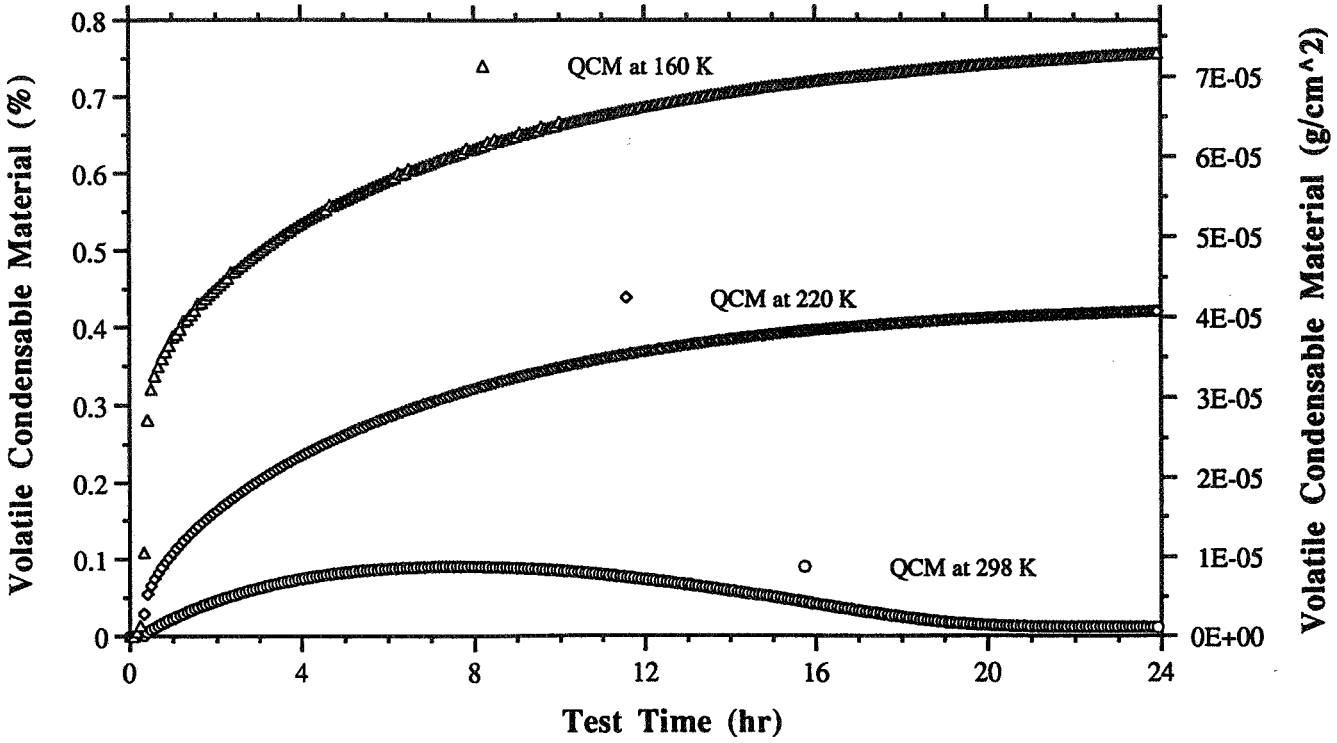


Figure 5. Volatile Condensable Material for QCMs at 160 K, 220 K, and 298 K as a Function of Time during the Isothermal Outgassing Test on Chemglaze Z306/Deft Primer at 125°C.

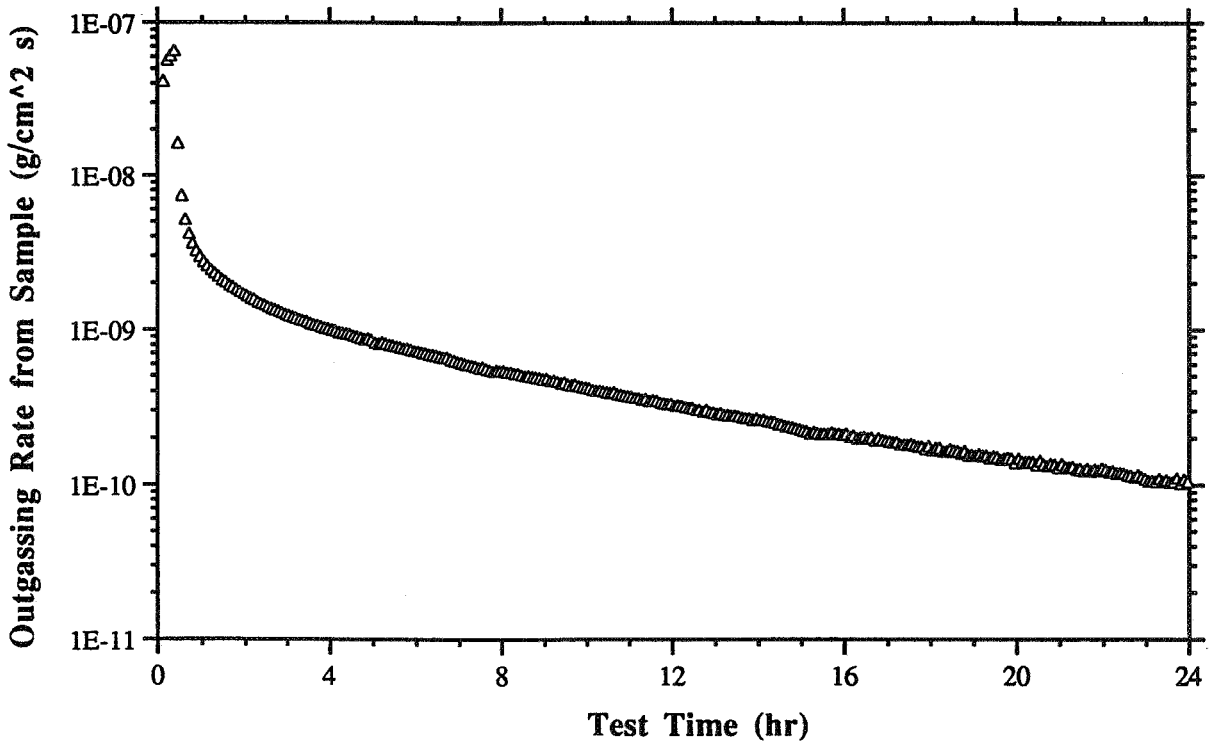


Figure 6. Outgassing Rate from the Sample as a Function of Time during the Isothermal Outgassing Test on Chemglaze Z306/Deft Primer at 125°C.

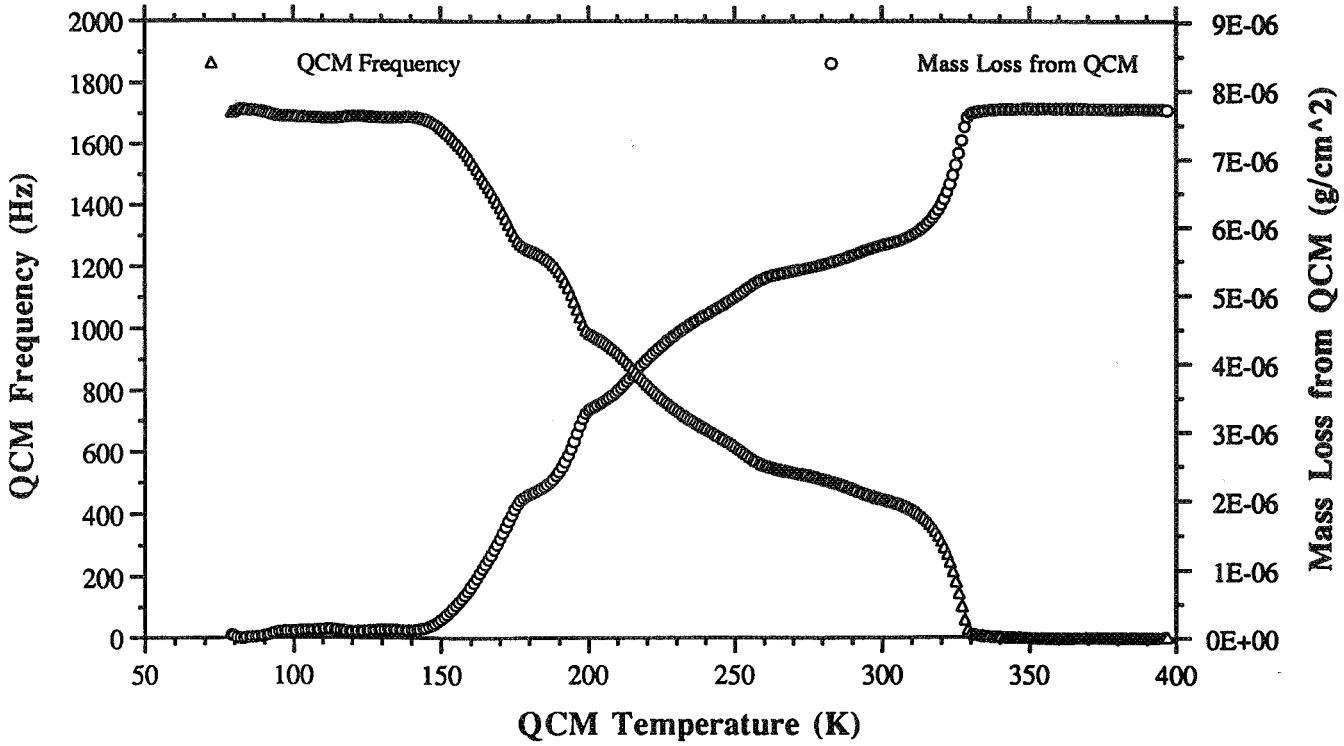


Figure 7. Mass Loss from the 80 K QCM as a Function of QCM Temperature during the QTGA of the Collected Deposit from Chemglaze Z306/Deft Primer at 125°C.

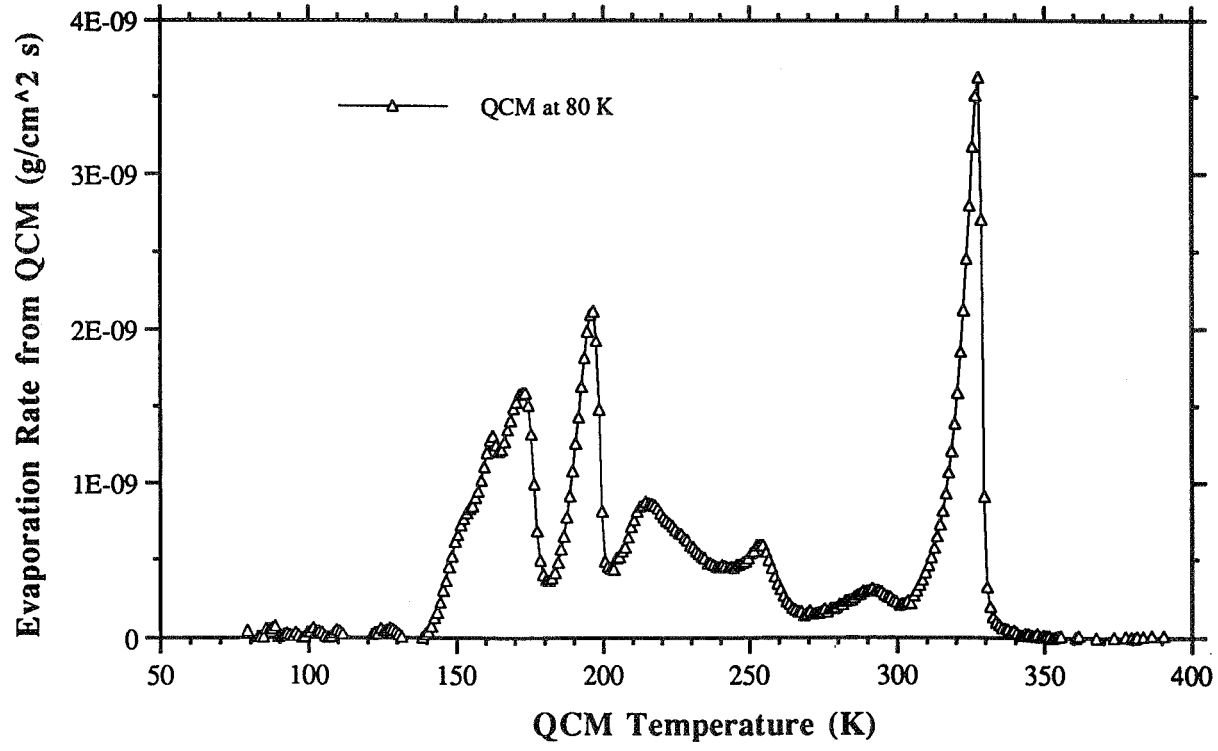


Figure 8. Evaporation Rate from the 80 K QCM as a Function of QCM Temperature during the QTGA of the Collected Deposit from Chemglaze Z306/Deft Primer at 125°C.

# SELF CONTAMINATION EFFECTS IN THE TAUVEX UV TELESCOPE: GROUND TESTING AND COMPUTER SIMULATION

Y. Lifshitz, Y. Noter, E. Grossman, L. Genkin, M. Murat
Soreq NRC, Yavne 81800, Israel

N. Saar, A. Blasberger
El-Op Electrooptics Industries Ltd.
P.O.Box 1165
Rehovot 76111, Israel

## ABSTRACT

The contamination effects due to outgassing from construction materials of the TAUVEX (Tel Aviv University UV Telescope) were evaluated using a combination of ground testing and computer simulations.

Tests were performed from the material level to the system level including:

- High sensitivity CVCM ($10^{-3}$%) measurements of critical materials.
- Optical degradation measurements of samples specially contaminated by outgassing products at different contamination levels.
- FTIR studies of chemical composition of outgassed products on above samples.
- High resolution AFM studies of surface morphology of contaminated surfaces.

The expected degradation of TAUVEX performance in mission was evaluated applying a computer simulation code using input parameters determined experimentally in the above tests. The results have served as guidelines for the proper selection of materials, cleanliness requirements, determination of the thermal conditions of the system and bakeout processes.

## 1. INTRODUCTION

Contamination during mission due to outgassing of spacecraft materials is a major failure mode of space optical systems in general and of UV optical systems in particular[1]. The contamination levels accumulated on spacecraft surfaces are very often evaluated for specific space projects[2-4]. The degradation of the system's optical performance is then calculated[4], taking into account experimental relations between contamination levels and transmission losses. The present paper focuses on the degradation of the optical performance of TAUVEX due to outgassing in mission for a simplified geometry but for the actual materials and temperature profiles. The study gives a critical review of the system's design as far as contamination in mission is concerned, attempting to assure that its optical performance would be within specification limits.

The work consists of two main phases: (a) contamination measurements at the material level providing input data for the second phase and, (b) Monte Carlo calculations of the transmission losses of TAUVEX vs. time after launch.

This paper is thus organized in two parts corresponding to the above phases.

# PART I - CONTAMINATION MEASUREMENTS AT THE MATERIAL LEVEL

## 2. EXPERIMENTAL

### 2.1 Materials and Test Samples

Several types of materials were selected to represent typical contamination sources:

(i) Two critical materials that were identified to be the two major possible contamination sources for TAUVEX: (a) the graphite/ester cyanate composite structural parts, and (b) the silicone rubber that serves as a sealant in several locations of the telescope.

(ii) Two other materials that were studied to evaluate the influence of their chemical nature on the contamination effects (using the same contaminant thickness): (a) Solithane 113, a typical polyurethane based elastomer used as a thermal conductive conformal coating, and (b) a "Buna N" O-ring, a butadiene acrylonitrile polymer, a typical elastomer with a high contamination potential.

Various test plates on which the contamination products were deposited were used. For UV and visible transmission measurements $CaF_2$ and quartz plates were chosen. $CaF_2$ is transparent down to 130nm while quartz is transparent only down to about 200nm. The quartz surface is however smoother, a fact which is beneficial for atomic force microscopy (AFM) measurements. For FTIR measurements NaCl and germanium plates were applied.

The contaminated samples were prepared using a standard micro VCM (Volatile Condensable Materials) outgassing measuring system (conforming to the ASTM E-595[5] method). The contaminating materials were heated to 125°C for 24 hours under vacuum conditions ($p<10^{-6}$torr). The outgassed condensable contaminants were collected on test plates kept at 25°C. The areal contamination density (or thickness) was determined by precise ($\pm 1\mu g$) measurements of the weight gain of adjacent collector plates exposed to the same heated materials simultaneously with the test plates.

### 2.2 Optical Measurements

Optical measurements (190nm-800nm) were performed using a diode array 8452 Hewlett Packard spectrophotometer. Vacuum UV (VUV) measurements will be performed when a VUV sprectrophotometer is available. Since the contamination was nonuniform, 8mm diameter slits were employed for the optical and FTIR measurements (paragraph 2.4) at several (~5) different positions (to achieve an averaged value of the contamination effects).

### 2.3 Atomic Force Microscopy (AFM) Measurements

The AFM measurements were performed under ambient conditions using a Digital Instrument Nanoscope II system. The surface morphology of the test samples (pristine and contaminated samples) was measured with a resolution up to 1nm. The measurements were performed using the minimal force possible since the adherence of the

contamination to some of the test plates was very poor and the AFM probe could displaced the contamination molecules. At present best results were obtained for $CaF_2$ test plates having stronger adhesion compared to other substrates.

## 2.4 FTIR Measurements

FTIR measurements were performed using a Nicolet model 740 system. A 8mm diameter slit was used and several measurements were performed for each test sample at different locations, applying the same method adopted for the optical measurements in order to overcome the problem of the nonuniformity of the contaminant distribution on the test samples.

## 2.5 CVCM (Collected Volatile Condensable Materials) Measurements

CVCM measurements were performed using a standard micro VCM system conforming to the ASTM E595 method. The accuracy of the standard CVCM measurements is $5 \times 10^{-3}$%. This accuracy is insufficient for the present project. A special adaptor enabling the introduction of 3g of the tested materials to the heated crucible (10 times larger than in the standard method) was developed, achieving an accuracy of $5 \times 10^{-4}$%. The equivalence of the extended method to the standard one was confirmed by testing high CVCM materials using the two methods. The same system was used for preparation of contaminated test samples as described above.

# 3. RESULTS

## 3.1 Optical Measurements

Optical transmission measurements were performed on test plates with different contamination thicknesses for the four contaminated materials mentioned before. Typical spectra of plates with three different thicknesses of outgassing products of graphite/ester cyanate are shown in Fig. 1. The optical measurements of all contaminated test plates revealed loss of transmission characterized by:

1) loss of transmission for the entire spectrum (190-800nm) with different absorption peaks for different materials.
2) all test samples exhibited an absorption peak at ~206nm.
3) the transmission loss (or the optical density $OD=\log_{10} I_0/I_t$) tends to increase with the weight of the contaminating material but the behavior is highly irregular, probably due to the nonuniformity of the contamination layer.

VUV measurements were available only for Solithane 113. Again, a strong absorption peak at $\lambda$=206nm was observed, with a smaller peak at $\lambda$=165nm. This result suggests that the 206 nm absorption peak represents a conservative measure of the transmission losses for the spectral region of 140nm-280nm relevant for TAUVEX (for a variety of materials).

## 3.2 AFM Measurements

Reliable AFM measurements were performed at present time only with $CaF_2$ test plates contaminated with outgassing products of graphite/ester cyanate and Solithane 113. In both cases the contaminated area was irregular and consisted of randomly dispersed islands (Fig. 2).

## 3.3 FTIR Measurements

The FTIR measurements exhibited absorption peaks that characterize the outgassed products (OP) of the contaminating materials. The graphite/ester cyanate OP exhibit the typical absorption peak of hydrocarbons at $\lambda$=2925cm$^{-1}$ and a peak at $\lambda$=1735cm$^{-1}$ which is typical of esters. The OP of the silicon rubber exhibits peaks at 805, 1026, 1090, 1260cm$^{-1}$ which are indicative of methyl silicones and at 2963cm$^{-1}$ which was not identified. The OP of Solithane 113 showed peaks at 1465, 1735 and 2925cm$^{-1}$ indicating a hydrocarbon/ester nature of the contaminant. The intensities of the peaks can be translated to contamination areal densities using published calibration curves [6]. This option was found to be important especially for graphite/ester cyanate where the CVCM values were lower than the detection limit of our system.

## 3.4 CVCM Measurements

The CVCM of the two critical materials of TAUVEX (graphite/ester cyanate and the silicone rubber) were precisely measured. The CVCM of the graphite/ester cyanate composite is less than the detection level (CVCM < 5 x $10^{-4}$%) while for the silicone rubber an average value of CVCM = 0.028% was determined. The measured CVCM were used also for evaluation of the contamination level of the test plates.

# 4. DISCUSSION

The purpose of the contamination measurements was to establish the correlation between the contamination areal density and the optical transmission loss. This correlation is needed as an input parameter when evaluating the optical degradation of TAUVEX due to molecular contamination during mission. Complementary studies were performed aiming at a better understanding of the contamination buildup on the optical surfaces.

If one assumes a linear correlation between the incremental transmission loss dI and an incremental areal contaminant density dC then

$$dI/I = a\,dC$$

or

$$I_t = I_0\, e^{-aC}.$$

If $\alpha$ is defined as $\alpha = a\,(\log_{10} e)$, then the optical density $OD = \log_{10}(I_0/I_t)$ is given by $OD = \alpha \,.\, C$.

A linear correlation between the optical density and the contaminant areal density is thus expected. In our previous work [7] performed with Solithane 113 and "Buna N" O ring, such a correlation was indeed obtained and the linear coefficient $\alpha$ was derived and used for the calculation of the expected optical degradation of TAUVEX. In the present work two independent measurements were used in order to evaluate the contaminant areal density C: (i) the measured CVCM value of the contamination source (ii) the FTIR peak intensity using conventional calibration curves. For both methods no linear correlation between OD and C was found for the two critical materials of TAUVEX (graphite/ester cyanate and silicone rubber). Moreover, different $\alpha$ values were obtained for different contaminants for similar contamination areal densities. The UV and visible OD spectra had different absorption peaks for different materials except a common peak at 206nm that can serve for a conservative evaluation of TAUVEX performance. The AFM analysis indicates that the contamination builds up in an irregular way, i.e. by chaotically dispersed island growth, rather than a continuous smooth layer. This result may explain the nonlinear dependence of OD on C.
The OD spectra indicates some material dependent absorption, but scattering due to the rough nature of the contamination is also possible. The IR spectra apart from being used for the $\alpha$ values also reveals the chemical nature of the deposits (i.e. a hydrocarbon type contaminant has a strong absorbtion band at 2925cm$^{-1}$, a methyl silicone type contaminant at 805cm$^{-1}$ etc.). These results suggest that the best input data for evaluation of the optical degradation in mission is a table of the maximal OD's (i.e. at $\lambda$ = 206nm) vs. C and not a single value of $\alpha$ as was done in the previous work.

# PART II. MONTE CARLO CALCULATIONS OF THE TRANSMISSION LOSSES OF TAUVEX OPTICAL SYSTEM VS. TIME

## 5. THE SOREQ CODE FOR CALCULATION OF CONTAMINATION

Calculations of outgassing induced contamination of spacecraft surfaces are performed by either analytical models[2,8] or computer codes[9,10,11]. This section briefly describes a code that was developed for the present work. The Soreq 3D code for evaluation of the contamination of spacecraft systems due to outgassing follows the history of contaminant molecules. The approach is based on classical trajectories with initial conditions randomly selected applying a Monte Carlo technique. The initial distribution of the contaminant molecules is introduced as an input to the program. Each molecule represents a finite fraction of the contaminant material and has a probability of escaping its initial position (depending on its outgassing "kinetic" properties[2,8,9] and the temperature profile of the system). The direction of the escaping molecule is randomly chosen by the program and it moves in a straight line until it impinges on the next surface where it can either be trapped or reflected according to its "sticking probability"[2,8,9]. The program follows the individual trajectory of each of the preselected number

of different molecules. The number of contaminant molecules on each surface of the system is counted at certain specific times thus giving the contaminant molecules areal density vs. time. The input parameters are: (i) the geometry of the system, (ii) the temperature profile of the surface, (iii) the quantities and kinetic constants of the contaminants, (iv) the initial distribution of the contaminants in the system, and (v) the definition of the sensitive surfaces for which the contaminant areal distribution should be calculated. The output files include the contaminant areal density (C) of each individual surface vs. time. The data derived in part I (transmission loss vs. C for different thicknesses and different materials) was introduced to the program and calculations of the transmission losses of each optical surface as well as the total loss of the system are also available.

# 6. BASIC ASSUMPTIONS AND INPUT PARAMETERS

## 6.1 TAUVEX Geometry

The TAUVEX telescope system consists of three boresighted 20 cm aperture telescopes mounted in a rectangular housing as shown in Fig. 3. All three telescopes have an identical Ritchey - Chretien optical layout. Each telescope consists of nine optical surfaces which are sensitive to contamination effects: the primary mirror, the secondary mirror, the first correction lens (2 surfaces), the second correction lens (2 surfaces), the filter (2 surfaces) and the detector window. A detailed description of TAUVEX is given elsewhere[12]. For the present work, a simplified geometry was used. Only one telescope was taken into account assuming that the contaminant distributions in each separate telescope would be the same (to a good approximation) as in the entire system. Fig. 4 describes the simplified geometry assumed for a single telescope. Three sensitive surfaces were evaluated: (i) the primary mirror (ii) the secondary mirror (iii) the front lens. The pumping apertures leading to the other optical surfaces are so small that they cannot be treated by the computerized code, but are treated with a good accuracy by simplified analytical calculations[2,8].

## 6.2 Modes of Operation and Temperature Profiles

TAUVEX temperature profiles are affected by its operation modes. TAUVEX orbiting duty cycle consists of two main phases: (i) operational phase in which it serves for astronomical observations (ii) survival mode (10 h duration) when it passes through the earth radiation belts. At this mode, the power is off and the telescope cover may be closed. During the operational phase different telescope orientations may result in "hot" and "cold" modes. Additional "outgassing mode" is planned for the beginning of TAUVEX flight mission. Special heaters attached to the telescope optical elements are operated, aiming at a forced outgassing and cleaning of these elements during the first weeks in space. This mode may be operated also further in mission, in case of severe optical degradation due to contamination. Table 1 gives the different temperature profiles of TAUVEX calculated by El-Op for the above modes. This table served as input data for the present work for evaluation of specific (extreme) conditions. Intermediate profiles are however also possible. It can be immediately observed that the outgassing cycle only

affects the temperature of the optical surfaces, but does not affect the main body of the telescope (compared to operational conditions) for hot conditions and only slightly affects the temperature of the body for cold (nominal) conditions.

## 6.3 Materials

In this section the critical materials, their quantities and outgassing properties are presented.

### 6.3.1 Critical materials of TAUVEX

TAUVEX was specially designed to be constructed mostly from inorganic (i.e. metals and ceramics) materials, that are contaminant free as far as outgassing is concerned. All the organic materials used for TAUVEX were however selected to meet the ASTM E595 specifications[5], were listed, and a budget of their potential contaminant hazard was prepared. It was found that the critical materials, contributing to more than 95% of the total potential contaminant weight are: (i) the graphite/ester cyanate composite structural parts and (ii) the silicone rubber from which two sealings pads are made: an external sealing pad between the shield and the external cover, and an internal one between the bezel and the shield.

### 6.3.2 Quantities of critical materials and potential contaminant hazard

The total weight of the graphite/ester cyanate in the system is 250g and its CVCM is less than $5 \times 10^{-4}$% as derived in part I. The total weight of the silicone rubber is 220g and its measured CVCM equals 0.028%.

### 6.3.3 Outgassing properties (kinetic constants)

The kinetic constants of the critical materials for TAUVEX calculations were taken as equal to those of similar materials cited in other works. For graphite/ester cyanate an activation energy $E_b$ = 11.3 kcal/mole and a residence time $\tau$(298°C) = 26.6 h cited [12,13] for graphite epoxy were adopted, while for the silicone rubber two sets of values for two different silicone based polymers were used (for PSG - 120 D[9] $E_b$ = 8.35 kcal/mole, $\tau$(298°K) = 91.5h, and for Methyl-Phenyl 3-siloxane[2] $E_b$ = 25 kcal/mole and $\tau$(298°C) = 77.8 h). Only the higher contamination levels obtained using the PSG - 120 D values are presented in this work.

## 6.4 Maximal Permissible Contamination Level

The maximal allowable contamination levels for NASA and ESA projects range from $10^{-7}$ g/cm$^2$ to $10^{-6}$ g/cm$^2$ [4,14]. These levels are derived from optical properties losses. For a level of $10^{-7}$ g/cm$^2$ our own data for $\lambda$ = 206 nm show a transmission loss of 4% for the graphite/ester cyanate and 2% for the other meassured materials. Since the TAUVEX telescope has 9 optical surfaces it follows that even contamination levels of

$10^{-7}$ g/cm$^2$ on all surfaces is associated with a total transmission loss of ~30% (it may be larger if reflections are taken into account since a contaminant on a reflecting surface absorbs light twice[15], i.e. should cause a higher transmission loss per $10^{-7}$ g/cm$^2$).

A maximal permissible contamination level of $10^{-7}$ g/cm$^2$ thus seems logical and not too conservative for TAUVEX. The following evaluations will consider this value for the elucidation of the necessary CVCM values for the graphite/ester cyanate and the silicone rubber.

# 7. RESULTS

## 7.1 General

Calculations of contamination levels vs. time were done for the following operational modes: (i) nominal (cold) operational conditions, (ii) hot operational conditions, (iii) forced outgassing and (iv) survival conditions with a closed cover. As an example, only the first two will be presented here, since they are the most important modes of operation in which the TAUVEX telescope is used for astronomical observations. The calculations will be presented using CVCM = 5 x $10^{-4}$% for graphite/ester cyanate and CVCM = 0.028% for the silicone rubber.

## 7.2 Contamination Levels for Nominal (Cold) Operational Conditions

Figure 5 shows the contamination levels accumulated vs. time after launch on the three main optical surfaces of TAUVEX, i.e. the primary mirror, the secondary mirror and the front lens. The contamination initially increases with time, reaches a maximal value of ~7 x $10^{-8}$ g/cm$^2$ after ~800 h and then decreases with time to reach the $10^{-8}$g/cm$^2$ level in ~4000h. The contamination is concentrated mainly on the primary mirror while the levels on the secondary mirror and the lens are much lower. The main contaminant is graphite/ester cyanate while the contribution of silicone rubber is negligible. Since the maximal allowable areal contaminant density is $10^{-7}$g/cm$^2$ it follows that the assumed CVCM of 5 x $10^{-4}$% for graphite/ester cyanate is in accordance with this criterion.

## 7.3 Contamination Levels for Hot Operational Conditions

The contamination levels for the hot operational conditions are presented in Fig. 6 for graphite/ester cyanate and in Figs. 7 and 8 for silicone rubber. The maximal contaminant levels are ~5 x $10^{-7}$g/cm$^2$ and ~1 x $10^{-7}$g/cm$^2$ respectively and the time to reach the maximal values is ~80 h for graphite/ester cyanate and ~800 h for the silicone rubber. Initially it is the graphite/ester cyanate that contributes to the contamination, but after 800 hours the silicone rubber dominates. The CVCM values needed to achieve the allowable contamination level of $10^{-7}$g/cm$^2$ are $10^{-4}$% for graphite/ester cyanate and the measured 0.028% for the silicone rubber respectively.

# 8. DISCUSSION

The contamination levels on the TAUVEX main optical surfaces were calculated for the different operational modes taking into account two critical materials, i.e. graphite/ester cyanate and silicone rubber (in two locations.) It should be noted that the actual operational conditions and contamination levels can be intermediate between the different modes defined in paragraph 6.2 that correspond to extreme conditions. Calculation of the contamination levels of graphite/ester cyanate shows that the CVCM value for the hot operational mode should be kept below $10^{-4}$ % and for the cold mode below $5 \times 10^{-4}$% in order to guarantee a contamination level lower than $10^{-7}$g/cm$^2$. The graphite/ ester cyanate parts were specially baked out at 90°C for 72h under vacuum conditions to guarantee a minimal CVCM value. However, we currently cannot measure the CVCM value with the proper accuracy ($10^{-4}$%). For the silicone rubber the measured CVCM value of 0.028% is sufficient to guarantee this contamination level.

Fig. 9 exhibits the transmission loss of TAUVEX for the hot mode due to its three main optical surfaces, assuming three different CVCM values (the recommended $10^{-4}$ %, $2\times10^{-4}$% and $5\times10^{-4}$% which is the detection limit of our sustem) of graphite/ester cyanate and the measured CVCM value of silicone rubber (0.028%). The calculations were performed for $\lambda$ = 206 nm using the experimental correlation between contamination level and transmission loss (paragraph 3.1). For contamination areal density up to $5\times10^{-7}$ g/cm$^2$, $\alpha$ values of $1.78\times10^4$ cm$^2$/g and $8.9\times10^3$ cm$^2$/g for graphite/ester cyanate and silicone rubber respectively were assumed. First the transmission loss of each optical surface was calculated, considerering both the contributions of the graphite/ester cyanate and the silicone rubber contaminants. Then the overall transmission loss was calculated by multiplying the transmission values of the three surfaces. In Fig. 9 it is assumed that each contaminated mirror surface contributes only once to the transmission loss. This leads to a maximal ~8% reduction in transmission for the recommended CVCM value. One may however consider a loss mechanism in which the light is alternated twice[15] (upon incidence and upon reflection). Using this assumption the maximal transmission loss for the hot mode is ~12%. Fig. 9 also indicates that even for the worst case (CVCM value of $5\times10^{-4}$%), the maximal transmission loss will be 30%, but within 1 month the surfaces will be cleaned by self outgassing so that the transmission loss will be lower than 10%. For twice the recommended CVCM ($2\times10^{-4}$%) the maximal transmission loss of 15% will be reduced to below 10% within 3 weeks. Fig. 10 shows the TAUVEX total transmission loss in the cold mode, assuming the recommended CVCM=$5\times10^{-4}$% for graphite/ester cyanate and the measured value of 0.028% for the silicone rubber. The maximal loss is 3% (~5% when each mirror is accounted twice). The thermal-vacuum experiment which is planned in the near future will supply evidence for the actual transmission vs. time behavior of the TAUVEX system.

The calculations assume kinetic outgassing parameters adopted from the literature (activation energies and residence times). The literature values however vary and may be very different from the actual values of the materials used in TAUVEX. Calculations of the contamination levels of the silicone rubber using two very different activation

energies (8.35[9] and 25[2]kcal/mole) taken from different sources however show that similar maximal areal contamination densities are achieved and only the time scale of the evolution of the contamination (both increase and decrease periods) is significantly affected by the variation of the activation energy.

The calculations treated only the three main optical surfaces. The other optical surfaces are located in regions into which the flow of outgassing products from the main TAUVEX volume is negligible. The contamination of these surfaces should be treated by a much simpler analytical approach[2,8] assuming an even distribution of all potential contaminants on the system surfaces (a most conservative assumption). For TAUVEX the transmission loss due to these extra surfaces is less than 10% as long as the CVCM of the contaminating structural materials of the detector unit is kept below 0.01%.

## 9. SUMMARY AND CONCLUSIONS

The present work can be summarized as follows:

a) The contamination products of two TAUVEX materials (graphite/ester cyanate and silicone rubber) and two other materials were evaluated using CVCM, optical, AFM and FTIR measurements.

b) Optical measurements were performed in the 190-800nm range for all contaminants with additional VUV (140-190 nm) measurements for Solithane 113 contaminants. All contaminants showed an absorption peak at 206 nm. Optical degradation could be best described by a table of OD's (optical densities) vs. areal concentrations rather than a linear dependence between the two.

c) A 3D Monte Carlo program for the calculation of contamination due to outgassing of spacecraft materials was developed and applied for TAUVEX.

d) An evaluation of the degradation of the performance of TAUVEX optical surfaces due to self contamination by outgassing in space was carried out for different operational modes.

The main conclusions of the above evaluation are:

a) Strict CVCM values are needed for the graphite/ester cyanate ($10^{-4}$% for the hot operational mode and $5x10^{-4}$% for the cold operational mode).

b) Since no contaminants were found in outgassing tests of graphite/cyanate ester, its CVCM is lower than $5 \times 10^{-4}$% (detection limit of our outgassing system). This is acceptable for the cold mode. The behavior during hot mode operation will be tested in a future thermal-vacuum test.

c) The measured CVCM value of the silicone rubber (0.028%) is acceptable in all modes.

**Acknowledgment:** This work was partially supported by the Israeli Space Agency (ISA), the Israel Ministry of Science and the Israel Ministry of Absorption. The authors are gratful to Dr. L. Singer of ISA for helpful discussions and support.

## 10. REFERENCES


(1) C.R. Maag, "Effects of the Contamination Environment on Surfaces and Materials" in "proceeding of NASA/SDIO Space Environmental Effects on Materials Workshop", June 28 - July 1, Hampton, Va, 1988, NASA, CP-3035 part I, 353, 1989.

(2) J.J. Scialdonne, "A Preliminary Assessment of the Self Induced Environment and Contamination of the Space Telescope", proc. of Symp. on Spacecraft Materials in a Space Environment, Toulouse, 8-11 June 1982, ESA SP-178, 107, 1982.

(3) L.E. Mauldin, W.P. Chu, "Optical Degradation due to Contamination on the SAGE/SAGE II Spaceflight Instruments", SPIE vol. 338, 58, 1982.

(4) S. Volf, a. Zwaal, "Hipparchos Cleanliness Policy", Proc. of the 3rd European Symp. on Spacecraft Materials in Space Environment, Noordwijk, 1-4 Oct., 1985, ESA SP 232, 49, 1985.

(5) ASTM E595-90, "Standard Test for Total Mass Loss and Collected Volatile Condensable Materials from Outgassing in a Vacuum Environment", ASTM Annual Book of Standards.

(6) ESA PSS-01-705, "The detection of organic contamination of surfaces by infrared spectroscopy", October 1982.

(7) G. Nahor, M. Baer, M. Anholt, M. Murat, Y. Noter, Y. Lifshitz, N. Saar, O. Braun, "Degradation of TAUVEX optical system performance due to contamination by outgassed spacecraft materials", SPIE Vol. 1971, 288, 1992.

(8) J. Dauphin, "Outgassing and Contamination Predictions", Proc. of Symp. on Spacecraft Materials in a Space Environment", Toulouse, 8-11 June 1982, ESA-SP-178, 55, 1982.

(9) J. Guillin, J.F. Gory, "Simulation de la Contamination Vol par le Logiciel CONTAMI 2", ibid, p. 81.

(10) C. Koeck, M. Frezet. "Calculation of Environmental Effects on Spacecraft Surface Using Monte Carlo Technique - Application to Contamination and Atomic Oxygen", 4th Symp. on Spacecraft Materials in a Space Environment, September 6-9, 1988, CEPADUES Press, 263, 1989.

(11) A. de Leuze, G. Barbier, "Models and Analysis Tools for the Columbus Contamination Environment", Proc.of ESA workshop on Space Environment Analysis, ESTEC, Noordwijk, 9-12 October, 1990, ESA WPP-23, p. 3.1.

(12) J.M. Topaz, O. Braun and N. Brosch, "The TAUVEX UV Astronomical Telescope", SPIE Vol. 1764, 94, 1992.

(13) D.J. Tenerelli, ed. "Contamination Control Working Group (CCWG) Meeting Notes", Lockhead Missiles & Space Co. inc., Space System Division, LMS/D79/3009 Org. 64-10, B579, Feb. 2, 1981.

(14) R. Hansen, C.R. Maag, "Development of Contamination Requirement for Spacecraft Instrumentation", SPIE Vol. 777, 68, 1987.

(15) O.F. Hall, "Current Flight Results from the P78-2 (SCATHA) Spacecraft Contamination and Coatings Degradation Experiment", Proc. of Symp. on Spacecraft Materials in a Space Environment, Toulouse, 8-11 June 1982, ESA - SP - 178, 143, 1982.

Table 1. - Temperature profiles of TAUVEX at different operational modes.

| Mode | Outgassing | | Survival | Operational | |
|---|---|---|---|---|---|
| | Nominal | Hot | | Cold | Hot |
| Primary mirror | 45 | 45 | -10 | -10 | 30 |
| Secondary mirror | 45 | 45 | -10 | 10 | 35 |
| Lens | 30 | 30 | 20 | 20 | 30 |
| Filter | 30 | 30 | 0 | 0 | 35 |
| Sensor | 30 | 30 | 10 | 10 | 35 |
| Bezel | 30 | 30 | -10 | 0 | 30 |
| Shield | -40 | 85 | -40 | -90 | 85 |
| Secondary mirror baffle | -15 | 35 | -35 | -40 | 35 |
| Primary mirror baffle | -5 | 35 | -30 | -30 | 35 |
| Cover | - | - | -40 | - | - |
| Struts | -20 | 30 | -20 | -20 | 30 |

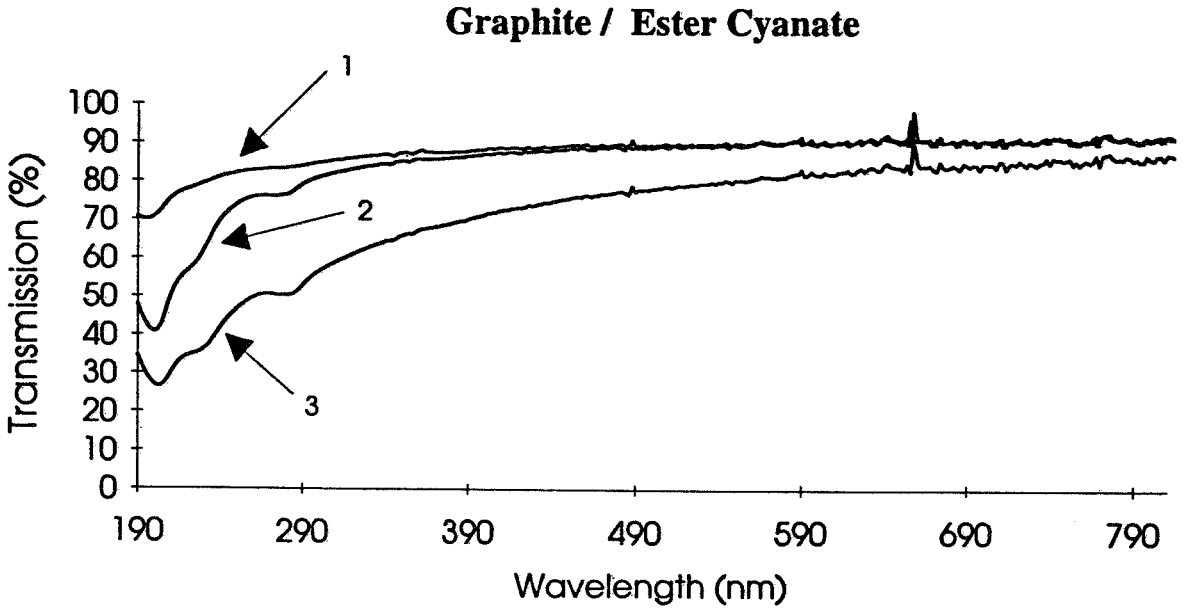


Fig. 1. Typical spectra of $CaF_2$ test plates contaminated with outgassing products of graphite/ester cyanate. Contaminant concentrations are: (1) ~$3x10^{-7}$ g/cm$^2$, (2) ~$5x10^{-7}$ g/cm$^2$, (3) $1.2x10^{-6}$ g/cm$^2$.

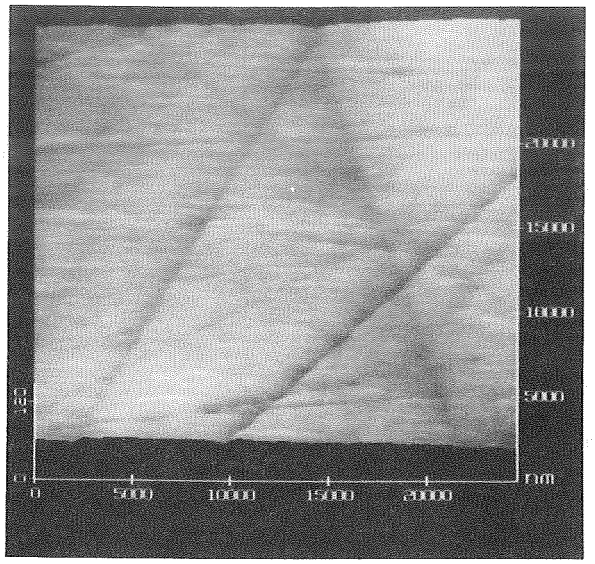


a

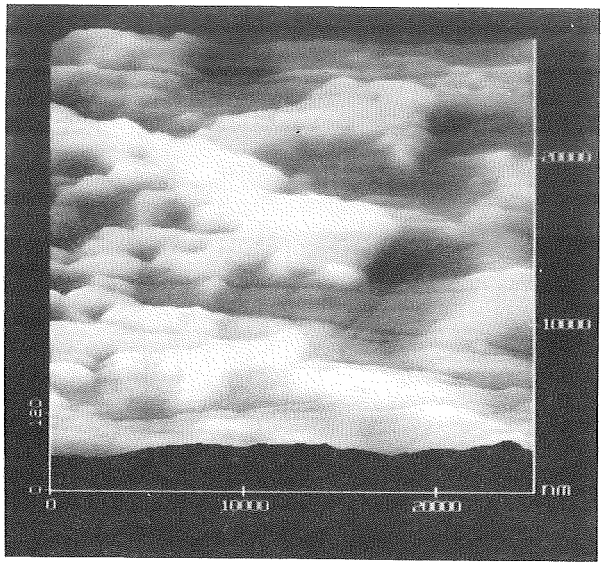


b

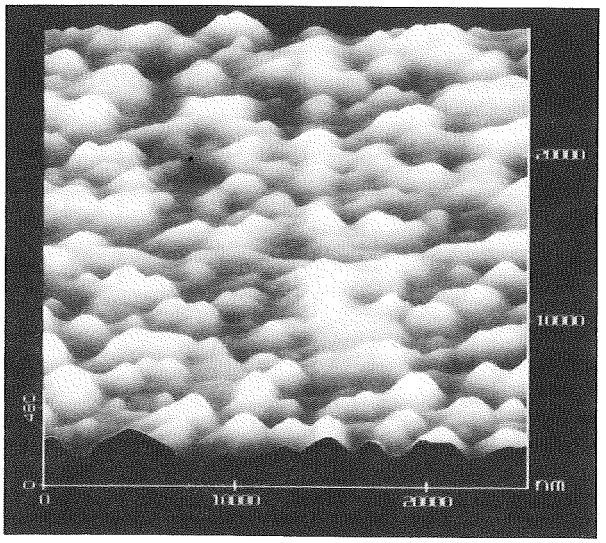


c

Fig. 2. AFM measurements of $CaF_2$ test plates contaminated with outgassing products of graphite/ester cyanate. Image size is 25 by 25 microns. Vertical dimension is 120 nm for (a) and (b) and 480 nm for (c).

(a) Clean $CaF_2$, (b) $CaF_2$ contaminated with ~$1.5 \times 10^{-6}$ g/cm$^2$, (c) $CaF_2$ contaminated with ~$5 \times 10^{-6}$ g/cm$^2$.

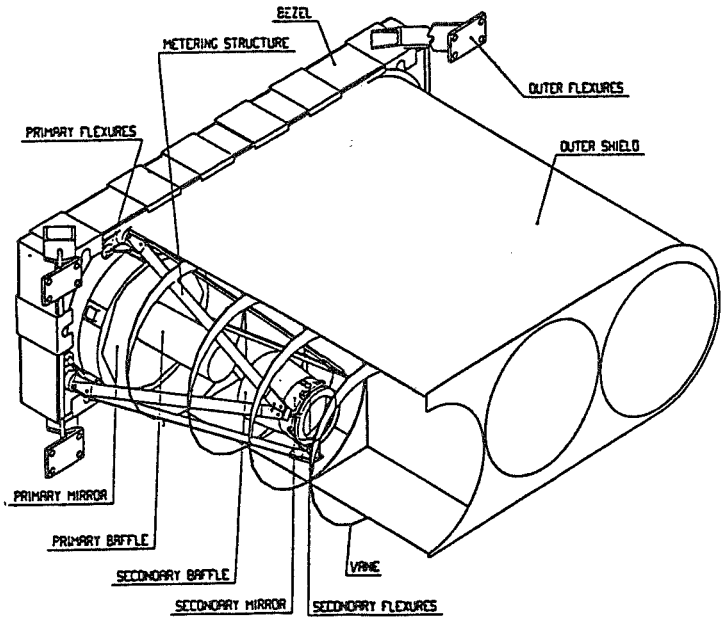


Fig. 3. TAUVEX - A view of the optical module.

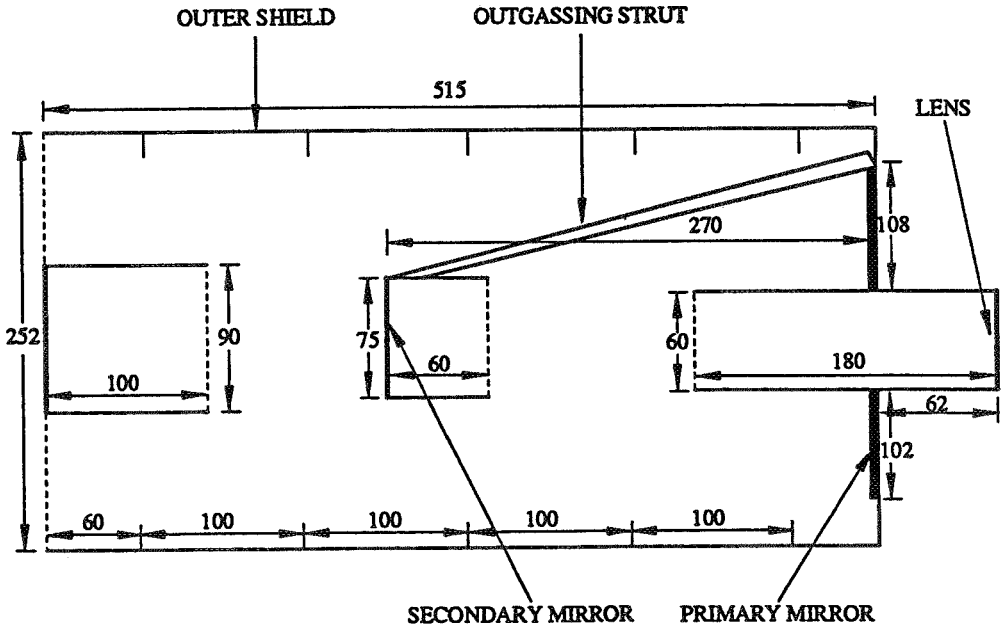


Fig. 4. A simplified model of TAUVEX used for 3D Monte Carlo calculations. Only one of the six struts is shown for the sake of clarity.

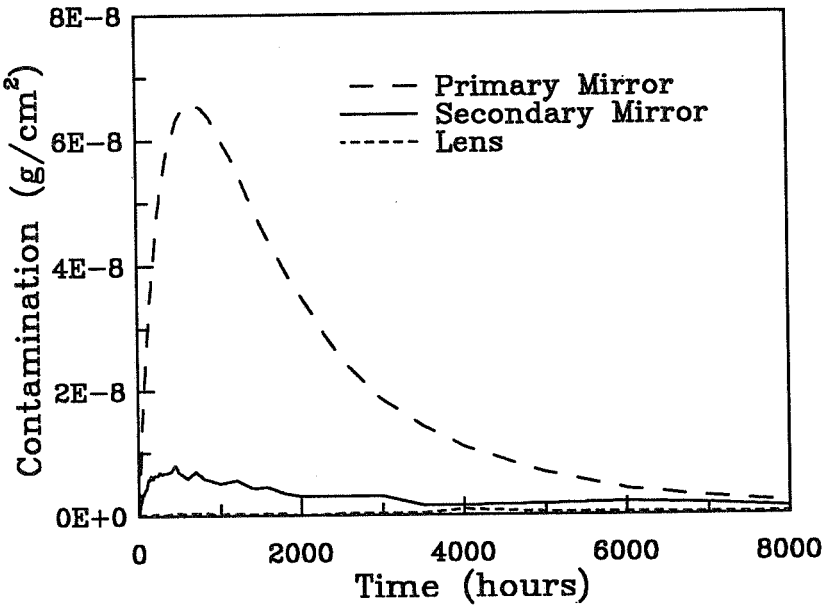


Fig. 5. Contamination levels vs. time after launch from graphite/ester cyanate for three TAUVEX principal optical surfaces: (i) primary miror, (ii) secondary mirror and (iii) front side of first correction lens. The calculations are for CVCM=0.0005% and assume cold conditions.

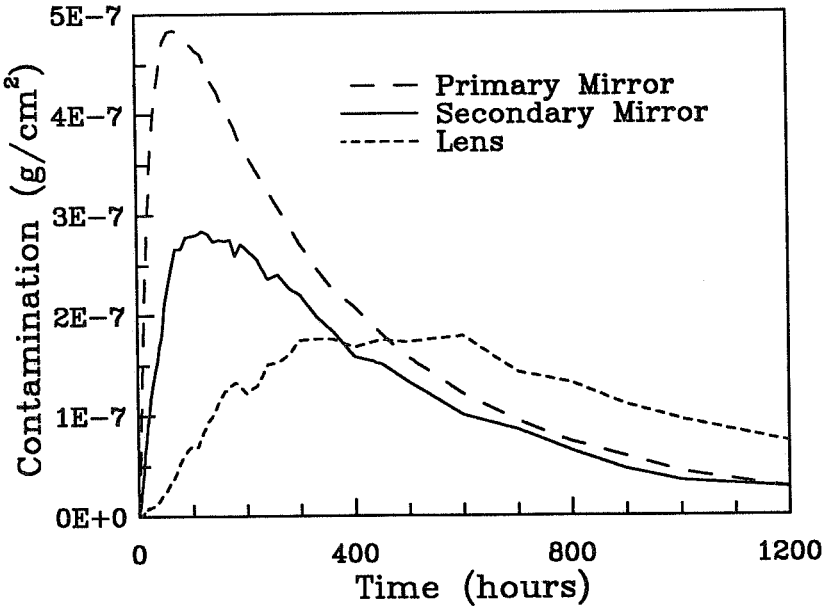


Fig. 6. Contamination levels vs. time after launch from graphite/ester cyanate for three TAUVEX principal optical surfaces: (i) primary mirror (ii) secondary mirror and (iii) front side of first correction lens. The calculations are for CVCM=0.0005% and assume hot conditions.

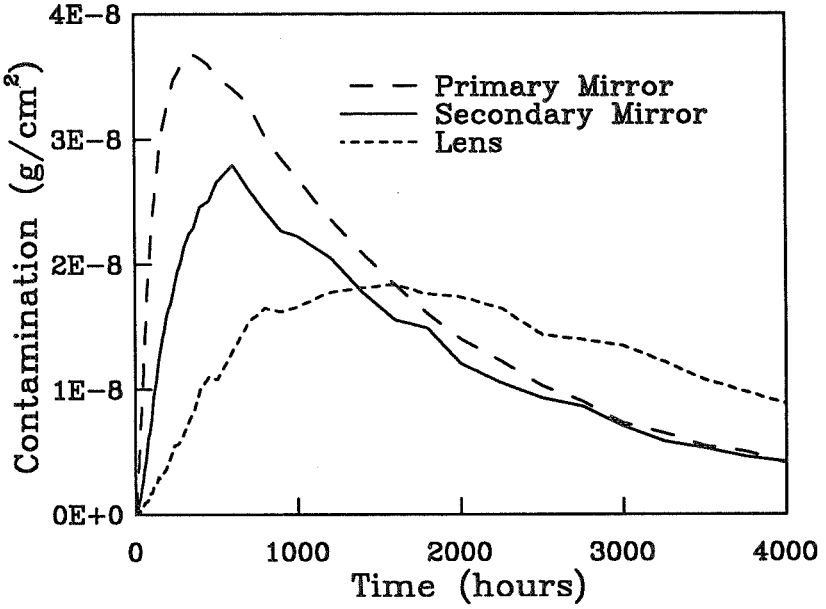


Fig. 7. Contamination levels vs. time after launch from external silicone rubber sealant for three TAUVEX principal optical surfaces: (i) primary mirror, (ii) secondary mirror and (iii) front side of first correction lens. The calculations are for CVCM=0.028% and assume hot conditions.

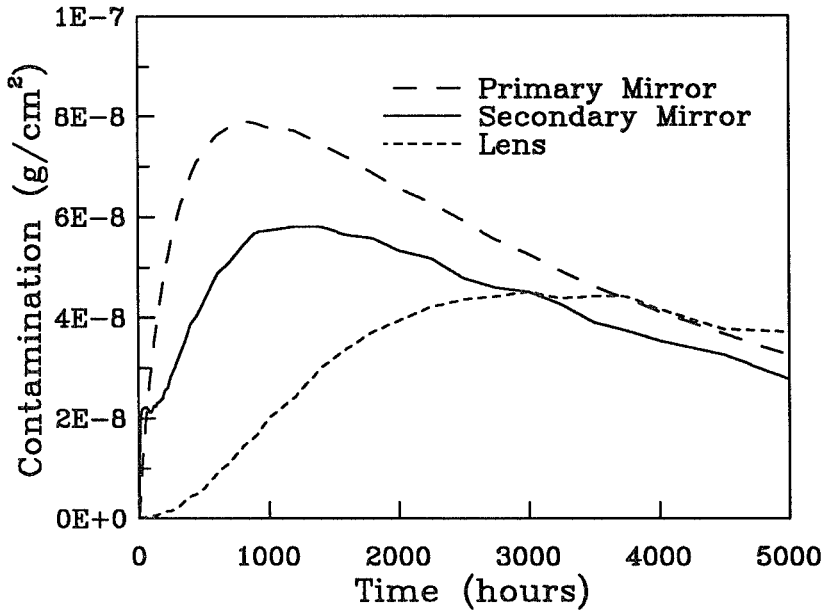


Fig. 8. Contamination levels vs. time after launch from internal silicone rubber sealant for three TAUVEX principal optical surfaces: (i) primary mirror, (ii) secondary mirror and (iii) front side of first correction lens. The calculations are for CVCM=0.028% and assume hot conditions.

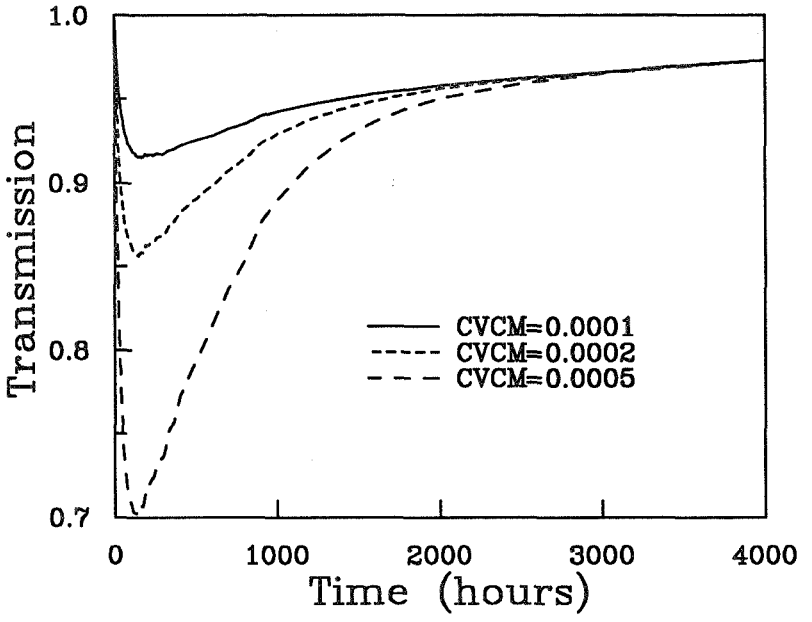


Fig. 9. Transmission loss vs. time after launch for TAUVEX. The calculations assume hot conditions. Results are shown for various CVCM values for graphite/ester cyanate (0.0001%, 0.0002%, 0.0005%) and the measured CVCM=0.028% for silicone rubber.

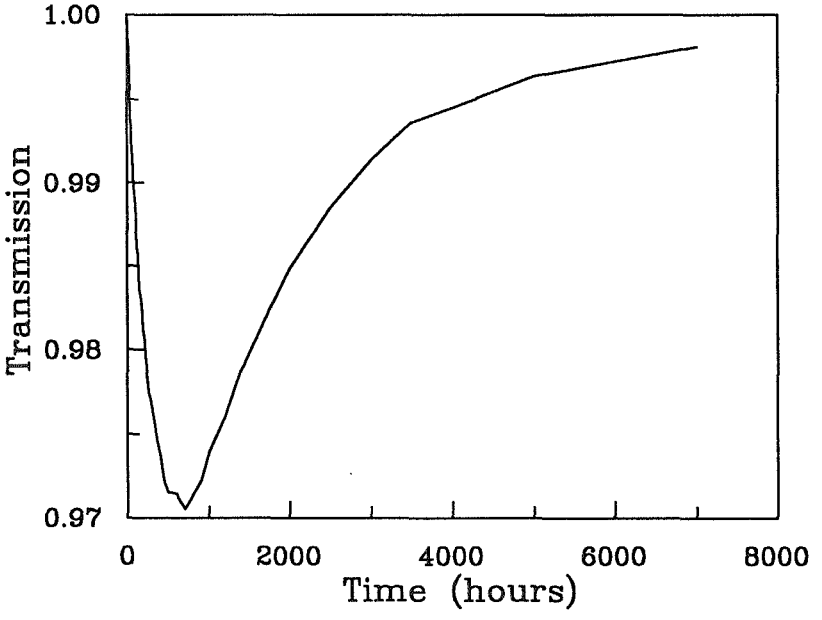


Fig. 10. Transmission loss vs. time after launch for TAUVEX. The calculations assume cold conditions. Result is shown for CVCM=0.0005% for graphite/ester cyanate and the measured CVCM=0.028% for silicone rubber.

# HUBBLE SPACE TELESCOPE SERVICING MISSION SCIENTIFIC INSTRUMENT PROTECTIVE ENCLOSURE DESIGN REQUIREMENTS AND CONTAMINATION CONTROLS

Patricia A. Hansen, David W. Hughes
Swales and Associates, Incorporated

Randy J. Hedgeland
NASA Goddard Space Flight Center

Craig J. Chivatero
Lockheed Missiles and Space Company

Robert J. Studer and Peter J. Kostos
Fairchild Space

## ABSTRACT

The Scientific Instrument Protective Enclosures were designed for the Hubble Space Telescope Servicing Missions to provide a benign environment to a Scientific Instrument during ground and on-orbit activities. The Scientific Instruments required very stringent surface cleanliness and molecular outgassing levels to maintain ultraviolet performance. Data from the First Servicing Mission verified that both the Scientific Instruments and Scientific Instrument Protective Enclosures met surface cleanliness level requirements during ground and on-orbit activities.

## INTRODUCTION

The 15 year mission of the Hubble Space Telescope (HST) is to provide scientific data on the constituents of our universe. Collectively, the HST scientific objectives are to determine: "the constitution, physical characteristics, and dynamics of celestial bodies; the nature and processes which occur in the extreme physical conditions existing in stellar objects; the history and evolution of the universe; and whether the laws of nature are universal in the space-time continuum".[1] On-orbit manned servicing missions are critical in fulfilling these objectives. The successful December 1993 Space Transportation System (STS) 61 mission was the first step in upgrading the HST Scientific Instrument (SIs) and restoring the scientific capabilities of the HST through the installation of Orbital Replacement Units (ORUs). The ORUs consisted of two SIs [the Wide Field and Planetary Camera-2 (WFPC-2) and the Corrective Optics Space Telescope Axial Replacement (COSTAR)], Solar Arrays (SAs), Solar Array Drive Electronics, magnetometers, a coprocessor for the DF-224 flight computer, two rate sensor units, two gyroscope electronic control units, several fuse plugs, and a Goddard High Resolution Spectrograph redundancy kit.

The First Servicing Mission (FSM), shown in Figure 1, used a three Carrier system configuration that included: the Solar Array Carrier (SAC), the Orbital Replacement Unit Carrier (ORUC), and the

Flight Support System (FSS). The 15' x 15' x 15' SAC functioned as a load isolation system for the SAs, and it was used for temporary stowage of the replaced SAs during Extravehicular Activity (EVA). The 12' long x 15' wide x 15' high ORUC, shown in Figure 2, was the most contamination sensitive Carrier. The ORUC housed the WFPC-2 and COSTAR in Scientific Instrument Protective Enclosures (SIPEs). The two SIPEs, the Radial SIPE (RSIPE) for WFPC-2 and the Axial SIPE (ASIPE) for COSTAR, provided a thermal environment equivalent to that inside of the HST, and they were mounted on a load isolation system which provided a low-g vibration environment to the SIs. The warm thermal environment not only ensured that the SIs would remain within their temperature limits during the EVA, but also ensured that any outgassing inside the SIPEs, which could otherwise affect optical performance, would not condense on the SIs. The 5' long x 15' wide x 15' high FSS was used as the maintenance platform to berth the HST to the Shuttle throughout the mission.

The SIPEs were designed to provide a protective environment for the SIs during activities which posed a particulate and molecular degradation threat to the SIs. The RSIPE design, shown in Figure 3, was the most complex design, and as such, this paper will focus on the RSIPE design requirements and the contamination controls which were implemented to preserve the cleanliness and optical performance of the SIs. Similar design requirements and contamination controls were also implemented for the ASIPE. The SI contamination requirements will be described as the basis for the SIPE design requirements. Verification of the contamination cleanliness levels for the SIs and SIPE will be presented.

## SIPE DESIGN

The RSIPE provided structural interfaces for mounting to the ORUC and ASIPE; access for EVA removal and insertion of the SI; protection of the SI from mechanical damage during an EVA; controlled thermal, acoustical, and contamination environments; and an electrical interface to the SI. The SIPE was made of an aluminum honeycomb composite. This design used a large amount of adhesive in the manufacturing process; therefore, contamination control methods were incorporated in the design and processing phases to control and reduce outgassing.

The candidate bonding adhesives for the panel facesheets, inserts, and edge member closeouts were initially screened to determine the outgassing rates at the on-orbit predicted temperatures. FM 73 adhesive, by American Cyanamid Company, was used for the RSIPE and FM 123 LVC, by American Cyanamid Company, was used for the ASIPE. For both samples, initial outgassing test yielded acceptable results. To further reduce the honeycomb panel outgassing and increase venting for more efficient vacuum baking, the exterior facesheets were perforated with 0.028 inch diameter holes approximately one inch apart on center. The interior facesheets were not perforated. The facesheet perforations allowed for directional venting away from the SI during Orbiter ascent and on-orbit operations. Prior to the buildup of the SIPEs, the honeycomb panels were vacuum conditioned to decrease outgassing during system certification.

A monitoring system was incorporated into the SIPE designs to effectively verify the surface cleanliness of the SIPEs. Figure 4 shows the RSIPE baseplate contamination witness plates, and

vertical and flat optical witness mirrors (OWMs). The witness plate is a 9" x 9" aluminum surface used to measure surface molecular cleanliness levels. The oblique and viewing port mirrors are shown in Figure 5. These OWMs were used to measure surface ultraviolet reflectance and particulate levels. The SIPE was designed so that the OWMs were accessible without opening the RSIPE to preclude compromising the cleanliness level of the RSIPE or the SI. The viewing port was incorporated into the RSIPE design for the insertion of a Quartz Crystal Microbalance (QCM) during the system level vacuum outgassing test to measure the total outgassing rate of the RSIPE with all the hardware installed.

Because the WFPC-2 required a dry purge at all times, the RSIPE design incorporated a purge interface as shown in Figure 6. The purge system, which is attached to the RSIPE baseplate, utilized stainless steel tubing for controlling moisture and surface cleanliness levels. The purge gas entered the RSIPE through a port at the bulkhead fitting location interfacing with the WFPC-2 pick-off mirror cover after installation of the WFPC-2 into the RSIPE.

A vent filter system, detailed in Figure 7, was developed to sustain an effective purge, control particulate migration from the external environment into the RSIPE, allow for pressure differentials during launch and ascent, and reduce molecular backstreaming into the RSIPE. The location of the vent on the RSIPE is shown in Figure 3 in the middle of the protective cover assembly. The mounting frame was a 10" x 10" component that contains a stainless steel filter element (nominal 30 micron pore size) and protective screen to preclude damage to the filter element. A restrictor plate, equipped with a purge flow monitor (not shown), covered the entire mounting frame. This plate increased the efficiency of the purge to the WFPC-2 by reducing molecular backstreaming into the RSIPE.[2]

## SIPE CLEANLINESS REQUIREMENTS

The SI cleanliness requirements evolved from the HST Aft Shroud (AS) cleanliness requirements which were driven by the Faint Object Spectrograph detector operating temperature. To preclude potential cross-contamination between the SIPEs and the SIs, the SIPEs were subject to the AS outgassing requirements and surface cleanliness level requirement of 400B per MIL-STD-1246.

### SI Cleanliness Requirements

For the Servicing Missions, the SIs are the critical elements for establishing the overall contamination requirements and budgets. The SIs are directly exposed to the SIPEs during ground and on-orbit operations, and therefore the SIPEs were assessed for the cleanliness impact to the SIs. The SI requirements dictated the necessity for a continuous gaseous purge to maintain a dry, hydrocarbon-free environment for internal SI surfaces.

The science goal for WFPC-2 was to experience no greater than a one percent loss in UV throughput in any 30 day period at a wavelength of 1470 Å. Mass transport modelling determined that this goal equates to less than or equal to 4.7 Å accumulation on a -70°C charge couple device (CCD). To meet this goal significant improvements were made to the WFPC-2 and are discussed in detail in

References 3 and 4. External WFPC-2 surface cleanliness level requirements were much less stringent than the CCD requirement evolving from the HST AS cleanliness requirements. The WFPC-2 external surface outgassing requirement is less than 1 Hertz (Hz) per hour measured by a 15 MHz QCM set at -20° C. The external surface cleanliness level is Level 400B (i.e., less than 2.0 mg/ft$^2$) per MIL-STD-1246.

The COSTAR science specification required the M1 and M2 mirror end-of-life spectral throughput of 56 percent at 1216 Å, equating to a 12 Å deposition for a 1 percent reflectance loss for every 1.5 Å deposited. The external COSTAR surface cleanliness level requirements were much less stringent than the M1 and M2 mirror requirements, and as with WFPC-2 its cleanliness requirements evolved from the HST AS cleanliness requirements. The COSTAR external surface outgassing requirement was less than 1 Hz per hour measured by a 15 MHz QCM set at -20° C. The external surface cleanliness level was Level 400B.

**SI Purge Requirements**

To preserve the WFPC-2 ultraviolet performance, an ultra-clean gaseous nitrogen purge was instituted from the completion of system thermal vacuum testing through integration and testing to launch. For simplicity, the WFPC-2 purge requirements, the most stringent of the nitrogen purge requirements, were instituted as the FSM purge requirements. The WFPC-2 purge requirements are shown in Table 1.

Table 1. WFPC-2 Purge Gas Requirements

| Outlet Gas Specification | Requirement |
|---|---|
| Purity | 99.5% (5000 ppm total impurities) |
| Purge Line Particulate | Level 21 per MIL-STD-1246 (< 15 particles of > 5 microns shed per SCF) |
| Total Hydrocarbons (as $CH_4$) | < 1.0 ppm |
| Dew Point (at 21°C, 760 mm Hg) | > -73.4°C |
| Water | < 1.5 ppm (molar fraction) |

A gaseous nitrogen purge was implemented to ensure an ultra-clean environment for the SIs during the long period of testing and integration prior to launch. Gaseous nitrogen was chosen as the purge gas due to its low cost and ready availability, at relatively high purity, at both Goddard Space Flight Center's (GSFC) integration and test facilities and at Kennedy Space Center's (KSC) launch integration facilities. To meet the WFPC-2 purge requirements additional filtration was required. This was provided by a series of portable filtration units, purge carts, which provided the SIs with

isolation from molecular contamination sources, including those within the already clean purge supply gas.

A total of six purge carts were ultimately required to support the continuous purge requirements of the SIs and SIPEs. Two carts were required for each instrument, (one active, one backup), with two remaining for the carriers and transport containers. Continuous purge was defined as no more than a one hour outage, for any reason, before clean gas flow was re-established. Implementing this requirement was the most challenging part of the purge operation. Multiple backups were established including in-place spare purge carts, with redundant parallel filtration, and backup purge gas supplies, (K-bottle 6 packs), with pressure actuated shuttle valves to automatically provide backup in case of facility outage. In addition a computer system radio-paged project personnel if the nitrogen supply pressure was lost.

The purge carts provided a gaseous nitrogen purge not only during integration activities in the NASA cleanroom, but also during transport between facilities (GSFC to KSC, payload cannister transport between KSC facilities, and in the Orbiter). One purge cart actively supplied an SI while another purge cart was staged and certified in the next facility to be occupied by the SI. This method ensured that a fully tested, certified purge gas supply was ready for an SI immediately upon its arrival to a facility and allowed for a straight forward transfer from facility purge to transport purge and back to facility purge (a frequent, if irregular, occurrence).

## FSM MONITORING RESULTS

The SIPE surface cleanliness level (particle and molecular) degradation was budgeted from the end of system level thermal vacuum testing through Orbiter integration and on-orbit activities. As shown in Figure 8, periodic cleaning of the RSIPE was scheduled to maintain cleanliness levels during integration and test. The particle level excursions shown in Figures 8-9 were the result of crew training which involved inserting mass model instruments into the respective SIPEs. This training was conducted in a Class M 5.5 cleanroom, but due to the number of excess people observing the activity, the particle levels of the SIPE grossly exceeded the requirement. As a result of this monitoring, the instrument insertion procedure was modified to minimize personnel in the SIPE area.

Monitoring, using image analysis of the SIPE OWMs and tapelifts, provided a particle fallout measurement while the SIs were installed in the SIPEs. The modified procedure minimizing personnel resulted in a clean SIPE and SI, well within the HST budget. Figures 8 and 9 provide the particulate and molecular budgets for the RSIPE and ASIPE, respectively. Post-mission data, image analysis of the OWMs and tapelifts verified that the particle level inside the SIPEs did not exceed the HST requirement of particle level 400. Rinse data, prior to the installation of the SIs into the RSIPE and post-mission, show that the molecular contamination level was less than 0.5 $mg/ft^2$, well within the HST budget.

The WFPC-2 external particulate level budget shown in Figure 10 was based upon HST AS particle level requirements, and the pick-off mirror particle level was imposed by obscuration requirements dictated in the WFPC-2 contamination control plan. Actual particle level results on external surfaces,

shown in Figure 10, were determined by tape lift sampling and/or image analysis. Figure 11 shows the WFPC-2 molecular level budget and the actual data as determined by chemical analyses and/or OWM reflectance measurements. The WFPC-2 exterior surface particulate and molecular cleanliness levels, Level 300 and 0.1 mg/ft$^2$, respectively, were much less than the HST requirement of Level 400 and 2.0 mg/ft$^2$.

Figure 12 shows the budgeted particulate contamination allocations for the COSTAR M1 and M2 mirrors. The COSTAR exterior surface particulate contamination level was less than Level 200, well below the HST requirement of Level 400. An OWM program was used to monitor the M1 and M2 degradation; verification was performed throughout the COSTAR build-up, testing, integration, and launch activities. Figure 13 details the COSTAR molecular contamination budget for the external surfaces and M1 and M2 mirrors. The actual obscuration for the M1 and M2 mirrors (not shown) ranged from 0.5 to 3.5 percent.

## CONCLUSION

As a result of incorporating important cleanliness controls early in the design phase of the SIPEs, an effective program for fabricating a protective enclosure to preclude degradation of the FSM SIs was developed. The design strategy included material screening beyond ASTM E595 selection criteria, high temperature component bakeouts, honeycomb panel directional venting, a purge system and vent design, and a monitoring scenario using witness plates, molecular rinses, tapelifts and OWMs. The implementation strategy employed stringent contamination controls during the SIPE fabrication, integration, test, instrument integration, Orbiter integration, and on-orbit activities to minimize potential surface contamination of the FSM SIs.

## REFERENCES


1. "Space Telescope Systems Descriptions Handbook", ST/SE-02, LMSC/D974197B, 31 May 1985.
2. M. Peterson and B. Choudhury, "HST/SM SIPE Contamination Analysis", LMSC Memorandum EM: SPS 644A, 5 February 1992.
3. J.B. Barengoltz, J.M. Millard, T. Jenkins, and D.M. Taylor, "Modeling of Internal Contaminant Deposition on a Cold Sensor", SPIE 1329: 337-351, 1990.
4. J.B. Barengoltz, S. Moore, D. Soules, and G. Voecks, "The Wide Field/Planetary Camera 2 (WFPC-2) Molecular Adsorber", JPL Publication 94-001, 15 January 1994.

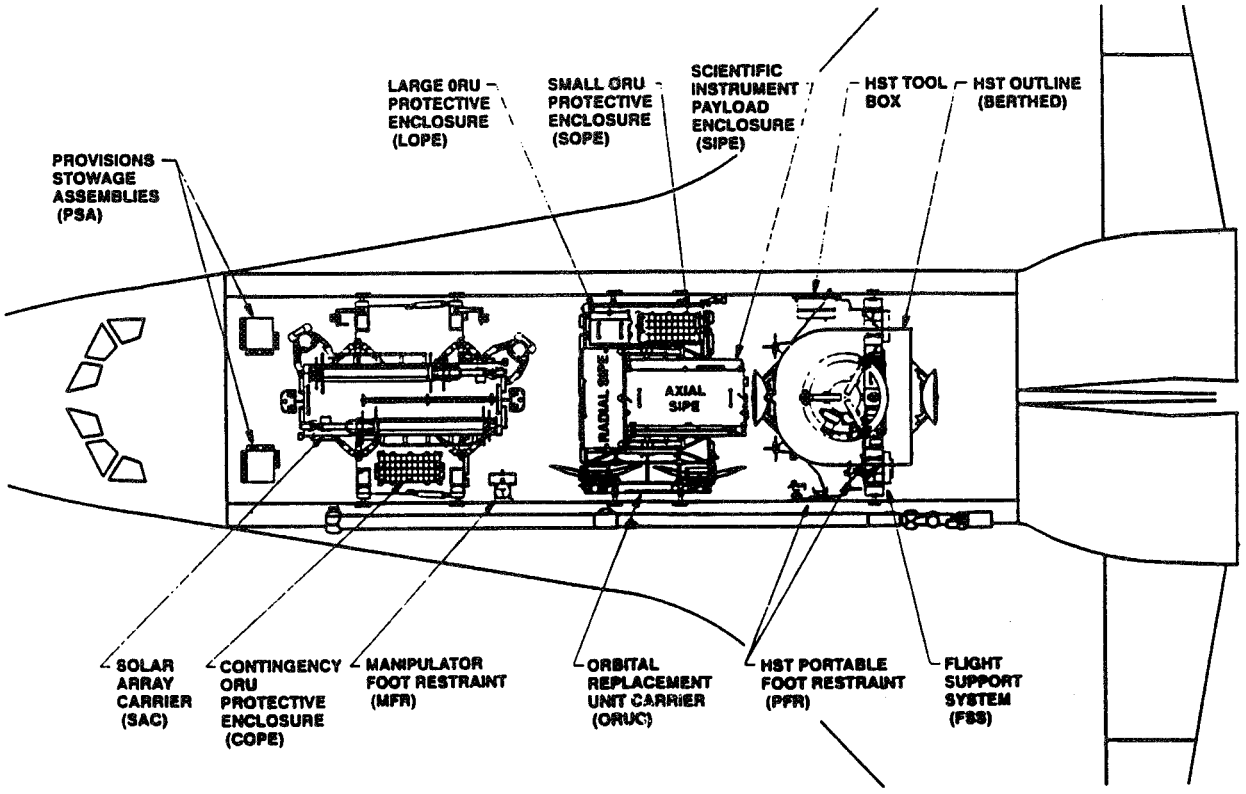


Figure 1. HST First Servicing Mission (STS-61) Cargo Configuration

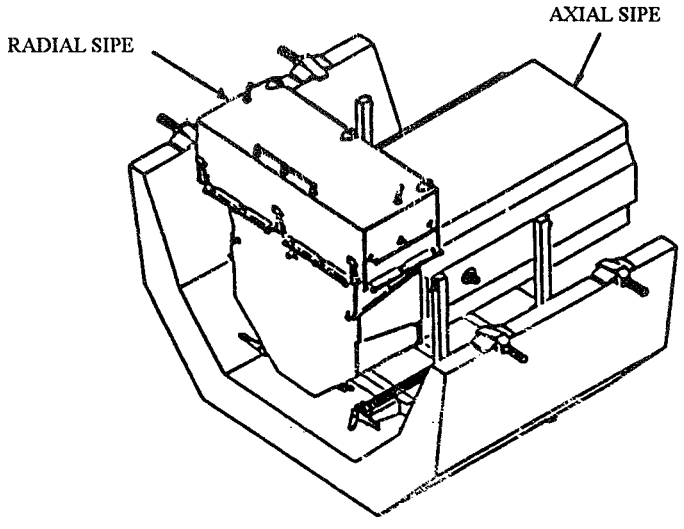


Figure 2. ORUC with SIPEs Integrated

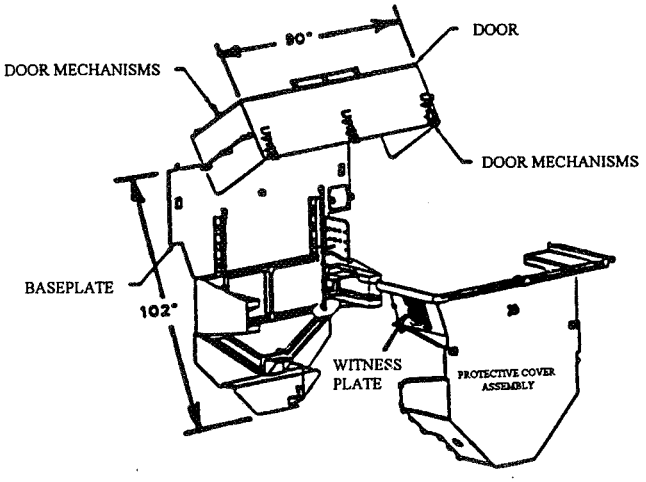


Figure 3. RSIPE Components

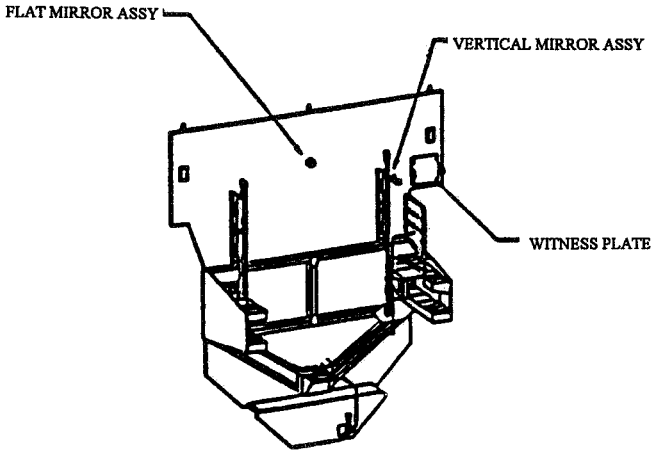


Figure 4. RSIPE Baseplate Contamination Monitors

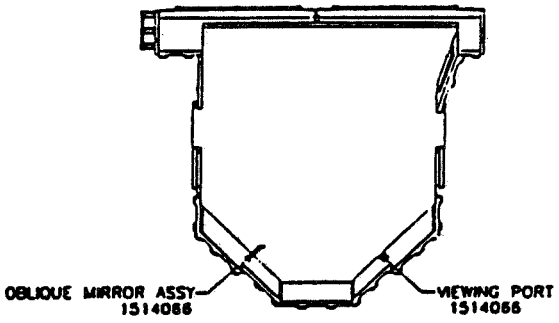


Figure 5. RSIPE Oblique Mirror and QCM Port

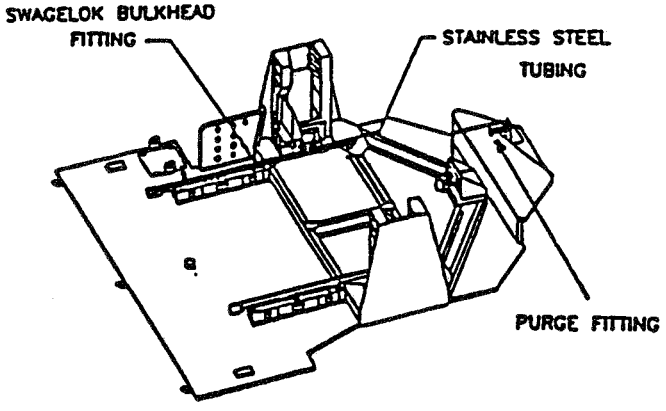


Figure 6. RSIPE Purge System

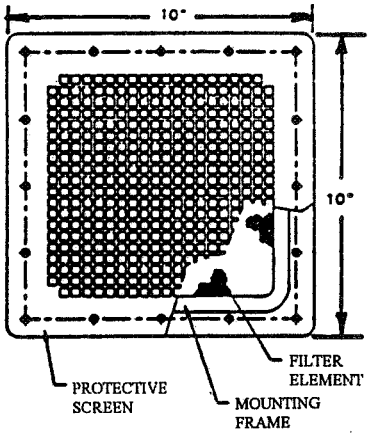


Figure 7. SIPE Vent Filter Design

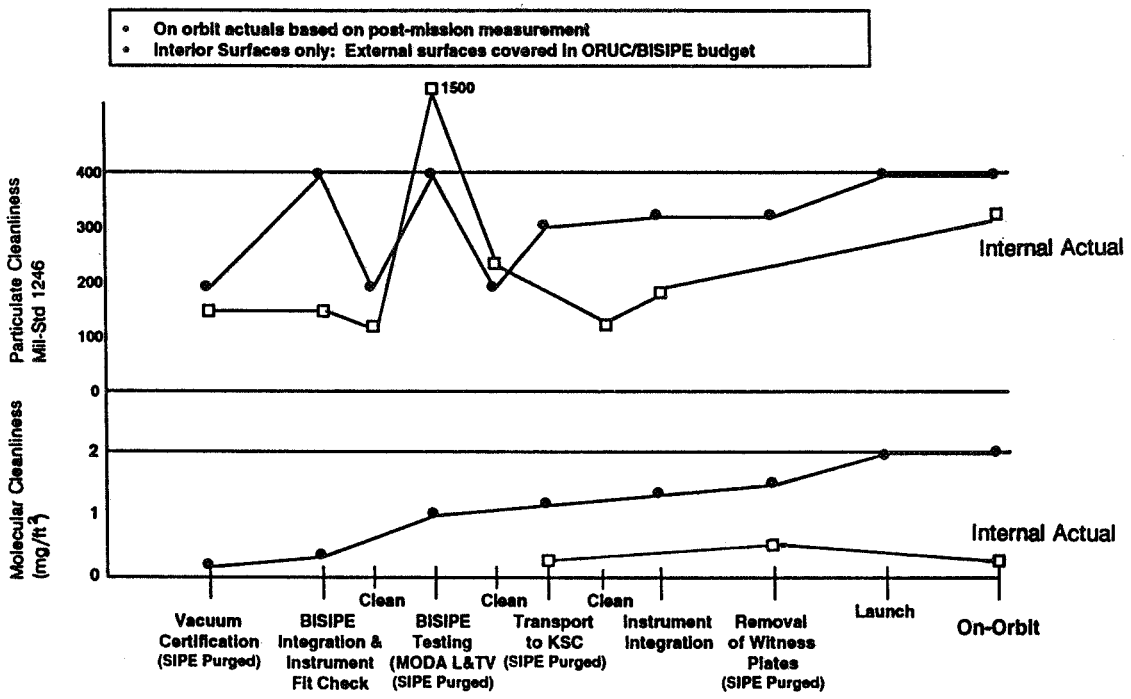


Figure 8. RSIPE Contamination Budget

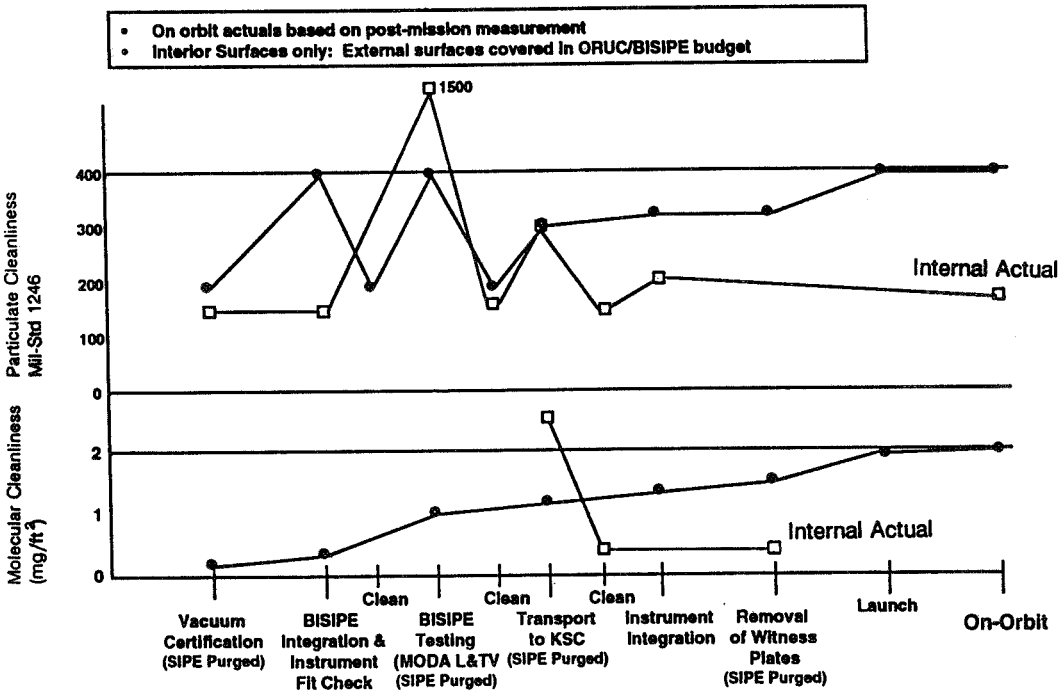


Figure 9. ASIPE Contamination Budget

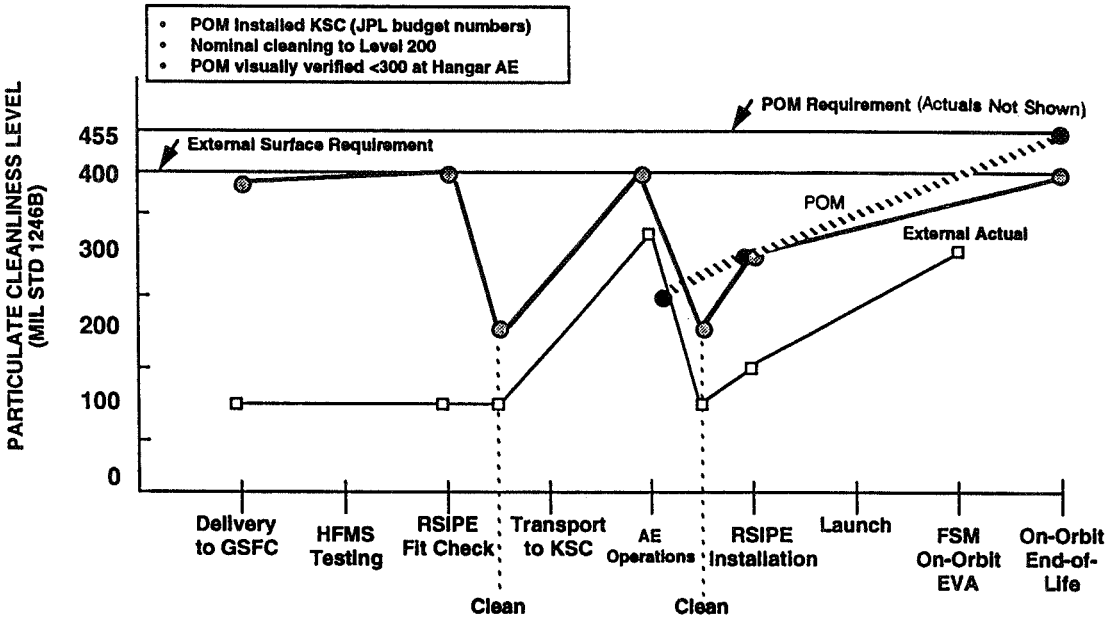


Figure 10. WFPC-2 Particulate Contamination Budget

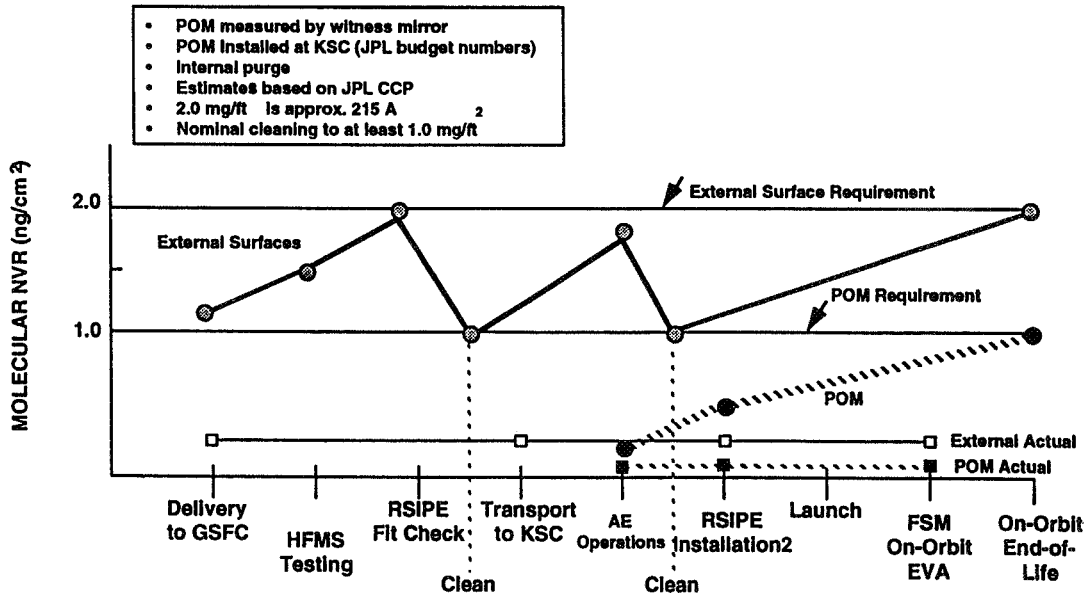


Figure 11. WFPC-2 Molecular Contamination Budget

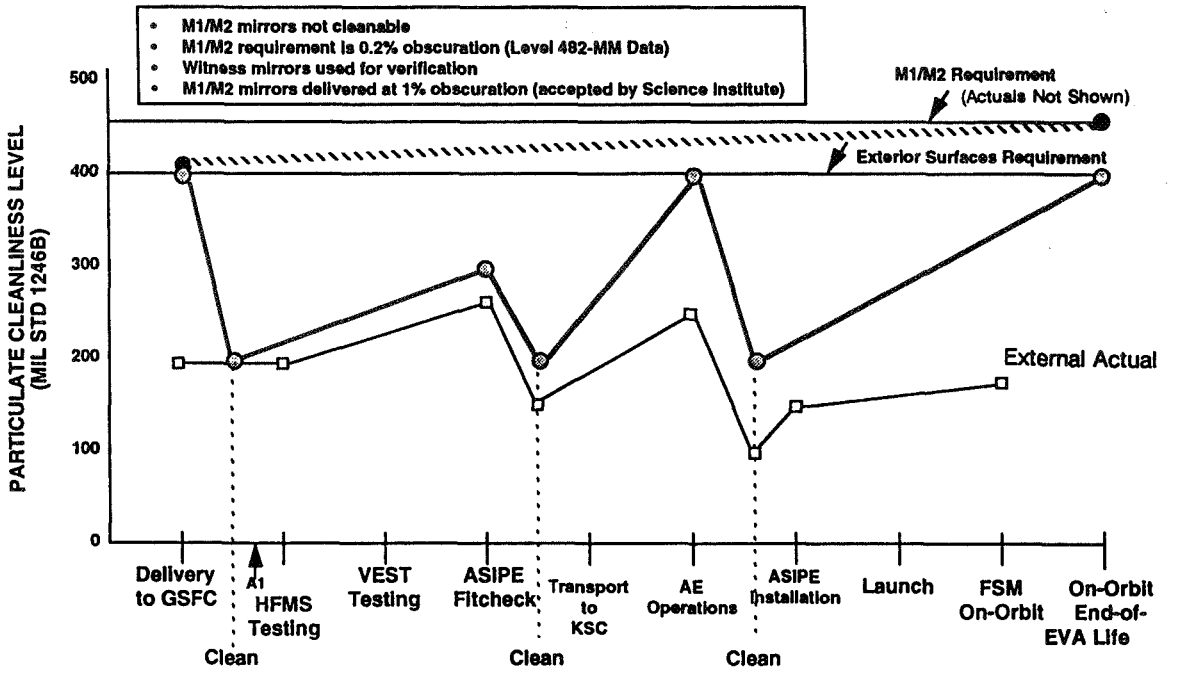


Figure 12. COSTAR Particulate Contamination Budget

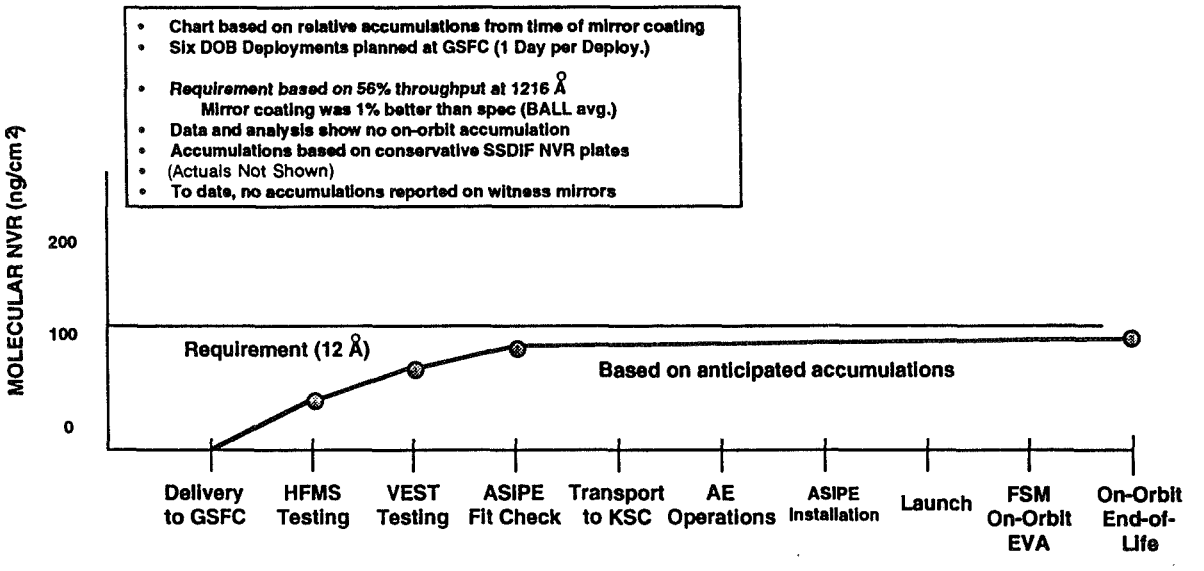


Figure 13. COSTAR Molecular Contamination Budget

# USING A TEMPERATURE-CONTROLLED QUARTZ CRYSTAL MICROBALANCE IN A SPACE EQUIPMENT CLEANROOM TO MONITOR MOLECULAR CONTAMINATION

William J. Mitchell
McDonnell Douglas Space Systems Company
NASA, Goddard Space Flight Center

**ABSTRACT**

There is a need for continuous monitoring for molecular contamination in cleanrooms where spaceflight equipment is assembled, integrated, and tested to insure that contamination budgets are met. The TQCM (temperature-controlled quartz crystal microbalance) can be used to provide both a real time warning and a cumulative measurement of molecular contamination. It has advantages over the other measurement methods such as witness mirrors, NVR(non-volatile residue) plates, and gas analyzers. A comparison of the TQCM sensitivity and ease of operation is made with the other methods. The surface acoustic wave microbalance (SAW), a newly developed instrument similar to the TQCM, is considered in the comparison. An example is provided of TQCM use at Goddard Space Flight Center when the Wide Field Planetary Camera 2(WFPC-2) and the Corrective Optics Space Telescope Axial Replacement(COSTAR) were undergoing integrated testing prior to their installation in the Hubble Space Telescope on its first servicing mission. Areas for further investigation are presented.

**INTRODUCTION**

Molecular contamination is a serious concern when spaceflight equipment is assembled, tested, and integrated in cleanrooms at government and industry facilities. Molecular contamination, sometimes called non-volatile residue (NVR), is the result of emitted gas, vapors, or aerosols condensing on a surface. The molecular layers will degrade performance of optics and sensors by reducing their throughput. As part of system performance considerations, the loss of signal due to contamination must be budgeted. For example, the total allowable molecular contamination coating for the COSTAR optics was determined and then budgeted for the various stages of assembly, test, integration, and on-orbit life. Eight (8) angstroms of molecular contamination was allowable during the integration and testing stage at GSFC. If the budget was exceeded, cleaning, with its inherent risks, would be necessary to prevent a degradation in performance. It is therefore desirable to monitor the contamination deposited at each stage and to know as early as possible if excessive contamination is occuring.

Although contamination deposited directly on critical surfaces such as optics or sensors is the immediate concern, contamination on other surfaces may later desorb and transfer to the critical areas particularly in the vacuum environment of a test chamber or space as temperatures of the surfaces change.

In some cases, contamination of a critical surface can be measured directly by checking transmission, reflectivity, or detector response with a standard source. In other cases, the contamination may be inferred from sample collection of contamination made in the vicinity of the spaceflight equipment. This has traditionally been done with witness mirrors and NVR collection plates. More recently the TQCM is being used for this purpose(ref. 1) and the surface acoustic wave (SAW) microbalance, a newly developed instrument similar to the TQCM, is in limited use(ref. 2). Gas analyzers, although more difficult to relate to deposited molecular contaminion, give an indication of molecular contaminants in the cleanroom atmosphere.





C-2

The purpose of this paper is to compare the TQCM with the other measuring techniques in terms of sensitivity and ease of operation and to describe in more detail the TQCM use. The advantages of each technique will be discussed and the need for a coordinated use of the various techniques is stressed. An example of TQCM use in a clean room at Goddard Space Flight Center(GSFC) will be presented including a description of the installation, operation, results, and analysis. Areas for investigation in the use of the TQCM are discussed.

## MOLECULAR CONTAMINATION MONITORING METHODS

The molecular contamination monitoring methods discussed herein are the witness mirror, NVR plate, gas analyzer, TQCM, and SAW.

### Witness Mirrors

Witness mirrors are typically one inch diameter by one quarter inch thick flat glass mirrors front-surface coated with aluminum and magnesium flouride or some other coating that is representative of the optics of concern. They are made with a highly uniform reflective surface and are normally serialized for easy identification. A baseline reflectivity measurement is made of a control mirror and a test mirror in one or more wavelenghts using a reflectometer and typically ranges from 75 to 85%. The test mirror is placed in the vicinity of the spaceflight equipment. It is periodically removed and returned to the lab for reflectivity measurement where a decrease in reflectivity is an indication of contamination. The control mirror is transported and handled in the same manner as the test mirror except that it is not exposed to the environment being monitored. The mirrors must be carefully handled to avoid scratches, smudges, or any other damage or contamination that would give misleading results. The purpose of the control mirror is to determine if any damage or contamination occurs in transportation and handling as well as provide a check on the reflectometer.

For the purpose of comparison of the different measuring methods, the ability to detect a change equivalent to one molecular layer of water will be discussed. (Some forms of contamination have considerable greater molecular thickness than water). The measuring accuracy of the reflectometer is usually +,-1.5% (or greater) for a uncertainty range of 3% (see Table 1). A typical conversion factor (depending on measuring wavelength and contaminant material) is 0.5%/angstrom. Therefore the 3% range of measurement uncertainty is equivalent to 6 angstroms. Thus, the mimimum thickness that can be detected would be slightly over six angstroms. One molecular layer of water is about 3 angstroms(ref. 9) and could not be detected by a witness mirror.

The advantage of the witness mirror is that it can be coated similar to the optics in space equipment and measured in the wavelength of interest. If positioned properly it should be a very representative sample. The disadvantage is in the careful handling required, the lack of sensitivity to low levels of contamination, and the lack of real time warning capability.

### NVR Plates

NVR plates are normally 1 foot square polished aluminum plates. They are cleaned to an ultraclean level and then carefully transported to the cleanroom and installed in a holder. It is common to position four or more plates in a large cleanroom on wall mounts with their collecting surface parallel to the wall facing into the room. After a period of time (usually one to six months) the plate(s) are removed and carefully transported to the lab for analysis. Analysis is by solvent wash, evaporation of solvent, and weighing of the remaining non volatile residue (NVR). Normal lab procedures would not detect much less than 0.1 mg/ft$^2$ (see Table 1). This is equivalent to about 10.8 angstorms of coating(using the density of water). Obviously one monolayer of 3 angstroms is beyond detection level.

The advantage of the NVR plates is that the NVR produced can be analyzed by infrared and mass spectroscopy and the contents, such as esters, phthalates, silicones, and aliphatic hydrocarbons, can be identified. This can sometimes reveal the source and allow for corrective action. A periodic check with NVR plates is a nice facility control measure. The disadvantages are lack of sensitivity which requires fairly long collection time and the laboratory time and effort required for processing the plates.

**Gas Analyzer**

Gas analyzers can be used in cleanrooms to collect air samples, analyze the samples, and print out results on a near real-time basis. They are usually Fourier transform infrared spectrometers that periodically sample the air and measure content of water, carbon dioxide, methane, hexane, etc., in parts per million. The results are printed out and displayed on a screen and alarm levels can be set. An increase above normal range could indicate increased molecular contamination being deposited and investigation and corrective action can be taken. However, the vapor pressure of many of the species detected by the analyzer may not allow their condensation on optics at clean room temperature and pressure. Thus, the measurements of air content cannot be correlated to the thickness of the contamination being deposited on the spaceflight equipment. Thus, the sensitivity of parts per million (Table 1) cannot be compared to the other methods.

The advantage of the gas analyzer is that it provides a real time measurement which can be used to take timely corrective action. The disadvantage is it cannot be correlated with levels of molecular contamination being deposited.

**TQCM**

The TQCM is an instrument that uses quartz crystal oscillators operating in the dual difference mode to measure the mass of small amounts of molecular contamination deposited on the exposed crystal (see Figure 1 for an illustration of TQCM sensors). The mass deposited results in an increase in the TQCM frequency which is normally directed to a computer and displayed on its screen, printed out, and recorded on disk. The screen and printout can be monitored on a periodic basis and limits can be set for investigation. The sensitivity is such that the TQCM can provide a real time warning of contamination events in a clean room. Also, the recorded frequency can be compared over any length of time to get an indication of cumulative deposit. Table 1 shows the sensitivity of a 10 MHz TQCM and a 15 MHz TQCM. Note that the minimum thickness that can be detected is shown for comparison with other methods. The conventional expression for sensitivity is shown at the bottom of the table in mass per unit area to cause 1 Hz change. This is converted to frequency change caused by one a angstrom thick coating assuming that the molecular contamination has the density of water. The measuring accuracy of the TQCM, +,- 2 Hz or a range of 4 Hz, is divided by the conversion factor to result in the minimum thickness detected.

A 3 angstrom layer of molecular contamination would result in about 19 Hz change on the 15 MHz TQCM, well within its ability to detect. For the 10 MHz TQCM, a three angstrom deposit would result in about 7 Hz change, more than the range of uncertainty of 4 Hz. Thus, both TQCMs could detect the hypothetical 3 angstrom layer.

The advantage of the TQCM is that it can provide a real time warning and cumulative record of molecular contamination, it does not require laboratory effort, and it is more sensitive than the witness mirror or NVR plate. The disadvantage might be the greater equipment cost (estimate $10,000 to $20,000 for one TQCM and support equipment). Also it is difficult to analyze the small quantities deposited on the crystal to identify molecular species.

**SAW**

The SAW microbalance also uses quartz crystals operating in the dual difference mode. However its frequency is developed by a "surface acoustic wave" as opposed to a shear wave(ref. 5). It operates at a higher frequency and has considerably greater sensitivity(ref. 3, 4). See Table 1 for the improvement in sensitivity over the TQCM. The practical benefit of the considerably greater sensitivity, particularly at less than one molecular layer where surface behavior may not be uniform, is still to be demonstrated.

**TQCM/SAW Advantages**

Due to their greater sensitivity, the TQCM and SAW can provide near real time indication of molecular contamination. Their results can be displayed on computer screen and limits set for allowable increases over various time periods. They can also provide a cumulative measurement over any period of time as the frequency is recorded for later reference. Their data is easily recorded and displayed and no separate laboratory procedures and measurements are required. Their frequency increase is directly relatable to deposit on a surface where the gas analyzer measurements are not.

**Coordinated Use**

Other methods should not be discarded because the TQCM and SAW have certain advantages in sensitivity and ease of recording and use of data. The witness mirror may give the optical designer the most direct measurement of the effect of contamination on a specific optical surface at a specific wavelength if mimimum detectable levels of contamination are exceeded. (The TQCM might allow for a similar reflectance measurement from the exposed crystal depending on reflectometer configuration and crystal size.) The NVR plate is a good long-term measurement of contamination that allows for chemical analysis of the contamination constituents. The gas analyzer supplements the TQCM real time capability.

It is important to take a coordinated look at all methods available. If NVR plates are analyzed on a three month basis as a facility check, the TQCM readings for that period of time should be presented and a comparison made. Witness mirrors and NVR plates can corroborate each other if their results are obtained for the same time period and compared to historical trends. If there is an important space instrument in the cleanroom, additional witness mirrors and NVR plates can be installed at the start of the period and analyzed at the end to provide cumulative data for comparison with the TQCM.

**USE OF TQCMs AT GSFC**

TQCMs have long been used at GSFC in vacuum chamber testing to measure outgassing of condensible products. In March 1993, several TQCMs were installed in the cleanroom of the Spacecraft Systems Development and Integration Facility. The temperature of the TQCMs was controlled at a few degrees Farenheit below nominal room temperature. Two TQCMs were selected for their stability and were returned to the manufacturer for coating with magnesium flouride, similar to the optics of the flight instruments for the first HST Servicing Mission, the WFPC-2 and the COSTAR. The TQCMs were then installed in the clean room and operated before and during the period that the instruments were there and have been operating since as a facility monitor.

**Installation**

Figure 2 illustrates the TQCM installation. Each TQCM (Faraday Mod. 82-E with 15 MHz crystals) was connected to a controller (Faraday Mod. 72-DET) with a 15 foot long electrical cable. The controller allows for setting and controlling of the operating temperature of the TQCM. It also provides the temperature diagnostic and TQCM frequency thru a coax cable to the data acquisition unit (Hewlett Packard Mod. 3421A) which is connected to a Hewlett

Packard Integral Personal Computer. The data acquisition unit and the computer are located outside the clean room in a test control room where personnel are available to monitor the TQCM data.

One TQCM was installed on a specially built platform in the High Fidelity Mechanical Simulator (HFMS), a test station that simulates the aft section of the HST where the instruments are located. During testing of the WFPC-2 and COSTAR they are placed in the HFMS with their optics exposed. (At other times they are covered and purged). Thus, this TQCM was located as close as possible to the critical optics.

The other TQCM was located in the northeast corner of the clean room at the input air filter bank and is more indicative of the input air to the clean room.

**Operation**

TQCM frequency and temperature were displayed on the computer screen and printer every half hour. (Interval can be set as desired and recording can be more or less frequent then printout). During the time the critical instruments were in the cleanroom, the responsible personnel would monitor the readings hourly. Limits were set for notification of the contamination engineer and project personnel.

**Results**

WFPC-2 arrived at GSFC on June 4, 1993, and was in the clean room for 74 days thru August 17, 1993. The TQCM data is shown in Figure 3. TQCM #3, located in the NE corner, showed no change for the period. There was very little personnel or equipment activity in this area, so TQCM #3 is indicative of the input air quality. TQCM #4 was located in the enclosed HFMS hub area near the WFPC-2 and COSTAR. Its frequency increased from 913 to 932 Hz, a difference of 19 Hz. At 6.4 Hz/angstrom (see Table 2) this amounts to about a 3 angstrom coating. This was well within the WFPC budget of 108 angstroms.

The WFPC budget was based on external surface degrading from 1 milligram per square foot to 2 milligram per square foot (MIL-STD 1246B, Level B). The budget considered the planned cleaning after the testing at GSFC, the fact that the flight pickoff mirror would be installed at the launch site, and the fact that the internal optics were protected by an aperture cover and purge.

Note on Figure 3 (point 2) that the TQCM frequency increased about 8 Hz on June 23, the highest single day increase. This day marked the start of a period of heavy activity in and around the HFMS which included the installation and removal several times of large tooling using the overhead crane and a balance beam. As many as six people were needed inside and immediately outside the HFMS. Thus, the increase in TQCM frequency occured during a period of peak personnel and tooling activity. Note that TQCM #3, which is not in the area, did not react to the activity.

TQCM #3 did react to its physical movement (point 1), and to cleanroom input air variations at point 3 where temperature was lowered from 68F to 65F and TQCM temperature from 19C(66.2F) to 17C(62.6F), and at point 4 where the cleanroom relative humidity increased from 44 to 56% before returning to 44%. It has been noticed on numerous occasions that the TQCM frequency is affected by changes in humidity and temperature and by changes in physical orientation or the vibration associated with relocation.

The COSTAR arrived at GSFC on July 9, 1993, and was in the clean room for 50 days until it was installed in its shipping container on August 27. The TQCM readings are shown for this period in Figure 4. TQCM #3 readings showed no significant change during this period. TQCM #4 increased from 930 to 934 Hz, a difference of 4 Hz which is less than one angstrom of molecular coating. Part or all of the increase could be due to instrument random variation. The 4 Hz increase is negligible when compared to the budget of 48 Hz (8 angstroms). Note

that the COSTAR budget was much more stringent than that of WFPC-2 due to greater exposure of the flight optics.

Thus, the TQCM data indicated that both instruments were well within their molecular contamination budgets while at GSFC.

A total of nine witness mirrors were placed in the HFMS during the time the WFPC-2 and COSTAR were at GSFC. No statistically significant change was seen in the mirrors when considering the measuring accuracy of the reflectometer (+,-1.5%) although a slight trend toward a reflectance decrease could be seen when all data was viewed together. This correlates with the TQCM data as the 3 angstroms coating indicated by the TQCM for the WFPC and less than 1 angstrom for the COSTAR are below the measuring accuracy of a witness mirror (see Table 1).

NVR plates were not read to correlate with the period of time that WFPC and COSTAR were in the clean room.

**Analysis of Deposition on Crystal**

Several methods were considered for analyzing the contaminant deposited on the TQCM. Problems result due to the very small mass and thickness of coating available for analysis. The 19 Hz frequency increase noted during the WFPC II exposure in the cleanroom indicates about 3 angstroms coating or 0.008 micrograms on the approximately 0.6 cm diameter crystal.

McKeown et. al. reported on analysis of the TQCM crystal surface done with a Nicolet MX-1 FTIR spectrometer with a specular reflectance attachment(ref. 6). The IR beam was reflected off the crystal at near normal incidence and compared to the signature of a clean crystal for reference. However, in this case there weas about 25 micrograms deposit. This method "detects films down to a few hundred angstroms region" and is not feasable for the small amount detected above.

Experiments are currently underway at GSFC using a Nicolet Model 710SX Infared Spectrometer and IR microscope with grazing angle objective to analyze thin films on a TQCM crystal.

Thermogravimetric analysis is a method by which the crystal temperature is increased at a controlled rate and the TQCM frequency monitored to determine the temperatures at which desorbtion takes place(ref. 7). If there are a small number of species involved and they are placed on the crystal in the right order, they can be identified by their desorbtion temperature. In practice, the more volatile species tend to sweep the less volatile from the surface (ref. 8).

**AREAS FOR INVESTIGATION**

Three areas for future investigation have been noted. They are the stability of the TQCM, methods of calibration, and the analysis of the deposition on the crystal.

**Stability**

All TQCMs operated to date in the GSFC cleanroom at temperatures a few degrees below room temperature appear to require some time from hours to days to stabilize. The frequency usually increases initially and then levels off.

Once the TQCMs have stabilized after initial turn-on, they have a random variability that may be due to the cooling device cycling, electronic noise, and variation of the temperature and humidity in the room. More work could be done in this area. The standard deviation for three TQCMs over an eight day period was calculated and ranged from 0.7 Hz to 1.2 Hz.

The TQCMs will vary with temperature and humidity. See Figure 5 for an instance where cleanroom humidity went out of control but temperature was held

fairly constant. In this case the TQCM frequency immediately followed the relative humidity and varied about 0.5 Hz per 1% RH change. It has been suggested that a crystal coated with magnesium flouride, as was the case in this example, is hydroscopic and will react in this manner. As the reference crystal was not coated with magnesium flouride, it would not be expected to react to the humidity. It would be advantageous to eliminate or reduce the reaction to temperature and humidity. At present the TQCMs can only be used in a well controlled area where any significant change due to humidity or temperature is known and allowed for.

**Calibration**

There is no method for periodic calibration of the TQCM. If a method could be developed to apply a known mass to the exposed crystal for calibration purposed and then remove it by physical means or heating, confidence in the readings would be improved.

**Analysis of the Deposition on the Crystal**

The analysis of the molecular contamination deposited on the crystal is important so the source of the contamination can be identified and corrected. More effort needs to be applied to methods such as thermogravimetric and spectroscopic analysis of the adsorbed material.

**CONCLUSIONS**

The TQCM is considerbly more sensitive to molecular contamination than witness mirrors and NVR plates. When operated in a cleanroom at ambient pressure, the TQCM provides a real-time warning of low levels of molecular contamination and reliable and convenient measurement of cumulative contamination deposition.

**REFERENCES**

1. W. J. Mitchell, "Monitoring deposition of molecular contamination of optics using a temperature controlled quartz crystal microbalance (TQCM)", SPIE Vol. 2261, Optical Systems Contamination, pp. TBP, 1994. (TBP = to be published)

2. P. A. Mogan, "Real time measurements of nonvolatile residue contamination in cleanroom environments", SPIE Vol. 2270, NASA Spin Off Technologies, pp. TBP, 1994.

3. D. A. Wallace, W. D. Bowers, "Mass flux comparisons of a 200-MHz SAW resonator microbalance to a 15 MHz TQCM in a high vacuum environment", SPIE Vol. 2261, Optical Systems Contamination, pp. TBP, 1994.

4. A. P. M. Glassford, J. W. Garrett, W. D. Bowers, "Mass sensitivity calibration of the SAW QCM at ambient temperature", SPIE Vol. 2261, Optical Systems Contamination, pp. TBP, 1994.

5. W. D. Bowers, "A high sensitivity real time NVR monitor", SPIE Vol. 1754, Optical Systems Contamination, pp. 344-351, 1992.

6. D. McKeown, J. A. Fountain, V. H. Cox, and R. V. Peterson, "Analysis of TQCM Surface Contamination Adsorbed During the Spacelab I Mission," AIAA Shuttle Environment and Operations Conference, pp. 108-115, November 13-15, 1985, Houston, Tx.

7. D. A. Wallace and S. A. Wallace, "Use of a cryogenically cooled TQCM in conjunction with a programmable data acquisition system to detect and examine ecreted mass on the sensing crystal caused by environmental contamination," SPIE Vol 1165 Scatter from Optical Components pp. 424-431, 1989.

8. R. J. Bryson, A. B. Bailey, B. L. Seiber, W. T. Bertrand, J. H. Jones, and B. E. Wood, "Cryogenic quartz crystal microbalance - characterization and calibration for Midcourse Space Experiment (MSX) program," SPIE Vol. 1754, Optical Systems Contamination, pp. 205-214, 1992.

9. E. H. Kennard, Kinetic Theory of Gasses, McGraw Hill, 1938, p. 149.

**Table 1. Sensitivity of Molecular Contamination Measuring Devices**

| | MEASURING ACCURACY | CONVERSION FACTOR | DETECT 1 MONOLAYER (3 angstroms) | MINIMUM THICKNESS DETECTED (angstroms) |
|---|---|---|---|---|
| **WITNESS MIRROR (reflectance measurement)** | +,-1.5% | 0.5% per angstrom | No | 6 |
| **NVR PLATES, 1 ft. square rince, weigh** | 0.1mg/ft$^2$ minimum | 9.26x10$^{-6}$ g/ft$^2$/ang. | No | 10.8 |
| **FTIR GAS ANALYZER** | +,-1 ppm | * | No | * |
| **TQCM 10 MHz** | +,-2 Hz | 2.3 Hz/ang. | Yes | 1.7 |
| **TQCM 15 MHz** | +,-2 Hz | 6.4 Hz/ang. | Yes | 0.63 |
| **SAW 200 MHz** | +,-2 Hz | 920 Hz/ang. | Yes | 0.0043 |

For Reference:

| | TQCM SENSITIVITY | |
|---|---|---|
| | ngm/cm$^2$ - Hz | Hz cm$^2$ - ng |
| 10 MHz TQCM | 4.42 | 0.23 |
| 15 MHz TQCM | 1.56 | 0.64 |
| 200 MHz SAW | 0.0109 | 92.0 |

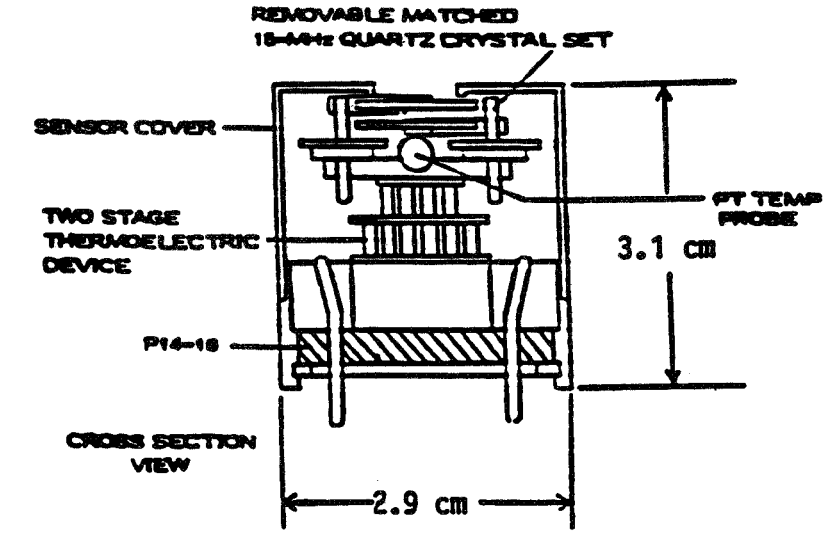


TQCM Sensor Design, Faraday Labs, La Jolla, CA.

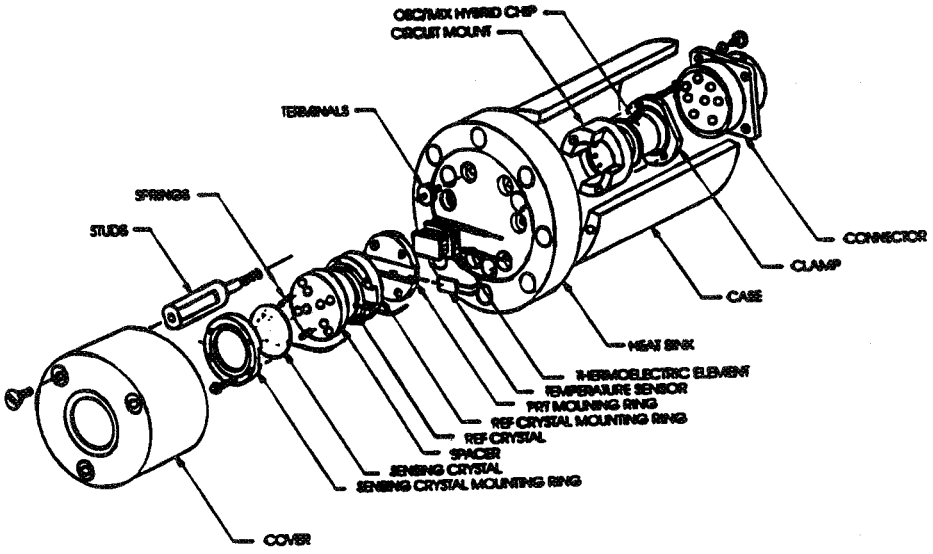


TQCM Sensor Design, QCM Research, Laguna Beach, CA.

**Figure 1 : TQCM Sensor Design**

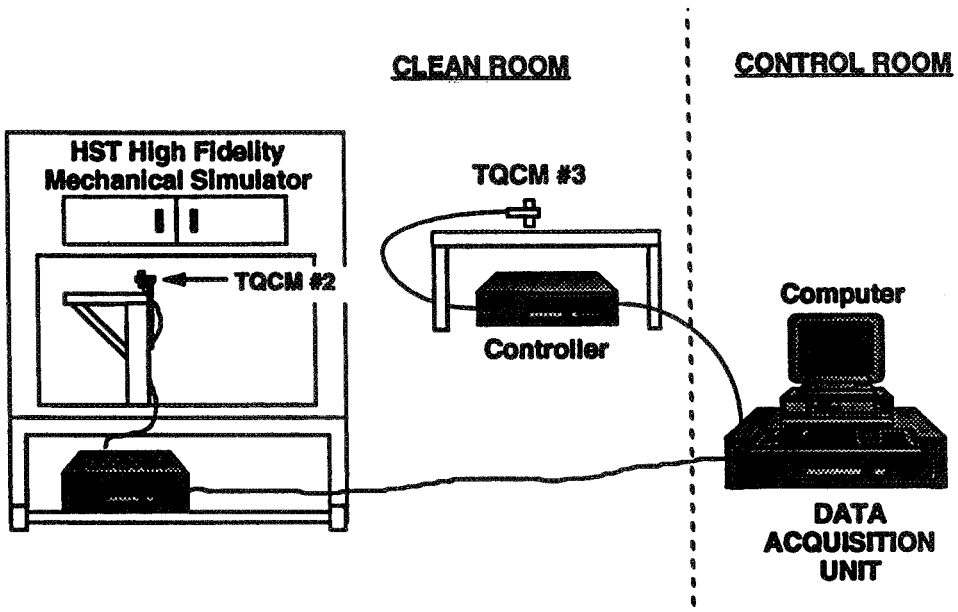


Figure 2 : TQCM Installation

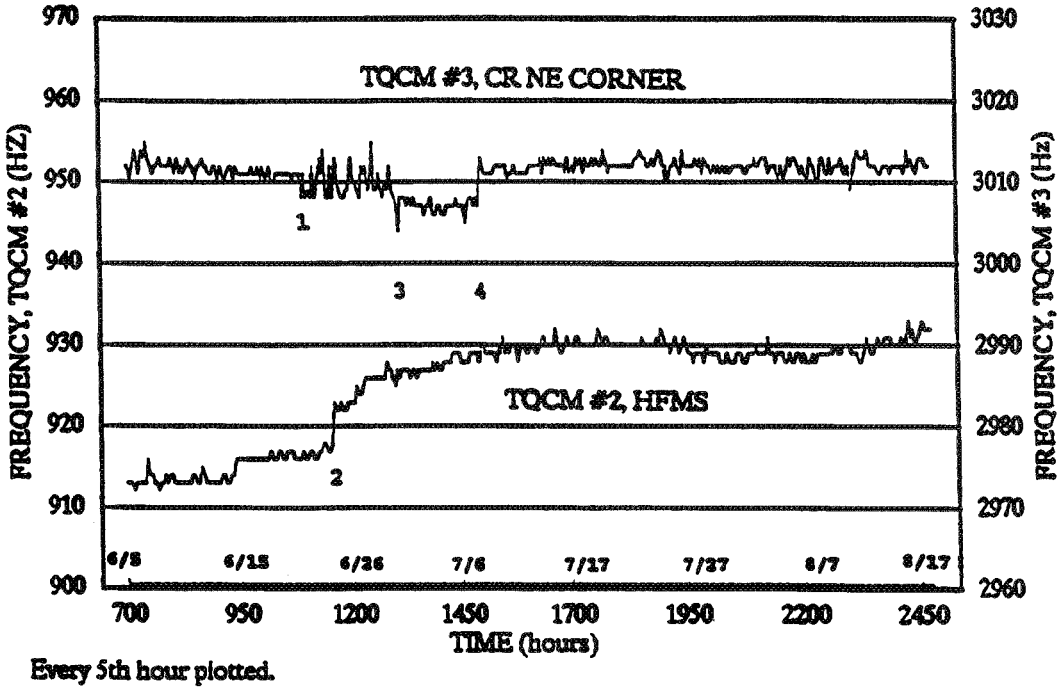


Figure 3 : TQCM Readings, WFPC II Integration and Test at GSFC

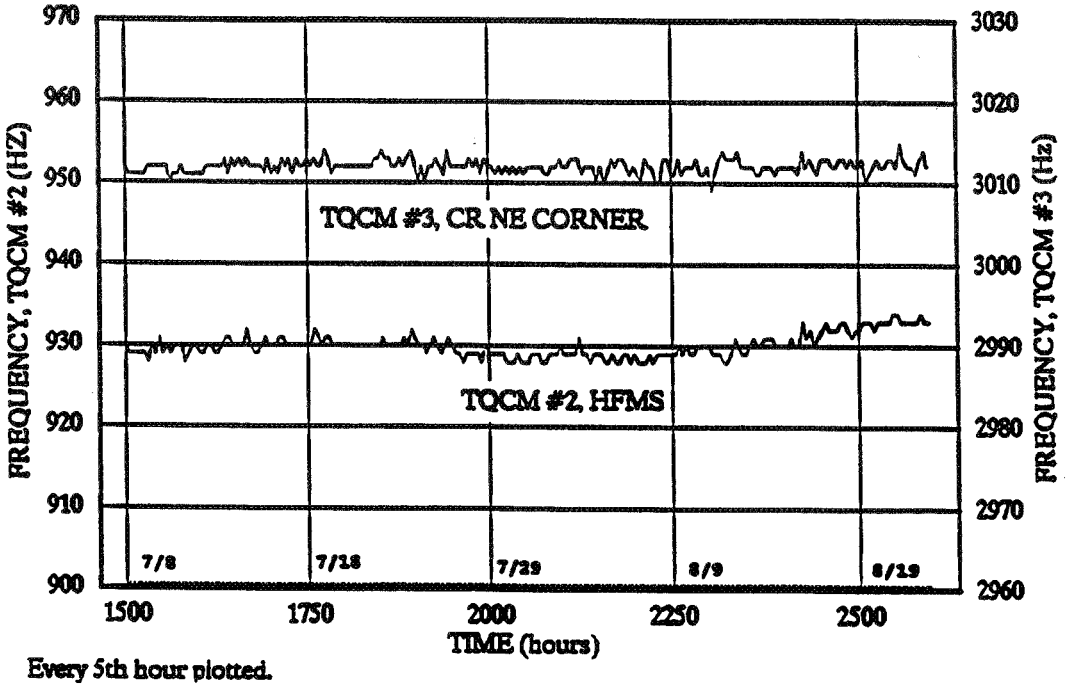


**Figure 4 : TQCM Readings, COSTAR Integration and Test at GSFC**

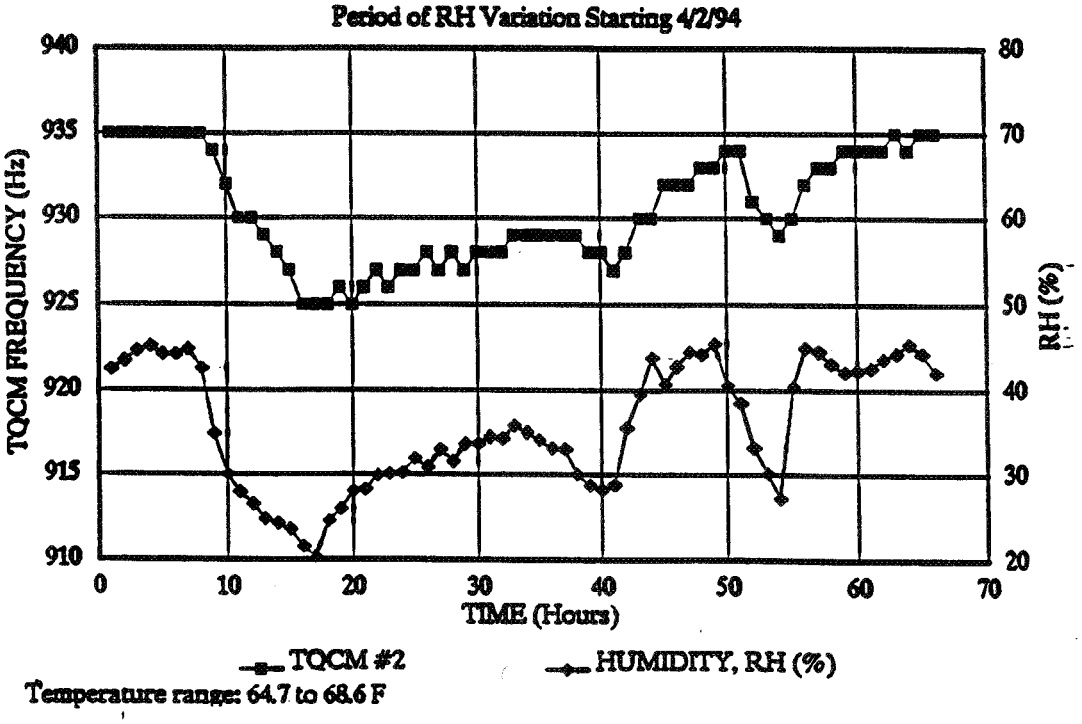


**Figure 5 : TQCM #2 Correlation with Humidity**

# CLEAN ASSEMBLY AND INTEGRATION TECHNIQUES FOR THE HUBBLE SPACE TESLESCOPE HIGH FIDELITY MECHANICAL SIMULATOR

David W. Hughes
Swales and Associates, Beltsville MD

Randy J. Hedgeland
NASA Goddard Space Flight Center

## ABSTRACT

A mechanical simulator of the Hubble Space Telescope (HST) Aft Shroud was built to perform verification testing of the Servicing Mission Scientific Instruments (SIs) and to provide a facility for astronaut training. All assembly, integration, and test activities occurred under the guidance of a contamination control plan, and all work was reviewed by a contamination engineer prior to implementation. An integrated approach was followed in which materials selection, manufacturing, assembly, subsystem integration, and end product use were considered and controlled to ensure that the use of the High Fidelity Mechanical Siumulator (HFMS) as a verification tool would not contaminate mission critical hardware. Surfaces were cleaned throughout manufacturing, assembly, and integration, and re-verification was performed following major activities. Direct surface sampling was the preferred method of verification, but access and material constraints led to the use of indirect methods as well. Although surface geometries and coatings often made contamination verification difficult, final contamination sampling and monitoring demonstrated the ability to maintain a class M5.5 environment with surface levels less than 400B inside the HFMS.

## INTRODUCTION

It has been well established within the contamination control community that clean assembly and integration are essential elements in the creation of a clean test or manufacturing facility. This principle applies to aerospace test equipment (also called ground support equipment, or GSE) because of the large size and complex interaction of the GSE with flight hardware; cross contamination of sensitive thermal and optical surfaces can cause deleterious effects. An alignment and envelope verification tool, the HFMS, was built for the HST Servicing Missions. The HFMS was manufactured, assembled, and tested within the cleanliness constraints imposed by the HST contamination control program for use with contamination sensitive Scientific Instruments (SIs).

This paper reports on the unique contamination problems associated with creating a mock-up of a large structure for use in testing sensitive hardware. The HFMS and its cleanliness requirements will be described, and the approach to HFMS contamination control will be presented. The practical aspects of implementing this approach and some lessons learned during the construction and certification of the HFMS will be discussed.

## HIGH FIDELITY MECHANICAL SIMULATOR

### Physical Description

The HFMS is a mechanical mock-up of the HST Aft Shroud and contains a support system for 5 SIs, 3 Fine Guidance Sensors, electrical harnesses, thermal blankets, and an equipment shelf for electronics. The HFMS is comprised of four major parts. The Aft Shroud Mock-up (ASM), a 5 meter high, 5 meter diameter cylinder, supports the Main Ring Simulator (MRS) (Figure 1). In the HST, the Primary Mirror is supported by the Main Ring (Figure 2). Suspended from the MRS is the Focal Plane Deck (FPD) and Scientific Instrument Support Structure (SISS) (Figure 3). Light collected by the HST is directed into SI apertures in the Hub area of the FPD. Access to the SISS is through three sets of doors in the ASM; an opening above one of these doors provides access into the FPD for a radial SI. Three sets of doors allow access to the other radial bays. Within these bays are guiderails and latches for insertion and capture of SIs. As a "high fidelity" simulator, the interior finish and astronaut interfaces have the same appearance and function as

the HST Aft Shroud interior (Figures 4-6).

**Developmental Stages**

In order to understand the sequential imposition of contamination constraints, the HFMS developmental stages must be delineated. The HFMS was assembled and integrated at Goddard Space Flight Center (GSFC). Certain subassemblies were received from the manufacturer already assembled; these were the FPD, the MRS, and the ASM. Other parts were fabricated at GSFC and transferred to the Spacecraft Systems Development and Integration Facility (SSDIF) for assembly. The SSDIF is a class M5.5 cleanroom capable of supporting the integration of two Shuttle payloads concurrently. Integration of the HFMS began with disassembly and cleaning of the MRS, and mating of the MRS with the FPD. After SI latches were installed and aligned on the FPD, the SISS was added to the assembly. Again, latches were installed, and alignment and metrology verification activities occurred. The equipment shelf and blankets were added to the structure, and the structure was integrated with the ASM. Cables were routed and final blanket closeout was performed. A significant milestone in the contamination control program was the integration of the HFMS interior parts with the ASM. This integration virtually eliminated access to the Hub area, and greatly restricted access to the FPD and MRS underside. As access to various surfaces became more restricted, the contamination requirement became more stringent.

**Requirements**

The contamination requirements are derived from the intended uses of the HFMS: envelope verification of SIs, astronaut familiarization with HST interfaces and Orbital Replacement Unit (ORU) installation, SI confocality and alignment verification, and SI thermal vacuum operational tests. The intimate contact between the SIs and the HFMS imposes a surface cleanliness requirement upon the HFMS interior equal to the most stringent of the SI external surface requirements: Level 400B per Mil-Std 1246. Contact between the astronauts and the exterior surfaces of the HFMS provides the opportunity for cross contamination of the interior during crew familiarization; therefore, all external hand rails and astronaut interfaces must also be Level 400B. Other exterior surfaces are Visibly Clean, Highly Sensitive (VCHS) per JSC-SN-C-0005. During some operations, SI optics are exposed to the Hub area for extended periods of time without a direct purge or covering. The most stringent cleanliness requirement imposed to protect the First Servicing Mission (FSM) SI optics was Level 200A in the Hub area. Although the HFMS was not used in a vacuum for the FSM, a requirement exists not to preclude outgassing certification at the SI requirement of 1 Hz/hr on a 15 Mhz Quartz Crystal Microbalance at -20° C with the hardware at the maximum on-orbit temperature. An unusual requirement for GSE, internal air cleanliness of class M5.5 or better, is mandated by the enclosed nature of the HFMS and the class M5.5 environmental requirement of all HST SIs and Aft Shroud ORUs.

These primary requirements led to the development of secondary requirements which were not applicable to the flight HST: materials used inside the ASM must not generate particles when contacted by cleanroom garments, interior surfaces must be sufficiently static dissipative to prevent the attraction of particles, and the Hub area must be purgeable to prevent contamination of the SI optics in the unlikely event the cleanroom goes out of specification. To maintain the class M5.5 air cleanliness, constraints were placed on the orientation of the HFMS in the cleanroom air flow, HFMS door opening, and the number of persons permitted inside the ASM. Implementation of these requirements is discussed below.

**IMPLEMENTATION**

An early management commitment to contamination control facilitated implementation of contamination controls. Concurrence from the contamination control engineer (CCE) was required for all work authorizations, and the CCE was involved in daily test team meetings. With this guidance, the test team personnel were able to implement the spirit of the contamination control program during all phases of development. Standard operating procedures and contamination status memos were issued as necessary to communicate the level of cleanliness to which the hardware was being maintained. These documents proved to be a valuable addition to the contamination control plan because they were specific to the work at hand.

Because of resource limitations and surface morphology constraints, not every surface could be verified to Level 400B after each operation. HFMS surfaces were categorized according to the cross contamination risk they posed to the SIs,

and verification requirements consistent with these risks were established. The contamination risks were assessed by evaluating the pontential for SI contamination due to the following transfer mechanisms: direct contact, airborne mobility of contaminants, vacuum outgassing, and indirect transfer by personnel contact. Although surface cleanliness cleanliness requirements differed, the precision cleaning procedure by which all surfaces were cleaned was invariant. This procedure had been previously proven capable of producing surfaces meeting Level 250A; Quality Assurance audits demonstrated the repeatability and consistency of the results. Molecular verification of HFMS surfaces, because of the geomety and access constraints, required the development of techniques other than the standard solvent rinse.

Materials selection was also considered an important aspect of the integrated approach to contamination control. Selection of materials which would not generate particles or cause static discharge during testing of SIs required an elaborate test program.

**Personnel Management**

Personnel constraints formed the basis of success for the HFMS contamination control program. Because the integration team personnel were all experienced in cleanroom assembly and testing, it was possible to concentrate on specific work patterns and priorities rather than general cleanroom behavior. Issues that were addressed included personnel access to the HFMS interior, when to notify contamination engineering of an operation requiring support, and how to minimize cross contamination between surfaces. The cooperation of the integration personnel in following the standard operating procedures was essential for the success of the contamination control program.

**Standard Operating Procedures**

During contamination generating activities, active involvement by contamination control technicians limited the accumulation of contaminants. All obvious contamination generating operations, such as drilling, cutting, or reaming, required simultaneous vacuuming and a follow-up wipe with isopropyl alcohol (IPA). In addition, any time fasteners were installed or removed, tape or optical targets were removed, or a subassembly was integrated with the HFMS, the areas involved were wiped with IPA. To minimize particle fallout accumulation on difficult to clean surfaces, such as the SI latches, bagging material was used to cover the hardware when access was not required.

In addition to the cleaning already mentioned, maintenance cleaning was performed bi-weekly at the subassembly level and weekly at the assembly level. Routine cleaning was mandated by the high activity levels in the cleanroom and the large surface area of the HFMS.

**Verification Requirements**

The verification requirements for HFMS parts during assembly and integration are shown in Table 1. Temporary mating surfaces, such as surfaces mated for match drilling, could be cleaned after the part was removed. Reflecting the cleanable nature of these surfaces, verification to VCHS was considered acceptable. Similarly, non-mating surfaces that were accessible for cleaning were verified to VCHS. Using a VCHS requirement instead of a 400B requirement allowed operations to continue without waiting for tapelift data. Surfaces which would become inaccessible for verification due to the HFMS geometry were a concern because of airborne contaminant transport. Both direct and indirect contamination transfer mechanisms were a concern because these surfaces could be contacted by personnel or hardware. Accordingly, these surfaces were verified to Level 400B. Because mated surfaces are not a source for direct contact, indirect contact, or particle transport under ambient conditions, particulate cleanliness was not required to be verified prior to mating. The possibility of volatile condensible contaminants from mated surfaces cross contaminating other surfaces under ambient conditions was considered negligible due to the lack of a transport mechanism. To minimize future outgassing due to surface Non Volatile Residue (NVR), each mating surface was wiped with IPA prior to mating. Mating surfaces which could be de-mated during crew familiarization in the HFMS had to meet the same requirements as surfaces which were inaccessible. The modifications to the verification requirements which were necessary to accommodate the different surface finishes and geometries are discussed further in the Verification Methods section.

A similar analysis was performed for the HFMS GSE. Small tools were cleaned to the level of the hardware with which they interfaced. Larger GSE, such as the Optical Telescope Assembly (OTA) dolly, were cleaned according to

the cross contamination risk that was posed. Surfaces in contact with the HFMS were verified to 400B or VCHS, depending on the requirement of the surface with which they interfaced. Surfaces not in direct contact with the HFMS were cleaned to VCHS (the same requirement as the HFMS exterior), except for those surfaces which were not accessible to personnel. Because of the difficulty in reaching and verifying inaccessible surfaces, those surfaces were cleaned for entry into the cleanroom or covered with bagging material and verified to Visibly Clean on a periodic basis. These requirements are summarized in Table 2.

**Verification Methods**

The principle surface verification methods were the tapelift and solvent rinse. Unfortunately, not all surfaces were amenable to these methods. Alternative verification methods were developed for painted surfaces, surfaces with geometries that prohibited rinsing, and parts with less than the appropriate sampling area.

The solvent rinse technique often is not compatible with painted surfaces because the solvent will extract paint components from the surface or react with the paint. In some cases, this can be solved by the choice of solvent; however, for the HFMS only IPA was used to perform rinses. Rather than attempt to verify that no contamination was present, the approach taken was to monitor incremental changes. This allowed the use of solvent swabs, which do not contain enough solvent to endanger the paint integrity. The species detected were compared with previous swab samples to ensure that no new source of contamination had impacted the surface. This approach was dependent upon confidence in the initial cleanliness level. Maintenance of the painted surfaces in controlled environments following painting provided this confidence.

Some surfaces and assemblies could not be rinsed because the geometry of the part prohibited collection of a solvent rinse. These parts were swab sampled to determine qualitatively if any contaminant species were present. Once the cleanliness of the part was established, routine cleaning was used to maintain the surfaces. Monitoring of nearby parts confirmed the absence of volatile condensible contamination. Personnel training with respect to cross contamination mechanisms assisted in maintaining the cleanliness of the surfaces.

Small parts, such as fasteners, shims, and standoffs, presented less surface than the standard sampling area. To rinse these items, similar parts were grouped together after cleaning and rinsed as a batch. Once the parts were integrated with a larger structure, the structure became the controlling surface for rinse sampling.

To improve confidence in the cleanliness of the surfaces which were not amenable to standard rinse techniques, the entire HFMS was regularly inspected using an ultraviolet (UV) light. Many hydrocarbons fluoresce when illuminated with UV light. To ensure that the critical Hub area, to which the SIs would be exposed, was free from condensible hydrocarbons, a real-time NVR deposition monitor was installed: a Temperature Controlled Quartz Crystal Microbalance (TQCM) with a magnesium fluoride ($MgF_2$) coating operating three degrees centigrade below room temperature was used to record NVR deposition. To eliminate possible unkonwn surface effects, the $MgF_2$ coating was used to mimic the coating on the SI optics. Although $MgF_2$ coated TQCMs are sensitive to humidity (surface water mass is indistinguishable from hydrocarbons), the assumption that all accumulation is caused by hydrocarbons was conservative. Analysis of the TQCM response indicates a 1 Hz increase for a 2% relative humidity increase. Relative humidity was usually 45% at 68 °F. The use of the TQCM in ambient conditions is discussed in detail in reference 1.

**Materials Selection**

Materials used inside the HFMS had to be cleanable to 400B, low outgassing, static dissipative, and abrasion resistant. Verification of these criteria required an extensive test program. The test procedures were customized for each material based upon the use and location of the material. The HST structure is a graphite-epoxy composite covered with aluminum tape on the outside and multi-layer insulation (MLI) on the inside. The test process is depicted in Figure 7. After screening the material for low outgassing properties (less than 1% TML and 0.1% CVCM per ASTM E595) and the ability to meet Level 400 by tapelift before and after cleaning, the material entered a concurrent test period. Static dissipation, NVR rinse, and dry abrasion testing were performed concurrently. Static dissipation was checked for single layer and overlapped layers of tape. Abrasion testing was performed using a dry wipe; both the wipe and the sample were microscopically examined. Finally, a vacuum outgassing test was performed in the Molecular Kinetics (Molekit) facility.

Two materials, the aluminum tape used on the exterior of the HFMS and the beta cloth blankets intended for the interior of the HFMS, illustrate the necessity for a comprehensive test program. The HST flight aluminum tape was tested for use on the exterior and certain parts of the interior of the HFMS. In general, bare aluminum is a particle generating material because the oxide is easily abraded from the surface. Although most failed to meet the criteria for internal use, certain tape samples met Level 400 when tapelifted; this may be due to mechanical hardening during the tape fabrication process. Because the samples which passed were from the same roll as samples which failed, the tape was rejected for use inside the ASM. The samples were inspected to VCHS and approved for use on the exterior of the HFMS.

Many of the HFMS internal surfaces are covered by blankets. To simulate the HST, black betacloth blankets were baselined for use. The betacloth is a teflon coated fiberglass which is etched to produce the black color. This etching process weakens the betacloth such that the material was easily abradable by personnel contact. A test plan similar to the tape test plan was followed for several candidate blanket materials. In the case of the tape testing, the only cleaning that was tested was solvent wiping with IPA. For the blanket samples, different cleaning methods were tested, including non-contact vacuuming and solvent rinsing. The material which was chosen was manufactured without the use of silicone oil lubricant and was the only one which was non-porous. The non-porous aspect improved rinsability, cleanability, and abrasion resistance, and permitted verification to Level 400B.

## DISCUSSION

### Cleanliness Data

During assembly and integration of the HFMS, cleanliness samples were required whenever contamination generating activities were completed. While the HFMS interior assembly was separate from the ASM, access for cleaning was not precluded. Following integration with the ASM in April 1993, access for cleaning was restricted. From that point forward, maintaining cleanliness was paramount. Cleanliness levels found during routine sampling of the HFMS showed that the interior of the HFMS was better than Class 200. During heavy activity, cleanliness levels increased slightly, but stayed below Level 400. Rinses taken from the FPD during integration and closeout were in the tenths of milligrams per square foot. Selected routine sampling data is shown in Table 3; the July data was taken during operation of the HFMS.

In May 1993, after the HFMS was integrated, a TQCM was installed in the hub area to monitor contamination generated by cable routing and blanketing operations. The data from May through the end of June is shown in Figure 8. Two interesting items are evident on the graph: a 12 Hz jump in mid-May and a sudden increase in the contamination rate in June. An investigation of the 12 Hz jump indicated that the jump was not caused by contamination but was intrinsic to the TQCM.[1] The sudden increase around June 21 was caused by final closeout activities. Though not shown, the rate of contamination remained low once the HFMS was operational; the TQCM frequency at the end of SI testing was 935 Hz, compared with 930 Hz at the beginning. From the time of integration until commissioning, the total NVR accumulation in the Hub area was $4.3 \times 10^{-2}$ mg/ft$^2$ (30 Hz at $1.56 \times 10^{-9}$ g/cm$^2$/Hz). Optical witness mirrors placed near the TQCM showed no degradation at 121.6 nm during this period. Because swab samples of the Hub taken before integration showed no materials other than the swab background, confidence was high that the Level B requirement was maintained in the Hub area.

### Lessons Learned

Several significant contamination lessons were learned during the HFMS program. Some of these are related to surface treatment, and others are relevant to cleanroom management.

It was found during assembly of the MRS that brush irridited aluminum does not possess the same resistance to particle generation as dip irridited aluminum. Tapelifts from the brush irridited surface ranged from Level 500 to Level 750, whereas dip irridited surfaces were better than Level 300. Bare aluminum surfaces produced particles too numerous to count.

Tape coverings for surfaces which will be used in vacuum are often perforated to prevent air bubbles. The direction of perforation of paper backed tape is important; perforating from the backing side through to the tape surface causes

fibers to be trapped in the perforations. The ASM was covered with perforated tape, and efforts to remove the fibers by cleaning failed. The only solution was to re-cover the surface with unperforated tape.

Black beta-cloth is sometimes used as a thermal blanket on flight hardware. When ground simulators are used, the temptation is to use the same material for visual fidelity. Etched beta-cloth, however, easily generates particles when contacted because the fiberglass ends are weak. An alternative material which does not generate particles should be used in the cleanroom.

The direction in which the HFMS was oriented was found to have an impact on air flow into and out of the simulator. To minimize particle accumulation, the HFMS was oriented for each activity such that the air flow was tangent to the open doors - thus carying personnel and activity generated contamination downstream, rather than into the HFMS. Related to this phenomenon, the top of the HFMS, between the MRS and the ASM, was open. To prevent cross contamination from other cleanroom activities, this opening was covered with bagging material.

To control particle accumulation in the HFMS, a series of clean zones within the cleanroom were designated. Entrance to the clean zone required passing over a tackymat, and entrance to the HFMS required wiping the soles of one's booties with IPA. By controlling personnel access, the amount of contamination introduced into the HFMS was minimized. This process is discussed in more detail in Reference 2.

## SUMMARY

The use of clean assembly and integration techniques is as important for GSE as it is for the flight hardware which that GSE will contact. Using an integrated contamination control approach to materials selection, integration, and use of GSE will minimize the cleanliness impact to sensitive hardware. Cleanliness data collected during the HFMS assembly, integration and use validates this approach.

## REFERENCES

1. Mitchell, W. J., "Monitoring Deposition of Contamination on Optics Using a Temperature Controlled Quartz Crystal Microbalance (TQCM)", Presented at SPIE *Optical System Contamination - Effects, Measurement, Control IV Conference*, 25-29 July 1994, San Diego, California.

2. Hedgeland, R. J., et al; "An Integrated Approach to Contamination Verification and Control for the HST First Servicing Mission", Presented at SPIE *Optical System Contamination - Effects, Measurement, Control IV Conference*, 25-29 July 1994, San Diego, California.

**Table 1. Verification Requirements, HFMS Surfaces**

| Surfaces | Metal or Tape | Painted (Note 1) | Rinse Prohibited |
|---|---|---|---|
| Cleanroom entry | 400B | 400B + swab | 400 + UV |
| Non-mating or temporary mating | VCHS | 400 + swab | VCHS |
| Prior to becoming inaccessible | 400B | 400B + swab | 400 + UV (Note 2) |
| Prior to permanent mating | None (Note 3) | None (Note 3) | None (Note 3) |
| Prior to mating if de-mating may occur with ORUs present | 400B | 400B + swab | 400 + UV |

Note 1. Solvent restrictions exist
Note 2. Consult the CCE concerning contamination impact
Note 3. Alcohol wipe prior to mating

**Table 2. Cleaning and Verification Requirements, GSE Surfaces**

| Surfaces | Clean to | Verify to |
|---|---|---|
| Contact HFMS non-critical surface | 400B | VCHS |
| Contact HFMS critical surface | 400B | 400B |
| No contact with HFMS surfaces | VCHS | VCHS |
| Not accessible to personnel | Per cleanroom entry requirements | Per cleanroom entry requirements |

**Table 3. HFMS Cleanliness Data**

| Date/Activity | Axial Bay | Radial Bay | ASM Interior | Hub Area |
|---|---|---|---|---|
| 4/9 Pre-integration | 100B | 50B | 150 | 100 |
| 4/9 Post-integration | 200 | (Note 1) | 300 | (Note 2) |
| 5/17 Routine Inspection | 100 | (Note 1) | 100 | (Note 2) |
| 6/5 Routine Inspection | 100 | 100 | 150 | (Note 2) |
| 7/9 Pre-Use | 150B | 150B | 100 | (Note 2) |
| 7/9 Post-Use | (Note 1) | 200 | 200 | (Note 2) |
| 7/28 Pre-Use | 150B | 100B | (Note 1) | (Note 2) |

Note 1. Not sampled at this time
Note 2. Not accessible for sampling

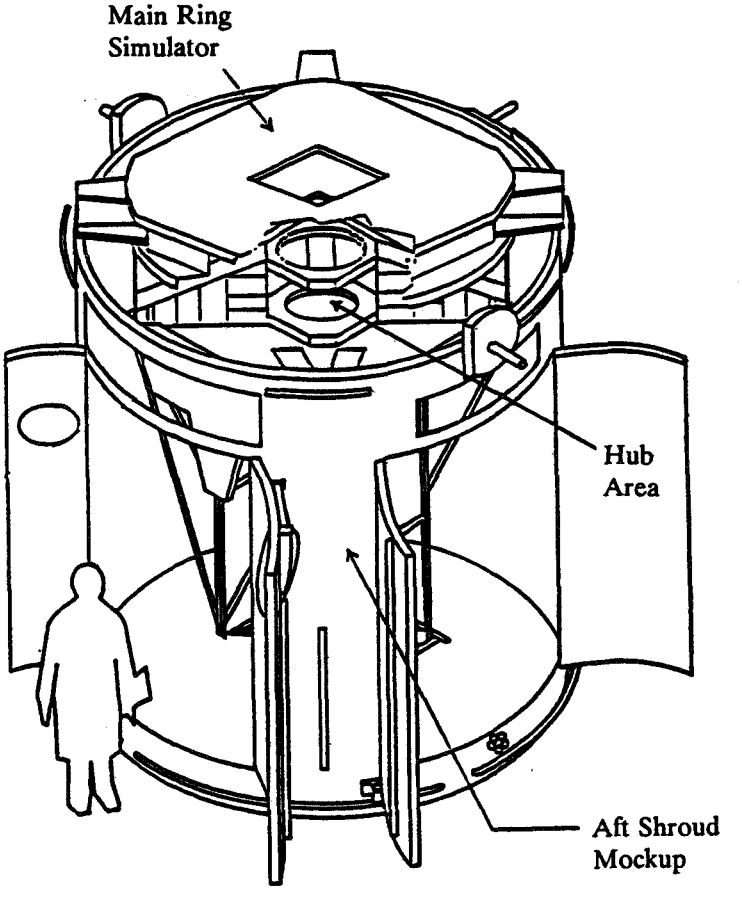


**Figure 1 : HFMS Aft Shroud Mockup**

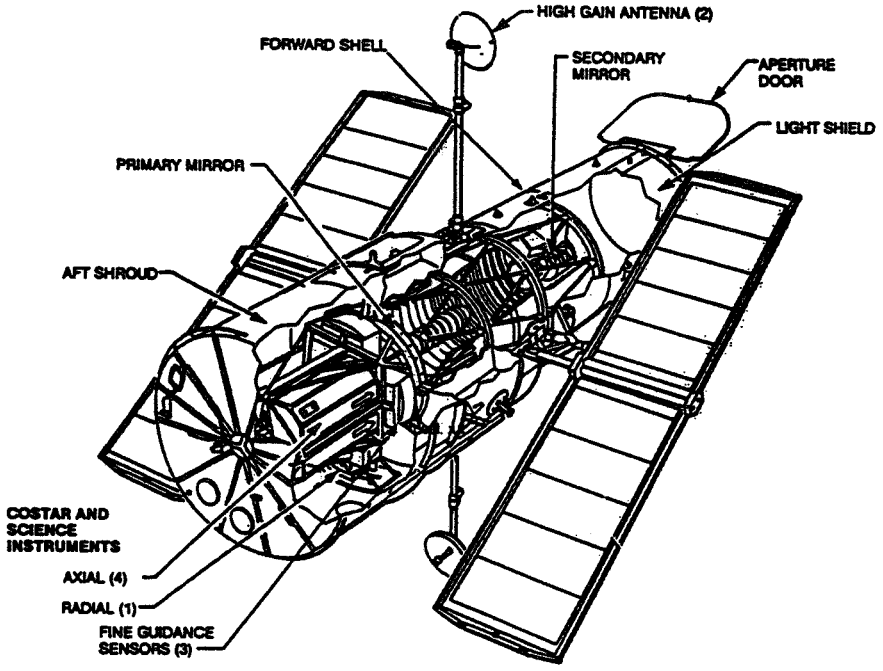


**Figure 2 : HST Showing Location of Aft Shroud**

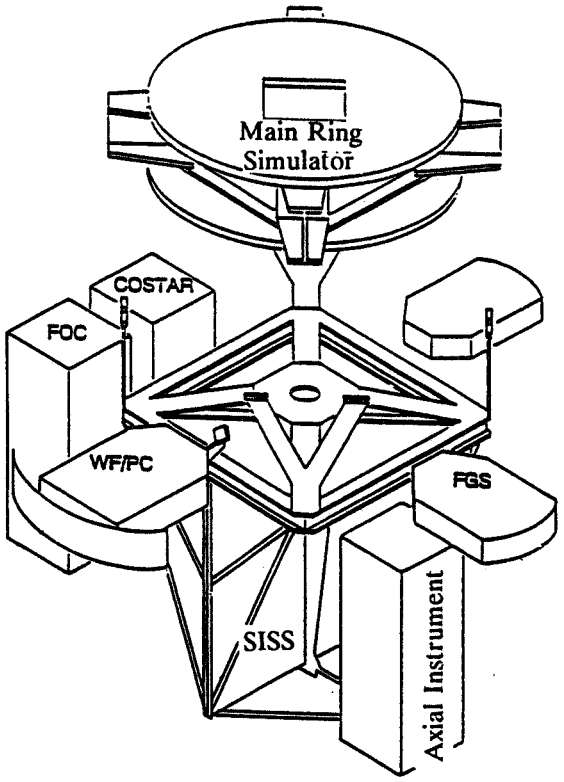


**Figure 3 : HFMS Internal Components**

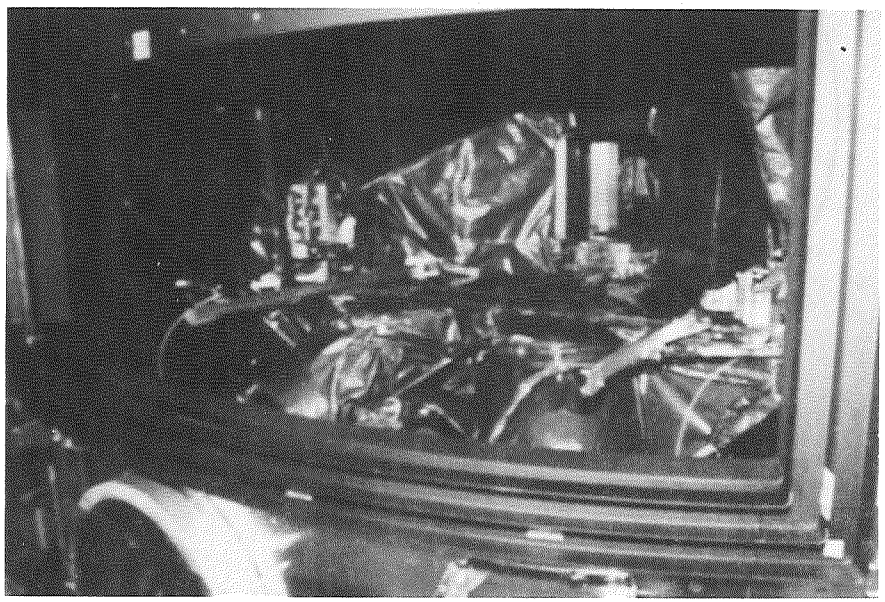

Figure 4 : Radial Bay

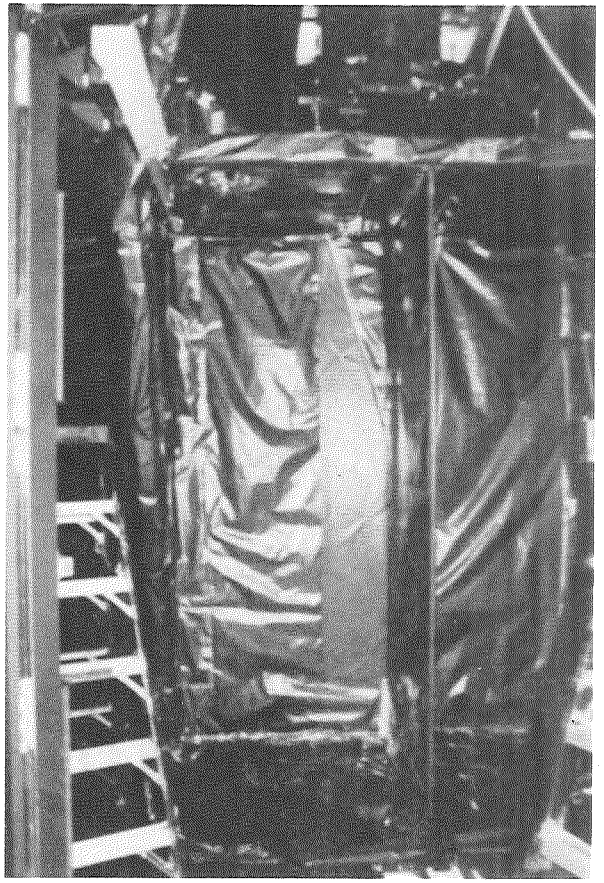

Figure 5 : HFMS Axial Bay

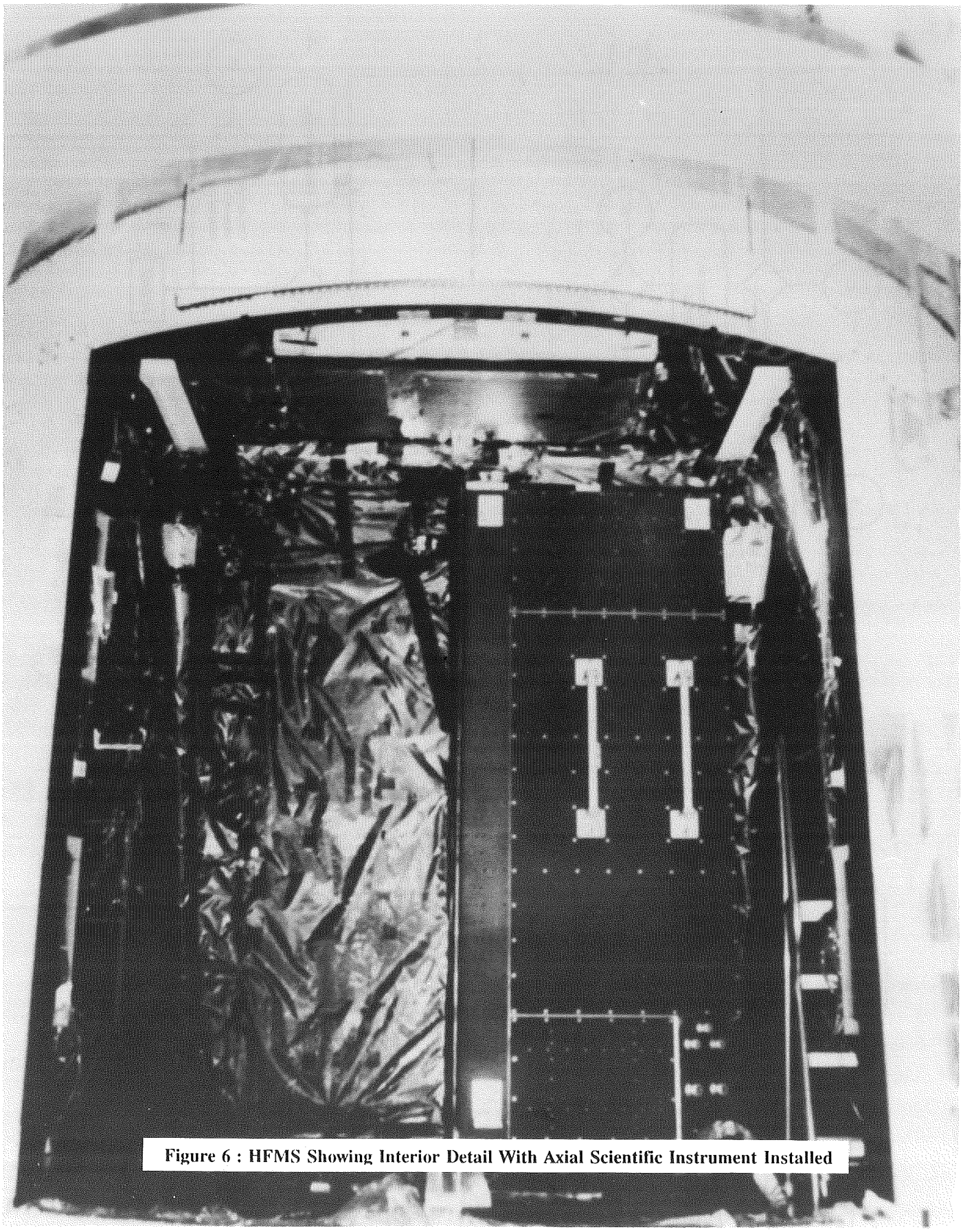

**Figure 6 : HFMS Showing Interior Detail With Axial Scientific Instrument Installed**

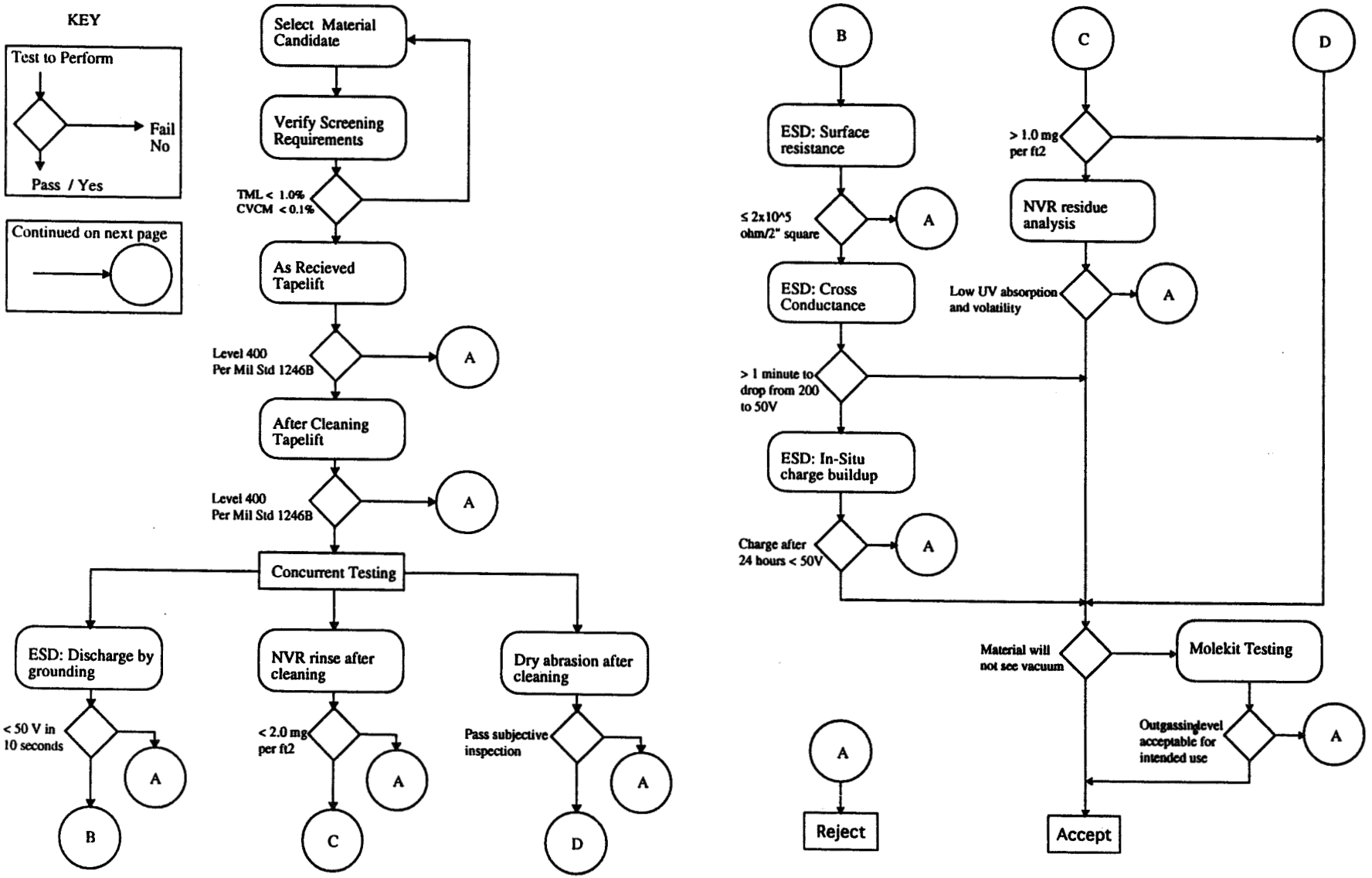


**Figure 7 : Materials Testing Flow Chart**

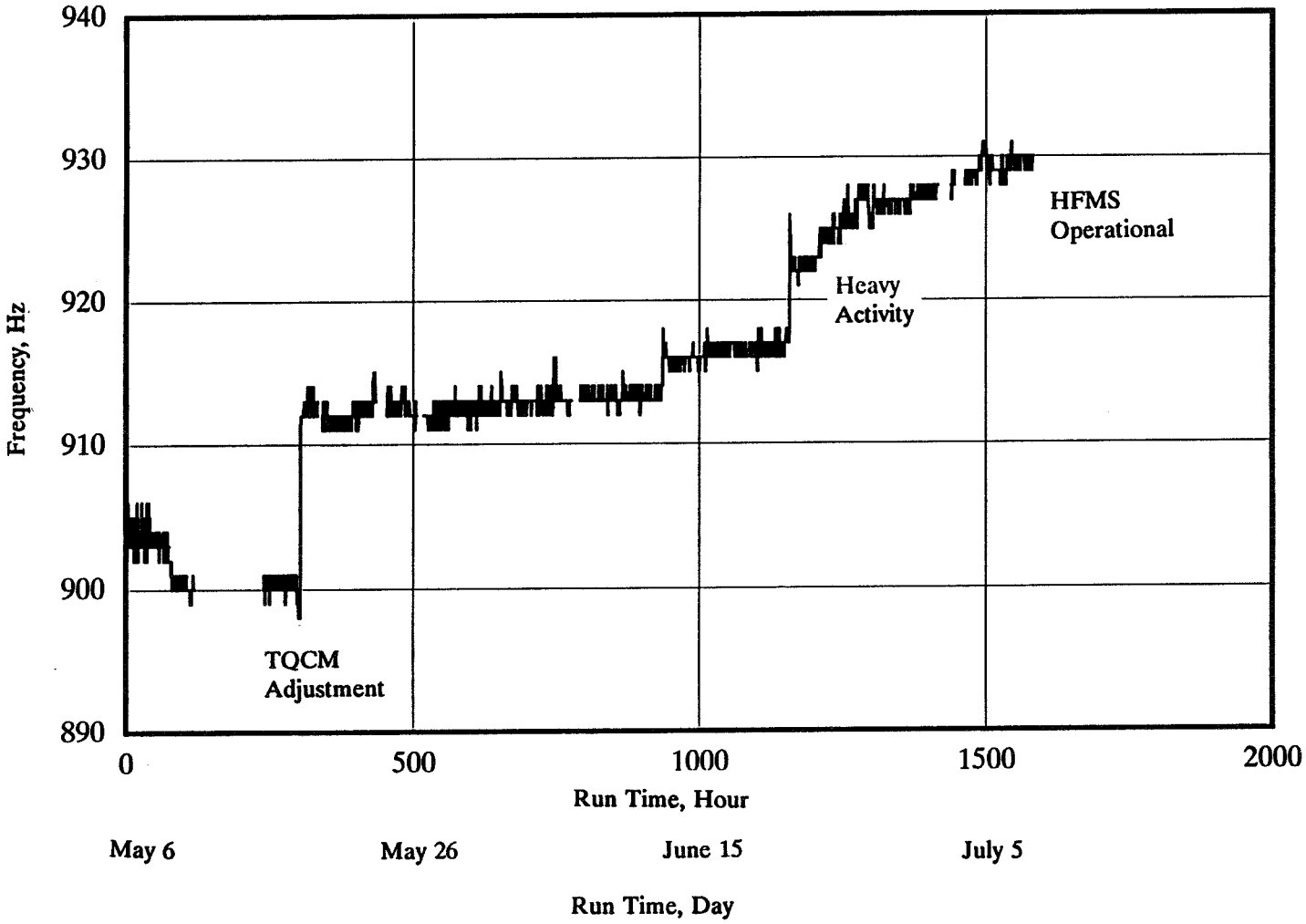


**Figure 8 : TQCM data from the HFMS Hub area, May - June 1993**

# LABORATORY SIMULATION OF LOW EARTH ORBIT (LEO) ATOMIC OXYGEN EFFECTS*

George E. Caledonia, Robert H. Krech and David B. Oakes
Physical Sciences Inc.

## ABSTRACT

PSI's pulsed fast oxygen atom source has been used extensively over the last 7 years to investigate the effects of ambient oxygen atoms impacting materials placed in LEO. During this period we have irradiated well over 2000 material samples with 8 km/s oxygen atoms generated in our source. Typical irradiance level is 3 x $10^{20}$ O atoms/cm$^2$ although some materials have been irradiated to fluence levels as high as 6 x $10^{21}$ O atoms/cm$^2$.

We will review the operating principles and characteristics of our source along with the diagnostic and handling procedures appropriate to material testing. We will then present representative data on the velocity dependence of oxygen atom erosion rates (the PSI source provides oxygen atoms tunable over the velocity range of 5 to 12 km/s) as well as the dependence on material temperature. Specific examples of non-linear oxidative effects related to surface contamination and test duration will also be provided.

## INTRODUCTION

We developed a pulsed fast oxygen atom beam in the mid 1980's[1] under NASA funding to provide a ground test facility to qualify materials to be used in low earth orbit (LEO). This was in response to a number of early space shuttle observations[2-5] of material erosion and property change resulting from interactions with the LEO ambient atmosphere, which is dominantly atomic oxygen. These interactions occur at orbital velocities, ~8 km/s, and for a while there was a frenzied activity to develop atomic oxygen beams which operate at this velocity. The manifold of developed ground sources has been reviewed previously[6] and to our knowledge ours is the only system that provides a high flux neutral oxygen atom beam with wide area operating capability at the desired velocity of 8 km/s. Sets of materials (2.5 x 2.5 cm samples) have been simultaneously irradiated to 8 km/s oxygen atom fluences of 6 x $10^{21}$ cm$^{-2}$ in our facility.

Simultaneous with the development of ground test facilities, a number of flight programs dedicated to evaluating the effect of the LEO environment on materials were also configured and flown. Notable examples of these include the Long Duration Exposure Facility[7-9] and the Evaluation of Oxygen Interactions Shuttle Experiments,[10-11] the most recent of which, EOIM-3, flew in August 1992.

A large data base on LEO environment material effects has been developed as a result of these flight and ground testing activities. Some of this data base is scattered and much can be difficult to interpret due, for example, to contaminant effects on flight tests and the lack of characterization of ground facilities.

Flight tests of materials are preferable but considerably more expensive than ground evaluation. Furthermore, it is difficult to acquire material aging data from flight tests which, LDEF notwithstanding, are generally limited to less than 2 weeks experiment duration. Lastly, the flight data represent an average over the orbital environmental conditions of the flight. Many materials exhibit an increased rate of oxidative behavior with increased temperature, e.g. Ref. 12. Materials can vary in temperatures between -40° C to +65° C as the surface exposure varies from deep space to solar illumination (pathological materials excluded). Thus a measurement over a short shuttle experiment may not be reliably extended to a longer mission with different orbits, even if the aging effects can be linearly extrapolated.

The use of ground test data has been problematical both because facility definitions have been vague and because standardized measurement techniques have not been applied. The need for a measurement protocol is clear. Banks et al. have recently discussed this for asher systems[13] (a technique which has seen some abuse in the past,[14]) and Minton[15] has recently

*This work was supported in part by the Defense Nuclear Agency, monitored by Dr. William Blumberg of the Geophysics Directorate of the USAF Phillips Laboratory, and by the NASA Lyndon B. Johnson Space Center, monitored by Mr. Steve Fitzgerald.

presented version 1 of a detailed protocol. NASA Langley has responsibility under the SEE program to ultimately provide a definitive protocol.

PSI has performed commercial evaluation of LEO materials since 1987 and has developed a measurement protocol very similar to that outlined by Minton. The first step in such a protocol is the clear definition of the capabilities and operating properties of the fast oxygen atom facility. Since the PSI O-atom beam source has been used for material evaluation for the past 7 years, a significant effort has been dedicated to characterizing its operating properties in detail.

The operating principles and characteristics of our device are described below. This discussion is followed by some representative results of material behavior under simulated LEO conditions.

**The Fast Atom Source**

The hyperthermal oxygen atom source and experimental configuration have been described previously[16,17] and will be discussed only briefly here. A schematic of the experimental system is shown in Figure 1. It is comprised of two stainless steel six-way crosses, including an 8 in. cross source chamber housing a pulsed oxygen valve/nozzle assembly, connected to a 16 in. cross expansion chamber. The system is pumped by a cryopump attached to the large cross which maintains a base pressure of $3 \times 10^{-7}$ Torr.

The oxygen atoms are generated in a pulsed laser discharge of pure $O_2$ as described by Caledonia et al.[1] A 12-J/pulse $CO_2$ laser is focused with a 100 cm focal length $BaF_2$ lens into the throat of a 20-deg full angle, 12.5 cm long conical expansion nozzle which has been partially filled with $O_2$ by a pulsed beam valve. The plasma, ignited at the throat, expands out the nozzle dissociating the molecular oxygen in front of it. The nozzle was designed to allow ion and electron recombination while the slower kinetics of atom/atom recombination maintains a highly dissociated beam. The result, at 8 km/s, is an approximately 50 μs pulse of highly dissociated oxygen (> 80% atoms) with less than 1% ion content (the beam is charge neutral). The general beam properties are provided in Table 1 while the diagnostics used in evaluating these properties are summarized in Table 2.

The beam velocity (5 to 12 km/s) is selected by varying the time delay between the pulsing of the $O_2$ valve and the triggering of the $CO_2$ laser. The delay determines the mass of $O_2$ processed by the pulsed discharge which is inversely related to the beam velocity. The velocity is determined by measuring the time of flight of the pulse between two radiometers attached to the source chamber, mounted along the beam axis and separated by 7.6 cm, and filtered to monitor the $^5S$-$^5P$ oxygen atom line (777 nm) (see Figure 1).

We have estimated the flux of oxygen atoms generated per pulse by measuring the mass of $O_2$ processed per pulse. This was determined by using the known time delay between the pulsing of the oxygen valve and the firing of the laser, monitoring the flow of oxygen with a mass flow meter and measuring the temporal profile of the molecular oxygen pulse (laser off) with a pressure transducer aligned along the beam axis. With this measure of the $O_2$ processed per pulse, the flux at any point down stream can be estimated if the expansion characteristics of the beam are known. The expansion properties have been determined previously[13,17] by measuring the fast O-atom erosive mass loss of polyethylene samples mounted 75 cm downstream from the nozzle throat as a function of radial position. The expansion half angle (to 1/e times the on-axis flux) was found to be 14 deg. These calibrations have been cross checked by measuring the absolute oxidation rates of materials and comparing them with equivalent space flight measurements. More recently, as discussed in the next section, the oxidation rate of thin silver films has been used as a calibration standard.

Although the beam is charge neutral, it does have a small but finite ion content. The charge concentration can be decreased by up to a factor of eight using a pair of pseudo-Helmholtz coils as shown in Figure 2. Thus any effects due to charged rather than neutral species can be delineated. Control of the ionic concentration is critical in that some materials are efficiently oxidized by $O^+$ and not by O. The local charge concentration can be measured through use of a retractable Langmuir probe, Figure 2. The probe is positionable both horizontally and vertically and it has been found that the spatial and temporal shape of the ion distribution matches that of the neutral distribution.[17]

We have recently measured the $O(^1D)$ concentration of the beam by monitoring the emission from the forbidden $O(^1D \rightarrow {}^3P)$ transition using a specially constructed bank of narrow-band interference filters. The $O(^1D)$ concentration was found to be $\leq$ 0.4% for a beam velocity of 8 km/s and to increase monotonically with beam velocity over the velocity range of 6 to 12 km/s.

We have also evaluated the translational temperature of the beam. This was done by passing the O-beam through a 0.15 cm diameter circular aperture and measuring the oxidation pattern on a thin silver film witness plate placed 5 cm behind the aperture. Any growth in the beam beyond the slit width is due to the Maxwellian motion of the O atoms and can be related to an effective temperature for an 8 km/s velocity beam. This temperature was deduced by be ~ 300 K at a distance of 85 cm from the nozzle throat. The beam temperature will be higher closer to the throat and is calculated to be ~ 1000 K at the nozzle exit plane.

Lastly, we have measured the VUV/UV content of the beam and find that it is somewhat less then the equivalent LEO value per oxygen atom. Since the beam is pulsed, the VUV radiation can be chopped allowing independent examination of VUV effects on materials.

Our O-beam facility has been employed on several occasions to pre-test materials which were subsequently flown in space experiments. In general, the comparison between flight data and ground test data has been quite good. The most recent large ground test was for the SEE program on materials for the EOIM-3 flight.[18] We irradiated 84 materials to a fluence of $2 \times 10^{20}$ $cm^{-2}$ 8 km/s oxygen atoms and followed a careful protocol of pre- and post-test weighing taking account of water uptake. The Jet Propulsion Laboratory performed subsequent surface analysis. With a few understood exceptions, the comparison between our ground test results for these materials and the flight observations was quite good,[18] demonstrating our ability to simulate LEO conditions.

## EXAMPLE MATERIAL STUDIES

Material oxidation rates can be significantly affected both by the test environment and the test system parameters. In this section we will briefly examine the effect of sample temperature and o-atom velocity on two materials, a thin silver film and μ-crystalline carbon. In the case of the thin silver film the effect of two additional parameters, test duration and surface contamination will be addressed.

We have performed investigations of the temperature dependent oxidative behavior of several materials over the temperature range of 0 to 85° C. An example of such studies is our observations of the oxidative behavior of thin films of silver (600Å)[19] and μ-crystalline carbon (1 μm) which were vacuum deposited onto the crystals of quartz crystal monitors (QCM's). QCM's are the diagnostic of choice for monitoring mass change as the measurements are performed continuously in-situ. Unfortunately in many instances the materials to be tested cannot be coated on a crystal. Then weight change is monitored by pre- and post-testing weighing using our Mettler analytical balance and Cahn micro-balance. (Here a careful protocol must be followed to account for moisture uptake).

The silver and carbon films are good examples for consideration in that the silver gains mass upon oxidation while the carbon loses mass. In these experiments, the QCM was mounted directly onto a temperature-controlled aluminum block and thus the quartz crystal, which is in intimate thermal contact with the QCM base, was maintained to ±0.5° C (material coupons can be monitored in the same manner). Temperature regulation of the QCM was necessary since the oscillator frequency is temperature dependent. Therefore, a change in temperature could be erroneously interpreted as a mass gain or loss.

The silver films are particularly interesting since because of their high oxidation efficiency we feel that they can be used as a standard for laboratory flux calibrations. Furthermore, they have been successfully used in both flight[19] and laboratory[17] studies to study the distributions or hyperthermal oxygen atoms scattered off of selected surfaces. The oxidation behavior of these films exhibits several intriguing effects. Our studies in this are described in detail in Ref. 20 and presented briefly below.

Typical thin film silver oxidation histories for irradiation by 8 km/s oxygen atoms at room temperature are shown in Figure 3. Shown is oxidation depth versus the number of impinging O-atom pulses as determined by the measured mass increase for two film thicknesses. Two important features can be seen. First, no oxidation occurs during the first two hundred pulses. This is typically observed and we relate it to the required removal of a contamination layer on the silver film. Indeed, if we first irradiate the film with several hundred pulses of a fast argon beam and then shortly thereafter impinge it with fast oxygen atoms, we find that oxidation initiation is immediate. Second, after oxidation initiation, the oxidation depth increases linearly with O-atom fluence for approximately the first 250Å of the silver film and then the oxidation rate slows down. We believe the oxidation rate becomes diffusion controlled at these thicknesses and thus only very thin films are useful as a linear calibration source. Note that the observed oxidation rate continues to decrease very dramatically in the case of the 1 μm thick film.

Note that in the interpretation of the QCM data it is important to understand the oxidation process. During the course of our work we realized that the poly-crystalline silver oxidized to the peroxide, AgO, rather than $Ag_2O$. This was determined by

measuring the mass uptake of a totally oxidized film with known silver loading, and verified both by heating the film to 200° C to form $Ag_2O$ and by X-ray diffraction analysis of the film.

These limited tests on silver films demonstrate a number of interesting features. From the perspective of a ground test facility, the two that are most important are the demonstrated role of surface contamination and the observation of the time (thickness) variation in the oxidative behavior.

In further studies we examined the temperature dependence of the silver and carbon oxidation rate over the range of 0° to 85° C. These results are shown in Figure 4, (For convenience, all results are normalized to a silver reactivity of unity at 273 K). Although there is some scatter in the data, the silver oxidation rate is apparently independent of temperature, unlike that for carbon. Thus, we believe that these silver films will provide a good standard for relative investigation of high velocity oxidation behavior of materials. On the other hand, the oxidation rate for this particular form of carbon varies significantly with temperature, a critical effect for predicting lifetime if this material were to be used in an engineering design.

We've also investigated the effect of O-atom velocity on the oxidation rate. This study is complicated by the fact that the number of oxygen atoms per pulse in our beam decreases as the beam velocity increases. Rather than go into the details of our velocity dependent calibration we will only discuss the relative oxidation behavior of the thin silver film and carbon samples as the beam velocity is varied.

The carbon and silver film samples were irradiated simultaneously at velocities of 8, 10 and 12 km/s at a pulse frequency of 2 Hz. The observed oxidation depth versus time of the thin silver film is shown in Figure 5a. The decreasing oxidation rate with increasing velocity correlates with the decreased number of oxygen atoms produced per pulse as the velocity is increased. Indeed within the uncertainty of our calibration the silver film oxidation efficiency remained constant over the velocity range. (This is not surprising since the oxidation efficiency is near unity.)

This result is contrasted with the observed etched depth histories in the carbon sample as shown in Figure 5b. Here it can be seen that the etch rate increased with velocity even though the O-atom fluence decreased. Thus the carbon sample studied shows a strongly velocity dependent oxidation rate. We have observed a similar trend over the velocity range of 6 to 11 km/s in other materials, such as kapton.**

Thus oxidative effects on materials can also depend on the velocity of the O-beam employed in the testing. We have shown one instance where different velocity scalings pertain. Assuredly, these will be others. To avoid errors, it is clear that ground testing for lifetime estimates should be performed at the appropriate LEO velocity.

## SUMMARY

Ground testing provides a critical adjunct to the evaluation and validation of material applicability for low earth orbit operations. Care must be taken, however, to ensure that the ground test facility can provide valid test results. In the case of hypersonic oxygen atom testing, proper material evaluation and data interpretation require both a clear understanding of the characteristics of the test facility as well as a standardized measurement protocol.

Details of the PSI fast oxygen atom source have been provided. This system has been used to evaluate materials since 1987, over 2000 material samples have been tested. Good comparison with space test results has been demonstrated. All major beam parameters, e.g., VUV, metastable content, beam velocity spread, have been evaluated and a standard measurement protocol has been applied.

Example test data has been presented for 8 km/s oxygen atom beam irradiation of a think silver film and a sample of micro-crystalline carbon. Although these data are of interest in their own right, they also demonstrate the importance of controlling test parameters such as contamination level, sample temperature, and beam velocity.

---

**Krech, R.H., "Determination of Oxygen Erosion Yield Dependencies Upon Specific LEO Environments," Physical Sciences Inc. TR-1176, March, 1993.

**REFERENCES**


1. Caledonia, G.E., Krech, R.H., and Green, B.D., AIAA J. 25/1, 59 (1987).

2. Leger, L.J., Spiker, I.K., Kuminecz, J.F., and Visentine, J.T., AIAA Paper 83-2631, Oct. 1983.

3. Leger, L.J., Visentine, J.T., and Kuminecz, J.F., AIAA Paper 84-0548, Jan. 1984.

4. Visentine, J.T., Leger, L.J., Kuminecz, J.F., and Spiker, I.K., AIAA paper 85-0415, Jan. 1985.

5. Green, B.D., Caledonia, G.E., and Wilkerson, T.D., J. Spacecraft, 22, 500 (1985).

6. Caledonia, G.E., in Rarefied Gas Dynamics: Space Related Studies, eds. E.P. Muntz, D.P. Weaver and D.H. Campbell, Vol. 116, Progress in Astronautics and Aeronautics, AIAA, Washington, D.C., pp. 129-142, 1989.

7. Levine, A.S., ed., "LDEF - 69 Months in Space, First Post-Retrieval Symposium," NASA Conf. Pub. 3134, 3 vol., June 2-8, 1991.

8. Levine, A.S., ed., "LDEF - 69 Months in Space, Second Post-Retrieval Symposium," NASA Conf. Pub. 3194, 4 vol., Second, June 1-5, 1992.

9. Levine, A.S., ed., "LDEF - 69 Months in Space, Third Post-Retrieval Symposium," Abstracts, NASA CP 10120, Third, Nov. 8-12, 1993.

10. Visentine, J.T., compiler, "Atomic Oxygen Effects Measurements for Shuttle Missions STS-8 and 41-G," 3 vol., NASA TM 100459, Sept. 1988.

11. Leger, L., Koontz, S., Visentine, J., and Hunton, D., "An Overview of the Evaluation of Oxygen Interactions with Materials III Experiment," LDEF Material Results for Spacecraft Applications Conference, Huntsville, AL, Oct. 26-28, 1992. Also AIAA-93-0497, January 1993, Reno, NV.

12. Kamenetzky, R.R., Linton, R.C., Finckenor, M.M. and Vaughn, J.A., "Effects of Atomic Oxygen on Polymeric Materials Flown on EOIM-3) AIAA 93-4103, AIAA Space Programs and Technologies Conference and Exhibit, Sect. 21-23, 1993, Huntsville, AL.

13. Banks, B.A., Aver, B.M., Rutledge, S.K., and deGroh, K.K., "Atomic Oxygen Durability Evaluation of Protected Polymers Using Thermal Energy Plasma Systems," Int. Conf. on Plasma Synthesis and Processing of Materials, Denver, CO, 1993.

14. Koontz, S.L., Albyn, K., and Leger, L.J., J. Spacecraft, 28, 315 (1991).

15. Minton, T.K., "Protocol for Atomic Oxygen Testing of Materials in Ground-Based Facilities, version Number 1," JPL Publication 94-02, April 1, 1994.

16. Caledonia, G.E., Krech, R.H., Upschulte, B.L., Sonnenfroh, D.M., Oakes, D.B., and Holtzclaw, K.W., AIAA Paper 92-3974, 1992.

17. Caledonia, G.E., Krech, R.H., Upschulte, B.L., Holtzclaw, K.W., and Oakes, D.B., AIAA 94-2638, 1994.

18. Chung, S.Y., Brinza, D.E., Minton, T.K., Stiegman, A.E., Kenny, J.T., and Liang, R.H., "Flight- and Ground-Test Correlation Study of BMDO SDS Materials," JPL Publication 93-31, 1993.

19. Gregory, J.C. and Peters, P.N., "Measurement of the Angular Distribution of 5 eV Oxygen Scattered Off a Solid Surface in Earth Orbit," in Proc. 15th International Symposium on Rarefied Gas Dynamics, Grado, Italy, 1986, eds. V. Boffi and C. Cerignani, pp. 644-656.

20. Oakes, D.B., Krech, R.H., Upschulte, B.L., and Caledonia, G.E., "The Oxidation of Polycrystalline Silver Films by Hyperthermal Oxygen Atoms," submitted to J. Appl. Phys.

**Table 1. Fast O-Beam Properties**

| | |
|---|---|
| Velocity | 8 km/s ± 15% (5 to 12 km/s range) |
| Fluence | ~$10^{18}$ O-atoms/pulse, 3 Hz |
| Composition | >80% oxygen atoms |
| Size | Expandable to >1000 $cm^2$ area |
| Charge content | <1% ions (controllable by pseudo-Helmholtz coils) |
| Metastable content | O($^1$D) concentration <0.4% |
| Temperature | T ≈ 300 K |
| VUV/UV content | One photon per $10^4$ O atoms (similar to LEO) |

**Table 2. O-Beam Diagnostics**

| | |
|---|---|
| Velocity, temporal pulse shape | Radiometers, mass spectrometer (standard quadrupole and TOF) |
| Pulse fluence | Mass flow meter, thin silver film actinometer |
| Beam composition | Mass spectrometer |
| Excited state concentrations | Spectrometer, bandpass filters |
| Charge content (beam is charge neutral) | Langmuir probe |
| Beam shape | Erosive witness samples, positionable Langmuir probe, 2D visible imaging |
| Beam translational temperature | Slitted thin silver film target chamber |

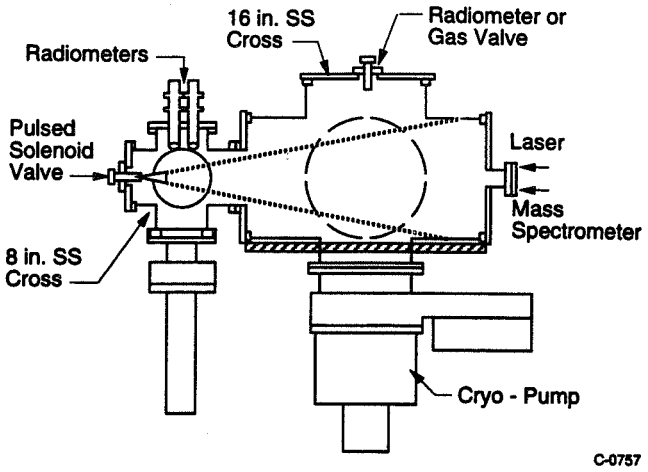


**Figure 1. Schematic of the Fast-2 System**

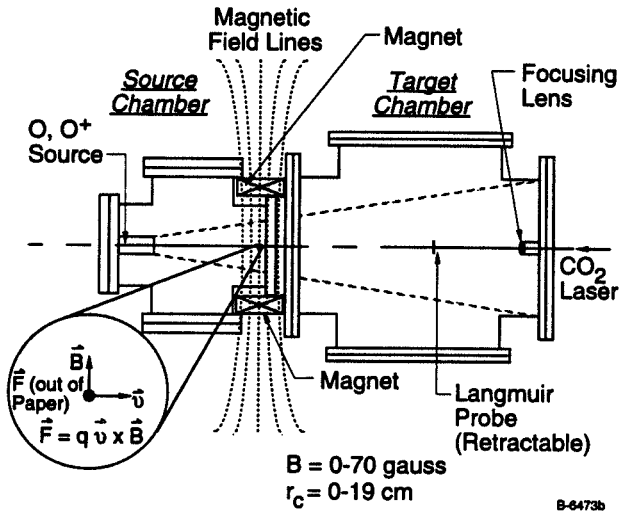


**Figure 2. Schematic of beam ion control system.**

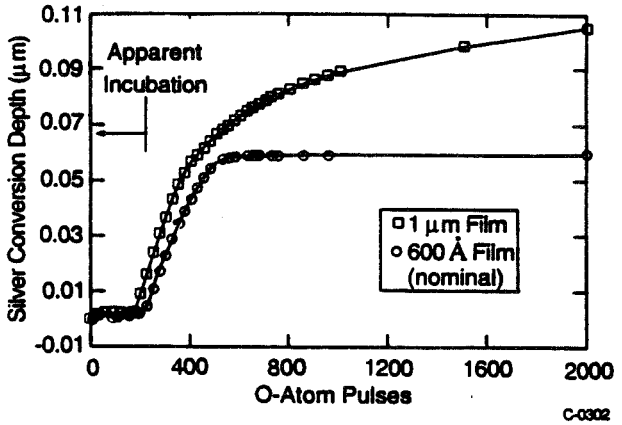


**Figure 3. Oxidation behavior of thin silver films coated on QCM crystals (O-atom velocity = 8 km/s, room temperature).**

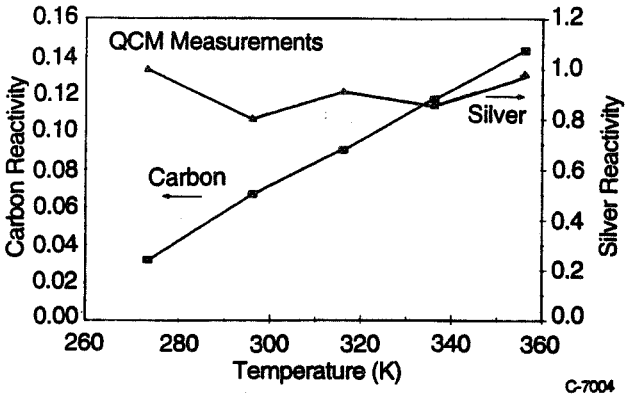


**Figure 4. Measured silver and carbon reactivity vs temperature (O-Atom velocity 8 km/s).**

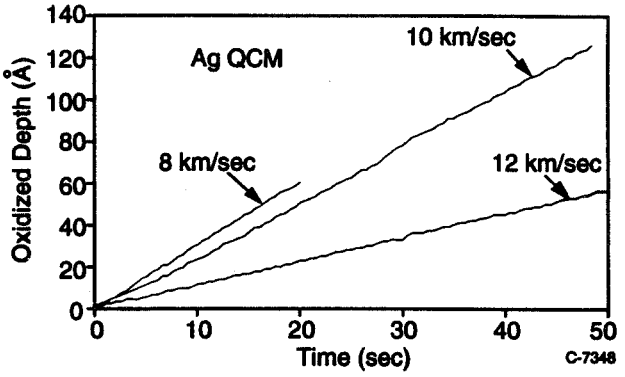


**Figure 5a. Observed silver oxidation depth vs time for 3 O-atom velocities. Pulse repetition frequency was 2 Hz.**

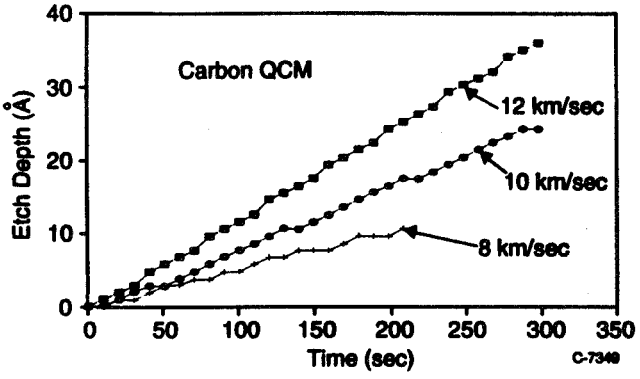


**Figure 5b. Observed etch depth of carbon vs time for 3 O-atom velocities. Pulse repetition frequency was 2 Hz.**

# A FACILITY TO PRODUCE AN ENERGETIC, GROUND STATE ATOMIC OXYGEN BEAM FOR THE SIMULATION OF THE LOW-EARTH ORBIT ENVIRONMENT

Andrew D. Ketsdever, David P. Weaver and E.P. Muntz
Collaboration for Nonequilibrium Technologies
United States Air Force Phillips Laboratory and University of Southern California

## ABSTRACT

Because of the continuing commitment to activity in low-Earth orbit (LEO), a facility is under development to produce energetic atmospheric species, particularly atomic oxygen, with energies ranging from 5 to 80 eV. This relatively high flux facility incorporates an ion engine to produce the corresponding specie ion which is charge exchanged to produce a neutral atomic beam. Ion fluxes of around $10^{15}$ $sec^{-1}$ with energies of 20-70 eV have been achieved. A geometrically augmented inertially tethered charge exchanger (GAITCE) was designed to provide a large column depth of charge exchange gas while reducing the gas load to the low pressure portion of the atomic beam facility. This is accomplished using opposed containment jets which act as collisional barriers to the escape of the dense gas region formed between the jets. Leak rate gains to the pumping system on the order of 10 were achieved for moderate jet mass flows. This system provides an attractive means for the charge exchange of atomic ions with a variety of gases to produce energetic atomic beams.

## INTRODUCTION

Atomic oxygen is the predominant species in the low-Earth orbit (LEO) environment between 180 and 650 kilometers. Oxygen atoms, primarily in the ground ($^3P$) state, results from the photodissociation of molecular oxygen by solar ultraviolet radiation. In the thermosphere (> 80km), it is present at nearly thermal energies (~0.01eV); however, the relative kinetic energies encountered during collisions with spacecraft in LEO is about 5 eV with fluxes in the range of $4 \times 10^{14}$ to $2 \times 10^{15}$ $cm^{-2}$ $sec^{-1}$ normal to the ram direction. Atomic oxygen is observed to be the major source of spacecraft material degradation and glow. Spacecraft which operate in LEO must be designed to withstand the adverse effect of atomic oxygen on sensitive optical instruments, solar arrays, and even structural components. Because of the observations of many satellite and Shuttle missions, several ground based facilities capable of reproducing the LEO environment were developed (ref. 1,2,3). Ground based systems are more adaptable, cost efficient, and practical than dedicated satellite missions.

With this in mind, the Department of Aerospace Engineering at the University of Southern California in conjunction with the United States Air Force's Phillips Laboratory has been developing a facility capable of producing a ground state, energetic O atom beam with energies and fluxes similar to those encountered in LEO (ref. 4,5). Figure 1 shows the general schematic of the energetic atomic beam facility at USC. Ion engine technology has been incorporated to produce a beam of energetic ions. Because the engine can be run on several gases, simulation of any atmospheric specie can be achieved; however, atomic oxygen is the specie of interest in this paper. The ions are accelerated to the desired energy range using electrostatic grids producing a well-collimated beam which is energy selected using a Wien filter (ref. 6). The remaining atomic ions undergo a charge exchange process in molecular hydrogen (large charge exchange cross section, small scattering angle per collision) in the reaction

$$X^+ + H_2 \rightarrow X + H_2^+$$

to produce energetic atoms. In the USC facility, energies upwards of 80 eV with continuous fluxes estimated around $10^{15}$ $sec^{-1}$ should be achievable. This places this facility in an operational energy region which is much higher than other facilities, using microwave discharges or laser discharges expanding through nozzles, whose energies may just reach 5 eV. Descriptions and results of the major system components are the main focus of this paper.

This work is supported by the Air Force Phillips Laboratory (A. Ketsdever-Palace Knight Program) and the University of Southern California.

## BACKGROUND

The USC atomic beam facility consists of three major components. The first is the ion engine which consists of the hollow anode ring jet (HARJ) plasma source and a secondary discharge chamber. The second is the Wien energy filter which consists of an electromagnet and two electrostatic plates. The Wien filter is capable of rejecting ions produced in the ion engine which do not meet the experimental energy requirements. The Wien filter is described in detail in reference 6 and will not be discussed here. The final component is a geometrically augmented inertially tethered charge exchanger (GAITCE) which contains the dense charge exchange gas. The subsequent sections discuss the ion engine and GAITCE in detail.

### Hollow Anode Ring Jet (HARJ) Plasma Source

In order to obtain an energetic beam of neutral atoms by the method outlined earlier, it is first necessary to produce the corresponding ion which can then be accelerated to the desired energy. Ions are formed using a hollow anode electrical discharge plasma source first investigated fifty years ago (ref. 7) for electron beam production in cathode ray tubes. Recently sources of this type have been used for electron beam welding and material processing. The hollow anode plasma source is contained inside a high vacuum facility with molecular oxygen fed into its discharge chamber. Neutrals, ions and electrons all emerge from the aperture in the anode with a relatively dense gas cloud formed in the vicinity of the anode aperture to accommodate a higher degree of ionization and dissociation. To accomplish this, the concept of an inertially tethered gas cloud formed by a ring jet (ref. 8) is used. A ring jet is a series of orifices or a continuous slot through which gas being supplied by a stagnation chamber flows. The orifices or slot are arranged so that their axes are at an angle $\omega$ to the normal of the plane defined by the ring. For the purposes of the hollow anode ring jet (HARJ) used here and shown on the left in Figure 2, the stagnation chamber is the hollow anode discharge chamber.

The HARJ exploits the low pressure, high voltage glow discharge, i.e. discharges operated on the left side of the Paschen curve. In a gas discharge of this nature when a potential is supplied to the cathode, electrons are emitted from the cathode material based on that material's work function. Each electron that leaves the cathode is accelerated toward the anode ionizing the gas in the discharge chamber on the way. Some of the positive ions produced drift towards the cathode and become sources of more electrons by secondary emission due to ion bombardment. The region of interest in this work is that of the abnormal glow with the Aston dark space, cathode glow, Crookes dark space, and the negative glow filling up parts of the discharge chamber. Electrons produced in the discharge have energies close to that corresponding to the cathode fall and are slowed both inside and outside of the anode. Maximum electron beam energy is obtained when the cathode fall occupies the entire discharge chamber; otherwise, the electrons are slowed in the negative glow region before exiting the chamber.

Typical pressures in the discharge chamber range from 1 to 150 μm Hg. At these pressures the discharge occurs for voltages from 1 kV to 5 kV with currents ranging from 10 - 200 mA. This range of discharge characteristics is consistent for a variety of gases such as $0_2$, $N_2$, Ar, $CO_2$, Ne. The discharge voltage has an upper bound which is determined by the temperature the hardware can withstand and by the transition from a glow discharge to the undesired arc discharge. The input power, discharge chamber pressure, and chamber geometry all must be considered when attempting to determine the degree of ionization. In the schematic shown in Figure 2, the plasma is given a preferred direction by the ring jet angle $\omega = 45°$. The source has a stainless steel cathode surrounded by ceramic insulators. The anode is made of aluminum and water cooled to reduce the HARJ operating temperature. The working gas is introduced into the discharge chamber through small radially positioned orifices in the anode cone.

The new generation HARJ has several interesting features. First, the source is omnivorous and can be operated with several different discharge gases. Only the discharge pressure and input power need to be modified for optimum operating conditions. Second, there appears to be no serious erosion of the cathode material due to high energy ion bombardment over several hours of operation. Third, there are no problems starting the discharge. The discharge initiates spontaneously at low currents (~10mA), and the current increases in a controlled manner as the voltage to the discharge is increased. Transition from a glow discharge to an arc discharge is not observed for this source operating at up to 200 mA. Finally, the source is simple in design and easy to operate.

#### Reactions in an Oxygen Discharge

In a discharge of the type mentioned earlier, several chemical processes are available to electron-molecule or electron-atom collisions. Among these are

$$O_2 + e \rightarrow O_2^* + e \quad \text{(Excitation)} \quad \text{(R-1)}$$

$$O_2 + e \rightarrow O_2^+ + e + e \quad \text{(Ionization)} \quad \text{(R-2)}$$

$$O_2^+ + e \rightarrow O^+ + O + e \quad \text{(R-2a)}$$

$$O_2 + e \rightarrow O^+ + O + e + e \quad \text{(R-3)}$$

$$O_2 + e \rightarrow O + O + e \quad \text{(Dissociation)} \quad \text{(R-4)}$$

$$O + e \rightarrow O^+ + e + e \quad \text{(R-4a)}$$

$$O^+ + e + M \rightarrow O + M \quad \text{(Recombination)} \quad \text{(R-5)}$$

$$O_2^+ + e + M \rightarrow O_2 + M \quad \text{(R-6)}$$

$$O^+ + O_2 \leftrightarrow O + O_2^+ \quad \text{(R-7)}$$

This set of reactions is by no means complete and is only meant to show some of the more important reactions taking place within the discharge. Of particular importance are the ionization processes of reactions (R-2), (R-2a), (R-3), and (R-4a) and the ion destruction processes of reactions (R-5) and (R-6). From the ionization cross sections given in reference 9, it is clear that the (R-2) $\rightarrow$ (R-2a) branch for the creation of atomic ions is preferred over the direct dissociative ionization of reaction (R-3) for the range of electron energies from 50-300 eV. The ionization cross-section for reaction (R-4a) is approximately 1.5 x $10^{-16}$ $cm^2$ for an incident electron energy of 100 eV (ref. 10). A consequence of the relatively high cross-sections for reactions (R-2) and (R-2a) is that the emerging beam will have a considerable part of its total current produced by molecular ions. The relative portion of the total beam current produced by $O^+$ ions can be reasonably approximated by the ratio of the cross-sections $q_i(R-2) / \{q_i(R-2) + q_i(R-3)\}$ yielding about 35%.

Figure 3 shows the fraction of oxygen ions in an excited state (ref. 11) being produced by a gas discharge source similar to the one used for this study. The vast majority of the ions produced in both cases are in the ground states for incident electron energies less than 20 eV. However, this fraction of ions in an excited electronic state rises to about 30% for electron energies greater than 50 eV. The ionization reactions (R-3) can be further broken down by (ref. 12)

$$e\,(18.9\text{ eV}) + O_2\,(X^3\Sigma_g^-, v=0) \rightarrow O^+\,(^4S) + O\,(^3P) + 2e \quad \text{(R-3a)}$$

$$e\,(22.2\text{ eV}) + O_2\,(X^3\Sigma_g^-, v=0) \rightarrow O^+\,(^2D) + O\,(^3P) + 2e \quad \text{(R-3b)}$$

Reaction (R-3a) results in the formation of ground state ions by electrons which are 6.84 eV above the 12.06 eV ionization potential. The energy difference between ground $O^+$ ($^4S$) and the first excited state $O^+$ ($^2D$) is 3.32 eV. Thus, the minimum electron energy required to produce excited $O^+$ ($^2D$) ions in reaction (R-3b) is 22.2 eV. As can be seen in Figure 4, the jump in relative concentration of electronically excited ions produced in a gas discharge source occurs near 20 eV.

*Lindholm and Gustafsson* (ref. 13) have also found that $O^+$ ions produced in discharge sources from CO, $N_2O$, and $CO_2$ have different properties. In beams from $CO_2$ the ground state ions seem to be more prevalent than the metastable $O^+$ ($^2D$, $^2P$) states. Beams from CO and $N_2O$ as well as $O_2$ appear to maintain the metastable ($^2D$, $^2P$) states as equally important. The importance of the electronic states of the ions becomes evident when cross sections for the ions neutralization to form O atoms is investigated.

**Incorporation of the HARJ into an Ion Engine**

Although the HARJ produces a relatively large degree of ionization by itself, nearly 60% of the oxygen molecules will escape the HARJ discharge chamber and ring jet flow field un-ionized. For this reason and to allow for acceleration of the ions produced, the HARJ has been incorporated into an ion engine assembly shown in Figure 2. Beyond the exit of the HARJ discharge chamber, the partially ionized plasma forms an inertially tethered gas cloud (due to the ring jet configuration) whose charged particles are partially contained in a secondary discharge volume. In this second discharge, an external electric and magnetic field increases the number of collisions creating a higher degree of ionization and a higher fraction of dissociated molecules.

The positive potential supplied to the secondary discharge volume's anode accelerates the electrons to energies capable of ionizing and dissociating the molecular oxygen. The magnetic field is set up by permanent magnets radially positioned around the anode. The magnetic field strength was designed such that the electrons emerging from the HARJ would acquire a radius of gyration

$$r_g = \frac{m v_{o\perp}}{qB} \quad (1)$$

(where m is the particle mass, $v_{o\perp}$ is the velocity perpendicular to **B**, and B is the magnitude of the magnetic field) on the order of the secondary discharge volume radius. This increases the electrons path length to a few mean free paths within the secondary volume allowing more time for collisions with gas particles. The ions produced in the ion engine are then extracted from the secondary discharge volume through the use of electrostatic grids forming an energetic ion beam. This beam must then be energy selected and neutralized to be of use for degradation studies.

**Ion Charge Exchange Process**

Because of the near resonant charge exchange situation (implying a large charge exchange cross section) and the beneficial 16:1 mass ratio, (implying a small scattering angle) atomic hydrogen is a very attractive charge exchange target gas. However, it is difficult to produce and maintain pure hydrogen atom gas clouds. Cross sections for oxygen ion charge exchange in molecular hydrogen have also been investigated. This process may indeed have two branches due to the added modes introduced by the hydrogen molecule. These branches are

$$O^+ + H_2 \rightarrow O + H_2^+ \qquad \text{(Charge Exchange)} \qquad \text{(R-8)}$$

and

$$O^+ + H_2 \rightarrow OH^+ + H \qquad \text{(R-9)}$$

where the energy defect for (R-8) for ground state ions and molecules is $\Delta E = 1.81$ eV. Obviously if the process expressed by (R-9) dominates the flow field chemistry, molecular hydrogen must be excluded as a viable charge exchange gas.

Previous studies (ref. 14,15) have concluded that (R-9) is the major branch for oxygen ions with incident energy near thermal energies (~0.01 eV). The rate constant found in reference 9 for reaction (R-9) obtained from a gas discharge on $CO_2$ (i.e. mostly ground state $O^+$ ions produced) was $1.58 \times 10^{-9}$ $cm^3$/sec which is in reasonable agreement with the other studies at thermal energies. *Kim, et al.* (ref. 15) found evidence that the rate constant for reaction (R-9) is decidedly less for gas discharges on $O_2$ than it is for $CO_2$ discharge. This was found to be caused by the relatively high percentage of metastable ions ($^2D$, $^2P$) produced by gas discharge sources operating on pure molecular oxygen (ref. 11). Therefore, the electronically excited $O^+$ ($^2D$, $^2P$) ions have a significantly smaller reaction rate constant then ground state ($^4S$) ions at thermal energies. As mentioned earlier, the HARJ is expected to produce anywhere from 20 - 40% of metastable oxygen ions. This fact coupled with incident ion energies, which are an order of magnitude or two larger than thermal energies (and enough to overcome the energy defect of 1.81 eV), indicates that the reaction branch (R-9) will probably be negligible.

The charge exchange reaction (R-8) can be further described by

$$O^+ (^4S) + H_2 (X'\Sigma_g^+, v''=0) \rightarrow O (^3P) + H_2^+ (X^2\Sigma_g^+, v') \qquad \text{(R-8a)}$$

$$O^+ (^2D) + H_2 (X'\Sigma_g^+, v''=0) \rightarrow O (^3P) + H_2^+ (X^2\Sigma_g^+, v') \qquad \text{(R-8b)}$$

$$O^+ (^2D) + H_2 (X'\Sigma_g^+, v''=0) \rightarrow O (^1D) + H_2^+ (X^2\Sigma_g^+, v') \qquad \text{(R-8c)}$$

The energy defect for reaction (R-8a) is 1.81 eV which is sufficiently large that the probability of charge transfer is small. Reaction (R-8b) only has an energy defect of about 0.1 eV when the product ion vibrational level v' is 6 or 7. For v'=0 in reaction (R-8c), the energy defect is 0.46 eV. Due to the low $\Delta E$ for (R-3b) and (R-3c), the cross sections for these reactions are expected to be large. The charge exchange cross-sections for reaction (R-8a) have been experimentally determined by a variety of sources. Figure 4 (ref. 12,13) shows the relative cross sections for the reactions (R-8b,c) as a function of the incident ion kinetic energy for metastable ions formed in the discharge. As Figure 3 shows, the amount of metastables produced is dependent on the electron energy. Above about 25 - 30 eV, the relative concentration of metastable ions is around 30%. Figure 4 shows that the cross section for charge exchange is larger for the metastable ion reactions than that of the ground state. This is consistent with the statements made earlier in the section. The ratio of the charge exchange cross sections for atomic and molecular hydrogen, up to large ion energies, ranges from about 1 to 2 indicating that not much is lost using molecular hydrogen as the charge exchange gas. Cross sections for various ion/molecule charge exchange and scattering collisions are shown in Table 1.

The creation of fast neutral species, for the case of fast ions impinging on a cloud of charge exchange gas is given by (ref. 4)

$$d(n_{of}) = (n_{if} Q_{ce} - n_{of} Q_{ion} - n_{of} Q_{sc})\, d(I_n) \qquad (2)$$

where $n_{of}$ is the number density of the fast neutrals produced, $n_{if}$ is the number density of the fast incoming ions, $I_n$ is the column depth of charge exchange gas, and $Q_{ce}$, $Q_{ion}$, and $Q_{sc}$ are the charge exchange, ionization, and scattering cross sections.

It is assumed that $n_{of}$=0 when $I_n$=0, and that a near-resonant process is taking place, i.e. $Q_{ion} \ll Q_{ce}$. The solution to (2), using the results in Table 1 for $O^+/H_2$ charge exchange, gives the maximum degree of neutralization as nearly 45% which occurs for a column depth of charge exchange gas of $1.44 \times 10^{15}$ $cm^{-2}$. This assumes that two scattering collisions are allowed for the entire process. This column depth must be maintained within the central region of the GAITCE in order to produce a high neutral atom yield

**Geometrically Augmented Inertially Tethered Charge Exchanger (GAITCE)**

The ions which pass through the Wien filter undergo a charge exchange process via collisions with a charge exchange gas within the confines of the geometrically augmented inertially tethered charge exchanger (GAITCE) producing a neutral atomic beam. The GAITCE configuration is shown in Figure 5. In a typical experiment, reducing the mass flow of charge exchange gas into the vacuum system is always of interest. The charge exchange gas is introduced to the GAITCE geometry by opposed jets, with the jet flows acting as collisional barriers to the escape of relatively dense gas trapped in the central region. The GAITCE is differentially pumped to remove the gas which has passed through the perforated pumping screen and no longer available for charge exchange. Skimmers are added in the flow field to further aid in the containment process. This design allows for a column depth of charge exchange gas adequate for a high degree of neutralization while minimizing the mass flow to the high vacuum portion of the atomic beam pumping system.

The opposed containment jets of the GAITCE are basically free jets expanding into a relatively low-density (compared to the jet stagnation density) background gas. The density of the free jet flowfield decreases as the inverse square of the distance R from the source as measured along a streamline. The density varies from streamline to streamline by (ref. 16)

$$\frac{\rho(R,\theta)}{\rho(R,0)} = \cos^2\left(\frac{\pi\theta}{2\phi}\right) \tag{3}$$

where R is the distance from the source measured along a streamline, $\theta$ is the angle of the streamline measured from the source center line, and $\phi$ is a constant based on the gas used ($\phi$ = 1.365 for $\gamma$ = 1.67 and 1.662 for $\gamma$ = 1.40). A simple physical model for free jet penetration into a background gas has been developed by *Muntz, et al.* (ref. 17). The background gas density is reduced from its equilibrium value far from the containment jet by collisions with jet species.

An important dimension in this formulation is the distance from the jet at which the background density has been reduced by 1/e of its value far away from the jet. This distance is known as the radius of penetration, $r_p$. As a function of $\theta$ from the jet centerline, $r_p$ is given by (ref. 17)

$$r_p(\theta) = \left(\frac{V_{rel}}{C_B}\right)\pi\sigma_{JB}^2\, n_{J_o} c_J(\gamma)\, D_o^2 \cos^2\theta \tag{4}$$

where

$$V_{rel} = v_{J\infty} + C_B \;;\; v_{J\infty} = \sqrt{\frac{2\gamma}{\gamma-1}\frac{kT_J}{m_J}} \;;\; C_B = \sqrt{\frac{8kT_B}{\pi m_B}} \;;\; \sigma_{JB} = \frac{\sigma_J + \sigma_B}{2}$$

Here, $v_{J\infty}$ is the jet limit velocity, $C_B$ is the mean thermal speed of the background gas, $\sigma_{JB}$ is the combined collision diameters, $n_{J_o}$ is the jet stagnation number density, $D_o$ is the jet orifice diameter, and $c_J(\gamma)$ is a constant ($c_J(\gamma)$ = 0.15 for $\gamma$ = 1.67 and 0.0863 for $\gamma$ = 1.40), $m_J$ and $m_B$ are the mass of the jet and background gases, and $T_j$ and $T_B$ are their temperatures, respectively.

The radius of penetration can be nondimensionalized by $D_o$ to give $R_p = r_p / D_o$. For conditions where $R_p < 1$, the background gas begins to penetrate the jet flowfield up to the jet itself. For the application of background gas containment by opposed jets, which is of interest here, it is important to keep $R_p \gg 1$ or $r_p \gg D_o$. As can be seen from equation (4), $r_p(\theta)$ goes to zero as $\theta$ approaches 90°. Thus, the background gas can penetrate and in fact escape the central region of the GAITCE through the skimmer openings of the charge exchanger at these large angles causing "leaks" to the high vacuum portion of the system. To counter this adverse effect, the containment jets were positioned on traverses so that the angle $\theta$ to the edge of the skimmer openings of the charge exchanger could be varied.

There are two competing factors which determine the most efficient jet placement along the GAITCE centerline (z-direction). The first is the amount of the jet mass flow, $\dot{M}_{jet}$, which is rejected by the skimmer, thus not entering the central region of the GAITCE. As z increases and thus $\theta$ ( $\theta = \text{atan}(R_{opening}/z)$ ) decreases, the jet flow which does not enter the skimmer, $\dot{M}_{ne}$, increases as equation (3) suggests. $\dot{M}_{ne}$ is lost to the chamber pumping system. This factor is counteracted by the

effect of the radius of penetration. As z increases, the effective radius of penetration in the direction of the edge of the skimmer opening, $r_{p,edge}$, increases as equation (4) shows. A larger $r_{p,edge}$ implies more containment of the background gas in the central region of the GAITCE is expected. Because the jet stagnation number density is a governing parameter of $r_p$, larger values of $\dot{M}_{jet}$ are also expected to contain more efficiently.

## EXPERIMENTAL FACILITY

The atomic beam facility is cryogenically pumped using gaseous (24-26 K) helium and is capable of maintaining pressures of about $1 \times 10^{-5}$ Torr when the mass flow from all sources is 20 mg/sec. This vacuum facility is backed by two large diffusion pumps (8500 l/sec) and a 1000 l/s turbopump to remove any incondensibles. The facility is fitted with a variety of instrumentation and diagnostic tools including a quadrupole mass spectrometer, an electron beam, a baratron with scanning valve capable of reading multiple pressure ports, and a traversing system capable of moving the entire length of the chamber.

The first step in acquiring experimental data was to investigate the discharge characteristics of the ion engine. An electrostatic energy analyzer (EEA) was used to obtain the ion energy distributions and fluxes as a function of the ion engine parameters ($p_{dc}$, $I_{dc}$, $I_{sd}$, and $V_{acc}$). The EEA probe is shown in Figure 6. It is similar in design to the one used by *Lipschultz, et al.* (ref. 18) in that it has a three grid assembly preceding the collection cup. The first grid, G1, is used to repel unwanted species, namely electrons. For this study it is kept at the same potential as the ion engine accelerating grid ($V_{acc}$) so that the incident ions are not accelerated in the probe. The bias $V_2$ to the second grid, G2, is varied to limit the collection of positive ions to those with a velocity greater than

$$v_c = -\sqrt{\frac{2q(V_2 - V_p)}{m_i}} \tag{5}$$

where q is the elemental charge, $V_p$ is the local plasma potential, and $m_i$ is the ion mass. The last grid, G3, is normally biased to suppress secondary electron emission from the collecting cup. However, previous work using the EEA have shown little evidence of a secondary emission. Therefore, the potential on grid 3 and the collecting cup are normally held at $V_{acc}$ so that no ion acceleration takes place within the probe. The EEA ion current measurements are used to estimate the total ion flux from the engine.

Next, the GAITCE was investigated as a stand alone component. The general experimental set up for the charge exchanger is shown in Figure 5 with one exception. In the experimental configuration, the back opening of the GAITCE was blocked off (GAITCE length = 50.2 cm) with the reflection of molecules off the back wall modeling the presence of an opposing jet. The differential pumping of the central region is done through a perforated cylinder to evenly distribute the pumping throughout. Two pumping ports on the side of the GAITCE are open to the chamber in this experiment because of the availability of a large cryopump. However as a component in an atomic beam system, the charge exchanger will be differentially pumped by a high throughput turbopump. Typically the open area of the perforated cylinder is half of the combined pumping port area. Although charge exchange with molecular hydrogen is desired, molecular nitrogen is used as a model gas in this experiment due to cryopumping restrictions

The containment jet is mounted on a traverse which allows movement in the z-direction on the GAITCE centerline. A skimmer of half-angle 30° is attached to the front of the GAITCE to aid in containing the background gas. The skimmer was made from available materials; thus, the half-angle was not considered in the initial design. For future work, there may be an advantage to matching the skimmer angle to the angle from the jet (at some position, z) to the edge of the front opening. The containment jet diameter, $D_o$, is 0.246 cm, and the diameter of the front opening of the GAITCE is nearly 7.0 cm. Note that the jet diameter is only a few percent of the skimmer opening diameter; thus, the blockage of ions, caused by the presence of the jet, into the GAITCE is negligible. Pressure inside the central region and outside the pumping cylinder are recorded using an MKS baratron with a scanning valve. An impact pressure probe provided pressure readings outside the skimmer opening of the GAITCE. Generally, the probe was one skimmer opening radius downstream (+z-direction) of the opening from the charge exchanger and able to traverse in the +x-direction, giving pressure profiles across the skimmer opening.

## RESULTS

### Ion Engine

Figure 7 shows the HARJ discharge chamber voltage versus current characteristic curve (no secondary discharge). As the voltage is increased, the current across the discharge chamber increases steadily and in a well-behaved manner. The locus of

points of the characteristic curve shift to the right as the HARJ discharge chamber pressure increases. The transition from a high voltage, low current glow discharge to the low voltage, high current arc discharge was not seen in the pressure and voltage ranges used in this experiment. After an initial warm up period of a few minutes, the HARJ discharge current remained relatively constant over a period of several hours. The source has run consistently for over 100 hours without any servicing.

Figure 8 shows a typical EEA current ($I_{probe}$) versus the potential on the second grid, $V_2$, for $p_{dc}$= 100 μm Hg, $I_{dc}$= 50 mA, $I_{sd}$= 100 mA, and $V_{acc}$= 0 V. The EEA was positioned one secondary discharge radius downstream of the accelerating grid. Normalized energy distributions also shown in Figure 12 are derived from

$$E(V_2) = \left[\frac{d(I_{probe})}{dV_2}\right] / E_{max}. \tag{6}$$

The energy distribution has a defined peak at 20 eV with a full-width half maximum of about 8 eV. By increasing $I_{sd}$ by a factor of two, the total ion current from the ion engine increases by a factor of 2.25 and increases by more than a factor of 4 by tripling $I_{sd}$. The ion flux of positive ions per unit area per second is then easily calculated by dividing the probe current by the factor (e $A_p$) where e is the elemental charge and $A_p$ is the area of the probe collection cup (3.14 $cm^2$). Ion fluxes obtained at these experimental conditions range from 0.66 to 2.7 x $10^{12}$ $cm^{-2}$ $sec^{-1}$. The total ion flux per second over the entire discharge volume ranges from 0.29 to 1.2 x $10^{15}$ $sec^{-1}$.

The ion current measurements can be significantly modified by shielding the teflon exterior of the EEA to reduce repulsion due to space charging. Also the assumption made above was that the EEA was completely accessible to incident ions; however, each of the three grids is only about 50% transparent. Without careful alignment of the grid mesh, blockage of the cup may be on the order of 75-85%. This suggests that the flux estimates made earlier may be a factor of 2-4 too low.

### Charge Exchanger

The GAITCE performance is measured by the observed gain in background gas containment using the containment jet configuration over a configuration with the same central region pressure where the gas is able to diffuse freely from the neutralizer's interface with the high vacuum. The gain is given by

$$Gain(\dot{M}_{jet}, z) = \frac{\dot{M}_{diff}}{\dot{M}_{esc} + \dot{M}_{ne}} \quad ; \quad \dot{M}_{diff} = m_B \frac{n_{cr} C_B}{4} A_o \tag{7}$$

where $\dot{M}_{diff}$ is the mass flow diffusing out the skimmer opening assuming no containment jet is used, $\dot{M}_{esc}$ is the mass flow escaping out the skimmer opening with the jet operating, as interpolated from an impact pressure probe measurement, $\dot{M}_{esc} + \dot{M}_{ne}$ represents the load on the vacuum system, $m_B$ is the background gas molecule mass, $n_{cr}$ is the background gas number density in the GAITCE central region, and $A_o$ is the skimmer opening area. $\dot{M}_{diff}$ is essentially constant over a reasonable range of the jet's position.

Figure 9 shows the gain as a function of z and $\dot{M}_{jet}$ for a nitrogen ($\gamma$=1.40) gas flow. As expected the gain increases for a given mass flow by increasing z a moderate amount (~0.6 cm). Also plotted is $r_{p,edge}$ nondimensionalized by the distance from the jet to the skimmer edge $d_{edge}$. At small values of z, the effect of increasing $r_{p,edge}$ dominates the gain equation. However as z increases, $\dot{M}_{ne}$ takes over as the major loss to the chamber pumping system.

## CONCLUSIONS

Figure 9 suggests that reductions of the leak rate from the GAITCE to the high vacuum portion of the beam system can approach a factor of 10 for moderate $\dot{M}_{jet}$. This is a tremendous benefit to systems which require low chamber background pressures to maintain beam collimation and physical properties such as internal states and neutral atomic species. As anticipated the gain increases as $r_{p,edge}$ and $\dot{M}_{jet}$ increase. Increases in $\dot{M}_{jet}$ act to increase $r_p$ across the entire skimmer opening thus increasing the relative background gas containment. The GAITCE makes an attractive charge exchanger for atomic oxygen ions with molecular hydrogen.

Previous studies (ref. 19) have indicated that the ion beam produced by the ion engine under consideration here has nearly a 1:1 ratio of molecular ions to atomic ions. Therefore, if the molecular ions are removed from the beam, this implies that approximately half of the ion flux produced by the ion engine will be removed from the flow field. If the ion energy distribution of the $O^+$ ions is narrowed to ±1 eV in the Wien filter, the ion flux is expected to be reduced by about an order of magni-

tude. The maximum possible conversion of the remaining ions to fast neutrals using molecular hydrogen as a charge exchange gas is only about 45%, further reducing the atomic beam flux. In order to achieve a fast neutral flux on the order of $10^{15}$ $sec^{-1}$ an initial flux of ions of $5x10^{16}$ $sec^{-1}$ must be produced by the ion engine taking these reductions into consideration. This is about an order of magnitude higher than the ion flux measured for the ion engine currently in the atomic beam facility. Significant improvements in the flux (up to 10x) can be expected from the next generation of ion engines by designing a larger plasma source and by running the source at higher discharge currents.

## REFERENCES


1. Cross, J. and Blais, N.,"High Energy/Intensity CW Atomic Oxygen Beam Source," *Rarefied Gas Dynamics*, Progress in Aeronautics and Astronautics, Vol. 116, AIAA, Washington D.C., 1989, pp. 143-155.

2. Caledonia, G., Krech, R., Upschulte, B., Sonnenfroh, D., Oakes, D. and Holtzclaw, K.,"Fast Oxygen Atom Facility for Studies Related to Low Earth Orbit Activities," AIAA Paper 92-3972, 1992.

3. Stidham, C., Stueber, T., Banks, B.,Dever, J., Rutledge, S. and Bruckner, E.,"Low Earth Orbital Atomic Oxygen Environmental Simulation Facility for Space Materials Evaluation," NASA Tech. Memorandum 106128, 1993.

4. Ketsdever, A., Weaver, D. and Muntz, E.P.,"A Molecular Hydrogen Ring Jet Charge Exchanger for the Production of Energetic Oxygen Atoms," AIAA Paper 94-0371, 1994.

5. Muntz, E.P., Boyd, I. and Ketsdever, A.,"Rarefied Flow Testing in the 1990's: Measuring Those Phenomena that are Difficult to Calculate," AIAA Paper 94-2631, 1994.

6. Teal-Quiros, E., and Prelas, M.,"New Tilted-Poles Wien Filter with Enhanced Performance," *Review of Scientific Instruments*, **60**(3), 1989, pp. 350-357.

7. Dugdale, R., Maskrey, J., Ford, S., Harmer, P. and Lee, R.,"Glow Discharge Beam Techniques," *Journal of Material Science*, **4**, 1969, pp. 323-335.

8. Muntz, E. P., Kingsbury, D., De Vries, C., Brook, J. and Calia, V.,"Inertially Tethered Clouds of Gas in a Vacuum," *Rarefied gas Dynamics*, B. G. Teubner Stuttgart, Germany, 1986, pp. 474-485.

9. Farchi, A., Aubert, J., Wartski, L., Coste, P. and Mardirossian, C.,"A Broad Beam Microwave $O^+$ Ion Source," *Journal of Physics D*, **25**(7), 1992, pp. 1149-1151.

10. Heinrich, F., Stoll, H., Scheer, H. and Hoffmann, P.,"Energy Analysis of Neutral Atoms in Broad Oxygen Ion Beams by Doppler-Shift Measurements," *Journal of Applied Physics*, **68**(11), 1990, pp. 5428-5434.

11. Turner, B., Rutherford, J. and Compton, D.,"Abundance of Excited Ions in $O^+$ and $O_2^+$ Ion Beams," *Journal of Chemical Physics*, **48**(4), 1968, pp. 1602-1608.

12. Moran, T. and Wilcox, J.,"Charge Transfer Reactions of Ground $O^+(^4S)$ and excited $O^+(^2D)$ State Ions with Neutral Molecules," *Journal of Chemical Physics*, **69**(4), 1978, pp. 1397-1405.

13. Gustafsson, E. and Lindholm, E.,"Ionization and Dissociation of $H_2$, $N_2$, and CO in Charge Exchange Collisions with Positive Ions," *Arkiv för Fysik*, **18**(13), 1960, pp. 219-239.

14. Smith, D., Adams, N. and Miller, T.,"A Laboratory Study of the Reactions of $N^+$, $N_2^+$, $N_3^+$, $N_4^+$, $O^+$, $O_2^+$, and $NO^+$ Ions with Several Molecules at 300 K," *Journal of Chemical Physics*, **69**(1), 1978, pp. 308-318.

15. Kim, J., Theard, L. and Huntress, W.,"ICR Studies of Some Hydrogen Atom Abstraction Reactions: $X^+ + H_2 \rightarrow XH^+ + H$," *Journal of Chemical Physics*, **62**(1), 1975, pp. 45-52.

16. Ashkenas, H. and Sherman, F.,"The Structure and Utilization of Supersonic Free Jets in Low Density Wind Tunnels," *Rarefied Gas Dynamics*, Academic Press, New York, 1966, pp. 84-105.

17. Deglow, T. and Muntz, E.P.,"Isoptope Separation by Jet-Background Interaction," *Journal of Applied Physics*, **50**(2), 1970, pp. 589-594.

18. Lipschultz, B., Hutchinson, I., LaBombard, B. and Wan, A.,"Electric Probes in Plasmas," *Journal of Vacuum Science Technology A*, **4**(3), 1986, pp. 1810-1816.

19. Pham-Van-Diep, G., Muntz, E. P. and Weaver, D.,"Ring-Jet Neutralization of Low Energy Oxygen Ion Beams," *Rarefied Gas Dynamics*, VCH, 1991, p. 1553.

**Table 1. Charge Exchange and Scattering Cross Sections for Collisions Partners at 10 eV**

| Charge Exchange Partners | $Q_{ce}$ ($\times 10^{-16}$ cm$^2$) | $Q_{sc}$ ($\times 10^{-16}$ cm$^2$) | $\theta_{max}$ (degrees) |
|---|---|---|---|
| $O^+$ in $O_2$ | 5.0 | 8.0 | > 90 |
| $O^+$ in O | 35 | 5.0 | 90 |
| $O^+$ in H | 16 | 3.0 | 3.5 |
| $O^+$ in $H_2$ | 9.0 | 6.9 | 7.5 |
| $O_2^+$ in $O_2$ | 30 | 10 | 90 |
| $N_2^+$ in $N_2$ | 35 | 12 | 90 |

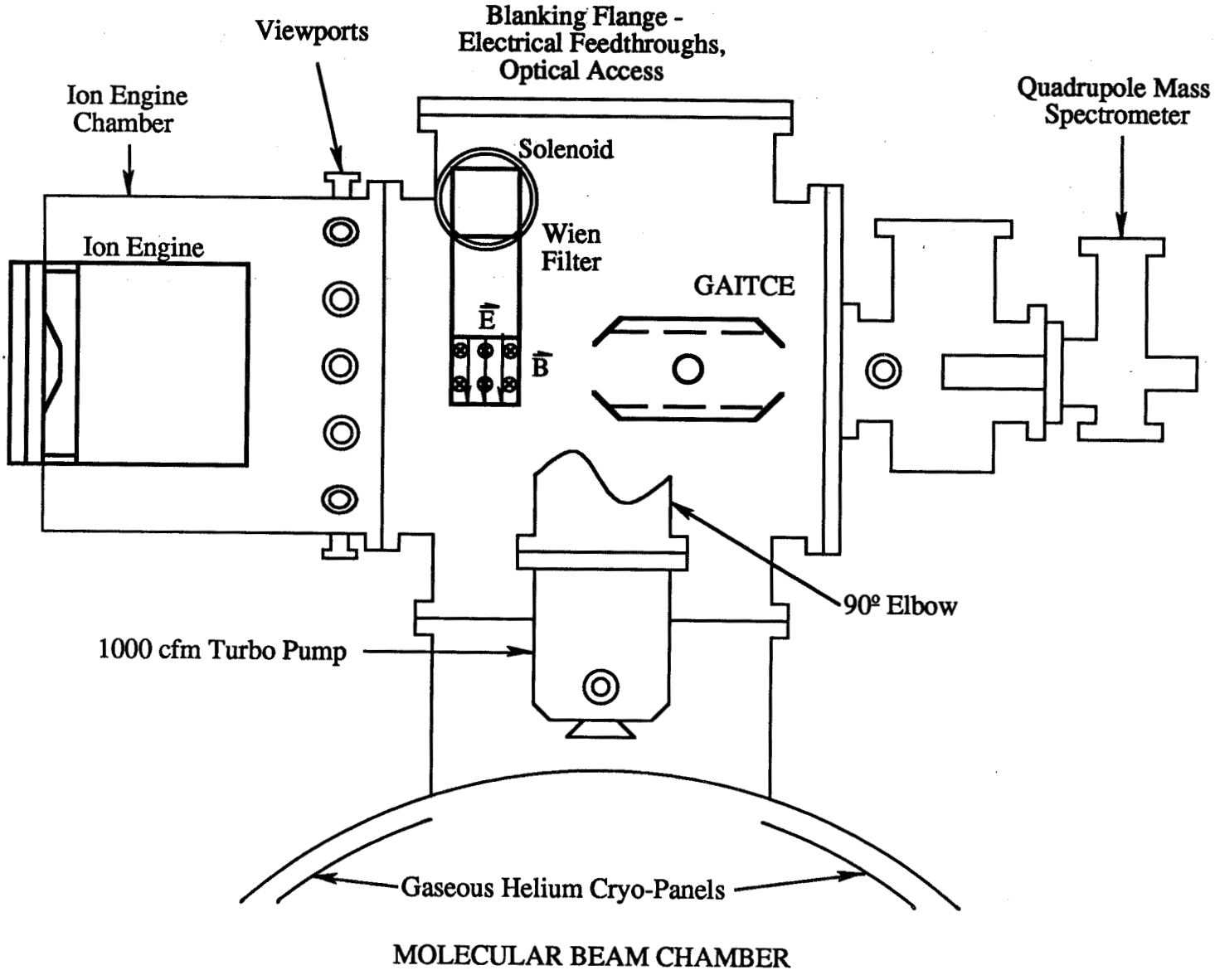


FIGURE 1

USC/Phillips Laboratory Atomic Beam Facility

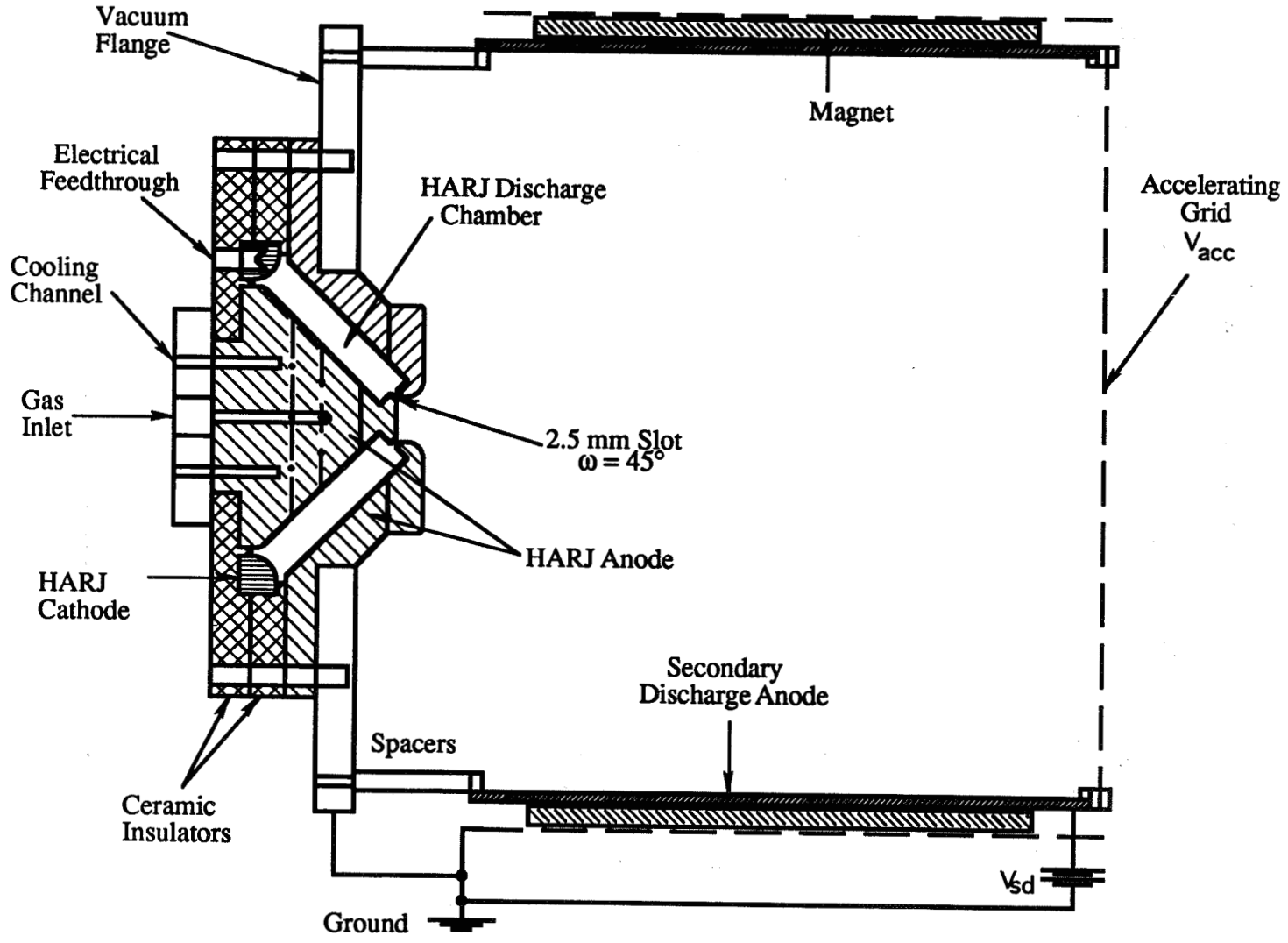


FIGURE 2

Ion Engine (HARJ/Secondary Discharge Chamber) Schematic

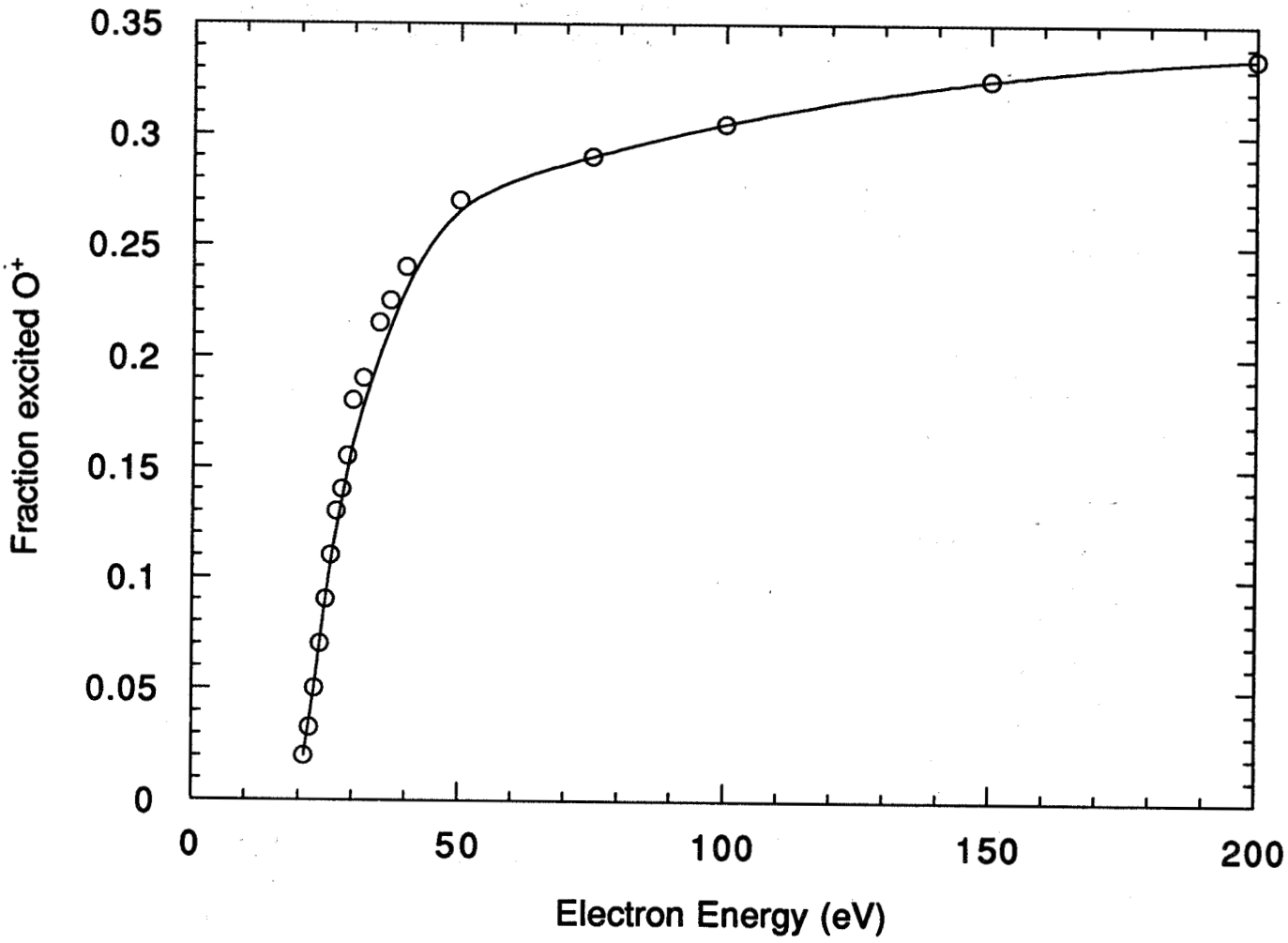


FIGURE 3

Faction of Electronically Excited State $O^+$ Ions as a Function of Electron Energy in a Typical Discharge

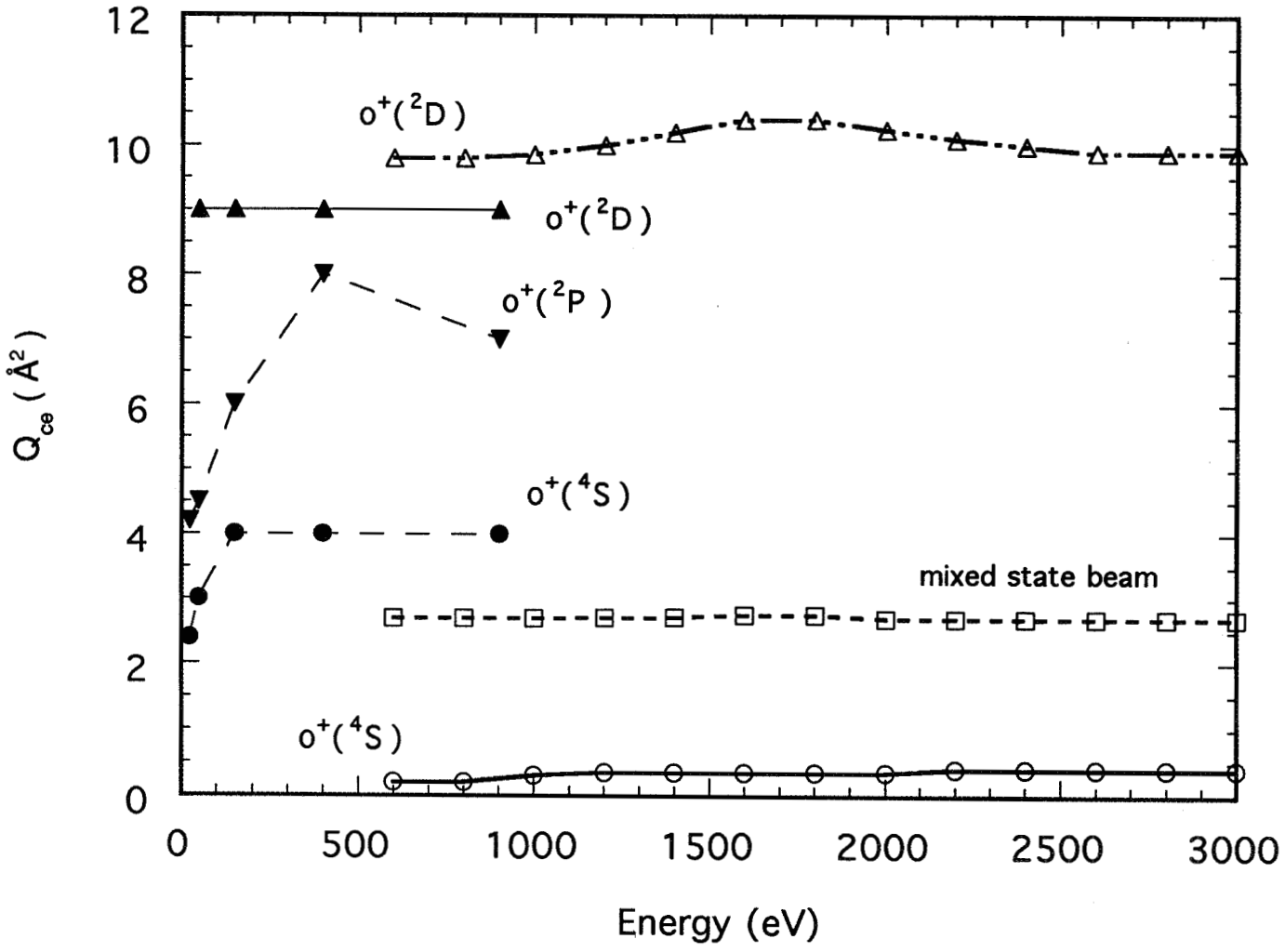


FIGURE 4

Charge Exchange Cross Sections for $O^+/H_2$ Reaction as a Function of Incident Ion Energy

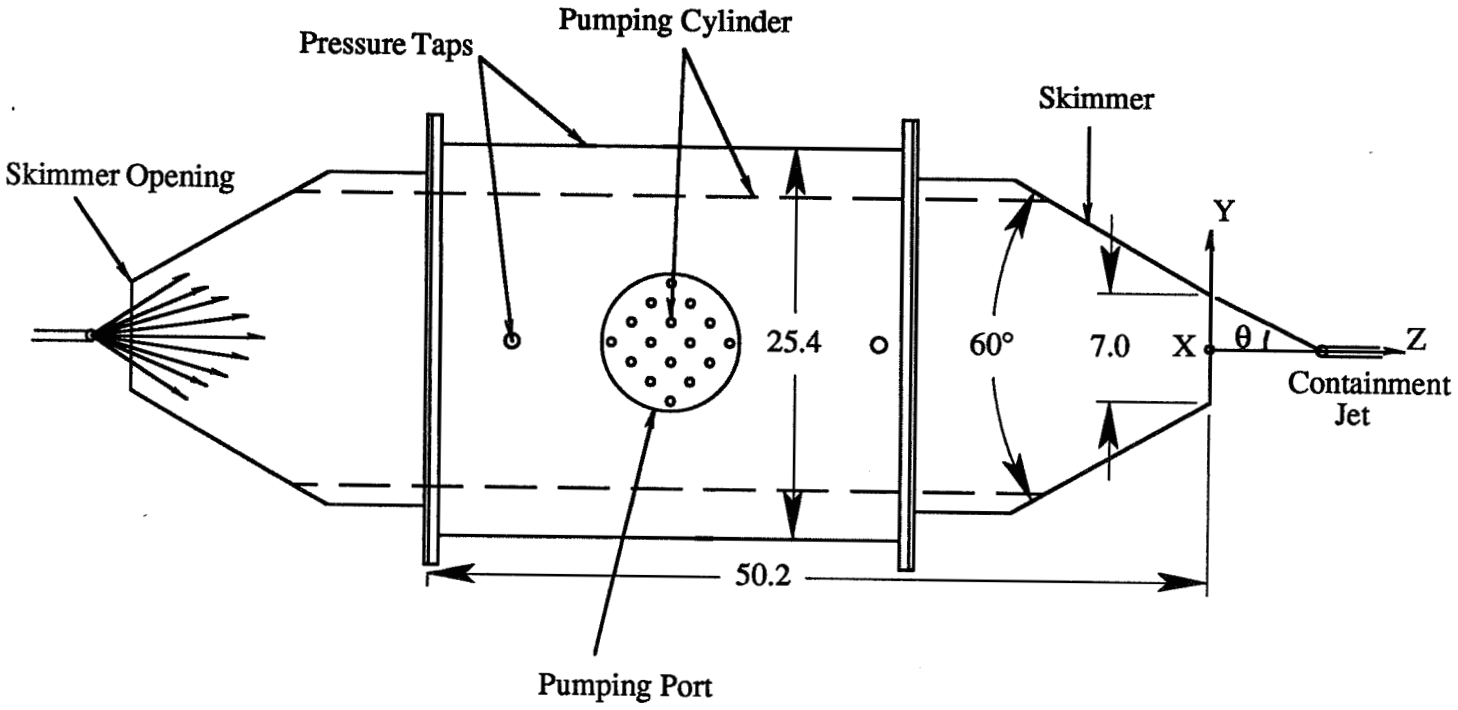


FIGURE 5

GAITCE Schematic. All Dimensions in Centimeters.

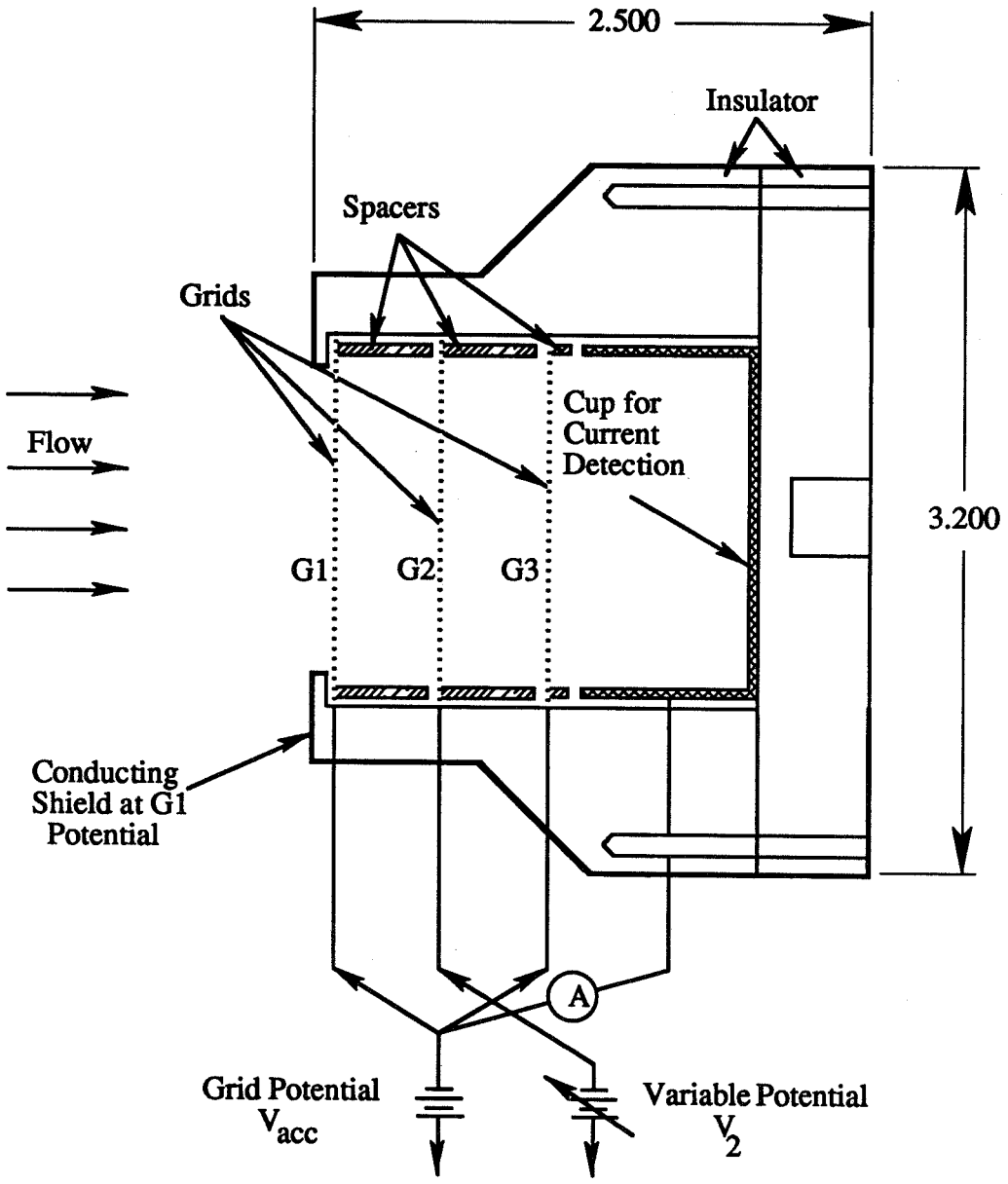


FIGURE 6

EEA Schematic. All Dimensions in Centimeters.

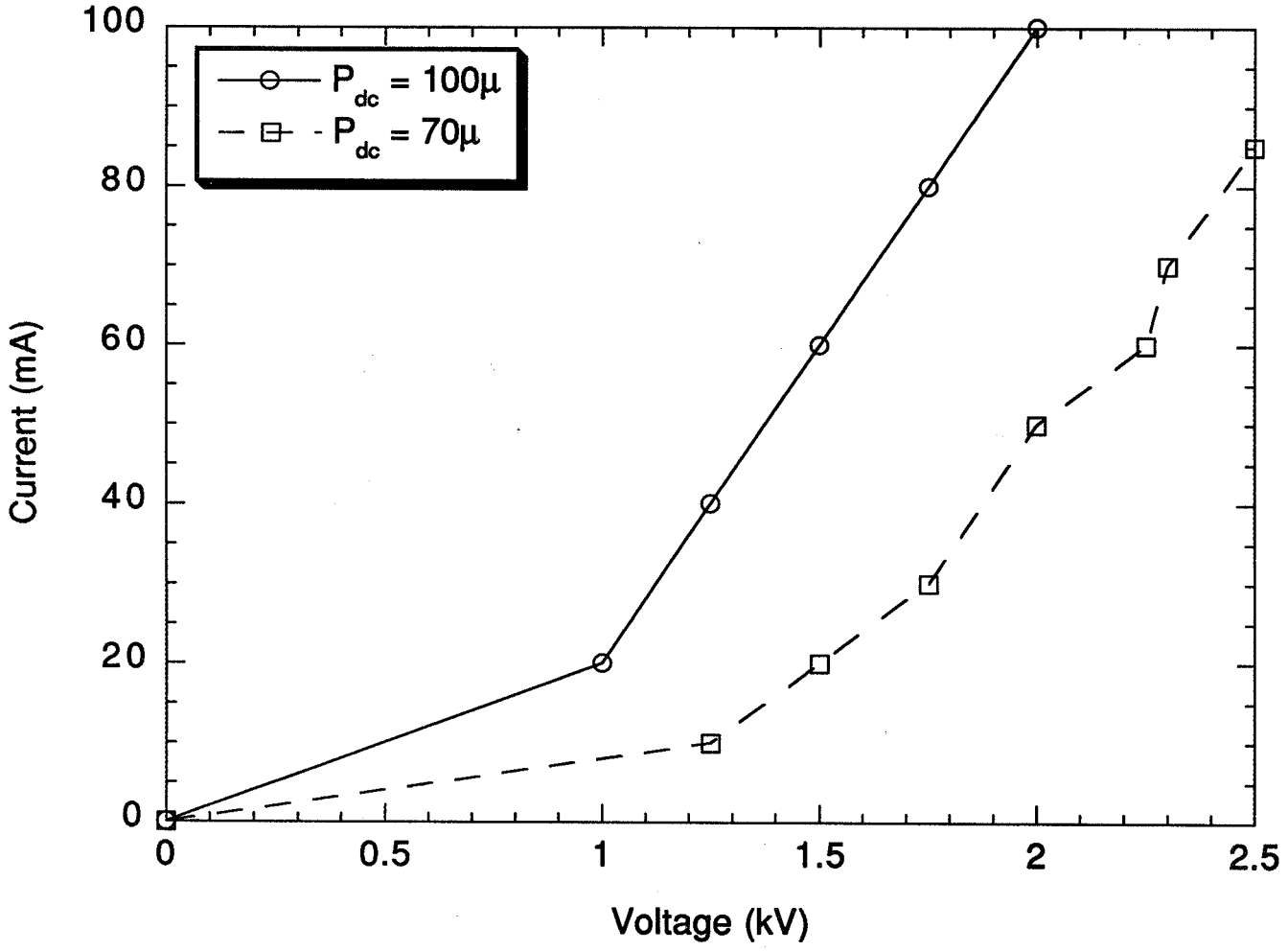


FIGURE 7

Typical HARJ Discharge Characteristics

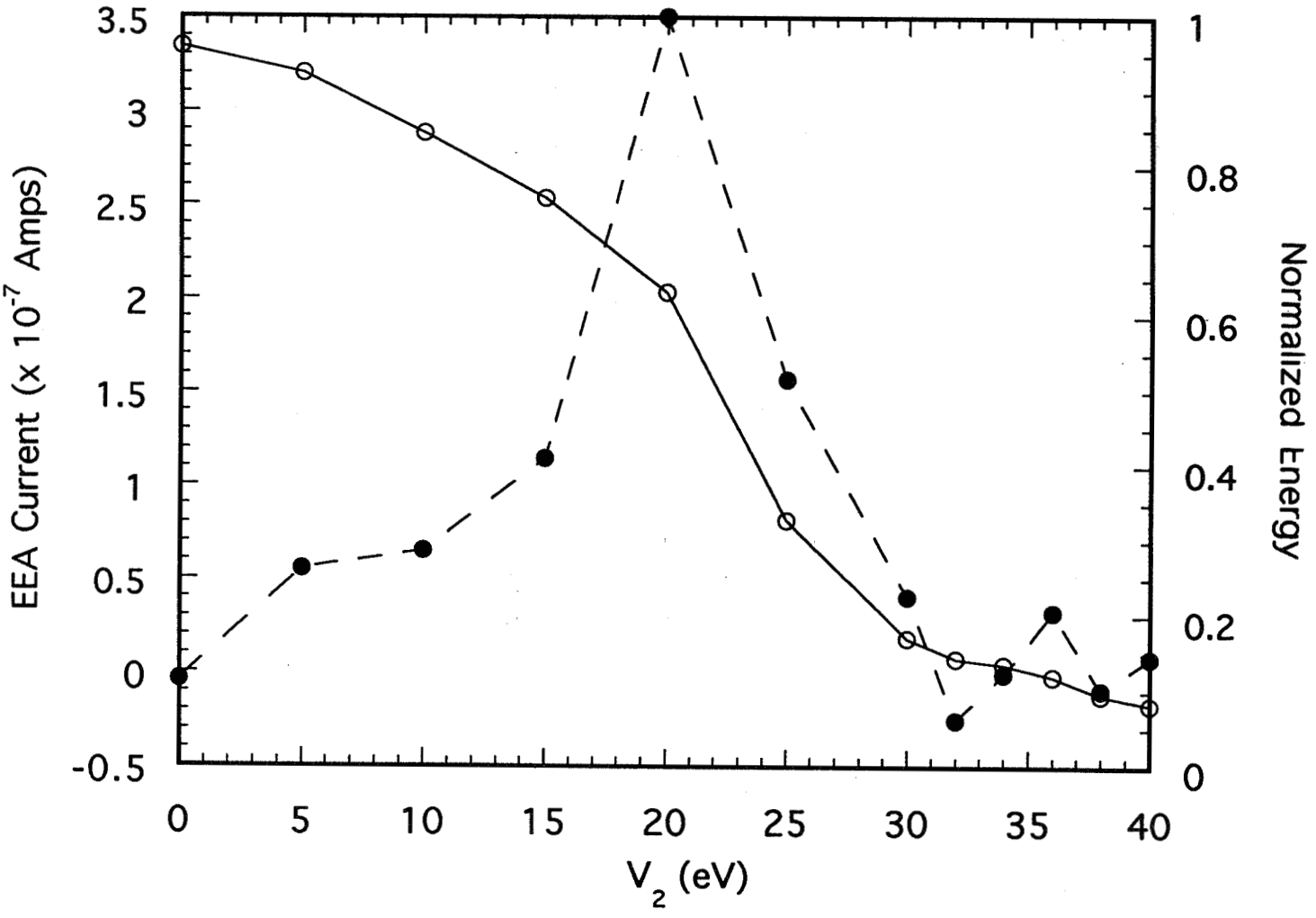


FIGURE 8

Ion Engine Current and Normalized Ion Energy versus EEA Grid 2 Voltage ($V_2$). Energy: Solid Symbols.

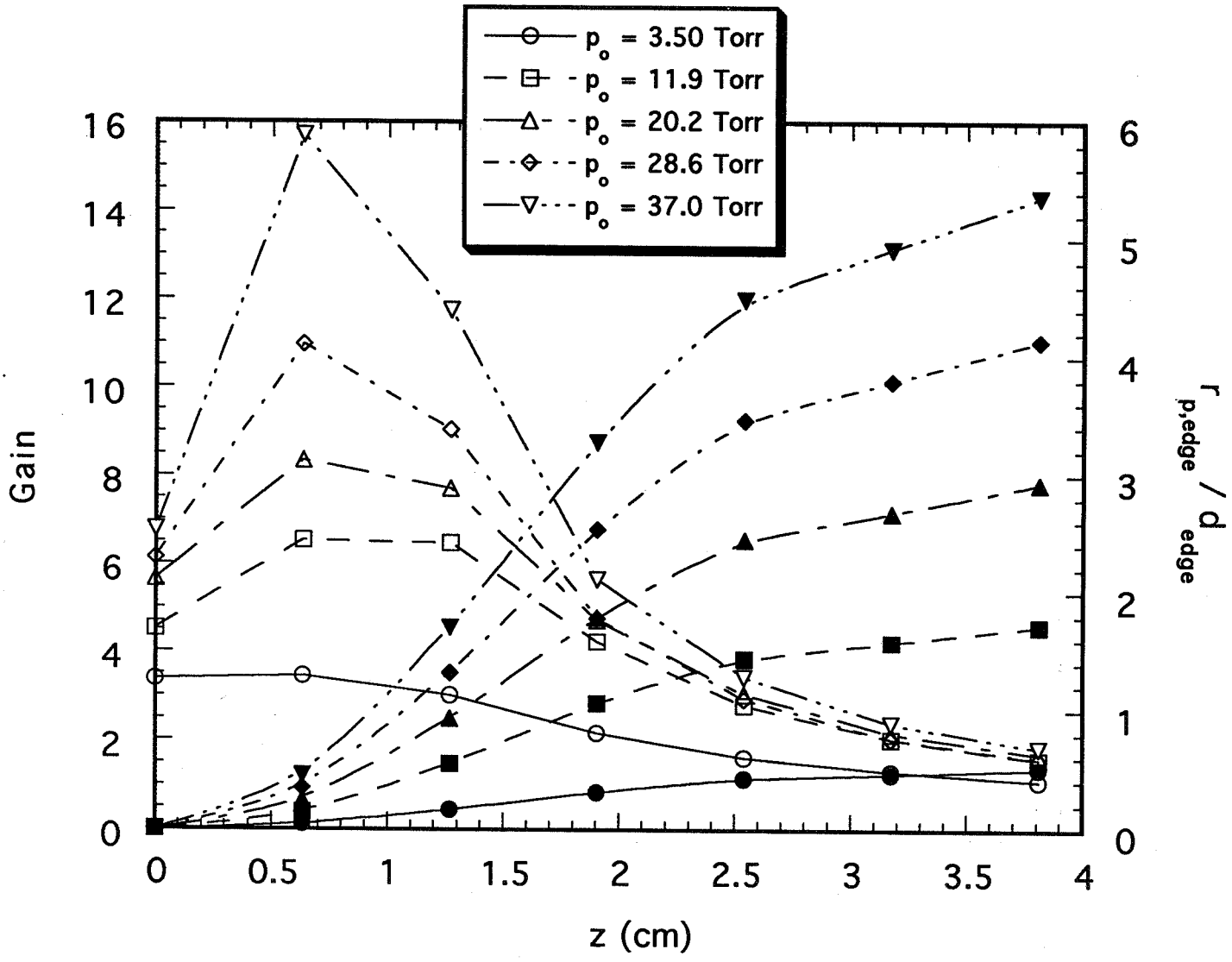


FIGURE 9

GAITCE Gain and $r_{p,edge}/d_{edge}$ as a Function of z for Various Jet Stagnation Pressures (Nitrogen). Gain: Open Symbols.

# ATOMIC OXYGEN (ATOX) SIMULATION OF TEFLON FEP AND KAPTON H SURFACES USING A HIGH INTENSITY, LOW ENERGY, MASS SELECTED, ION BEAM FACILITY

R. Vered, E. Grossman, G.D. Lempert and Y. Lifshitz
SOREQ NRC, Yavne 81800, Israel

## Abstract

A high intensity (> $10^{15}$ ions/cm$^2$) low energy (down to 5 eV) mass selected ion beam (MSIB) facility was used to study the effects of ATOX on two polymers commonly used for space applications (Kapton H and Teflon FEP). The polymers were exposed to $O^+$ and $Ne^+$ fluences of $10^{15}$ - $10^{19}$ ions/cm$^2$, using 30eV ions. A variety of analytical methods were used to analyze the eroded surfaces including: (i) atomic force microscopy (AFM) for morphology measurements (ii) total mass loss measurements using a microbalance, (iii) surface chemical composition using X-ray photoelectron spectroscopy (XPS), (iv) residual gas analysis (RGA) of the released gases during bombardment.

The relative significance of the collisional and chemical degradation processes was evaluated by comparing the effects of $Ne^+$ and $O^+$ bombardment. For 30 eV ions it was found that the Kapton is eroded via chemical mechanisms while Teflon FEP is eroded via collisional mechanisms.

AFM analysis was found very powerful in revealing the evolution of the damage from its initial atomic scale (roughness of ~ 1 nm) to its final microscopic scale (roughness > 1 μm). Both the surface morphology and the average roughness of the bombarded surfaces (averaged over 1 μm x 1 μm images by the system's computer) were determined for each sample. For 30 eV a non linear increase of the Kapton roughness with the $O^+$ fluence was discovered (a slow increase rate for fluences $\Phi < 5 \times 10^{17}$ $O^+$/cm$^2$, and a rapid increase rate for $\Phi > 5 \times 10^{17}$ $O^+$/cm$^2$).

Comparative studies on the same materials exposed to RF and DC oxygen plasmas indicate that the specific details of the erosion depend on the simulation facility emphasizing the advantages of the ion beam facility.

## 1. Introduction

Erosion of surfaces by atomic oxygen (ATOX) has been the subject of many investigations in the past ten years[1-3]. It is now very well established that external surfaces of space systems orbiting with a velocity of 8 km/sec in low earth orbits (LEO) collide with the residual oxygen atoms at an effective energy of ~3-7eV and a flux of $10^{14}$-$10^{15}$ O/cm$^2$ sec. Flight

experiments have demonstrated that most organic surfaces are severely erroded by this exposure [1-6]. The ATOX problem initiated many studies of surface erosion by oxygen applying a variety of ground exposure facilities [7-13]. The complex nature of most of these systems in terms of a wide energy range and a mixture of species imposes severe difficulties in understanding the atomic oxygen erosion mechanisms and in establishing reliable ground simulation experiments for space applications. Contradictory models were proposed to explain the energy dependence of the degradation efficiency of Kapton [2,14].

The present work describes studies performed using a unique mass selected ion beam facility capable of providing a high $O^+$ flux and medium and low (5eV-45keV) energy. In this facility most of the relevant physical parameters (ion nature, flux, energy) can be controlled and varied. Two other less sophisticated systems, commonly used for ATOX simulation, RF plasma ("plasma asher") and DC plasma were also used for comparative studies. The present work is focused on ATOX effects in two commonly used polymers (Kapton H and Teflon FEP) by atomic oxygen. The work also demonstrates the possibilities offered by atomic force microscopy (AFM) for ATOX erosion studies detecting the erosion from the initial stage (nm scale) to the final stage (μm scale). Other diagnostic methods employed were scanning electron microscopy (SEM), X-ray photoelectron spectroscopy (XPS), mass loss measurements and residuale gas analysis (RGA) during bombardment. Since energetic oxygen bombardment of surfaces may involve a combination of collisional and chemical effects, $Ne^+$ bombardment representing pure collisional effects was also investigated using the same mass selected ion beam facility.

## 2. Experimental

### 2a Targets

Two polymer materials commonly used for space applications were studied, i.e. Kapton H and Teflon FEP supplied by du Pont. The polymers chemical structure is:

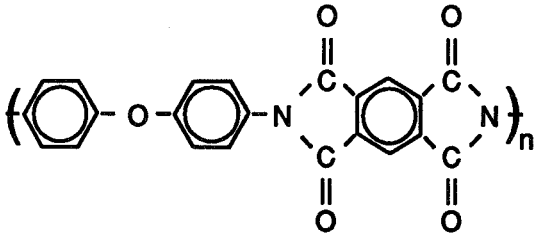

KAPTON H

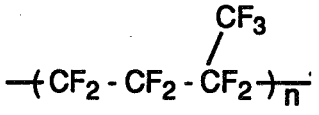

TEFLON FEP

The samples were cleaned prior to bombardment in isopropanol and dried by freon spraying.

## 2b. Irradiation facilties

### The ion beam facility

The main irradiation facility used for the present research was the ion beam facility [15] where $O^+$ and $Ne^+$ irradiations were carried out (fig. 1). This is a high-output isotope separator operating at a maximum beam energy of 45 keV, to which a beam deceleration stage has been added to produce ions at energies down to 5 eV. For $O^+$ bombardment, $O^+$ and other ions are generated in a $CO_2$ fed discharge ion source. The ions are extracted and accelerated to 20 keV, electromagnetically mass separated and then focused onto a grounded slit before entering the ion deceleration stage. The $O^+$ ions are then decelerated to an energy E by means of an electrode at a voltage of 20 keV - E. Special care is taken to prevent electrons from being accelerated towards the target. Prior to target bombardment, the $O^+$ ions are deflected and separated from energetic 20 keV neutrals generated by charge exchange along the beam path. The bombardment is thus of pure, low- energy $O^+$ ions. A specially designed electron flood gun neutralizes the $O^+$ charge on insulating targets surfaces. Mechanical rastering is used to achieve uniform irradiations (± 10% over 1x1 $cm^2$). The 5eV $O^+$ flux of this facility was low so that 30eV was selected as a compromise. At this energy the flux was $10^{15}$ ions/$cm^2$ sec impinging on a mechanically rastered sample (3 x 1.5 $cm^2$) masked to give an exposed area of 2 $cm^2$. The masked surface was used as a reference for comparison with the bombarded area. The pressure during bombardment was $10^{-6}$ torr.

### The RF and DC plasma facilities

Two complementary facilities utilized for the present research are a RF plasma system and a DC plasma system. The RF plasma system is a conventional plasma cleaner ("plasma asher") model PDC-3XG manufactured by Harrick Scientific Corporation. This is a 15 watts, 9.3 MHz system with a 25 cm long 7 cm diameter cylindrical chamber. The oxygen plasma is excited at a typical pressure of $8x10^{-2}$ torr. The thermal energy oxygen plasma composition of plasma ashers has been described in many publications [2,11-13]. The DC plasma unit is a home made system where the plasma is generated by a DC discharge between two parallel electodes. The diameter of the circular electrodes is 10 cm and the distance between the electrodes is 4 cm. The typical working oxygen pressure is $7x10^{-2}$ torr. The system is pumped by a standard diffusion pump to a pressure of $10^{-6}$ torr before introduction of the oxygen and starting the DC plasma discharge. A square 2x2 $cm^2$ probe is used to detect the plasma current and potential. At typical conditions the current provides a flux of $5x10^{13}$-$5x10^{14}$ ions/$cm^2$ sec with an energy of 30-150 eV depending on the operational conditions. For both plasma systems the fluxes are not uniform and the exact operational conditions are difficult to control and reproduce.

## 2c. Analyses

### Mass loss analysis

The samples were weighed before irradiation (after being kept at a pressure < 2 x $10^{-6}$ torr for four hours) and after irradiation, by a Mettler UM3 microbalance having a precision of 0.1μg. The bombarded Kapton gained weight during the first minutes of its exposure to atmospheric pressure so that the Kapton measurements were inaccurate within 0.1 mg/$cm^2$. The Teflon bombarded samples did not exhibit the same behavior and its weighing accuracy was within ±10μg.

### Residual gas analysis

Residual gases in the irradiation chamber were monitored by a Dycor M200 quadrupole gas analyzer, manufactured by Ametek. Gas release from the irradiated samples was evaluated by substraction of the spectra prior to irradiation from those during irradiation.

### Atomic Force Microscopy (AFM)

AFM studies were performed under atmospheric pressure using a Digital Instrument Nanoscope II system with two different (15μm and 140μm) scan heads. The surface morphology of the insulating bombarded materials was detected with a sufficient resolution from the 1nm scale without the need of depositing a thin conductive layer (as required for SEM analysis). The evolution of the surface morphology through irradiation by $O^+$ and $Ne^+$ fluences of $10^{15}$ ions/$cm^2$ to $10^{19}$ ions/$cm^2$ was detected. The surface vertical roughness was measured and statistically averaged by the system.

### Scanning Electron Microscopy (SEM)

SEM analysis was performed by a Phillips 525/535 SEM. The analyzed surfaces were coated by a few hundred angstroms of gold to provide good conductivity and high resolution . The SEM images (typically 10μm x 10μm or larger) were compared to the AFM images of the largest scale (also 10μm x 10μm).

### X-ray Photoelectron Spectroscopy (XPS)

Bombarded samples were studied by XPS (555 Perkin Elmer system), analyzing the chemical composition of the surfaces. Previous XPS studies[16] of irradiated Kapton however indicated its chemical composition changes due to exposure to atmospheric pressure. Another indication to the bombarded Kapton interaction with the atmospheric environment is its weight gain discussed previously.

## 3. Results

### 3a. Kapton H

#### AFM studies

30 eV $O^+$ bombardment of Kapton H surfaces using the mass selected ion beam system resulted in significant morphology changes due to surface erosion, (fig. 2). The pristine surface was completely amorphous. Upon successive $O^+$ bombardment the surface exhibited, in the large scale, a certain roughening and a formation of grain-like features which increased with fluence. Strong changes were also detected in the molecular scale. While the pristine structure exhibited a disordered zigzag pattern with a typical periodicity of about 32Å, a similar analysis performed on top of a grain-like structure in the $10^{19}$ $O^+/cm^2$ bombarded surface exhibited a smaller periodicity of about 19Å. This latter result may not represent the bombarded surface itself, but reflect its interaction with the ambient atmosphere as previously discussed.

The vertical roughness of pristine and $O^+$ bombarded surfaces was also investigated (fig. 3). It increased from 10Å for the pristine sample to 0.4 μm for the $10^{19}$ $O^+/cm^2$ bombarded sample. For $O^+$ fluences smaller than $5x10^{17}$ $O^+/cm^2$ (low fluence region) the roughness increased very slightly with fluence, while for fluences higher than $5x10^{17}$ $O^+/cm^2$ (high fluence region) a sharp increase of two orders of magnitude of the surface roughness was observed for a fluence increase of only one order of magnitude. The results of $O^+$ bombardment were compared to those of $Ne^+$ bombardment, in order to distinguish between collisional and chemical effects. 30 eV $10^{19}$ $Ne^+/cm^2$ bombardment of Kapton produces precisely the same roughness as that of 30 eV of $10^{15}$ $O^+/cm^2$.

AFM images of Kapton exposed to RF or DC plasmas of oxygen show surface erosion and roughening that increases with fluence. The roughness of RF and DC exopsed Kapton is comparable to that of ion beam eroded surfaces for similar mass loss (fig. 4). The exact morphology of samples exposed to the RF and DC oxygen plasmas is different than the morphology following exposure to an $O^+$ beam. Row-like ordering of the erosion was observed in all heavily eroded samples using the RF and ion beam systems.

#### SEM studies

SEM analysis of the same severely bombarded ($1 x10^{19}$ $O^+/cm^2$) Kapton surfaces (fig. 5) displayed porous morphology with needle-like ordering as has been previously reported[1,9]. The SEM images reveal the same row-like ordering that was observed by the AFM. It should be noted that using the same magnification, the AFM and SEM images (figs. 4c and 5, respectively) of the same samples are similar. This similarity indicates that the AFM probe did not induce any artifacts in the present results. AFM was however capable of detecting the development of the damage from its initial stage (several nm scale) that could not be detected by the SEM.

## XPS studies

XPS studies of both $O^+$ and $Ne^+$ bombarded Kapton did not reveal a significant chemical composition change between pristine and bombarded surfaces.

## Mass Loss Analysis

The mass loss of Kapton increased linearly with fluence upon $O^+$ bombardment (fig. 6). The average reaction yield for 30 eV $O^+$ bombardment was 3.5 $x10^{-23} cm^3$/atom. The mass loss upon $Ne^+$ bombardment was at least one order of magnitude lower than for $O^+$ irradiation. The accuracy of the mass loss measurements of Kapton is limited ($\pm$0.1mg) due to the interaction between the atmospheric environment and the bombarded sample, and no reliable mass loss of Kapton can be detected for fluences < 4 $x10^{18}$ $O^+/cm^2$.

The mass loss of Kapton exposed to both RF and DC oxygen plasmas increased linearly with the fluence. The reaction yield for the DC plasma exposure can be estimated by assuming that the flux impinging on the sample is equal to the current measured by a probe inserted into the plsama. The reaction yield thus obtained was comparable (slightly lower) to the $O^+$ beam exposure i.e., 1.7 x $10^{-23} cm^3$/atom. The mass loss rate of Kapton exposed to RF plasma was $2x10^{-3}$ $mg \cdot cm^{-2} \cdot min^{-1}$.

# 3b. Teflon FEP

## AFM studies

AFM studies of pristine and 30 eV $O^+$ and $Ne^+$ bombarded Teflon (fluence up to $10^{19}$ ions/$cm^2$) were performed. Similar effects were observed for $O^+$ and $Ne^+$ bombardment, in contrast to the Kapton bombardment data. The pristine surface structure (Fig. 7a) is built of small features ~150x150 nm in size, scattered in a chaotic way. The heavily ($3x10^{18}$ ions/$cm^2$) bombarded Teflon exhibited a strong surface modification both in the μm scale and in the nm scale. In the μm scale (Fig. 7b) the surface is characterized by randomly dispersed hollows (~1μm diameter) embedded in a rather smooth area. A higher resolution analysis of these smooth areas reveals a configuration of densely-packed chains 70 nm wide.

AFM images of Teflon exposed to RF and DC plasmas were characterized by a significant nonuniformity of the erosion features. Craters were observed but no 1μm hollows. The surface roughness of the Teflon eroded by plasmas was higher than the area between hollows for the $O^+$ exposure.

## SEM studies

SEM studies (~20μm x 20μm scale) of gold deposited $O^+$ bombarded Teflon (Fig. 8) reveal eroded surfaces for $3x10^{18}$ ions/$cm^2$ exposure with ~1 μm holes embedded in a rather smooth matrix similar to that observed by AFM. The roughness of the $Ne^+$ bombarded surfaces is similar to the $O^+$ bombarded surfaces, but the morphology of the $Ne^+$ bombarded Teflon surface looks a little different (the area between the holes is not smooth, but eroded and wrinkled).

## XPS studies

XPS analysis of $O^+$ and $Ne^+$ bombarded Teflon yielded a strong increase in the C percentage and a corresponding decrease of the F percentage leading to the reduction of the F/C ratio from 2 to 1. A similar phenomenon was reported by others[6,17]. The O percentage slightly increased (to 2.6%) following $Ne^+$ bombardment and more significantly increased (to 8.8%) following $O^+$ bombardment.

## Mass Loss analysis

The mass loss of Teflon also increased with 30 eV $O^+$ and $Ne^+$ bombardment fluence (fig. 9). In both cases a reaction yield of ~ $6.5 x10^{-22}$ $cm^3$/atom was measured, with no significant difference between $O^+$ and $Ne^+$ bombardments.

For both RF and DC oxygen plasmas the mass loss of the exposed Teflon increased with fluence. The mass loss rate of Teflon exposed to RF plasma was $3x10^{-3}$ $mg \cdot cm^{-2} \cdot min^{-1}$. The reaction yield of Teflon exposed to DC plasma (assuming that the flux impinging on the sample is equal to the current measured by a probe inserted into the plsama) was $3.2x10^{-23}$ $cm^3$/atom, an order of magnitude lower than for 30eV $O^+$ irradiated Teflon. In both plasma systems the reaction yield of Teflon is higher by a factor of 2 than that of Kapton.

## RGA analysis

RGA measurements during 30eV $Ne^+$ bombardment indicated the release of $CF_2$ and $CF_3$. Similar measurements of 10keV $Ne^+$ bombardment of Teflon yielded additional peaks, such as $C_3F_3$, $C_2F_4$, $C_3F_4$ and $C_3F_5$.

# 4. Discussion

The ATOX environment in space involves fluxes of neutral 3-7eV atomic oxygen. The main simulation system employed in the present research (the MSIB facility) involves 30eV $O^+$ ions, and the surface is neutralized by flooding the exposed surface with electrons simultaneously with the 30eV $O^+$ ions.

The 5eV $O^+$ flux of this facility was low so that 30eV, (for which a flux of $10^{15}$ $O/cm^2$ sec and more was obtainable) was selected as a compromise. At this energy, as for higher energies used in many ATOX studies, the bombardment of surfaces with energetic species is associated with several processes occurring in three distinct time scales[18]: (i) the collisional stage (~$10^{-13}$ sec) where the ions transfer their kinetic energy to target atoms; (ii) the thermalization stage (~$10^{-11}$ sec) in which target atoms participating in the collision cascade lose their excess kinetic energy reaching a thermal equilibrium with the surrounding atoms; (iii) the long term relaxation stage ($10^{-10}$ sec - 1 sec) in which the final structure of the material is determined and chemical reactions with the residing species may occur. In the collisional stage, the ions lose energy via ionizations, phonon excitations and atomic displacements. In this stage physical sputtering occurs when target atoms are displaced with sufficient energy towards the surface. Surface reconstruction and chemical sputtering are possible during the thermalization stage. Chemical sputtering may be induced by chemical interactions between the bombarding species and the target atoms that form volatile species. Polymer bombardment is more complex than that of inorganic materials since the pure collisional processes (ionizations and atomic displacements) may induce chemical reactions at a later stage due to the formation of radicals, or may initiate cross-linking and scissioning. ATOX simulation facilities may involve species with energies ranging from thermal (< 0.1 eV) to 1 keV. For E < 1 eV the processes are purely chemical and no collisional effects occur. For E = 1 keV the oxygen atom penetrates deep into the polymer (typical range 100Å) creating significant collisional damage along its track and the chemical effect of the oxygen atom trapped at its final position is negligible compared to the collisional effects. For E ~ 5 eV, chemical effects should be dominant but the role of collisional effects must also be determined. Koontz et al. [2] have analyzed the reactivity of Kapton to oxygen as a function of the O energy (in the range of 0.05-5 eV) and suggest a purely chemical degradation process that follows an Arrhenius like expression $R = Ro \exp(-0.4/E)$ (where R is the mass loss rate and E is the energy) having an activation barrier of 0.4 eV. Ferguson[14] performed the same analysis for the energy region of 0.08-800 eV to reach the relation $R = Ro\ E^{0.68}$. Ferguson's expression can be explained in terms of purely collisional effects where the degradation increases with the energy deposited via collisions.

The Kapton exposure data given in the present work indicates that for 30 eV $O^+$ bombardment, chemical effects dominate, while collisional effects (determined from $Ne^+$ bombardment) are smaller by at least one order of magnitude. The reaction yield values obtained in the present work (E = 30 eV) are in accord with earlier published data. Since the Kapton degradation by oxygen in space (E ~ 5 eV) is one order of magnitude lower than our data for E = 30 eV, it follows that in contradiction to the model presented by Koontz et al.[2] the chemical degradation by oxygen is energy dependent for $5\ eV \leq E \leq 30$ eV and does not reach a saturation value when exceeding the activation energy of the rate limiting degradation channel. This may be explained by the initiation of additional reaction channels not considered by Koontz et al., or by the increase of the number of target atoms exposed to atomic oxygen following the increase of the $O^+$ energy. This high reaction yield

value may also be associated with the ionic nature (instead of neutral state in space) of the atomic oxygen used. Another interesting phenomenon associated with Kapton exposure to 30 eV $O^+$ ions is the nonlinear behaviour of the degradation with $O^+$ fluence, revealed by the AFM. This behaviour is currently not understood, and may be associated with an increase of the degradation efficiency due to the increase of the bombarded Kapton roughness. The XPS studies indicated that the chemical composition of the bombarded Kapton is very similar to that of the pristine samples. This XPS data may however be misleading since as was previously reported[23] the bombarded Kapton is attacked by the ambient atmosphere upon its release from the vacuum chamber, going back to the original Kapton atomic composition. Indeed, the bombarded Kapton samples gain significant weight during their first moments of exposure to the ambient atmosphere. This weight gain may be related to absorption/chemical-interaction processes that occur upon exposure to air.

The Teflon was found to have a different response to 30 eV $O^+$ and $Ne^+$ bombardment than Kapton. Since for both ionic species the bombardment of Teflon yields similar mass loss values it can be concluded that for Teflon and 30 eV ion energy, the oxygen degradation is via a collisional process. In accordance to this conclusion, a Teflon FEP bombardment by 750 eV $Ar^+$ has been reported[16] to have a similar reaction yield of $2 \times 10^{-21} cm^3$/ion. It should be noted that the reaction efficiency of Teflon by 30 eV $O^+$ is larger by three orders of magnitude than for ATOX in space[1,2,8] (20 times larger than Kapton erosion by 30 eV $O^+$). The reason for these high reaction values at E = 30 eV is currently unclear. Residual gas analysis during bombardment indicated the release of $CF_2$ and $CF_3$ which was followed by the reduction of the F/C ratio in the bombarded surface from 2 to 1. It thus seems that the energy loss in the collisional process of 30 eV bombardment of Teflon FEP releases very efficiency $CF_m$ gaseous species, possibly via scissioning.

The erosion processes of Teflon by 5 eV oxygen are still unclear. It is believed[2] that Teflon is only very slightly eroded by 5 eV O (reaction yield smaller by a factor of 50 then for Kapton) and that a simultaneous exposure to VUV enhances its reactivity to be similar to that of Kapton. Future experiments by our laboratory will probe the reactivity of Teflon for the whole $O^+$ range of 5-30 eV in order to understand the sharp increase of reactivity of 3 orders of magnitude in this small energy region.

The previous discussion was focused on the data obtained by the MSIB system. Two additional systems (i.e. RF and DC plasmas) were also used for comparison. The data available from the three systems employed is very much affected by the nature of the three systems. Both plasma systems have a complex nature regarding the species ($O^+$, $O^+_2$, excited atoms and molecules, etc.) and the energy spread (E < 0.1eV for the RF, an unknown distribution of tens up to several hundred eV for the DC plasma). Under such conditions the determination of the flux and the fluence is also difficult. Kapton mass loss serves as a calibration standard, especially for the RF system, while the probe current served as a measure of the flux in the DC system. The comparison between the MSIB data and that of the plasma systems is thus very limited.

For the RF system a comparison of the AFM images can be made for similar mass losses. For Kapton the roughness is similar but the exact surface morphology is different. For Teflon the surface morphology of the eroded surfaces is different, and so is the reaction yield relative to Kapton (~2 for RF and DC and ~20 for MSIB). The actual reaction yields measured using our RF and DC plasma systems are in accord with published data [2,9]. The reaction yield of Kapton for the DC plasma is similar to the MSIB but the roughness (for the same mass loss) is much higher. The reaction yield for Teflon is one order of magnitude lower for the DC plasma and the surface morphology is different. It should be noted that the erosion in both plasmas is highly irregular and large variations exist between different tests performed under the same conditions. No such variations were observed for the exposures in the MSIB system. Reaction products of Teflon in different oxygen plasmas were claimed to be responsible for the realtively high reaction yield in these systems [9]. This explanation is not applicable for the MSIB system, where relatively higher reaction yields were measured.

The present work has demonstrated that MSIB, where the different physical parameters relevant for erosion studies can be controlled, is capable of elucidation of degradation mechanisms. Specifically it demonstrated that the two commonly used polymers in space applications have entirely different degradation processes for 30eV $O^+$ exposure. This, along with the comparison to the RF and DC plasmas, indicates that the use of ground ATOX simulation facilities for space materials qualification may lead to erroneous conclusions if the specific erosion mechanisms are not understood.

## Summary and Conclusions

The present work can be summarized as follows:

(i) Chemical processes dominate the degradation of Kapton by 30eV $O^+$ bombardment.

(ii) Collisional processes dominate the degradation of Teflon by 30eV $O^+$ bombardment.

(iii) Teflon erosion by 30eV $O^+$ bombardment is 3 orders of magnitude higher than 5eV ATOX erosion in space, indicating different erosion mechanisms for Teflon for these two cases.

(iv) MSIB offers better control and research possibilities than RF and DC plasmas.

(v) AFM is an efficient analysis method for the investigation of ATOX erosion from its initial stage to its final stage (1nm-1μm scales).

## Acknowledgments

This work was partially supported by the Israel Space Agency (ISA), by the Israel Ministry of Science, and by the Israel Ministry of Absorption. The authors are grateful to Dr. L. Singer of ISA for helpful discussions and support.

## REFERENCES


1. L.G.Leger, S.L. Koontz, J.T. Visentine and J.B. Cross, *Proc. of Spacecraft Materials in Space Environment Sympos.*, Toulouse, France, pp. 393-404 (1988).
2. S.L. Koontz, K. Albyn and L.J. Leger, *J. Spacecraft* **28(3)**, 315 (1991).
3. M.R. Reddy, N. Srinivasamurthy and B.L. Agrawal, *ESA Journal* **16**, 193 (1992).
4. K. deGroh, B. Banks, *Proc. of 1st LDEF Post-Retrieval Symposium*, Kissimmee, Florida, June 2-8, 1991.
5. B.A. Banks, S.K. Rutledge, K.K. deGroh, M.J. Mirtich, L. Gebauer, R. Olle and C.M. Hill, *Proc. of 5th Int. Symp. on Materials in a Space Environment*, Cannes-Mandelieu, France, September 16-20, 1991.
6. T.L. Cheeks and A.L. Ruoft, *Mat. Res. Soc. Symp. Proc.* **75** , 527 (1987).
7. R.C. Tennyson, *Can. J. Phys.* **69**, 1190 (1991).
8. W.D. Morison, R.C. Tennyson, J.B. French, T. Braithwaite, M. Moisan and J. Hubert, *Proc. of Spacecraft Materials in Space Environment Sympos.*, Toulouse, France, pp. 435-452 (1988).
9. M. McCargo, R.A. Dammann, T. Cummings and C. Carpenter, *Proc. of Spacecraft Materials in Space Environment Sympos.*, Noordwijk, 1985, **ESA SP-232** (1985).
10. K.T. Kern, P.C. Stancil, W.L. Harries, E.R. Long, J. and S.A. Thibeault, *Sample Journal*, **29(3)**, 29 (1993).
11. A.F. Whitaker, B.Z. Jang, Sampe Journal, 30(2), 30-41 (1994).
12. A.F. Whitaker, B.Z. Jang, J. Appl. Poly. Sci. 48, 1341-1367 (1993).
13. T. Wydeven, M.A. Golud, N.R. Lerner, J. Appl. Poly, Sci., 37, 3343-3355 (1989).
14. D.C. Ferguson, *Proc. of the 13th Space Simulation Conference*, Orlando, FL, 1984, **CP-2340**, 205 (1984).
15. I. Chavet, M. Kanter, I. Levy, H.Z. Sar-El, *Proc. 8th Int. EMIS Conf.*, Skovde, Sweden (Institute of Physics, Sweden, p. 191 (1973).
16. K.S. Sengupta and H.K. Birnbaum, *J. Vac. Technol.* A. **9(6)**, 2928 (1991).
17. H.B. Gjerde, T.R. Chun, S.J. Low, *Proc. of the 18th International SAMPE Technical Conference, 1986,* 262 , (1986).
18. B.W. Dodson in *Material Research Society Symposium Proceeding (MRC, Pittsburgh, 1989).* **128**, 127 (1989).
19. J.S. Sovey, *J. Vac. Sci. Technol.* **16(2)**, 813 (1979).

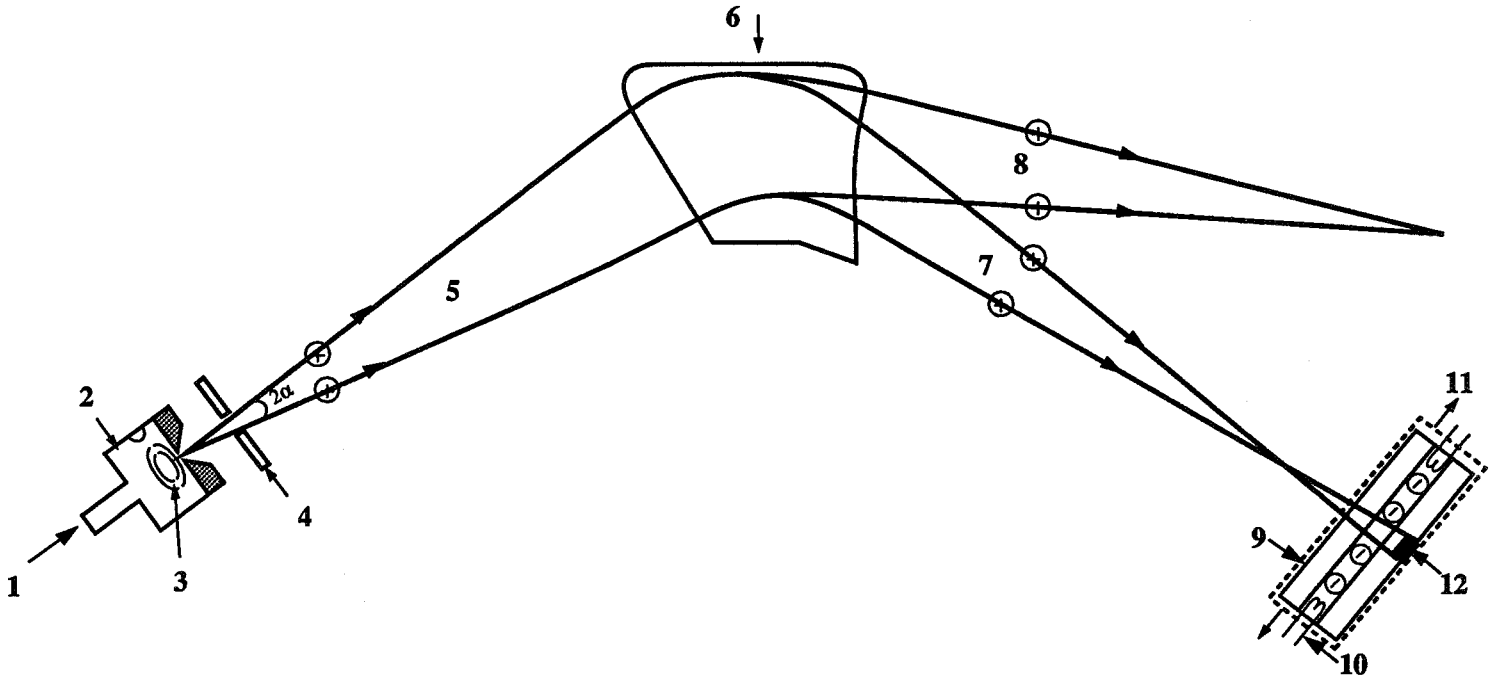


Fig. 1 - Schematic view of the mass selected ion beam facility: 1. $CO_2$ or Ne Gas inlet, 2. Ion source, 3. Electric arc, 4. Acceleration electrode, 5. High energy $C^+$,$O^+$, $CO^+$, $CO_2^+$, ions, 6. Separation magnet, 7. $O^+$ or $Ne^+$, 8. $C^+$, $CO^+$, $CO_2^+$, 9. Deceleration assembly, 10. Surface charge neutralization, 11. Mechanical scanning assembly, 12. Substrate

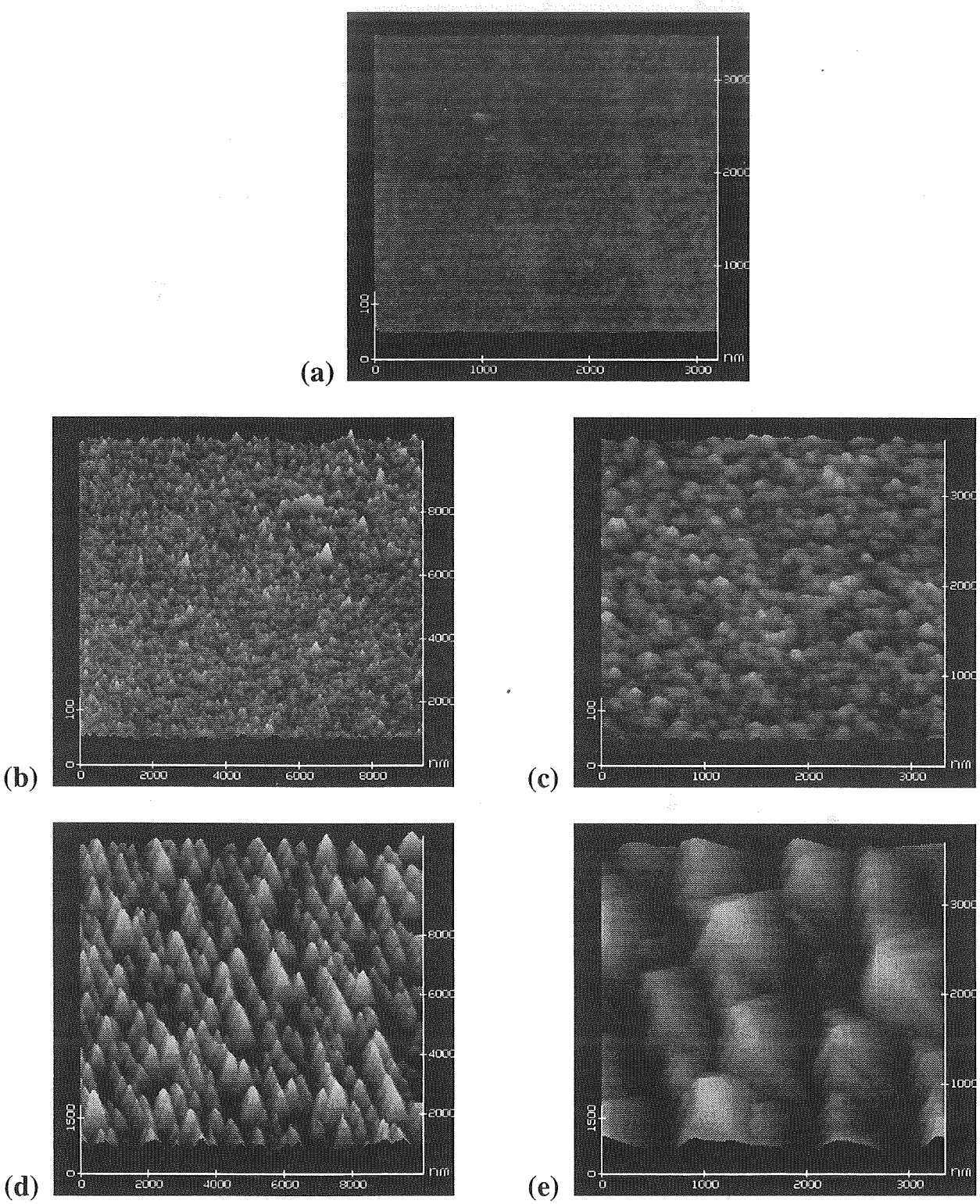


Fig. 2 - AFM images Kapton at different stages of 30 eV $O^+$ bombardment. (a) Pristine.
(b) 10 μm x 10 μm and (c) 3.3 μm x 3.3 μm - $O^+$ flux of $5x10^{17}$ ions/cm$^2$
(d) 10 μm x 10 μm and (e) 3.3 μm x 3.3 μm - $O^+$ flux of $1x10^{19}$ ions/cm$^2$
Note the different z scales: 100 nm for (a), (b) and (c), and 1500 nm for (d) and (e).

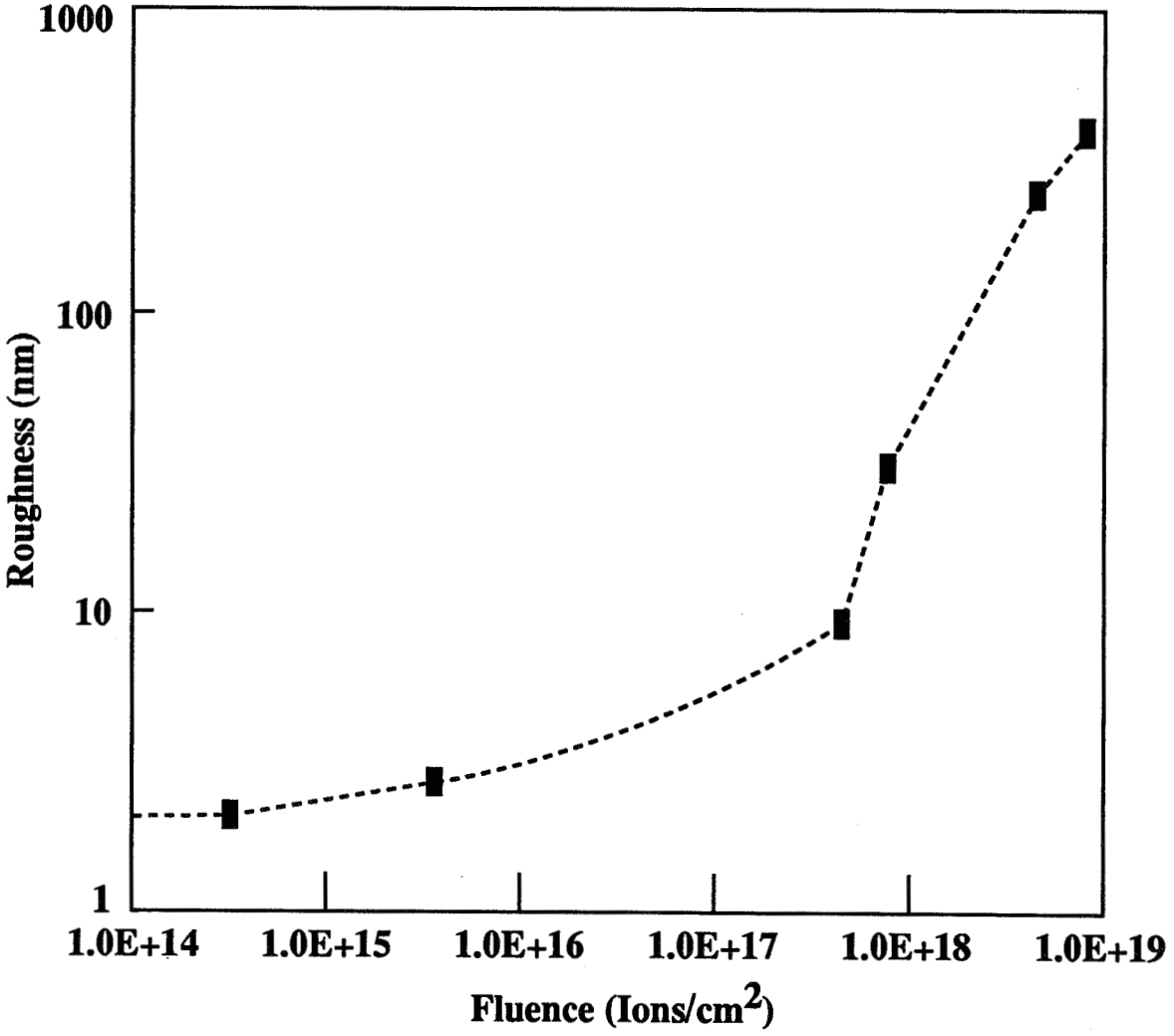


Fig. 3 - The vertical roughness of 30 eV $O^+$ bombarded Kapton surfaces (studied by AFM) as a function of fluence.

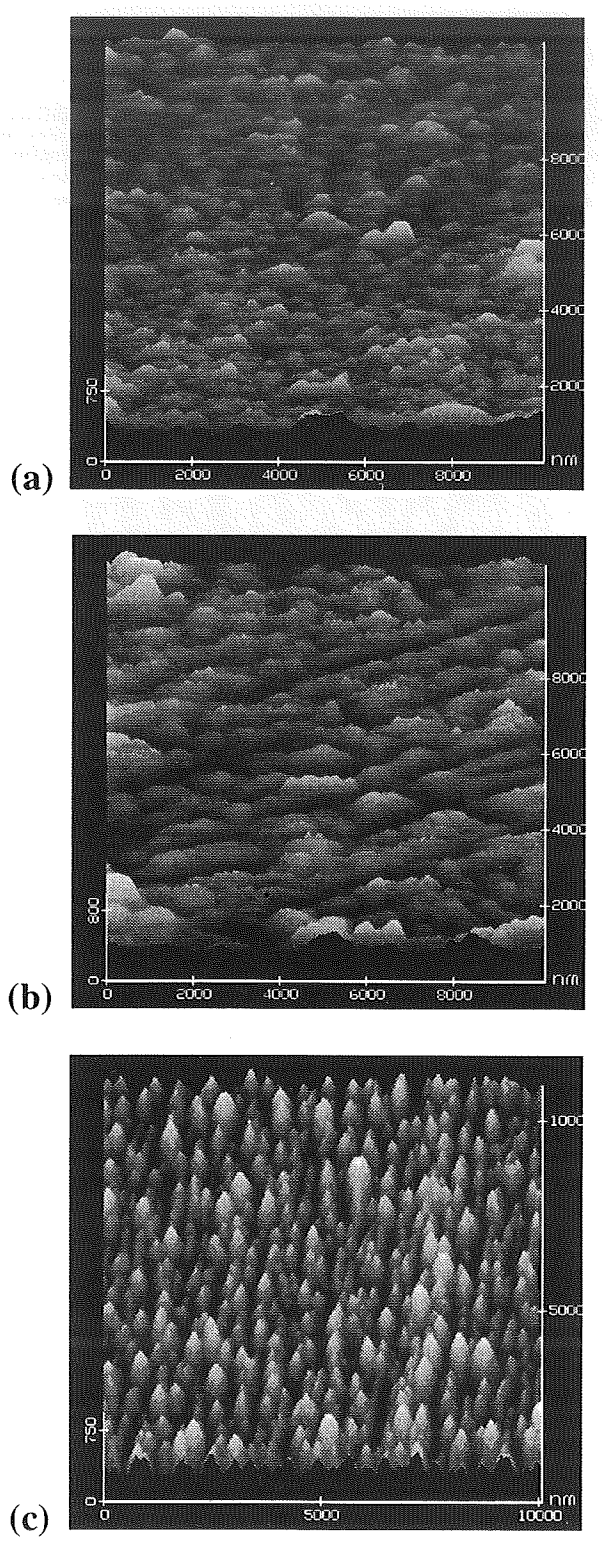


Fig. 4 - AFM images (10 μm x 10 μm) of Kapton exposed to oxygen with a similar mass loss of 0.2 mg/cm$^2$ (a) DC plasma, fluence of 5x10$^{18}$ O$^+$/cm$^2$; (b) RF plasma, fluence of 5x10$^{20}$ O$^+$/cm$^2$;

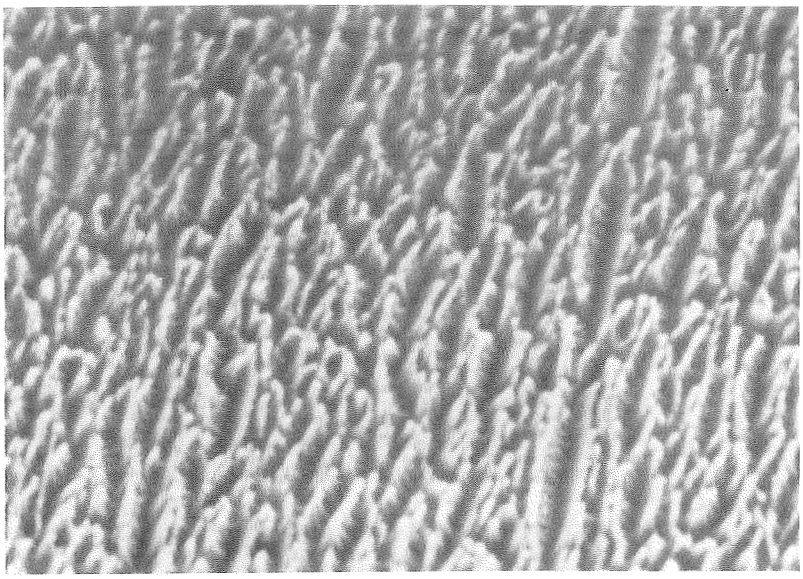

Fig. 5 - SEM image (10μmx10μm) of a Kapton surface eroded by 30 eV $O^+$ at a fluence of 1 x $10^{19}$ ions/$cm^2$.

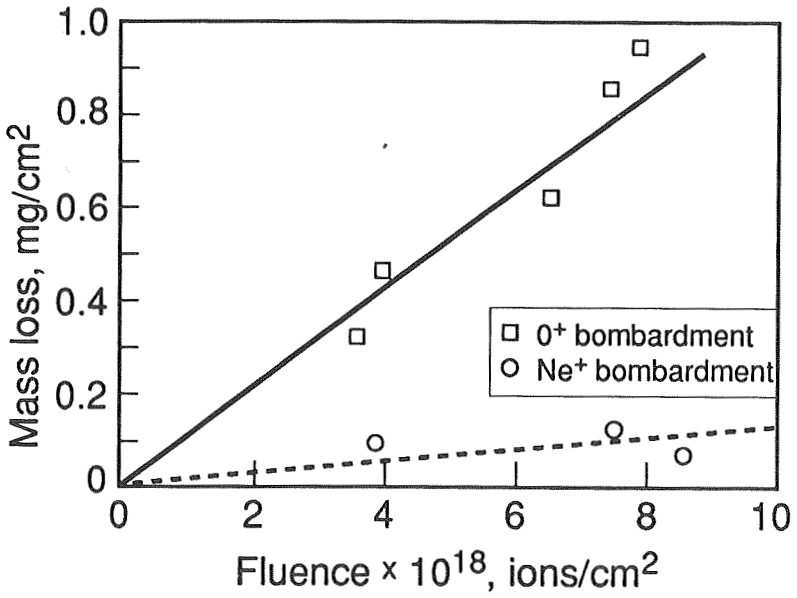


fig. 6 - The mass loss of Kapton surfaces as a function of fluence at 30 eV $O^+$ and $Ne^+$.

Note: (i) significant erosion by $O^+$, small erosion by $Ne^+$; (ii) the Kapton eroded surfaces gained weight upon exposure to atmospheric pressure leading to an inaccuracy of 0.1 mg in the measurements.

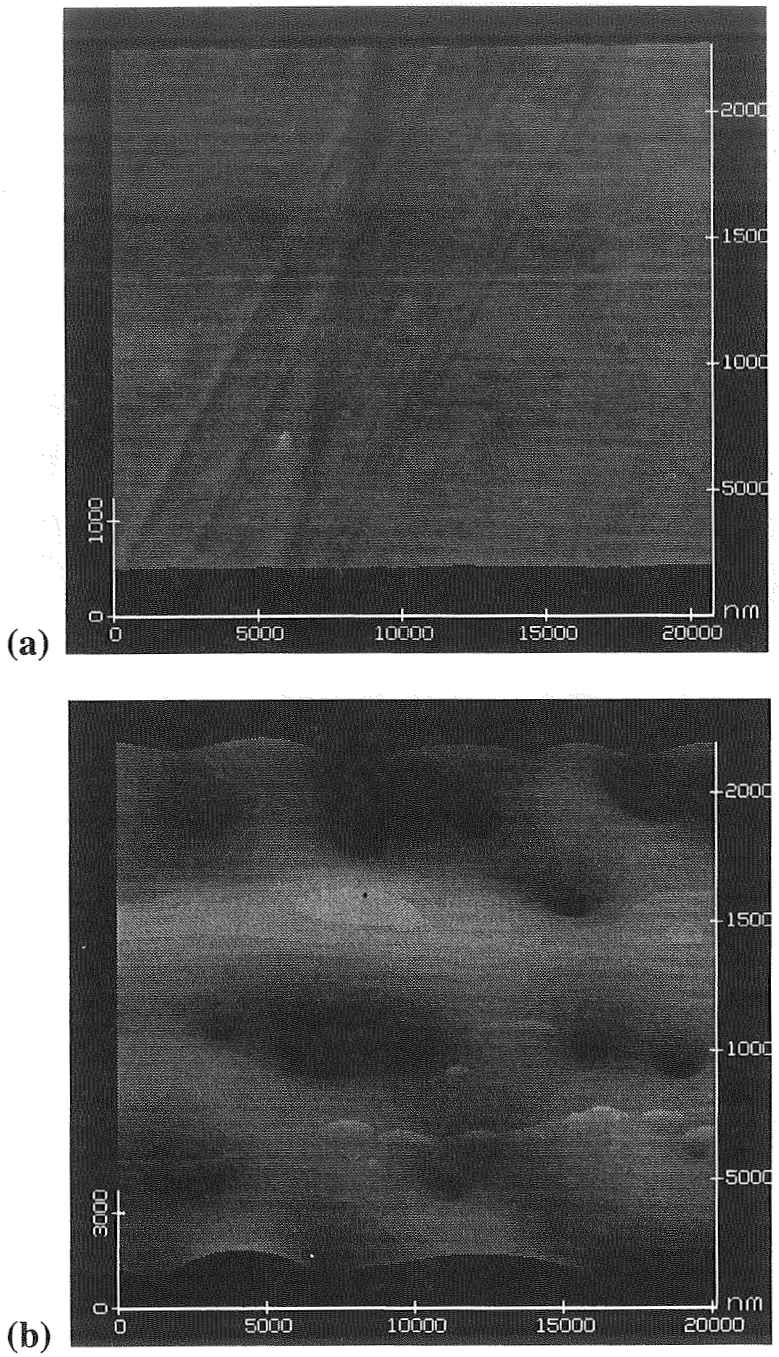


Fig. 7 - AFM images (20 μm x 20 μm) of Teflon. (a) pristine; (b) after 30 eV $O^+$ bombardment at a fluence of $3x10^{18}$ ions/$cm^2$;
Note the different z scale, 1000 nm for (a) and 3000 nm for (b).

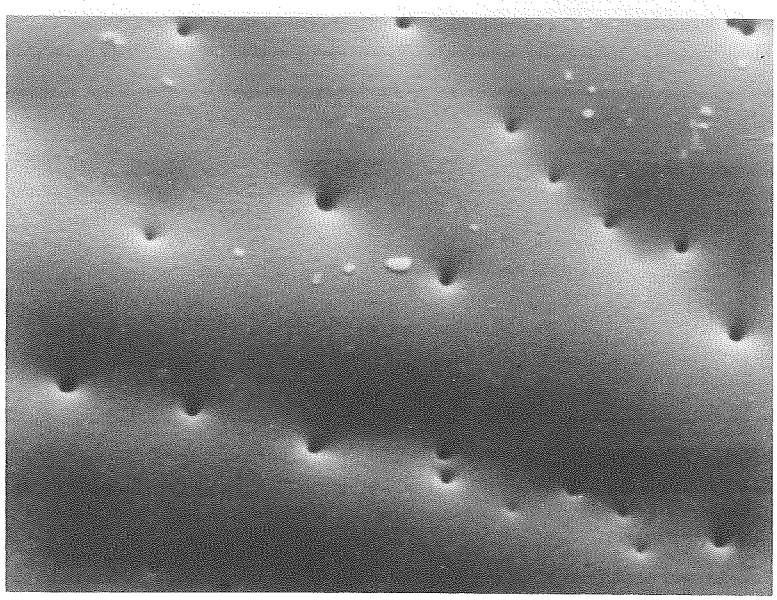

Fig. 8 - SEM image (20μmx20μm) of Teflon eroded by 30 eV $O^+$ ions at a fluence of 3 x $10^{18}$ ions/$cm^2$.

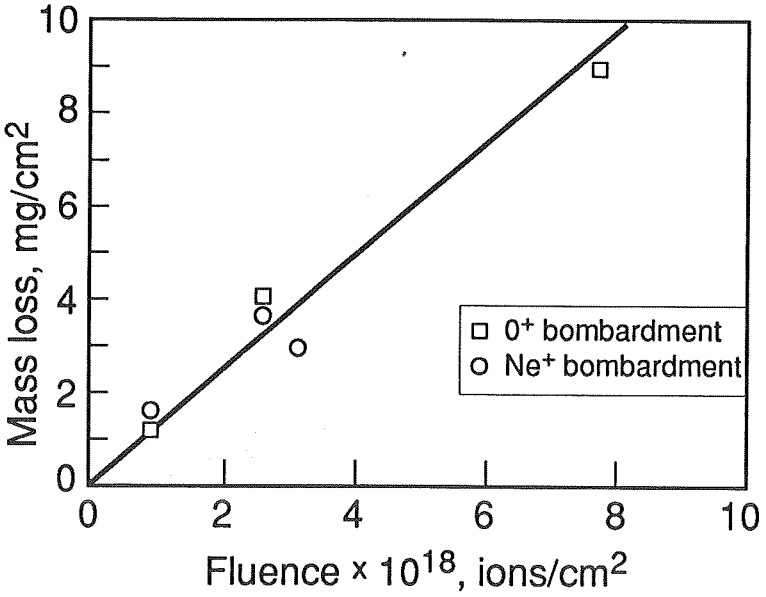


Fig. 9 - The mass loss of Teflon surfaces as a function of fluence at 30 eV $O^+$ and $Ne^+$ bombardment.

Note: similar erosion by $O^+$ and $Ne^+$.

# THE EFFECT OF LOW EARTH ORBIT EXPOSURE ON SOME EXPERIMENTAL FLUORINE AND SILICON-CONTAINING POLYMERS

John W. Connell[1], Philip R. Young[1], Carol G. Kalil[2], Alice C. Chang[3] and Emilie J. Siochi[3]

[1]NASA Langley Research Center

Hampton, VA 23681-0001

[2]Analytical Services and Materials

Hampton, VA 23666

[3]Lockheed Engineering and Sciences

Hampton, VA 23666

## ABSTRACT

Several experimental fluorine and silicon-containing polymers in film form were exposed to low Earth orbit (LEO) on a Space Shuttle flight experiment (STS- 46, Evaluation of Oxygen Interaction with Materials, EOIM-III). The environmental parameters of primary concern were atomic oxygen (AO) and ultraviolet (UV) radiation. The materials were exposed to $2.3\pm0.1X10^{20}$ oxygen atoms/$cm^2$ and 30.6 UV sun hours during the flight. In some cases, the samples were exposed at ambient, 120°C and 200°C. The effects of exposure on these materials were assessed utilizing a variety of characterization techniques including optical, scanning electron (SEM) and scanning tunneling (STM) microscopy, UV-visible (UV-VIS) transmission, diffuse reflectance infrared (DR-FTIR), x-ray photoelectron (XPS) spectroscopy and, in a few cases, gel permeation chromatography (GPC). In addition, weight losses of the films, presumably due to AO erosion, were measured. The fluorine-containing polymers exhibited significant AO erosion and exposed films were diffuse or "frosted" in appearance and consequently displayed dramatic reductions in optical transmission. The silicon-containing films exhibited minimum AO erosion and the optical transmission of exposed films was essentially unchanged. The silicon near the exposed surface in the films was converted to silicate/silicon oxide upon AO exposure which subsequently provided protection for the underlying material. The silicon-containing epoxies are potentially useful as AO resistant coatings and matrix resins as they are readily processed into carbon fiber reinforced composites and cured via electron radiation.

## INTRODUCTION

Evaluation of Oxygen Interactions with Materials-III (EOIM-III) is the third in a continuing series of materials exposure experiments flown aboard the space shuttle. This particular experiment was flown in August 1992 aboard Atlantis (STS-46). The primary parameters of concern for organic polymeric materials aboard EOIM-III were atomic oxygen (AO) and ultraviolet (UV) radiation. Other parameters that can

affect organic polymeric materials such as vacuum, thermal cycling, particulate radiation, and micrometeoroids and debris are less important for short term low Earth orbit (LEO) space flight experiments. The materials in this flight experiment were exposed to $2.3\pm0.1X10^{20}$ oxygen atoms/$cm^2$ and 30.6 ultraviolet sun hours. Some of the samples were also exposed at different temperatures (ambient, 120° and 200°C). AO is known from previous space flight experiments, of both short and long duration, to cause substantial erosion and mass loss of organic polymers[1-4]. Certain perfluorinated polymers, such as copolytetrafluoroethylene have exhibited good resistance to AO in both ground based and space flight exposure experiments. However, simultaneous exposure to AO and UV radiation can dramatically increase the rate of degradation of this material[5,6]. Coatings of inorganic oxides such as aluminum oxide[7], silicon oxide[7], chromium oxide[8] and indium-tin oxide[9], as well as decaborane-containing polymers[10], have been shown to protect organic materials from oxygen plasma and/or AO erosion. To provide maximum protection, the coatings need to be ~500-2000 Å thick, relatively uniform and defect free.

High performance polymers, such as polyimides, have been modified by the incorporation of silicon in the form of siloxane groups, either in the polymer backbone or pendant on the polymer chain. In addition to other favorable effects, the incorporation of silicon-containing groups into these polymers has been observed to enhance oxygen plasma/AO resistance through the formation of inorganic silicon (i.e. silicates/silicon dioxide) species by interacting with AO or oxygen plasma.[3,5,11-17] Other polymers containing silicon, such as poly(carborane siloxane)s, have also exhibited excellent oxygen plasma resistance.[18]

UV radiation present in LEO is of sufficient energy to cause organic bond cleavage. Organic polymeric materials can undergo UV induced chain scission and crosslinking reactions resulting in darkening, thermal conductivity, optical and mechanical property changes, embrittlement and loss of strength. These material property changes can dramatically affect spacecraft performance and lifetime.

Many of the experimental polymers flown on this experiment had shown promise in regards to AO and/or UV resistance in ground based exposure experiments. Low color, fluorinated polyimides[19] have been shown to be relatively resistant to electron and UV radiation in ground based experiments. Fluorine-containing poly(arylene ether)s had been shown to be resistant to electron radiation[20]. The silicon-containing materials had exhibited lower weight loss rates than Kapton®HN when exposed to oxygen plasma.[15,16] The intent of the work described herein was to increase our understanding of space environmental effects on fluorine and silicon-containing high performance polymers to aid in the design of future, lightweight materials with improved space environmental durability. The results of LEO exposure on these materials are discussed and, where relevant, compared to results from ground based exposures.

## EXPERIMENTAL

### Fluorine-Containing Polymers

The fluorine-containing polyimides[21] were prepared using the following general procedure. Stoichiometric quantities of the appropriate diamine and dianhydride were placed in N,N-dimethylacetamide (15-20% solids). The resulting solution was stirred at room temperature under nitrogen for 16-24 hr to form a viscous poly(amide acid) solution. This solution was subsequently cast onto plate glass and placed in a flowing dry air chamber until the film was tack-free. The tack-free film was placed in a forced air oven and heated for 1 hr each at 100, 200 and 300°C to effect imidization and solvent removal. The film was removed from the glass and characterized. The fluorine-containing poly(arylene ether)[22] and the copoly(imide-arylene ether)[23] were prepared as previously reported. The chemical structures of the fluorine-containing polymers are presented in Figure 1.

### Silicon-Containing Polymers

The epoxy functionalized siloxanes (EFS) were synthesized and cured using a UV source as previously described.[24] The polyimide containing pendent siloxane groups was prepared as previously reported.[15] The chemical structures of the silicon-containing polymers are presented in Figure 2.

Thin films (0.001-0.003 in. thick) were prepared and characterized prior to integration onto the EOIM-III experimental platform. Both control and flight experiment specimens were taken from the same piece of film. It should be noted that some of the flight specimens were exposed at elevated temperatures while the controls were stored under ambient conditions and did not receive additional thermal treatment. The characterization data determined on the flight specimens presented herein is relative to that of the control specimens which had been stored on Earth for ~2 years.

### Characterization

Ultraviolet-visible (UV-VIS) transmission spectra were recorded on a Perkin-Elmer Lambda 5 spectrometer. Infrared spectra were obtained by diffuse reflectance on a Nicolet Magna-IR System 750 spectrometer (DR-FTIR). Scanning tunneling microscopy (STM) was performed in air on a Nanoscope II instrument (Digital Instrument, Inc., Santa Barbara, CA) using a tungsten tip and G-Head accessory. Specimens were prepared by coating with a 5-8 nm of gold-palladium using a Hummer IV sputtering system (Anatech, Ltd., Alexandria, VA). A Cambridge Stereoscan 240 (Cambridge Instruments, Deerfield, IL) scanning electron microscope (SEM) was used to obtain SEM photomicrographs of Au-Pd coated specimens. Glass transition temperature (Tg) determinations were conducted on a DuPont 9900 Computer/Thermal Analyzer-Model 943 Thermomechanical Analyzer (TMA) at a heating rate of 5°C/min.

The approach used to make solution property measurements has been previously reported.[25] Gel permeation chromatography (GPC) was performed on a Waters 150C GPC at 35°C in chloroform using a $10^3/10^4/10^5/10^6/$Å Microstyragel™ HT column bank. The chromatograph was interfaced with a Waters

differential refractometer and a Viscotek (Viscotek Corp., Porter, TX) Model 150R Differential Viscometer (DV). A universal calibration curve was generated using Polymer Laboratories (Polymer Laboratories Inc., Amherst, MA) narrow dispersity polystyrene standards. GPC-DV analyses were conducted after samples had been in solution overnight.

## RESULTS AND DISCUSSION

The chemical structures of the experimental polymers are presented in Figures 1 and 2. The polymers are separated for convenience into fluorine-containing and silicon-containing. Fluorine-containing polymers flown in this experiment consisted of hexafluoroisopropylidene (6F)-containing polyimides, one poly(arylene ether) and one copoly(imide-arylene ether). The silicon-containing polymers consisted of four epoxy functionalized siloxanes (EFS) and one polyimide containing pendent siloxane groups (PISOX-1). The structures shown in Figure 2 for the EFS resins are prior to cure via UV radiation. These are one-part resins which contain ~1% of a photoiniatior catalyst (onium salt) and react via a cationic mechanism.[24]

Visual inspection of the two classes of exposed specimens revealed a marked difference in appearance. Fluorine-containing polymers were "frosted" or diffuse in appearance. In contrast, the silicon-containing polymers generally remained transparent and exhibited limited effects attributable to exposure. The two classes of polymer films were characterized by a number of analytical techniques. Thermo-mechanical analyses of the films showed no detectable change in $T_g$s of exposed films.

The initial weights, and weight losses of the films after LEO exposure are presented in Table 1. For comparative purposes, the weight loss data for FEP Teflon® on EOIM-III is included. The samples were either 1.0 in. or 0.5 in. in diameter and 0.001-0.003 in. thick. Consequently, the initial weights varied considerably. The fluorine-containing films exhibited higher weight losses after LEO exposure than either FEP Teflon® or the silicon-containing films. The weight losses for the fluorine-containing films were also higher with increasing exposure temperature, particularly when exposed at 200°C.

Most of the silicon-containing films were only exposed at 120°C due to limited space on the ambient exposure tray. They were not exposed at 200°C because of outgassing and subsequent contamination concerns. In general, silicon-containing films exhibited weight losses after 120°C exposure comparable to that exhibited by FEP Teflon® after ambient exposure (Table 1). The initial sample weights are included in Table 1. The ambient LEO exposed film from EFS-1 was brittle and broke apart during deintegration. Thus the weight loss could not be obtained. The ambient LEO exposed film from PISOX-1 exhibited a slight weight gain. This observation is reasonable since the silicon-containing polymers can gain weight by reacting with the AO to form silicate/silicon oxide. The overall trend exhibited by the weight loss data correlates well with observations from other analyses such as STM and XPS discussed later in this section.

Table 1. Weight Losses of Films after Exposure

| Film Sample | Initial Weight, mg | Weight Loss, mg | | |
|---|---|---|---|---|
| | | Ambient Exposed | 120°C Exposed | 200°C Exposed |
| 6F-PI-1 | 6.45 (120°C) | ——— | 0.63 | |
| | 28.92 (200°C) | | | 12.45 |
| 6F-PI-2 | 7.61 (ambient) | 0.79 | | ——— |
| | 8.84 (120°C) | | 0.92 | |
| 6F-PI-3 | 10.51 (ambient) | 0.48 | | |
| | 11.31 (120°C) | | 0.49 | |
| | 53.20 (200°C) | | | 27.32 |
| 6F-PAE-1 | 3.76 (ambient) | 0.42 | | ——— |
| | 3.66 (120°C) | | 0.38 | |
| 6F-Co-PAE/PI-1 | 5.58 (ambient) | 0.67 | | |
| | 7.03 (120°C) | | 1.23 | |
| | 28.75 (200°C) | | | 13.10 |
| EFS-1 | 8.37 (120°C) | not available | 0.36 | ——— |
| EFS-2 | 31.27 (120°C) | ——— | 0.01 | ——— |
| EFS-3 | 30.48 (120°C) | ——— | 0.21 | ——— |
| EFS-4 | 43.55 (120°C) | ——— | 0.11 | ——— |
| PISOX-1 | 7.93 (ambient) | +0.30 (weight gain) | | ——— |
| | 24.69 (120°C) | | 0.01 | |
| FEP Teflon® | 15.60 (ambient) | 0.03 | ——— | ——— |

**UV-VIS Spectroscopy**

Films which acquired a "frosted" appearance with exposure exhibited significantly less UV-VIS transmission when compared to control films than did exposed films which did not appear "frosted". This phenomenon is illustrated in Figure 3 for each of the two classes of materials and is representative of spectra obtained for other fluorine and silicon-containing films. The decrease in transmission with exposure is attributed to light refraction and reflectance from surface roughness caused by AO erosion. The incorporation of fluorine into these type of materials was anticipated to reduce AO erosion since highly fluorinated vinyl polymers such as fluorinated ethylene propylene (FEP Teflon®) exhibit outstanding stability to the LEO environment.[5,6,26] There appeared to be a trend between higher exposure temperature and reduction of UV-VIS transmission (Figure 3). This observation correlates with the trend observed for higher weight loss with higher temperature exposure described earlier.

The silicon-containing films performed as expected, exhibiting no reduction in optical transmission by UV-VIS spectroscopy (Figure 4). The organically bound silicon (siloxane) was oxidized to inorganically bound silicon (silica/silicate) by atomic oxygen (see XPS section). The thin $SiO_x$ layer subsequently provided protection from further AO attack. This chemical transformation has been known and utilized in the microelectronics industry for some years.[27] This phenomenon has also been observed with other silicon-containing materials flown on several space flight exposure experiments.[28-31]

**Infrared Spectroscopy**

Selected representative specimens were examined by FTIR spectroscopy. Since control and exposed films were too thick for high quality transmission spectra, somewhat lower quality diffuse reflectance spectra were obtained. Differences between control and exposed samples were difficult to assess visually. However, subtle differences could be detected by subtracting the two spectra.

The result of subtracting the exposed EFS-1 spectra from that of the control is presented in Figure 5. An upward inflection is indicative of more of a particular component in the control specimen. While differences in DR-FTIR subtraction spectra were generally not dramatic, several trends were noted.

DR-FTIR spectra of the fluorine-containing polyimides tended to exhibit 5-10 $cm^{-1}$ frequency shifts with exposure for the 1720, 1380 and 720 $cm^{-1}$ imide-related bands. While shifts were observed previously for other LEO-exposed polyimide films[31,32], similar shifts have also been observed in our laboratory for thermally cured films which were not exposed in LEO. Thus, this feature remains uninterpreted. Most exposed silicon-containing polymers exhibited less aliphatic character with loss of methyl bands around 2970 $cm^{-1}$. Film thinning was also observed with exposure as evidenced by an upward inflection in subtraction spectra of most specimens. The band around 3350 $cm^{-1}$ in the exposed film is presumably due to moisture absorption (hydration) of the $SiO_x$ surface which formed upon AO exposure.

**Solution Property Measurements**

Only two sets of specimens were soluble before and after exposure. These two sets consisted of a fluorinated poly(arylene ether) (6F-PAE-1, Figure 1) exposed at ambient and 120°C and a fluorinated polyimide (6F-PI-1, Figure 1) exposed at 120 and 200°C, as well as the respective controls. Molecular weight analyses could only be conducted on these six films.

Number average ( $\overline{M}_n$), weight average ( $\overline{M}_w$), and Z average ( $\overline{M}_z$) molecular weight data along with the polydispersity ratio and intrinsic viscosities obtained by GPC-DV for the two soluble polymers are presented in Table 2. The fluorinated poly(arylene ether) appeared to undergo chain extension or possibly, slight crosslinking as evidenced by increases in ( $\overline{M}_n$), ( $\overline{M}_w$), and ( $\overline{M}_z$), and a 40% increase in hydrodynamic volume. These effects are attributable to UV degradation. This effect may be greater with elevated temperature exposure as the 120°C LEO exposed film exhibited larger increases in ( $\overline{M}_n$) and ( $\overline{M}_z$) compared to ambient LEO exposed and control films (Figure 6). The fluorinated polyimide appeared

to be stable to LEO exposure at all temperatures as no significant changes in the GPC data were evident. The apparent decrease in intrinsic viscosity with exposure for this material is not fully understood.

The molecular weight distributions for these two fluorinated polymers are presented in Figures 6 and 7. Distributions for the fluorine-containing poly(arylene ether) in Figure 6 show an increase in the high molecular weight component with exposure along with a corresponding decrease in the low molecular weight component. This observation is consistent with ( $\overline{M}_n$), ( $\overline{M}_w$), and ( $\overline{M}_z$) data given in Table 2. Molecular weight distributions for the fluorine-containing polyimide (Figure 7) show only minor differences with exposure.

Several polymers which received various LEO exposures have been characterized in previous studies. A polysulfone [i.e. poly(arylene ether)] film was found to undergo both chain scission and crosslinking after 10 months of LEO exposure onboard the Long Duration Exposure Facility (LDEF).[33] A sulfone-containing polyimide exhibited primarily crosslinking under identical exposure conditions on LDEF while a polyimide which contained isopropylidene and ether linkages (i.e. like polysulfone) exhibited no change in molecular weight.[32] A polysulfone film flown on a separate EOIM-III experiment also exhibited molecular level effects.[34] Thus, changes in various molecular weight parameters of soluble polymers resulting from LEO exposure can be readily characterized by GPC-DV. It appears that among aromatic polymers, not only is polymer family (i.e. imide vs. arylene ether) significant in regards to LEO stability, but the arrangement and type of connecting groups (i.e. ether, sulfone, carbonyl, etc.) is also important. However, our ability to predict how a particular polymer will respond to LEO exposure needs to be refined.

Table 2. Summary of GPC Results

| Sample ID | ( $\overline{M}_n$) g/mole | ( $\overline{M}_w$) g/mole | ( $\overline{M}_z$) g/mole | Polydispersity | Intrinsic Viscosity, dL/g |
|---|---|---|---|---|---|
| **6F-PAE-1** | | | | | |
| Control | 9408 | 35,930 | 68,600 | 3.81 | 0.459 |
| Exposed (Ambient) | 13,910 | 44,740 | 133,800 | 3.21 | 0.436 |
| Exposed (120°C) | 13,750 | 67,870 | 494,000 | 4.94 | 0.429 |
| **6F-PI-1** | | | | | |
| Control | 38,330 | 129,900 | 273,200 | 3.38 | 0.699 |
| Exposed (120°C) | 34,530 | 143,600 | 310,000 | 4.16 | 0.608 |
| Exposed (200°C) | 44,040 | 145,100 | 313,200 | 3.29 | 0.632 |

**Surface Analysis**

As mentioned earlier, LEO exposed fluorine-containing films exhibited a "frosted" appearance both visually and by optical microscopy. Further detailed data from STM and SEM analyses are shown in Figures 8 and 9, respectively. The fluorine-containing films appeared heavily eroded and shared identical marble-like erosion patterns unique in comparison to similar polymers flown of LDEF which exhibited an egg-crate-like erosion surface.[35]

The silicon-containing films exhibited no discernible differences between exposed and control samples by optical microscopy. However, analyses by SEM and STM indicated that some surface erosion did occur. The STM line plot of EFS-4 is presented in Figure 10. Note that when comparing the erosion depths in Figures 8 and 10 that the depth profile scales are different. STM spectra of the LEO exposed film shows the beginnings of the egg-crate-like pattern seen previously in AO exposed polymer films.[35] Presumably, initial AO erosion occurs until a sufficient layer of $SiO_x$ is formed from the reaction of the oxygen atoms with the silicon.

Table 3. XPS Results of EFS-1

| Photopeak | Control | LEO upside ambient exposed | LEO downside ambient exposed | LEO upside 120°C exposed | LEO downside 120°C exposed |
|---|---|---|---|---|---|
| **C1s** | | | | | |
| Binding Energy ,eV | 284.6 | 284.6 | 284.6 | 284.6 | 284.6 |
| Atomic Concentration , % | 65.9 | 38.7 | 61.7 | 18.3 | 73.6 |
| **O1s** | | | | | |
| Binding Energy ,eV | 532.1 | 532.8 | 532.6 | 533.1 | 532.0 |
| Atomic Concentration , % | 19.5 | 38.5 | 27.1 | 53.1 | 17.9 |
| **Si2p** | | | | | |
| Binding Energy ,eV | 101.8 | 103.7 | 101.9 | 103.2 | 101.4 |
| Atomic Concentration , % | 14.6 | 21.4 | 9.1 | 28.2 | 7.0 |
| **N1s** | | | | | |
| Binding Energy ,eV | — | 399.0 | 399.9 | 399.5 | 399.8 |
| Atomic Concentration , % | — | 1.4 | 2.2 | 0.5 | 1.5 |

**X-Ray Photoelectron Spectroscopy (XPS)**

X-ray photoelectron spectroscopy was performed at Virginia Polytechnic Institute and State University under NASA Langley Grant NAG1-1186. Representative samples of control and exposed fluorine and silicon-containing films were analyzed using XPS. The fluorine-containing polyimide (6F-PI-2) for the most part indicated little difference in the control sample and either side of the exposed samples. However, there was some difference in the atomic concentration of the fluorine on both LEO exposure sides of the ambient and 120°C exposed films. Silicon contamination was identified on both control (~2%) and exposed (1-3.8%) samples.

XPS data for EFS-1 exposed at both ambient and 120°C is presented in Table 3. There was a clear difference in XPS data from upside versus downside LEO exposed films. The upside LEO exposed films exhibited dramatic changes in surface chemistry. The downside of the films did not receive AO or UV exposure and consequently exhibited no changes in surface chemistry (Table 3). The silicon was oxidized to silicate/silicon oxide as evidenced by the increases in binding energy of the Si2p electrons on the LEO upside

Table 4. XPS Results of PISOX-1

| Photopeak | Control | LEO upside ambient exposed | LEO downside ambient exposed | LEO upside 120°C exposed | LEO downside 120°C exposed |
|---|---|---|---|---|---|
| **C1s** | | | | | |
| Binding Energy ,eV | 284.6 | 284.6 | 284.6 | 284.6 | 284.6 |
| Atomic Concentration , % | 69.2 | 26.7 | 58.7 | 29.3 | 68.7 |
| **O1s** | | | | | |
| Binding Energy ,eV | 532.1 | 532.8 | 532.6 | 533.1 | 532.0 |
| Atomic Concentration , % | 19.1 | 46.0 | 27.8 | 45.4 | 21.9 |
| **Si2p** | | | | | |
| Binding Energy ,eV | 101.6 | 103.1 | 102.4 | 103.4 | 101.6 |
| Atomic Concentration , % | 9.3 | 25.7 | 11.5 | 24.2 | 5.5 |
| **N1s** | | | | | |
| Binding Energy ,eV | 400.2 | 399.9 | 399.7 | 399.8 | 400.1 |
| Atomic Concentration , % | 2.4 | 0.9 | 1.9 | 1.1 | 3.9 |

exposed films. In addition, the atomic concentration of Si on the LEO upside exposed films increased from 14.6% (control) to 21.4 and 28.2%, respectively for the ambient and 120°C exposures. The oxygen 1s electron binding energies showed slight increases as did the atomic concentration of oxygen for the LEO exposed side of the films (Table 3). There were differences in the XPS data of the ambient LEO upside exposures compared to those of the 120°C exposures. The atomic concentrations for silicon and oxygen were higher for the 120°C exposed films. The XPS data for EFS-2 exhibited the same general trends as those described for EFS-1.

The polyimide containing pendent siloxane groups (PISOX-1) exhibited similar behavior in regards to the increases in binding energies of the silicon and oxygen electrons and atomic concentrations of the LEO exposed (upside) films (Table 4). These increases in binding energies and atomic concentrations are consistent with AO induced organo-silicon to silicate/silicon oxide chemical transformations. After exposure, the silicon-containing materials typically exhibited a ratio of silicon:oxygen of approximately 1:2. There appeared to be a trend between ambient exposed and elevated temperature exposed specimens of silicon-containing polymers in that the atomic concentration of silicon and oxygen were higher for the samples exposed at elevated temperature. Similar behavior, with respect to organo-silicon to inorgano-silicon chemical changes, has been observed for copoly(imide-siloxane) flown on LDEF.[28-31] The silicon and oxygen in these materials exhibited increases in binding energies and relative concentrations that were attributed to $SiO_X$ formation as a result of the AO exposure. In addition, these materials exhibited lower erosion rates than other non-silicon containing organic polymers.

## SUMMARY

A series of experimental fluorine and silicon-containing polymer films were exposed to LEO at several different temperatures aboard the STS-46 materials exposure flight experiment EOIM-III. The fluorine-containing materials were dramatically affected by relatively short term AO and UV exposure. They exhibited "frosting" with corresponding reductions in optical transmission as a result of AO exposure. The 6F-PAE-1 exhibited changes in molecular weight distribution characteristic of UV induced degradation while the 6F-PI-1 exhibited little, if any changes. The weight loss and UV-VIS data suggest that samples exposed at elevated temperature in LEO exhibited more pronounced AO effects (i.e. higher weight loss and greater reduction in optical transparency) compared to ambient LEO exposed samples. The fluorine-containing films exhibited a unique erosion pattern different than those observed on films flown on LDEF. Fluorine-containing materials of this type obviously would need to be protected from AO exposure.

The silicon-containing polymers exhibited little effects of the LEO exposure. The films remained clear with no significant reductions in optical transparency. Conversion of the organo-silicon to silicate/silicon oxide was evident from the XPS data and formation of this $SiO_X$ surface layer undoubtedly

protected the underlying material from further erosion. Initial erosion due to AO was observed. This is necessary to allow sufficient reaction of the atomic oxygen with the silicon to form an in-situ $SiO_x$ protective coating. Further work will focus on the effects of longer duration ground based exposures of these materials.

## REFERENCES


1. P. N. Peters, R. C. Linton and E. R. Miller, *J. Geophys. Res. Lett., 10*, 569 (1983).
2. D. E. Bowles and D. R. Tenney, *SAMPE J., 23*(3), 49 (1987).
3. W. S. Slemp, B. Santos-Mason, G. F. Sykes Jr. and W. G. Witte Jr., *AO Effect Measurements for Shuttle Missions STS-8 and 41-G, Vol 1, Sec 5*, 1 (1985).
4. *LDEF-69 Months in Space. First Post Retrieval Symposium. NASA Conference Publication 3134 Part 2*, A. Levine Ed., 1991.
5. L. J. Leger, J. T. Visentine and B. Santos-Mason, *SAMPE Quaterly, 18*(2), 48 (1987).
6. A. E. Stiegman, D. E. Brinza, M. S. Anderson, T. K. Minton, G. E. Laue and R. H. Liang, *Jet Propulsion Laboratory Publication 91-10*, May 1991.
7. B. A. Banks, M. J. Mistich, S. K. Rutledge and H. K. Nahra, *Proc. 18th IEEE Photovoltaic Specialists Conf.*,1985.
8. L. J. Leger, I. K. Spikes, J. F. Kuminecz, T. J. Ballentine and J. T. Visentine, *STS Flight 5, LEO Effects Experiment*, AIAA-83-2631-CP (1983).
9. K. A. Smith, *Evaluation of Oxygen Interactions with Materials (EOIM), STS-8 AO Effects*, AIAA-85-7021 (1985).
10. S. Packrisamy, D. Schwam, and M. Litt, *Polym. Prepr., 34*(2), 197 (1993).
11. J. T. Visentine, L. J. Leger, J. F. Kuminecz and I. K. Spiker, *AIAA-85-0415*, AIAA 23rd Aerospace Conf., Jan. (1985).
12. C. A. Arnold, J. D. Summers, Y. P. Chen, R. H. Bott, D. H. Chen and J. E. McGrath, *Polymer, 30*(6), 986 (1989).
13. C. A. Arnold, J. D. Summers, Y. P. Chen, T. H. Yoon, B. E. McGrath, D. Chen and J. E. McGrath, in *Polyimides: Materials, Chemistry and Characterization*, C. Feger, Ed., Elsevier Science Publishers B. V., Amsterdam, 1989, pp. 69-89.
14. C. A. Arnold, D. H. Chen, Y. P. Chen, R. O. Waldbauer, Jr., M. E. Rogers and J. E. McGrath, *High Perf. Polymers*, 2(2), 83 (1990).
15. J. W. Connell, D. C. Working, T. L. St. Clair and P. M. Hergenrother, in *Polyimides: Materials, Chemistry, and Charactization*, C. Feger, Ed., Technomic Pub. Co., Lancaster, PA, 1992, pp. 152-164.
16. J. W. Connell, J. G. Smith, Jr. and P. M. Hergenrother, *J. Fire Sci., 11*(2), 137 (1993).

17. P. R. Young and W. S. Slemp, LDEF Materials Workshop '91, *NASA Conf. Pub. 3162 Part 1*, 376-378 (1991).
18. J. Kulig, G. Jefferis and M. Litt, *Polym. Matl. Sci. Eng., 61*, 219 (1989).
19. A. K. St. Clair, T. L. St. Clair and W. S. Slemp, in *Recent Advances in Polyimide Science and Technology*, W. D. Weber and M. R. Gupta, Eds., Soc. Plast. Eng., Poughkeepsie, NY, 1987, pp. 16-36.
20. J. W. Connell, E. J. Siochi and C. I. Croall, *High Perf. Polymers, 5*, 1 (1993).
21. M. K. Gerber, J. R. Pratt, A. K. St. Clair and T. L. St. Clair, *Polym. Prepr., 31*(1) 340 (1990). F. W. Harris, S. L.-C. Hsu and C. C. Tso, *ibid.*, 342 (1990). R. A. Buchanan, R. F. Mundhenke and H. C. Lin, *ibid., 32*(2), 193 (1991).
22. R. N. Johnson, A. G. Farnham, F. A. Clendinning. W. F. Hale and C. N. Merriam, *J. Polym. Sci., 5*, 2375 (1967).
23. B. J. Jensen and S. J. Havens, *Polym. Prepr., 33*(1), 1084 (1992).
24. J. V. Crivello and J. L. Lee, *J. Polym. Sci. Polym. Chem. Ed., 28* 479 (1990).
25. P. R. Young, J. R. J. Davis and A. C. Chang, *Soc. Adv. Matls. and Proc. Eng. Ser., 34*(2), 1450 (1989).
26. P. R. Young, W. S. Slemp, *NASA Technical Memorandum 104096*, (Dec. 1991).
27. N. J. Chou, C. H. Tang, J. Paraszcak and E. Babich, *Appl. Phys. Lett., 46*(1), 31 (1985).
28. P. R. Young, W. S. Slemp, W. G. Witte and J. Y. Shen, *Soc. Adv. Matls. and Proc. Eng. Ser., 36*(1), 403 (1991).
29. M. J. Meshishnek, W. K. Stuckey, J. S. Evangelsides, L. A. Feldman, R. V. Peterson, G. S. Arnold and D. R. Peplinski, *NASA Technical Memorandum 100459, Vol. II*, Sec. 5-1 to 5-33 (1988).
30. W. S. Slemp, B. Santos-Mason, G. F. Sykes and W. G. Witte, *ibid., Vol. I*, Sec. 5-1 to 5-15 (1988).
31. P. R. Young, W. S. Slemp and C. R. Gautreaux, *Soc. Adv. Matls. and Proc. Eng. Ser., 37*(1), 159 (1992).
32. P. R. Young, A. K. St. Clair and W. S. Slemp, *Soc. Adv. Matls. and Proc. Eng. Ser., 38*(1), 664 (1993).
33. P. R. Young, W. S. Slemp, E. J. Siochi and J. R. J. Davis, *SAMPE Tech. Conf. Proc., 24*, T174 (1992).
34 P. R. Young, W. S. Slemp and E. J. Siochi, *Soc. Adv. Matls. and Proc. Eng. Ser., 39*, 2243 (1994).
35. C. R. Kalil and P. R. Young, *Soc. Adv. Matls. and Proc. Eng. Ser., 39*(1), 445 (1993).

The use of trade names of manufacturers does not constitute an official endorsement of such products or manufacturers, either expressed or implied, by the National Aeronautics and Space Administration.

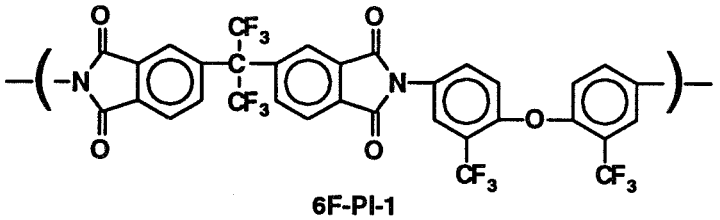

6F-PI-1

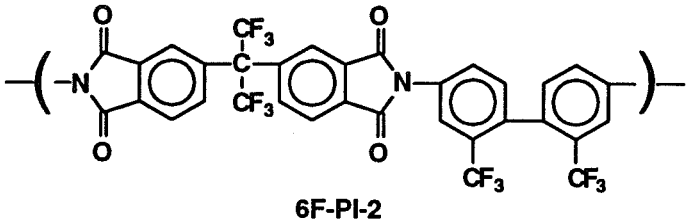

6F-PI-2

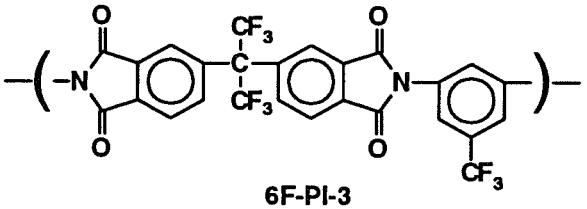

6F-PI-3

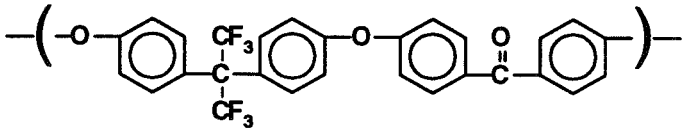

6F-PAE-1

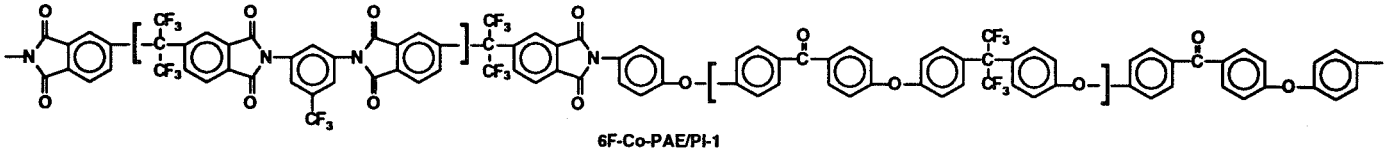

6F-Co-PAE/PI-1

Figure 1. Chemical structures of fluorine-containing polymers.

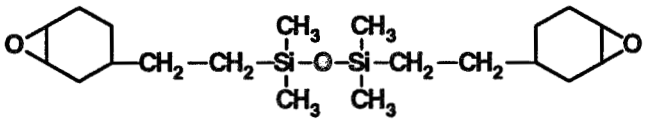

EFS-1

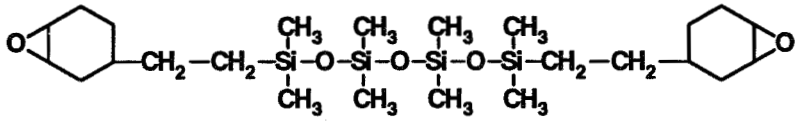

EFS-2

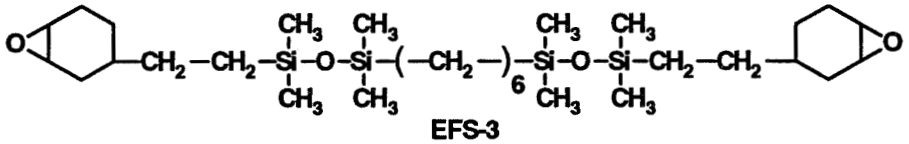

EFS-3

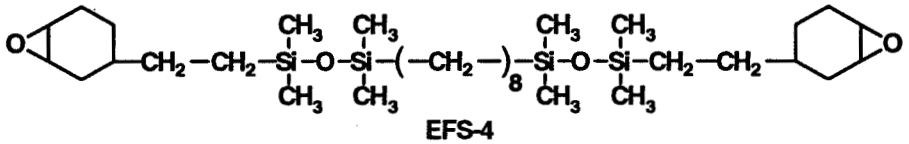

EFS-4

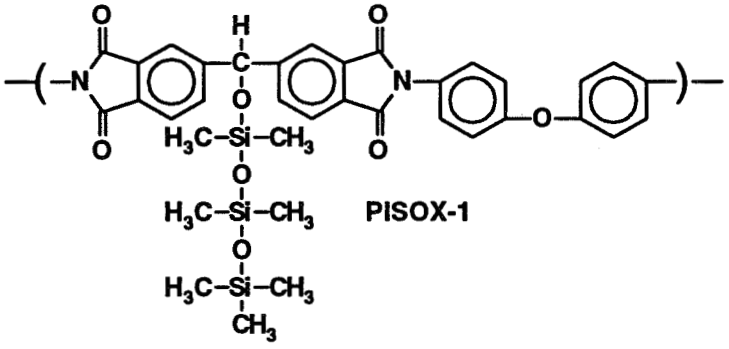

PISOX-1

Figure 2. Chemical structures of silicon-containing polymers, the structures given for the EFS compounds are prior to curing with a UV source.

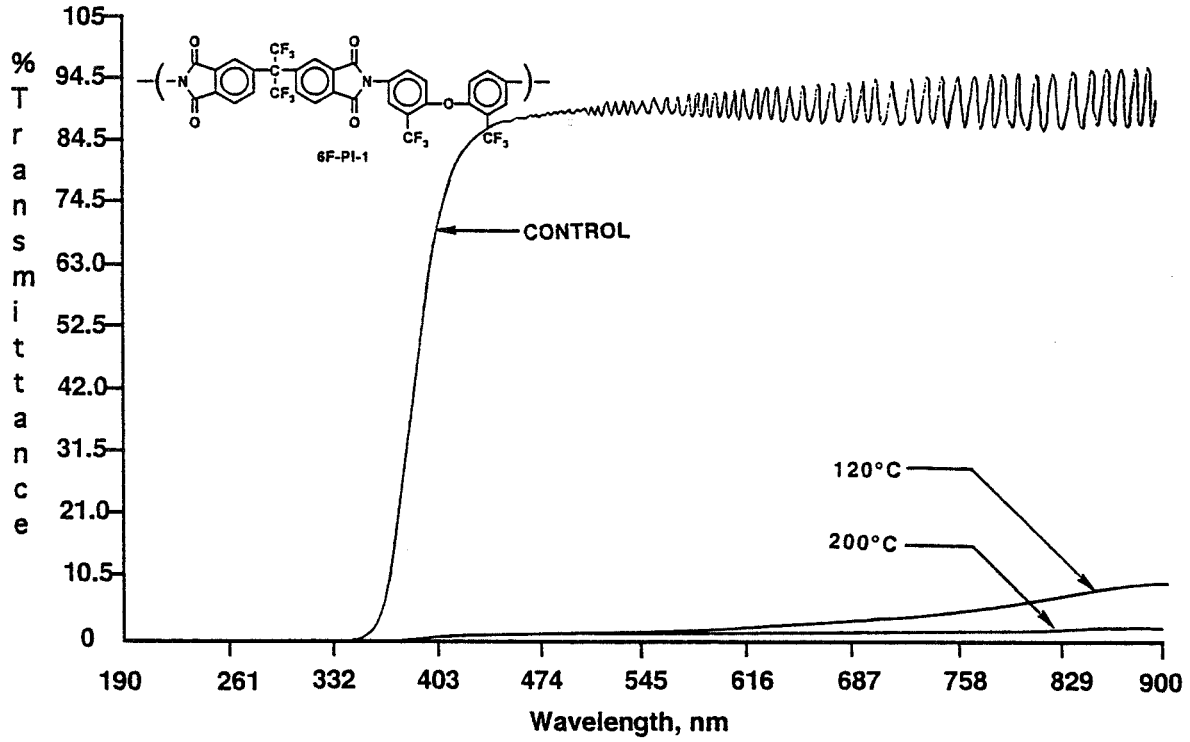


Figure 3. UV-VIS overlay spectra of fluorine-containing polyimide (6F-PI-1) before and after LEO exposure.

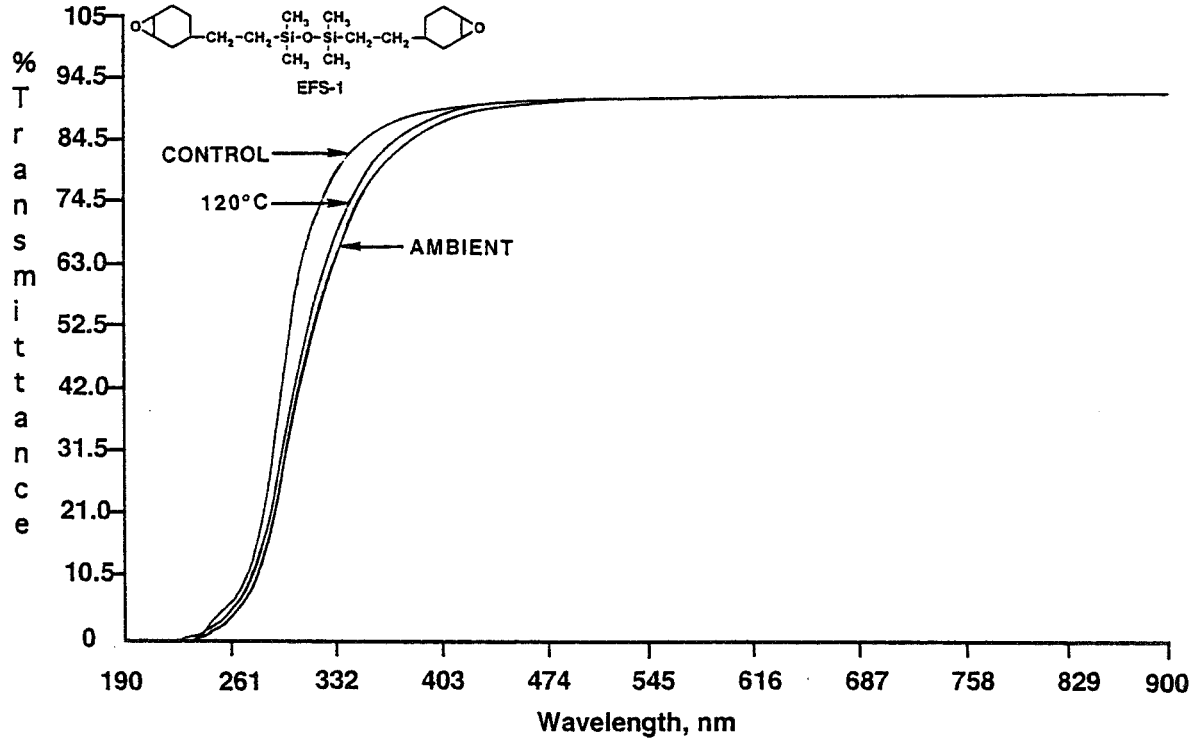


Figure 4. UV-VIS overlay spectra of silicon-containing epoxy (EFS-1) before and after LEO exposure.

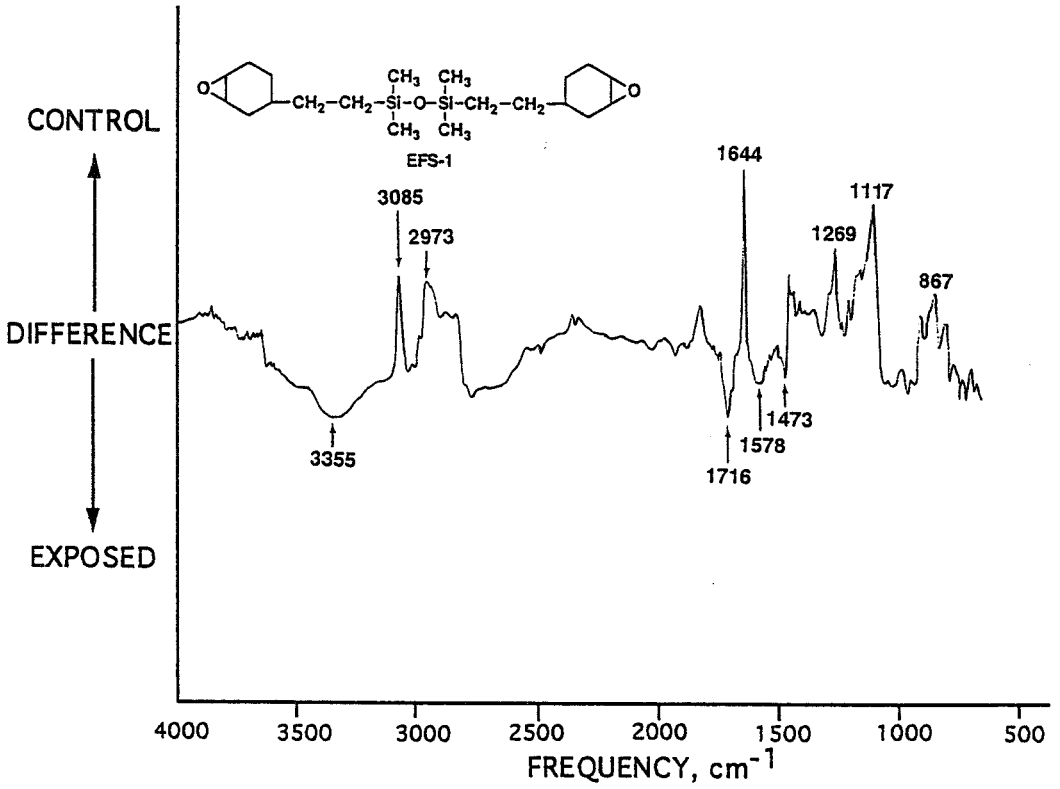


Figure 5. DR-FTIR subtraction spectrum of silicon-containing epoxy (EFS-1) before and after LEO exposure.

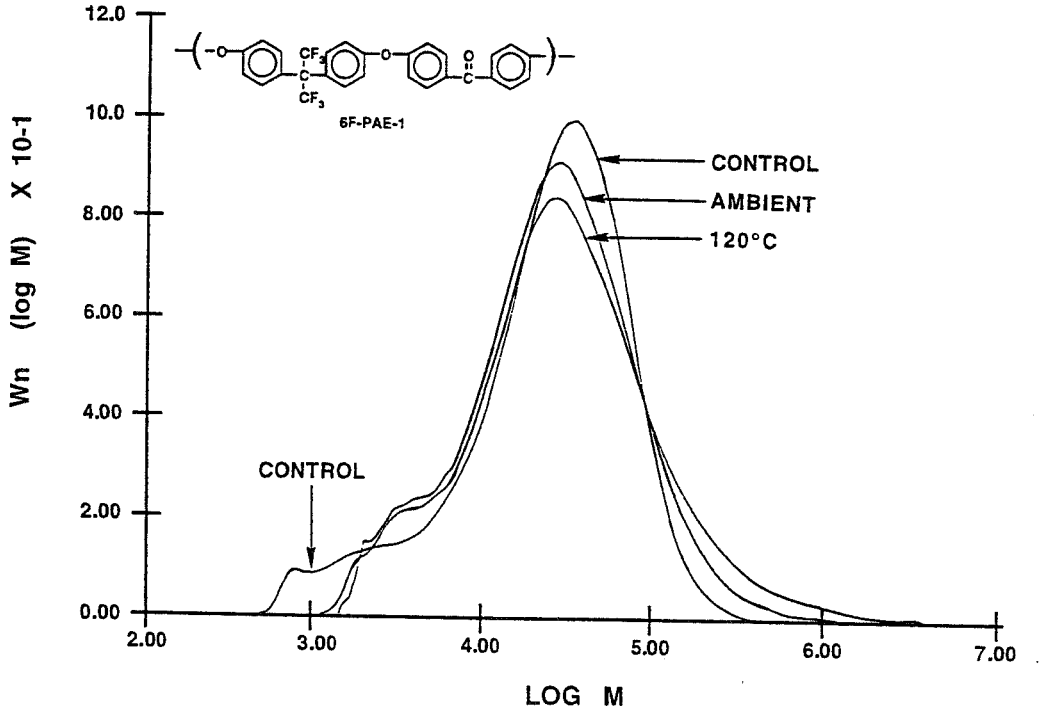


Figure 6. Overlay of molecular weight distributions of fluorine-containing poly(arylene ether), 6F-PAE-1, before and after LEO exposure.

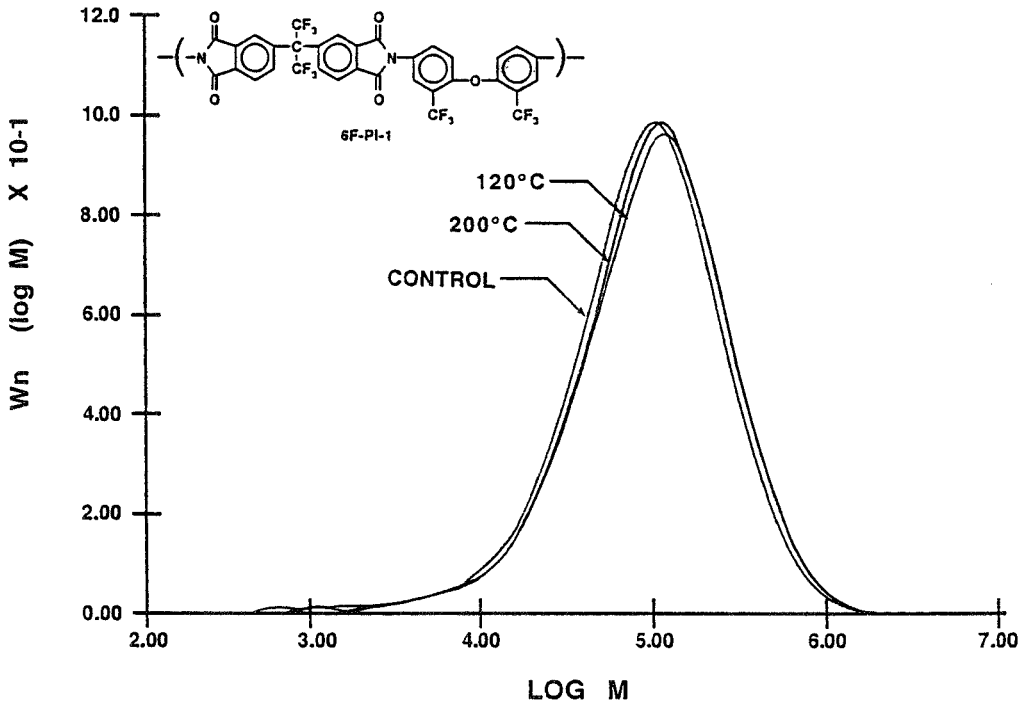


Figure 7. Overlay of molecular weight distributions of fluorine-containing polyimide, 6F-PI-1, before and after LEO exposure.

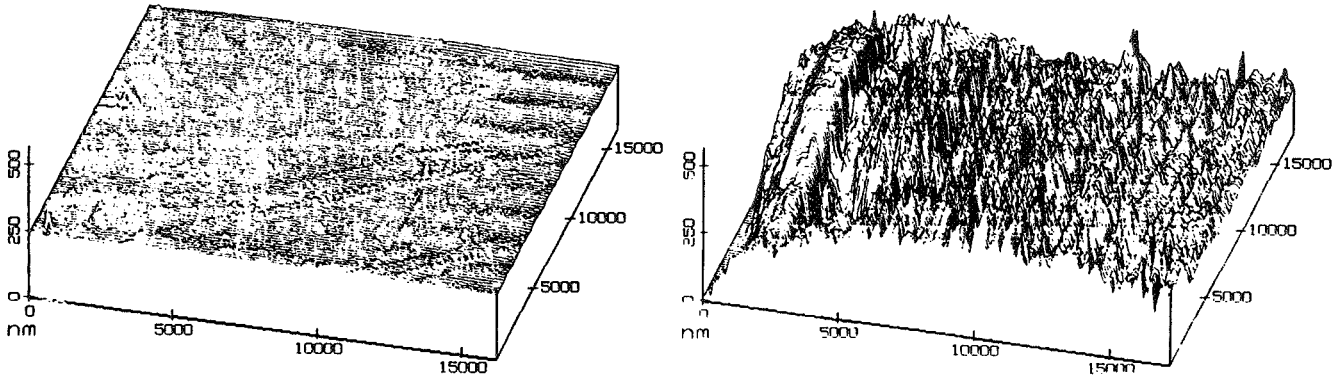


Figure 8. STM of fluorine-containing poly(arylene ether), 6F-PAE-1, before and after LEO exposure.

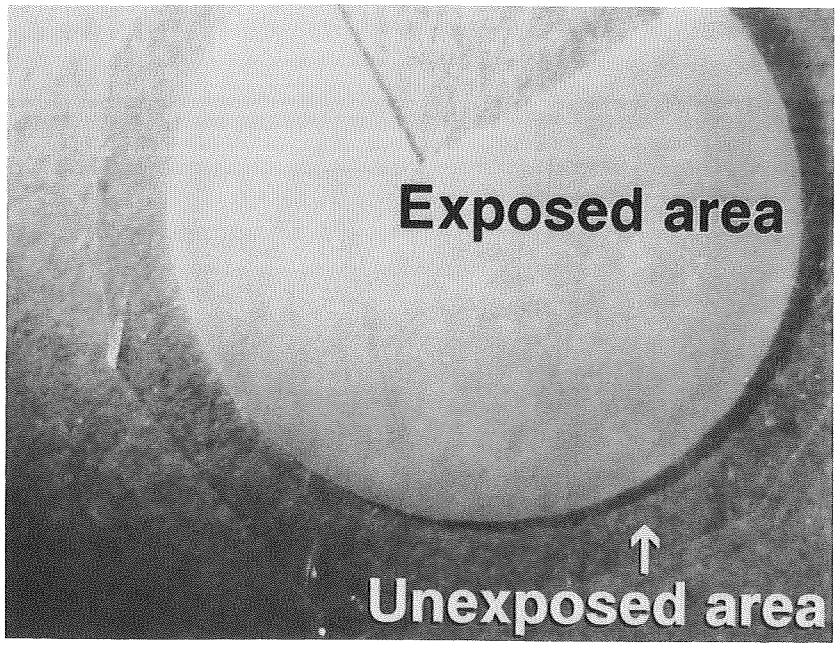


Optical microscopy (8X)

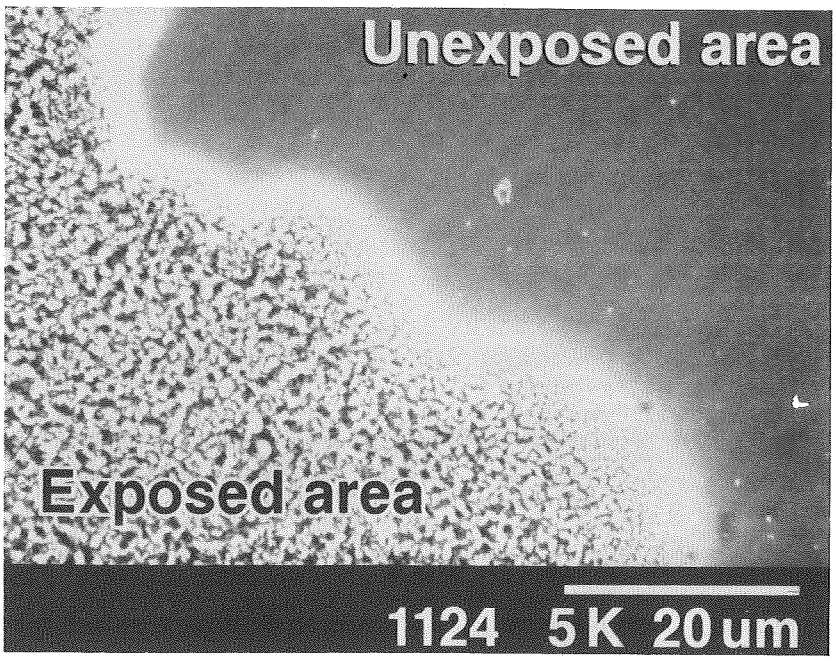


Scanning electron microscopy

Figure 9. Photomicrographs of fluorine-containing poly(arylene ether), 6F-PAE-1, before and after LEO exposure.

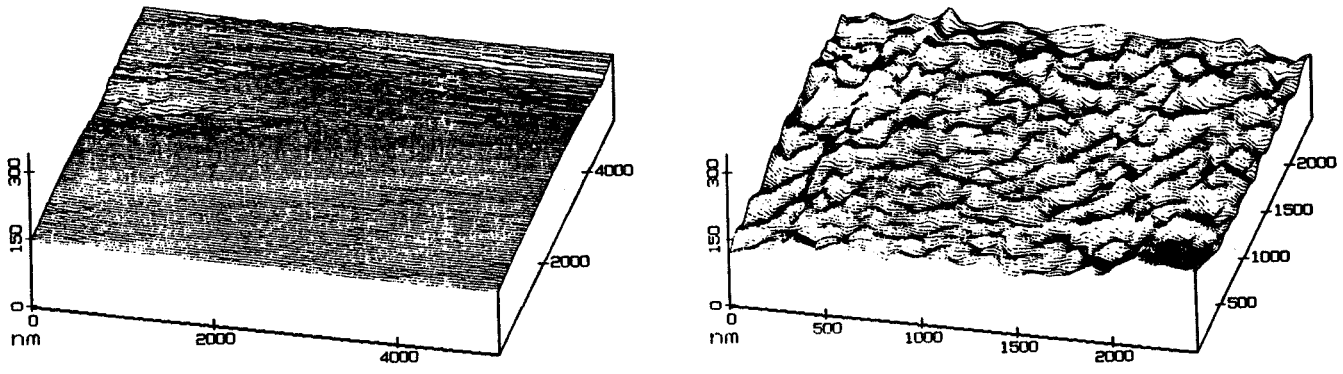


**CONTROL** **EXPOSED**

Figure 10. STM of silicon-containing epoxy (EFS-4) before and after LEO exposure.

# A SIMULATION FACILITY FOR TESTING SPACE STATION ASSEMBLY PROCEDURES

Ankur R. Hajare, Daniel T. Wick, and Nagy M. Shehad
Enhanced Technologies
Houston, Texas

## ABSTRACT

NASA plans to construct the Space Station *Freedom* (SSF) in one of the most hazardous environments known to humankind - space. It is of the utmost importance that the procedures to assemble and operate the SSF in orbit are both safe and effective. This paper describes a facility designed to test the integration of the telerobotic systems and to test assembly procedures using a real-world robotic arm grappling space hardware in a simulated micro-gravity environment.

## INTRODUCTION

NASA plans to construct the Space Station *Freedom* (SSF) in one of the most hazardous environments known to humankind - space. It is of utmost importance that telerobotic systems and procedures to assemble and maintain the SSF are both safe and effective. In addition, it is equally important that the mechanical attachment devices of the SSF function as planned. To ensure that the systems and procedures will meet all safety requirements, NASA is developing the Space Systems Automated Integration and Assembly Facility (SSAIAF). This facility will test the *integration* of flight systems, the telerobotic systems, and humans that will be involved in the assembly and maintenance of the SSF. Both mechanical and dynamic performance of these elements in a micro-gravity environment will be tested using real-time simulations.

Traditionally, the approach to building such hardware-in-the-loop, human-in-the-loop simulations has involved development of unique software to support each scenario. This scenario-specific approach results in continuous software development and maintenance, which consumes large portions of a project's budget and can adversely affect a project's schedule. A proposed SSAIAF software architecture, Simulation and Control Environment (SCE), will support the development of generic software components, called modules, that can be reused in numerous simulation scenarios. This approach will reduce the requirements for new simulation development.

This paper presents a brief overview of the SSAIAF. This is followed by a more in-depth description of the SCE proposed to be used by SSAIAF in developing the real-time simulations. The paper concludes with a description of how the SSAIAF can support the development of telerobotic procedures and space systems.

## SSAIAF SYSTEMS

SSAIAF systems will provide the resources for all testing and development activities undertaken in the facility. The SSAIAF systems are shown graphically in Figure 1.

### Computing Resources

Computing systems in this environment include hardware with sufficient processors, memory and I/O capacity to support two simultaneous tests on SSAIAF systems. The currently envisioned system will include three host computers, peripherals, and computer control consoles.

### Manipulator Development Facility

The Manipulator Development Facility (MDF) is a stand-alone system that provides a realistic test and training environment for astronauts who will use the Shuttle arm. The MDF permits astronauts or test engineers to lift structural components out of a mockup of the Space Shuttle Orbiter cargo bay and position them for deployment or erection.

### Mobile Remote Manipulator Development Facility

The Mobile Remote Manipulator Development Facility (MRMDF) is a stand-alone system that provides a realistic test and training environment for astronauts who will use the Space Station arm. The MRMDF permits astronauts or test engineers to grapple and position a station payload, a platform, and another object for deployment or erection on the Space Station.

### Air -Bearing Floor

The Air-Bearing Floor (ABF) is a large, smooth surface area (21.3 meters by 27.4 meters) upon which pallets can float on a cushion of air. Each pallet can carry over 453.6 Kg (1000 lb) of weight. The cushion of air permits the pallets to move in two dimensions as if there were no friction. Thus, the air-bearing floor simulates weightlessness in two dimensions.

### Six-Degree-of-Freedom Dynamic Testing System

The Six-Degree-of-Freedom Dynamic Testing System (SDTS) is a computer-controlled hydraulic table (Stewart Platform) that can move in six planes of motion at one time (right/left, back/forward, up/down, pitch, yaw, and roll). The SDTS can lift large objects weighing up to 4536 Kg (10,000 lb) and move them to a position, as directed, within a tolerance of 0.25 cm (0.1 inch). The orientation of the SDTS is such that it usually moves objects vertically.

### Simulation and Control Environment

The Simulation and Control Environment (SCE) is a software system that integrates all elements required for the development of SSAIAF real-time simulations in a comprehensive and cost effective application generation environment. The modular approach allows the reusability of software developed for previous simulations. The SSAIAF simulations developed using the SCE will execute on the test computing systems. SCE development activities utilizing a user-friendly, icon-driven user interface will be accomplished on development/maintenance workstations. The SCE architecture and usage is further discussed below.

## THE SIMULATION AND CONTROL ENVIRONMENT

### SCE Architecture

The proposed software architecture for SCE will include both Commercial-Off-the-Shelf (COTS) and custom components. SCE uses a layered architecture (Figure 2) that supports modular and reusable software modules as well as application generation techniques that provide fast development and ease of change. The SCE has been designed in a modular architecture for three reasons. First, this modular approach supports the maintenance of the entire system. This permits system maintainers and developers to revise and update any particular module without affecting the entire SCE. This modular design is also POSIX compliant so that it can be easily migrated to other platforms as hardware continues to evolve.

The second reason for this architecture is to support an automated approach to the development of simulations. The SCE is designed to maximize the reuse of previous development efforts. To this end, a developer can select a highly developed software module or portions of previous simulations and incorporate those in a new effort. For example, a developer could select arm models from one simulation and propulsion models from another and combine those in a new simulation. Thus, a developer has the ability to reuse software at any level that is most appropriate for the development effort being undertaken.

The third reason for this architecture is to facilitate simulation generation by automating many attributes traditionally determined by the simulation designer. For example, a simulation executive/scheduler within the SCE will automatically allocate software modules (processes) to one or more CPUs communicating through shared memory, in order to maximize the efficiency of the simulation. In the traditional approach these decisions would be made by a designer in an arbitrary way and evaluated in a trial-and-error manner.

### Major SCE Elements

The SCE is comprised of four major elements (Figure 3). First, the math models are implemented in the form of modules and can be considered as building blocks for the simulation developer. The modules themselves are built using lower level primitives.

The second element is an icon-based user interface that allows the simulation developer to define a particular simulation using a flow diagram-like notation that expresses the data-dependencies between the various modules, the simulation rates, delays, etc. The data representing a particular simulation are then stored as a set of Simulation Definition File(s). The third element is an application generator that translates the data created by the simulation definition element into another set of files called the Simulation Data File(s) and Executive Input File(s). The Executive Input File(s), which are generated following test computer dependent directives, are then shipped to the test environment, in addition to the simulation initialization data. The fourth element of the SCE, which is resident on the test computer complex, uses the Executive Input File(s) to setup the execution environment at run time and actually schedules and controls the simulation and automatically allocates parallel processes (when available) to multiple CPUs.

### Simulation Life Cycle Using SCE

The use of the SCE in the simulation life cycle is displayed in Figure 4. The life cycle begins with the generation of simulation requirements. If existing SCE capabilities cannot support these requirements, SCE or Module developers will develop additional capabilities, e.g. a robot model, to support the simulation requirements.

Once the necessary capabilities are available, a simulation is defined and developed. This might include combining a Space Station Freedom model, a robot model, and ephemeris modules (gravity, solar, etc.) into a simulation. The simulation is generated using pre-developed modules and tested. Once the simulation is verified, the end user will run the simulation and evaluate the results.

## DEVELOPING ON-ORBIT PROCEDURES

### Rapid Procedures Development

The SCE will support rapid prototyping of procedures by permitting the user to select modules ranging from simple to complex, and to combine the modules in a simulation to investigate the action of these systems in space. The system will contain modules for the Space Station systems and environment (gravity and solar), and it will automatically combine these complex modules into a testable simulation. These will be displayed in the trainer's workstation screen. The trainer will then run a simulation using various scenarios.

### Procedures Test and Verification

The SSAIAF will be designed to move flight-like articles as they would move in space to provide form-and-fit verification testing over a range of possible conditions. The SCE will support the evaluation of the complex dynamics and forces that cannot be tested elsewhere. The procedures using actual space systems can be tested utilizing SSAIAF test systems. Repeated and long term testing is possible, as well as off-nominal operations (e.g., collisions).

### Astronaut Training

Upon procedure verification, the SCE will support training of astronaut-robot teams to ensure that their tasks can be accomplished in a safe and efficient manner. Experience has shown that real-time simulation cannot provide all the hands-on training required to successfully complete mission training. Astronauts will be trained in the SSAIAF using either real space systems or volumetrically identical mock-ups. In addition, on the Space Station humans will have to work in conjunction with a robotic systems. Thus, actual or simulated testing of human-robot teams must be performed. The SSAIAF will provide as close to a realistic training environment for astronaut-robot teams as possible on earth.

### Problem Resolution

Experience in space operations has shown that anomalous situations occur which require real-time resolution (e.g., utilizing a robot in an untested scenario). The SCE could support rapid prototyping of possible solutions and testing of untested robotic operations. Interfaces with Johnson Space Center operations could include data and voice links with Shuttle and Space Station astronauts as they try to resolve on-orbit problems.

### A Repository of Simulation Objects

Finally, the SCE will serve as a repository of space systems models that can support the training required by future space systems. Future space systems will be designed and tested. The SCE will support the archiving of simulation modules and the results of prior testing for the benefit of future training program developers.

## CONCLUSION

Space is one of the most hazardous environments in which humans must work. The difficulty of assembling, maintaining, and repairing systems has led NASA to develop a facility where the integration of procedures and systems can be tested simultaneously. Testing space systems prior to launch requires a simulated environment. As stated above, the traditional approach to building, such as human-in-the-loop simulations, has involved development of unique software to support each scenario. However, in the SSAIAF the SCE approach represents a departure from tradition. The modular design maximizes the reuse of previously developed simulations. An entire simulation need no longer be developed from "scratch." Instead, developers can combine components of previous efforts and concentrate their efforts on the unique elements of the new simulation. In addition, the modular design of the SCE supports its own maintenance and permits migration to new platforms as hardware continues to evolve. The result of this approach is an adaptable software environment that supports the rapid development and test of space systems and the procedures they require in a cost-effective manner.

## ABBREVIATIONS

| | |
|---|---|
| ABF | Air-Bearing Floor |
| COTS | Commercial Off-the-Shelf |
| CPU | Central Processing Unit |
| Kg | Kilogram |
| MDF | Manipulator Development Facility |
| MRMDF | Mobile Remote Manipulator Development Facility |
| NASA | National Aeronautics and Space Administration |
| SCE | Simulation and Control Environment |
| SDTS | Six-degree-of-freedom Dynamic Testing System |
| SSAIAF | Space Systems Automated Integration and Assembly Facility |
| SSF | Space Station *Freedom* |

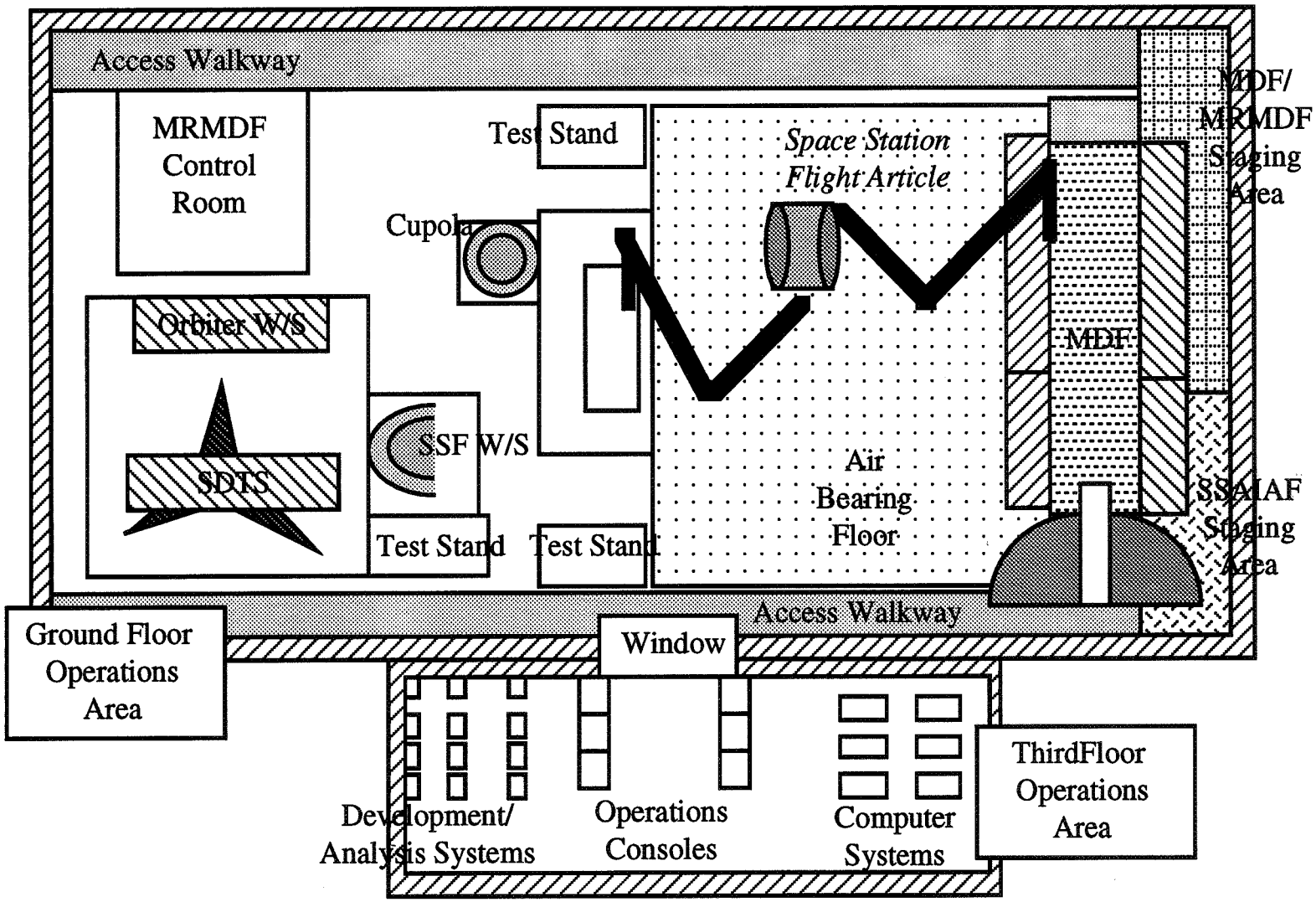


Figure 1. SSAIAF Systems

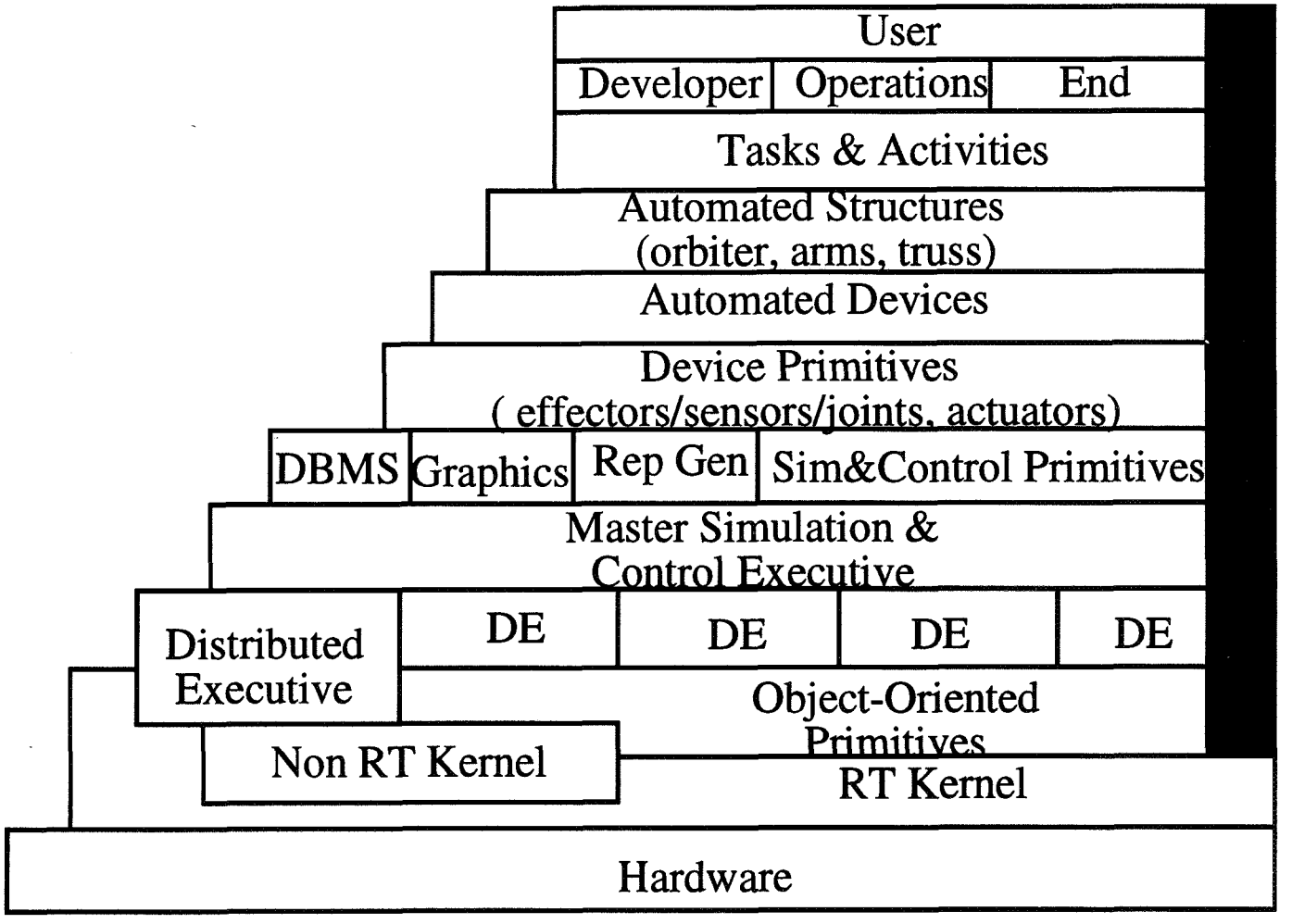


Figure 2. SCE Modular Design

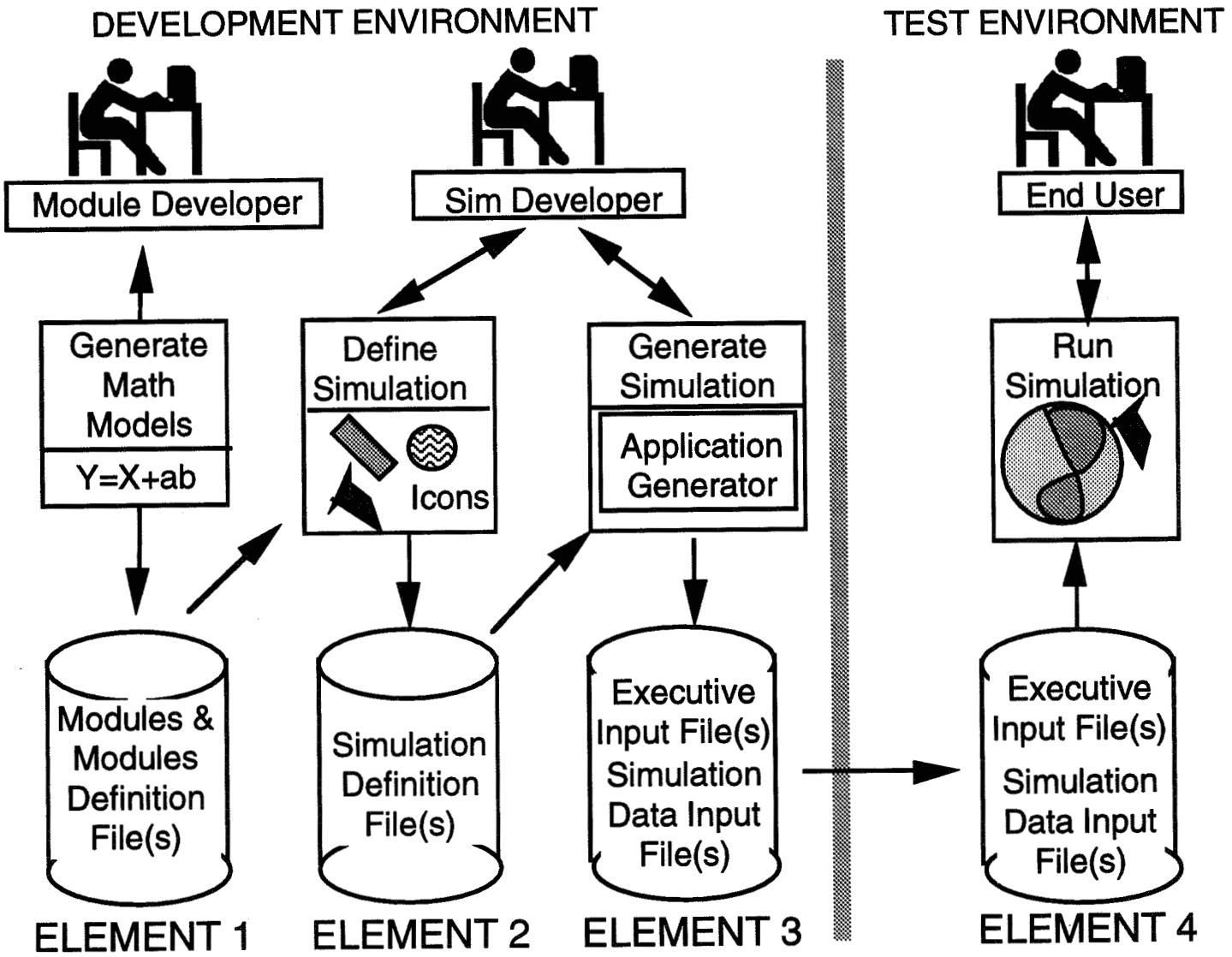


Figure 3. Major SCE Elements

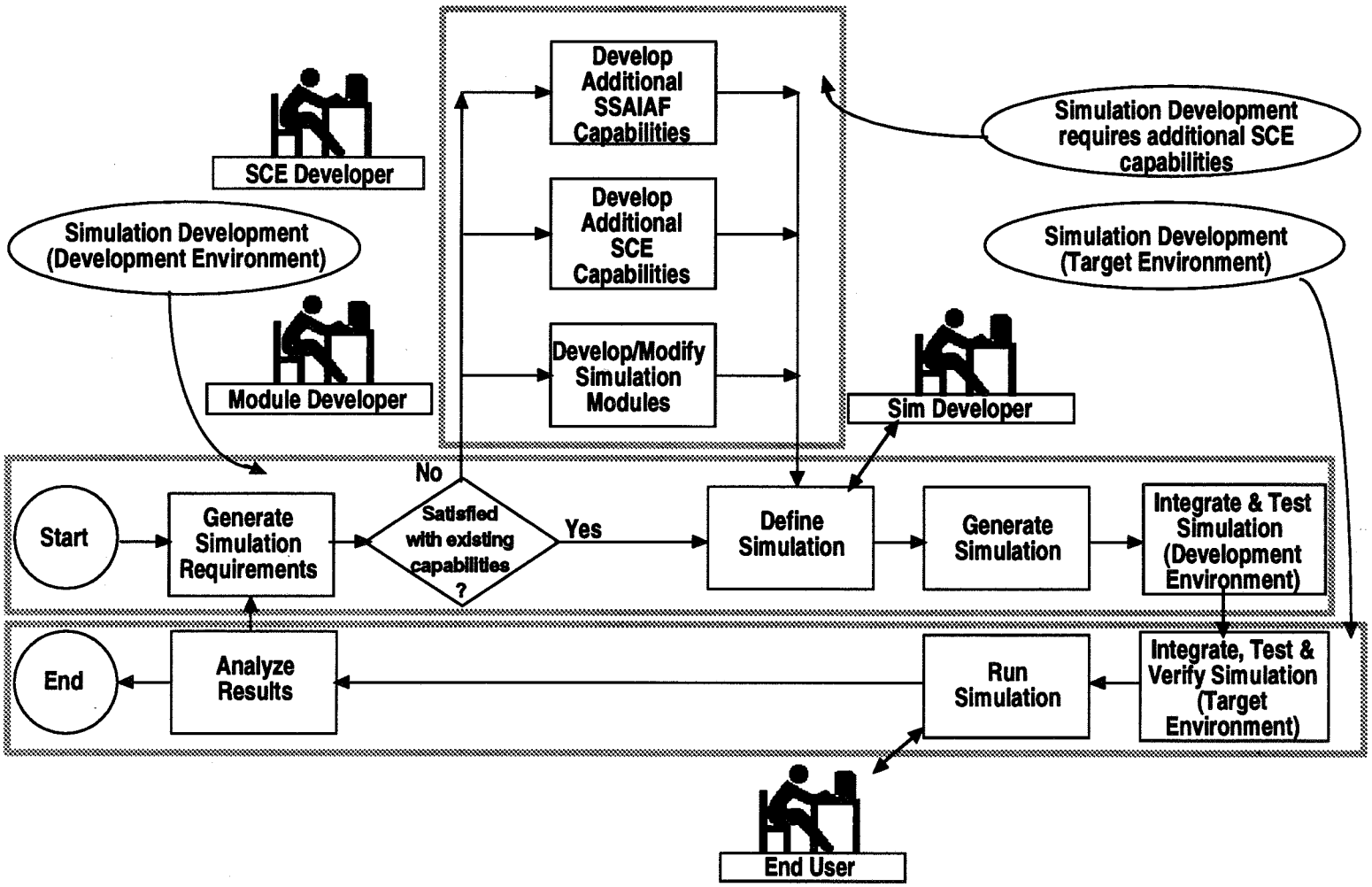


Figure 4. Simulation Life Cycle Using the SCE

# MARTIAN ENVIRONMENTAL SIMULATION FOR A DEPLOYABLE LATTICE MAST

Robert M. Warden
AEC-Able Engineering Co., Inc.

## ABSTRACT

The Mars Pathfinder mission (formerly Mars Environmental Survey or MESUR) is scheduled for launch in December 1996 and is designed to place a small lander on the surface of Mars. After impact, the lander unfolds to expose its solar panels and release a miniature rover. Also on board is the Imager for Mars Pathfinder (IMP) binocular camera which is elevated by a deployable mast to obtain a panoramic view of the landing area.

The design of this deployable mast is based on similar designs which have a long and successful flight history. In the past when this type of self-deployable mast has been used, a rate limiter has been incorporated to control the speed of deployment. In this application, to reduce weight and complexity, it was proposed to eliminate the rate limiter so that the mast would deploy without restraint. Preliminary tests showed that this type of deployment was possible especially if the deployed length was relatively short, as in this application. Compounding the problem, however, was the requirement to deploy the mast at an angle of up to 30 degrees from vertical. The deployment process was difficult to completely analyze due to the effects of gravitational and inertial loads on the mast and camera during rapid extension. Testing in a realistic manner was imperative to verify the system performance.

A deployment test was therefore performed to determine the maximum tilt angle at which the mast could reliably extend and support the camera on Mars. The testing of the deployable mast required partial gravity compensation to simulate the smaller force of Martian gravity. During the test, *mass* properties were maintained while *weight* properties were reduced. This paper describes the testing of a deployable mast in a simulated Martian environment as well as the results of the tests.

## TEST ARTICLE

The IMP Mast Assembly consists of a deployable triangular lattice structure, a base section, a tip section, a launch restraint/release device, and the Imager Camera payload (Figure 1). The camera is mounted to the tip plate and the base plate is mounted to the spacecraft. The lattice structure, when it is retracted, is surrounded by a thin metal cylinder covered by the tip plate and the base plate. Permanently attached to the middle of the tip plate is a center post which is a small rod that extends down through the center of the stowed mast to the base plate where it is captured by a pyrotechnically actuated pin-puller. The center post and pin-puller are needed to hold the stowed mast assembly together and support the camera throughout launch and landing. When the pin-puller is actuated, the center post is released which allows the mast to deploy. The base plate also encloses a set of three springs which are needed to provide the necessary initial deployment force. The extension of the mast assembly lifts and supports the camera above the Mars lander. Electrical cabling is attached along the length of the mast to connect the camera to the spacecraft.

### Deployable Lattice Structure

The lattice structure consists of unidirectional fiberglass/epoxy rods, aluminum fittings, stainless steel diagonal cables and stainless steel fasteners. The structure extends and retracts by twisting about the longitudinal axis. When stowed, it acts like a compressed spring that, when released, pushes out toward the extended position. Once fully deployed, the structure becomes rigid. This type of structure has been used frequently in space but every program requirement is somewhat different. A new 18.3 cm (7.2-in.)-diameter mast was needed for this program which was based on similar designs that range in size from 20.3 cm (8.00 in.) diameter to 76.2 cm (30.0 in.). Preliminary tests using an existing mast showed that it was marginally capable of deploying the camera at a 15-degree tilt angle (from vertical) and was unable to deploy the camera at 30 degrees. The design for the new unit has been scaled from existing designs but uses proportionally stronger structural elements while minimizing the weight of all other components.

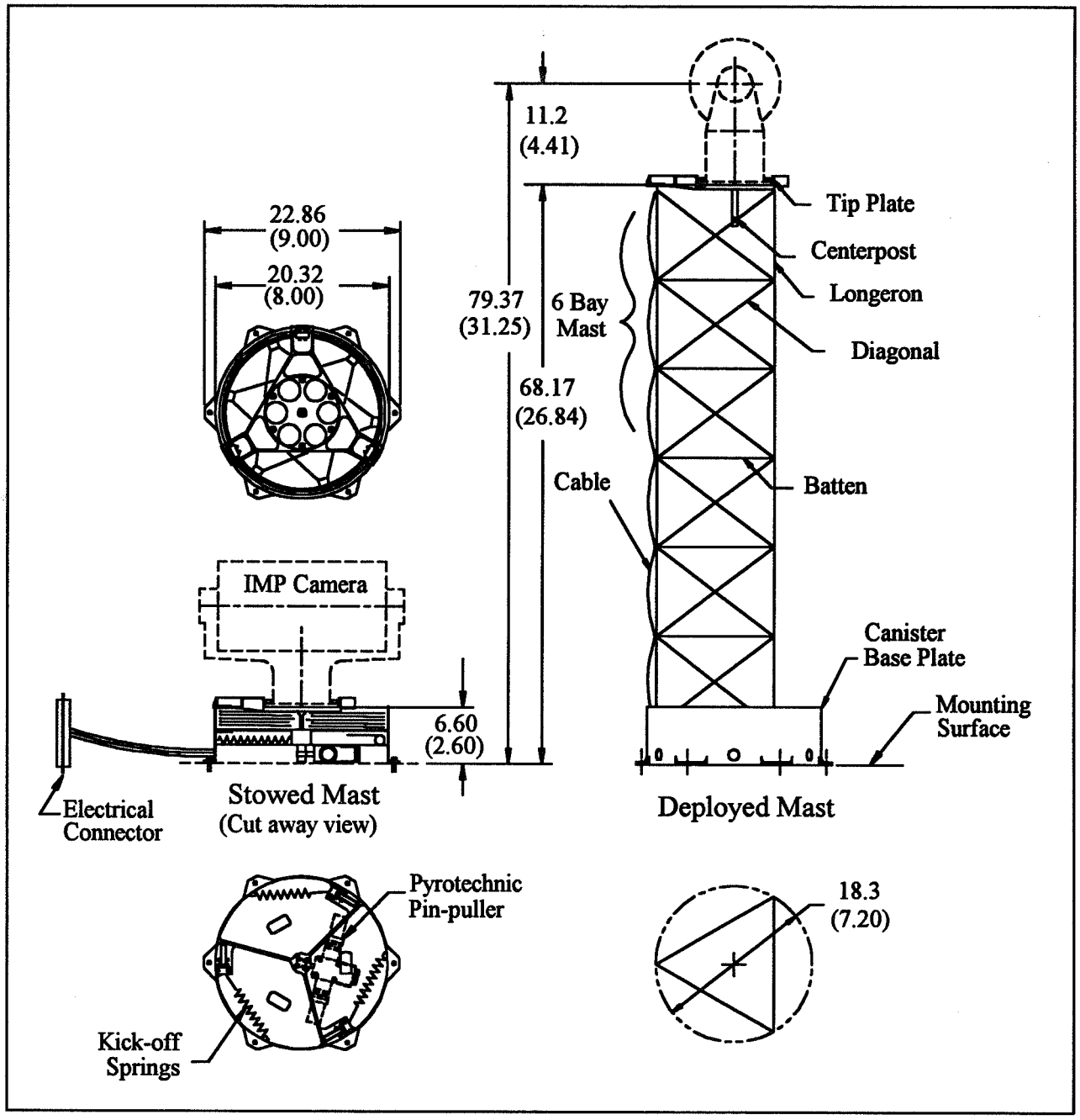


**Figure 1: IMP Outline Drawing**

**Electrical Cables**

Attached to the outside of the lattice structure are three electrical cables which are used to electrically connect the camera to the spacecraft. Electrical cables, when attached this way, have previously been shown to have had a negligible effect on the deployment of the mast. For this program, however, the electrical cables are jacketed in a conductive rip-stop nylon jacket. This type of covering promises to be lighter weight but because it is a much looser construction, there was some concern that it may interfere with the deployment of the mast.

**Camera Simulator**

A camera simulator was needed to simulate the actual flight camera for use in the testing. The mass of the flight camera was specified at 1.4 kg. The mounting configuration and exact moment of inertia had not been determined, so some reasonable assumptions were made to approximate the properties of the camera:

Total Mass: 1.4 kg (3.08 pounds, Earth weight)
Mounting holes: 6X #6-32, 3.00 in. BCD
Moment of Inertia: 0.0044 kg-$m^2$
Distance from camera mounting surface to CG: 0.0678 m

**TEST APPROACH**

The main problem in performing the deployment test was how to accurately simulate the deployment conditions on Mars. The force of gravity on Mars is much less than on Earth but the deployment force of the mast and the mass of the components are constant. The 1.4 kg mass of the camera by far dominates the 1.9 kg mass of the total system. To simplify the test, the differences in the weights of all components except for the camera were ignored because they were small compared to the weight of the camera and the push force of the mast. Figure 2 shows the forces involved in the deployment on Mars. Several approaches were considered to try to accurately simulate this condition on Earth.

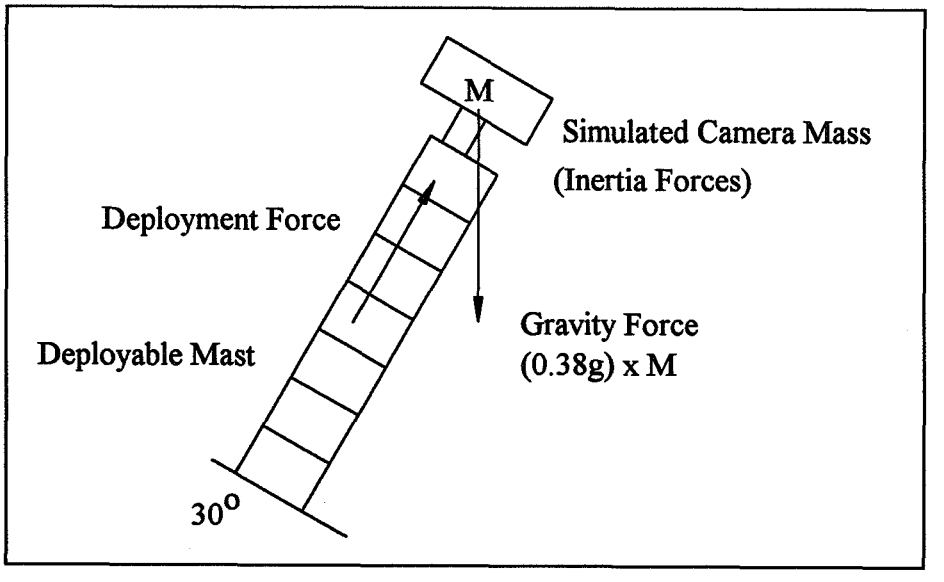


**Figure 2: Simple Surface Oriented Force Diagram**

Preliminary deployment tests simply used a lighter weight payload to simulate the reduced force of gravity on Mars. The rotational moment of inertia of the flight camera about the axis of deployment was specified by the customer. The simulated payload was configured in such a way as to produce the specified rotational mass moment of inertia and weigh 0.38 times the Earth weight of the camera. The simulated mass ended up looking like a dumbbell with most of the weight on the ends. This method accurately simulated the gravity on Mars and the rotational inertia of the camera but the axial inertia was reduced along with the tip mass.

During deployment of the mast, the tip plate rotates and extends at the same time. When the mast is fully extended, the tip plate over-shoots the end position and continues to rotate due to the rotational inertia of the payload This causes the mast to partially retract as the rotation slows down. At this point, the rotation and extension have momentarily stopped, but the tip plate is still subject to significant lateral motion. The tip plate then reverses direction and the mast deploys again only to over-shoot in the other direction. After a few cycles, the rotational oscillation of the tip plate damps out and after a few more cycles, the lateral vibration damps out.

In order to provide the proper dynamic forces on the mast during deployment, the proper rotational and translational inertia was required as well as the proper gravitational force. Without the correct tip mass, the resulting acceleration and deceleration would be significantly higher which could produce unrealistic loads on the mast. During deployment, the mast is less capable of resisting lateral loads than it is when fully deployed which makes the simulation of the true force balance even more important.

To perform the angled deployment test, an accurate setup was needed which would maintain the rotational and axial inertia of the camera while simulating the proper forces on the mast. The best way to do this is to use the actual camera mass and inertia but simulate the proper g-loading by partially off loading the weight of the camera. Figure 3 shows a more complete description of the forces. A constant-force-suspension system was designed to counterbalance the additional forces imposed by earth gravity. The camera simulator is partially suspended by a long lanyard which is attached to a spring reel device as shown in Figure 4. The spring force acts vertically through a lanyard, opposite the force of gravity. During an inclined mast deployment, the long suspension system closely simulates the force balance on the mast system that will occur on Mars.

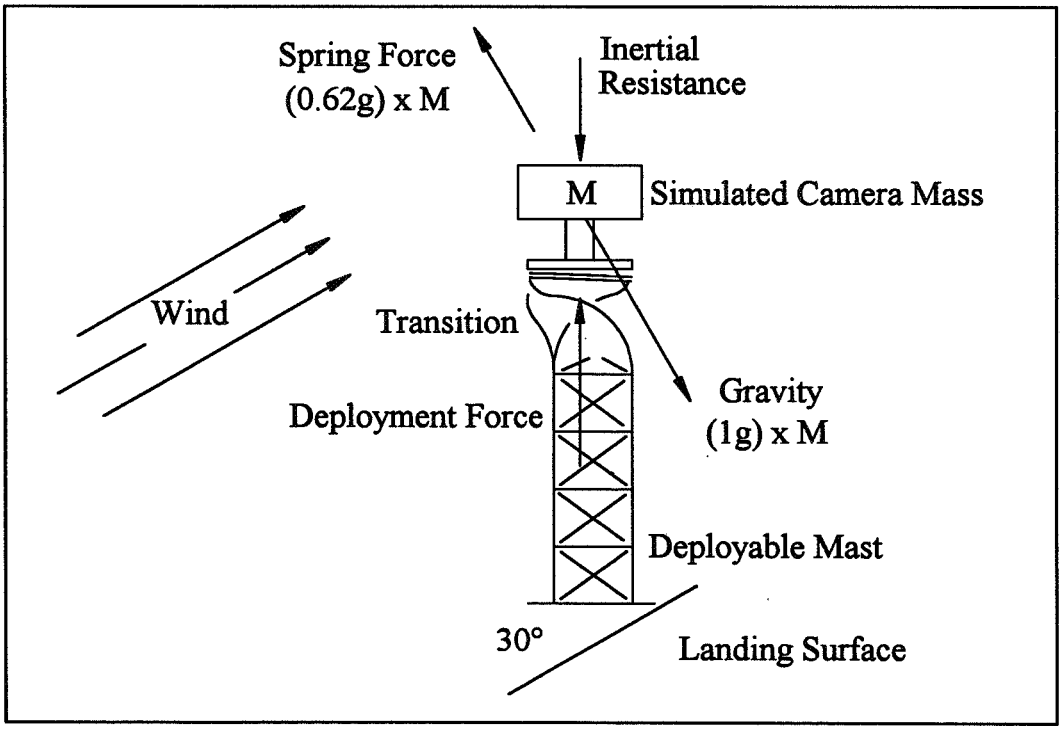


**Figure 3: Mast Oriented Force Diagram**

The counterbalance spring device was mounted as high as possible to reduce the error caused by the change in angle. Any angle in the counterbalance system is undesirable because it introduces an effective lateral component to the lanyard force. By using a long lanyard, the effect of the lateral displacement during inclined deployment is minimized. The counterbalance was positioned so that the lanyard was vertical when the mast was fully deployed. In this way, the load condition would be most accurate at the end of deployment which is where the dynamic conditions are the most uncertain. In this test, the angle of the lanyard was less than 3.5° from vertical and the error was calculated to be insignificant.

During deployment, the counterbalance system allows the tip of the mast to rotate without resistance whether the spring reel is paying out or reeling in the lanyard. As the tip of the mast deploys, retracts, twists and bends, the counterbalance maintains the correct force orientation on the camera simulator.

It is important to note that the suspension system was designed to be lightweight and very fast acting to allow the lanyard to retract as the mast deployed. In this way, a known vertical force on the mast assembly is maintained throughout the deployment. The lanyard load was set in a static state with analysis indicating only a small decrease in lanyard load during deployment accelerations. The force output of the spring reel was not perfectly constant over the deployment length but the error was disregarded because it was small compared to the push force of the mast and the force of gravity on the camera. The fast response of the spring reel was due to the small weight and size of the components.

## TEST DESCRIPTION

An adjustable base structure was constructed with a large flat mounting surface onto which the mast assembly was bolted (Figure 4). The mounting surface was capable of being tilted to simulate an inclined lander position on the surface of Mars. The angle of the mounting surface was adjustable in 5-degree increments. To simulate the lower gravity of Mars, a spring reel device was bolted to the ceiling and then attached to the camera simulator. The mast was first deployed vertically several times. The base was then tilted 5 degrees and the mast was again deployed several times. The tilt angle was increased at 5-degree increments until the mast failed.

Because the mast is triangular, its bending strength varies with its azimuthal orientation. At each tilt angle the mast was mounted in different azimuthal orientations and deployed several times to examine the effect of the mounting condition. The intent of the test was to keep increasing the angle of deployment until the mast broke, then shorten the mast and repeat the test. Preliminary estimates were that the mast could deploy at an angle of only 20 to 30 degrees. Exact predictions were nearly impossible due to the complex nature of the deployment process.

### Test Equipment

Base structure with adjustable mounting surface.
Coilable lattice mast.
Camera simulator attached to the top of the mast.
Spring reel attached to the ceiling.
Lanyard to attached the spring reel to the camera simulator.

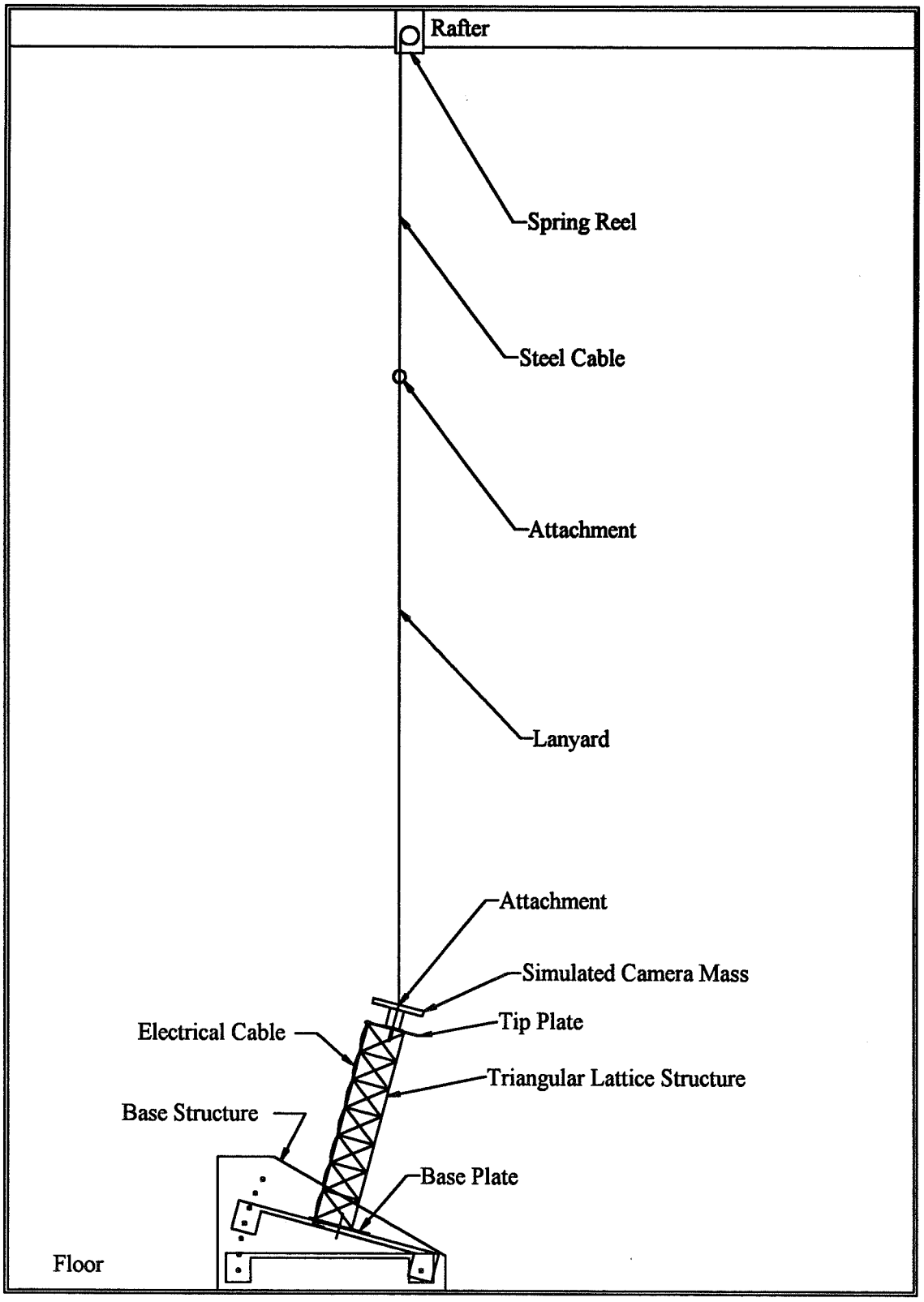


**Figure 4: Angled Deployment Test Set-up**

## TEST RESULTS

Surprisingly, the mast did not fail at the predicted tilt angle of 30 degrees so the tilt angle was increased further at 5-degree increments until the mast finally failed at 55 degrees after being deployed a total of 75 times. The mast was frequently examined for damage. An incipient fracture was finally observed in the fiberglass about three-fourths of the length up the mast after the second deployment at 50 degrees. Another deployment caused the fracture to grow. The angle was then increased to 55 degrees and the mast again deployed successfully but the damage was severe (less than 50% of the fibers were intact). The mast was then carefully retracted and allowed to deploy a final time during which it broke completely. Even in the broken condition, however, the mast successfully deployed and supported the payload, although the strength and stiffness were greatly reduced.

The mast failure was probably not caused by the increased deployment angle. The break may have been exacerbated by excessive handling of the mast (considerable torque was necessary to retract the mast) but it is more likely that the failure was due to fatigue. From these tests, it appears that the mast is life-limited when subject to uncontrolled deployments and after approximately 70 cycles, the fiberglass in the mast began to degrade.

The deployment of the mast was quite rapid and at first appeared to be uncontrolled. The deployment was, in fact, well controlled and very repeatable. The deployment rate of the mast was consistent in these tests and only minimally affected by the angle of deployment. The rapid deployment does cause a significant impact load onto the mounting surface which may be important in the design of the spacecraft.

The camera mass and moment of inertia are probably factors in the cycle life. It is unclear, however, whether an increased mass would improve or degrade the system performance. An increased moment of inertia would slow down the deployment acceleration and deceleration which may be a factor in the mast fatigue. The deployment of the base of the mast is critical to the successful extension of the system. Establishing good base strength early in the deployment sequence ensures good payload support, almost independent of deployment angle or tip mass. The electrical cables appeared to have no effect on the deployment.

## CONCLUSION

The deployment test shows that a simple functional test can be performed with successful results in lieu of an extremely complicated analysis. Many simplifications were incorporated into this test in order to make the test less complicated and to reduce the cost. The force of Martian gravity was simulated by partially off-loading the weight of the camera mass simulator. In this way, the actual camera mass and moment of inertia were also simulated.

# SPACE SIMULATION TECHNIQUES AND FACILITIES FOR SAX STM TEST CAMPAIGN

**Pietro Giordano, Giacomo Raimondo, Piero Messidoro**

**Alenia Spazio S.p.A.**
**Torino - Italy**

## ABSTRACT

SAX is a satellite for X-Ray astronomy. It is a major element of the overall basic Science Program of the Italian Space Agency (ASI) and is being developed with the contribution of the Netherlands Agency for Aerospace Programs (NIVR).

The scientific objectives of SAX are to carry out systematic and comprehensive observations of celestial X-Ray sources over the 0.1 - 300 KeV energy range with special emphasis on spectral and timing measurements. The satellite will also monitor the X-Ray sky to investigate long-term source variability and to permit localization and study of X-Ray transients.

Alenia Spazio is developing the satellite that is intended for launch in the second half of 1995 into a low, near-equatorial Earth orbit.

At system level a Structural Thermal Model (STM) has been conceived to verify the environmental requirements by validating the mechanical and thermal analytical models and qualifying satellite structure and thermal control. In particular, the following tests have been carried out in Alenia Spazio, CEA/CESTA and ESTEC facilities:

Modal Survey, Centrifuge, Acoustic, Sinusoidal/Random Vibration and Thermal Balance.

The paper, after a short introduction on the SAX satellite, summarizes the environmental qualification program performed on the SAX STM. It presents test objectives, methodologies and relevant test configurations. Peculiar aspects of the test campaign are highlighted. Problems encountered and solutions adopted in performing the tests are described as well. Furthermore, test results are presented and assessed.

## 1. INTRODUCTION

The SAX satellite will observe celestial X-Ray sources in the broad energy band from 0.1 to 300 KeV to achieve a systematic, integrated and comprehensive exploration of galactic and extra-galactic sources, providing, with respect to previous missions, an astrophysics facility for more complete and extensive studies of known and new celestial X-Ray sources (see Ref. 1).

The SAX satellite development is part of the joint SAX program managed by the Italian Space Agency (ASI) and the Netherlands Agency for Aerospace Programs (NIVR), which decided to fund in response to the scientific interest of the Italian and Dutch scientific community.

The launch of the SAX satellite is planned for the end of 1995, for a minimum operative life of two years. The ATLAS 1 launcher will inject Sax into its operative orbit at 600 Km altitude with an inclination of less than 5° over the equator.

A pictorial view of the SAX satellite is shown in Fig. 1 (following page). In particular, it consists of three modules.

- The **Service Module** (SVM) which includes a central cone, lower and upper floors, eight side panels (the batteries are mounted on dedicated panels) and six shear panels. It houses all the electronic units, attitude control sensors and actuators, one S-band Antenna and provides the interfaces with the launcher.
- The **Payload Module** (PM) with a box structure which provides attachments for all the science instruments. The PDS is mounted internally, the HP-GSPC, WFCs and Concentrators externally. Three Star Tracker sensors are also externally mounted on dedicated supports.
- The **Shade Structure** consists of a panel framework surrounding the PM. It supports the third Sun Acquisition Sensor, the second S-band Antenna and the Science Instrument Thermal Baffles (HP-GSPC and WFCs).

The SVM and the Shade Structure provide the interfaces of two solar array wings and a body mounted solar panel.

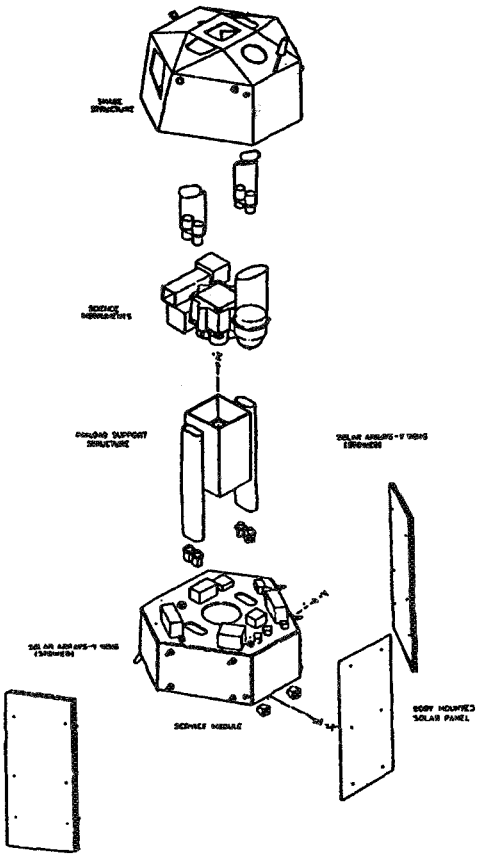

**Fig. 1 - SAX Satellite Overall View**

## 2. SYSTEM VERIFICATION APPROACH

The verification approach of the SAX satellite is based on three models (Ref. 2).

- Structural Thermal Model (STM) which was subjected to a full mechanical and thermal qualification test campaign.
- Engineering Model (EM) which is undergoing the electrical functional testing.
- Protoflight Model (PFM) which is intended for flight after environmental screening and final performance testing.

An overview of the system test approach is given in the table of Fig. 2 (see following page). Details of the SAX design, verification philosophy and system test approach are contained in Refs. 2 and 3.

In the frame of the system verification approach, a fundamental aspect is the STM activities. In fact, the overall satellite design, or essential portion of it, is governed by the thermal and mechanical requirements.

Qualification versus the above requirements is in this way a relevant part of the verification process.

Techniques used in simulating the environments acquire importance in providing the necessary confidence that the satellite meets the assigned operative role.

This paper will give evidence that methods and facilities used to qualify the mechanical and thermal design were adequate for its scope.

## 3. MECHANICAL REQUIREMENTS

The mechanical performances which have to be met by the SAX satellite can be split into two categories: one concerns the launch phase, and the other one the in-orbit life.

During the launch phase, the spacecraft structure must be able to withstand the high generated load environments. It must also be decoupled from the major low frequency excitation modes of the launcher, and the loads transmitted to the equipment must be acceptable to them.

| TYPE OF TEST | TEST DESCRIPTION | SAX STM | SATELLITE EM (S/C) | MODELS PFM |
|---|---|---|---|---|
| PHYSICAL PROPERTIES | Mass | X | -- | X |
| | MoI/CoG | X | -- | X |
| | Balancing | X | -- | X |
| STRUCTURAL TESTS | Modal Survey | X | -- | -- |
| | Acceleration | X | -- | -- |
| | Vibration | X | -- | -- |
| | Acoustic | X | -- | -- |
| | Pyroshock | -- | -- | X |
| THERMAL TESTS | Thermal Balance | X | -- | -- |
| | Thermal Vacuum | -- | -- | X |
| ALIGNMENT | | X | -- | X |
| COMPATIBILITY | EMC\EMI | -- | -- | X |
| LEAK TESTS | | X | -- | X |
| FUNCTIONAL | ISST | -- | X | X |
| PERFORMANCE TESTS | IST/ISC | -- | -- | X |
| DEPLOYMENT/RELEASE | Solar Array | X | -- | X |
| | C/S Shutter | X | -- | X |
| SPECIAL TESTS | P/L Calibration | -- | -- | X |
| | Ground Segment Comp. | -- | -- | X |
| | Match Mate Test | -- | -- | X |
| | Magnetic Field Measur. | -- | -- | X |

**Fig. 2 - System Test Approach Overview**

During the in-orbit life, the mechanical performances to be traced are the relative dimensional stability existing between several pieces of equipment, especially belonging to the Attitude and Orbit Control S/S (AOCS) and science instruments. This part of the verification process will not be dealt with in this paper.

The mechanical development of the SAX satellite was performed with the strong support of Mathematical Models and Analysis and a Structural Mathematical Model of the spacecraft was built for this scope and validated through the Modal Survey Test.

Mechanical requirements applicable to the SAX satellite and relevant to the launch phase can be furtherly split into subcategories:

- stiffness requirements
- launch load requirements

The stiffness requirements were verified within the frame of the validation of the mathematical model as described in section 4.1.

The ATLAS 1 launcher imposes a complex combination of mechanical loads which can be split into three major constituents:

- Quasi-static loads
- High Frequency loads
- Shock loads

*Quasi-Static Loads*

The transient response environment during ATLAS 1 flight is characterized by a combination of low frequency dynamic and steady-state responses. Steady-state responses were specified in terms of equivalent design load factors for use in designing the Primary Structure.

These values were conservative for preliminary design purpose only and reflected the recommended frequency constraints. They were representative of the g-loading at the spacecraft centre of gravity and did not include a dynamic uncertainty factor. This load factor information did not replace the need for satellite/launch vehicle coupled Transient Loads and Clearance Analysis for the more critical flight events.

The response of the spacecraft to launch vehicle transients depends on its mass properties, stiffness, and amount of axial-lateral coupling.

The above analyses are required to ensure that all the structural components have adequate margins.

A preliminary Transient Load Analysis was performed with a Spacecraft Dynamic Model representing the preliminary sizing of the hardware to provide a more accurate load distribution on the spacecraft for both Primary and Secondary Structure. These preliminary response data were used as a reference for the Stress Analysis Calculation and during the qualification test campaign on the Structural Model. A Dynamic Uncertainty Factor of 1.2, was applied to account for the potential design changes or modal correction prior to the final load cycle.

The final design load cycle is going to be run with the Test-Validated Dynamic Model for determination of the maximum expected flight loads. These response data will be used for calculation of the minimum margin of safety and therefore for the final verification of the qualification status of the spacecraft. The low frequency dynamic input was specified in terms of equivalent sinusoidal base acceleration.

Verification of minimum factor of safety was accomplished through a combination of static and sinusoidal base acceleration testing of the Structural Model. Primary structure interfaces are most easily loaded during Static Test, while the more complex dynamic responses are generated during the sinusoidal base acceleration test. For the Static Test it was chosen to perform a Centrifuge Test.

During the Vibration Test, notching of the base input was allowed in the 0 - 50 Hz range in order not to exceed the design loads and was based on flight equivalent levels as related to spacecraft damping.

*High Frequency Loads*

The high frequency random vibration that the spacecraft will experience is primarily due to the acoustic noise field, with a very small portion being mechanically transmitted from the engines. The acoustically excited random vibration environment is the design driver for component and small structure supports. The high frequency vibration level will vary from one location to another depending on the physical properties of each area of the spacecraft. Since the vibration level at the spacecraft interface depends on the adjacent structure above and below the interface, the exact interface level depends on the structural characteristics of the lower portion of the spacecraft, the particular Payload Launcher Adapter, and how the acoustic field is influenced by the particular spacecraft. The acoustic test of the spacecraft more accurately simulates the high frequency environment that it undergoes in flight than does a random vibration test. If the spacecraft is mounted to a test fixture that has structural characteristics similar to the Payload Launcher Adapter, then the vibration levels at the interface are similar to the flight levels.

Since the SAX satellite was attached to a rigid fixture during the Acoustic Test, a random test at low level was performed to provide evidence of the correct random vibration spectra specified for the unit located close to the spacecraft interface. The Launcher Adapter was not available at that time.

*Shock Loads*

There are four pyrotechnic shock events during flight on the ATLAS 1 Launcher. These are Insulation Panel Jettison, Payload Fairing Jettison, Centaur Separation from Atlas sustainer, and Spacecraft Separation. Since the system for Centaur Separation from Atlas is located far from the spacecraft, the shock is highly attenuated by the time it reaches the spacecraft and does not produce a significant shock at the spacecraft interface. The separation device for IPJ and PFJ are located closer to the spacecraft, and thus the shock at the spacecraft interface is noticeable. The Spacecraft Separation Device is at the Spacecraft/Centaur interface and produces the highest shock. Verification of the Spacecraft compatibility for Clamp Band Separation System will be performed on the Flight Model and as such it will not be described in this paper. This choice was dictated by the incomplete representativeness of both Structural and Engineering Models.

The launch load requirements verification tests are presented in sections 4.2 to 4.4.

## 4. STRUCTURAL MODEL TESTS SUMMARY

A summary of the mechanical tests performed on the SAX Structural Model is provided.

The Structural Model, as part of the STM, is fully representative of the Flight Model. It consists of a flight standard structure equipped with structural dummies of the several units, science instruments and mass representative harness.

An exception is the Solar Array -Y wing which was replaced by dedicated dummy masses.

The STM in full configuration is shown in Fig. 3 (following page).

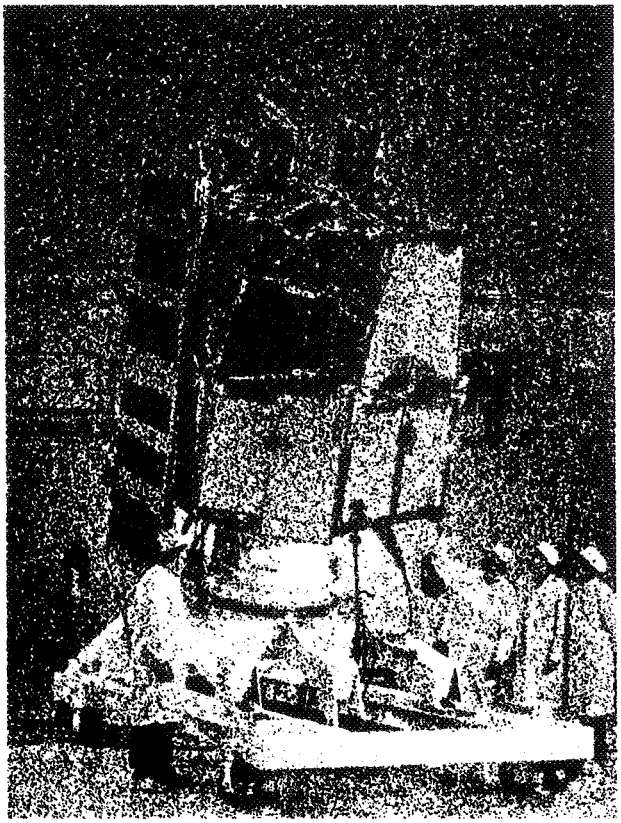

Fig. 3 - SAX Structural Model

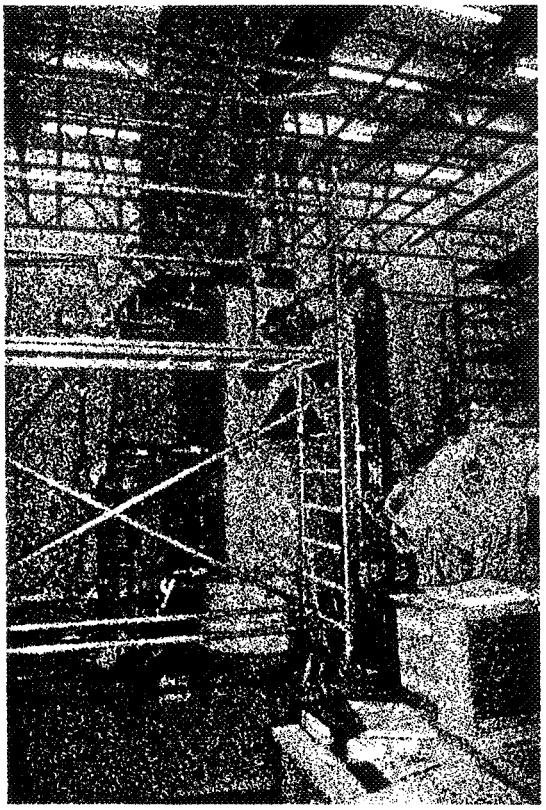

Fig. 4 - Modal Survey Test Set-up

### 4.1 Modal Survey Test

The primary purpose of the SAX Modal Survey Test was to measure all significant vibration modes over the frequency range 5 - 60 Hz and therefore the verification of the stiffness constraints. An additional purpose was to acquire frequency response functions up to 100 Hz. The test data were used to validate the SAX Structural Mathematical Model and to achieve a full understanding of how it behaves dynamically.

The test was carried out at the Integration Hall of Alenia Spazio in Turin using IABG's Modal Survey Test System. Modal Survey Test Set-Up is shown in Fig. 4.

The Flight Mathematical Model was modified to the STM Modal Survey Test Configuration. The changes introduced were mainly concerned with the missing hardware, mass distribution, modelling of the mass dummies instead of equipment, and the incorporation of the adapter used to realize the fixed-free conditions. It is worth mentioning that the missing hardware was responsible only for some local modes and had no influence on the global modes of the structure. This was necessary to operate a reasonable reduction of the modes limiting the number to that of particular interest for the subsequent correlation analysis and to guarantee a more uniform and significant energy distribution within the structure through a direct excitation of internal structural parts. The applied test technique was the Phase Separation Method with Multipoint Random Excitation.

Nine excitation points and 310 measurement points (response acceleration and excitation forces) were used. Applying random excitation forces, preparatory single points tests with the nine exciters and final multipoint tests with two exciter configurations were carried out. Additionally, measurements for linearity checks, Frequency Response Function measurements with an extended frequency range (5 - 100 Hz) and measurements for integrity checks were performed.

There were 28 modes expected in the frequency range to be examined. The number of the target mode was 18. From the two data sets from multipoint excitation, 17 and 18 modes were identified. For all these modes the modal parameters were determined. During the test, the results were carefully checked and comparisons were made between test and analysis results.

In general, the model was approximately 10% too flexible because of manufacturing contingencies. Minimum thickness and nominal Young's Module values were used. This is a conservative approach necessary for the Stress Analysis.

| DESCRIPTION : | Global Y first lateral mode | | | | | | | | | | |
|---|---|---|---|---|---|---|---|---|---|---|---|
| MODE | FREQ. | DEVIATION ( % ) | | DAMPING | Effective Mass ( % ) | | | | | | Generalized |
| NUMBER 1 | [ Hz ] | TEST 1 | TEST 2 | | MX | My | Mz | Mrx | Mry | Mrz | Mass [ Kg*m^2 ] |
| TEST 1 | 16.58 | - | - | 0.009 | 9.60 | 50.20 | 0.00 | 83.80 | 16.00 | 0.00 | 396.60 |
| TEST 2 | 16.57 | - | - | 0.009 | 11.90 | 48.40 | 0.10 | 79.30 | 20.20 | 0.00 | 470.20 |
| PREDICTION | 14.74 | -11.10 | -11.04 | - | 16.20 | 43.90 | 0.00 | 72.40 | 26.90 | 0.00 | 371.92 |
| CORRELATED | 16.38 | -1.21 | -1.15 | - | 18.92 | 37.33 | 0.00 | 66.14 | 33.88 | 0.00 | 422.49 |

| DESCRIPTION : | Global X first lateral mode | | | | | | | | | | |
|---|---|---|---|---|---|---|---|---|---|---|---|
| MODE | FREQ. | DEVIATION ( % ) | | DAMPING | Effective Mass ( % ) | | | | | | Generalized |
| NUMBER 2 | [ Hz ] | TEST 1 | TEST 2 | | MX | My | Mz | Mrx | Mry | Mrz | Mass [ Kg*m^2 ] |
| TEST 1 | 16.71 | - | - | 0.007 | 53.40 | 7.90 | 0.10 | 13.00 | 86.20 | 0.00 | 415.10 |
| TEST 2 | 16.69 | - | - | 0.007 | 56.60 | 3.90 | 0.10 | 6.80 | 92.30 | 0.00 | 396.90 |
| PREDICTION | 14.70 | -12.03 | -11.92 | - | 43.20 | 16.40 | 0.20 | 27.30 | 72.60 | 0.00 | 431.15 |
| CORRELATED | 16.43 | -1.68 | -1.56 | - | 37.08 | 19.12 | 0.00 | 33.50 | 65.64 | 0.00 | 430.95 |

| DESCRIPTION : | Global X second lateral mode | | | | | | | | | | |
|---|---|---|---|---|---|---|---|---|---|---|---|
| MODE | FREQ. | DEVIATION ( % ) | | DAMPING | Effective Mass ( % ) | | | | | | Generalized |
| NUMBER 3 | [ Hz ] | TEST 1 | TEST 2 | | MX | My | Mz | Mrx | Mry | Mrz | Mass [ Kg*m^2 ] |
| TEST 1 | 31.30 | - | - | 0.013 | 2.50 | 0.00 | 1.40 | 0.00 | 0.00 | 0.00 | 185.30 |
| TEST 2 | 31.24 | - | - | 0.014 | 2.70 | 1.00 | 1.40 | 0.00 | 0.00 | 0.00 | 179.60 |
| PREDICTION | 28.53 | -8.85 | -8.67 | - | 4.40 | 0.00 | 1.00 | 0.00 | 0.20 | 0.00 | 165.59 |
| CORRELATED | 31.03 | -0.86 | -0.67 | - | 3.23 | 0.00 | 1.20 | 0.00 | 0.19 | 0.00 | 184.19 |

| DESCRIPTION : | Global Y second lateral mode | | | | | | | | | | |
|---|---|---|---|---|---|---|---|---|---|---|---|
| MODE | FREQ. | DEVIATION ( % ) | | DAMPING | Effective Mass ( % ) | | | | | | Generalized |
| NUMBER 4 | [ Hz ] | TEST 1 | TEST 2 | | MX | My | Mz | Mrx | Mry | Mrz | Mass [ Kg*m^2 ] |
| TEST 1 | 31.64 | - | - | 0.007 | 0.20 | 1.10 | 0.00 | 0.00 | 0.00 | 3.30 | 161.50 |
| TEST 2 | 31.60 | - | - | 0.008 | 0.10 | 1.10 | 0.00 | 0.00 | 0.00 | 3.10 | 157.30 |
| PREDICTION | 29.92 | -5.44 | -5.32 | - | 0.00 | 1.80 | 0.00 | 0.00 | 0.00 | 1.10 | 164.83 |
| CORRELATED | 31.44 | -0.63 | -0.51 | - | 0.11 | 1.80 | 0.00 | 0.00 | 0.00 | 0.64 | 161.47 |

**Fig. 5 Comparison between Test, Prediction and Correlated Modes**

In addition, the idealization of the Adapter to Launch Vehicle Adaptor (LVA) Ring connection allowed local rotations which did not occur in practice.

The stiffness of each area of the model was increased altering the thickness and Young Module's to average or top tolerances values. As a result the frequencies of the global satellite modes were accurate to better than 2 %.

Local Models of the Hydrazine Tank, Batteries and Concentrators were affected by the modelling of the cleats, straps and brackets. The assumptions used to derive their stiffness were introduced in the model. In particular, the Payload Support Structure Cleat Tension/Compression stiffness was increased in line with the values obtained during dedicated development tests. The idealization of the Concentrator Upper Trunnion Brackets was found to be too simplistic and coarse models were replaced by detailed models of each component.

During the correlation, no changes were made to the mass distribution and modelling. In general, the modifications which have been outlined result in uniform stiffness changes. In the areas in which the stiffness is increased locally it will be necessary to review the analysis. However, none of the modifications which have been introduced will affect the overall load distribution and behaviour of the model. The results of the correlation activity are reported in Fig. 5 together with the test predictions and frequency constraints.

All the above modifications were reflected into the Flight Mathematical Model which was provided to General Dynamics for the final Coupled Load Analysis.

Detailed information about the test, test results and correlation activity are contained in the documents of Ref. 4., Ref. 5. and Ref. 14.

### 4.2 Centrifuge Test

The second step of the mechanical verification was the demonstration of the capability of the primary structure to withstand the quasi-static loads. For this purpose a centrifuge test was performed.

The test was carried out at the CEA CESTA Facility in Bordeaux (F). The centrifuge facility has the capability of generating a static acceleration, including those associated with satellite launches, in a fast and reliable way. It is constituted by a rotating arm with, at one extremity, 8.4 m from the rotating axis, an interface to the adaptor-specimen. It provides a static acceleration from 0 to 100 g corresponding to about 0.01 to 0.2 rad/sec$^2$.

The specimen is located inside a container (Nacelle) at the above defined interface. The most important aspects to be solved in using such a facility are related to the correct load distribution and the combination of axial and lateral loading.

The former is due to the different distance of each piece of hardware from the rotating axis which gives different accelerations along the satellite. This can be solved by increasing the masses locally to achieve the more realistic load distribution. The latter is due mainly to the dimensional constraints of the Nacelle ( 3 meters max diameter).

Detailed stress analyses were conducted in order to solve the above two problems.

First of all the stress analysis revealed the most critical load condition for each structural part. Only these load conditions were to be simulated by test because all the others were well enveloped by them. As it is not possible to reproduce the worst load case relevant to each structural part simultaneously, because they require different tilting angles, and because of the limited dimensions of the Nacelle, the following approach was followed:

* to identify the maximum obtainable tilting angles
* to compensate the reduced lateral load factor by increasing the axial load factors and by introducing dedicated compensation masses.

Two test cases corresponding to two different STM configurations and together providing the best possible coverage of the qualification load envelope were identified. Taking into account the STM shape, different rotation angles were used to cover a wider spectrum of lateral load factors.

The first test case was carried out with the fully integrated STM as shown in Fig. 6. Dummy masses were installed at the interfaces of the missing Solar Array Wing. The STM was inclined by 10° and rotated by 30°. The effective load factors at the CoG of the STM were:

* Axial Load Factor = -9.24 g
* Lateral Load Factor = 2.64 g

The second test case was carried out without the Shade Structure, Body Mounted Solar Panel and Solar Array Wing. Furthermore the dummy units installed inside the Concentrator Tubes were replaced by increased dummy masses. Dedicated dummy masses were also installed at the lower interfaces of the Body Mounted Solar Panel.

The STM was inclined by 36° but not rotated (see Fig. 7). The effective load factors at the CoG of the STM were:

* Axial Load Factor = - 4.69 g
* Lateral Load Factor = 4.64 g

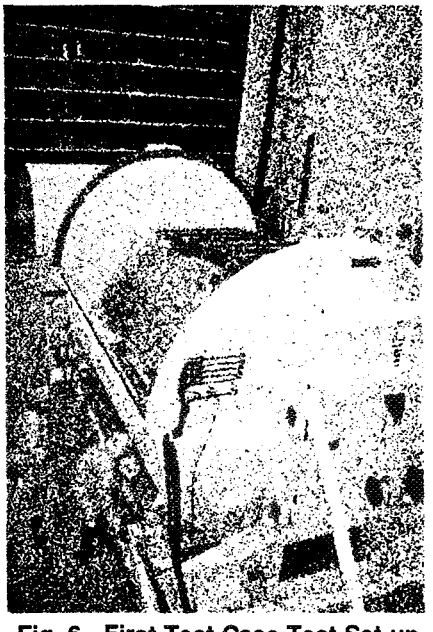

Fig. 6 - First Test Case Test Set-up

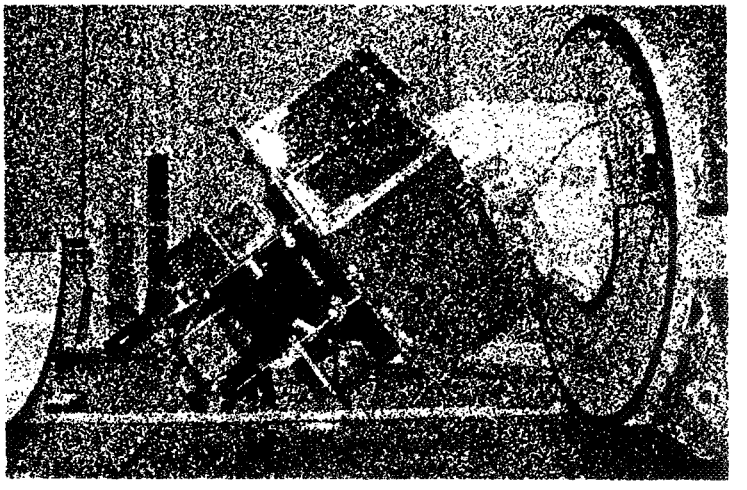

Fig. 7 - Second Test Case Test Set-up

| NOMINAL/TEST LOAD CASES | S/L - LVA RING | | S/M | | PSS | | C. TUBES | | SHADE S. | | HPGSPG S.S. | | PDS BRKTs | |
|---|---|---|---|---|---|---|---|---|---|---|---|---|---|---|
| | AX | LAT | AX | LAT | AX | LAT | AX | LAT | AX | LAT | AX | LAT | AX | LAT |
| BECO 1 | **-9.15** | **0.3** | **-9.15** | **0.3** | **-9.15** | **0.75** | **-9.15** | **0.75** | **-9.15** | **0.75** | **-9.15** | **0.75** | **-9.15** | **0.75** |
| BECO 2(*) | **-4.2** | **4.5** | **-4.2** | **4.5** | -3.75<br>**-1.48** | 7.05<br>**4.68** | **-3.75** | **7.05** | **-4.5** | **9.75** | -3.75<br>**-1.48** | 7.05<br>**4.68** | -3.75<br>**-1.48** | 7.05<br>**4.68** |
| BPJ (*) | -3.6 | 3.45 | -3.6 | 3.45 | -2.85<br>**-1.48** | 5.55<br>**4.68** | -2.85 | 5.55 | -4.5 | 7.2 | -2.85<br>**-1.48** | 5.55<br>**4.68** | -2.85<br>**-1.48** | 5.55<br>**4.68** |
| MECO | -8.1 | 0.6 | -8.1 | 0.6 | -8.1 | 1.95 | -8.1 | 1.95 | -8.25 | 4.05 | -8.1 | 1.95 | -8.1 | 1.95 |
| 1°TEST CASE | **-9.24** | **2.65** | **-9.62** | **2.71** | **-8.78** | **2.56** | **-8.82** | **2.5** | **-8.63** | **2.53** | **-8.89** | **2.58** | **-8.73** | **2.55** |
| 2°TEST CASE | **-4.69** | **4.64** | **-4.87** | **4.77** | **-5.31** | **5.33** | **-7.47** | **7.61** | | | **-4.52** | **4.52** | **-4.44** | **4.46** |
| | | | | | | | | | | | | | | |

(*) Non-bold values are relevant to coupled analysis results for non-time consistent events

**Fig. 8 - Comparison between Nominal Qualification and Test Load cases**

The STM was supported by a special inclined adapter constituted by two dismountable elements necessary to provide the correct orientation for the two test cases. The adapter was fitted with a flight standard interface flange.

The STM was equipped with 91 uniaxial and 30 triaxial strain gauges, with 9 displacement transducers and four accelerometers. Four runs were performed for each test case.

Detailed information about the test is contained in the documents of Refs. 6 and 7.

Using these test cases the nominal qualification loads were reached at the important interfaces. In particular, the first load case covered the qualification envelope relevant to flight conditions with high axial loads, while the second one covered the qualification envelope relevant to flight conditions with high lateral loads.

The comparison of the test load factors with the nominal ones is reported in Fig. 8.

The strain gauges behaviour, with the exception of 4 installed on the LVA Ring, was linear. The non-linearities were caused by local effects of Clamp Band tensioning and settling effects. However, even if non-linear effects were detected the measured strains were well below the yield limit.

All the test results are contained in the report of Ref. 8. No anomaly with the structure was detected.

### 4.3 Acoustic Noise Test

The objectives of the Acoustic Noise Test were:

* to qualify the secondary structure, including MLI and SSM's bonding vs the high frequencies broad band random vibration
* to verify the qualification random vibration criteria specified for the various equipments/instruments
* to verify alignment stability requirements of the item of interest.

The test was carried out in the Large European Acoustic Facility at ESTEC. The test set-up is shown in Fig. 9 (see following page).

The STM was instrumented with 251 accelerometers. They were located at areas expected to give high responses, or placed adjacent to equipment in order to confirm acceleration responses at these critical locations. Furthermore the acoustic noise spectrum was controlled by averaging the outputs of 13 microphones installed all around the Test Article (T/A).

The Acoustic Test consisted of the following runs:

- reverberation chamber preparation and equalization runs (chamber empty)
- low and intermediate equalization runs (T/A inside the chamber)
- qualification level run
- low level final run

Detailed information about the test is contained in the document of Ref. 9.

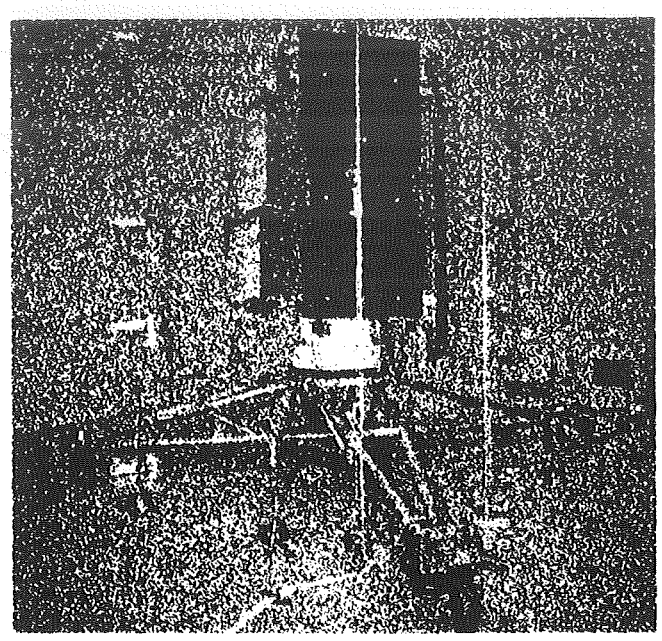

Fig. 9 - Acoustic Test Set-up

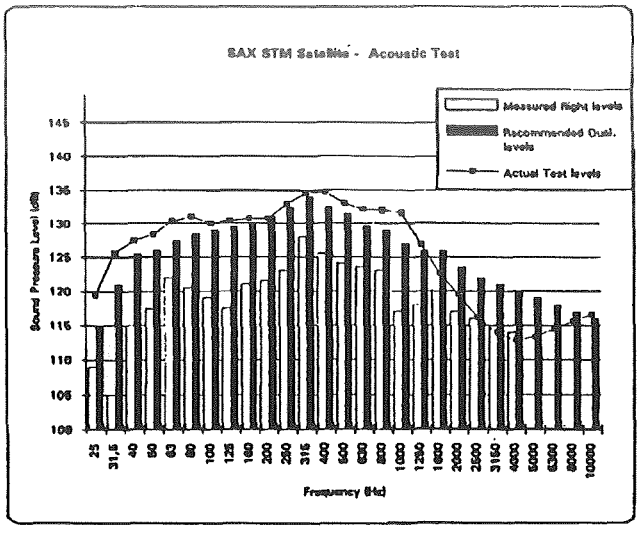


Fig. 10 - Acoustic Noise Levels

The comparison between nominal and qualification acoustic noise spectra is shown in Fig. 10. The in-flight measured noise spectrum is included as well. The sound pressure levels were well controlled within the required test tolerances with the exception of some unimportant frequency bands. The goal was to reproduce the correct sound pressure levels over the frequency range 31.5 - 2000 Hz neglecting higher frequencies. The sound pressure levels between 2000 to 10000 Hz are very low and component responses are significantly attenuated at these frequencies. The overall sound pressure level was exceeded by some 1.5 dB. No anomaly with the structure was detected.

The acceleration responses were compared to the spectrum specified for equipment/instruments qualification random vibration test. Apart from only a few units, both external and internal, a close agreement between the measured and predicted responses was detected.

As expected, because of a rigid test adapter, the Acoustic Noise Test did not induce a realistic and adequate excitation at the areas close to the mounting interface. The measured response accelerations at the interface areas were well below the typical ones. Furthermore, an essential reduction of the qualification input spectrum for all the P/L instruments was detected.

All the test results are contained in the report of Ref. 10.

### 4.4 Vibration Test

The Sinusoidal Vibration Test was performed to qualify the structure for the low frequency transient peak responses by applying an equivalent sinusoidal base input.

Even if not specifically required by the Launcher Authority, a Low Level Random Vibration Test was also performed. This was to complete the verification of the random vibration criteria of those units installed close to the mounting interface (mainly the ones located on the Tank Support Floor) and not adequately excited by the Acoustic Noise Test.

The vibration tests were carried out at the ESTEC Test Facility. The STM in full test configuration is shown in Fig. 11 (see following page).

For the Sinusoidal Vibration Test, the SAX STM was instrumented with 224 accelerometers. They were located at selected locations in order to provide information of either local and overall behaviour of the structure. The strain gauges, mainly located on the LVA Ring and PM and already used for the Centrifuge Test, were reutilized.

The same accelerometers as used for the Acoustic Noise Test was reutilized for the Random Vibration Test. The input spectra were controlled by 4 Pilot and 12 Copilot accelerometers installed on the Dynamic Adapter.

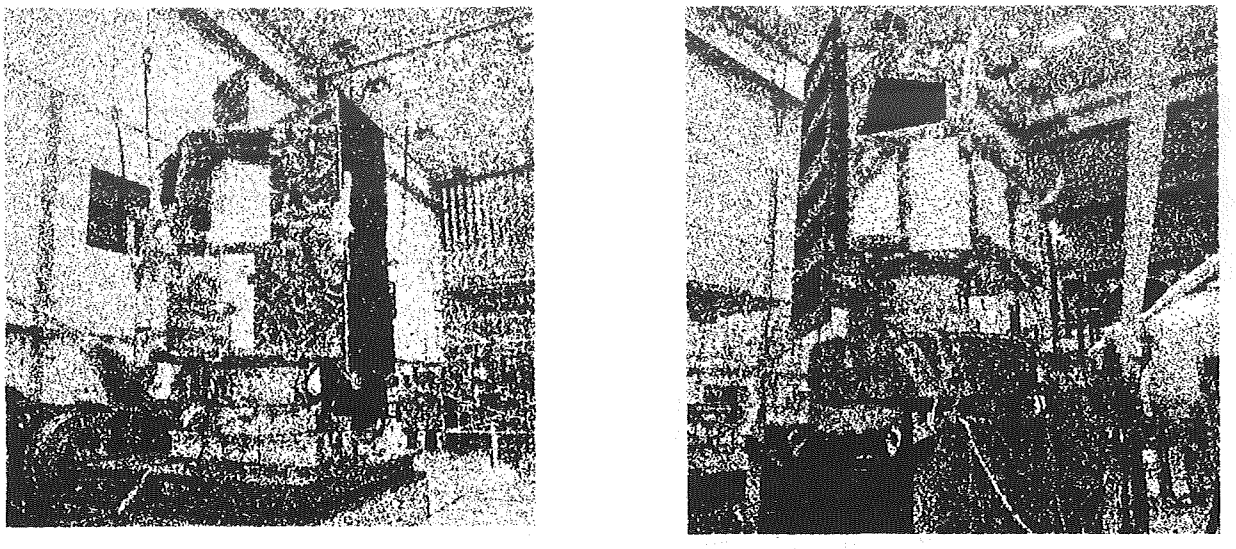

**Fig. 11 - Vibration Test Set-up**

The STM was subjected to the following test sequence for each axes:

***Sinusoidal Vibration Test***

- Low Level Run (0.2 g over the frequency range 5 - 2000 Hz)
- Intermediate Level Run (flight level over the frequency range 5 - 100 Hz)
- Qualification Level Run (flight level x 1.5)
- Final Low level Run

***Random Vibration Test***

- Low level Run (10 dB below the in-flight measured spectrum)

The vibration test was performed on the basis of the ATLAS 1 input spectra. Nevertheless, the sinusoidal input spectrum was reduced (notching) in order not to overstress the overall satellite, local structures and equipment.

Two different procedures were adopted depending on the frequency range:

**Frequency range up to 50 Hz**

The input spectrum was reduced in the frequency bands of the resonance of the primary structure such that the test loads experienced at each critical location of the structure did not exceed the design load.

**Frequency range from 50 to 100 Hz**

The input spectrum was reduced so as not to exceed at each critical location of the structure the maximum responses based on the amplification factors as provided by the Launcher Authority. A safety factor of 1.25 was used in this frequency range.

No notching was performed for the Random Vibration Test. A detailed description of the test is given in the document of Ref. 11. The input spectra together with the nominal ones are given in Fig. 12 a/b/c/d (see following page).

The Sinusoidal Vibration Test allowed to successful completion of the qualification of the primary structure against a safety factor of 1.5. A comparison between experimental and analytical base fluxes is reported in Fig. 13 (following page).

The results of the Random Vibration test were used only for the units of interest, i.e., the ones located on the Tank Support Floor. They were extrapolated at qualification level, considering a realistic damping factor coming from the results of the Sine Test. Higher levels than the ones obtained during the Acoustic Noise Test, but still enveloped by the specified random vibration criteria, were detected. All the test results are contained in the Report of Ref. 12.

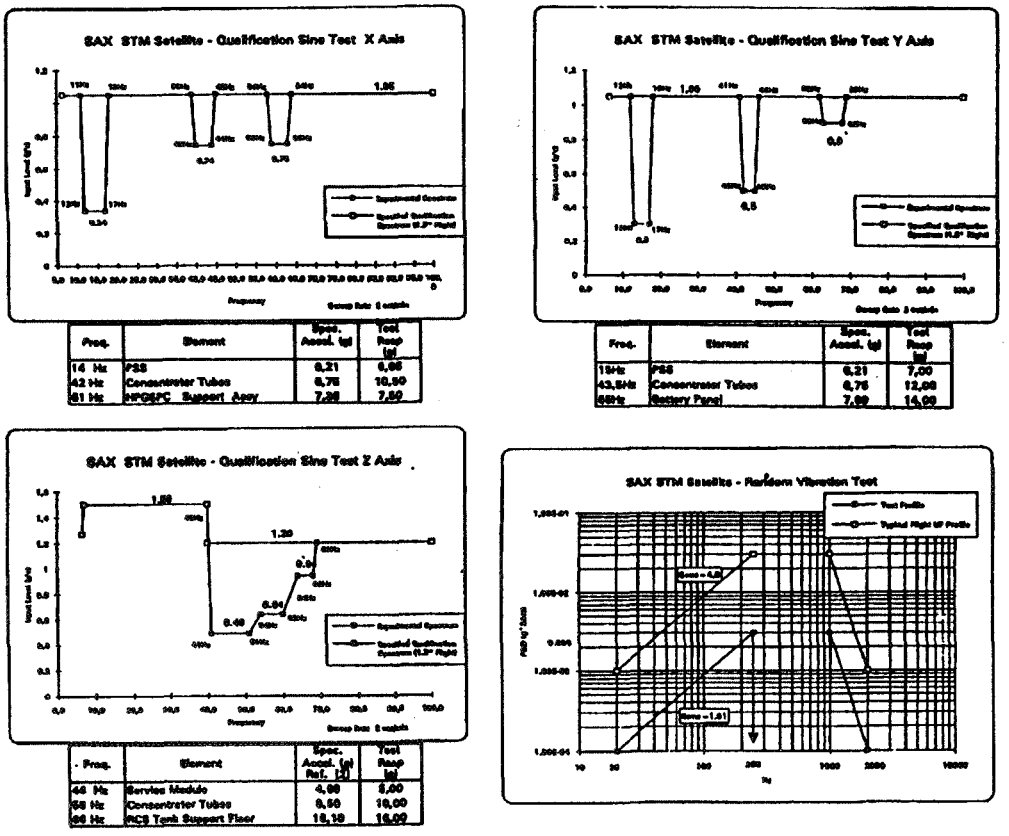


Fig. 12 - Qualification Input Spectra

## 5. THERMAL REQUIREMENTS

During its life, the SAX satellite is subjected to thermal induced environments which drive the design of thermal control. These environments are strictly related to the mission profile to be performed and they can be split mainly into launch and operative conditions.

Launch conditions were evaluated by using a dedicated Thermal Mathematical Model and judged of low importance with respect to the operative conditions because of the short duration of the tranfer phase.

The SAX operative mission profile includes several cases differing from each other in boundary conditions or attitude.

A Thermal Balance Test was performed in order to evaluate the satellite behaviour, but only the extreme cases were covered, identified by the analysis, simulating as far as possible the real flight condition. The test included both steady state and transient phases to correlate the TMM and to evaluate the Thermal Control design performances respectively.

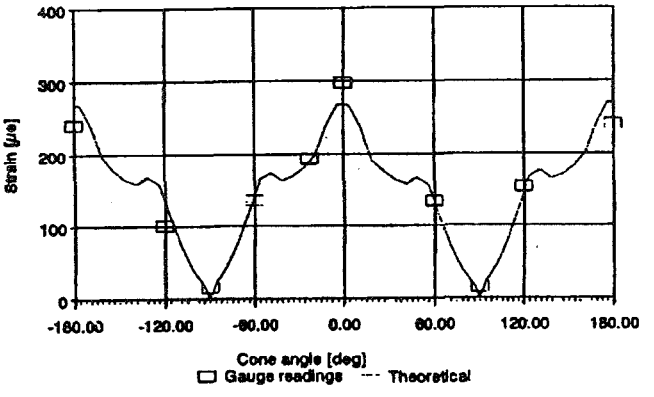


Fig. 13 - Comparison between Analytical and Experimental Base Fluxes (X axis)

| TASK N° | 1 | 2 | 3 | 4 | 5 | 6 | 7 |
|---|---|---|---|---|---|---|---|
| PHASE DESCRIPTION | PUMP DOWN & COOL.:e DOWN | 0° SAA COMMISSIONING SUMMER SOLSTICE | + 45° SAA SUMMER SOLSTICE | SUMMER SOLSTICE ECLIPSE | + 30° SAA WINTER SOLSTICE | - 30° SAA WINTER SOLSTICE | CHAMBER RECOVERY |
| TEST CASE | REACHING TEST COND. | STEADY STATE | STEADY STATE | TRANSIENT | STEADY STATE | STEADY STATE | REACHING AMBIENT C. |
| EXTIMATED DURATION | 15 HRS | 65 HRS | 50 HRS | 8 HRS | 30 HRS | 20 HRS | 15 HRS |
| SPACECRAFT ORIENTATION AND ATTITUDE | 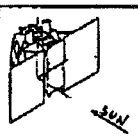  | 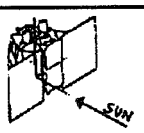  | 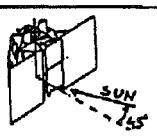  | 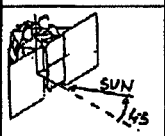  | 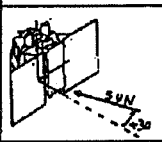  | 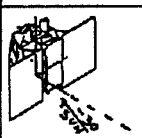  | 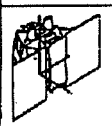 |
| SOLAR INTENSITY | FROM 0 TO 900 W/m2 | 840 W/m2 | 840 W/m2 | 0 - 1320 W/m2 | 900 W/m2 | 900 W/m2 | 0 W/m2 |
| CHAMBER VACUUM | FROM AMBIENT TO 10e-5 mbar | 10e-5 mbar OR BETTER | 10e-5 mbar OR BETTER | 10e-5 mbar OR BETTER | 10e-5 mbar OR BETTER | 10e-5 mbar OR BETTER | FROM 10e-5 mbar TO AMBIENT |
| SHROUDS TEMPERATURE | FROM AMBIENT TO 100 °K | 100 °K | 100 °K | 100 °K | 100 °K | 100 °K | FROM 100 °K TO AMBIENT |
| COMMENTS | | COLD CASE FOR P/L | COLD CASE FOR S/L | VERIFICATION OF TRANSIENT ECLIPSE PERFORMANCE | HOT CASE FOR P/L | HOT CASE FOR S/M | |

**Fig. 14 - Thermal Balance Test Phases**

## 6. THERMAL BALANCE TEST

The objectives of the Thermal Balance Test (see Ref. 15) are:

* to validate the Thermal Mathematical Model
* to demonstrate the validity of the Thermal Control Subsystem (TCS) design
* to anticipate any possible manufacturing/assembling problems.

The Thermal Balance Test covered only a few extreme mission cases which are considered significant for all the susequent correlation analysis. In particular the STM was subjected to the following test phases (see Fig. 14):

- **Commissioning Case - 0° Sun Aspect Angle (SAA)**
  (Steady State, worst cold case for the Payload Module)
- **Summer Solstice: 45° SAA**
  (Steady State, worst cold case for the satellite)
- **Summer Solstice Eclipse: 0° SAA**
  (Transient, orbital simulation)
- **Winter Solstice: 30° SAA**
  (Steady State, worst hot case for the Payload Module)
- **Winter Solstice: -30° SAA**
  (Steady State, worst hot case for the Service Module)

The test has been carried out in the Large Space Simulation Chamber (LSS) at ESTEC (NL).

The STM was fully representative of the Flight Model (see Fig. 15, following page) with the exception of the solar array wings which were replaced by shadowing panels (truncated panels) sized to avoid a direct sun impingement on the satellite during the summer solstice phase. They simulated the thermo-optical properties of the flight wings. The effect on the view factors of the reduced length of truncated panels was negligible. The dummy unit heaters were set at fixed power levels with the exception of the orbital simulation phase where for some units, mainly of the Electrical Power Subsystem (EPS), the same profile of the flight units was implemented. Also the Thermal Control heaters were set to a fixed level.

The S/L was installed on the Spin Box/Gimbal Stand via Thermal Test Support Rig. The Test Adaptor was designed such that it had minimum shadowing effects during the test phases and heat flux from S/L. In order to avoid heat exchange with the S/L it was also equipped with Guard Heaters. A thermostatic control was implemented for the Guard Heaters.

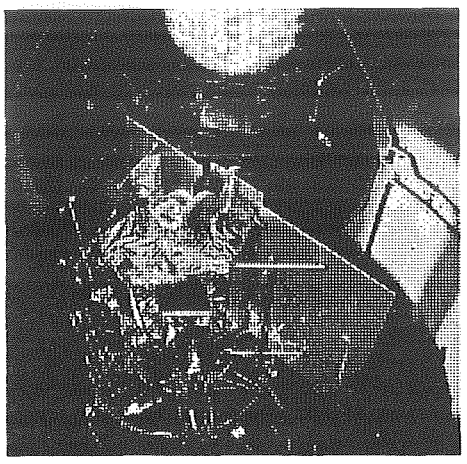

**Fig. 15 - Thermal Balance Test Set-up**

Radiative Plates were installed partially all around the satellite and in front of SVM Lower Platform in order to reproduce the Albedo and Earthshine effects. Thermostatic control, based on the average of two thermocouples for each plate, was implemented. The solar intensity, during the steady cases, reproduced the average value of the orbit for the summer solstice and winter solstice cases.

During the eclipse phases the real value of the Sun intensity along the complete orbit was simulated. The effect of Deep Space was simulated by Chamber Shroud (cooled by liquid nitrogen) all around the S/L. A stabilization criteria of 1°/22 h was used. This allowed to reach the equilibrium temperature with an accuracy of 0.5 °C.

Test results were not directly comparable with the analytic ones because of the slight changes occurring in the boundary conditions. A new Thermal Analysis including the actual boundary conditions was run. The modelling of the Thermal Test Adaptor was included and a more detailed model of the truncated panels substitued the coarse model. Comparison was made between the new analytical data and experimental results. This is documented in Ref. 16. In spite of this, in general, the STM was colder than the prediction. Differences for some units were detected between the two data sets. For the time being, the correlation activity is still in progress.

It is involving both the refinement of the modelling (refinement of the values of the thermo-optical properties, contact conductances, view factors, etc.) and modification of thermal control hardware. Local modifications were already identified, for example the Concentrators tubes will be completely covered by multilayers and heater supports will be modified, Second Surface Mirror area in correspondance of the batteries will be reduced to allow an higher temperature, etc.

Furthermore, a new allocation of the Thermal Control Power could be possible. Anyway, it is worth mentioning that the modification of the Thermal Control hardware as well as the power allocation will be such to confirm the thermal environments specified in the equipment design documentation.

## 5. CONCLUSIONS

An extensive test campaign was performed on the Structural Model of the SAX satellite. The test program was fully compliant with Launcher Authority recommendations but tailored to the specific technical needs and program constraints of the SAX program.

- The validation of the Mathematical Model as well as the successful verification of the stiffness requirements were accomplished through the classical Modal Survey Test. Slight differences between the experimental and analytical test results, mainly caused by the manufacturing contingencies and an underestimate of the stiffness of some structural components, were detected. An additional survey was performed over an extended frequency range (up to 100 Hz). The measured data were used in conjunction with the results of the Frequency Response Analysis to get more reliable predictions for the Sinusoidal Vibration Test. The mathematical model was updated and provided to the Launcher Authority (General Dynamics) for the final load cycle.

- The qualification against the static loads was reached through the Centrifuge and Sinusoidal Vibration Tests. They were conducted on the basis of the maximum acceptable loading as derived from the coupled load analysis with the launcher.

  * **Centrifuge Test**
    Two test cases corresponding to two different STM configuration and together providing the best possible coverage of the qualification load envelope were performed. Using these test cases the qualification was reached at the important interfaces.

  * **Sinusoidal Vibration Test**
    Purpose of the Sinusoidal Vibration test was to apply the maximum expected low frequency quasi-sinusoidal loads and to complete primary structure qualification.

  The qualification against SAX project requirements was correctly met. However, the final confirmation of the correct qualification against the quasi-static loads has still to be made based on the results of the final coupled load analysis with the launcher.

- Concerning the high frequency loads, the STM was successfully subjected to a complete qualification against the Acoustic Noise Test. Apart from only a few units, a good agreement between the predicted and measured response accelerations was detected. An essential reduction of the qualification input spectra of the Science Instruments was possible.
  Due to the presence of a rigid adapter, the Acoustic Noise Test did not induce a sufficient excitation over the areas near the mounting interface. In order to overcome this problem and therefore to verify the random vibration criteria of the units/equipments mounted on the Tank Support Floor correctly, a random vibration test, at low level, was performed. The extrapolated spectra of the units of interest were well enveloped by the specified random qualification spectra.

No problems arose with the structure all along the test campaign.

Test results allow to conclude that the SAX structural design conforms to the ATLAS 1 requirements. Nevertheless, the mechanical verification process will be completed only on the Flight Model which will undergo the Separation Shock Tests.

In order to cope with the thermal requirements derived by the particular SAX mission, a Thermal Balance test was performed on the Thermal Model refurbished from the Structural Model.

Only a few critical cases of the mission profile were simulated, providing anyway the necessary confidence in the capability of the satellite to meet thermal requirements. The test included both steady state and transient phases to correlate the Thermal Mathematical model and to evaluate the Thermal Control design performances. The Thermal Balance test was carried out with some deviations, but they were understood and a more reliable Thermal Model was implemented and run.
The new data set was the basis of the correlation analysis which, even if it is still to be completed, provided good evidence of the Thermal Control Subsystem performance.

Nevertheless, the thermal verification process will be completed only on the Flight Model where, during the Thermal Vacuum test, a thermal cycle will be used to verify the Thermal Mathematical Model correlated on STM and so definitevely provide confirmation of the requirement satisfaction.

**REFERENCES**


1. C. Butler, L. Scarsi - *The SAX Mission for X-Ray Astronomy*, SPIE-1344, July 90, S. Diego (CA-USA)

2. P. Giordano, G. Raimondo, P. Messidoro - *System Test Approach For The SAX Satellite*, 17th Space Simulation Conference, Nov. '92, Baltimore (ML - USA)

3. G. Finocchiaro, P. Santoro, P. Attinà - *SAX Satellite Design and Verification*, 12nd AIDAA Congress, July '93, Como (I)

4. G. Raimondo - *Modal Survey Test Specification*, Alenia Spazio Document, SXSP-AI-015

5. *SAX STM Modal Survey Test Report* , IABG Document, B-TR 0858/32

6. G. Raimondo, M. Patara - *STM Centrifuge Test Specification*, Alenia Spazio Document, SX-SP-AI-012

7. G. Raimondo - *First Assessment of Potential STM Centrifuge Test Cases*, Alenia Spazio Document, SX-TN-AI-218

8. *Centrifuge Test Report* , CEA CESTA Document, CESTA/DT/EX/ENV/ No DO 2143/93

9. G. Raimondo, M. Patara - *Acoustic Test Specification*, Alenia Spazio Document, SX-SP-AI-014

10. *SAX STM Acoustic Test Report* , ESTEC Document, No 1934

11. G. Raimondo - *Vibration Test Specification*, Alenia Spazio Document, SX-SP-AI-013

12. *SAX STM Vibration Test Report* , ESTEC Document, No 1935

13. G. Raimondo, M. Patara - *SAX PFM Acoustic Test Specification*, Alenia Spazio Document, SX-SP-AI-071

14. *SAX Modal Survey Test : Analytical - Measured Results Correlation and Mathematical Model Updating*, Alenia Spazio Document, SX-RP-AI-116

15. D. Monaldi, G. Raimondo, G. Poidomani - *Thermal Balance Test Specification*, Alenia Spazio Document, SX-SP-AI-0016

16. D. Monaldi, G. Raimondo - *Thermal Balance Test Verification Report*, Alenia Spazio Document, SX-RP-AI-0155

# ENVIRONMENTAL TESTING TO PREVENT ON-ORBIT TDRS FAILURES*

Robert M. Cutler
The MITRE Corporation
6305 Ivy Lane, Suite 500, Greenbelt, MD 20770
Voice (301) 901-9230, FAX (301) 901-9207
Internet: rcutler@mitre.org

Institute of Environmental Sciences
18th Space Simulation Conference
Baltimore, Maryland
November 1, 1994

## ABSTRACT

Can improved environmental testing prevent on-orbit component failures such as those experienced in the Tracking and Data Relay Satellite (TDRS) constellation? TDRS communications have been available to user spacecraft continuously for over 11 years, during which the five TDRSs placed in orbit have demonstrated their redundancies and robustness by surviving 26 component failures. Nevertheless, additional environmental testing prior to launch could prevent the occurrence of some types of failures, and could help to maintain communication services. Specific testing challenges involve traveling wave tube assemblies (TWTAs) whose lives may decrease with on-off cycling, and heaters that are subject to thermal cycles. The development of test conditions and procedures should account for known thermal variations. Testing may also have the potential to prevent failures in which components such as diplexers have had their lives dramatically shortened because of particle migration in a weightless environment. Reliability modeling could be used to select additional components that could benefit from special testing, but experience shows that this approach has serious limitations. Through knowledge of on-orbit experience, and with advances in testing, communication satellite programs might avoid the occurrence of some types of failures, and extend future spacecraft longevity beyond the current TDRS design life of ten years. However, determining which components to test, and how much testing to do, remain problematical.

## INTRODUCTION

### The NASA Space Network

The NASA Space Network includes five geostationary TDRSs controlled by ground terminals located primarily at White Sands, New Mexico. The TDRSs, from their high orbits, can view almost the entire surface of Earth. Each TDRS relays commands from a ground terminal to user spacecraft in low earth orbit (LEO). Each TDRS also relays data and telemetry from user spacecraft to the ground terminal. User spacecraft benefit from the Space Network's ability to communicate between fixed ground facilities and rapidly-moving spacecraft at almost any time, and at almost any location in LEO. Some examples of user spacecraft are included in Table 1.

*Work performed by The MITRE Corporation for the National Aeronautics and Space Administration, Goddard Space Flight Center, Code 405 under Contract NAS5-32607.

**Table 1. Examples of TDRS User Spacecraft**

Advanced X-Ray Astrophysics Facility (AXAF)
Cosmic Background Explorer (COBE)
Earth Observing System (EOS)
Earth Radiation Budget Satellite (ERBS)
Extreme Ultraviolet Explorer (EUVE)
Gamma Ray Observatory (GRO)
Hubbell Space Telescope (HST)
Landsats (LSATs)
Ocean Topography Experiment (TOPEX)
Space Shuttle Orbiters Atlantis, Columbia, Discovery, and Endeavour
Space Station Alpha (SSA)
Tropical Rainfall Measurement Mission (TRMM)
Upper Atmospheric Research Satellite (UARS)
X-Ray Timing Explorer (XTE)

### Replenishment and Reliability

To ensure the continuity of Space Network services, NASA monitors the state of health of the TDRSs, plans for changes in user requirements, and replaces or supplements TDRSs as necessary. Constellation replenishment planning depends on accurate estimates of TDRS lives. TDRS lives are predicted by reliability models. These models perform Monte Carlo simulations of the failures of all components except those already known to have failed. In most cases, a TDRS has a primary and a back-up component for each required function. Thus, most component failures do not prevent a TDRS from performing its mission. A partial or complete communication failure occurs only if both a primary component and its back-up components fail.

## COMPONENT FAILURE HISTORY

### Predicted Failures

Failure predictions are based on the "parts count" method and a constant failure rate for each class of part in operation, i.e., whose failure would be observable from the relayed data or from telemetry. Predictions are made using random or pseudo-random number generators to reflect the uncertainty of future events - even though the events may ultimately be physically explainable and thus non-random. Predicted failure rates are based on MIL-HDBK 217D (ref. 1). The "reliability drivers" are the components that most significantly affect the reliability of a TDRS's communication service, based on their predicted failure rates considered in combination with their duty cycles and the availability of back-up components. These reliability drivers are listed in Table 2.

**Table 2. TDRS Reliability Drivers**

| Component | Ten-Year Reliability |
|---|---|
| Decrypter | 0.81 |
| Return Processor | 0.89 |
| TT&C Transponder | 0.93 |
| Encrypter | 0.94 |
| Forward Processor | 0.94 |
| Traveling Wave Tube Amplifier Assemblies | 0.94 |
| Master Frequency Generator | 0.95 |
| Multiple Access Transmitter | 0.96 |
| Multiple Access Receiver | 0.97 |
| Ku-Band Receivers | 0.98 |
| Solar Array Drive Assembly | 0.99 |
| Telemetry Unit | 0.99 |
| Thruster Module | 0.99 |
| Wheel Drive Assembly | 0.99 |
| All Others | 0.91 |
| All | 0.42 |

The total predicted component failure rate of 1.10 per TDRS per year is constant for any TDRS except for the usually minor decreases that occur after a primary component and its back-up both fail, or if there is a single-point failure (one with no design back-up). TDRS 6's predicted failure rate is slightly lower than the rate for the earlier TDRSs because of the substitution of higher-reliability low noise amplifiers for the previously used parametric amplifiers in the single-access return telecommunication chains (ref. 2). The TDRS 7 failure rate will be even lower because its single-access services will use solid state power amplifiers (SSPAs) instead of TWTAs (ref. 3).

The total predicted failure rate of the TDRS constellation is approximately proportional to the number of TDRSs on orbit. Therefore, the total predicted failure rate for the constellation increased with each successfully launched TDRS. Depending on the future survival and operation of older TDRSs, the total predicted failure rate of the constellation may continue to increase. The TDRS launch dates and current ages are shown in Table 3.

**Table 3. TDRS Launch Dates and Ages (as of July 1, 1994)**

| Satellite | Launch Date | Age in Years |
|---|---|---|
| TDRS 1 | April 4, 1983 | 11.24 |
| TDRS 2 | January 1985 | Launch failed |
| TDRS 3 | September 29, 1988 | 5.75 |
| TDRS 4 | March 13, 1989 | 5.30 |
| TDRS 5 | August 2, 1991 | 2.91 |
| TDRS 6 | January 13, 1993 | 1.46 |
| TDRS 7 | June 29, 1995 (planned) | Unlaunched |
| TDRS 8, 9, and 10 | Unscheduled | Unlaunched |

**Observed Failures**

The component failures considered in this paper include those that appear to reflect imperfections in the design, manufacturing, or operation of a TDRS in the space environment, and that would be expected to significantly and irreversibly impair TDRS communication service in the absence of back-ups or a prior failure of the service. The failures on TDRS 1 of the primary thruster bank and the back-up negative roll thruster, which appear to have resulted from problems at launch with the booster rocket, and the failure of TDRS 2 to be carried into orbit by Challenger, are not counted for the purposes of this paper. Also not counted are failures that would affect the non-Space Network equipment on board, which is neither modeled nor fully monitored.

A TDRS can be neither inspected in orbit nor returned to earth for study. The state of health of a TDRS is surmised based on telemetry and the quality of communication services. The compilation of a component failure list is subjective, and opinions about whether a component has failed, and when it failed, may differ. More than one hundred Spacecraft Orbital Anomaly Reports (SOARs) document events that are not considered to be failures as defined in this paper, and it is possible and perhaps likely that some component failures have not been detected. Also, the attribution of a failure to a specific component may differ depending on whether the component caused the failure or was affected by the failure. In this paper, the affected component, which appears to have its function impaired or absent, is the one that is named. The cause of the failure is often less certain. The failures are listed in Table 4.

**Table 4. TDRS Component Failure History**

| Date | Component Description | TDRS | Age (Yr.) | SOAR |
|---|---|---|---|---|
| 07-17-83 | Gyro (# 1/2) | 1 | 0.28 | 1 |
| 10-19-83 | Diplexer, Ku-Band Forward East | 1 | 0.54 | 7 |
| 10-28-83 | TWTA, Ku-Band East ,Primary | 1 | 0.57 | 7 |
| 11-01-83 | TWTA, Ku-Band West, Primary | 1 | 0.58 | 8 |
| 04-15-85 | TWTA, Ku-Band Downlink, Primary (#5) | 1 | 2.03 | 43 |
| 06-27-85 | Indicator, East Pitch, Primary | 1 | 2.23 | 55 |
| 04-02-86 | Heater (at parametric amplifier), East, Primary | 1 | 3.00 | 61 |
| 11-28-86 | Diplexer, S-Band Forward East | 1 | 3.65 | 64 |
| 08-08-87 | TWTA, S-Band East, Primary | 1 | 4.34 | 67 |
| 08-11-87 | TWTA, S-Band East, Redundant | 1 | 4.35 | 68 |
| 03-14-89 | Indicator, West Pitch, Primary | 4 | 0.00 | 86 |
| 07-05-89 | Phased Array Receiver, S-Band, Primary (#10) | 1 | 6.25 | 93 |
| 08-30-89 | Synthesizer, S-Band Return East, Primary | 1 | 6.41 | 96 |
| 09-28-89 | Indicator, East Pitch, Redundant | 1 | 6.49 | 97 |
| 11-11-89 | TWTA, Ku-Band Downlink, Primary (#4) | 1 | 6.61 | 95 |
| 01-16-90 | Switch, West Polarization | 3 | 1.30 | 100 |
| 04-03-90 | TWTA, Ku-Band East, Redundant | 1 | 7.00 | 102 |
| 08-07-90 | Indicator, West Pitch, Redundant | 4 | 1.40 | 108 |
| 04-09-91 | Earth Sensor Electronics, Primary | 4 | 2.07 | 111 |
| 07-05-91 | Master Frequency Generator, 955 MHz, Primary | 4 | 2.31 | 115 |
| 09-04-91 | Processor (?), S-Band Return East, Primary | 1 | 8.42 | 119 |
| 04-03-92 | TWTA, Ku-Band West, Redundant | 1 | 9.00 | 125 |
| 05-29-92 | Heater (at parametric amplifier), East, Primary | 4 | 3.21 | 131 |
| 01-13-93 | Thermistor (on solar array) | 6 | 0.00 | 138 |
| 08-31-93 | TWTA, Ku-Band Downlink, Redundant (#6) | 1 | 10.41 | 122 |
| 05-29-94 | TWTA, S-Band East, Primary | 5 | 2.82 | 161 |

The reader will notice that 18 of the 26 failures have occurred on TDRS 1 during its 11 years of service. Only one failure has occurred on the almost six-year-old TDRS 3. With five failures in its five years, TDRS 4 has an average history. TDRS 5 has had only one failure in almost three years, and TDRS 6 has one failure in a year and a half.

TDRS 1 failures are dominant, leading most program personnel to conclude that subsequent improvements in design, manufacturing, and testing have markedly lowered the failure rates of the later TDRSs. However, the data base is not sufficient to justify such a conclusion on a purely statistical basis. The ages of the components when they failed are neither predominantly low, indicative of "infant mortality," nor predominantly high, indicative of burnout or wearout, but are distributed more or less evenly. Most of the failures are attributed to design errors, manufacturing defects, and unknown but often recurring conditions, with few if any being random events.

**Observations Versus Predictions**

A historical comparison of the numbers of predicted and observed TDRS component failures is shown in Figure 1. Since the prediction is an expected value, it increases smoothly, while the observations can occur as only discrete integral values. The 95% upper and lower confidence limits are calculated above and below the predictions, based on binomial probabilities, to delineate a confidence zone.

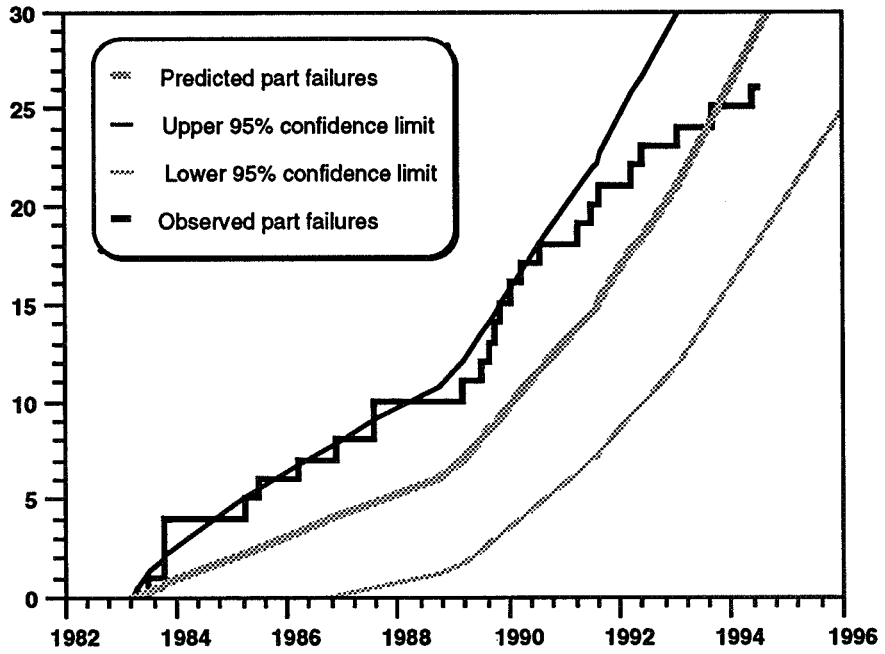


**Figure 1. TDRS Component Failures to July 1, 1994**

The observations tend to exceed predictions early in the program because many component failures occurred on the first TDRS. Recently, the observations fell behind predictions because of the better performance of the later TDRSs. Overall, the entire history of the TDRS 1 through TDRS 6 procurement appears to agree with predictions as well as can be expected. Future observations may fall further behind predictions. However, this trend could be halted by

either premature burnout or wearout on TDRS 1 through TDRS 6, or failures of new design features or part lots used beginning with TDRS 7.

The observed agreement is not entirely fortuitous. Three different sets of failure rates have been compiled for the TDRS design. The earliest set, based on MIL-HDBK 217B, included relatively high failure rates, and was replaced by MIL-HDBK 217D rates (refs. 4 and 5). The latter were considered to be *a priori* more appropriate, based on spacecraft experience in general but not on TDRS experience, which was then very limited and not yet fully compiled and analyzed. When the even lower MIL-HDBK 217E Notice 1 rates became available, they were found to under-predict historical TDRS failures, and thus they were not adopted for use in reliability and replenishment modeling (ref. 6). The most recently tabulated failure rates, in MIL-HDBK 217F Notice 1, have not been applied to the TDRS design, but could have been if a change to the new rates had been deemed necessary (ref. 7). In short, MIL-HDBK 217D failure rates have been used because they are consistent with total component failure experience.

For individual categories of components, observations do not mirror predictions. For example, the total predicted failure rate of 1.10 components per year is the sum of the rates for the TDRS bus and payload. The bus includes subsystems such as attitude control, electric power, propulsion, tracking, telemetry, and command (TT&C), and thermal control for these subsystems, with a total predicted failure rate of 0.44 components per year. The telecommunications payload has a total predicted failure rate of 0.66 components per year. However, only three of the 26 components failed to date are in the bus (viz., a gyro, an earth sensor, and a solar array thermistor). The reason for the better reliability of the TDRS bus is believed to be that its design was previously developed, tested, and improved by the Navy's FLTSATCOM program, while the TDRS payload design represented an extension of existing technology. Thus, new designs may merit more testing than proven designs.

## TRAVELING WAVE TUBE ASSEMBLIES

### Traveling Wave Tube Assembly Failures

Ten TWTAs have failed, including six (four Ku-band and two S-band) east and west TWTAs on TDRS 1, three Ku-band downlink TWTAs (the third having been turned on after the first one failed) also on TDRS 1, and one Ku-band east TWTA on TDRS 5. The design of the TWTAs used on TDRS 1 was defective, resulting in heat-induced stress failures. After the early TWTA failures on TDRS 1, the design of the TWTAs used on the later TDRSs was improved. Of course, TWTA failures continued to occur on TDRS 1.

Three of the TWTA failures occurred after operating times of less than 0.6 years, and may be considered to be examples of "infant mortality." Three of the failures, including the one on TDRS 5, occurred after operating times of about two to four years, and may be thought of as mid-life failures. The remaining five failures occurred after operating times of between six and nine years, and may be burnout failures.

Although TWTAs have been recognized from the beginning as being among TDRS life-limiting components, the TWTA failure history of TDRS 1 is obviously unsatisfactory. On the other four satellites, each with six operating TWTAs, the expected number of failures according to the average MIL-HDBK 217D rate of 2.0 per million hours is 1.4. Thus, the failure of a TWTA on TDRS 5 is consistent with the predicted rate. Since all TWTAs have back-ups, TDRS 5 communication service has not been affected.

### Traveling Wave Tube Assembly Testing

The TWTA failure experience on TDRS 1 might have been prevented by improved testing. Extended burn-in prior to launch might have prevented some of the "infant mortality" failures, but might have also reduced remaining TWTA life, thereby resulting in additional burnout failures. Therefore, extended burn-in of non-flight TWTA prototypes appears to be a better method of testing TWTA design and workmanship.

Some analysts have expressed concerns about limited TWTA cycle life. Although TWTAs remain on continuously under normal circumstances, the S-band TWTAs cycle when a TDRS experiences a loss of signal from the ground terminal, followed by a pre-programmed Emergency Time-Out (ETO). In addition, solar array disorientation can lead to a low-voltage cutoff of K-band TWTAs. Power cycling of non-flight TWTA prototypes could help to ensure adequate cycle life. (Also, a better definition of cycle life could lead to design and operational changes that conserve power by routinely cycling TWTAs in accordance with communication service schedules.)

Accelerated life testing could be performed with ambient temperatures and applied voltages that are more stressful than on-orbit operating conditions. This approach could have offered a very high likelihood of detecting design or manufacturing flaws resulting in "infant mortality," and a reasonable likelihood of detecting flaws leading to premature burnout. The accelerated life testing could incorporate both extended burn-in and power cycling.

## DIPLEXERS

### Diplexer Failures

Two diplexers have failed, one operating in the Ku-band and one in the S-band, but both connected to the east antenna of TDRS 1. The cause of these failures is believed to be short circuiting due to the presence of metallic particle contamination in the gaps between tuning screws and tuning cavity walls. Manufacturing improvements made after the TDRS 1 diplexer failures seem to have prevented similar failures on the other TDRSs.

The TDRS diplexer history is not satisfactory, especially because the diplexers are not redundant, and the failures disable the transmission of signals from the antennas. Of the two west diplexers remaining on TDRS 1, and the four east and west diplexers on each of the other four TDRSs, the expected number of additional failures at the MIL-HDBK 217D rate of 25.7 per billion hours is 0.02. The actual diplexer failure rate appears to have been considerably greater than the prediction.

### Diplexer Testing

If the hypothesized cause of diplexer failure, weightless migration of metal particles, is correct, then no amount of ordinary testing on earth would have revealed the problem. Only in the weightlessness of orbit would the particles have floated away from the diplexer walls and created short circuits. Testing in a weightless environment would not be practical. Perhaps functional testing accompanied by rotation or vibration to mobilize contaminating particles would be useful to simulate some of the effects of weightlessness. However, in the case of the failed diplexers, a simpler solution than improved functional testing appears to be ensuring the adequacy of tuning gaps and maintaining and verifying cleanliness through all stages of manufacturing.

## HEATERS

### Heater Failures

Two TDRS heaters have failed, and both are located near east parametric amplifiers on the three-year-old satellites TDRS 1 and TDRS 4. The first failure, on TDRS 1, was attributed to a design flaw in which the heater was placed too close to its controlling thermostat, resulting in excessive cycling. The design basis was 100,000 cycles, and the failure occurred after 525,000 cycles. The later TDRSs were modified to avoid this problem. Nevertheless, a second failure occurred, this time on TDRS 4. Since each TDRS has back-up heaters, and other back-up components that could be powered if more heat were needed, heater failures are very unlikely to threaten the TDRS mission.

### Heater Testing

Heater failures resulting from a flawed design with excessive cycling might have been avoided if heater performance and cycling were monitored during thermal-vacuum testing or other thermal environment simulation, for later comparison to design data. During a simulation of the thermal environment, it might be necessary to include conditions representative of a TDRS in sunlight (in different orientations) or in eclipse, with its various "hot" payload components powered or off, and with its thermal control material properties (e.g., absorptivities, reflectivities, conductivities, and heat capacities) represented as new or after aging. In this way, any condition that might result in excessive heater cycling might be discovered.

## ANTENNA POINTING INDICATORS

### Antenna Pointing Indicator Failures

After TWTAs, the components that have failed most often are parts of the gimbal drive electronics (GDE) used to read antenna positions. These parts are called null indicators. They are hermetically sealed, magnetically activated, mechanical switches with pin connectors and wiring. Their switching cycles are counted to determine the pitch (east-west) and roll (north-south) pointing positions of the east, west, and ground link antennas. Thus, there are six primary null indicators per TDRS, and each of these is accompanied by a back-up indicator. Another type of back-up exists in the form of ground station software that counts antenna movement commands to estimate pointing positions.

Null indicator failures were not predicted to be highly likely. The MIL-HDBK 217D failure rate of each indicator is very low, only a fraction of the 203 per billion hour failure rate of each GDE module. The expected number of GDE failures is 0.3, only a fraction of which would be null indicator failures.

Four null indicators have failed. All four failures affect pitch rather than roll indicators. Two of the failures are in the primary and back-up null indicators of the east antenna drive of TDRS 1. The other two failures are in the primary and back-up null indicators of the west antenna drive of TDRS 4. The times in service of the failed indicators were 0.00, 1.40, 2.23, and 6.49 years. The occurrence of the four failures in two primary/back-up pairs is remarkable for its random probability, based on the TDRS age distribution, of about 0.02. However, the pairings are unexplained, and convincing explanations of the failures are lacking.

### Antenna Pointing Indicator Testing

The apparently high rate of defects in the null indicators makes them good candidates for improved testing. On the other hand, the absence of an understanding of the cause of failure makes test specification problematical. The occurrence of the failures in primary/back-up pairs seems to indicate that the cause of the failures is in the design or environment of the switch pair, not internal to the switches. Thus far, ground testing of similar null switches under conditions somewhat representative of on-orbit operations has not resulted in a failure.

Test environment modifications that might appear to offer some possibility of reproducing the on-orbit failures include testing with thermal cycling, ionizing radiation, and, as in the case of the diplexers discussed above, rotation or vibration. Accelerated life testing of prototype null indicators, in which pertinent environmental factors are exaggerated, might also prove to be useful.

## GYRO

### Gyro Failure

The four TDRS 1 gyros were operated extensively to recover from a booster rocket failure during launch. One gyro failed three months later. Although each gyro exceeded its estimated 1500-hour design life by 1200 hours, the failure is counted in accordance with the criteria of this paper. Since each of the other three gyros continues to operate far beyond the design life (with current accumulated times in operation averaging 3900 hours), the failed gyro was probably defective rather than worn out.

The possibility remains that this failure at least in part is attributable to the failure of the booster rocket, not to TDRS 1 itself. However, this consideration is offset by the possibility that the uncounted thruster failures may not be entirely attributable to the booster rocket failure. In any case, since the very early gyro failure, no failures have occurred among either the three remaining gyros on TDRS 1 or any of the four gyros (some of which have logged almost 2000 operating hours) on each of the other four TDRSs in orbit.

### Gyro Testing

Any recommendation for additional gyro testing should account for gyro failure history. The TDRS gyro history is excellent, especially because each TDRS's long-term mission requires only one gyro. At the MIL-HDBK 217D failure rate of 2.06 per million hours, in the 26.3 TDRS-years of experience the expected number of additional failures is nine gyros, or an average of two per TDRS. Since none of these failures have occurred, the actual failure rate appears to be considerably lower. On the basis of on this experience, no additional testing of gyros is recommended.

## OTHER COMPONENTS

### Other Failures

The other TDRS components that have failed include the following:

Phased array receiver, S-band, primary (#10) on TDRS 1 at an age of six years (cause unknown)

Synthesizer, S-band return east, primary, on TDRS 1 at an age of six years (cause unknown)

West polarization switch stuck on TDRS 3 at an age of one year (caused by a short circuit, possibly related to thermal cycling, with insulation shrinkage and exposure of underlying wire)

Earth sensor electronics (ESE), primary, on TDRS 4 at an age of two years (cause unknown)

Master frequency generator (MFG), 955 megahertz output, primary lost on TDRS 4 at an age of two years (cause unknown)

Processor, S-band return east, primary (or possibly frequency synthesizer, S-band return east, back-up) on TDRS 1 at an age of eight years (cause unknown)

Thermistor on solar array of TDRS 6 during launch or deployment (caused by de-bonding)

The MIL-HDBK failure rates of these components are neither remarkably high nor low. The failures appear to be isolated and individually unpredictable events whose further description would not be useful here.

### Unfailed Component Types

All other components are unfailed. Interestingly, these include the TT&C transponders, encrypters, and decrypters, which are predicted to be TDRS reliability drivers. At the MIL-HDBK 217D failure rate of 14.5 per million hours, the total number of expected failures is 3.34. The probability of no failures when 3.34 are expected is 0.0354. Perhaps the unexpectedly good experience with the TT&C subsystem is attributable to its extensive early development, testing, and pre-launch operation.

### Other Component Testing

The predicted failure rates of other components do not appear to be particularly useful for planning a testing program. No additional testing of these components is recommended.

## CONCLUSIONS

The overall TDRS component failure history is consistent with high quality in design and workmanship, and with the total predicted failure rate from MIL-HDBK 217D. The philosophy of extensive redundancy combined with pre-launch performance and thermal-vacuum testing has been sufficient to ensure the continuous long-term availability of Space Network communication service.

Specific failures do not appear to have been predictable using MIL-HDBK methods. The types of components predicted to fail have not been the same as those that actually failed. Subsystems with extensive heritage have been much more reliable than predicted. Some new and modified payload components on TDRS 1 have been less reliable than predicted. However, the TDRS 1 failures led to design and manufacturing improvements on later TDRSs, whose reliabilities have been much better.

The principal components with an unsatisfactory failure history are the TWTAs on TDRS 1. These TWTAs have appeared to be subject to design error, resulting in both "infant mortality" and premature burnout. Their failures on orbit might have been avoided through sufficient accelerated life testing of prototypes, with both extended burn-in and power cycling. Without this testing, TDRS 1 failures had to occur before the TWTAs on later TDRSs could be targeted for improvement. The reliability of the improved TWTAs has been satisfactory.

The diplexer failure history presents an interesting testing challenge in which the migration of contaminating metallic particles in a weightless environment would need to be simulated. One approach could be the imposition of rotation or vibration during testing.

Accelerated life testing, rotation, or vibration might also be applied beneficially to antenna pointing indicators in order to determine the cause of their failures.

In the case of heaters, an accurate simulation of variations in on-orbit thermal conditions accompanied by monitoring of cycling rates might have prevented failures.

The TDRS reliability history appears to confirm the long-held view that additional testing can prevent on-orbit failures. Testing is particularly important for new and modified systems, subsystems, and components. From the failures experienced, it seems that accelerated life testing of prototypes including extended burn-in, cycling of applied power and ambient temperature, and rotation or vibration should receive especially strong consideration during the development of new spacecraft. However, identifying the types of components that merit more testing, and quantifying test conditions and durations so that they are consistent with procurement budgets and schedules, remain as major problems.

## REFERENCES


1. *Reliability Prediction of Electronic Equipment.* MIL-HDBK 217D, Department of Defense Rome Air Development Center, January 15, 1982.

2. TRW, *TDRSS Reliability Prediction/Assessment/Criticality Analysis Report Updates and TDRS Service Reliability Model,* March 1991.

3. TRW, *TDRSS Reliability Reports and Documentation - Reliability & Maintainability Analysis Updates - Final,* CDRL No. 511R03, June 23, 1989.

4. *Reliability Prediction of Electronic Equipment.* MIL-HDBK 217B, Department of Defense Rome Air Development Center, September 20, 1974, updated September 7, 1976.

5. TRW, *TDRSS Reliability Prediction/Assessment/Criticality Analysis Report,* Sequence No. RA-08, March 26, 1979.

6. *Reliability Prediction of Electronic Equipment.* MIL-HDBK 217E with Notice 1, Department of Defense Rome Air Development Center, October 27, 1986 and January 2, 1990.

7. *Reliability Prediction of Electronic Equipment.* MIL-HDBK 217F with Notice 1, Department of Defense Rome Laboratory, July 10, 1992.

# DAVID FLORIDA LABORATORY THERMAL VACUUM DATA PROCESSING SYSTEM

**Elie Choueiry**
David Florida Laboratory
Canadian Space Agency

## ABSTRACT

During 1991, the Space Simulation Facility, located at the David Florida Laboratory conducted a survey to assess the requirements and analyze the merits for purchasing a new Thermal Vacuum Data Processing System for its thermal vacuum testing facilities. A new, integrated, cost effective PC-based system was purchased and it uses commercial off-the-shelf software for operation and control. This system can be easily reconfigured and allows its users to access a local area network. In addition, it provides superior performance compared to that of the former system which used an outdated mini-computer and peripheral hardware.

This paper introduces the Canadian Space Agency's David Florida Laboratory then gives essential background on the old Data Processing System's features, capabilities, and the performance criteria that drove the genesis of its successor. This paper concludes with a detailed discussion of the Thermal Vacuum Data Processing System from its components, features, and its important role in supporting our space-simulation environment and our capabilities for spacecraft testing, here at DFL today. The Thermal Vacuum Data Processing System was tested during the ANIK E spacecraft test, and was in full operational mode at DFL in November 1991.

## INTRODUCTION

Located on the outskirts of Ottawa at Shirley Bay, the David Florida Laboratory (DFL) is the Canadian Space Agency's facility for the assembly, integration, and environmental testing of both satellites and other space hardware (spacecraft). DFL is available to domestic and foreign companies or organizations involved in aerospace and telecommunications. DFL's integration and assembly areas comprise three large temperature- and humidity-controlled clean areas.

The thermal vacuum (TV) facility contains multiple TV chambers used for space simulation testing. The infrared (IR) testing system is used to test and verify the thermal design, and the workmanship of spacecraft. Our customers use DFL's vibration facility to perform vibration tests and our staff do vibration and modal analyses to ensure that spacecraft structural integrity is maintained. Finally, antennas and RF payloads are evaluated using our anechoic chambers.

## BACKGROUND

### The Old Data Processing System (old DPS)

The old DPS was in use for more than a decade before its performance became questionable. Attempts to improve its reliability and efficiency were disappointing because its configuration was out-of-date. The old DPS's hardware was three DEC PDP 11 minicomputers (one 11/23 and two 11/34s), three 5 Mb hard disk drives for system control and temporary data storage, one 800 bpi tape drive for data archival, and peripherals for sampling input data and displaying output data from the old DPS. In the event of a system failure, one of the minicomputers was ready as a backup to the primary. If left to continue operating, the old DPS's hard disk glitches and computer outages could compromise DFL's capabilities. DFL policy is to safeguard expensive spacecraft.

At DFL we made a survey of customers and staff to assess the requirements of a replacement system that met the new industry specifications and provides the means to continue to successfully bid against other aerospace testing facilities. The following discussion of the old DPS's capabilities will provide the background against which we established its successor, the Thermal Vacuum Data Processing System (TVDPS).

## Old DPS Configuration and Capabilities

Software calibration curves to the 5th-order polynomial were done to all (64) telemetry input channels and half (384) of the available sensor input channels. At maximum configuration, the old DPS processed 64 telemetry input channels from two telemetry decommutation units as well as 768 sensor input channels from six dataloggers. Each datalogger processed a maximum of 128 sensor input channels. Sensor input channels used the standard inputs for thermocouples (TC), resistive temperature detectors (RTD), and voltage measurements, as well as special inputs such as calculations (averaging and rate-of-change determinations). As required by a TV test, alarm checking for all data was done and up to six sets of alarm limits were set by the users. Each set of alarm limits had four parameters such as low, lower, high, higher and all parameters, which could be modified during the test. A maximum of 420 old DPS outputs could be defined for CRT display; 168 of these displayed at any one time and of these, 45 were displayed graphically. In addition to its CRT displays, all old DPS outputs were displayed in either historical or single record hard-copy formats.

The old DPS temperature measurement system enabled temperatures to be accurately measured due to the configuration of the old DPS, the design of a Uniform Temperature Reference (UTR) block and case assembly, and the design of specialized feedthroughs. While maintaining a homogeneous temperature throughout all the attachment points, the UTR could accept up to 30 TCs. Two separate copper extension cable assemblies interfaced each UTR block to a datalogger. The reference temperature for the TCs therefore, became UTR temperature. This UTR temperature is measured by comparing it with a 0 °C reference TC immersed in an ice bath outside the vacuum environment.

## Requirements For The New Data Processing System (TVDPS)

The TVDPS must be capable of processing in excess of 1000 channels simultaneously and meet the following criteria:

1. High reliability. To ensure reliable TVDPS software and hardware, and that the TV chambers could operate 24 hours a day, seven days a week
2. Maintainability. A maintainability program is always active to ensure that preventative and remedial maintenance is performed on equipment as specified or necessary
3. Flexibility. Able to interface to industry-standard data acquisition and control equipment, including programmable logic controllers, board-level A/D converters, dataloggers, and high-performance external A/D converters. Interface communications to be standard IEEE-488 (GP-IB) or RS-232 (serial) connections through either a SCSI interface, or shared-RAM plug-in boards.
4. Versatility. TVDPS to be modular, users could add features such as graphical display devices and drivers, data storage and management options, and custom programming utilities.
5. User interface. TVDPS to allow users to quickly and efficiently master system commands from our graphical user interface's pull-down menus – each supplemented with on-line Help and editor screens.

## Market Research And In-House Testing Results

In 1991, during the ANIK E spacecraft testing, DFL staff finished the preliminary investigations into the requirements for the proposed TVDPS that could process more than 1000 channels simultaneously and meet the following:

The preliminary investigation used the following hardware:

- a file server (80386)
- a data acquisition computer (80286) with an 8-line serial interface to communicate with eight data loggers (Kaye)
- three user stations (80286/80386sx)
- Ethernet LAN cards and cabling
- a custom, serial I/O box for simultaneous monitoring of data loggers by both the old system and the new system
- Novell SFT Netware software.

Testing of the TVDPS software was performed by a software analyst using ASYST (scientific and engineering software that performs data acquisition using three type of interfaces, A/D, GP-IB/IEEE-488, and RS-232). ASYST tests on the TVDPS were done in parallel with the TV testing of the ANIK E satellites (Flight 1 and 2). Results were compared to those obtained from the old DPS. Although few software bugs were found in the TVDPS, testing results indicated that the TVDPS's reliability was satisfactory, its performance on the required tasks was slow but could be improved by using faster PCs (80386 or 80486) and state-of-the-art data monitoring software, and also using PC-based hardware and software that is capable of handling the functional requirements of a spacecraft data acquisition system.

The test results of the TVDPS allowed DFL staff to conduct a vendor survey of state-of-the-art data acquisition software. They reviewed the following software:

- Autonet by Imagination Systems Inc. (QNX)
- Scadix by Pioneering Controls Technology Inc. (UNIX)
- Labtech by Laboratory Technologies Corp. (UNIX)
- Paragon 500 by Intec Controls Corp. (DOS)
- FIX DMACS by Intellution Inc. (DOS)

As a result of the analysis, the Autonet software package was chosen to replace the old DPS software, mainly because Autonet met most of the listed requirements.

## THE TVDPS TODAY

The TVDPS controls one or several TV tests while acquiring raw-data, performing real-time computations on raw-data, and storing both the raw- and massaged-data. The TVDPS's human-factors engineered operator interface and its system reports, test reports, and process information, is easily understood by the technician, computer operator, and customer. For research scientists and engineering personnel, the TVDPS provides access to detailed historical system data and file management data. All of this information is available in soft-copy and hard-copy formats.

The TVDPS's operating system is real-time, multi-tasking, multi-user, with peer-to-peer distributed network capability. Depending upon the devices attached, TVDPS communication is serial (RS-232, 422, 485) or parallel (IEEE-488). The TVDPS monitors about 1000 data channels,

The integration of the current TVDPS was made at DFL with PC hardware from Dell Corporation. A distributed peer-to-peer architecture and built-in network capability was incorporated into the system integration plan.. Enhancements were made to existing patch panels (junction cabinets for data lines).

Major elements of the current TVDPS are: analog input devices, a primary node controlling analog input data, a user node, and local area network hardware. Any combination of TC, RTD, V and I inputs may be connected to the TVDPS dataloggers. Wherever UTRs are provided for interfacing sensor inputs to TVDPS dataloggers, temperature measurement accuracies of $\pm$ 0.5 °C are achieved for all TCs measuring temperatures between $\pm$200 °C (Error does not include TC inaccuracies of as much as 1 °C).

Major software components are: a QNX operating system with embedded network capabilities, and AUTONET data control software. AUTONET software receives input sensor data, and processes it with user-defined calculations and control algorithms, and also checks alarm limits (stored in an area of the central processor's memory called the point database). The TVDPS's QNX operating system can monitor, log, limit-check, and graphically display data as it is updated. Data-update rates and data-throughput rates are dependent on the specific data acquisition unit being used and TVDPS configuration. Historical data may be accessed alongside current data. A typical task switch rate is 140 µs on an 80386/20 MHz PC and 25 µs on an 80486/25 MHz PC.

## TVDPS HARDWARE

### Computers

The current TVDPS uses three 80386 based, and twelve 486 (80486/dx33-66 MHz) PCs (from the same manufacturer) of which, three of the 80486 PCs have high speed tape backup capability. Each PC has 8 Mb of RAM (minimum). On a distributed PC network, the benefits of using similar computers by the same manufacturer allow the system to be easily reconfigured at any time.

The PCs are divided into three categories: primary nodes, backup nodes, and user nodes. The primary nodes are the kernel of the networked data acquisition system and are of two Dell 80486/dx33 MHz computers with 12Mb of RAM and a 650 Mb hard disk. Two identical PCs are physically located beside these primary nodes and as backup nodes, they provide backup capability in the event of a primary node, system failure. Beyond this backup capability, a third identical PC is idle and can be configured as a primary node if ever required. The remaining PCs are user nodes dedicated for data display and data analysis when the spacecraft test is in progress.

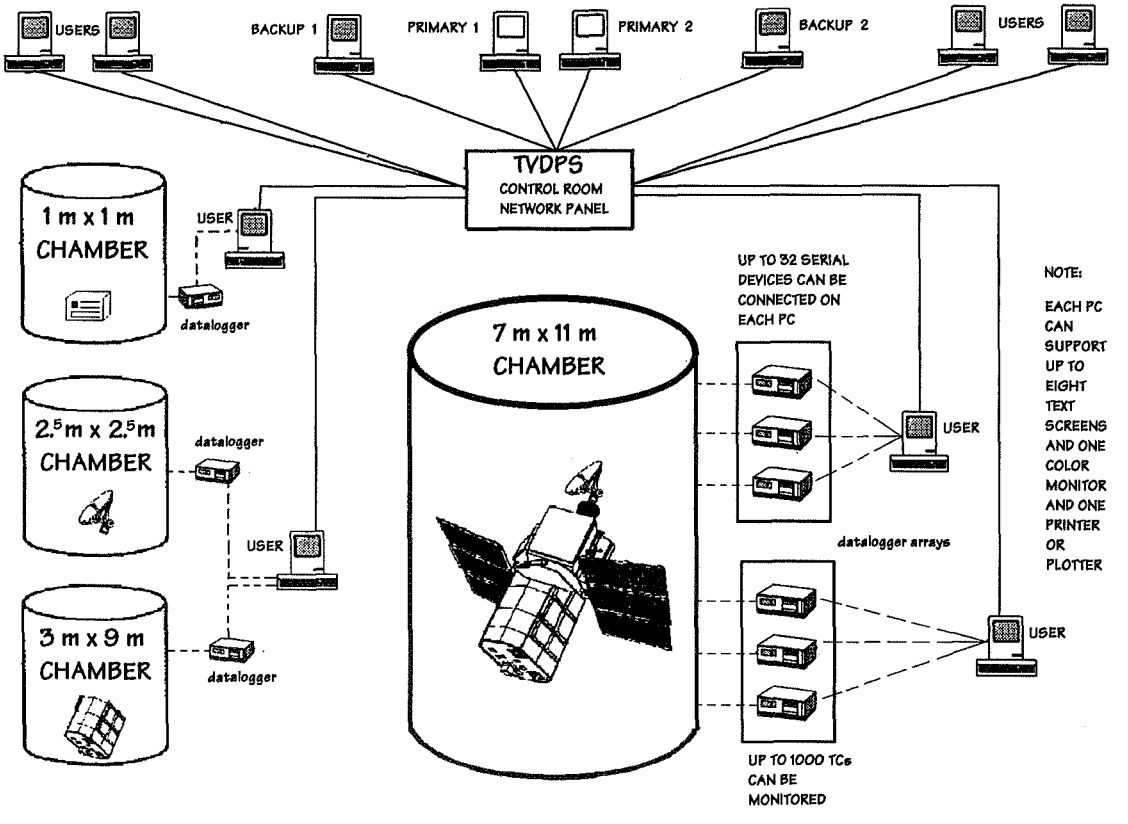


Figure 1. A Conceptual Schematic of the TVDPS

### Peripherals

Each PC has an Arcnet (token ring) LAN interface board, and a Connect Tech Intellicon-8, serial coprocessor board. The Arcnet card provides very high speed communications between as many as 254 different computers. The Arcnet board uses Arcnet as its physical transport layer. It is a token-passing protocol that implements a high-speed, error-free, acknowledged transfer of data between computers. This means that the network is virtually immune to noise. The bit rate is 2.5 Mb/s. Every byte is transferred in 11-bit synchronous form resulting in a usable data transfer rate exceeding 200 Kbytes/sec. Arcnet implements low-level buffer negotiation in hardware and automatically performs flow-control

data transfer between computers without the need for complex buffer management. The Connect Tech-8 serial coprocessor board consists of eight intelligent multiports used to format data displayed on node monitors. Also located on existing nodes, are several laser printers and ink-jet plotters that are accessed from the network to generate either graphs or hard-copy reports.

### LAN Hardware

All TVDPS PCs are connected to one another by an Arcnet LAN. The Arcnet LAN uses traditional star topology and can provide logical addresses for 256 devices. Active hubs connect up to eight PCs by coax cable (RG-62/U) to the LAN. As long as the rules for connecting LAN devices are observed, PCs can be removed or added to the LAN with ease. The LAN can be expanded by cascading up to eight hubs. Using coax cable, active hubs can be connected up to 2,000' apart.

### Analog Input Instrument

The TV facility has ten, Kaye Digi-4 Link dataloggers as its primary analog input devices. Inputs from these dataloggers (or their equivalent) can be any combination of the following:

- Type 'T' TC inputs, internally referenced, (using the data logger's isothermal referencing hardware) with a minimum system accuracy of ± 0.006%, + 0.25 °C @ 0.01 °C resolution, and ± .003%,+ 0.50 °C @ 0.1 °C resolution (based on a yearly calibration cycle)
- Type 'T' TC inputs, externally referenced using DFL's UTR blocks (isothermal uniform temperature reference) with a voltage-measurement accuracy (minimum) of 0.006% of reading + 1 count + 2 μV based on 16 bit, + sign, A/D conversion (based on a yearly calibration cycle) with a maximum V to temperature conversion error of +/- 0.06 °C
- Other major TC inputs, such as Type J, or K, internally referenced, @ 0.1 °C resolution;
- RTD inputs (10 ohms cu, or 100 ohms pt) @ 0.1C resolution
- Voltage inputs, 0 V to ± 12V with a minimum system accuracy of ± 0.006% of reading + 1 count + 2 μV based on a 16 bit A/D (+ sign) conversion (based on a yearly calibration cycle), with a four voltage ranges (minimum)
- All datalogger inputs are internally converted to engineering-unit outputs where applicable, with an output resolution of 4 1/2 digits plus polarity sign(minimum)

Other instruments include the DFL thermal chamber and static load facility data acquisition systems, manufactured by HP (HP 3852 data acquisition and control unit), and an in-house-designed Microprocessor Level Controlled power supply for the TV facility's heater rack inputs (associated processors are configured as two Kaye dataloggers to achieve maximum input device configurations for communications purposes). The processors generate P, I, or V engineering-units as output data for all 256, microprocessor-controlled power supplies.

Any operator can isolate any physical input device (data logger, heater rack, or telemetry unit) from scanning. Input data values may be checked using the Operator's data terminal. Custom software is used to enable such devices as the ion gauge readouts, Quartz Crystal Microbalance (TQCM), and mass spectrometers, and display these on the TVDPS.

## MAJOR SOFTWARE COMPONENTS OF THE TVDPS

### Network management

Arcnet's token ring architecture consists of passing predefined blocks of data (tokens) around the network, one node at a time, with each token requesting data. If a node wishes to place data on the network it waits for an empty token and then occupies it. If the token is filled, a busy signal is sent so that other nodes cannot intercept it. The destination node then accepts the data, empties the token so it can request data again. There are no data collisions since only one node can transmit at a time and likewise, only one node can receive at a time.

### Operating System

The TVDPS's QNX operating system runs under a modular real-time kernel similar to the UNIX operating system. The current QNX version (v.2.15) is highly efficient and occupies 150kb of RAM. Since the operating system is embedded in the TVDPS's software, access to the operating system by users is unnecessary.

### Real-Time Processing

The TVDPS's QNX operating system has the ability to monitor, log, limit check and graphically display data updates in real-time. Update rates and throughput rates are dependent on the data acquisition unit and the system configuration. Data from the point database can be directly accessed in real-time for output control, for plots or tabular data analysis, or for saving datalogging features to a hard disk drive. Historical data can be accessed when the TVDPS is operating. The typical task switch rate is 140 μs on an 80386/20 MHz PC and 25 μs on an 80486/25 MHz PC.

### Multi-Tasking

The TVDPS O/S allows the operator to multitask. In other words, it permits the TVDPS to perform multiple tasks concurrently. Examples of multitasking include: the receipt of sensor values from data acquisition units, the monitoring of system alarm conditions, transmitting data to a printer, processing graphics on CRTs, and enabling data to be stored disk. A maximum of 200 concurrent tasks may be run at a given time.

### Multi-User

The TVDPS supports multiple users on each PC, locally or on the LAN. Nodes can connect physically or by modem to a remote PC as required. When a node is in terminal mode, only text based screens may be accessed.

## AUTONET'S SPECIFIC FEATURES

Autonet offers multiple features that can be exploited depending on the requirements of the host system and the complexity of the host network. Some of the specific features include the following:

- Easy to Use and Set-up
- Menu Driven, Range Checking, Pop-Up Windows, Menu Security
- Real time operator displays
- Tools such as: Bar graphs, Panel Meters, Dial Meters, Circular Charts, Trend Graphs, Strip Charts, X-Y Plots, X-Y-Y profile, Spreadsheets, Instrument and Control Panel.

The Trend Display option offers the capability to define both real-time and historical Trend Displays with the following features:

- definable time base to display the data in seconds, minutes, hours, or days
- independent, user-definable, left and right Y axis scaling
- up to 15 different channels displayed on one trend graph
- select from 16 different colors for the each channel
- select from 12 different symbols to uniquely identify each channel on the node's viewscreen or its hard-copy printout
- select data from that stored on the hard disk (for any time period) to create an absolute, or relative-trend display on the node's viewscreen or its hard-copy printout
- the historical trend display allows a trend plot over a practical length of time to be seen on the node's viewscreen or its hard-copy printout
- horizontal orientation with dynamic scrolling from right to left on the node's viewscreen.

The instrument and control panel feature allows the operator to replace or supplement electro-mechanical instruments. With emulation of over 100 different instruments, each instrument and control panel is easily configured through a menu-driven fill-in-the-blank process. The instrument and control panel feature can update at a speed of 60 Hz.

### Logging administrator capabilities

The TVDPS provides various methods of logging sensor data to the host workstation's hard disk drive. The logging method is dependent on the type of data acquisition unit used.. Multiple and varied logging schedules can run concurrently. The summary logging routine summarizes interval-based data that was previously logged to the host workstation's hard disk. The summary log performs the following calculations for all previously recorded data that was logged in the selected time period: minimum and maximum value with time of occurrence, average, total, and total number of logged values. Logged data is available for display on a node's viewscreen, for historical trend reports, and for conversion to standard DOS file format. Logged data can be grouped for summarizing as often as once per minute, as infrequent as once per day, or even over a period of a range of days.

The File Transfer feature provides the export of historical data to a variety of formats. Data may be exported to a floppy disk, hard disk, or RS-232 serial port in the following data formats: ASCII, DIF, PRN, DFBIII and SCN. It also supports Kermit transfer protocol and host login script activation.

### Alarm administrator capabilities

The alarm administrator offers the following capabilities: real-time alarm monitoring, file management, and utilities.

Real time alarm monitoring has the following features:

- Up to four threshold limits and one rate of change limit per channel
- Option for user acknowledgment of each alarm
- Alarms automatically time-stamped and logged to disk
- Viewed via alarm summary screen, color coded and prioritized
- User-defined alarm limit video display colors
- Alarm reports and acknowledgments (check-time for alarm limits is $< 50$ μs).

### Utilities (Serial I/O Module)

The serial I/O module is capable of transferring scanned data from a TVDPS node, from remote and local RS-232 communications, to another TVDPS node, as well as receive data from an RS-232 device. The RS-232 output utility permits the transfer of real-time data over an RS-232 communications link, direct-connect or modem, from one TVDPS node or host computer to another host computer. The Kermit communications protocol ensures error-free file transfer. Output scans for multiple devices can be defined by the user. Each output scan can be configured to include scan rate, communications parameters, record separators, and so on, for use in transferring real-time data to remote TVDPS graphics workstation, or a non-TVDPS computer.

### Performance of the TVDPS

Since replacing the old DPS, the TVDPS system has proven to be the right choice for our aerospace testing facility. The new hardware proved very reliable with only few, infant-mortality type failures during the first months of operation. Our current software had some bugs not detected earlier due to the mode and complexity of network operation. However, all reported bugs were corrected by Autonet's manufacturer for its next version, but we are using the existing version because we have a reliable workaround to sustain us during the current work schedule. As a result, a new I/O Ram Cache card was installed on the primary node to accelerate the recovery time of the data base in the event of a node failure. The design of the TVDPS's user interface has reduced the learning curve to produce real savings in time required for test setup, definition of I/O channels, and data displays (graphical and tabular formats supported).

So far, over 90 tests were done and the number of TCs used in these tests ranged from only a few to over a thousand. For example, MSAT's complex IR test required the setup of over 1460 input channels on the TVDPS. They were as follows: 710 devoted to MSAT spacecraft and the IR rig structure, 240 for telemetry , 210 for thermal control, 165 for calculations, and 139 for miscellaneous inputs. Immense processing power was required to compare telemetry data with the MSAT spacecraft's temperatures during each phase of the test. For this purpose, one TVDPS node was connected to the MSAT spacecraft telemetry system (DEC 4000/200 VAX). An interface routine was implemented to serially receive ASCII formatted data at 9600 baud from the DEC 4000/200 VAX. This information was sequentially

retrieved and stored in the TVDPS's internal database. Then, real-time or historical time plots could be generated to correlate any number of activities, at any time, during the test.

Intermittent node failures due to unreported bugs only interrupt our datalogging for at most, only a few minutes. DFL's future plans are to upgrade the existing Autonet version within six months. The plans include using the new features of Autonet's modular software. These new added features will permit the TVDPS to be more versatile, flexible, and continue to maintain the open architecture concept needed to integrate new computer platforms as required.

## TVDPS BENEFITS

Major improvements have been achieved since the introduction of the TVDPS into the DFL. These benefits include the following:

- Significantly improved system reliability and diagnostic capability
- Increased efficiency of test article data monitoring from using state-of-the-art software and 32-bit PC hardware. Also, the TVDPS hardware configuration provides 100% backup of the TVDPS's real-time data monitoring capability (old DPS backup capability was 50%). Historical data processing capabilities will run concurrently with full-up spacecraft real-time data monitoring
- Elimination of adverse impacts on customer testing that resulted from failure of the old DPS and current computers and peripheral hardware. Simplified switchover to backup system support due to main node system failure
- Significant enhancements to test article mnemonics definitions, calculation capabilities, display, print spooling capabilities, hard-copy and data transfer capabilities to remote PCs, and so on. Also, data storage requirements will be streamlined, cutting permanent data storage costs by 75% to 85%. Capability to support future requirements for the expected sophisticated, knowledge-based, data acquisition design enhancements will be supported
- Significant reductions in hardware maintenance costs. Expect over $100K in savings over the first five years
- Significant reductions in software maintenance costs from substantial usage of off-the-shelf software
- Significant cost reductions in both hardware and software procurement costs during future expansions of the facility due to increased usage of PCs
- Sharing of resources in a peer to peer LAN PC workstation providing clear test, or process information in formats familiar to the technician or computer operator as well as providing detailed historical analysis and file management functions useful to research or engineering personnel.
- Test data can be transferred on different media on diskette or tape using standard data compression routines (can be up to 100:1 compression on test data files). Test data can be in an data interchange format ready for user analysis (post-test) on any standard PC spreadsheet program. This method will save an tremendous amount of data storage space and resources as compared to the old DPS methods (which was mainly hard-copies).

## CONCLUSION

The TVDPS has proven profitable for DFL's requirements. Its main advantage is the relative low cost of today's powerful PC based systems vs. higher priced workstations and mainframe computers. The TVDPS is also flexible enough to allow it to be reconfigured and redesigned as necessary, and its user friendliness is appreciated by first time customers. Also, output data can be transferred on different media (floppy, tape, compact disk). Finally, the ability of the operator to develop customized applications makes the TVDPS very beneficial to the customer.

# THERMAL BALANCE TESTING OF MSAT 2 SPACECRAFT

Serge Samson
Spar Aerospace, Ste-Anne-de-Bellevue

Elie Choueiry
David Florida Laboratory, Canadian Space Agency

## ABSTRACT

The present work reports on the recently completed infrared thermal balance/thermal vacuum testing of a MSAT satellite, the first satellite to provide mobile communications service for all of continental North America. MSAT is a two spacecraft program, using a three-axis stabilized Hughes HS-601 series Bus as the vehicle for the Canadian designed Payload. The thermal tests which were performed at the Canadian Space Agency's David Florida Laboratory in Ottawa, Canada, lasted approximately 35 days.

The infrared (IR) heating rig was designed to provide radiant heat inputs into seven spacecraft zones during Thermal Vacuum (TV) testing. The TV test was divided into multiple phases. It began with a thermal balance cold phase, followed by a thermal cold cycle and a hot balance phase, complemented by a thermal hot cycle to finish with a thermal cycle with continuous monitoring of the Bus and Payload. The spacecraft's external heat fluxes were provided by IR lamp sources. To ensure flux uniformity, highly reflective baffles and IR East and West faces; the Earth facing (Nadir); and the inside of the thrust cylinder. The aft-end panel heat fluxes were provided by a heated $LN_2$ shroud. The radiation flux intensity on the spacecraft zones from the various rig elements was measured using Monitored Background Radiometers (MBRs) and compared with direct calculations and with pretest predictions.

The temperature measurement system was based on Uniform Temperature References (UTRs) located inside the chamber such that all feedthroughs were copper-copper. This system was devised to achieve a temperature measurement accuracy of +/- 0.5°C for over 850 thermocouples used in the test. A PC- (QNX-based) based real-time data acquisition system was ultilized to provide continuous monitoring of all channels based on a 30-second time scan. In addition, the data acquisition system was able to retrieve telemetry stream from the Satellite Test Equipments (STE) station for real-time data manipulation.

Preliminary results showed the test to be successful from both the thermal balance side and the electrical testing side.

# THE REALUMINIZING OF THE 7-METER-DIAMETER SOLAR SIMULATOR COLLIMATING MIRROR

E. W. Noller
Jet Propulsion Laboratory
California Institute of Technology
Pasadena, CA

## BIOGRAPHY

E.W. Noller has been involved with space hardware design and the development of special space simulation techniques for flight projects at the Jet Propulsion Laboratory. He is a member of the original engineering team that designed the solar simulation system for the 7.62-m (25-ft) Space Simulator Facility. He has designed thermal vacuum simulator systems, beginning with Viking solar panels and continuing with the Magellan and TOPEX spacecraft solar-panel testing systems. He has researched vacuum deposition of thin and thick films on large composite reflectors, antenna elements, and metal optics. He is currently the cognizant mechanical engineer for the vector helium magnetometers on the Ulysses and Cassini spacecraft.

## ABSTRACT

This paper describes the modification of a three-electron-beam (EB) gun system for vacuum depositing a highly reflective aluminum coating on a 7.01-m (23-ft) -diam nickel-plated aluminum collimating mirror. The mirror is part of the JPL 7.62-m space simulator that was recently modernized with a new high vacuum pumping system, solar lamp power supplies, solar optic lens system, and refurbished collimating mirror.

The 7.01-m 12,700-kg (14-ton) spherical collimating mirror was removed from this facility for replating with 381 μm (0.015 in.) of electroless nickel and polished to a specular finish for realuminizing. The space chamber served as the vacuum coating vessel for the realuminizing coating process. The mirror is the primary reflector for the solar simulation system and the aluminized reflective surface is its most critical performance element. The uniformity of thickness and high reflectivity of the coating in visible and near-ultraviolet (UV) light governs the accuracy of the beam for solar testing. The uniformity of the thin-film thickness also controls the durability of the mirror over time. The mirror was polished to a 64-percent reflectivity with a uniformity of 1.5 percent. The performance goal for the aluminizing was 89 percent with +/— 0.5-percent variation over the mirror.

## KEY WORDS

Solar simulation; aluminizing; mirror.

## INTRODUCTION

Aluminizing the 7.01-m-diam mirror with a 508-cm (200-in.) spherical radius was one of the major tasks in refurbishing the solar simulation system as part of modifications to the 7.62-m space simulator facility. These modifications are to be completed in this calendar year. Reconditioning and modifying the facility's mirror-coating equipment was part of the support activity required to complete the replating, reconfiguring, and polishing of the large mirror. The evaporation system, which had not been used for many years, needed reengineering and replacement of obsolete elements that were no longer reliable or serviceable. The goal for recoating the mirror was to improve control of the uniformity of reflectivity and the symmetry of aluminum thickness over the mirror's large area. The original system, developed in 1964, is part of the facility's support equipment. The mirror and simulator facility recently underwent a major modernization to the vacuum-pumping system and the solar simulation optical system. The 7.01-m-diam 12,700-kg spherical collimating mirror was electroless nickel plated and polished to a specular reflectance (Fig. 1).

The realuminizing process is one of the most critical elements in the performance and quality of the simulated solar environment. The reflective coating, in its uniformity of reflectivity in the visible and near UV, governs the accuracy of the beam for solar testing. The uniformity of the thin-film thickness controls the quality and durability of the mirror for

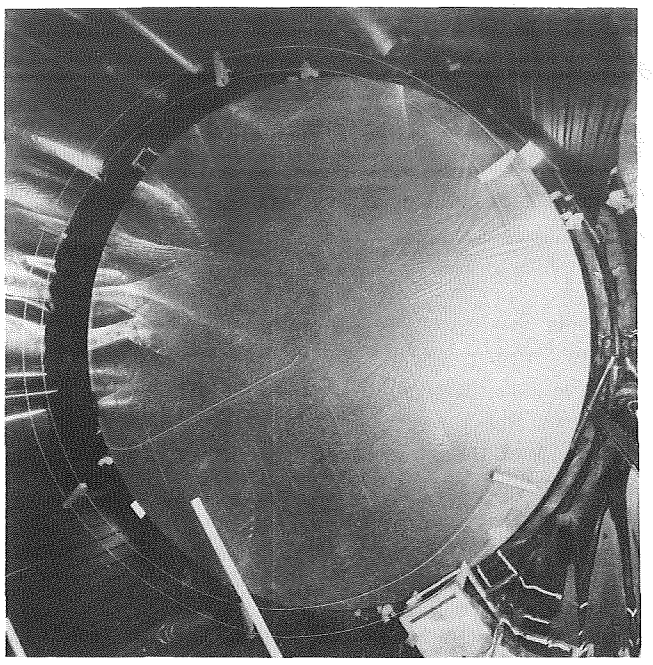

**Fig. 1. 7-m mirror with cover bag.**

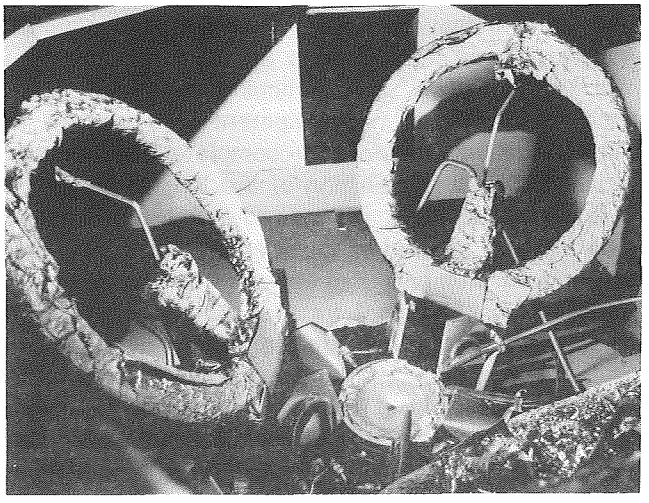

**Fig. 2. EB gun source.**

testing space hardware. Figure 2 shows the modifications to a three EB gun evaporation system used in the aluminizing process.

## REQUIREMENTS FOR COLLIMATING MIRROR PERFORMANCE

The primary element in the solar simulation system is the collimating mirror, which relays the output of 37 lamps through two sets of lenses that are the integrating optics for collecting and projecting light onto the collimating mirror that then relays the light to the chamber testing area. The performance requirement is for a +/— 5-percent uniformity over the 5.63-m-diam solar beam test area. The mirror nickel surface was polished to a 64 percent reflectivity with a uniformity of 1.5 percent. To realize maximum reflectance (e.g., 90-percent reflectivity with 2.5 percent variation over the mirror diameter) from this high-quality surface, improvement in the control of the vapor source was needed. The operational cost savings in power consumption and Xeone lamp burn life and the high cost of recoating the mirror also drove the requirement for Optima coating, since it delivers a long usable service life in the testing environment.

## SPACE SIMULATOR FACILITY CONFIGURATION FOR VACUUM-COATING OPERATION

The 25.9-m (85-ft)-high space simulation chamber has fully cryo-shrouded walls and floor, ten 121.9-cm (48-in.) cryo pumps with gate valves, and two turbo pumps. The 8.22-m (27-ft)-diam vacuum vessel has a test volume of 7.62-m (25 ft) diam inside the cryo shroud (Fig. 3). The mirror is located 24.3 m above the chamber floor in the horizontal position for aluminizing. The normal position for the mirror in the system is 7.5 deg off vertical. The mirror is supported from the chamber roof, and by three wiffel trees to 12 connections to the mirror rim. The mirror hangs face down and is leveled for optimum geometry for coating. The normal system location for the collimator is tilted 7.5 deg to relay the beam into the test volume. The aluminizing source is located at the center of a service work platform that is positioned 8.71 m (28.5 ft) below the mirror. The platform itself is located 9.14 m (30 ft) below the mirror and supported by cables inside the vacuum chamber during the aluminizing operation (Fig. 4). System control and operation is conducted from the cryo pump room, located half way between the mirror and source. Ports are clustered for utilities, viewing windows, and mechanical feed throughs for exposing the vapor source (Fig. 5). Power supplies are located nearby for the high-voltage bus supply to the guns. Transformers for the glow discharge system are also collocated (Fig. 6). All instrumentation and the control racks are on the platform surrounding the viewing port for the coating operation, along with

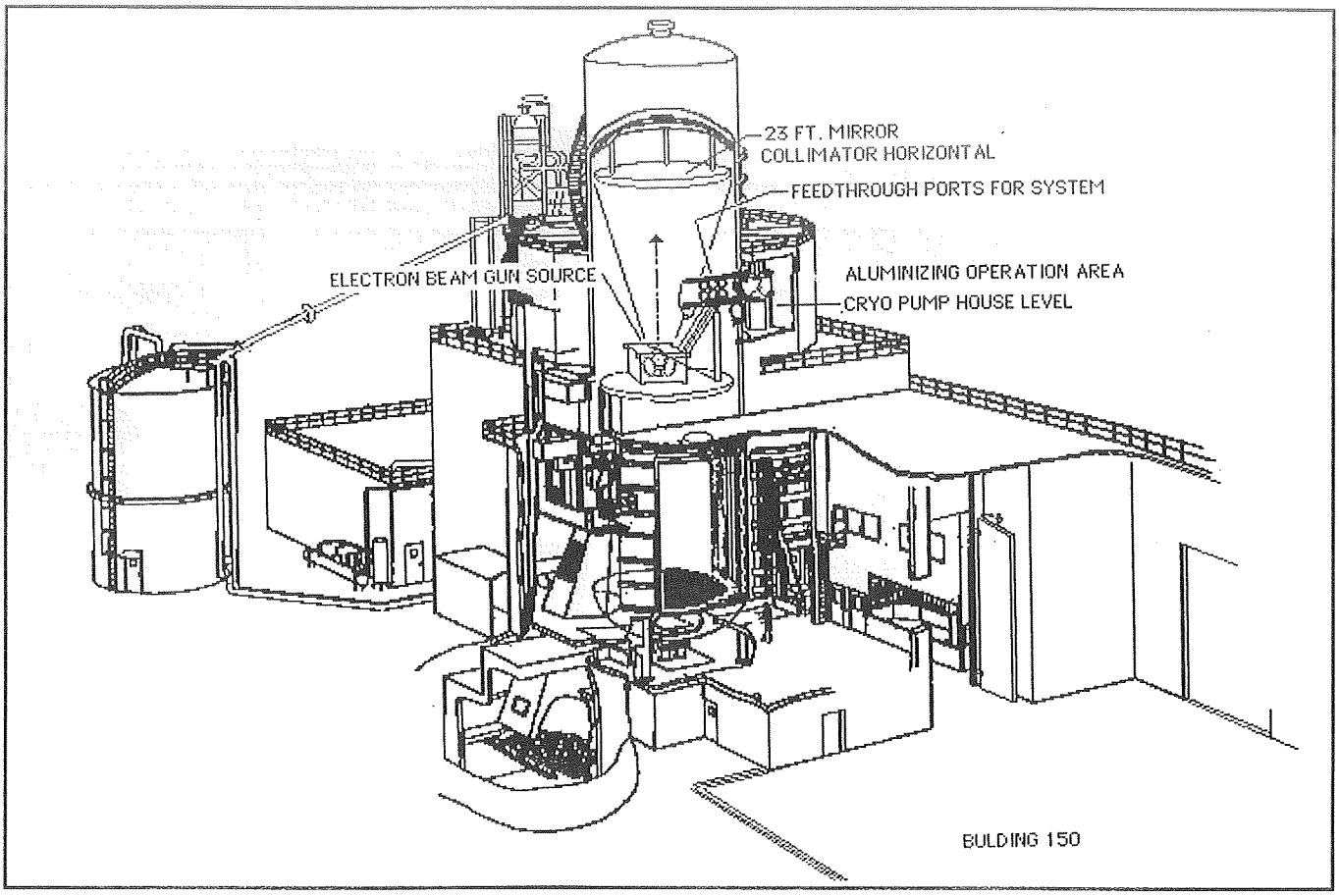


**Fig. 3. View of the Space Simulator Facility.**

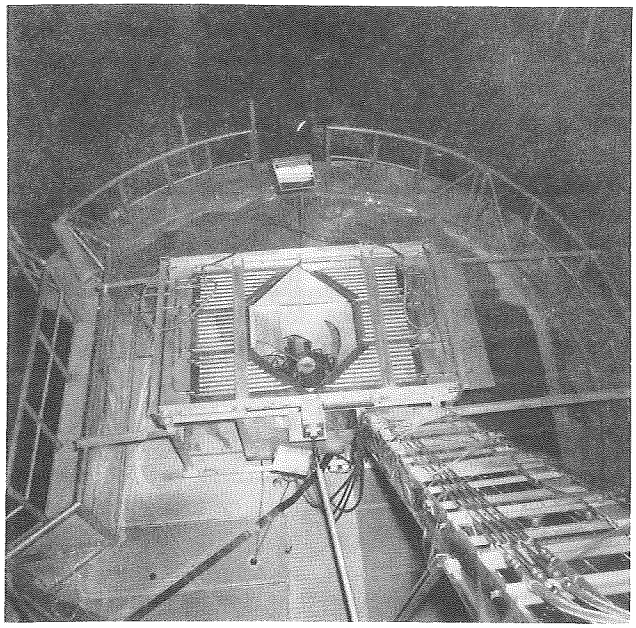

**Fig. 4. Aluminizing equipment platform.**

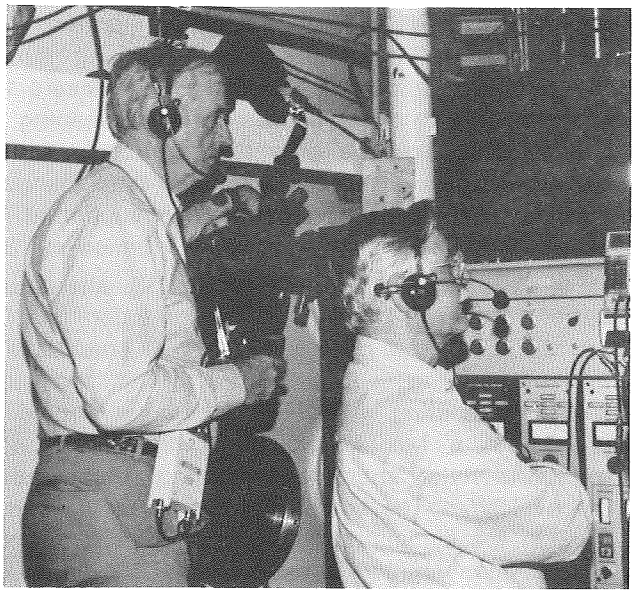

**Fig. 5. Control center for aluminzing process.**

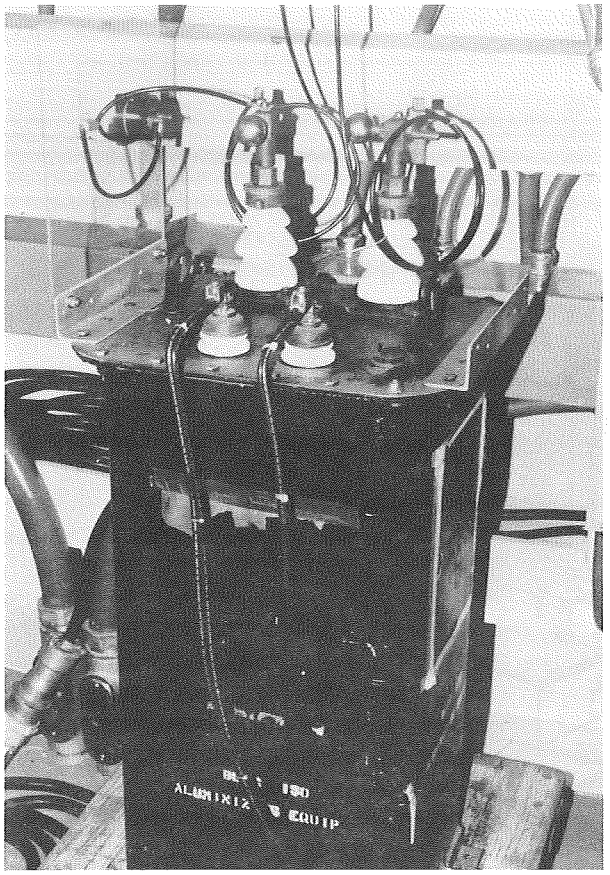

**Fig. 6. Glow discharge transformer.**

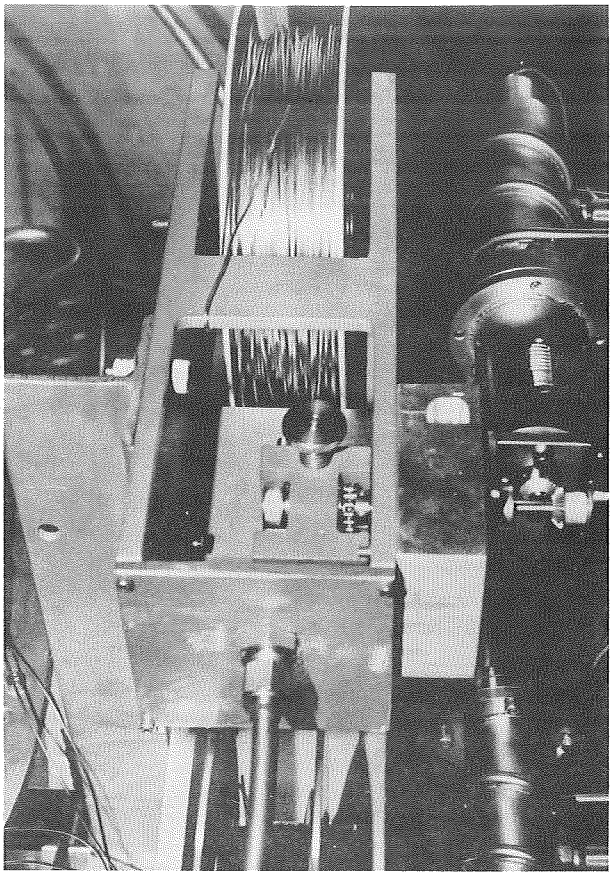

**Fig. 7. Dual wire-feed assembly.**

two telescopes and a television monitor. A vacuum-rated TV camera with a turning mirror looks through a port in the EB gun enclosure for close-up visual observation. Plasma cleaning is accomplished using a glow discharge source that consists of two concentric aluminum rings hanging 1.82 m (6 ft) below the mirror face supported by cables. The glow discharge was performed at 13.3 mPa ($10^{-4}$ torr) at 10,000 volts (V) alternating current (ac) with partial pressure of argon gas for 20 minutes. The chamber cryo wall shrouds are masked by hanging mylar panels to keep the walls free from coating. The EB gun vapor source is located in a box-like housing with a horizontal guillotine-style shuttered opening that opens mechanically. The source is exposed to the mirror through the symmetrically wedged aperture formed by the open shutter halves. Three 270-deg guns are symmetrically positioned around a 14.6-cm (5.75 in.)-diam crucible supported on a water-cooled hearth. Two aluminum-wire-feed mechanisms adjacent to the crucible replenish the aluminum (Fig. 7). Five quartz-crystal-thickness monitors are located around the edge and a sixth is at the center of the mirror.

## ELECTRON-BEAM GUN SYSTEM MODIFICATION

The EB gun system was developed in the early years of the space program for aluminizing the collimating mirror. The mechanics for steering the electron beams in the crucible were primitive and incapable of producing controlled beam movement at the high sweep rates required to affect vapor distribution. The primary change to the system was the use of a three-phase frequency generator with adequate power to drive the gun's primary focus coils above 10 Hz. The three-phase Helmholtz sweep coils are located at 30-deg off-vertical on each gun axis and are primary in keeping the beams from crossing over each other, which could cause superheated eruptions in the molten aluminum. The three-phase-

induced fields are used to move the beam from right to left along the axis of each electron gun. High-temperature thermocouples that sense cruci-ble temperature during evaporation were added to better monitor the thermal inertia in the molten aluminum during the aluminizing process. The experimental coating cycles that were made showed a direct correlation between beam power, aluminum level in the crucible, and evaporation rates. To supply adequate aluminum to the crucible for high-evaporation rates, a dual aluminum wire-feed system was added. To calibrate the system, five crystal-thickness monitors were used around the periphery of the mirror and one at the center during pratice coating runs.

## EXPERIMENTAL DETAILS

Secondary electromagnetic steering coils are used to control the energy exchange between the surface of the molten pool of aluminum and the thermal energy in the beam. The blooming or defocusing beam enlarges the area of the beam image for heating the beam evaporation and is also used to counter wave action that distorts distribution to the mirror. The higher the power level in the gun, the more the evaporation rate increases ionization coupling and the better support for a secondary distribution source as a sole source distribution to the mirror.

A number of beam patterns were evaluated to sweep and raster the beam over the melt. The controlled beam-sweep system superimposed the two sweep signals to interdigitate the magnetic fields within the crucible area. The gun focus coil was moved in and out to preset limits at 10 Hz, and lateral Helmholtz sweep coils were set to 60 cycles at 3-phase 75 V ac.

The object of pattern change was to identify the beam excursion that gave the best symmetrical distribution pattern to the aluminum coating. The mechanism for uniformity improvement is thought to be a higher vaporization rate to increase the ionization coupling and form a new virtual source of distribution and thus help to obscure the beam image at the mirror surface. The unusually long path of up to 27.4 m magnifies the images of the source in the aluminized surface. Attempts have been made to image the source at the center and edges of the mirror with a pin-hole camera using plated glass.

The goal of generating a point source effect by patterning the beams over the crucible of molten aluminum was achieved by combining the sweep rates and patterns of the two magnetic coil systems. The results of changing the magnetic power in the two fields was observed in real time in the sensor at the center and in the sensors spaced symmetrically around the edge. The magnetic steering effect on source distribution was clearly observed, but when the beam power rate was raised significantly above 30 kW, it caused the beam to suppress the molten aluminum surface, resulting in waves on the surface with higher thickness ratios of 5:1 between the center and edge of the mirror coating and a nonsymmetrical coating thickness around the mirror edges. Deposition rates and coating thicknesses were displayed on the crystal monitors for finetuning the system. The best uniformity and thickness ratio produced from the practice testing was a 2:1 ratio (Fig. 8). The inverse square law and cosine-law distribution for open-crucible sources are generally reflected in the distribution pattern, but are difficult to calculate due to the dynamics of the beam-image size over the molten aluminum.

A procedure was then established from the test runs that produced a detailed set of conditions and control values for specific thermal levels, power/frequency settings, and subjective visual observations to position the beams properly for the coating operation. The dynamics and scale of a coating operation in such a large chamber produce an almost-unlimited number of variables that can influence the process. The protective mylar panels that cover the wall shrouds carry large surface deposits of aluminum from the coating operation and trap surface water. One of many variables to consider is thermal radiation from the evaporation source when the shutter exposes the hot source and causes the subsequent overcoating with fresh aluminum.

We used an aluminizing evaporation rate of 0.5 nm/s that was much slower than the normal standard of 1.0 nm/s for highly reflective coating. However, this slow deposition rate was offset by our ability to control surface water in the chamber by cooling the wall shrouds with liquid nitrogen and by the large number of cryo pumps. This water vapor control was crucial in achieving high-quality reflectivity and proper adhesion of the aluminum. Details of the final aluminizing operation are as follows:

## MIRROR CLEANING AND PREPARATION

Final preparation of the mirror surface for aluminizing was accomplished as part of the termination process in the final polishing operation by a Tinsley Laboratory optician. The cleaning process consisted of washing the mirror surface with deionized filtered water and detergent and blowing it with dry nitrogen gas to remove all droplets of moisture. The mirror was fitted with a stainless steel wire grid supporting a cover bag that provided a nitrogen gas purge to protect the nickel surface for coating. This provided a water-mark-free surface without streaks.

## CONCLUSION

Although this research represents preparation and qualifying tests for an adequate procedure for coating the mirror, a number of additional equipment modifications and variables in the process remain to be explored for a better thin-film coating. These variables can only be explored in the full scale dynamics of the vacuum facility. However, the facility's cost of operation precludes much experimentation beyond the specific reflectivity requirement for the collimator. Durability of the present coating should be usable for many years to come.


## ACKNOWLEDGMENTS

The author would like to acknowledge the expertise and years of distinguished experience in large metal optics that was brought to the mirror task by Peter Taylor and Thomas Brooks, consultants to the Tinsley Laboratory. Their teamwork effort made the mirror preparation for coating a success.


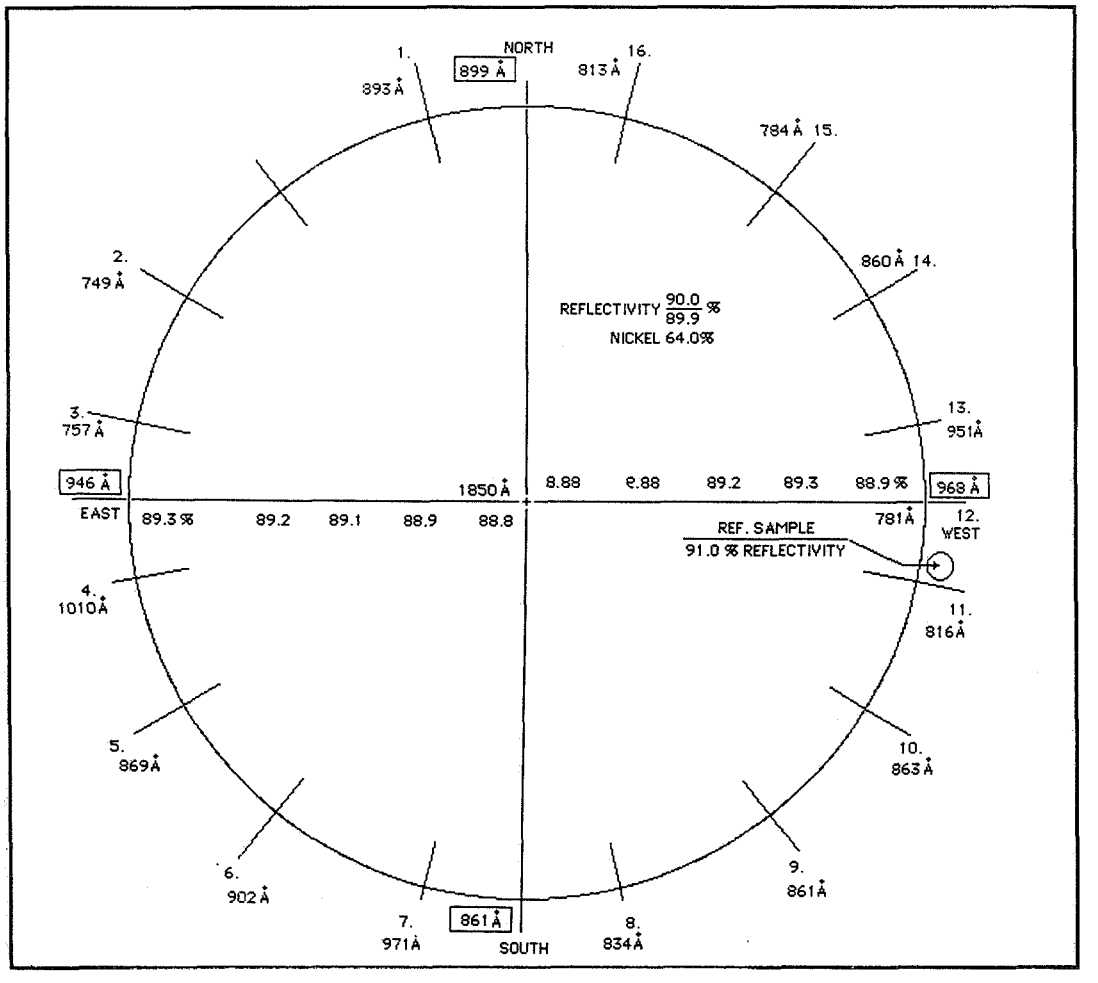


**Fig. 8. Thickness and reflectivity map.**

**Table 1. Final aluminizing performance data.**

| Item | Performance Data |
|---|---|
| CHAMBER PRESSURE | |
| - At start of process | 0.2 mPa (1.6 x $10^{-6}$ torr) |
| - End of run | 1.2 mPa (9 x $10^{-6}$ torr) |
| PUMPING CAPACITY | |
| - 10 cryo pumps | @ 45,000 liters (l)/s = 450,000 l/s |
| - 2 turbo pumps | @ 2,200 = 4,400 l/s |
| CHAMBER WALL SHROUDS | 120 °C |
| DEPOSITION | |
| - Rate | 0.5 nm/s |
| - Total time | 2 min, 59 s |
| POWER | |
| - Per EB gun | 11 kW |
| - Total | 33 kW |
| CRUCIBLE TEMPERATURE | 1625 ° C |
| REFLECTIVITY | |
| - Test sample (Fig. 8) | 91 percent |
| - Nickel test plate (15.2-cm diam) | 64 percent |
| - Mirror at edges in visible light | 90/89.98 percent (12 hrs at atmosphere) |
| - Mirror edge-to-center average | 88.8/89.3 percent (post conditioning) |
| - Reflectivity map (Fig. 8) | |

FURTHER ACKNOWLEDGMENT

The research described in this paper was carried out by the Jet Propulsion Laboratory, California Institute of Technology, under a contract with the National Aeronautics and Space Administration.

# THERMAL BALANCE TESTING OF THE MSAT SPACECRAFT

**Serge Samson**
Spar Aerospace Limited,
Ste. Anne-de-Bellevue, Quebec, CANADA

**Elie Choueiry**
David Florida Laboratory,
Canadian Space Agency,
Ottawa, Ontario, CANADA

**Kenneth Pang**
Hughes Aircraft Corporation,
El Segundo, California, U.S.A.

## ABSTRACT

This paper reports on the recently completed thermal balance/thermal vacuum testing of an MSAT satellite, the first satellite to provide mobile communications service for all of continental North America. MSAT is a two-spacecraft program, using a three-axis-stabilized HUGHES HS-601 series bus as the vehicle for the Canadian-designed payload. The thermal tests performed at the Canadian Space Agency's David Florida Laboratory in Ottawa, Canada, lasted approximately 32 days.

## Background

The infrared (IR) heating rig was designed to provide radiant heat inputs into seven spacecraft zones during thermal vacuum (TV) testing. The TV test was divided into multiple phases and began with a thermal balance cold phase, followed by a cold test phase and a hot balance phase, a hot test phase to finish, and finally a thermal cycle with continuous monitoring of the bus and payload. The spacecraft external heat fluxes were provided by IR lamp sources. To ensure flux uniformity, highly reflective baffles and IR lamp sources were used over six of the seven zones: the two Second Surface Mirror (SSM) radiators; the East and West faces; the Earth facing (Nadir); and the inside of the thrust cylinder. The Aft end panel heat fluxes were provided by a heated $LN_2$ shroud. The radiation flux intensity on the spacecraft zones from the various rig elements was measured using Monitored Background Radiometers (MBR), and compared with direct calculations and with pretest predictions.

The temperature measurement system was based on Uniform Temperature References (UTR) located inside the TV chamber such that all connectors and cabling were copper-copper. This system was devised to achieve a temperature measurement accuracy of $\pm$ 1 °C for over 850 thermocouples used in the test. A PC-based real-time data processing system (TVDPS) on a QNX operating system, provided continuous monitoring of all channels within a 30s time scan. Also, the TVDPS retrieved a telemetry stream from the Satellite Test Equipment (STE) station, and provided real-time data manipulation.

Preliminary results showed the test to be successful from both viewpoints - thermal balance and electrical testing.

## INTRODUCTION

MSAT is a three-axis-stabilized communications satellite designed to operate in a geostationary orbit over North America. The antennas and the SPAR-designed payload are integrated on a Hughes Aircraft HS-601 Bus. MSAT will be the first satellite to provide a mobile continental communication service. Two satellites are being tested. The first satellite (M1) will service Canada and will be operated by Telesat Mobile Inc. (TMI), while the second satellite (M2), owned by American Mobile Satellite Corporation (AMSC), will service United States territory. M1 and M2 respectively are planned to be launched in April and March 1995. Figure 1 shows MSAT with its receive and transmit L-Band antennas. Gain limitations inherent with mobile users have driven MSAT to offer high receive gain and high transmit power capabilities. The high power transmit feed is capable of radiating over 600 W RF in the L-Band frequency and is fed by 16 primary (and 4 redundant) High Power Amplifiers (HPAs). Ten HPAs are mounted on each of the North and the South radiators. Each HPA dissipates 120 W and when the forward repeater is operated, eight to ten HPAs dissipate simultaneously on the North and/or the South radiators. The HPA dissipation is distributed on the radiator surface using orthogonal imbedded heat pipes. The spreader heat pipes distribute the dissipation of each HPA in the Z axis orientation (aft-nadir) and header heat pipes are used to distribute the heat load between the HPAs themselves in the X axis orientation (East-West).

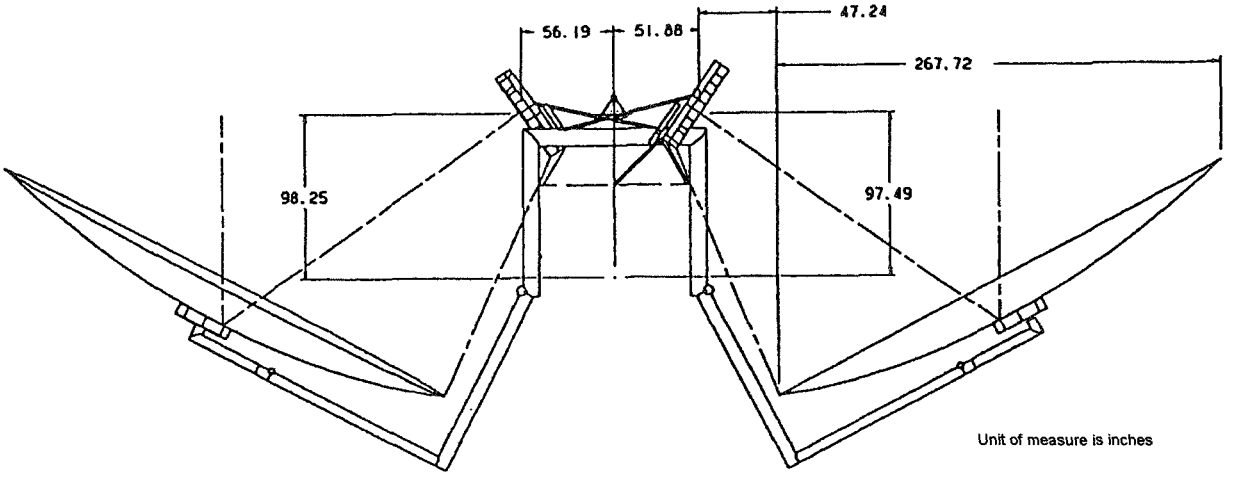


Figure 1. The MSAT satellite

Due to the MSAT program's schedule and flight hardware availability, two TV tests were performed on each satellite. Thermal balance, as well as bus and payload performance verification tests used the same setup (by using the same setup, DFL's resources were optimised and the testing time was reduced). The L-Band feeds were unavailable for the TV tests, so heated feed simulators were made to create the correct thermal boundaries for the payload. The feed thermal models were verified in a separate, thorough conductance test [Ref.1].

DFL's space simulation laboratory has integrated and tested numerous satellites and space sub-systems. Its facilities include anechoic chambers, vibration platforms, and several vacuum chambers to hold all sizes of spacecraft (7m x 11m maximum). Its anechoic chambers are used to evaluate antennas and RF payloads. Its vibration platforms are used for vibration and modal analysis to verify the structural integrity. Its vacuum chambers, in addition to providing hard vacuum testing, are also equipped for doing IR TV testing to verify the thermal design and workmanship of spacecraft. The IR TV tests are controlled and monitored in-house by the TVDPS.

## BACKGROUND

In the mid 1980's, SPAR, sponsored by DFL, developed orbital thermal simulator capability using infrared (IR) stimulation. The developed technique consisted of partitioning the appropriate spacecraft surfaces into isoflux zones each receiving an IR-equivalent radiant solar flux corresponding to a specified orbital position [Ref.4,7]. The IR fluxes were generated by IR lamps and Calrods. An IR rig structure supported the spacecraft and associated IR hardware. The use of baffles with a specular reflecting surface enhanced flux uniformity by containing flux spillover around the various zones. The total radiation input to the spacecraft surfaces was measured by specially designed Monitored Background Radiometers (MBR) [Ref.2]. The heating element configurations were determined using a software package developed by SPAR (IRFLUX) to calculate the absorbed heat flux distribution in individual zones. IRFLUX calculated both the initial heat source configurations, and the final data reduction of the measured zone flux values. The IR portion of the thermal balance test for the OLYMPUS spacecraft thermal model was carried out at DFL in the second half of January 1986, ([Ref.3] contains a detailed description of the test design). In 1990, the ANIK E (flight 1 and 2, GE Astro 5000 series) spacecraft thermal tests took place at DFL. A total of five different flux environments including eclipse, were simulated on the ANIK E spacecraft [Ref.5]. The thermal balance phase was performed first, and lasted seven days. The TV test setup enabled testing to progress directly from thermal balance to TV communications testing.

## MSAT THERMAL VACUUM TEST REQUIREMENTS

The TV tests were required to verify the Bus and Payload system performances over the qualification or acceptance temperature ranges. Spacecraft thermal balance phases were also performed to verify the satellite thermal design and correlate the thermal model. During the Bus and Payload test phases, the test heaters as well as the IR lamps are used to obtain the desired temperatures on the different subsystems.

The first TV test, identified as M2 CTV-1, was on the M2 satellite, and this test had two long performance testing phases (hot and cold), and five thermal balance phases. M2 CTV-1 lasted 32 days under vacuum. Figure 2 displays the test profile.

The second TV test, M1 CTV-1 was on the M1 satellite and consisted of Bus and Payload hot and cold testing (two phases). The next two tests (M2 CTV-2, M1 CTV-2) will consist of two system performance testing phases and some thermal balance phases.

During the thermal balance phases, the absorbed flux uniformity was required to be better than 5% over each IR zone. Every interface to the spacecraft had to be thermally isolated using a specially designed thermal blankets to minimize the heat exchange between them and the satellite. Those unwanted heat fluxes would cause inaccuracies in thermal balance correlation. Test heaters and specially designed heated multi-layer blankets (MLI) were used to maintain a temperature gradient of less than 3 °C at those interfaces between the spacecraft side temperature and the chamber side temperature.

### Thermal vacuum test design

The IR tests were performed in the 7m x 11m TV chamber. By an attachment ring, the satellite was supported horizontally inside the TV chamber. The conductive heat exchange between the spacecraft and the test structure was minimized by low-conductivity washers at their interface. The IR rig was held by the same structure (U-frame) which is supported onthe tilt-adjustable support frame. This assembly sits on a large tower erected inside the TV chamber. The IR rig was installed on top of the U-frame and surrounds MSAT. Figure 3 shows the unassembled IR rig.

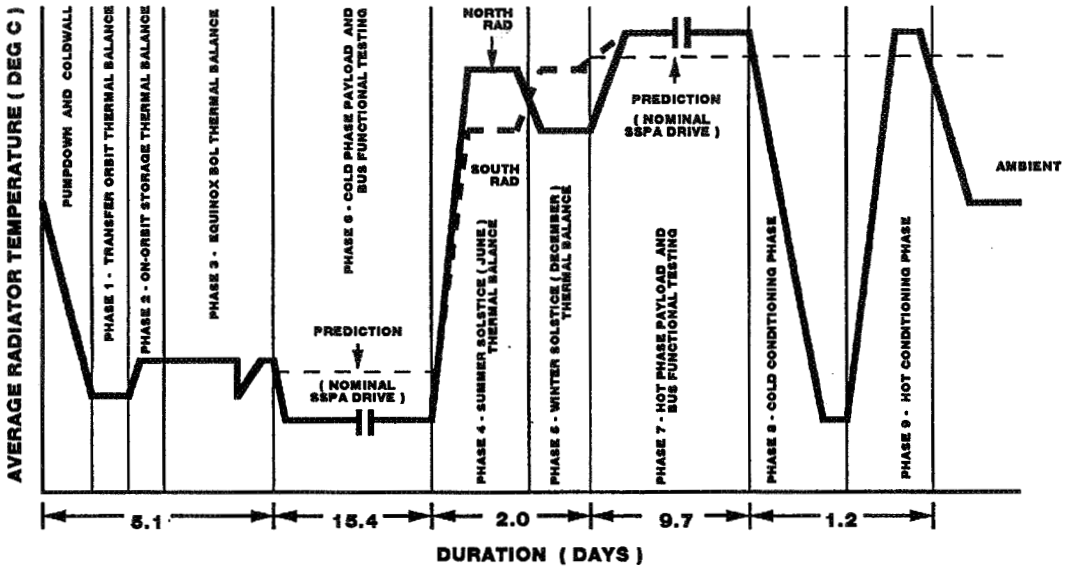


Figure 2. Test profile for M2 CTV-1 test on MSAT M2

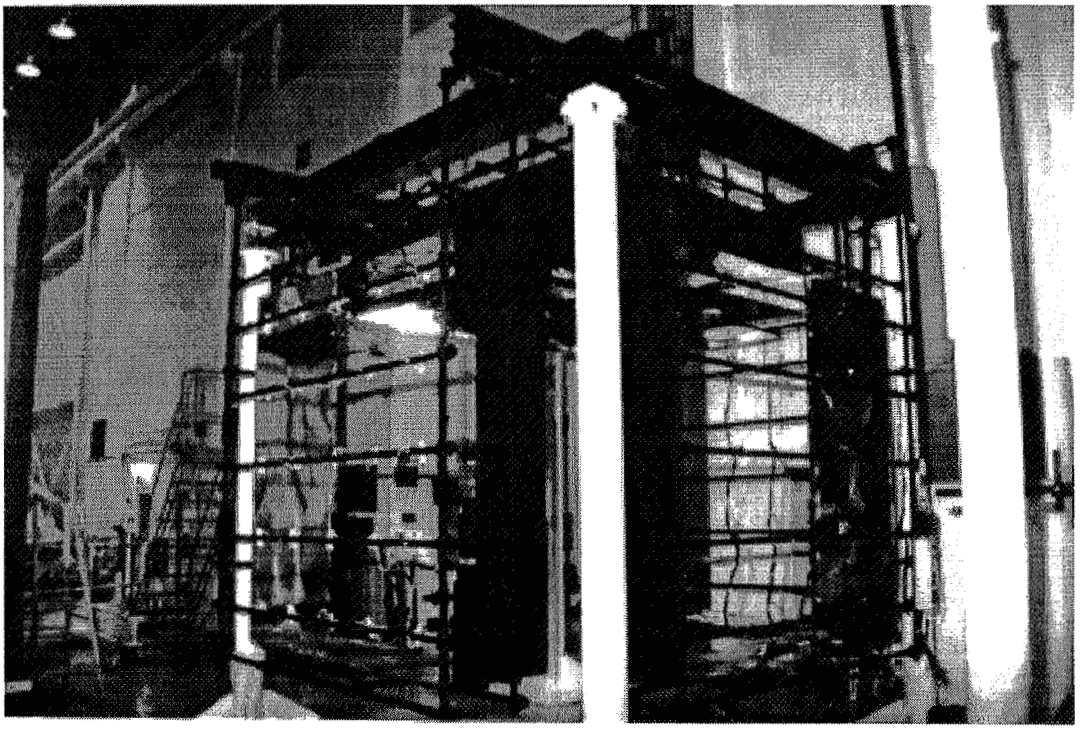

Figure 3. Unassembled IR rig assembly

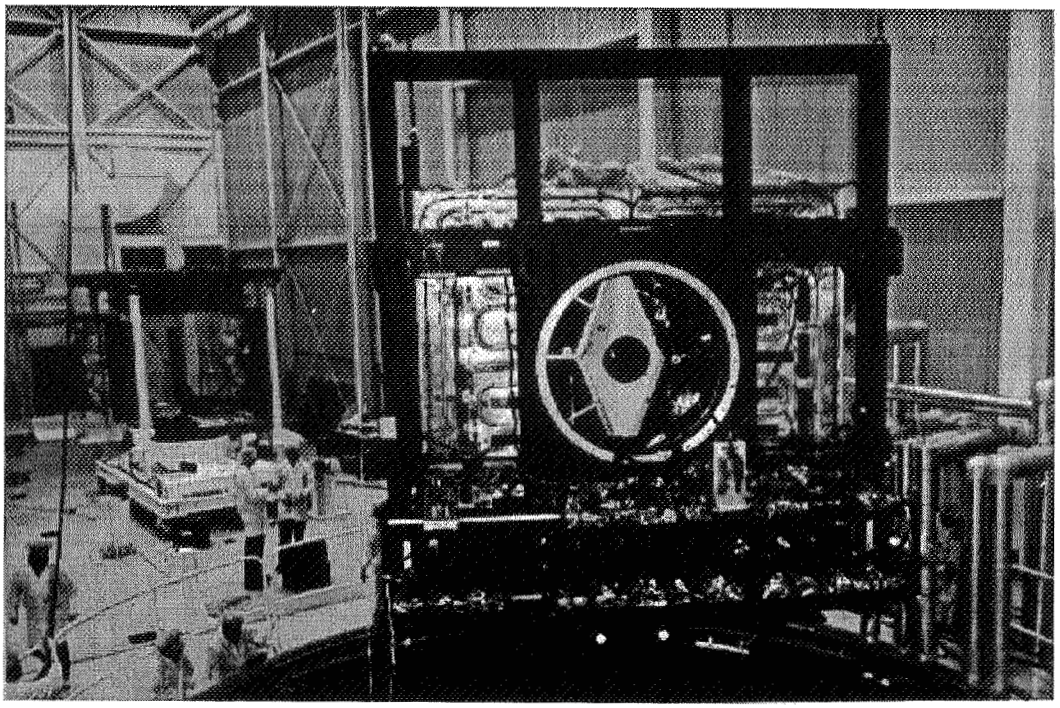

Figure 4. Complete IR assembly surrounds MSAT M2 prior to TV test

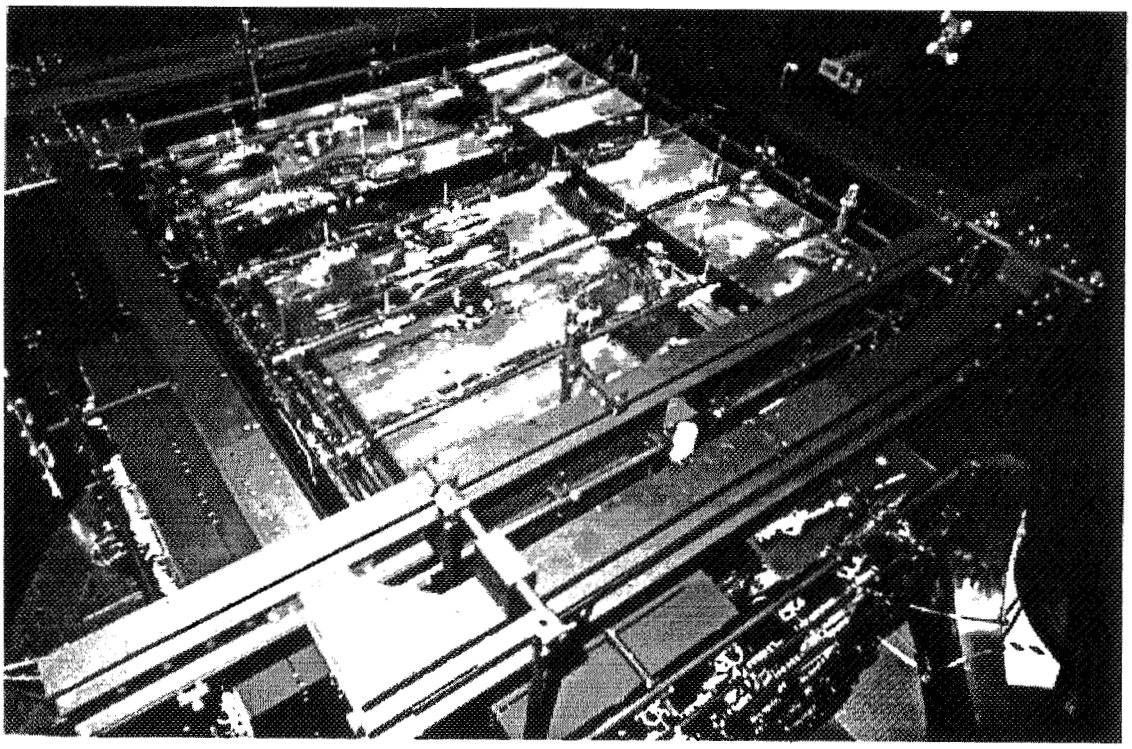

Figure 5. Complete IR assembly surrounds MSAT M2 in the 7 m x 11 m TV chamber

Figure 4 shows the complete IR assembly prior to testing, and includes the spacecraft within the IR rig. In order to prevent the satellite being affected by the IR rig and the tower structure, a high-emissivity $LN_2$ shroud is used in front of the North Radiator. The $LN_2$ shroud's high emissivity was achieved by bonding a black-painted 1" aluminum honeycomb over the $LN_2$ shroud.

The support frame is designed to maintain its horizontalability to within 2 mm/m. Two leveling devices called jactuators, are located below the support frame in the –Z side of the spacecraft (AFT). The +Z end of the support frame rests on a central spherical bearing allowing for two-axis adjustments using the jactuators. The leveling can be verified with X-axis (East-West) and Z-axis (AFT-Nadir) tilt sensors. Three sensors are located on the exterior surface of each radiator panel. A level setting adjustment is performed prior to pumpdown using a high accuracy level. The tilt sensor equations are then brought to a zero degree angle value. No tilt angle adjustment have been required after pump-down of any of the four CTV tests as both the X-axis and the Z-axis stayed within $\pm$ 0.05° off-angle.

Figure 5 illustrate the complete setup prior to testing in the 7 m x 11 m TV chamber. Including pump down and recovery, a total of seven Phases were performed - five of them required heat flux inputs from the IR rig: Equinox, Summer Solstice, Winter Solstice, transfer orbit, and on-orbit storage. At the beginning of each Phase, the IR lamps were adjusted to their nominal setting. The radiometer input could then be used to refine the power setting on the IR lamp if necessary, for individual zones. The eclipse test occurred after the Equinox Phase; during this test all the IR lamps and Calrods were turned off.

Each cable or bundle interfacing with the satellite is thermally guarded so as to eliminate any conductive heat exchange between the satellite and the test hardware. Unwanted heat fluxes would cause inaccuracies in the thermal balance test correlation, so a specially-designed, heated thermal blanket was used at the different test interfaces. A resistive wire was applied to the internal layer of the guard blanket using aluminum as well as Kapton tapes. Cable thermal management was also provided using similar heated blankets. This integrated heater/blanket design significantly reduced setup time by eliminating the individual guard heater installation at each interface. Velcro and reinforced blanket material are used to recover them for use in future tests. Modular baffles and a generic IR lamp mounting structure were built for this program and remain available for use in future tests.

Distributed on the TV chamber wall around the satellite, 16 recovery lamp poles were used to recover the TV chamber and were available for emergency recoveries as well.

### IR rig design

The satellite surface was divided into seven isoflux zones. IR Research Inc.'s 500 W IR lamp sources provided heat inputs for six of these zones, namely: the North and South radiators, the East and West faces, the earth facing (Nadir), and the inside of the thrust cylinder with its LAM (liquid apogee motor). The Aft end zone was controlled with two vertical $LN_2$-heated shrouds. As shown in Table 1, 122 IR lamps were used. IR lamp locations were computed using IRFLUX, a SPAR program developed to calculate the absorbed flux in the individual zones irradiated by IR lamps or Calrods.

IRFLUX treats each zone independently and that results in increased flexibility and reduction of execution time. The program analyzes zones either with, or without specular baffles. IRFLUX takes into account surface absorptivity variations as a function of angle of incidence and IR lamp power (radiated frequency spectrum). IRFLUX inputs are the required average absorbed flux value and the zone definitions (zone dimension, baffle locations and properties, satellite surface type). Then, IRFLUX generates the optimal IR lamp configuration and power levels required to obtain the requested average flux density. IRFLUX also provides a flux distribution matrix to produce isoflux contour plots.

Highly reflective Vacuum-Deposited Aluminum baffles delimited every zone. These baffles ensured maximum flux uniformity and contained flux spillover around various IR zones. The absorbed fluxes were accurately measured at 38 locations on the satellite's surface using 49 monitored background radiometers [Ref.3] (see Table 1).

At the beginning of each Phase, the IR lamps were adjusted to their nominal setting. The radiometer readings were compared to the IRFLUX predicted flux distribution, then appropriate corrections were made to the IR lamp power level.

Table 1. IR lamp and radiometer distribution

| IR ZONE | NUMBER OF IR LAMPS | NUMBER OF RADIOMETER LOCATIONS | NUMBER OF RADIOMETERS | NEW RADIOMETERS SURFACE TYPE | OLD RADIOMETERS SURFACE TYPE |
|---|---|---|---|---|---|
| NORTH RADIATOR | 20 | 7 | 9 | SSM | SSM (OLYMPUS) |
| SOUTH RADIATOR | 20 | 7 | 9 | SSM | SSM (OLYMPUS) |
| EAST | 25 | 5 | 7 | CLK** | BLACK PAINT (OLYMPUS) |
| WEST | 25 | 5 | 7 | CLK** | BLACK PAINT (OLYMPUS) |
| NADIR | 30 | 8 | 10 | CLK** | BLACK PAINT (OLYMPUS) |
| | | | | - | WHITE SUNSHIELD (ANIK-E) |
| THRUST CYLINDER | 2 | 4 | 4 | - | 1 MIL KAPTON (ANIK E) |
| | | | | WHITE PAINT | - |
| AFT | 0* | 2 | 3 | - | 1 MIL KAPTON (ANIK E) |
| TOTAL: | 122 | 38 | 49 | | |

* A heated shroud was used
** CLK : Carbon Loaded Kapton

Monitored background radiometers (MBRs)

The MBRs were designed and then calibrated to take a direct reading on the heat flux absorbed by a spacecraft surface. The MBRs are made of a sensing disk covered by a surface identical to the corresponding spacecraft surface and a body to form a background for the back of the sensing disk. A detailed error analysis [Ref.6] has shown that: for power levels greater than 130 $W/m^2$, the maximum, calculated error was less than 3 %; for fluxes of 40 $W/m^2$, it was 4.1 %; and for fluxes of 5 $W/m^2$, it was 20 %, (for 5$W/m^2$, this translates to less than $\pm$ 1 $W/m^2$).

## THERMAL VACUUM DATA PROCESSING SYSTEM (TVDPS)

DFL's Thermal Vacuum Data Processing System (TVDPS) was designed as an operator interface station to provide test or process information in formats clear and familiar to the technician or computer operator. Also, detailed historical analysis and file management functions useful to research or engineering personnel. The TVDPS's operating system is real-time, multi-tasking, multi-user, with peer-to-peer distributed network capability. Depending upon the devices attached, TVDPS communication is serial (RS-232, 422, 485) or parallel (IEEE-488). The complexity of the MSAT IR test required the setup of over 1460 input channels on the TVDPS. Channel allocations were broken down as follows: 139 miscellaneous inputs, 165 calculation channels, 210 thermal control channels, 240 telemetry channels, and 710 channels for the spacecraft and the IR rig structure.

The TVDPS can monitor, log, limit check, and graphically display data while changes occur. Update rates and throughput depend on the data acquisition unit and system configuration. Any historical (previously data logged) data may be accessed concurrently with ongoing data acquisition. Typical task switch rate is 140 µs on an 80386/20 MHz PC and 25 µs on an 80486/25 MHz PC.

Processing power in addition to the above was required to compare telemetry data with spacecraft temperatures during each phase of the test. For this purpose one of the TVDPS nodes was connected to the spacecraft telemetry system, which consisted primarily of a VMS-based DEC VAX 4000-200. An interface routine was implemented to serially receive ASCII formatted data at 9600 baud from the DEC VAX 4000-200. This information was sequentially retrieved and stored in the TVDPS internal database. Real-time or historical plots could be generated to correlate any number of activities at any time during the TV test.

## Temperature measurement system

The high accuracy of the temperature measurement system is maintained because the design of specialised feedthroughs, and the Uniform Temperature Reference (UTR) block-and-case assembly. Into each UTR, up to 30 thermocouples were plugged and this maintained a homogeneous temperature throughout all of the attachment points. Two distinct copper extension cable assemblies connect each UTR block to one TVDPS datalogger.The copper extension cable wires are connected by a 34-pin vacuum-feedthrough; two pins of which are used for connecting the common shields together. Thus the reference temperature for the thermocouples is now UTR temperature. UTR reference temperature is measured by comparing it with a 0 °C reference thermocouple which is immersed in an ice bath outside the vacuum environment.

## Thermal control system

The thermal control system has 256 microprocessor-controlled DC power supplies, each capable of delivering up to 2 kW of regulated and monitored output power into a resistive load. To minimize the consequences of hardware failure and increase the versatility of the user, the thermal control system is of a modular design. To reduce the size of the equipment and significantly increase its power efficiency beyond that achieved with linear control technology, switch-mode power control techniques are used. All channels are voltage controlled and power is an output variable. Because the lamps are wired in parallel circuits, failure identification techniques prevent the burnout of the second lamp.

Both prior to, and during testing, the parameters for output voltage and its limit level specification are set through the thermal control system's console. This console is also responsible for current channel status and alarm displays, and the measured load current is used to calculate the output power level. The console is connected to eight node controllers and each node controller controls 32 power supplies. These power supplies operate on a closed loop system to provide, regulate, and monitor the specified output voltage. Table 2 lists the operating limits of the thermal control system.

Protection and alarm facilities used by the thermal control system include channel set point level versus monitored level compliance, load detection and shutdown for open- or short-circuits, load-sense line alarms for open- or short-circuits, and out-of-limit alarms. In the event of a municipal power failure, emergency power to the thermal control system is provided by a diesel generator.

Table 2. Operating limits for the thermal control system

| | |
|---|---|
| NUMBER OF CHANNELS | 250, MAXIMUM |
| LOAD CURRENT / CHANNEL | 10 A (DC), MAXIMUM |
| OUTPUT VOLTAGE / CHANNEL | 240 V (DC), MAXIMUM |
| POWER INPUT | 208 V(AC), THREE PHASE 25 KVA |
| VOLTAGE CONTROL RANGE | 0 TO 100 % |
| PROGRAMMABLE VOLTAGE LEVEL RESOLUTION | 1 V DC |
| SYSTEM CONTROL ACCURACY | LESS THAN 1% OF SET VALUE |

## TEST RESULTS

The final infrared absorbed flux results for each IR zone in the MSAT CTV test design are listed in Table 5. The flux values are given for the thermal balance phases only (Phases 1 to 5). Figure 6 is the IRFLUX-generated contour plot for the Phase 3 Nadir IR zone and shows the absorbed flux distribution on the MSAT surface. The predicted radiometer readings, at their actual locations, are highlighted on the contour plots, as seen in Figure 6. For the North and South zones (radiators), additional simulations were performed to reflect the lamp height difference between the radiometer disk and MSAT's surface. More accurate predictions can therefore be used for the radiometer readings. For the East, West and Nadir zones, the radiometer height was not considered. However, the analyses showed that the predictions were not significantly affected by this. Table 3 is an example of radiometer correlations for the Nadir zone during Phase 3.

Table 3. Radiometer correlation for the Nadir zone during Phase 3

| NADIR ZONES | PREDICTED MBR FLUXES (required flux [CLK] is 969.0 w/m$^2$) | TEST RESULTS (required flux [CLK] is 969.0 w/m$^2$) | ERROR BETWEEN PREDICTIONS AND RELATIVE TEST RESULTS |
|---|---|---|---|
| + ZOSW (CLK) | 962.0 | 1019.0 | 0.06 |
| + ZOSE (CLK) | 974.7 | 973.5 | 0.00 |
| + ZOWEST1 (CLK)<br>+ ZMWEST2 (CLK) | 972.1 | 953.1<br>965.3 | – 0.02<br>–0.01 |
| + ZOEAST2 (CLK)<br>+ ZMEAST1 (CLK) | 975.0 | 993.4<br>986.9 | 0.02<br>0.01 |
| + ZONW (CLK) | 964.3 | 954.1 | – 0.01 |
| + ZONE (CLK) | 966.3 | 929.0 | – 0.01 |
| + ZMKUW (SUNSHIELD) | 525.0 | 529.5 | 0.01 |
| + ZMKUE (SUNSHIELD) | 529.9 | 516.9 | –0.02 |
| **AVERAGES** | | | |
| EQUIVALENT MBR AVERAGE (CLK) | 970.19 | n/a | 0.00 |
| EQUIVALENT MBR AVERAGE (SUNSHIELD) | 526.95 | n/a | – 0.01 |
| ZONE AVERAGE (CLK) | 968.0 | n/a | 0.00 |
| ZONE AVERAGE (SUNSHIELD) | 524.8 | n/a | 0.00 |

For the zones without lamp fluxes, the background radiation was calculated using the radiometer readings without the use of simulation analysis. For the East and West faces, the IR zone was subdivided in three regions, namely: Aft, Forward North, and Forward South. Both Forward regions represent two sides of each dummy feed. The flux uniformity in those regions was greatly affected by the following: the presence of the dummy feeds, the SMA cables, and the L-Band waveguides, as well as the removal of some IR lamps. Although IRFLUX cannot simulate the presence of obstructions inside an IR zone, the flux prediction inaccuracies were less than 10 %.

For the Nadir zone, absorbed fluxes are given for the carbon loaded Kapton blanket surfaces as well as for the Ku-Band antenna's white painted sunshield surface. Also, IRFLUX simulations were performed for both surfaces. The Aft end was subdivided into three regions, namely: the Bus Panel (external to the thrust cylinder), the Thrust Cylinder (inside) and the Plume Shield (white painted surface).

Table 4. IR flux results ($W/m^2$) for Phases 1 to 5

| ZONE/PHASE | PHASE 1 SPINNING | | PHASE 2 WEST SUN | | PHASE 3 NADIR SUN | | PHASE 4 EAST SUN | | PHASE 5 NADIR SUN | |
|---|---|---|---|---|---|---|---|---|---|---|
| | DATA | REQD | DATA | REQD | DATA | REQD | DATA | REQD | DATA | REQD |
| NORTH | 245.1 | 248.0 | 22.6 | n/a | 19.3 | n/a | 144.0 | 150.0 | 25.6 | n/a |
| SOUTH | 240.2 | 248.0 | 27.8 | n/a | 21.0 | n/a | 27.6 | n/a | 165.7 | 172.0 |
| EAST AFT | 345.8 | 398.0 | 25.1 | n/a | 20.1 | n/a | 1115.5 | 1152.0 | 32.6 | n/a |
| FWD NORTH | 320.0 | 398.0 | n/a | n/a | 23.8 | n/a | 617.5 | 1152.0 | 36.9 | n/a |
| FWD SOUTH | 235.2 | 398.0 | 41.1 | n/a | 40.1 | n/a | 883.6 | 1152.0 | 57.7 | n/a |
| WEST AFT | 349.6 | 398.0 | 1265.0 | 1286.0 | 18.0 | n/a | 27.6 | n/a | 28.1 | n/a |
| FWD NORTH | 254.8 | 398.0 | 689.0 | 1286.0 | 17.1 | n/a | 20.4 | n/a | 26.4 | n/a |
| FWD SOUTH | 273.0 | 398.0 | 1005.8 | 1286.0 | 16.0 | n/a | 18.5 | n/a | 23.6 | n/a |
| NADIR MLI | 16.1 | n/a | 15.7 | n/a | 968.0 | 969.0 | 12.6 | n/a | 1248.3 | 1259.0 |
| SUN SHIELD | 15.3 | n/a | 12.7 | n/a | 524.8 | 524.0 | 12.4 | n/a | 633.0 | n/a |
| AFT BUS PANEL | 18.4 | n/a | 12.8 | n/a | 12.3 | n/a | 15.4 | n/a | 16.0 | n/a |
| THRUST CYL. | 43.7 | n/a | 44.5 | n/a | 39.7 | n/a | 58.4 | n/a | 54.1 | n/a |
| PLUME SHIELD | 43.4 | n/a | 43.4 | n/a | 38.4 | n/a | 57.1 | n/a | 51.3 | n/a |

## Thermal model correlation

To compare the MSAT M2 CTV-1 test results, Hughes Thermal Group had modified the MSAT bulk model and detailed panel models. The MSAT bulk model provided boundary conditions for Hughes Aircraft's detailed panel models as well as providing predictions for all propulsion systems. Payload and bus unit mounting surface temperatures (UMS) came from four different detailed panel models (North Radiator, South Radiator, Subnadir Panel, and Bus Panel). SPAR provided the temperature gradients from the payload unit to the UMS. Hughes Aircraft HS-601 programs provided the temperature gradients of the bus units.

The correlation used five thermal balance phase results (transfer orbit, on-orbit storage, Equinox BOL no-drive, Summer EOL no drive, and Winter EOL no drive).

Heat pipe conduction in the detailed panel model was verified and validated by the results. In all five thermal balance phases, excellent correlations ($\Delta$ t less than 3°C) were made for heat pipe temperatures. MSAT's heater system was dependent on the heat pipes to distribute the heat to the essential units. Heat pipe temperature was a good indicator for radiator temperature distribution. MSAT's main heat-rejection paths were the North and South Radiator panels. Mounted to the heat pipe equipped radiator panel were all of the high-dissipating Ku-Band and L-Band units. The fixed-conductance heat pipes were primarily used to spread the heat evenly throughout the radiator to help cool down the high-heat-dissipating units and to help maintain the non-dissipating units within an acceptable temperature range.

Hughes Aircraft's detailed panel model was used to predict UMS temperature. The temperature gradient from an SSPA thermocouple or an LRV to the header pipe was needed to obtain the SSPA temperature for the test correlation. The average temperature gradient was 2.5°C for cold cases, and 2.0°C for hot cases; the $\Delta$t would then be used for the post-test correlation of the SSPA.

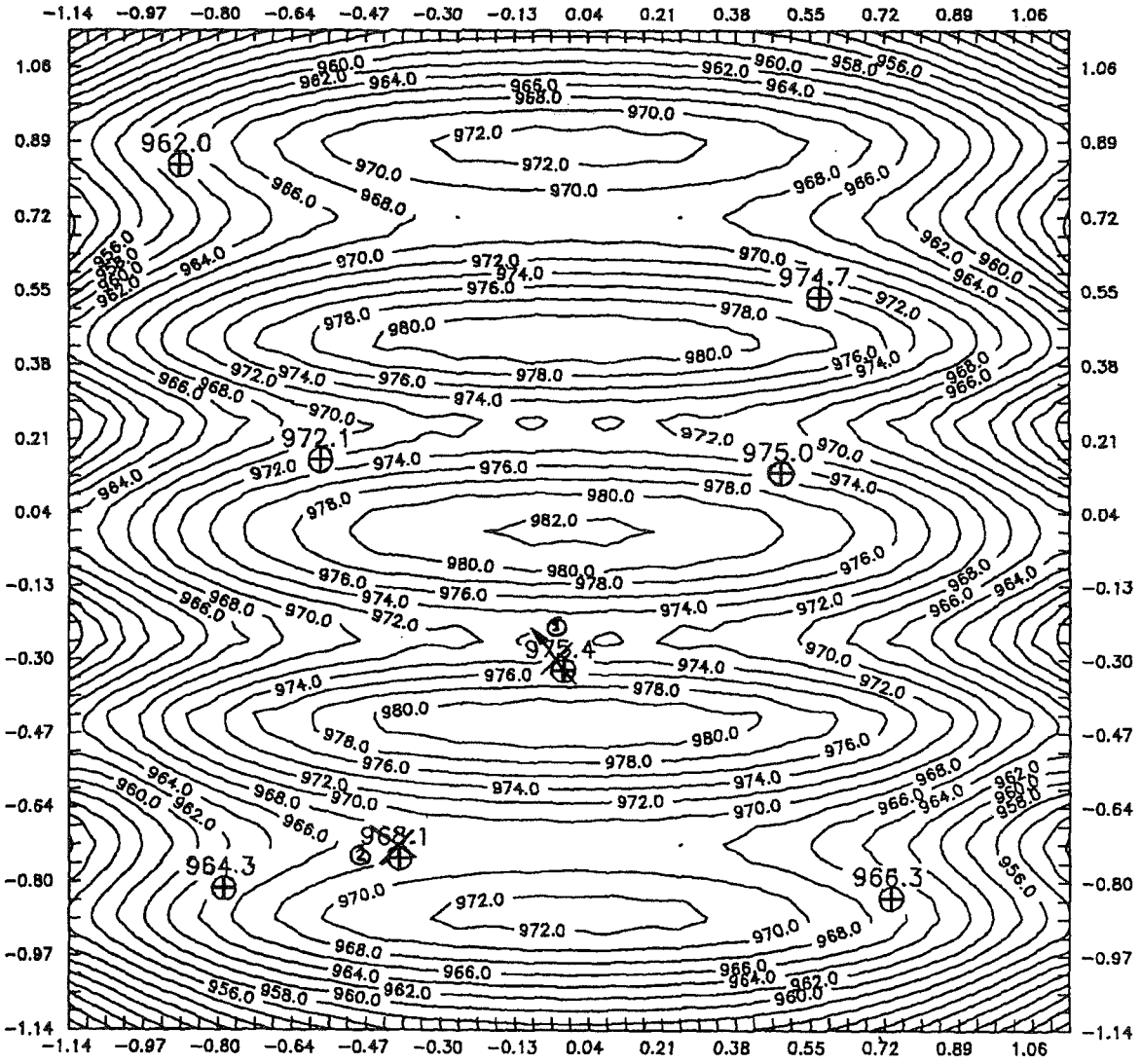


Figure 6. The contour plot generated by the IRFLUX application for the Phase 3 Nadir IR zone

IR lamps supplied heat fluxes to the spacecraft. Radiometers were used to determine the amount of the heat fluxes absorbed by the surfaces. The measured absorbed heat fluxes are listed in Table 4 for each thermal balance phase. Dummy feed temperatures were pre-determined and used as boundaries. The dummy feeds were controlled by the test heaters and adjusted by the E/W IR lamps. Thrust cylinder temperatures were controlled by the test heaters. The MSAT M2 CTV-1 unit predictions and test results are listed in Table 5.

### Transfer Orbit Thermal Balance (Phase 1)

All payload units were off and the bus and the TT&C units were on. The payload maintenance heaters and replacement heaters were disabled The spacecraft was assumed to be spinning with a summer sun perpendicular to the spinning axis (Z-axis). The IR lamps were used to apply an orbital average solar heat flux to the East/West blankets and to maintain the North/South exterior radiator temperatures to about 4 °C. The results show that all payload unit temperatures were within 2 °C of predicted values. The propulsion system, TT&C, and the bus units were within the 5 °C range.

Table 5. Thermal balance correlation for three phases

| SUB-ASSEMBLY and TV UNIT DESCRIPTIONS | EQUINOX BOL (Phase 3) | | | | SUMMER EOL (Phase 4) | | | | WINTER EOL (Phase 5) | | | |
|---|---|---|---|---|---|---|---|---|---|---|---|---|
| | ST | PRED | DATA | ΔT | ST | PRED | DATA | ΔT | ST | PRED | DATA | ΔT |
| **SUBNADIR FWD PANEL** | | | | | | | | | | | | |
| NORTH OUTPUT SWITCH | OFF | 1 | 3 | 2 | OFF | 35 | 35 | 0 | OFF | 30 | 29 | -1 |
| NORTH OUTPUT HYBRID MATRIX | OFF | 2 | 2 | 0 | OFF | 38 | 36 | -2 | OFF | 35 | 33 | -2 |
| OHM ISOLATOR TEMP NW | OFF | 2 | 4 | 2 | OFF | 43 | 39 | -4 | OFF | 39 | 35 | -4 |
| OHM ISOLATOR TEMP NE | OFF | 8 | 7 | -1 | OFF | 46 | 45 | -1 | OFF | 40 | 39 | -1 |
| SOUTH OUTPUT SWITCH | OFF | 0 | 2 | 2 | OFF | 25 | 25 | 0 | OFF | 35 | 36 | 1 |
| SOUTH OUTPUT HYBRID MATRIX | OFF | 1 | 3 | 2 | OFF | 31 | 31 | 0 | OFF | 38 | 37 | -1 |
| OHM ISOLATOR TEMP SW | OFF | 0 | 3 | 3 | OFF | 34 | 35 | 1 | OFF | 44 | 46 | 2 |
| OHM ISOLATOR TEMP SE | OFF | 0 | 2 | 2 | OFF | 36 | 36 | 0 | OFF | 44 | 45 | 1 |
| L-BAND RECEIVER | ON | 8 | 8 | 0 | ON | 30 | 29 | -1 | ON | 38 | 37 | -1 |
| KU LOOPBACK FILTER | OFF | 0 | 3 | 3 | OFF | 28 | 28 | 0 | OFF | 32 | 34 | 2 |
| LO DISTRIBUTION NETWORK | OFF | 1 | 4 | 3 | OFF | 26 | 27 | 1 | OFF | 32 | 34 | 2 |
| TELEMETRY ENCODER UNIT | ON | 8 | 8 | 0 | OFF | 31 | 31 | 0 | OFF | 27 | 26 | -1 |
| **SUBNADIR AFT PANEL** | | | | | | | | | | | | |
| 7-FREQUENCY LO | ON | 14 | 13 | -1 | ON | 44 | 44 | 0 | ON | 38 | 34 | -4 |
| 2-FREQUENCY LO DOUBLER | ON | 9 | 7 | -2 | ON | 44 | 43 | -1 | ON | 39 | 38 | -1 |
| COMMAND DECODER UNIT | ON | 5 | 7 | 2 | ON | 32 | 30 | -2 | ON | 35 | 32 | -3 |
| TELEMETRY ENCODER UNIT | OFF | 2 | 5 | 3 | ON | 40 | 39 | -1 | ON | 37 | 32 | -5 |
| **BUS PANEL** | | | | | | | | | | | | |
| IRU | OFF | 4 | 2 | -2 | OFF | 28 | 28 | 0 | OFF | 24 | 23 | -1 |
| MWA | ON | 20 | 21 | 1 | ON | 42 | 41 | -1 | ON | 43 | 43 | 0 |
| BDC | ON | 9 | 11 | 2 | ON | 35 | 33 | -2 | ON | 36 | 32 | -4 |
| SCP | ON | 14 | 17 | 3 | ON | 38 | 36 | -2 | ON | 39 | 36 | -3 |
| PDU | ON | 8 | 6 | -2 | ON | 33 | 31 | -2 | ON | 34 | 32 | -2 |
| VDU | ON | 5 | 4 | -1 | ON | 29 | 28 | -1 | ON | 29 | 28 | -1 |
| **PROPULSION** | | | | | | | | | | | | |
| LAM INJECTOR | ON | > 3 | 26 | -- | ON | > 3 | 24 | -- | ON | > 3 | 38 | -- |
| LAM VALVE | ON | > 3 | 30 | -- | ON | > 3 | 43 | -- | ON | > 3 | 43 | -- |
| OX TANK | ON | 3 | 5 | 2 | ON | 31 | 29 | -2 | ON | 32 | 30 | -2 |
| FUEL TANK | ON | 3 | 5 | 2 | ON | 31 | 32 | 1 | ON | 31 | 29 | -2 |
| HE TANK | ON | 3 | 5 | 2 | ON | 28 | 29 | 1 | ON | 28 | 27 | -1 |
| **NORTH RADIATOR** | | | | | | | | | | | | |
| SSPA | ON | 17 | 16 | -1 | ON | 46 | 44 | -2 | ON | 31 | 28 | -3 |
| SSPA ISOLATOR | OFF | 3 | 4 | 1 | OFF | 38 | 36 | -2 | OFF | 24 | 22 | -2 |
| KU RECEIVER | ON | 3 | 3 | 0 | ON | 31 | 29 | -2 | ON | 21 | 22 | 1 |
| KU UP-CONVERTER | ON | 5 | 6 | 1 | ON | 34 | 34 | 0 | ON | 21 | 17 | -4 |
| KU TWT | ON | 26 | 24 | -2 | ON | 62 | 57 | -5 | ON | 49 | 44 | -5 |
| KU EPC | ON | 4 | 6 | 2 | ON | 33 | 35 | 2 | ON | 22 | 21 | -1 |
| LINEARIZER | ON | 2 | 0 | -2 | ON | 31 | 33 | 2 | ON | 17 | 19 | 2 |
| HI-PWR ISOLATOR | ON | 0 | 2 | 2 | ON | 39 | 40 | 1 | ON | 25 | 26 | 1 |
| TWT R-SWITCH S13 | OFF | -4 | -2 | 2 | ON | 30 | 29 | -1 | ON | 17 | 18 | 1 |
| O/P LPF | OFF | -1 | 1 | 2 | ON | 36 | 34 | -2 | ON | 23 | 23 | 0 |
| RADIO ASTRONOMY FILTER | OFF | -5 | -2 | 3 | ON | 33 | 29 | -4 | ON | 20 | 18 | -2 |
| TM TRANSMITTER | ON | 7 | 7 | 0 | ON | 33 | 32 | -1 | ON | 22 | 20 | -2 |
| ULPC | ON | 6 | 7 | 1 | ON | 32 | 32 | 0 | ON | 21 | 20 | -1 |
| KU POWER MONITOR | OFF | 1 | 3 | 2 | ON | 28 | 29 | 1 | ON | 16 | 17 | 1 |
| EXTERNAL LOAD | OFF | 2 | 2 | 0 | OFF | 32 | 31 | -1 | OFF | 23 | 21 | -2 |
| **SOUTH RADIATOR** | | | | | | | | | | | | |
| SSPA | ON | 17 | 16 | -1 | ON | 28 | 27 | -1 | ON | 47 | 46 | -1 |
| SSPA ISOLATOR | OFF | 7 | 6 | -1 | OFF | 20 | 18 | -2 | OFF | 34 | 36 | 2 |
| L-BAND UP-CONVERTER | ON | 11 | 9 | -2 | ON | 21 | 18 | -3 | ON | 43 | 40 | -3 |
| COMMAND RECEIVER | ON | 3 | 5 | 2 | ON | 15 | 16 | 1 | ON | 34 | 34 | 0 |
| TELEMETRY TWT | ON | 17 | 15 | -2 | ON | 43 | 39 | -4 | ON | 56 | 53 | -3 |
| TELEMETRY EPC | ON | 10 | 12 | 2 | ON | 27 | 25 | -2 | ON | 42 | 43 | 1 |
| DC/DC CONVERTER | ON | 3 | 4 | 1 | ON | 16 | 16 | 0 | ON | 35 | 35 | 0 |
| EXTERNAL LOAD | OFF | 3 | 4 | 1 | OFF | 8 | 10 | 2 | OFF | 31 | 33 | 2 |

### On-orbit Storage Thermal Balance (Phase 2)

All the payload units were off and the bus and the TT&C units were on. The payload maintenance heaters and replacement heaters were enabled. The West IR lamps were used. The results show that all payload unit temperatures were within 2 °C. The propulsion system and TT&C units were within the 5 °C range, however some bus unit temperatures were at least 5 °C lower than the predictions. A comparison of the predicted vs. actual bus panel and thrust panel temperatures revealed a discrepancy of 5 °C; this discrepancy was attributed to the fact that the bus panel and thrust cylinder reacted more slowly than the radiators, and had not reached their steady state when the data was taken.

### Equinox BOL No Drive Thermal Balance (Phase 3)

IR lamps were not used. The bus and the TT&C units were on. The payload maintenance heaters were enabled and the replacement heaters were off. The SSPAs and Ku-TWTAs were on at no-drive. The environment was set as a steady state eclipse condition and should be the worst on-orbit cold case. Most units were within the 5 °C range. The 2-frequency local oscillator (LO) and the reference oscillator were 7°C cooler than the predictions. After post-test TC inspection, those TCs used in this Phase were found partially detached.

### Summer EOL No Drive (Phase 4)

East and North IR lamps were used. The bus and the TT&C units were on. The payload maintenance heaters were enabled and the replacement heaters were off. The SSPAs were at no-drive and the Ku-TWTA was at nominal drive. All units were within the 5 °C range. One of the external load in the South radiators was 7 °C cooler than the predictions. After the post-test TC inspection, the external load TC was found partially detached.

### Winter EOL No Drive (Phase 5)

Nadir and South IR lamps were used. The bus and the TT&C units were on. The payload maintenance heaters were enabled and the replacement heaters were off. The SSPAs were at no-drive and the Ku-TWTA was at nominal drive. All units were within the 5°C range.

## CONCLUSION

The stringent test requirements and the high power dissipation of the MSAT payload required the development of versatile IR radiating rigs to accurately simulate required test environments. The IR rig used 122 IR lamps to provide IR heat inputs into six of the seven spacecraft zones. Each zone is contoured with specular reflective baffles to provide < 5 % flux uniformity with a minimum number of lamps. To measure the absorbed flux at 38 spacecraft locations, 49 MBRs were used. The IRFLUX software was used to do simulations and perform post-processing on the six IR zones.

The radiometer test results correlated the software flux prediction and distribution very well. The IR technique developed by SPAR has proven to be an accurate method for correlating the internal thermal network of satellites. An additional advantage is the ability to perform consecutive thermal balance and TV tests. The MSAT bulk and detailed panel models were successfully updated to reflect the thermal balance test results, and the temperature correlations were generally within 2 °C. Four spacecraft tests were conducted with short preparation time and no major problems. DFL proved to be a very reliable test facility and their state-of-the-art equipment and well trained staff supported those tests efficiently.

## REFERENCES


1. S. Samson, P. Theophanous, J. Lemire & M. Donato, "Thermal Test Designs for the MSAT Satellites", 2nd International Symposium, Environmental Testing for Space Programmes, ESTEC, The Netherlands, 1993.

2. C. Ruel, M. Larouche & M. Donato, "Monitored Background Radiometer," 17th ICES Conference, 1987.

3. M. Donato, P. Messidoro & E. Choueiry, "Correlation of the Olympus Thermal Model Using IR Test Data", International Symposium on Environmental Testing for Space Programmes, 1990.

4. M. Donato, J. Green, D. St-Pierre & M. Reeves, "Evaluation of Infrared Test Method for the Olympus Thermal Balance Tests", *The Journal of Environmental Sciences,* 1987.

5. A. Golob, C. Ruel, D. St-Pierre & M. Donato, "Thermal Balance testing of Anik E Spacecraft", 1991

6. C. Ruel & P. Germain, "Error Analysis of the Monitored Background Radiometer", SPAR Report RML-009-88-017, 1988.

7. M. Donato, C. Ruel, A. Harris & B. Muir, "Absorbed Flux Predictions for Spacecraft IR Testing", 14th ICES Conference, 1983.

N95- 14083

# THERMAL DESIGN VERIFICATION TESTING OF THE CLEMENTINE SPACECRAFT: QUICK, CHEAP, AND USEFUL

Jeong H. Kim and Nelson L. Hyman
Naval Center for Space Technology, Naval Research Laboratory
Washington, DC

## ABSTRACT

At this writing, Clementine had successfully fulfilled its moon-mapping mission; at this reading it will have also, with continued good fortune, taken a close look at the asteroid Geographos. The thermal design that made all this possible was indeed formidable in many respects, with very high ratios of requirements-to-available resources and performance-to-cost and mass. There was no question that a test verification of this quite unique and complex design was essential, but it had to be squeezed into an unyielding schedule and executed with bare-bones cost and manpower. After describing the thermal control subsystem's features, we report all the drama, close-calls, and cost-cutting, how objectives were achieved under severe handicap but (thankfully) with little management and documentation interference. Topics include the newly refurbished chamber (ready just in time), the reality level of the engineering model, using the analytical thermal model, the manner of environment simulation, the hand-scratched film heaters, functioning of all three types of heat pipes (but not all heat pipes), and the BMDO sensors' checkout through the chamber window. Test results revealed some surprises and much valuable data, resulting in thermal model and flight hardware refinements. We conclude with the level of correlation between predictions and both test temperatures and flight telemetry.

# PARTIAL PRESSURE ANALYSIS IN SPACE TESTING[1]

Charles R. Tilford
National Institute of Standards and Technology
Gaithersburg, MD 20899

## ABSTRACT

For vacuum-system or test-article analysis it is often desirable to know the species and partial pressures of the vacuum gases. Residual Gas or Partial Pressure Analyzers (PPAs) are commonly used for this purpose. These are mass spectrometer-type instruments, most commonly employing quadrupole filters. These instruments can be extremely useful, but they should be used with caution. Depending on the instrument design, calibration procedures, and conditions of use, measurements made with these instruments can be accurate to within a few percent, or in error by two or more orders of magnitude. Significant sources of error can include relative gas sensitivities that differ from handbook values by an order of magnitude, changes in sensitivity with pressure by as much as two orders of magnitude, changes in sensitivity with time after exposure to chemically active gases, and the dependence of the sensitivity for one gas on the pressures of other gases. However, for most instruments, these errors can be greatly reduced with proper operating procedures and conditions of use. In this paper, data are presented illustrating performance characteristics for different instruments and gases, operating parameters are recommended to minimize some errors, and calibrations procedures are described that can detect and/or correct other errors.

## INTRODUCTION

There are many applications where it is desirable or essential to know not just the total vacuum pressure, but the partial pressures of different gas species. Partial pressure analysis is widely used as a general diagnostic of vacuum system performance, and it is essential when testing systems or components that can be damaged by contaminants (e.g. vacuum pump oil, water). For outgassing studies the identification of the gas species and their partial pressures are an invaluable tool in identifying gas sources and determining the possible interactions between the outgassed material and sensitive components on which it might impinge. These measurements can be made using Partial Pressure Analyzers (PPAs), also known as Residual Gas Analyzers (RGAs), which indicate the partial pressures, as a function of molecular weight, of the gases in a vacuum environment. Although originally developed for the qualitative diagnosis of residual gases in ultra high vacuum systems, the growing need for better contamination data and more sophisticated space experiments has encouraged the application of these instruments to quantitative measurements. However, the performance of these instruments varies significantly, depending on design and conditions of use. In the best cases, after proper calibration, they can be accurate to within a few percent; in other cases, they can have orders-of-magnitude errors. The unpredictable performance of some instruments has caused misleading results - frustrating users and probably discouraging the wider use of a potentially valuable instrument.

---

[1]This work was supported in part by the Applied Physics Laboratory of The Johns Hopkins University.

At a minimum, users can make better use of RGA results if they understand the potential problems and errors. It is also possible, with a reasonable effort, to detect and even minimize some of the more egregious errors. This paper discusses some of the observed performance characteristics of RGAs or PPAs, and suggests calibration or testing procedures that can help to detect and minimize undesirable behavior.

## INSTRUMENT BASICS

Residual gas analyzers are compact mass spectrometers that can be attached to vacuum systems as appendage instruments, or, with minor modifications, immersed directly in the vacuum. Generally, they can be baked, are constructed to be compatible with ultra high vacuum systems, and are designed for high sensitivity so that they can detect and analyze low-level residual gases in a vacuum system. They consist of an electron-impact ionizer, a mass filter, extraction electrodes to transfer ions from the ionizer to the mass filter, and an ion detector at the far end of the mass filter. Ion source designs are varied and can have a significant effect on instrument performance. In the simplest cases they resemble the filament and grid structure of a Bayard-Alpert ionization gage. In some instruments they are "closed" and may be differentially pumped so that the instrument operates at a reduced pressure and samples higher-pressure gases through a restricted conductance. A number of different mass filter types have been used and many of the early instruments used magnetic-sector analyzers. However, most modern commercial RGAs use quadrupole mass filters. In a quadrupole filter a combination of DC and megahertz-range radio frequency voltages impressed on the quadrupole rods increases the probability that ions with a selected mass-to-charge ratio will travel down the axis of the filter structure to the detector; the transmission probability for other ions is much smaller and they are deflected to the rods or the surrounding structure. The detector may be a Faraday cup or, for increased sensitivity, a secondary electron multiplier (SEM). The SEM may be used as an analog current amplifier, or combined with a fast-rise amplifier for ion counting.

Mass ranges for different instruments vary, but ranges of 50 to 200 mass-to-charge ratio are typical. The high-sensitivity design and small size limits the mass resolution of these instruments and it is often necessary to use cracking patterns to distinguish between molecules with small mass differences, e.g., $N_2$ and CO. The minimum-detectable partial pressure is determined by several factors, and ranges from $10^{-14}$ to $10^{-8}$ Pa ($10^{-16}$ to $10^{-10}$ torr; 1 torr = 133.3 Pa) for different instruments. The ion sources of these instruments typically can operate in pressures as high as 0.1 Pa, however, as will be shown, significant high-pressure nonlinearities can occur in some instruments at pressures of $10^{-3}$ Pa or lower. Differential pumping can extend the effective range of the instruments higher, but attention must be paid that sampling problems do not distort the partial-pressure spectrum.

## INSTRUMENT PERFORMANCE

The increased interest in using RGAs for quantitative analysis has prompted several systematic studies of their performance in recent years [Refs. 1-6]. The studies at the National Institute of Standards and Technology (NIST) [Refs. 5,6] have involved the repeated calibrations of more than a dozen different RGAs with partial pressures of different gases between $10^{-7}$ and $10^{-1}$ Pa. The performance of these instruments, especially mass resolution and sensitivity as a function of mass-to-charge ratio, will depend on a number of factors, including, ion energy, electron emission current, and both the dc and rf potentials in the quadrupole filter. In many instruments these factors can be varied by adjusting different instrument operating parameters. Unfortunately, most manufacturers provide little or no information on the overall performance effects of varying these parameters. Therefore, for some instruments these calibrations were

repeated with different combinations of instrument operating parameters. In some cases the calibrations were performed with pure gases, in others with combinations of two or three gases, each of which could be independently controlled and measured. The calibrations for inert gases were referenced to NIST primary vacuum standards [Ref. 7], either directly or with calibrated transfer gages. Water calibrations used a new NIST primary water vapor standard [Refs. 6, 8]. Examples of the NIST results are presented below. Further details and results obtained by other workers can be obtained from the references.

**Relative Sensitivities**

The sensitivities of ionization gages to different gases are generally presented as "relative sensitivities" - the ratio of the sensitivity for a specific gas to the sensitivity of the same gage for a reference gas, generally nitrogen or argon. Generally, for a given gas the relative sensitivities for different ionization gages do not vary by more than 10%. It is often assumed, both by users and some instrument manufacturers, that these same relative sensitivities can be used for RGAs. However, while the relative sensitivity of an ion gage is determined primarily by the ionization probability of the different gases, the relative sensitivities of RGAs are also strongly influenced by the mass-dependent transmission efficiency of the mass filter, which depends on instrument design and operating parameters. Data are presented in the references showing relative sensitivities for different instruments, operated with Faraday-cup detectors, that differ by as much as a factor of five from the values found for ionization gages, and in at least one case the sensitivity of a particular instrument for helium, relative to argon, could be varied by a factor of 10 simply by changing instrument operating parameters. The sensitivity of SEMs is also mass dependent, and their use will introduce additional variability in the relative sensitivities.

**Sensitivity as a Function of Pressure**

As a first approximation, the sensitivity of a hot-cathode ionization-type instrument is independent of pressure, i.e., the ion current is linear with pressure. However, with the more complicated RGAs the linearity can be strongly influenced by instrument design, operating parameters [Ref. 5], and even history of use [Ref. 2]. The most influential operating parameter is the ion-extraction voltage (labeled "ion energy" in many instruments), the potential difference between the center of the quadrupole filter and the anode of the ion source. The observed nonlinearities can be broadly categorized as "low-pressure", typically occurring at pressures of $10^{-4}$ Pa and below during operation with high ion-extraction voltage settings, and "high-pressure", typically occurring at pressures of $10^{-3}$ Pa and above during operation with low ion-extraction voltages.

The range of observed performance can be appreciated from Fig. 1. The data in this figure, discussed in detail in [Ref. 5], were selected from 27 different data sets obtained for each instrument with different ion-source operating parameters: emission current, electron-accelerating voltage, and ion-extraction voltage. To emphasize the changes in linearity, the data from each set have been normalized to a value of 1 at $10^{-4}$ Pa. The data presented were chosen to illustrate extremes of behavior: best linearity, maximum low-pressure nonlinearity, and maximum high-pressure nonlinearity. For PPA-D the performance illustrated by the line with no symbols (sensitivity constant to within a few percent up to $10^{-2}$ Pa) was obtained for a wide range of operating parameters, the high-pressure nonlinearity was observed only under extreme settings of the operating parameters, and virtually no low-pressure nonlinearity was observed. For PPA-A

significant nonlinearities were observed for all combinations of operating parameters. The line with no symbols was the best observed performance, and large low- and high-pressure nonlinearities were observed for a wide range of operating parameters. In particular, when operated at low ion-extraction voltages the sensitivity of this instrument changed by more than two orders of magnitude as a function of pressure.

The performance characteristics illustrated in Fig. 1 clearly depend in part on the design of the instrument, but the question remains, how well do these characteristics repeat from one unit to another of the same design? We have carried out brief testing of two additional units of instrument type A, and have found similar results to those illustrated in Fig. 1. We have carried out more extensive tests of three additional units of type D, and some of the results are illustrated in Fig. 2. In this test, the three additional units, D-2, D-3, and D-4, were operated with the same operating parameters (1 mA emission current, 100 V electron energy, and 10 V ion extraction voltage) found to give the most linear behavior for the original instrument, now labelled D-1. As can be seen, all four instruments exhibit very good linearity at low pressures, but there are significant differences for pressures above $10^{-3}$ Pa. It is quite possible that the limit of linear behavior could be extended to higher pressures for D-2 and D-4 by decreasing the ion energy (ion extraction voltage). One can reasonably conclude that instruments of a given manufacturer and model will probably give similar performance under similar conditions of use, but that for best performance individual instruments will have to be fine tuned.

**Background Gas Effects**

It is implicitly assumed that an RGA measures the partial pressure of one gas independent of the pressure of other gases. This assumption has been tested using calibration systems in which two or three gases can be simultaneously and independently controlled and measured [Refs. 2, 5]. The assumption is not always valid.

Figure 3 illustrates the results of such a test with two inert gases. The helium responses of several RGAs were simultaneously monitored as a function of the pressure of a second gas - argon. A helium pressure of $1.2 \times 10^{-4}$ Pa was maintained constant to within 1 % throughout the experiment. The experiment started with an argon pressure of $8.6 \times 10^{-5}$ Pa, which was then reduced to "zero" for the time indicated by the horizontal line on the figure, after which the argon pressure was restored. The changes in the helium responses of four instruments are shown; three are quadrupoles and instrument F is a magnetic-sector. As can be seen, the responses of all four instruments were stable with time, and that of instrument F was little affected by the change in the argon pressure. However, the helium sensitivities of the three quadrupoles variously increased or decreased by up to 12 % when the argon was "turned off". Not included in the figure were data for two other quadrupoles tested at the same time; their response was similar to F, i.e., they showed virtually no change in their helium sensitivity.

The results of Fig. 3 illustrate some of the types of responses observed with inert gases for different instruments. In general, the responses depend not only on the particular instrument, but also on the combination of gases. Typically, argon sensitivities are much less affected by changes in a helium pressure. On the other hand, instruments that are unaffected by changes in argon or helium background pressures can be significantly affected by a change in water pressure. Generally, with higher background pressures the sensitivity changes are larger; in some cases we have seen order-of-magnitude changes for background pressure changes in the $10^{-3}$ to $10^{-1}$ Pa range. And there is evidence that the characteristics of a particular instrument are affected by condition and duration of use [Ref. 2].

## Reactive Gas Effects

In addition to the prompt sensitivity changes illustrated in Fig. 3, reactive gases can cause changes that are slowly reversible. We have observed such changes during and after operation with $O_2$, $H_2O$, CO, $H_2$, and even $CO_2$. Figure 4 illustrates the results of such a test for three different instruments; two quadrupoles and one magnetic-sector (F). In this case an argon pressure of $1.3 \times 10^{-4}$ Pa and a helium pressure of $1.4 \times 10^{-4}$ Pa were maintained in the chamber. A water pressure of $4.4 \times 10^{-4}$ Pa was then "turned on" during the period indicated on the time axis by arrows. Again, the results differ from instrument to instrument. The argon signal of instrument F, the magnetic-sector which did not show a change in sensitivity in Fig. 3, does show a "prompt" change in the argon signal when water is added and taken away, as well as a residual shift in the argon signal after the water is "removed" (slow equilibration of the water pressure accounts for the time-response of the instrument signal). Instrument D-4, an instrument that showed no change in the helium sensitivity during the test illustrated in Fig. 3, shows a definite time-dependent change in argon sensitivity throughout the water exposure, but a prompt recovery with a residual offset when the water is removed. Instrument A-2, of the same type as PPA-A in Fig. 1, exhibits a complicated response to the water, and most notably exhibits a long-term recovery of the argon sensitivity after the water is removed.

Again, the data of Fig. 4 are only illustrative. For a number of other instruments we have observed both positive and negative sensitivity changes after exposure to different reactive gases, followed by long-time-constant decays, similar to that shown for A-2, back to their pre-exposure values. This effect will cause a hysteresis in the indicated partial pressures when the pressure of a reactive gas is increased and then decreased. Typically, we have not observed sensitivity changes greater than about 20%, and some instruments seem to be effectively immune to this behavior.

## Absolute Sensitivity and Minimum-Detectable Partial Pressure

As noted before, RGA sensitivities depend on pressure, gas species, and instrument operating parameters. There are also instrument design features that cause significant variations in sensitivity from one instrument to another. For instance, five instruments of different design, operated with Faraday-cup detectors and "nominal" operating parameters, had sensitivities ranging from 2 to $52 \times 10^{-8}$A/Pa for an argon pressure of $10^{-4}$Pa [Ref. 5]. The factors influencing absolute sensitivities and minimum-detectable partial pressures are discussed in some detail in Ref. 9, but the most important factor is the ion source design and the coupling of the ions from the source to the mass analyzer. For a given electron emission current, the ion production rate can be increased by electrostatically trapping the electrons to increase their path length within the ionizer. The ions must then be extracted from the source and injected into the mass analyzer; the efficiency of this process will depend on field gradients within the source and between the source and the analyzer - the fields between an ion source and a quadrupole analyzer are particularly important.

Unfortunately, using electron trapping to enhance the "brightness" of an ion source makes the source dependent on space charge and susceptible to the previously-discussed nonlinearities with pressure. Of the instruments tested in Ref. 5, the most sensitive was PPA-A of Fig. 1, the least sensitive was PPA-D. The space charge dependence and nonlinearities of some quadrupole instruments can be decreased, and the sensitivity increased, by operating at higher ion energies, but this will decrease the mass resolution, and can cause nonlinearities at lower pressures.

The minimal-detectable partial pressure will depend on the instrument sensitivity and the ion detection limit. For one-second sampling times the noise limit of high-quality ammeters and cables is about $10^{-16}$A, so the detection limit for PPAs with Faraday cup detectors can be in the range of $10^{-11}$ to $10^{-9}$Pa. However, not all ammeters are equal, and in some instruments the limit can be two to three orders of magnitude higher. Secondary electron multipliers can increase the ion current by as much as a factor of $10^7$, depending on SEM design and operating voltage. However, SEM noise and quantum limits (1 electron/s corresponds to $1.6 \times 10^{-19}$ A) will limit the minimum-detectable partial pressure to $10^{-14}$ to $10^{-12}$ Pa range. By using ion counting and longer sampling times this limit can be reduced somewhat. SEMs are also used to achieve improved, but modest detection limits with lower-cost, noisier ammeters.

As with other RGA characteristics, there is often a tradeoff between sensitivity, linearity, and mass discrimination, and the user should choose an instrument to suit the problem. It should also be noted that the detection limit for a given species can be obscured by overlap from strong neighboring peak - this performance characteristic is generally characterized as "abundance sensitivity". This problem will increase as the mass resolution decreases.

### Long-Term Stability

If Faraday-cup detectors are used and operation with active gases is avoided, the sensitivity of some instruments has been observed to change less than 10% over a period of months. At the other extreme, during this same time the sensitivity of other instruments changed by as much as a factor of five, although after several months operation the sensitivity of these instruments stabilized to within 25%. The gain of an SEMs can exhibit order-of-magnitude changes over periods of weeks, particularly when the SEM is new, so operation with SEMs results in sensitivities that can be significantly less stable than with Faraday-cup detection.

## CONTAMINATION

Contaminants generated in RGAs are a particularly serious problem since they cannot be distinguished from system gases and are generally present at relatively high partial pressures because of conductance limitations. Therefore, it is particularly important to use ultra high vacuum techniques in handling and using RGAs and highly desirable that they be baked.

However, even with a clean RGA, apparent contaminants or anomalous species can be generated by reactions between the hot filament and system gases. A notable example is water (Ref. 6). Operation in water of tungsten or thoria-coated filaments, or the high-voltage discharge in a cold-cathode gage, will generate significant quantities of hydrogen, carbon monoxide (which might be mistaken for nitrogen), and carbon dioxide. Variable amounts of oxygen will also be produced, depending on water pressure and time. Detectable amounts of atomic oxygen and $H_3O$ (hydronium, which can be confused with fluorine) are also produced. Since water is often the dominant gas in a vacuum system, and some space experiments, these reactions can cause the misidentification of species not present, or present in smaller quantities.

## RECOMMENDATIONS

If RGAs are to be used to their full potential it is clearly desirable to avoid or minimize the aberrant behavior that has been observed for some instruments. The most and least desirable instrument characteristics will depend on the application, and there is probably no perfect instrument for all

applications, although for almost any application it is probably undesirable for the sensitivity for one gas to depend on the pressure of other gases. As noted, there will be tradeoffs between characteristics, and there is not a perfect correlation between price and performance.

It is important that the user decide what mass range, minimum-detectable partial pressure, and mass resolution the application requires. Extending capabilities beyond actual requirements in any of these areas will incur penalties in other aspects of performance, and instrument cost. Having prioritized instrument requirements, three steps should be taken: select an RGA that most closely matches those requirements, adjust the instrument operating parameters to optimize its performance, and calibrate it with a mix of gases and over a range of pressures that approximate the actual conditions of use. This is clearly easier said than done, but not totally impossible.

As a first effort, ask the manufacturer for calibration data; if the RGA readout is in pressure units, demand calibration data. In many cases the manufacturers do not know or may not disclose much of the information of interest, so all three steps will probably require instrument testing and calibration by the user. NIST is currently developing simpler calibration systems of the type described in Ref. 5. These are designed to allow users to calibrate RGAs with several gases at once over a range of pressures. Until such systems are available, RGAs can be calibrated with pure inert gases by comparison with a Bayard-Alpert (BA) ionization gage (preferably a glass-envelope gage with opposed tungsten filaments) over a wide range of pressures. These ion gages are much more stable and linear than an RGA; with a good controller they will be linear and stable to within 10% over a wide range of pressures. For better accuracy, a Spinning Rotor Gage can be used (the operation of vacuum gages is discussed in Ref. 10). In general, calibration of the mass scale is not a problem, and it can be quickly checked with respect to common residual gases; e.g., $H_2$ at mass-to-charge ratio of 2, $H_2O$ at 18 and CO at 28. Further information on RGA evaluation and calibration procedures is given in Ref. 11.

The reasons why quadrupole instruments behave the way they do are not fully (or even well) understood, but it does appear that space charge in the ion source has a significant influence on the ion extraction process and the instrument sensitivity [Refs. 12, 13]. Charge exchange in the ion source can also be important, as well as surface contamination on quadrupole rods [Refs. 2, 14]. Space-charge effects will be enhanced when operating with low ion-extraction voltages. If an increase in the RGA sensitivity at high pressures is observed (e.g., as in Fig. 1), and the instrument allows the adjustment, try operating with higher ion-extraction voltages. It is generally believed that operating with lower emission currents will also reduce high-pressure increases in sensitivity; our experience is that this is true in some, but not all cases. On the other hand, if the sensitivity increases with decreasing pressure below $10^{-4}$ Pa, try operating with lower ion-extraction voltages. If a significant pressure dependence of the sensitivity still remains, expect that the sensitivities for different gases will depend on the pressures of other gases,

After optimum operating parameters are established, periodically repeat calibrations with one or more pure gases to check for stability. If an SEM is used, periodically compare it to a Faraday cup and adjust the SEM gain or correct the readings accordingly. As a general rule, we obtain the most reliable results with tungsten filaments. Extended operation at higher pressures in hydrocarbon-contaminated systems can deposit insulating films on the quadrupole rods [Ref. 14] and should be avoided.

With some instruments and under some conditions of use, we have found that after calibration we can make measurements with uncertainties of a few percent. With other instruments and/or conditions of use, it is difficult to keep errors below one or two orders of magnitude. At a minimum, users should have some idea which situation they are dealing with and interpret their results accordingly.

## REFERENCES


1. F. M. Mao, J. M. Yang, W. E. Austin, and J. H. Leck, "Residual gas analyzers and their use in high vacuum systems", Vacuum 37, 335-8 (1987).

2. Fu Ming Mao and J. H. Leck, "The quadrupole mass spectrometer in practical operation", Vacuum 37, 669-75 (1987).

3. R. J. Reid and A. P. James, "Characterization of a multiple head residual gas analyzer installation on an electron storage ring", Vacuum 37, 339-42 (1987).

4. J. D. Sankey and A. H. Bass, "A preliminary attempt at the calibration of a small quadrupole mass spectrometer in the ultra-high vacuum portion of its range", Vacuum 40, 309-312 (1990).

5. L. Lieszkovszky, A. R. Filippelli, and C. R. Tilford, "Metrological characteristics of partial pressure analyzers", J. Vac. Sci. Technol. A 8, 3838-3854 (1990).

6. C.R. Tilford, "Characteristics of Partial Pressure Analyzers", in James B. Breckinridge and Alexander J. Marker III (eds.), SPIE Vol. 1761, Damage to Space Optics and Properties and Characteristics of Optical Glass, Vol. 1761, SPIE, Bellingham WA, 1992, p. 119-129.

7. C. R. Tilford, S. Dittmann, and K. E. McCulloh, "The National Bureau of Standards Primary High-Vacuum Standard", J. Vac. Sci. Technol.A 6, 2853, (1988).

8. S.A. Tison and C.R. Tilford, "Low-Density Water Vapor Measurements; The NIST Primary Standard and Instrument Response", in Benjamin A. Moore and Joseph A. Carpenter, Jr. (eds.), RL/NIST Workshop on Moisture Measurement and Control for Microelectronics, NISTIR 5241, NIST, U.S.A., 1993, p. 19-29.

9. C.R. Tilford, "The Measurement of Very-Low Partial Pressures", J. Vac. Soc. Japan 37 no.7 (1994).

10. Charles R. Tilford, "Pressure and Vacuum Measurements", Chapter 2, Volume VI, Physical Methods of Chemistry, edited by Bryant W. Rossiter, John F. Hamilton, and Roger C. Baetzold, Interscience, New York, (1992).

11. J.A. Basford, M.D. Boeckmann, R.E. Ellefson, A.R. Filippelli, D.H. Hokeboer, L. Lieszkovszky and C.M. Stupak, "Recommended Practice for the Calibration of Mass Spectrometers for Partial Pressure Analysis", J. Vac. Sci. Technol. A 11, no. 3, pg. A22 (1993).

12 M.C. Cowen, W. Allison and J.H. Batey, "Electron space charge effects in ion sources for residual gas analysis", Measurement Sci. Technol. 4, 72 (1993).

13. M.C. Cowen, W. Allison and J.H. Batey, "Nonlinearities in sensitivity of quadrupole partial pressure analyzers operating at higher gas pressures", J. Vac. Sci. Technol. A 12, 228 (1994).

14. W.E. Austin and J.H. Leck, "Optimization of the operation of the small quadrupole mass spectrometer to give minimum long-term instability", Vacuum 41, 2001 (1990).

## FIGURE CAPTIONS

1. Normalized argon sensitivities for two different quadrupole RGAs (PPA types A and D) operated with different combinations of ion source parameters. The line without symbols illustrates the most linear behavior for each instrument, while the circles and squares illustrate extremes of high- and low-pressure nonlinearities.

2. Normalized argon sensitivities for four different RGAs, all of the same manufacturer and model (type D of Fig. 1), and all operated with the same emission current, electron energy, and ion extraction voltage.

3. Changes in the response of four different instruments to a helium pressure of $1.2 \times 10^{-4}$ Pa when an argon pressure of $8.6 \times 10^{-5}$ Pa is reduced to zero ("Ar Off) and then restored.

4. Changes in the response of three different instruments to an argon pressure of $1.3 \times 10^{-4}$ Pa when a water pressure of $4.4 \times 10^{-4}$ Pa is introduced and then removed.

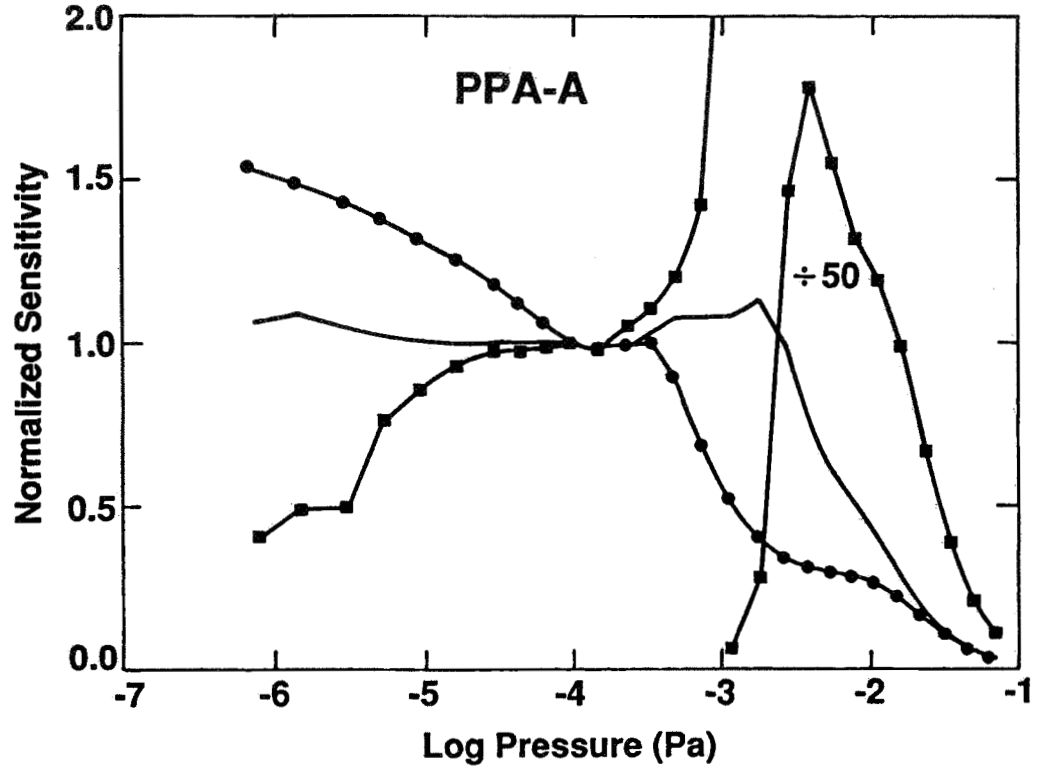
PPA-A
÷50
Normalized Sensitivity
Log Pressure (Pa)
2.0
1.5
1.0
0.5
0.0
-7
-6
-5
-4
-3
-2
-1

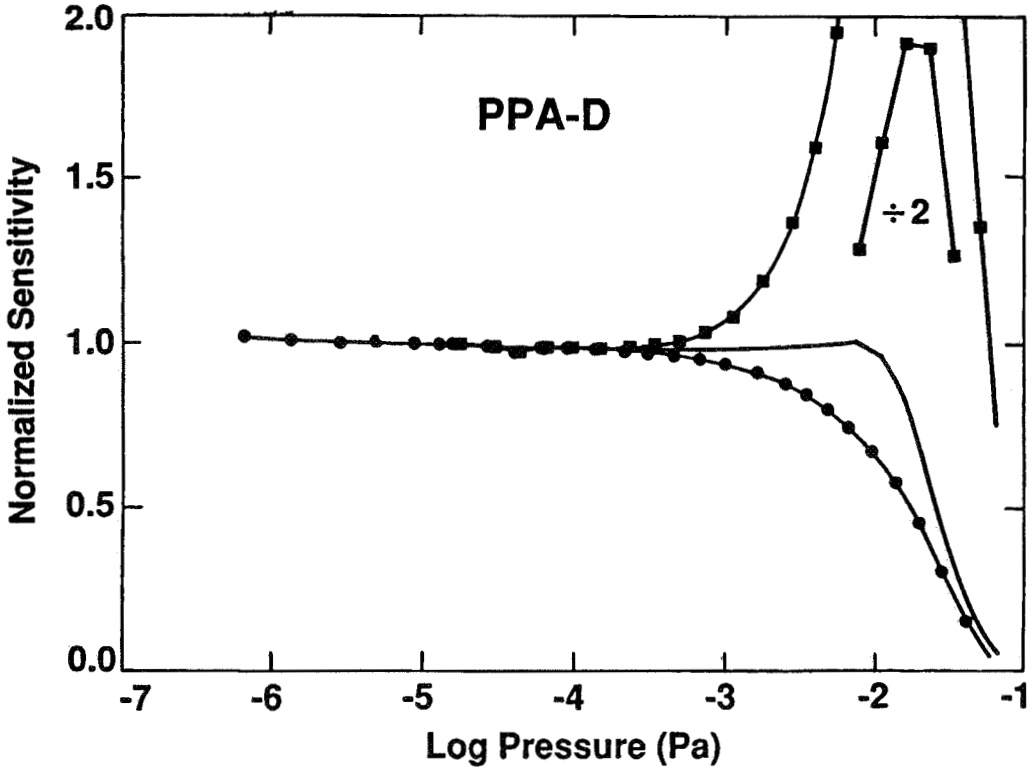
PPA-D
÷2
Normalized Sensitivity
Log Pressure (Pa)
2.0
1.5
1.0
0.5
0.0
-7
-6
-5
-4
-3
-2
-1

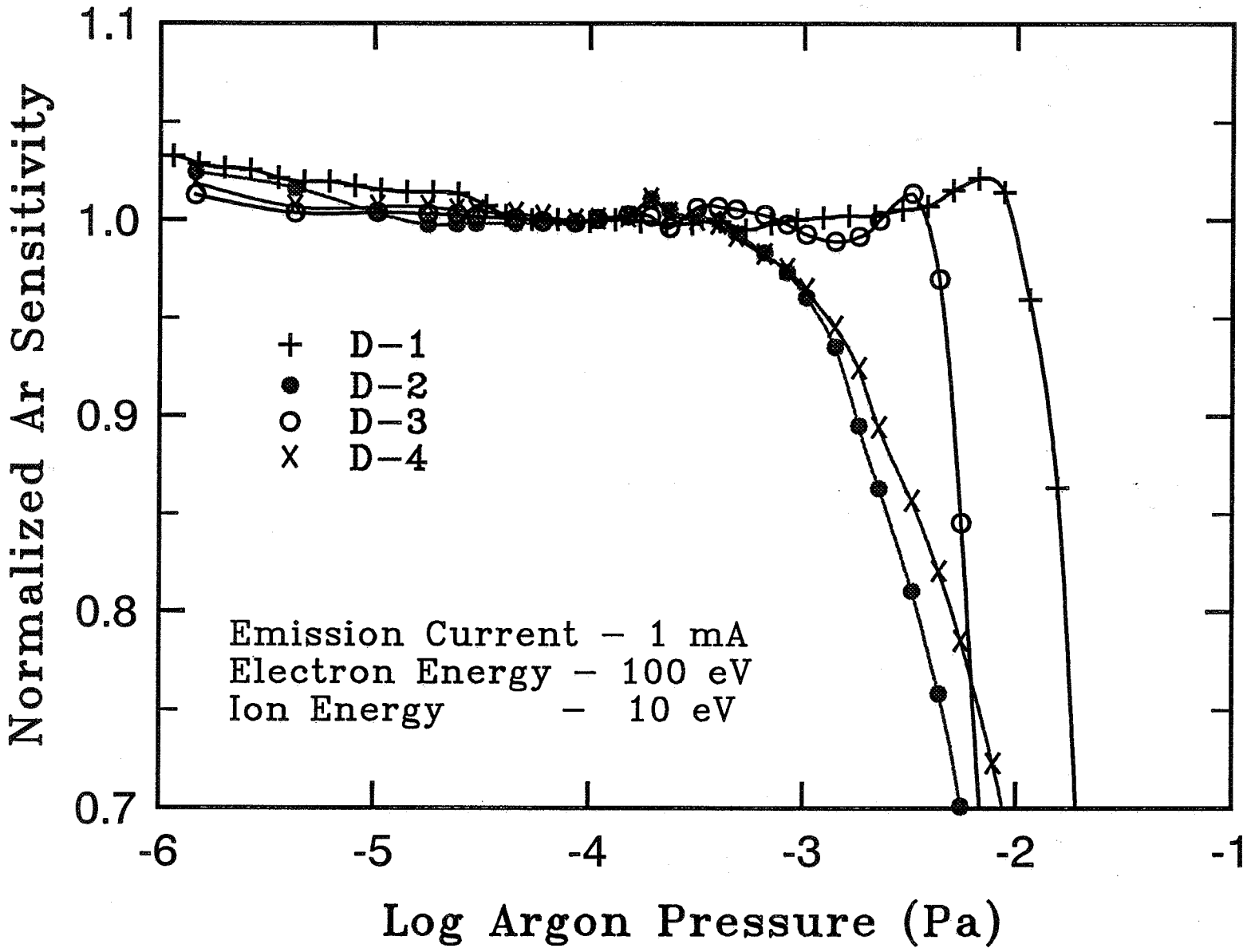
Normalized Ar Sensitivity
1.1
1.0
0.9
0.8
0.7
-6
-5
-4
-3
-2
-1
Log Argon Pressure (Pa)
+ D-1
● D-2
o D-3
x D-4
Emission Current - 1 mA
Electron Energy - 100 eV
Ion Energy - 10 eV

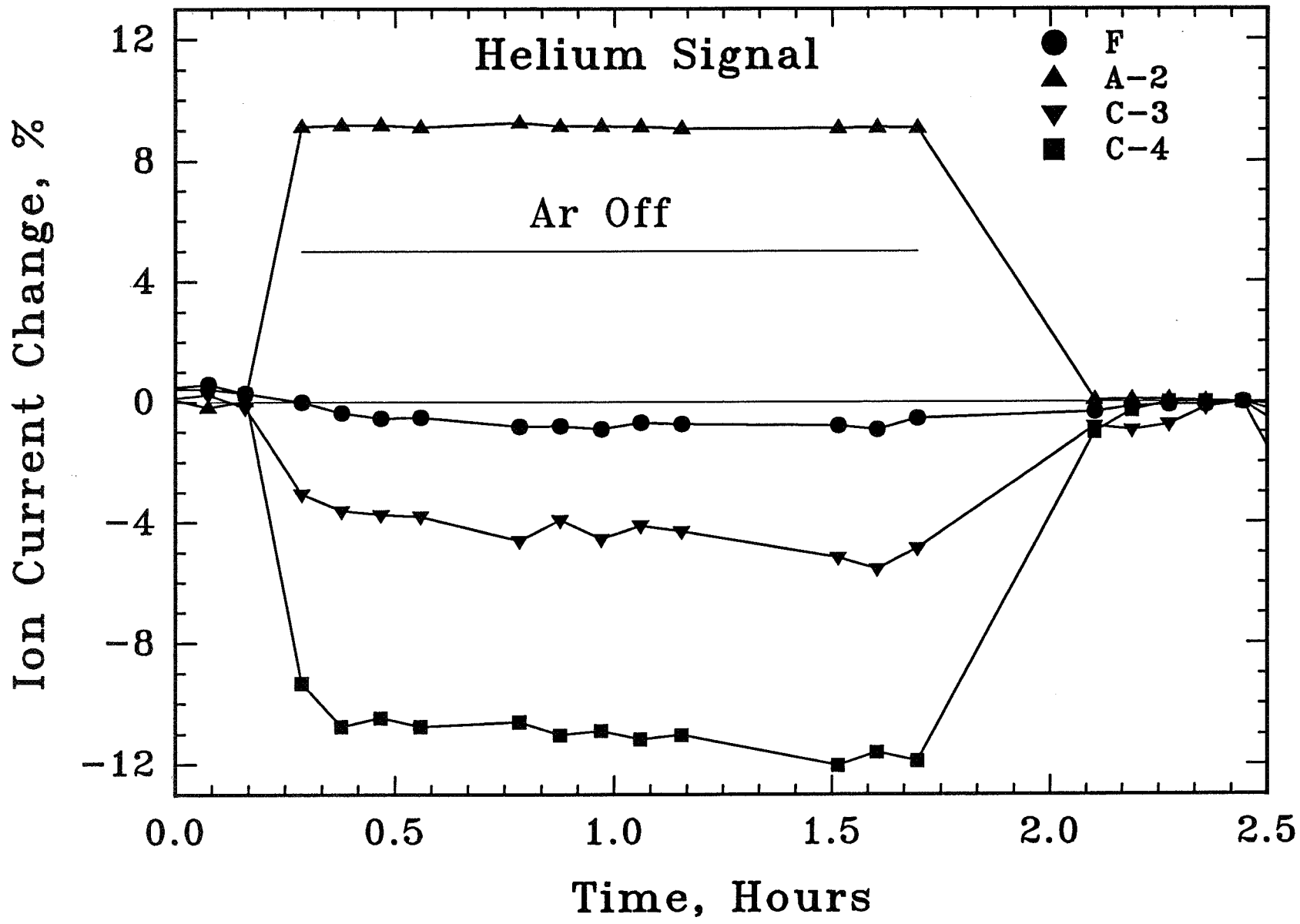
Helium Signal
F
A-2
C-3
C-4
Ar Off
Ion Current Change, %
12
8
4
0
-4
-8
-12
0.0
0.5
1.0
1.5
2.0
2.5
Time, Hours

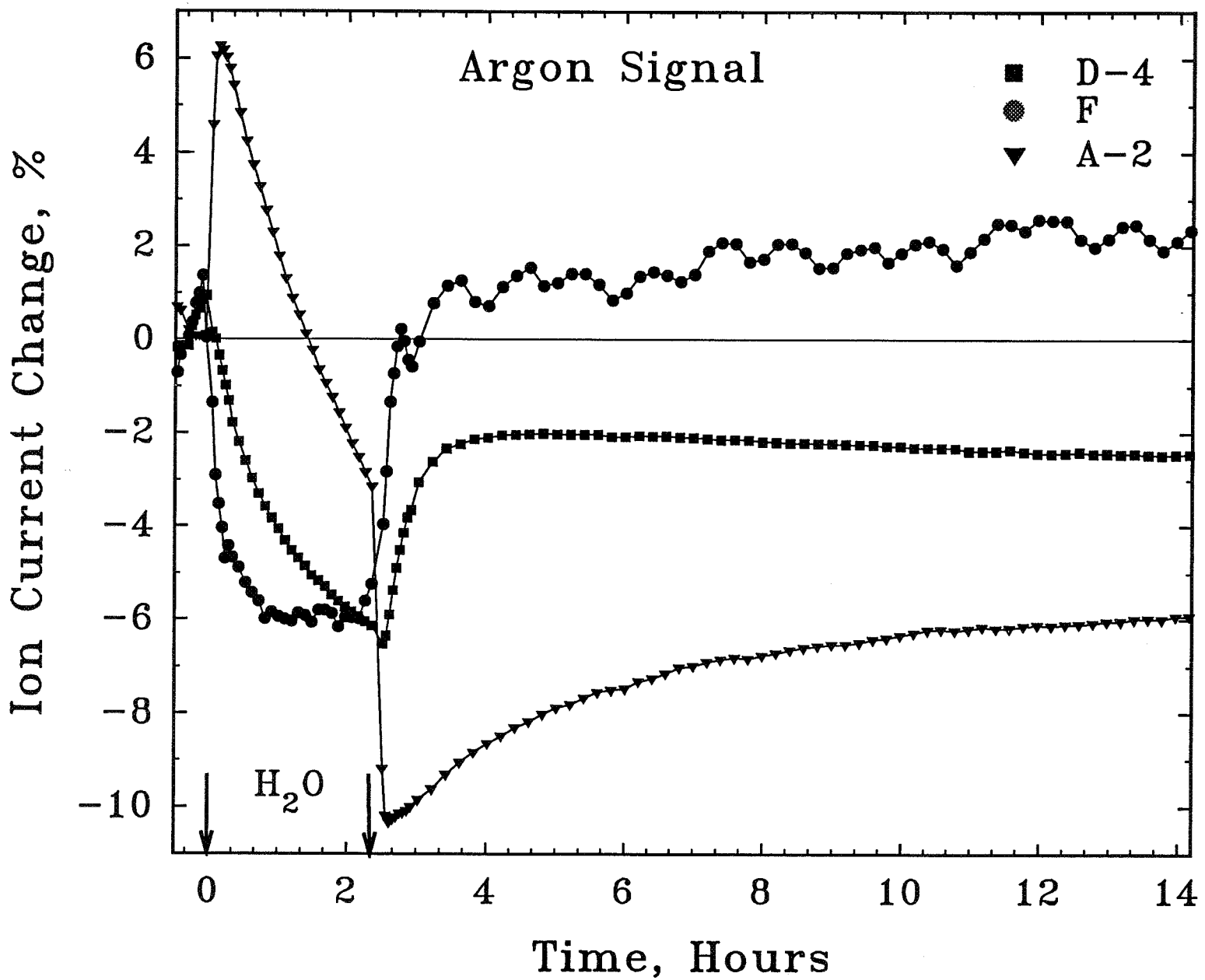
Argon Signal
D-4
F
A-2
Ion Current Change, %
6
4
2
0
-2
-4
-6
-8
-10
$H_2O$
0
2
4
6
8
10
12
14
Time, Hours

# REFURBISHMENT OF A 39' THERMAL VACUUM CHAMBER

Arthur A. Edwards
Space Systems/Loral
Palo Alto, California

## ABSTRACT

The 39' thermal vacuum chamber at Space Systems/Loral in Palo Alto, California, was built by CVI Corporation in 1969. Since then, it has been used to test numerous spacecraft including those of the GOES, Intelsat, Insat, Superbird, N-Star, NATO and other programs. Ten years ago, the aluminum $LN_2$ shroud experienced serious fatigue failures in the field welded jumper tubing, effectively shutting down the chamber for vacuum testing. (Refer to a paper presented by A. Edwards in 1984 at the 13th Space Simulation Conference titled **Fatigue Induced Cracking in Aluminum Shroud of 39 Foot Vacuum Chamber**). The problem was repaired at the time, but new failures began to reappear a few months ago and are now occurring at a rate that suggests that the shroud may again become inoperable. Consequently, Space Systems/Loral is spending in excess of $6 million to replace the shroud and the existing $LN_2$ equipment with a new, state of the art cryogenic system.

In May, 1994, a contract was awarded to PSI, Incorporated, to remove the existing shroud and $LN_2$ pumping system and replace it with a gravity fed shroud and distribution system. Included in the contract are eight skid mounted gaseous nitrogen pumping systems capable of controlling shroud zone temperatures between +150°C and -180°C. The project is scheduled to be completed in April 1995.

## HISTORY

The SS/Loral thermal vacuum chamber is a top loading 39 foot sphere with a subcooled, pressurized $LN_2$ system feeding an aluminum shroud (figures #1 and #2). The shroud is interconnected with jumpers in a series/parallel combination that separates it into six zones (figure #3). The liquid flow is large enough and the pressure high enough that the $LN_2$ remains as liquid throughout the shroud, vaporizing the secondary liquid when it reaches the

subcooler's heat exchanger. The advantage of the system is that is does not vapor lock with the thermal loads up to 300 KW. One of its disadvantages is that the pumps required to maintain this high pressure/flow rate introduce energy into the liquid which ends up as consumed $LN_2$. In addition, the liquid temperature is relatively high, because heat is absorbed by the $LN_2$ through a sensible process resulting in an increase in the liquid temperature as it travels through the shroud.

In 1984, the shroud's interconnecting jumper tubing began failing during each pumpdown cycle through a fatigue fracture mechanism that is explained in detail in the proceedings of the Space Simulation Conference held in Orlando that year. Many of the field welded jumpers were replaced, effectively stopping the failures. Since then, SS/Loral has successfully tested many spacecraft in the chamber, and the shroud has held together satisfactorily. However, during the past few months, fatigue failures have been occurring in tubing that was not replaced ten years ago. The failure rate has increased enough to indicate that something should be done to correct the problem before the chamber is once again unusable. The problem is compounded by the fact that SS/Loral has eleven thermal vacuum tests scheduled in the chamber during 1994 and 1995. To work around this situation, a plan has been devised to accomplish the refurbishment without disrupting the testing schedule.

## COURSE OF ACTION

It is obvious that the present shroud repair program is not a long term answer to the problem. A permanent solution had to be found. It was decided to remove and replace the entire shroud rather than repair it as it failed. Process Systems International of Westborough, Massachusetts, was selected to accomplish the refurbishment, and, together with SS/Loral, devised a plan to remove the existing system and replace it with a new shroud that will not experience fatigue failures. The new shroud will be supplied with a gravity fed $LN_2$ system that will provide the liquid flow required to handle a maximum 200 KW heat load at the lowest possible $LN_2$ consumption.

In addition to its $LN_2$ capability, each of the shroud's six zones can now be operated independently at any temperature between $+150^{o}C$ and $-180^{o}C$. A new 48" gate valve and roots blower will also be added to the vacuum system to reduce pumpdown time. In addition,

all the new $LN_2$ piping will be vacuum jacketed. To operate this equipment, a computer controlled operating console will be provided.

## SCHEDULE

The chamber testing schedule for the next two years was a serious concern to SS/Loral in its decision to approve this project. Because of this schedule, it appeared that there would not be sufficient time to replace the shroud within that period. During the initial design contract, however, the two companies worked together to develop an assembly and installation program that will allow the refurbishment project to be accomplished without interfering with testing. To do this, the installation sequence was separated into three phases:

> **Phase 1** - That work which can be accomplished at any time without regards to chamber activity.
> **Phase 2** - That work which can be accomplished between any early vacuum tests.
> **Phase 3** - That work which can only be accomplished in a period between satellite vacuum tests. This work cannot be stopped or postponed once it has started, and, if delayed, will delay the following spacecraft vacuum tests accordingly.

Scheduling of the work in the first two phases is not critical, and can be easily accomplished with good planning. The work associated with the third phase, however, is another matter. The third phase work includes such projects as removing the existing shroud, cutting penetrations through the chamber wall, installing the new $LN_2$ distribution system, installing the new shroud, removing the existing and installing the new operating console and interconnecting all of the new piping and electrical wiring. It is critical that the third phase work be accomplished within the openings of the existing test schedule. No delay in spacecraft testing can be tolerated.

Fortunately, SS/Loral's testing schedule shows a two month window between tests early in 1995, which is one of the few major breaks that will occur within the next two years. Consequently, PSI and SS/Loral developed an installation program that would fit into this window. The typical span to accomplish the amount of work in phase three has been as long as four months in previous projects. However, PSI and SS/Loral engineers worked together to develop a plan that

will allow the phase three work to be accomplished in the two month span available.

The essence of this plan is the pre-assembly of all the major components before the installation begins. For example, the new $LN_2$ shroud will be assembled into six structurally self supporting segments, assembled and leak checked on the high bay floor. When the window opens up, and the old shroud is removed, the segments will be set into the chamber and connected to their supports. No tubes will be welded inside the chamber, the final piping connections will be made with flexible cryogenic couplings. The $GN_2$ and $LN_2$ pumping skids will be assembled in PSI's shop and shipped ready for installation. This pre-assembly includes as much of the wiring and piping as possible. The new operating console and all of the vacuum jacketed $LN_2$ piping will also be pre-assembled and ready for installation. When the window opens, several teams will work in parallel to install the various components and systems within the two month span allotted. The success of this plan will be in the hands of PSI's site engineer and his installation teams, and will depend on the coordination efforts of the two companies.

## OPERATING COST CONSIDERATIONS

The operating cost of a thermal vacuum test chamber is very much dependent upon the thermal cycle of its $LN_2$ system. A typical thirty day thermal vacuum test in a chamber using a subcooled nitrogen system can cost as much as $150,000 in $LN_2$ consumption alone (at $.30 per gallon). This adds up to close to $1 million per year. Obviously, a reduction in $LN_2$ consumption can result in significant cost savings over a span of several thermal vacuum tests. Consequently, considerable thought was given to minimize the new system's $LN_2$ consumption. To accomplish this goal, the existing pressurized, subcooled system was abandoned and a gravity fed design was adopted. Basically, the system works like a ship's steam boiler. A large header is connected to the bottom of the shroud's vertical section from which the liquid flows vertically through finned tubing into a collection header attached to the top of the shroud. There is little $LN_2$ pressure, so its temperature is as low as possible. As the shroud is radiated by the heating rods or lamps (at a one sun maximum density), bubbles of $GN_2$ are formed inside the tubes and the heat is absorbed as latent thermal energy. These bubbles travel up the tubes and are collected in the top header and then returned, along with excess $LN_2$, to a separator tank. This

design maintains two phase (saturated) flow throughout the tubing, so that no part of the shroud is exposed to superheated gas or becomes vapor locked. This is accomplished by designing the liquid flow through the shroud tubes to be twenty times that of the $LN_2$ that is vaporized. A pump is not needed to accomplish this because the pressure difference between the liquid supply head and the partially vaporized return head is sufficient to circulate adequate liquid. The result is an effective cryogenic system, operating at the lowest possible temperature at a minimum $LN_2$ consumption rate.

To supplement the main shroud system, twelve auxiliary $LN_2$ zones are included to provide cooling to individual spacecraft components as required for each test. Because of the pressure drop and horizontal configuration in these zones, an $LN_2$ pump is used to transfer the liquid through these auxiliary zones.

## SYSTEM DESIGN

The new $LN_2$ shroud has approximately 3600 square feet of area and will be built in three segments, a top, bottom and cylindrical segment. Figure #4 shows a cross section of the three and their location in the chamber. The cylindrical segment is divided into four zones and the top and bottom segments are each a single zone. Each cylindrical zone will be fed from its own 300 CFM $GN_2$ skid. The top and bottom segments are constructed of vented extrusions connected to intermediate headers (figure #5). The top segment is 800 square feet and the bottom segment is 1000 square feet and each segment will be fed by its own 650 CFM $GN_2$ skid. To prevent vapor lock, there are no horizontal flow paths anywhere in the shroud. The cylindrical section is constructed of PSI's extruded tubing number HIV-42 at 7.5 inch centers as shown in Figure #6. The tubes are connected to a supply header at the bottom and a return header at the top (figure #7). All the vertical tubes are in parallel and there are no interconnecting jumpers in the shroud. This configuration is important because it eliminates the possibly of the fatigue failure problems that SS/Loral has experienced with its pressurized shroud. The side wall tubing with its overlapping fin design ensures optical density while providing a molecular conductance of 160 liters/sec.$ft^2$. With a side wall surface area of 1800 square feet, the total conductance through the cylinder is 290,000 liters/sec. All shroud sections will be fabricated from 6000 series aluminum.

Since there are no pumps in the $LN_2$ system, the key to its design is the driving force that is caused by the static head from the $LN_2$ separator tank. This tank is fed directly from the main $LN_2$ storage tank as demanded by a level sensor. The liquid is then fed to the shroud from the separator through a vertical supply header that enters the chamber near the bottom. After the $LN_2$ travels up through the shroud, it collects in the return headers and is routed back to the separator. There, the gas is vented and the liquid is returned to the shroud.

If no heat were introduced into the $LN_2$ throughout this cycle, there would be no liquid flow because the supply static head would be equal to the return static head. But heat is introduced into the liquid through heat leaks and through thermal energy directed onto the surface of the spacecraft. This heat load vaporizes less than 5% of the liquid in the tubes resulting in a vapor/liquid mixture in the exhaust which is lower in density than is the supply $LN_2$. This density difference results in a net driving pressure that circulates enough liquid through the shroud to remove the heat load and keep the liquid at $LN_2$ temperature. Figure #8 shows the various stages and flow patterns in a typical tube and how they change as a function of heat load. The new SS/Loral shroud will function in the "saturated nucleate boiling" region. The fluid flow rate is calculated to be twenty to fifty times greater than the heat load will vaporize. Figure #9 shows the system with a modulating valve in the $LN_2$ supply line to each zone. This valve controls the liquid/vapor ratio (density) of the liquid in the tube and therefore determines its supply pressure.

## THERMAL TESTING

Over the years, many aerospace companies have developed a standard procedure for performing thermal testing in vacuum chambers. Typically, an $LN_2$ shroud is used to simulate the cold black body of outer space, and a heating system, consisting of either cal rods or quartz lamps, is provided to simulate the sun's energy and counteract the cooling effects of the cryogenic shroud. Figure #10 shows a typical cal rod heater cage surrounding a part of a satellite. This technique has worked successfully, but has proven to be very costly in $LN_2$ consumption and in the associated efforts to build heater arrays, data systems and support structures. In the process of T/V testing, it has been discovered that a typical spacecraft operates during most of its orbital life not far from ambient

temperature. Consequently, the required thermal conditions can be attained by designing the shroud to operate at whatever temperature is appropriate for the orbital conditions under test. For example, if a surface of a spacecraft experiences a temperature of, say +30°C, then it is obvious that this temperature could be achieved by setting the segment of the shroud facing that surface at +30°C, or at whatever temperature will cause the surface to reach that level. In other words, little is gained by averaging two extreme temperatures of an $LN_2$ shroud and heater system bucking each other to reach the desired surface temperature somewhere in between (in this example, +30°C).

Millions of dollars in recurring and non-recurring testing costs can be saved by utilizing a segmented thermal shroud whose temperatures can be accurately controlled within the spacecraft's operating temperature range. To accomplish this, each of the six segments of the new shroud can be set at any temperature between +150°C and -180°C. The new thermal shroud will be segmented into six independently controllable zones, one to match each surface of the spacecraft, and each zone temperature will be programmed to simulate the conditions it will experience in orbit. Mylar covered reflectors will be used to thermally isolate each surface from the other. It is calculated that the probable $LN_2$ consumption rate using this technique will be less than ten percent of that which the SS/Loral 39' chamber is now experiencing. Significant non-recurring cost savings will also be realized because it will no longer be necessary to design and build large heater cages, heater power systems, special cryopanels, a fixture to support all of this and the hundreds of thermocouples to monitor the temperatures on all of this hardware. These non-recurring costs on a typical satellite program at SS/Loral have exceeded $2 million.

The refurbished SS/Loral chamber will have a dual capability. First of all, it will have the ability using $LN_2$ to simulate the thermal extremes found in orbital space as is presently available, and it will also be able to provide the required thermal conditions by using a temperature controlled segmented shroud, whichever a customer or contract requires. Under either condition, the cost of thermal vacuum testing will be significantly lower than SS/Loral, and many other companies in the industry, are now experiencing.

## DENSE GAS NITROGEN SYSTEM

Since a reliable $GN_2$ temperature control system is a relatively new technology in the thermal vacuum industry, and since it provides one part of the operation of the refurbished shroud, it is appropriate to describe its characteristics and capabilities.

Based upon their experience in the design and manufacture of first generation dense gas nitrogen systems, PSI has developed a new state-of-the-art second generation series called model TCU-1000 (figures #11, 12 and #13). This system includes a variable high speed centrifugal blower, a direct immersion electric heater and a compact spiral tube heat exchanger along with appropriate valves and sensors.

The control system provides precise temperature, dense $GN_2$ over a range of +150°C to -180°C within +/- 1° C. This control is achieved by maintaining a gas density of 0.4 lbs/ft$^3$ and gas flow at rates up to 650 CFM. During the cooling cycle, $GN_2$ flow is modulated through the heat exchanger to minimize $LN_2$ consumption and avoid using electric heat which is not needed. During the heating cycle, the appropriate power is provided by an SCR control. Although the method of control is sophisticated, operation is simple and precise. The only program required is the blower operating speed, temperature set point and ramp/soak cycle. All eight units are skid mounted, (caster mounting is available) with fully enclosed cabinets, and are completely insulated and purged to eliminate frost build up or condensation. The process piping is stainless steel and the units are available in 100, 300 and 650 CFM sizes.

## WORK TO BE ACCOMPLISHED

Initially, all of SS/Loral's existing cryogenic equipment and systems will be removed. Those items include:

- -$LN_2$ pumping skid and subcooler
- -Model 1200 helium refrigerator skid
- -Helium compressor skid
- -$GN_2$ warm up skid
- -48" Gate valve
- -Entire $LN_2$ shroud
- -All $LN_2$ piping
- -Vacuum and cryogenic operating console

After this equipment has been removed, and when the time is appropriate, the following will be installed and interconnected:

- -Gravity fed shroud including valves, lines and separator tank
- -Twelve auxiliary zones, including valves and $LN_2$ transfer pumps
- -48" High vacuum gate valve
- -Ambient starting roots blower
- -Eight temperature control and distribution skids with piping and valves
- -New vacuum and cryogenic control console

## CONTRACTOR SELECTION

The refurbishment project contract was not circulated for competitive bidding. When SS/Loral established its design, the vendor was selected who was considered to be the most appropriate to provide the equipment required. In addition, the schedule that would have been lost by writing a definitive specification, followed by a bid span of at least eight weeks ending in whatever time would be required to read and evaluate all of the proposals was not acceptable. Instead, PSI Incorporated was identified as the company with the appropriate equipment, engineering skills and management experience that were needed to accomplish the project within the technical, financial and schedule restraints previously noted. Initially, a study contract was awarded to PSI to design the systems, identify the costs and determine the schedule for the refurbishment work to follow. During this study, SS/Loral and PSI engineers worked together identifying requirements and sharing design ideas. This creative and interactive process produced a design that satisfied SS/Loral's requirements and gave PSI a clear understanding of what was required and how the new system will be used. This partner relationship between the two companies is somewhat unique in the industry, but has resulted in a greater understanding by both companies of all aspects of the job. In recent years, Dr. W. Edwards Deming has taught American industry that competitive bidding in a highly technical project is not necessarily as effective as the creation of a partner relationship between the user and supplier from which both parties benefit. This contract has so far confirmed the validity of that concept.

## CONCLUSION

There are many large thermal vacuum chambers throughout the aerospace industry that have been in operation for more than twenty five years. During that time, they have been used successfully to test spacecraft in various space and defense programs. Although some of the country's weapons systems programs have recently been reduced or eliminated, there appears to be future business in the communication and weather satellite area. It seems to be an important requirement that aerospace companies who intend to be competative have modern and efficient thermal vacuum test facilities. Of the aerospace firms that have their own, somewhat aging, thermal vacuum test chambers, the question arises of how to bring them up to modern standards. The stainless steel shells of these chambers are not likely to deteriorate. The aluminum shrouds and their associated cryogenic systems, however, are a different matter. The replacement of aging and failing shrouds seems to be an appropriate opportunity to take advantage of the new cryogenic systems now available. To increase operating efficiency, recent improvements in cryogenic equipment and $GN_2$ systems are now available that offer a low cost alternative to traditional thermal vacuum testing. To upgrade these facilities then, a refurbishment of the typical shroud and $LN_2$ system is a cost effective way to reach this goal and provide a state of the art facility without completely replacing or duplicating existing chambers.

ORIGINAL PAGE
BLACK AND WHITE PHOTOGRAPH

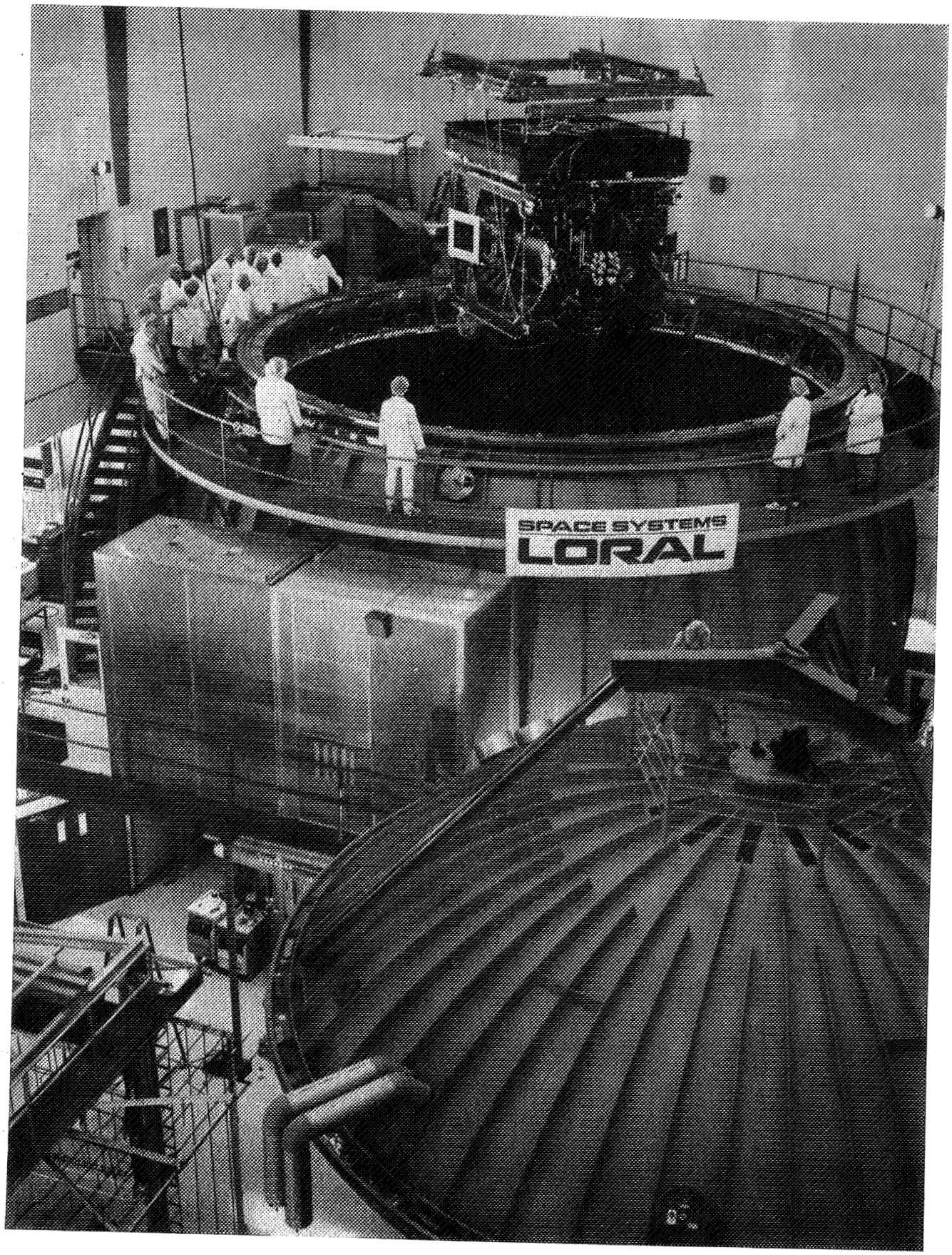


FIGURE 1

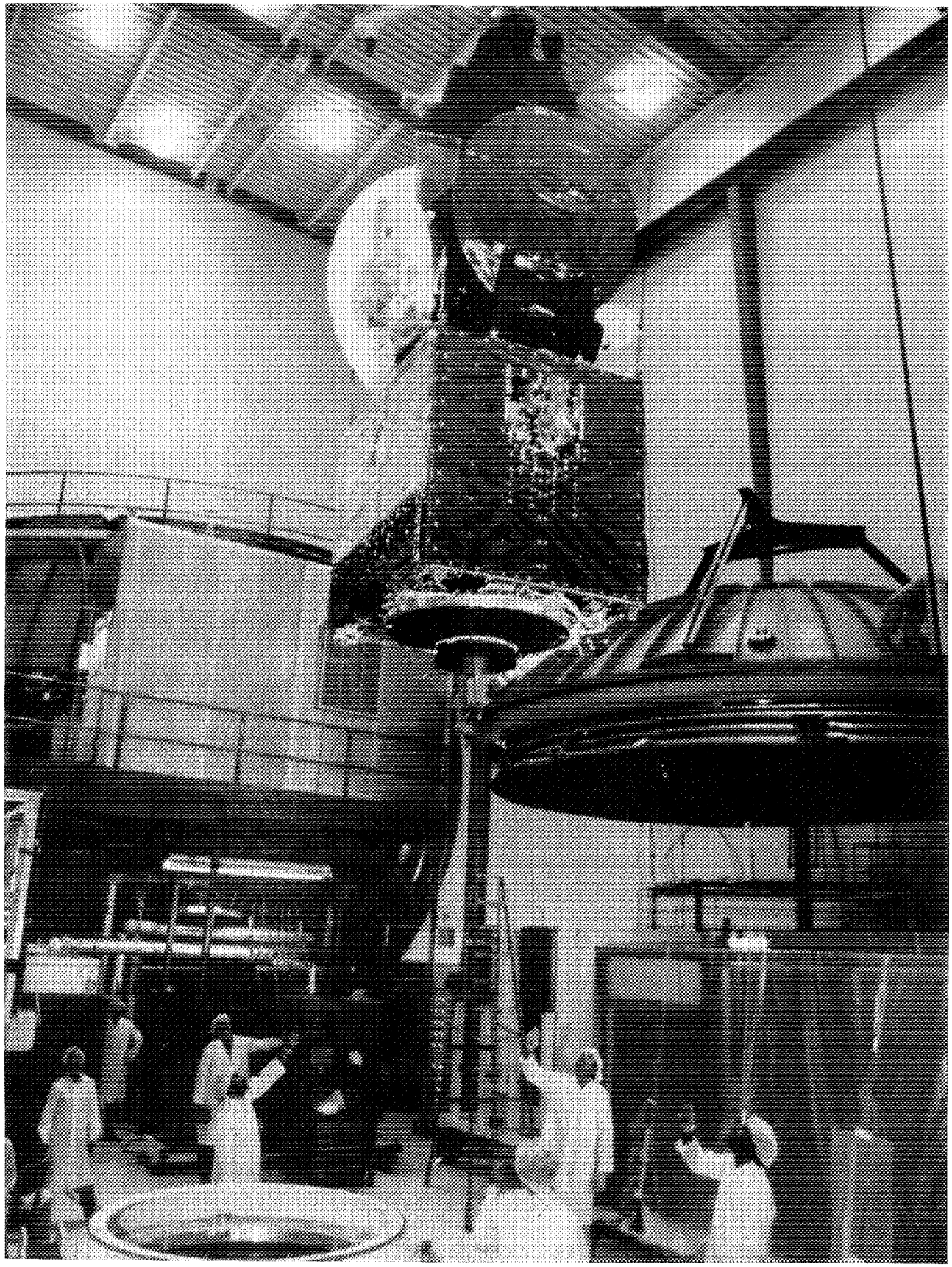

FIGURE 2

ORIGINAL PAGE
BLACK AND WHITE PHOTOGRAPH

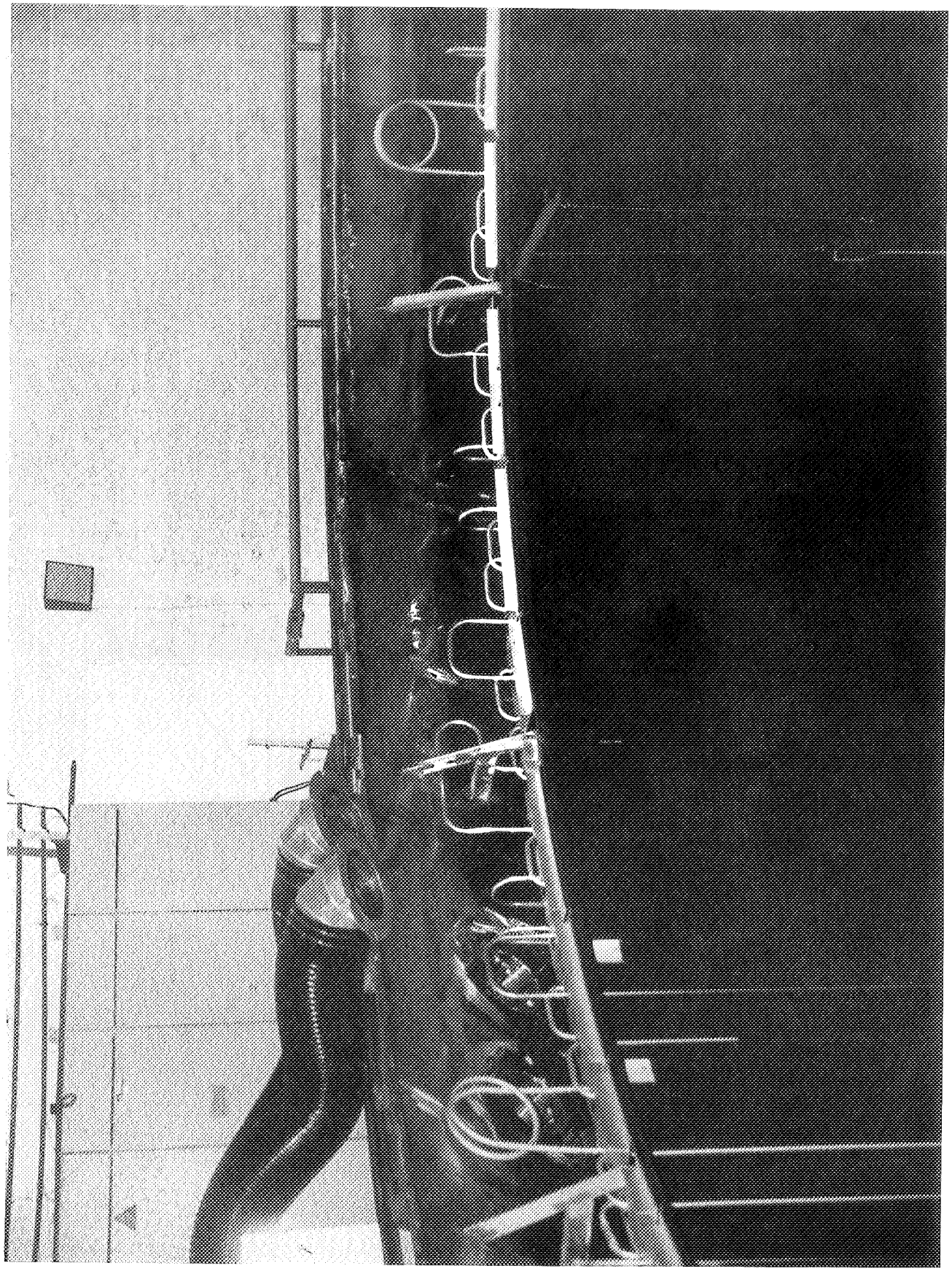

FIGURE 3

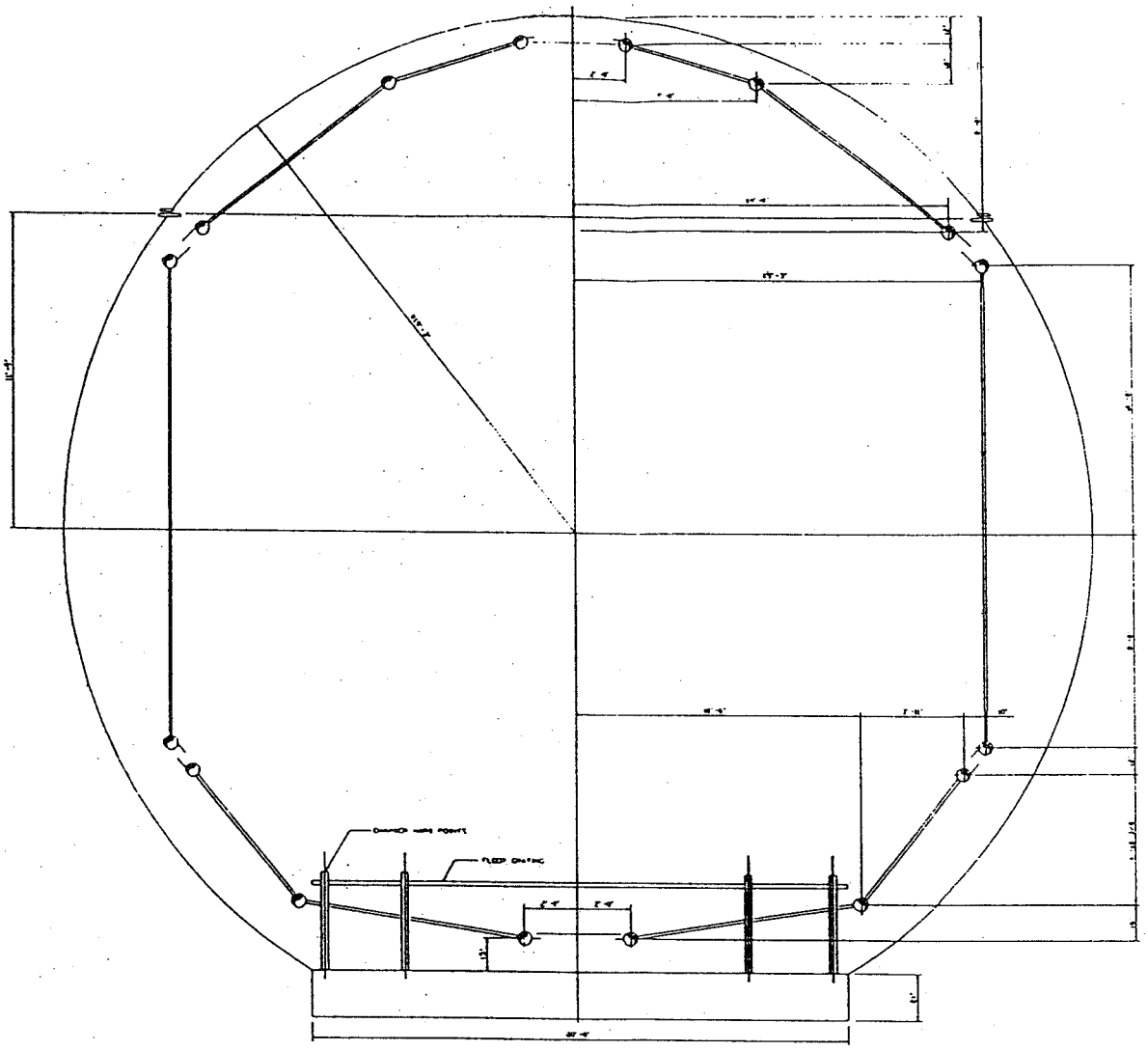

Figure 4

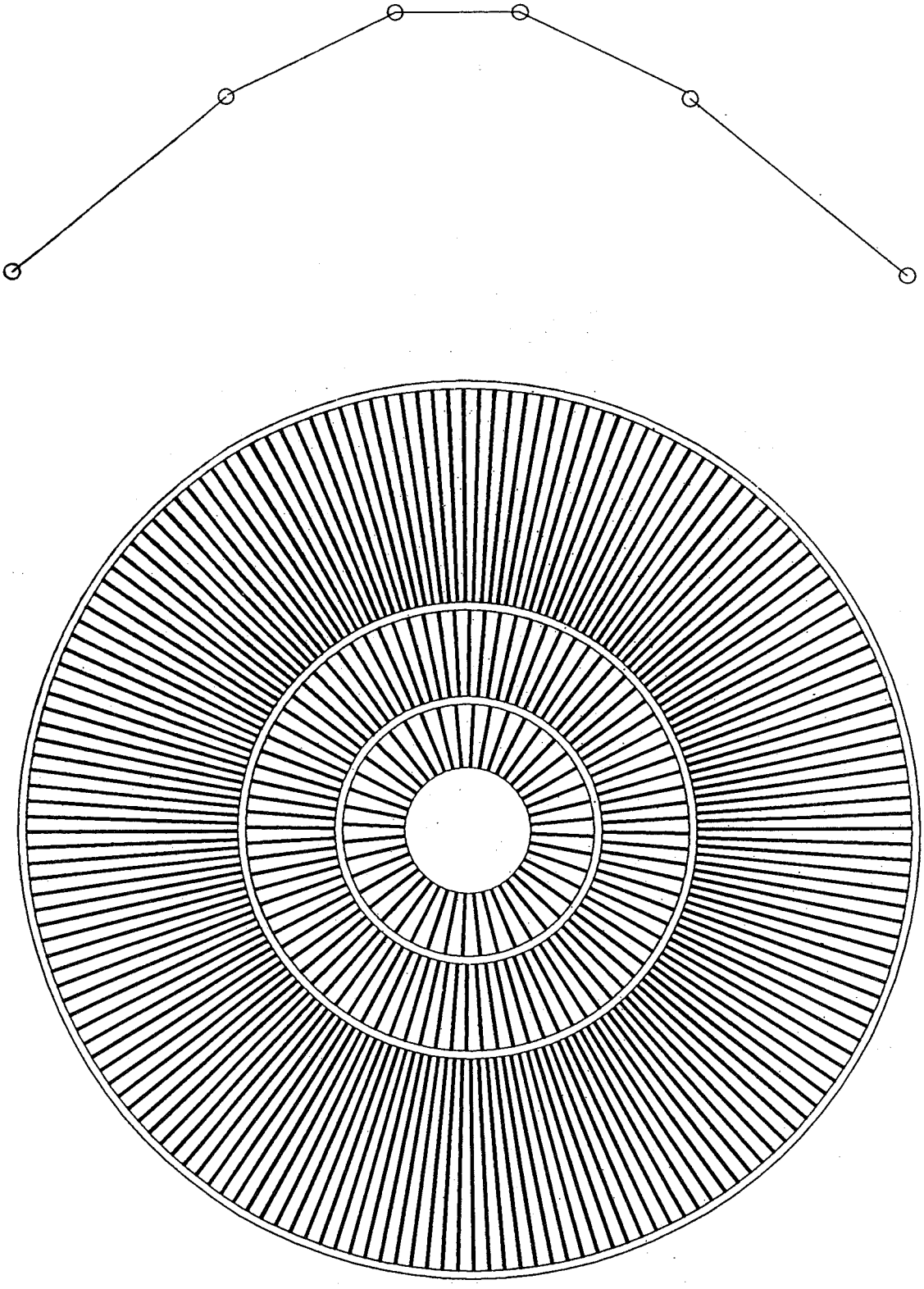

Figure 5

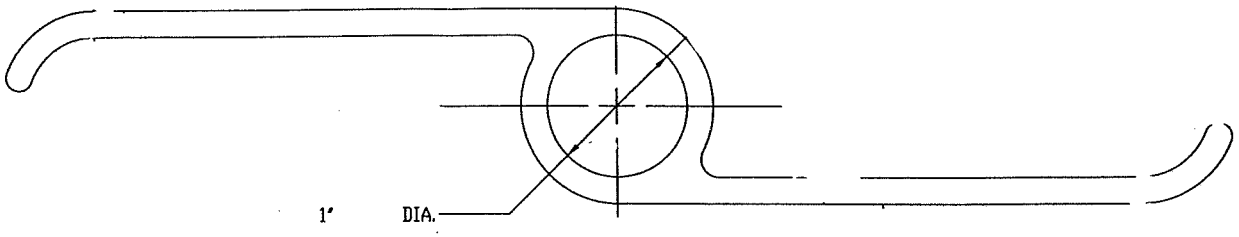


Figure 6

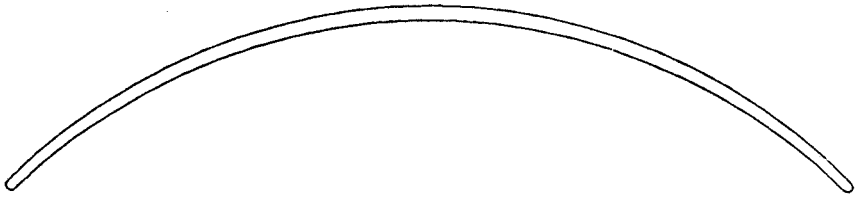

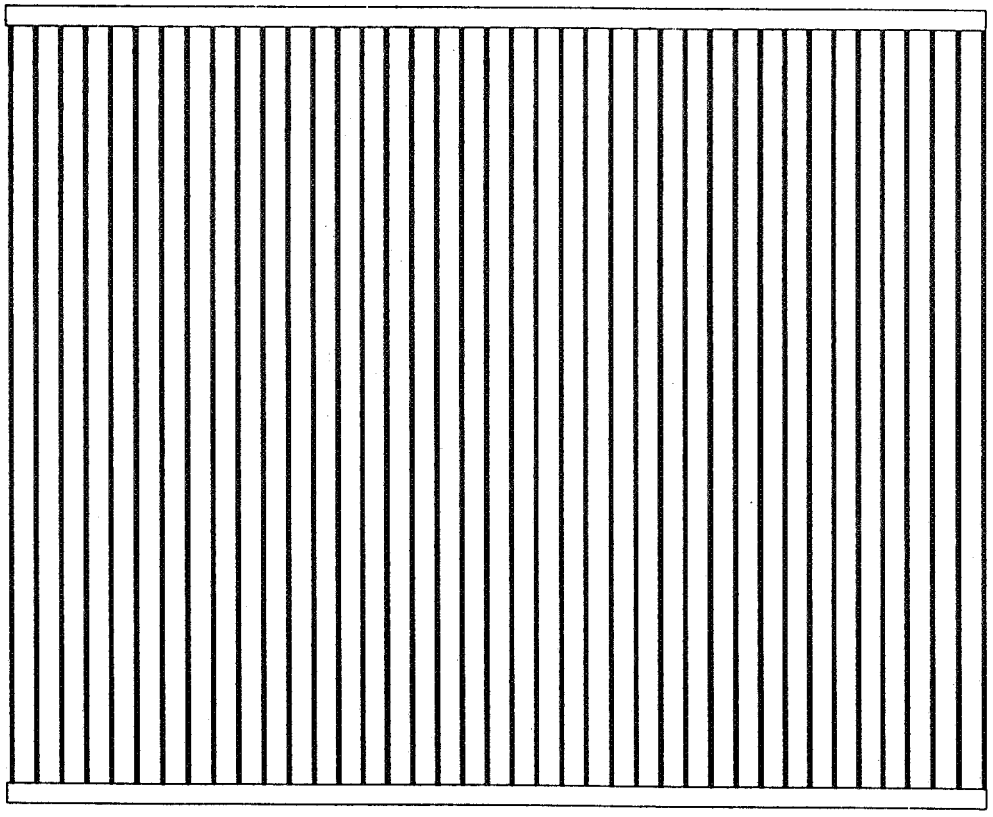

Figure 7

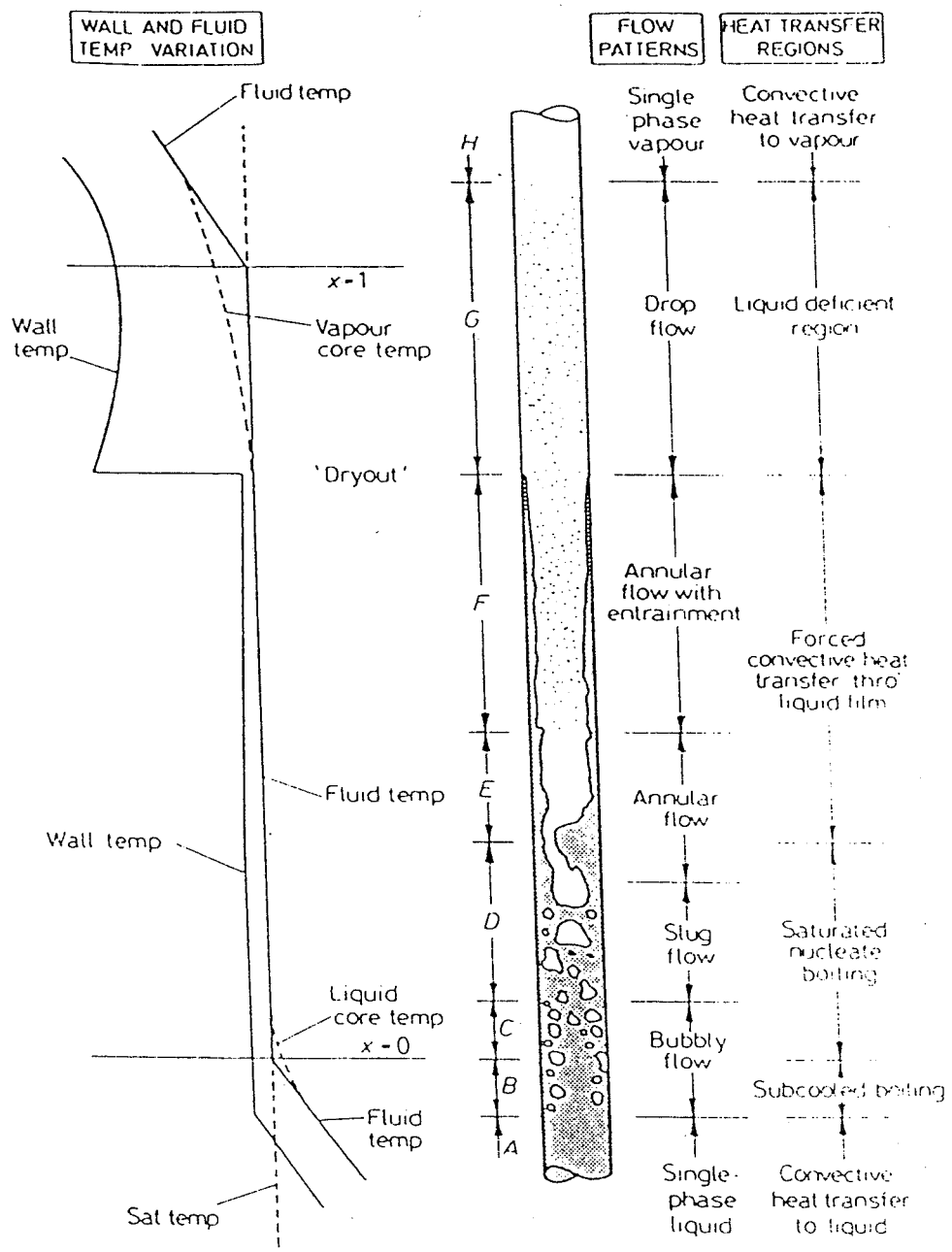
WALL AND FLUID TEMP VARIATION
FLOW PATTERNS
HEAT TRANSFER REGIONS
Fluid temp
x-1
Vapour core temp
Wall temp
'Dryout'
Fluid temp
Wall temp
Liquid core temp
x-0
Fluid temp
Sat temp
H
G
F
E
D
C
B
A
Single phase vapour
Drop flow
Annular flow with entrainment
Annular flow
Slug flow
Bubbly flow
Single-phase liquid
Convective heat transfer to vapour
Liquid deficient region
Forced convective heat transfer thro' liquid film
Saturated nucleate boiling
Subcooled boiling
Convective heat transfer to liquid

Figure 8

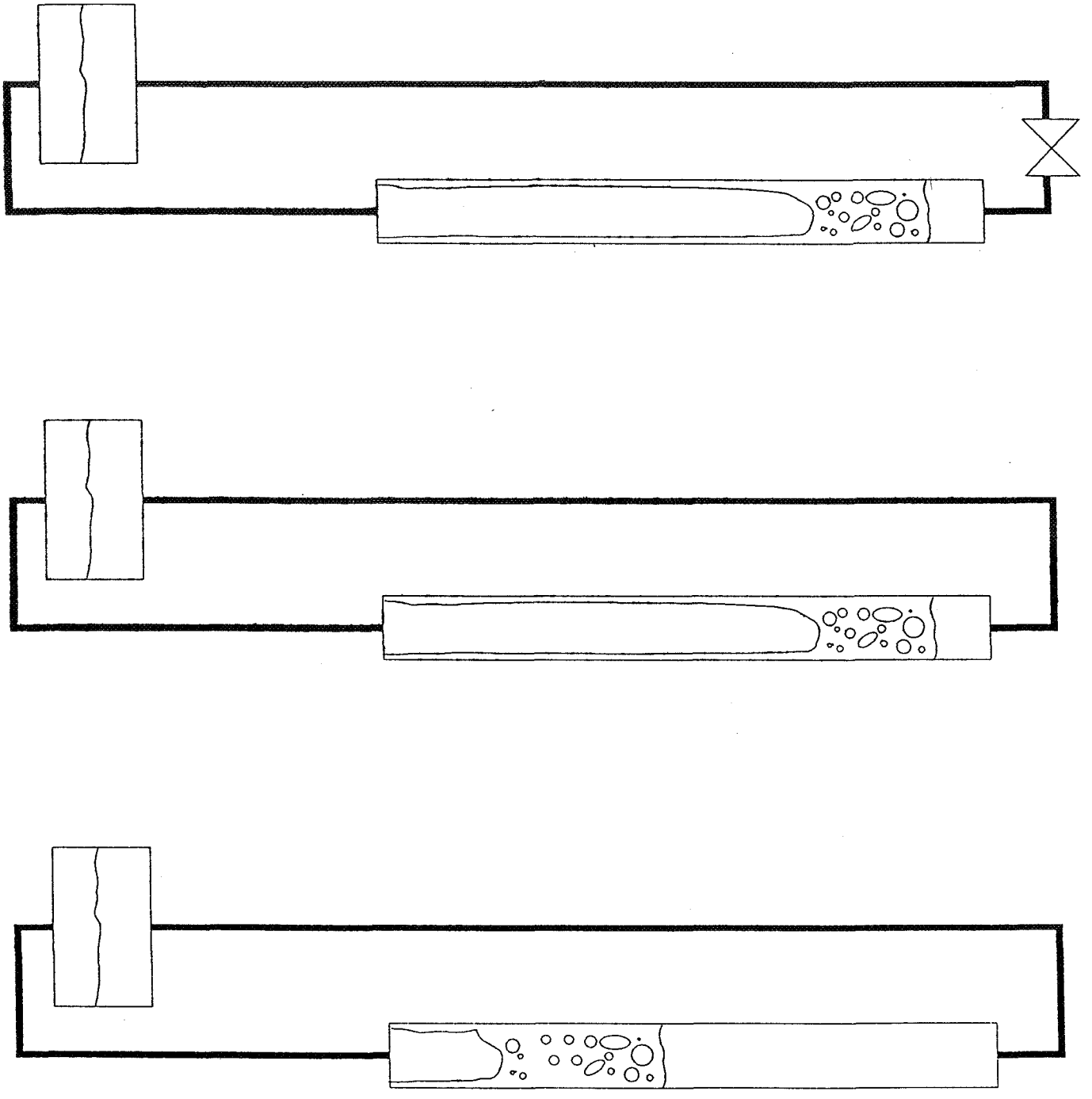

Figure 9

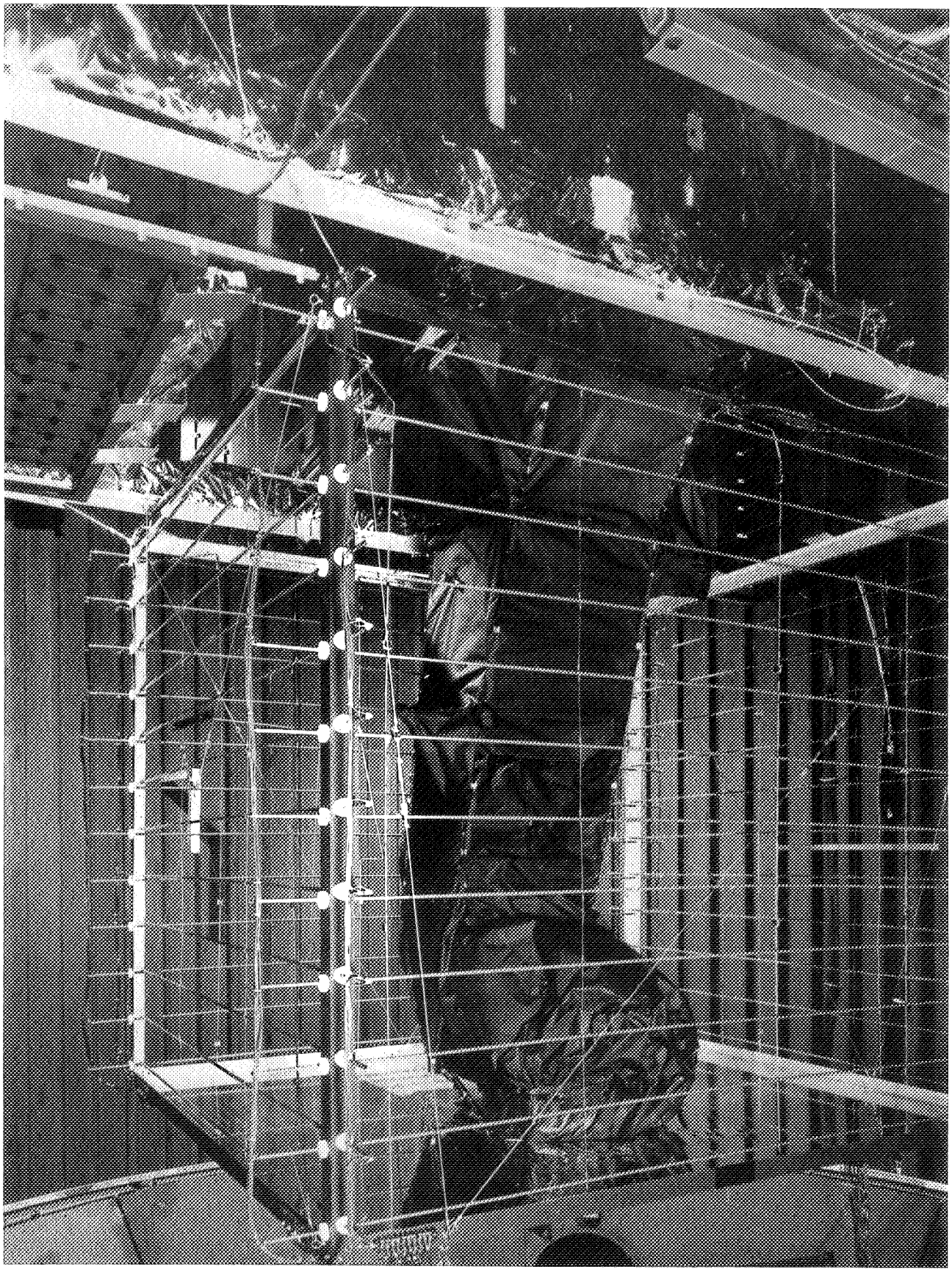

FIGURE 10

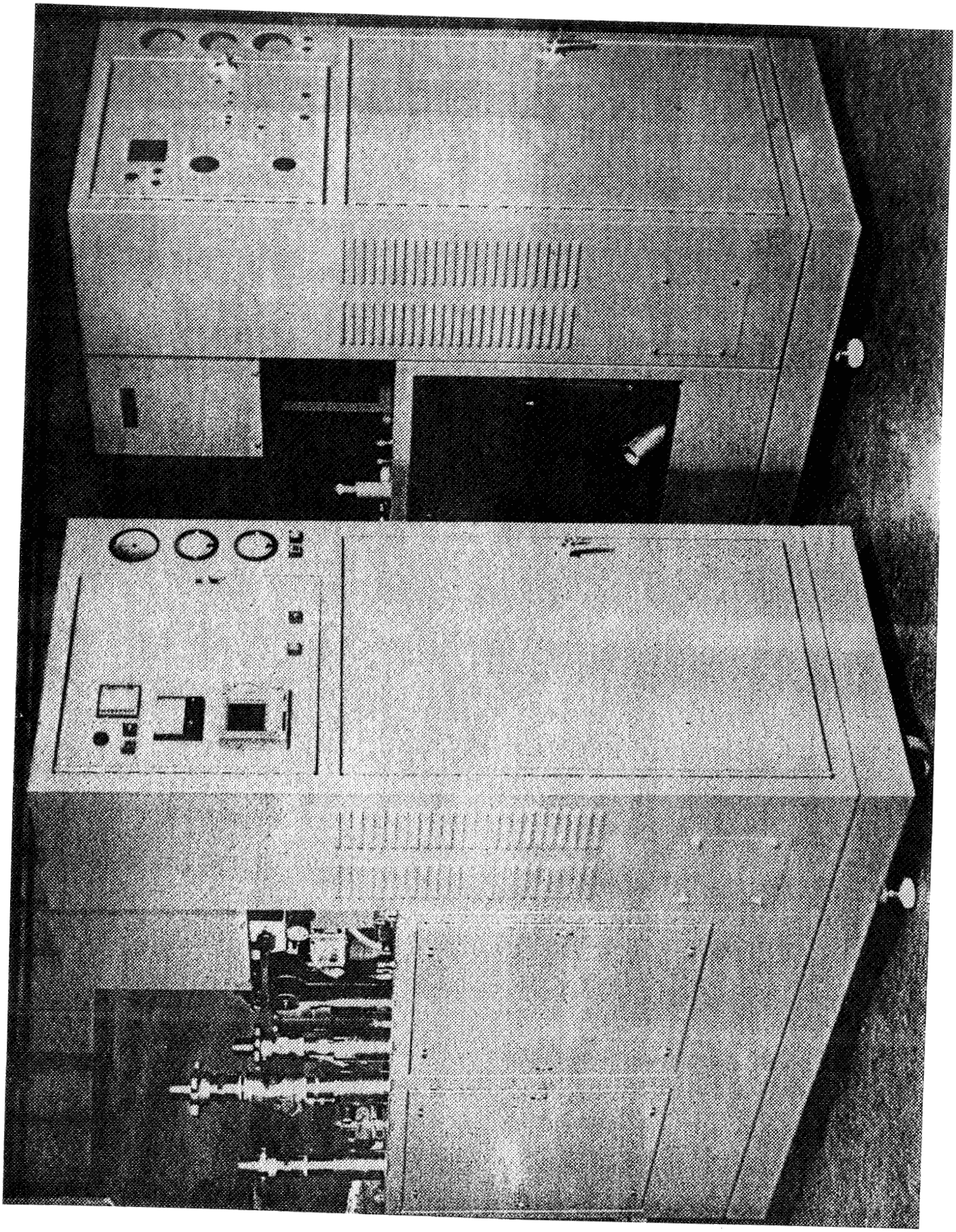

Figure 11

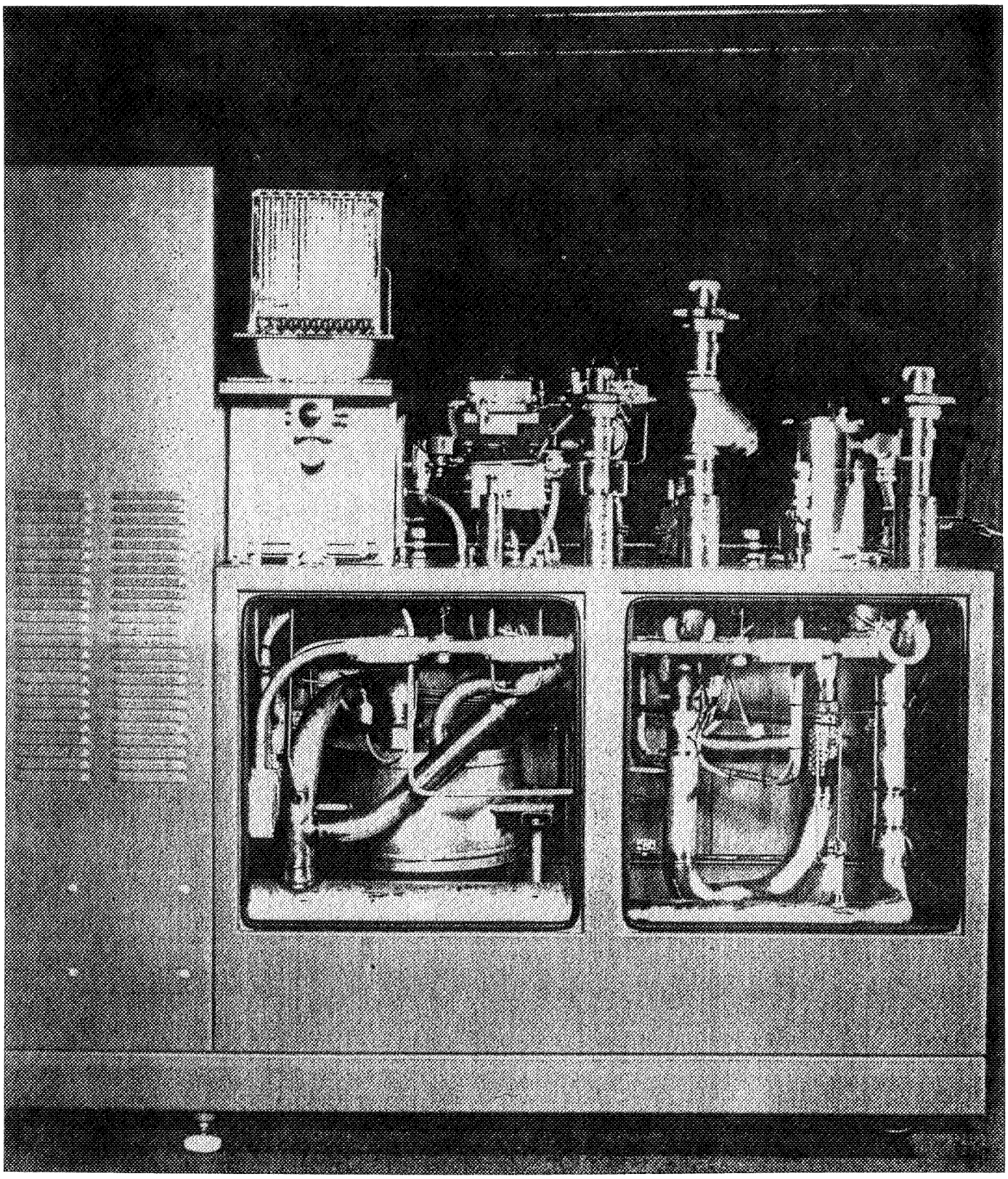

Figure 12

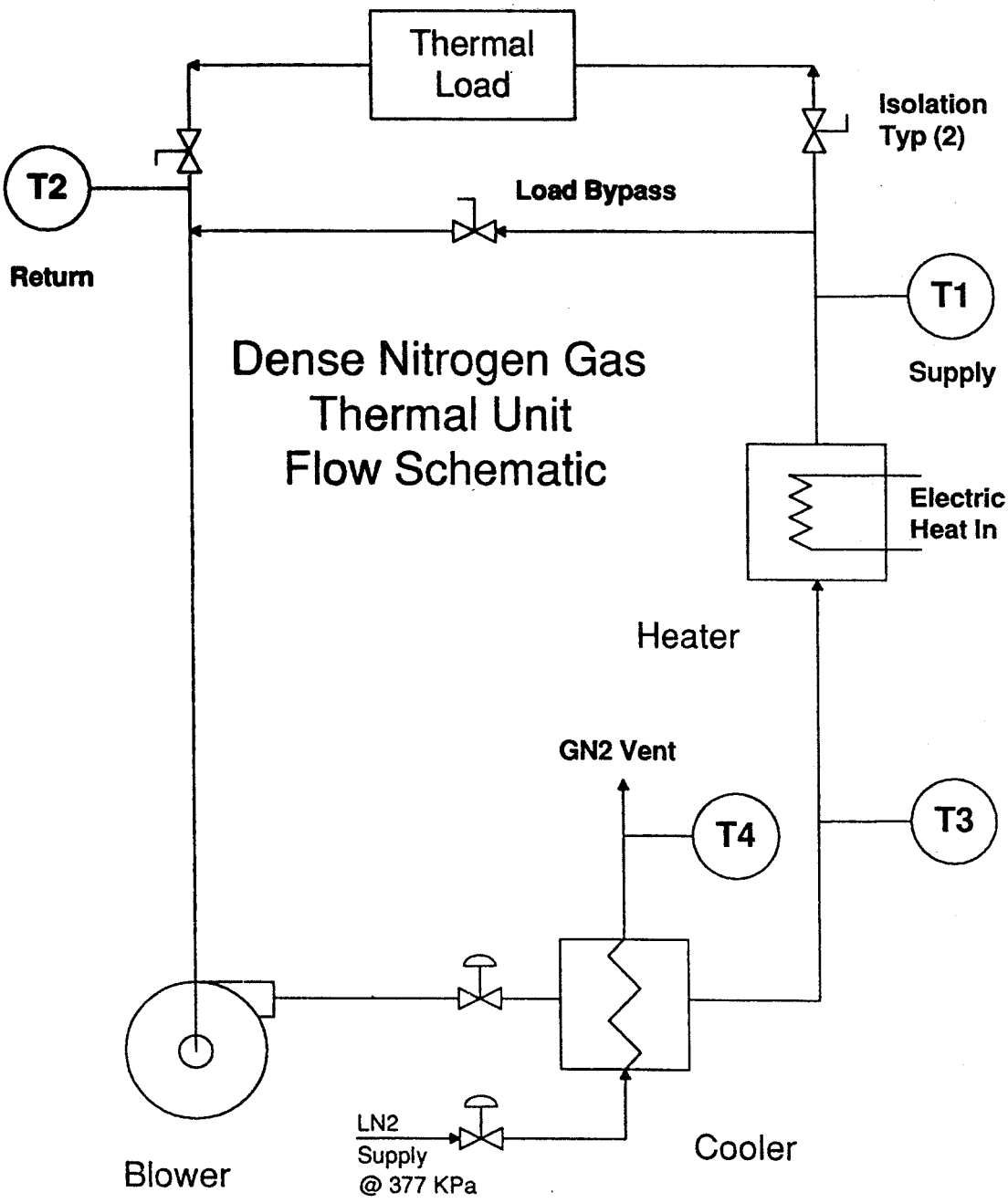
Thermal Load
Isolation Typ (2)
T2
Load Bypass
Return
T1
Supply
Dense Nitrogen Gas Thermal Unit Flow Schematic
Electric Heat In
Heater
GN2 Vent
T4
T3
LN2 Supply @ 377 KPa
Blower
Cooler

Figure 13

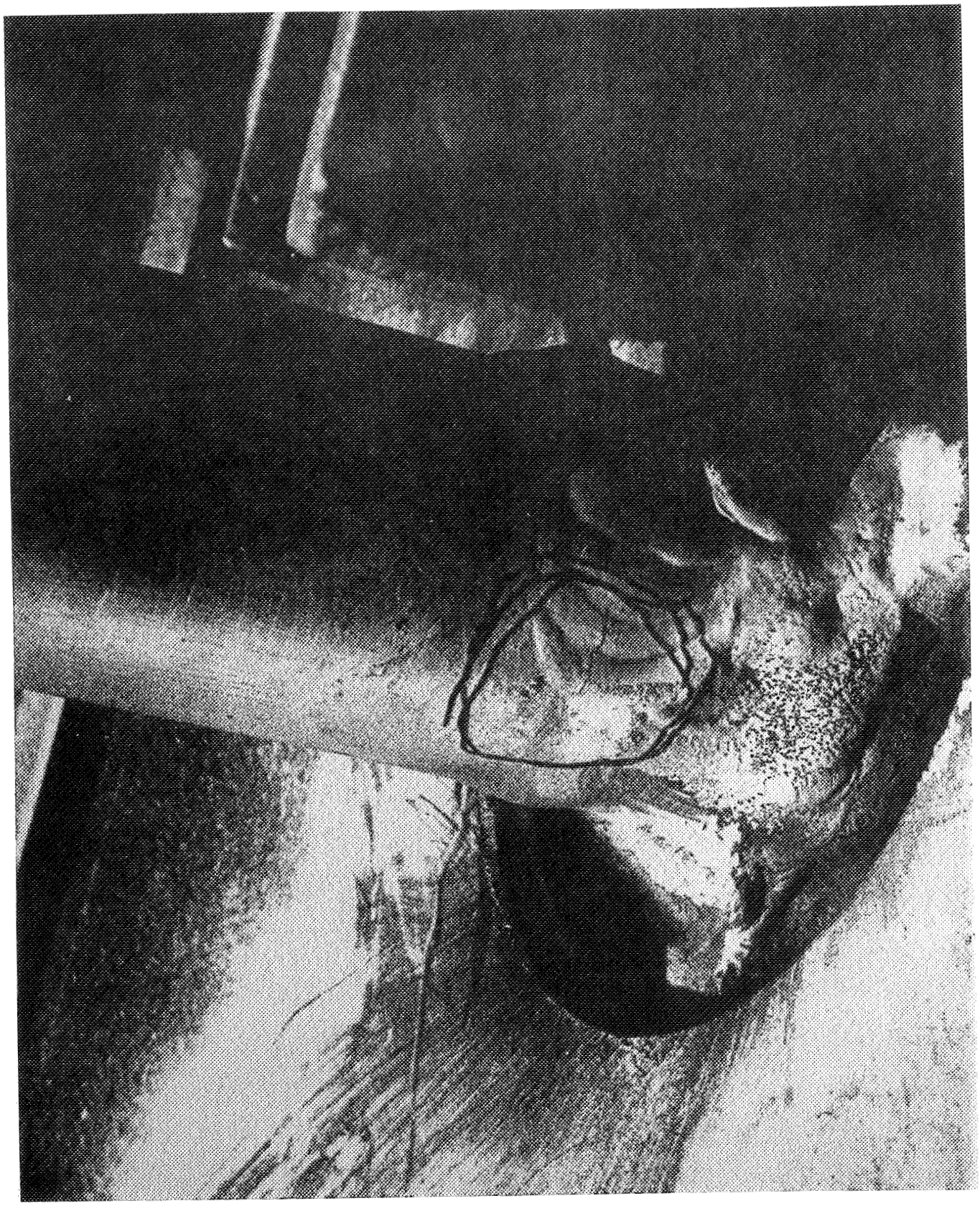

Typical Cracked $LN_2$ Tube
Figure 14

Satellite Surface: 388 ft^2
Satellite emissivity: 0.1

Warmup with GN2 System

Satellite warmup is based on 100MJ of heat capacity between -30C and +30C

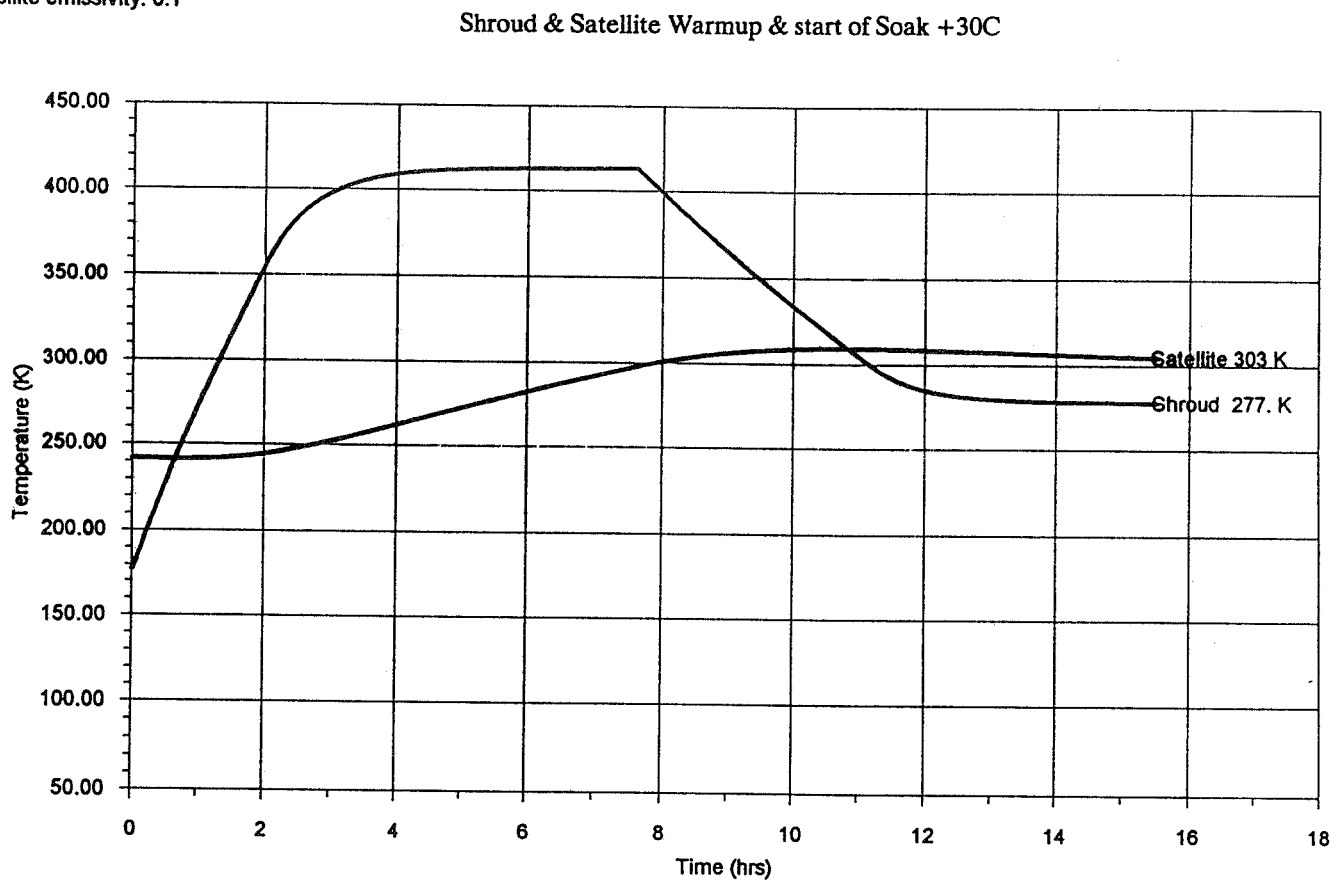


Figure 15

Temperature difference (supply - return) = 60K

SPACE SYSTEM / LORAL

Shroud Mass 9500 kg
Transfer Lines Mass 2200 kg
Shroud Enthalpy @ 85K 1.28E+8 Joules
@425K: 2.71E+9 Joules

SHROUD WARMUP to +150C using TCU's

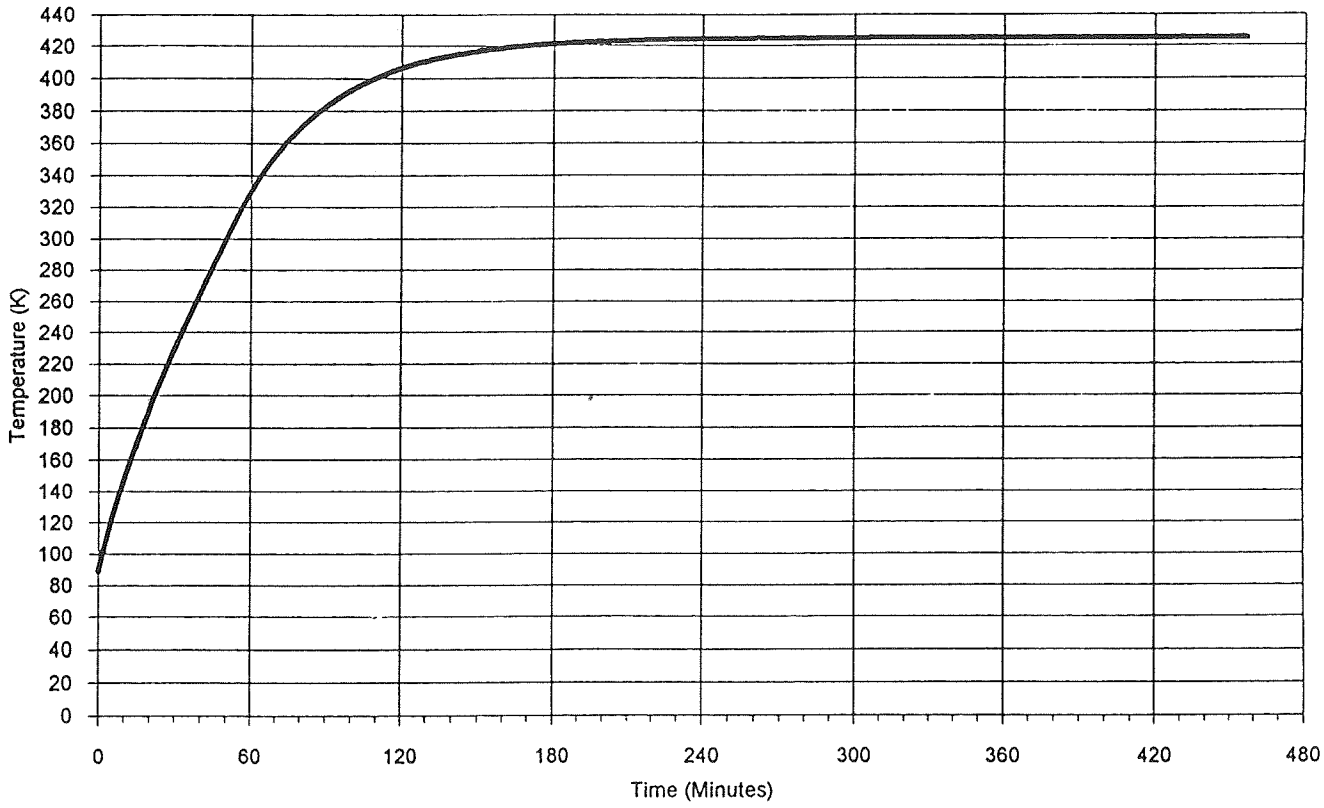


Figure 16

Supply Flowrate: 5.9 kg/s

SPACE SYSTEM / LORAL

Shroud Mass 9500 kg
Shroud Enthalpy @425K: 2.71E+9 Joules
@85K: 1.28E+8Joules

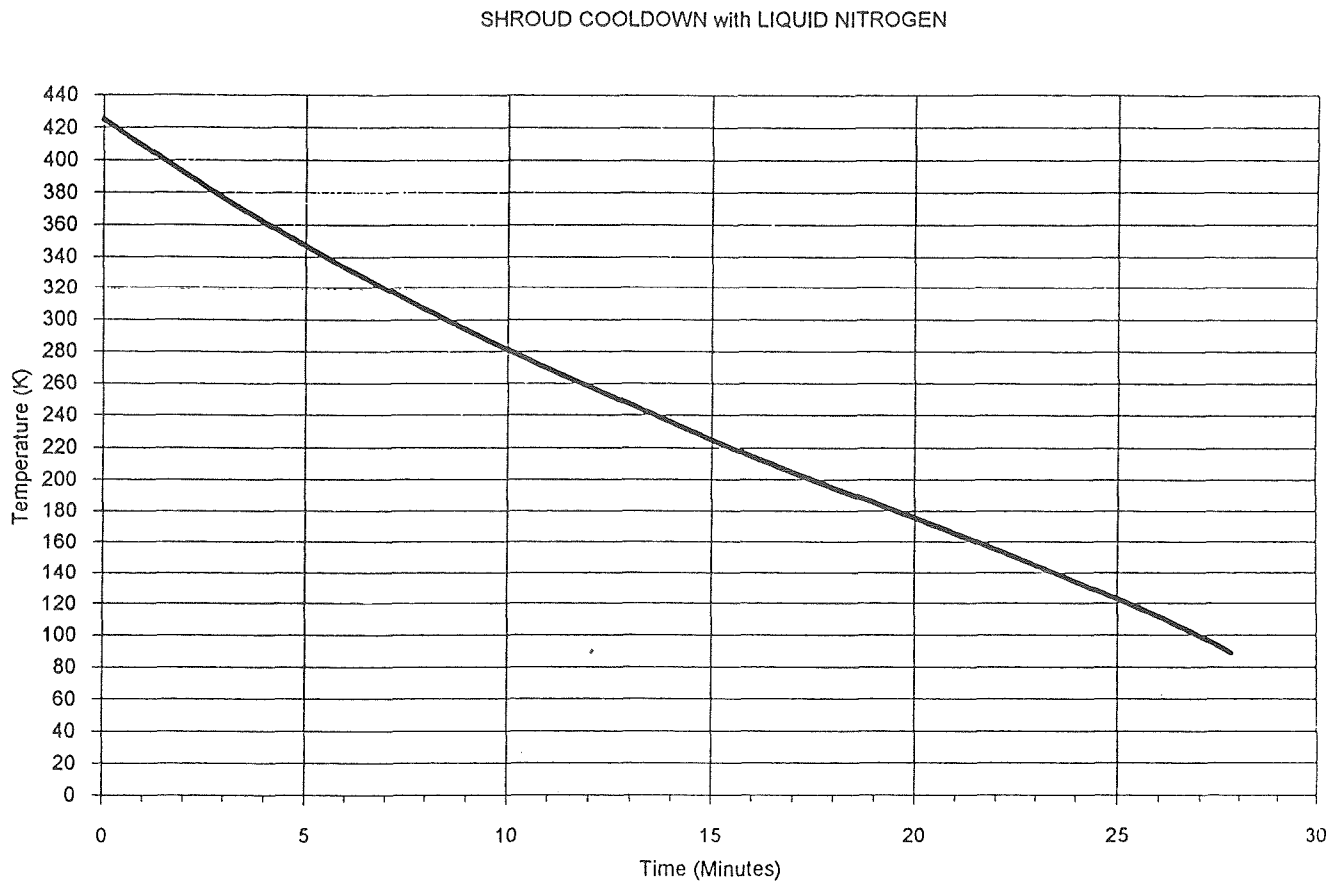


Figure 17

# HYDRA, A NEW TOOL FOR MECHANICAL TESTING

P.W. Brinkmann
ESA/ESTEC, Noordwijk, The Netherlands

## ABSTRACT

The introduction outlines the verification concept for programmes of the European Space Agency (ESA). The role of the Agency in coordinating the activities of major European space test centres is summarized.

Major test facilities of the environmental test centre at ESTEC, the Space Research and Technology Centre of ESA, are shown and their specific characteristics are highlighted with special emphasis on the 6-degree-of-freedom (6-DOF) hydraulic shaker. The specified performance characteristics for sine and transient tests are presented. Results of single-axis hardware tests and 6-DOF computer simulations are included.

Efforts employed to protect payloads against accidental damage in case of malfunctions of the facility are listed. Finally the operational advantages of the facility, as well as the possible use of the HYDRA control system design for future applications are indicated.

## INTRODUCTION

### Verification Concept for Spacecraft

In view of the very high cost of developing and launching satellites, it is essential to ensure that the design fulfils all specified requirements and that hardware and software are free from workmanship failures before the spacecraft is placed in orbit. The verification of space systems, however, cannot be limited to a series of environmental and functional tests at the end of the development programme after the integration of the flight models. The identification of problem areas and in particular of design deficiencies at a late stage in the programme would lead to significant schedule delays and cost overruns. Efficient verification consequently needs to start with the design and must continue throughout all project phases confirming at each phase that the programme objectives will be met. Hence the verification concept must deploy a series of verification steps including tests, which lead to satisfactory system performance without undue risks. Its purpose is to:

- qualify the design already in the early development phase of a project;
- permit timely selection of suitable materials and processes;
- ensure proper functioning of components, units, subsystems before final flight model integration;
- guarantee the integrity of system performance and identification of workmanship failures before launch.

Design verification requires the provision of computer models as well as breadboard or full scale satellite models, which are sufficiently representative with respect to the performance to be verified (e.g. structural, thermal, electrical models). Tests on satellite models are generally performed to update and qualify the corresponding mathematical models. Confidence in functional performance is built up by tests at different hardware levels, starting at component level and terminating with system performance verification. Therefore performance characteristics of the test facilities are regularly reviewed and adapted to the needs of future Agency programmes. In this context the Agency has recently decided to extend its satellite test facilities by implementing a 6-degree-of-freedom (6-DOF) hydraulic shaker until 1996.

### Facility Coordination

The European Space Agency has developed and maintains major environmental test facilities. Similarly some ESA member states have established test centres to support their national programmes. The facilities are at the disposal of industry, scientific institutes and projects to support Agency programmes as well as space programmes of ESA member states; but these can also be made available for non-ESA projects, when not utilized for Agency purposes.

Therefore European industry and scientific institutes do not have to procure those environmental test facilities, saving not only extensive investments but also significant costs for operation and maintenance. In order to avoid duplication of facilities and subsequent underutilization of facilities in Europe, ESTEC has established a close co-operation with its partners CNES/INTESPACE (France), IABG (Germany) and CSL (Belgium). This co-operation is not limited to operational aspects, but also includes consultation with respect to identification of requirements of future programmes and coordination of investments for new test facilities. This improves the utilization of facilities in Europe and avoids unnecessary redundancies or over-capacities. Whilst the national test centres are equipped for environmental tests on small and medium satellites, the ESTEC facilities are compatible with the requirements of the large spacecraft to be launched on Ariane-4 and Ariane-5. The test facilities of all centres are compliant with the stringent product assurance requirements of ESA for tests on space hardware.

## THE MAIN TEST FACILITIES IN THE ESA TEST CENTRE

The cut-out view in Fig. 1 illustrates the most important test facilities of the ESTEC Test Centre. The illustration already includes the test hall for the 6-DOF vibration facility, which is presently under construction.

The facilities shown in Fig. 1 are briefly described hereafter. All facilities are located in one building, which also contains integration halls, data handling and support facilities, such as meeting rooms, customer offices and storage areas. Hence, test campaigns involving various test disciplines can be efficiently executed with low transportation and handling effort.

Facility for Thermal Balance Tests

The Large Space Simulator (LSS) at ESTEC with a solar beam diameter of 6 m is the largest solar simulator within the ESA member states with unique performance characteristics. Fig. 2 illustrates the LSS and shows the main dimensions.

During the tests the pressure inside the test chamber is reduced to levels below $10^{-6}$ mbar with oilfree high vacuum pumps. For simulation of the deep-space heat sink, the vacuum chambers are lined with stainless steel shrouds, which are cooled down to temperatures of about 100 K by liquid nitrogen. In $GN_2$ mode they can be operated in the temperature range from + 80°C to - 100°C for thermal cycling. Simulated solar radiation is produced by 25 kW xenon-arc lamps and associated optics. Motion systems make it possible to simulate the spacecraft orientation with respect to the impinging solar beam.

**Electromagnetic Test Facilities**

o EMC facility

The EMC chamber has a surface area of 7.1 m x 6.1 m and a height of 5 m.
All emission and susceptibility tests in the frequency and time domain are fully automated. They are computer-controlled with online data reduction, narrow and broad-band identification. All evaluated data are corrected for probe factors, etc.

The facility is particularly well adapted to carry out electrostatic discharge tests on spacecraft and to verify the effects of the discharges. A high voltage unit, generating up to 30 kV, with a maximum discharge capability of 500 joules, is used for this purpose. A separate, multi-channel data acquisition and measurement system is used to verify the effects of electrostatic discharges on the test subject. The system, which has an overall dynamic range of 160 dB, includes active sensors for measurements of the magnetic and electric fields and of the surface current.

o Compact Payload Test Range (CPTR)

The CPTR permits the testing of the radiation links between ground stations and satellites. The CPTR is illustrated in Fig. 3. The overall size is about 25 m x 11 m x 10 m with a plane wave zone of 7 m x 5 m x 5 m. The reflector dimensions are 9.2 m x 8 m with a surface accuracy of 70 microns peak-to-peak. It permits measurements of critical system parameters such as EIRP (Equivalent Isotropic Radiated Power, PFD (Power Flux Density), beam steering, link budgets, etc. One of the facility's main features is its low cross-polar performance. The frequency range is from 1.5 to 40 GHz.

Facilities for Mechanical Tests

o Vibration facilities

The test centre at ESTEC is equipped with electro-dynamic vibrators, which operate in a frequency range from 5 to 2000 Hz and can perform sinusoidal, random and shock tests sequentially along the main orthogonal axes of the specimen.

The main vibration system consists of two 140 kN shakers which can either be used individually or in multishaker configuration. In the latter configuration, the two shakers are coupled to a dual-head expander for tests in the longitudinal (vertical) axis and to a large slip table for "lateral tests". Fig. 4 illustrates the multishaker configurations.

o Acoustic facility

The ESTEC facility is the largest one in Europe with a volume of approx. 1600 $m^3$. It operates with $GN_2$ and can produce noise levels of up 158 dB ($P_{ref} = 2 \times 10^{-5}$ Pa). During the test liquid nitrogen is evaporated and temperature controlled in two serial heat exchangers. The thermal energy is provided from a hot water reservoir fed by the central heating system of the plant.

## THE 6-DOF HYDRAULIC SHAKER

Considerable effort has been expended during the last decade in studying the possibilities for improvement of dynamic structure qualification in general and for system acceptance of Ariane-4 and Ariane-5 payloads in particular. These investigations have led to the concept of the 6-DOF hydraulic shaker (HYDRA), which is distinguished by the following improved features as compared with conventional electrodynamic shakers:

a) actuator force and stroke
b) frequency range extended below 5 Hz
c) active control of orthogonal motions
d) controlled excitation in 6-DOF permitting realistic flight load testing
e) improved test operations and safety

The design and engineering phase for HYDRA and the associated building has been performed during 1992/1993. The procurement, installation and acceptance phase of the building started in 1993, while the start of the shaker procurement has been delayed until August 1994 for budgetary reasons. The facility shall become operational in the second half of 1996 for tests on the structural model of the PPF/Envisat satellite (mass approx. 7000 kg). This ESA satellite is currently planned for launch in 1998 by Ariane-5.

## Performance Characteristics

### System configuration and forces

The geometry of the table and actuator arrangements was optimised by detailed trade-offs early in the design phase. These were based upon finite element models calculating the rigid body modes and the elastic modes of the loaded and unloaded table, taking into consideration stiffness, masses and the geometric configuration of all actuators. The actuator force requirements were calculated with a dedicated computer programme taking into account the kinematics of the loaded table. The results of the trade-offs (reported in Ref. 1) and subsequent engineering have led to an octagonal table with a span of 5.5 m and a mass of 22000 kg. The first flexible mode in loaded configuration, is 22% above the upper operational frequency limit of the shaker, which is at 100 Hz. According to DIN standard 4024 and taking into consideration the damping ratio for such a table, the first elastic mode will not have a remarkable influence on the table acceleration up to 100 Hz. The table is driven by 4 actuators in the vertical direction and 2 actuators for each lateral direction. Each of the 8 actuators has a stroke of ± 70mm, a maximum piston velocity of 0.8 m/sec and a force rating of 630 kN. The high force levels are required to accommodate the "overturning moments" created by the table and payload assembly during dynamic testing. In conventional testing with electro-dynamic shakers these need to be compensated for using bearing assemblies, i.e. passive elements. The 6-DOF hydraulic shaker counteracts these moments by the active control of the motions in all translational and rotational axes. In this way it will be possible to actively attenuate the parasitic orthogonal motions (often referred to as "cross-talk") for sine tests of large payloads. The cut-out view (Fig. 5) illustrates the PPF/Envisat satellite being tested on the HYDRA facility.

### Operational test modes

HYDRA has been designed for sinusoidal testing along each translational axis. Besides testing at selected discrete frequencies (sine-dwell), it is possible to perform sine sweeps with sweep rates in the range of 2 to 4 octaves per minute. Furthermore transient excitation signals in 6-DOF can be generated in addition.

### Dynamic performance

The dynamic range of HYDRA is shown in Fig. 6 and Fig. 7. The upper acceleration limits of the performance diagrams are applicable for a test article mass of 7000 kg with a centre of gravity 5 m above the table surface. The acceleration limits will increase as the test article mass decreases and vice-versa. The Ariane-5 qualification levels for sinusoidal vibration tests are indicated hereafter for comparison and show that margins exist even for payloads with higher masses.

| Ariane-5 (Ref. 2) | Frequency range (Hz) | Qualification levels (0-peak) recommended |
|---|---|---|
| Longitudinal | 4-5<br>5-100 | 12.4mm<br>1.25g |
| Lateral | 2-5<br>5-25<br>25-100 | 9.9mm<br>1g<br>0.8g |
| Sweep rate | | 2 oct/min. |

The specified performance tolerances are as follows:

a) Signal distortion for sine test mode
(differences between measured and reference signal)

peak values:
≤ 1.5 dB
or
≤ 0.025g, whichever is larger

RMS values:
≤ 1.0 dB
or
≤ 0.025g, whichever is larger

b) Parasitic cross-axis excitation in sine test mode in the unexcited orthogonal axes

≤ 10% of nominal excitation level
or
≤ 0.025 g, whichever is larger.

c) Signal distortion for transient test mode
(differences between measured and reference signal)

peak values (all maxima and minima):
≤ 1.5 dB
or
≤ 10% of the max. amplitude in all other degrees of freedom, whichever is larger

RMS values (difference between measured and reference signal):

≤ 1.0 dB

or

≤ 10% of the max. amplitude in all other degrees of freedom, whichever is larger

Total signal duration:

≤ ± 5%

Signal quality

Hydraulic exciters cannot reproduce acceleration signals free from distortion, mainly because of non-linearities of the hydro-dynamics in servovalves and actuators (Ref. 3). An example of this phenomenon is shown in Fig. 8. The graph shows the distorted acceleration at the table centre during a sine test at 4 Hz with an existing 6-DOF hydraulic shaker.

In order to reduce these distortions to an acceptable level, special effort has been put into the careful design of servovalves, actuators, and bearings and particularly into the actuator control system of HYDRA. The digital control system (Ref. 4) uses detailed mathematical models of the shaker system with the following features:

- non-linear control algorithms for servovalve/actuator
- on-line prediction of actuator motions
- on-line prediction of system kinematics

The functioning of the actuator control algorithm was verified by tests with an available actuator and a simplified control system. A typical result of these tests is shown in Fig. 9. Subsequently a 6-DOF computer model was set up, and initial investigations were performed at discrete frequencies from 0.5 Hz up to 100 Hz without yet employing table acceleration feedback and oil pressure feedback of the servovalves. Fig. 10 illustrates a typical result of these simulations, which shows good coincidence between the nominal and actual waveform; it also shows that the orthogonal motions ("cross-talk") are well below 10% of the nominal excitation. The 6-DOF simulations will be continued in order to perform sensitivity analyses and to test various feedback options for the final optimisation of the control software. Due to the delayed start of the implementation phase of the project, these results cannot be presented in this publication.

## Transient Testing

The introduction of a test method that reflects a more realistic representation of the space flight environment has been a major objective for the development of HYDRA. In preceding studies it has been concluded that the simulation of the multi-directional transients at the interface of launcher and spacecraft produces more realistic structural responses. In contrast, traditional sine tests lead to unrealistic responses and therefore involve an inherent risk of over- or under-testing (Ref. 5, 6, 7). Multi-degree-of-freedom hydraulic shakers designed for earthquake simulation have been used in the past to

demonstrate that the reproduction of transients is feasible after several iterations (Ref. 8). Recent advances in computer technology permit the control system of HYDRA to simulate transients in 6-DOF without iteration. Fig. 11 shows the simulation results of a representative transient for Ariane-5 at lift-off. The quasistatic portion of the transient signal as well as its frequency contents above 100 Hz have been filtered out to become compliant with the dynamic range of the facility.

## Operational Aspects

The 6-DOF hydraulic shaker allows the specimen to be tested along both the vertical and the lateral axes with one single test setup. It is therefore no longer necessary to dismount, re-locate and re-instrument the payload for the different excitation directions. This not only reduces the effort involved in handling and instrumentation, with consequent reductions in test durations and risk, but it also provides flexibility in the sequencing of tests. In particular, x-, y- and z-signature tests can be performed without particular effort before and after each single-axis test run.

The large octagonal test table is flush with the test floor. It facilitates the mounting of heavy and/or geometrically large specimens (e.g. appendages such as solar arrays). Due to the wide span of the table the complexity and mass of the adaptors can be kept low. All shaker equipment and supplies are located in the basement of the building, mechanically isolated from the clean test area (class 100.000 Fed.Std. 209). The gap between the aluminium test table and the test floor is closed by a flexible seal. This provides mechanical separation of the clean test area from the hydraulic equipment located below the table.

Detailed reliability and safety analyses were made during HYDRA's design, as outlined in the following diagrams. The control system has been designed in such a way that the failure events identified in the various analyses will not lead to a hazardous situation for facility or payload, because it will trigger a "soft facility shutdown" in time.

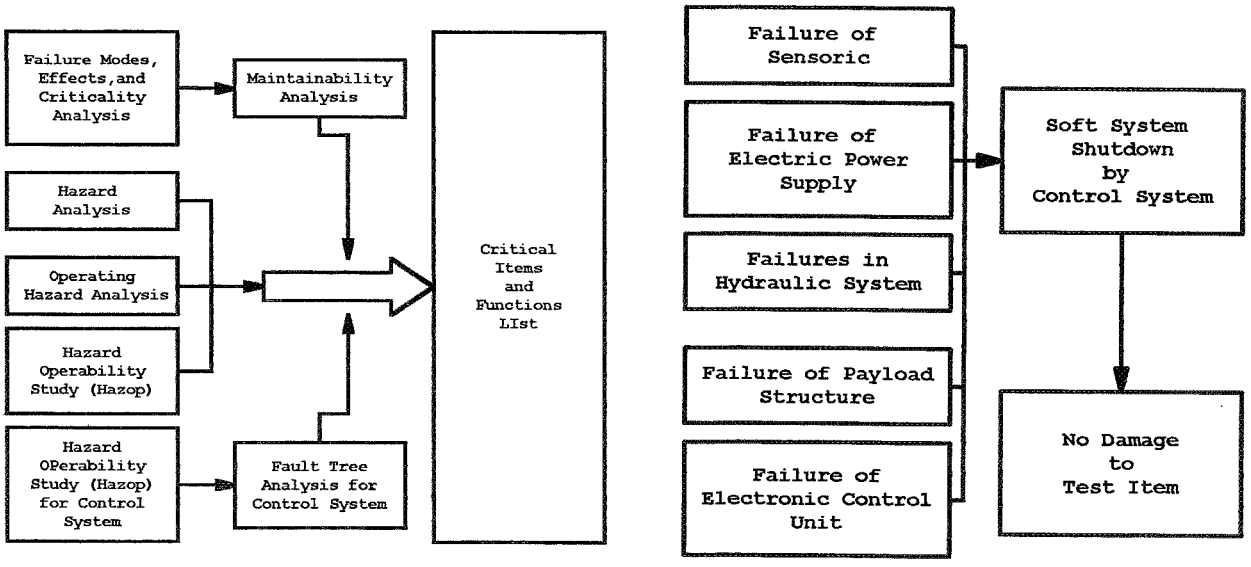

## CONCLUDING REMARKS

The installation of the hydraulic shaker will ensure that the ESA test centre at ESTEC, Noordwijk, remains compliant with the testing requirements evolving from the ongoing launcher developments, which lead to larger satellites with higher masses.

However, the new facility will not only extend the performance for applying traditional test methods, it will also provide ESA with the tool to verify the advanced test method of "transient testing" after more than one decade of intense theoretical study work and subsequently to apply this method for the qualification of satellite structures.

The control system design, once verified in practical application, will certainly have the potential to improve the performance characteristics of other machines and simulators driven by hydraulic actuators. In fact, the control algorithm for the HYDRA hydraulic system has already been successfully used for the control of the horizontal moving system of the 6-DOF driving simulator at Daimler-Benz, Berlin, Germany. Both the acceleration control accuracy and the time behaviour could be improved drastically compared to the previous analogue feedback control.

## REFERENCES


1. Brinkmann, P.W. , Kretz, D, 1992
   The Design Concept of the 6-Degree-of-Freedom Hydraulic Shaker at ESTEC, NASA Publication 3181

2. Arianespace, 1994
   Ariane-5 User's Manual, Issue 2, May 1994.

3. Lachenmayr, G, Krautwald W.,
   Development of High-Precision Computer Models of a Multi-Axis Vibration Test Facility and Usage for Control System Design and Test Prediction,
   ESA WPP-066, October 1993

4. Kretz, D., Grimm, A.,
   Design and Performance Characteristics and Control and Safety System of the Hydraulic Shaker at ESTEC,
   ESA WPP-066, October 1993

5. Brunner, O., Stavrinides C., Klein, M.,
   Transient Vibration Testing of Satellites,
   ESA SP-304, September 1990

6. Ams, A., Wedig, W.,
   Identification and Variation of Transients - A New Test Procedure for Space Structures, ESA WPP-066, October 1993.

7. Erben, E., Beig, H-G., Lachenmayr, G.
A Transient Test Method Applicable for Spacecraft Structure Qualification,
ESA WPP-066, October 1993.

8. Füllekrug, U., Sinapius, M.,
Simulation of Multi-Axis Vibration in the Qualification Process of Space Structures,
ESA WPP-066, October 1993

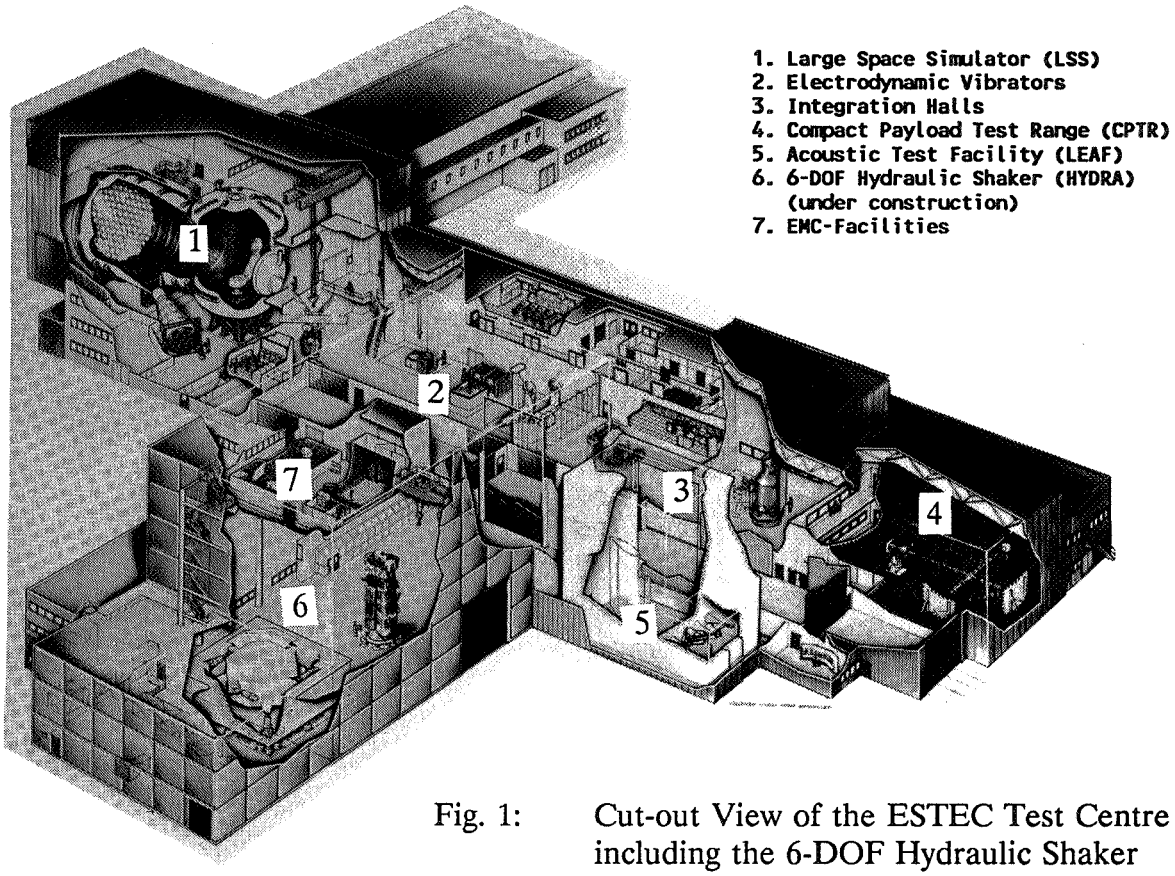


Fig. 1: Cut-out View of the ESTEC Test Centre including the 6-DOF Hydraulic Shaker

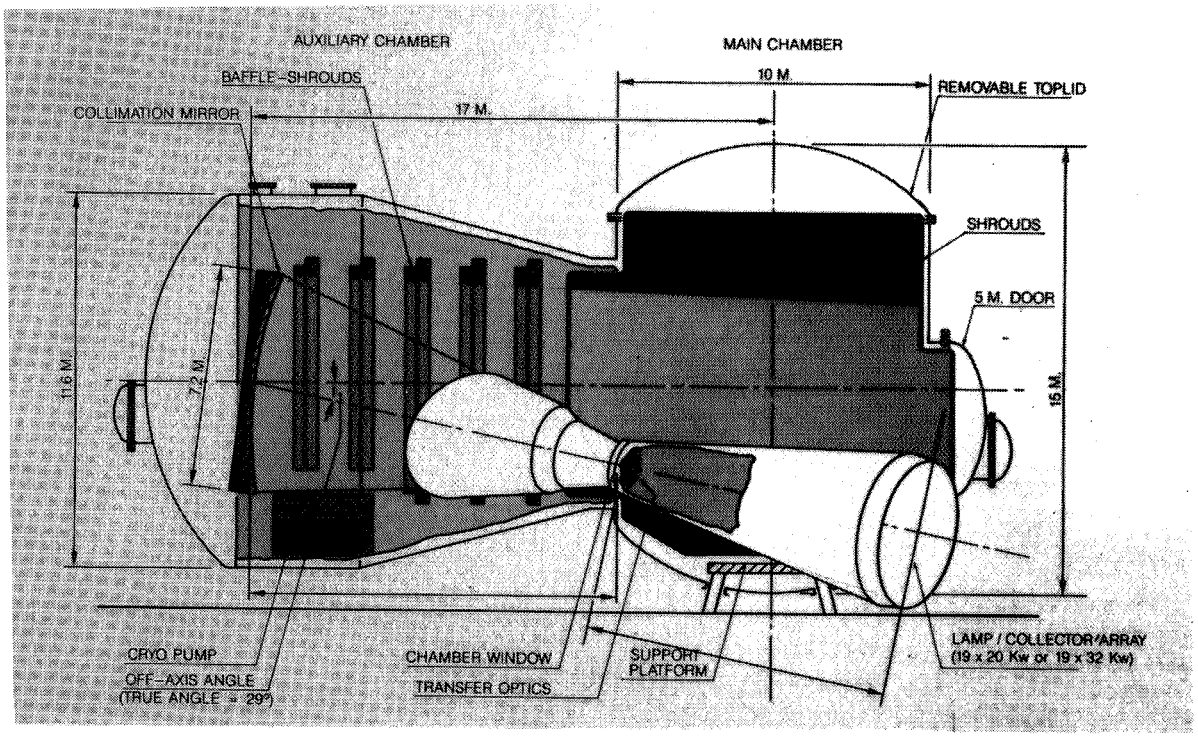


Fig. 2: Schematic of the Large Space Simulator (LSS) at ESTEC

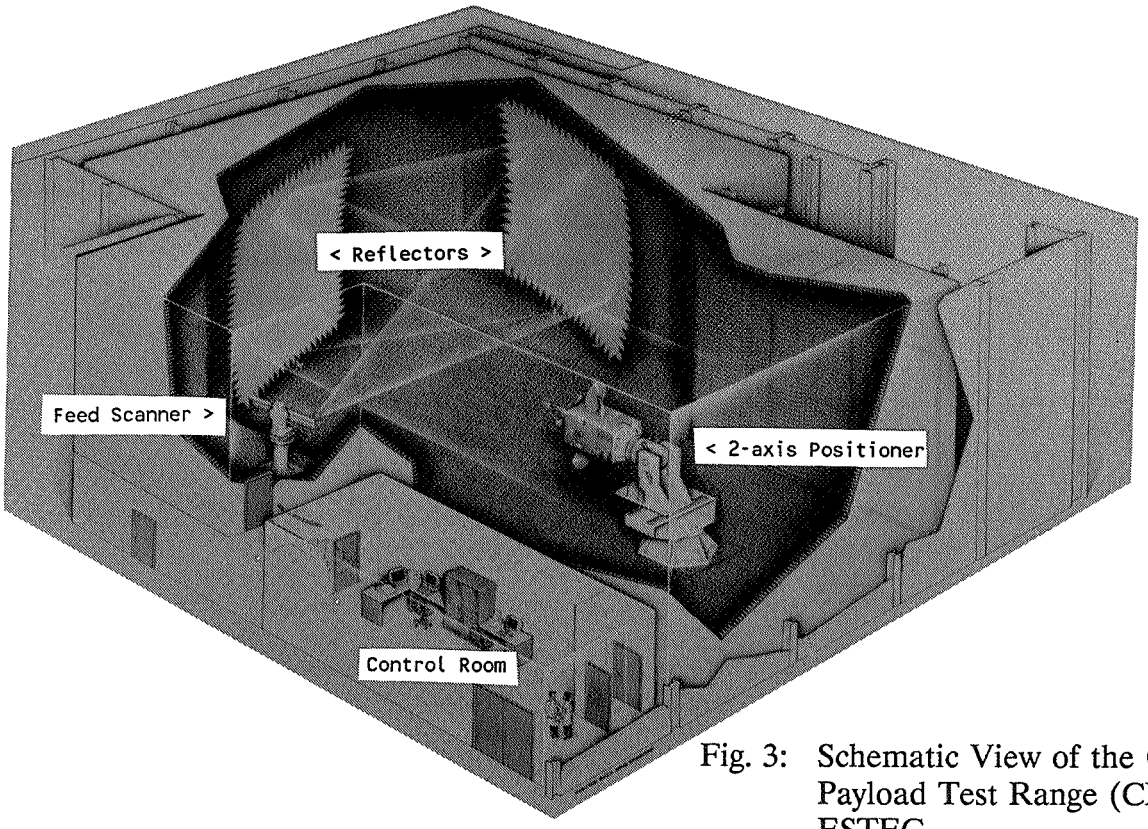


Fig. 3: Schematic View of the Compact Payload Test Range (CPTR) at ESTEC

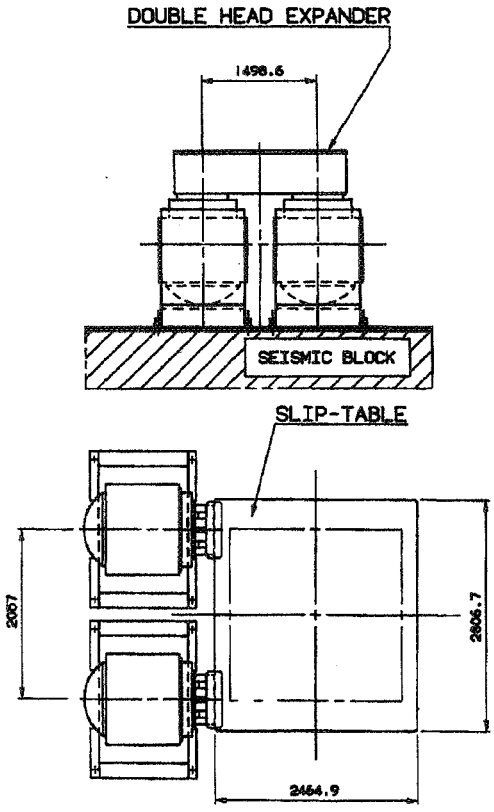


Fig. 4: The 280 kN Multi-axis Shaker in Vertical and Horizontal Configuration

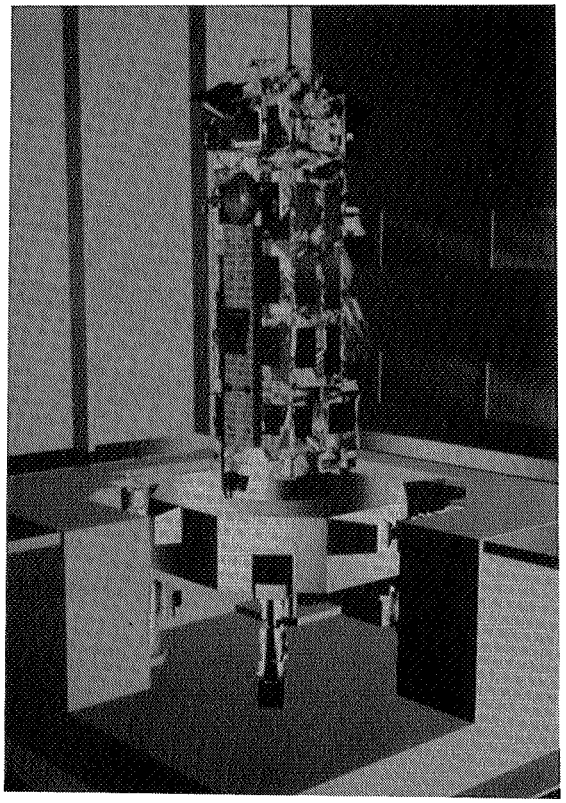

Fig. 5: HYDRA Test Configuration with the PPF/Envisat Satellite

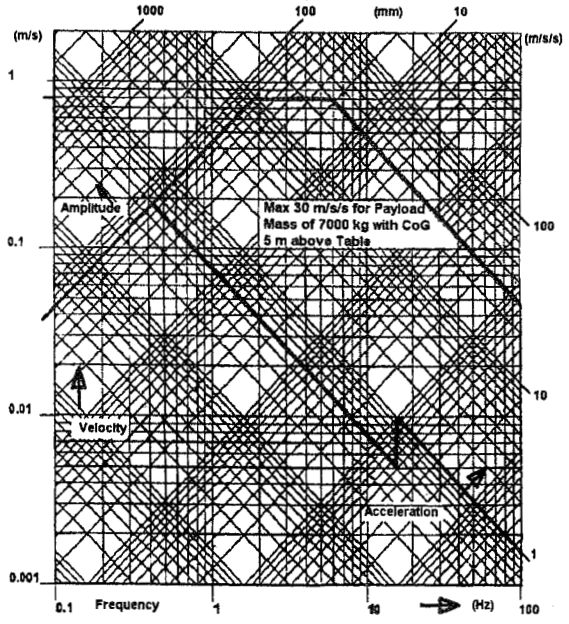


Fig. 6: HYDRA Performance for Lateral Excitation

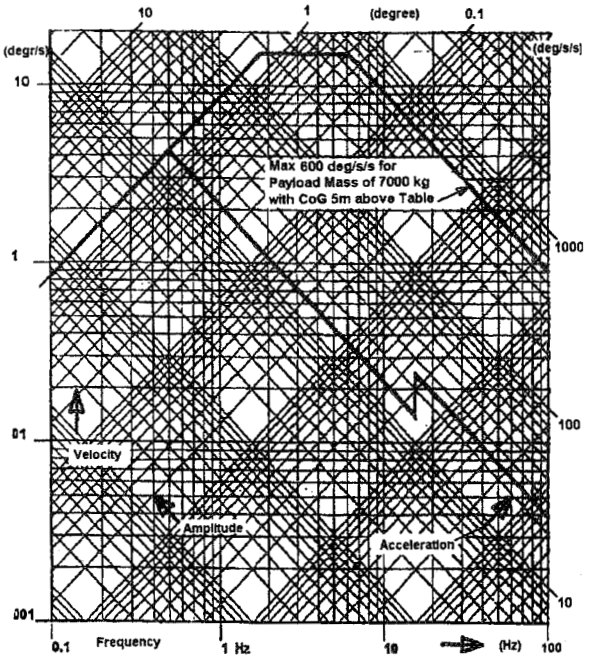


Fig. 7: HYDRA Performance for Rotational Excitation

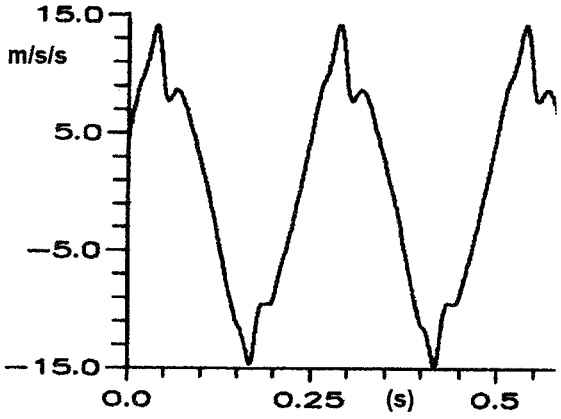


Fig. 8: Acceleration Time History with 4 Hz Sinusoidal Input of an Existing 6-DOF Earth Quake Simulator

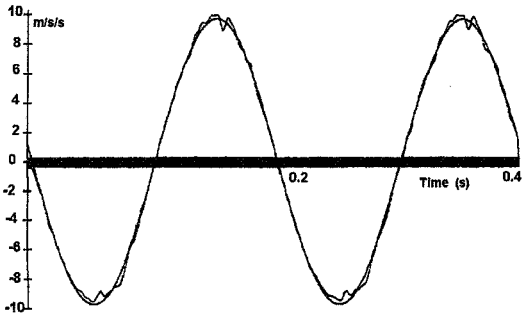


Fig. 9: Acceleration Time History Measured with Single Axis Test Rig Using a Simplified HYDRA Control (Input 5 Hz Superimposed)

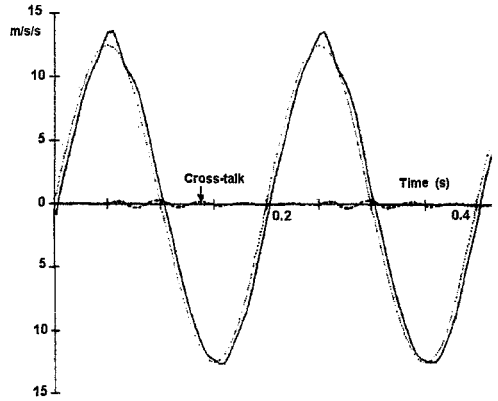


Fig. 10: Acceleration Time History simulated with the 6-DOF HYDRA Computer Model without Feedback Loops (Input 5 Hz Superimposed)

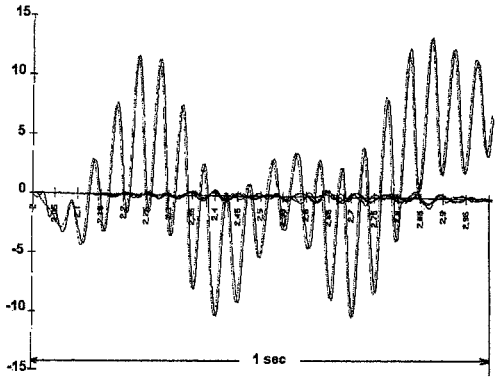


Fig. 11: A Transient Simulated with a HYDRA Mathematical Model (Input Superimposed)

# SYSTEM LEVEL MECHANICAL TESTING OF THE CLEMENTINE SPACECRAFT

James Haughton
Kinetic Research Corporation
Annapolis, Maryland

Joseph Hauser
Naval Research Laboratory
Washington, DC

William Raynor
Naval Research Laboratory
Washington, DC

Peter Lynn
Naval Research Laboratory
Washington, DC

## Abstract

This paper discusses the system level structural testing that was performed to qualify the Clementine Spacecraft for flight. These tests included spin balance, combined acoustic and axial random vibration, lateral random vibration, quasi-static loads, pyrotechnic shock, modal survey and on-orbit jitter simulation. Some innovative aspects of this effort were:

- The simultaneously combined acoustic and random vibration test
- The mass loaded interface modal survey test
- The techniques used to assess how operating on board mechanisms and thrusters affect sensor vision

## Definitions and Acronyms

| | |
|---|---|
| BMDO | Ballistic Missile Defense Organization - Co-sponsor of the Clementine Program |
| ELV | Expendable Launch Vehicle |
| EM | Engineering Model - High fidelity Prototype model of the Clementine Flight Spacecraft. |
| ISA | Interstage Adapter - Composite truncated cone adapter that interfaced the Solid Rocket Motor to the Clementine Spacecraft |
| LLNL | Lawrence Livermore National Laboratory - Supplied the lightweight sensors and cameras that were used for lunar mapping |
| NASA | National Aeronautics and Space Administration - Co-sponsor of the Clementine program, also supplied the use of the Deep Space Network for communications |
| NCST | Naval Center for Space Technology at the Naval Research Laboratory |
| NRL | Naval Research Lab |
| PA | Payload Adapter - aluminum truncated cone adapter that interfaced the Space Vehicle to the Titan IIG Launch Vehicle |
| Payload | The payload consists of the Payload Adapter (PA), the Interstage Adapter (ISA), Solid Rocket Motor (SRM) and Clementine Spacecraft. |
| SC | Clementine Spacecraft |
| SV | Space Vehicle - Assembly consisting of the Interstage Adapter, Solid Rocket Motor and Clementine Spacecraft |

## Introduction

The Clementine Spacecraft, designed, built, and integrated by the Naval Center for Space Technology at the Naval Research Laboratory, was launched on January 25,1994 on a Titan II ELV from Vandenberg Air Force Base. This was the culmination of a 22-month odyssey from concept to launch. The Clementine program was jointly sponsored by the Ballistic Missile Defense Organization (BMDO) and the National Aeronautics and Space Administration (NASA). Using an array of light weight sensors and cameras, supplied by Lawrence Livermore National Laboratory (LLNL), it successfully completed the most extensive mapping of the moon to date.

There were three fundamental problems that faced the Clementine program related to system level testing due to the "fast-track" approach that was required; 1) there was no tolerance for major schedule delays, 2) financial and schedule constraints precluded the implementation of a full qualification program, and 3) there were uncertainties with regards to the engineering issues associated with the new technologies. As a result, in order to provide an acceptable combination of time, money and risk, a hybrid qualification/protoflight approach was adopted.

Two identical spacecraft structures were fabricated. The first was designated as the Engineering Model (EM) and the second was identified as the Flight Model. The EM was assembled during the period of January 1993 to May 1993. System level testing on the EM was conducted from June 1993 through August 1993. This provided data early in the program that proved invaluable in support of the design development. The EM was also used for verification of the basic design, the systems engineering, and was a pathfinder for the flight unit. The EM system testing schedule was developed and performed in support of the flight spacecraft build. Assembly of the flight spacecraft begin in May 1993 and was completed in August 1993. Integration took placed from August 1993 to October 1993. System level testing at NRL started at the beginning of November 1993 and concluded at the end of December 1993. Clementine was shipped to Vandenberg AFB, CA, on December 30,1993 for launch preparation where final system integration and testing took place.

## Mission Background

Conceived as a implement for testing advanced lightweight space-based technologies, conceptual design of the Clementine mission began in the early spring of 1992. The mission objectives for Clementine were to demonstrate the latest in BMDO developed space-based imaging sensors and advanced lightweight component technologies on a long duration flight. This was to be achieved by employing as much existing BMDO technology as possible to perform a lunar mapping as well as an asteroid encounter. A "fast track" program philosophy was required to meet an early 1994 launch.

Utilizing targets such as the moon, the stars, and the spacecraft interstage assembly ( after separation ), the performance of these technologies were demonstrated. As an alternate objective to the primary military mission, but one of scientific importance to the international civilian community, was to digitally map the lunar surface. Clementine entered lunar orbit on February 19,1994. It gathered the most comprehensive lunar multispectral image collection to date, collecting over 1.8 million pictures, by May 3, 1994. The imaging of the lunar surface has been made available to the planetary science community. Figures 1 and 2 illustrate some of the images that were captured.

A secondary objective was developed during the mission design that utilized the spacecraft interstage assembly as a radiation and particle detection experiment. After separation from the spacecraft, the interstage assembly remained in a highly elliptical earth orbit for several months collecting valuable data at altitudes where opportunity for investigation has not been available.

The Clementine program successfully demonstrated the capability to produce, implement, and operate spacecraft of the "faster, cheaper, better" variety through cooperative efforts between national laboratories, DOD, NASA, Industry, and international space organizations.

## Mission Scenario ( and Resulting Environments )

- The Clementine Spacecraft was launched on a Titan IIG ELV from Vandenberg AFB into a low earth staging orbit ( LEO ) on January 25, 1994. ( Launch environments were a combined 11.0 Gpk axial and 3.5 Gpk lateral quasi-static loads as well as vibro-acoustic loads.)

- After achieving LEO, the launch Clementine payload separation was initiated by the Titan II ELV. This separation involved releasing the marmon clamp that mated the Clementine Space Vehicle to the Payload Adapter. ( Pyroshock event )

- After several days in LEO the payload was spun up to 60 RPM using the Spacecraft's attitude control thrusters. At this point, the Space Vehicle was injected into a trans-lunar trajectory using the Star 37FM SRM which was mounted in the Interstage Adapter. ( 12.5 Gpk quasi-static axial acceleration)

- Next the attitude control system thrusters were activated to stop the Space Vehicle Spin and the solar arrays were deployed by releasing the frange bolts. ( Pyroshock event )

- The Clementine Spacecraft then initiated separation from the Interstage Adapter and SRM by firing eight separation nuts. ( Pyroshock event )

- The expended SRM/ISA was left in a highly elliptical orbit while the Clementine Spacecraft was inserted into a stable lunar polar orbit using the Spacecraft 110 lbf. delta V thruster.

- Lunar mapping operations using the Clementine SC's mission sensors over a period of approximately two months.

## Clementine Design

Referring to figures 3 and 4, the Clementine payload was designed to provide structural, mechanical and electrical interfaces with the Titan IIG ELV. The payload consisted of:

- The Payload Adapter (PA) - An aluminum truncated cone with riveted forward and aft interface rings which connected the Clementine Space Vehicle to the Titan IIG Launch Vehicle. The PA weighed approximately 85 lbs.

- The Interstage Adapter (ISA) - A composite truncated cone with forward and aft ring which were riveted and bonded to the shell. The ISA housed the Solid Rocket Motor and interfaced it to the Clementine Spacecraft. The ISA weighed approximately 80 lbs.

- The Solid Rocket Motor (SRM) - The SRM provided 12,000 lbf. of thrust for lunar orbit insertion. The SRM bolted to the aft ring of the ISA at the Space Vehicle separation plane. The SRM weighed approximately 2500 lbs. and was by far the heaviest component.

- The Clementine Spacecraft which provided a stable platform and positioning for the optical mission sensors. The Spacecraft's structural components were a machined aluminum subfloor, two decks containing the Reaction Control System and thrusters, eight honeycomb aluminum sheer panels containing the electronic components/boxes and eight longerons attaching the subfloor with the decks and sheer panels. The Spacecraft weighed approximately 490 lbs. unfueled.

## Clementine Overall Test Philosophy

The Clementine Satellite best fits in the category of a Class C Space Vehicle. DOD-HDBK-343 describes Class C Satellites as a medium to high risk effort, single string design, small size and low to medium complexity. In order to provide the best mix of mechanical reliability and low cost, a combination Qualification / Protoflight test philosophy was adopted which had the following characteristics:

- Test environments and loads were based on using a Titian IIG Expendable Launch Vehicle to get the Space Vehicle into low earth orbit, and a Thiokol Star 37FM Solid Rocket Motor for putting the Spacecraft into lunar orbit.
- Separate Engineering Model and Flight Spacecrafts were built.
- Qualification test levels were defined as maximum expected flight levels plus 6 dB for two minutes duration. Protoflight test levels were defined as maximum expected flight levels plus 3 dB for one minute duration.
- The Engineering Model Spacecraft (EM) was tested to qualification levels.
- The Flight Spacecraft was acceptance tested to protoflight levels.
- Components with only flight units available underwent protoflight testing while components with both operational prototypes and flight units had qualification testing on the prototype and protoflight testing on the flight unit.
- Levels for loads testing were equal to 1.05 times expected flight loads. The structure was designed for yield at a minimum of 1.10 times flight loads.
- Low level random signature tests were performed before and after any system level test that input significant loads into the structure. Transfer functions from these pre and post test signatures were compared to see if any structural failure or degradation had occurred.

## Test Flow

The test flows for both the EM and Flight Spacecraft are shown below. The goal of the EM test program was to qualify the Clementine design and provide a pathfinder for future Flight Spacecraft testing. The goal of the Flight Spacecraft test flow was to verify workmanship and acceptability of Clementine in its entirety for flight.

**Engineering Model Test Flow**

The Engineering Model (EM) was a high fidelity, non-flight, mass and stiffness prototype of the Clementine Spacecraft which was tested to qualify Clementine's design. It contained mass simulators for all components as well as dummy solar arrays. For tests performed on the Space Vehicle ( S/V ) configuration, a mass simulated SRM and high fidelity prototypes of ISA and PLA were used instead of the flight items. The following flow chart illustrates the Engineering Model development test flow.

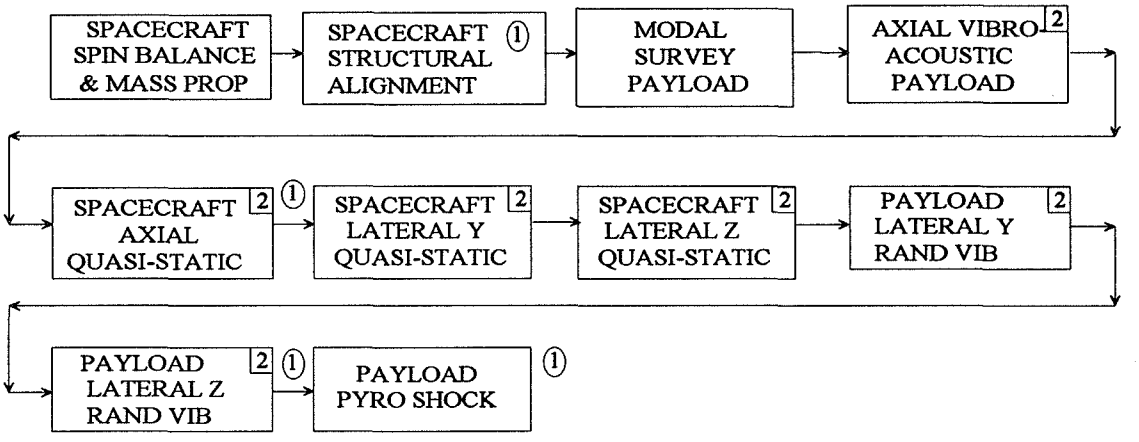


① PERFORM SENSOR ALIGNMENT VERIFICATION

[2] PERFORM PRE AND POST STRUCTURAL SIGNATURES

**Flight Structure Test Flow**

The Flight Clementine Spacecraft in launch configuration was acceptance tested to protoflight levels. The flight PLA and ISA were used for these tests, but for safety reasons the SRM mass simulator was used instead of the flight SRM.

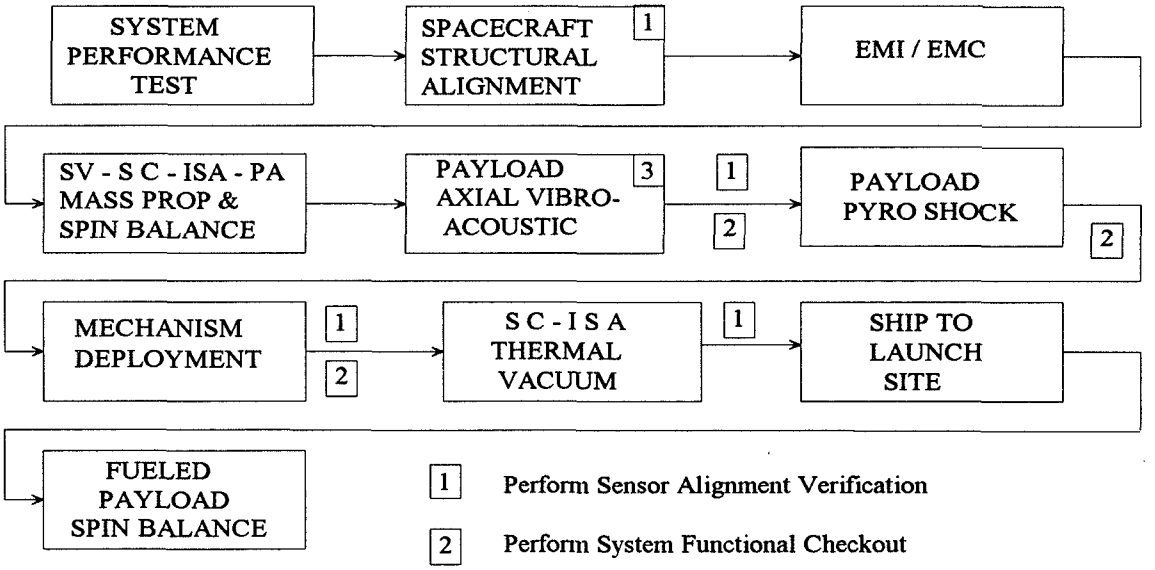


[1] Perform Sensor Alignment Verification

[2] Perform System Functional Checkout

[3] Perform Pre and Post Random Signatures

## Sensor Bench Location Alignment

Angular alignment verification of Clementine's optical sensors to one another was critical to mission success. Sensors were aligned before testing began and alignment was rechecked periodically during the test flow to determine sensitivity to dynamic and thermal loads. Translational alignment was not nearly as critical as angular alignment because the sensors were viewing subjects that were hundreds of miles away. The Alignments were also measured to provide a check on the overall structure integrity and thruster pointing. Similar alignments were done on both the EM and the Flight Spacecraft.

First, the centerlines of the sensors were aligned to each other, then the alignment of one of the sensors was measured to the reference axis of the Spacecraft. The alignment of the centerlines of the delta V thruster, attitude control thrusters, and Inertial Measuring Units were then also measured to the reference axis of the Spacecraft. Knowledge was required to within .005 degrees on all measurements. All measurements were periodically verified as shown in the test flow.

## Spin Balance and Mass Properties

Due to the 3 axis pointing requirements of the spacecraft during lunar orbit and 60 RPM spin during trans lunar flight, balancing and knowledge of mass properties were critical on Clementine.

### Engineering Model Structure

Several spin balance tests and mass properties measurements were performed on the Clementine EM as a pathfinder for the flight structure. Spin balance fixtures were balanced separately first. The first test was done on the EM Spacecraft alone ( Spacecraft Configuration ), mounted on the spin table via the S/V spin fixture and S/C adapter. Balance weights were added to the EM as required. The other spin balance test was done on the EM along with the interstage (ISA) and solid motor simulator ( Space Vehicle Configuration ). C.G., moments of inertia and products of inertia were measured on the EM S/C using an MOI machine.

### Flight Structure at NRL
### Engineering Model Spin Balance Pathfinder Activities

Pathfinder activities to prove the ability to accurately mate separate space vehicle components without violating the ACS unbalance condition requirements took place during the months of August 1993 through October 1993. The spacecraft EM and the interstage EM-SRM mass simulator assembly were balanced separately using the NRL spin balance machine. These two components were assembled and the unbalance was measured for the final assembly. Since the flight SRM manufacture was not complete at this time, the SRM mass simulator was configured into a worst case unbalanced condition based on past history of the SRM and contractual agreements with the manufacturer, Thiokol Corporation. The unbalance condition of the interstage EM was measured. The unbalanced SRM mass simulator was then mated to the interstage EM in a worst case configuration by aligning the phase angles of the unbalance properties for the two components. The static and dynamic unbalance of the interstage EM-SRM assembly was then corrected and measured. By mating in a worst case configuration, the allotted weight budget for counterweights was verified.

The spacecraft EM, a structural and mass simulator of the flight spacecraft (stowed wet launch configuration) was also dynamically balanced. The dynamic mode was used because it satisfied both the static requirement during spacecraft 3-axis stabilization and the dynamic requirement during space vehicle spin-stabilization. Static and dynamic unbalance was measured for the final correction. The spacecraft EM and interstage EM-SRM mass simulator were then mated with the use of optical alignment

tooling. The resulting unbalance condition was measured and verified to be within the ACS requirements. Therefore, the following was confirmed: 1) the validity of the spin balance flow, 2) the ability to accurately mate the separate space vehicle components, and 3) the allowed counterweight budget.

**Flight Vehicle Spin Balance Processing Operations**

During the months of November and December of 1993, the following spin balancing activities took place at Building A-59 of NRL. Using the NRL spin balance machine, both the dry flight spacecraft and the flight interstage-SRM mass simulator assembly were balanced separately. Static and dynamic unbalance was measured and corrected for the dry spacecraft in the stowed launch configuration. The SRM mass simulator representing the unbalance properties of the actual flight SRM was mated to the flight interstage. The unbalance of the SRM mass simulator was previously matched to simulate the actual unbalance of the loaded flight SRM as specified in the Thiokol STAR 37FM Rocket Motor Logbook. The unbalance properties of the SRM mass simulator are based on data collected during flight SRM spin balance operations conducted at NASA Wallops Flight Facility in October 1993. Thiokol Corporation was responsible for the balancing of the flight SRM. Static and dynamic unbalance was also measured and corrected for the flight interstage-SRM mass simulator assembly.

**Flight Structure at Vandenberg AFB**

Following spin balance operations, both the spacecraft and interstage were shipped to Vandenberg AFB for launch processing. After spacecraft propellant loading and interstage-flight SRM integration at Building 1610 of Vandenberg AFB, the two components were mated together in the space vehicle configuration. Final unbalance measurements of the space vehicle were made using the NASA spin balance machine. Based on the EM spin balance pathfinder activities and preliminary calculations, balance correction was not expected following mating of the flight space vehicle assembly. Final unbalance measurements were well within the required specifications and balance correction to the processed space vehicle was not necessary.

## Engineering Model Modal Survey

A modal survey was performed on the EM S/V to determine the global natural frequencies, modes shapes and damping coefficients. This data was used for the following purposes:

- To validate a Nastran model of the overall structure for coupled loads purposes
- To determine the in-orbit dynamics of the structure for assessing control loop interactions.
- Determine the local dynamic characteristics of key areas of the structure (panels, decks etc.)

A structural configuration was chosen for the test that would allow the primary vibration modes of the S/V to be measured while minimizing the influence of local modes and nonlinearities. In order to accomplish this, some components and subsystems were modified from the flight configuration. The following are examples:

- Deployable Solar Arrays - these were mostly non structural and mounted to the structure via hinges which would produce nonlinear responses.
- Sensor Bench - the mounting bench for the mission sensors was attached to the spacecraft via kinematic mounts. Although the sensor bench was left in for the test, an attempt was made to preload the mounts to reduce gapping.

- Propellant Tanks - Cylindrical steel mass simulators were used to simulate propellant filled tanks. The mounting flanges were flight like however.

The boundary conditions for the test were free-free with added interface mass. The free-free support system provides boundary conditions that are easily matched in an analytical model while the interface mass produces system mode shapes that have strain energy distributions that are similar to the modes see during launch. This was accomplished by mounting the S/V via the PLA to a 6 inch thick, 6 ft. X 12 ft. steel plate that weighed 15,000 lb. The whole system was then supported on a low frequency ( less than 5 hz. ) air bearing support system.

The modal shape vectors and frequencies from the modal survey were correlated with and used to refine the NASTRAN model; the final results for the first five modes are tabulated below.

| Analytical Frequency ( Hz ) | Test Frequency ( Hz ) | Mode Shaped Description | Comments |
|---|---|---|---|
| 21.3 | 23.7 | Mid-deck Bending | Matched by axial random vibration test |
| 32.7 | 33.8 | Payload Bending, My | Good Match |
| 35.2 | 38.2 | Payload Bending, Mz | Non-linear test data due to friction slip at propellant tank mount |
| 41.9 | 41.4 | Sub-floor bending | Good Match |
| 42.2 | 43.0 | Delta V Motor Base Bending | Good Match |

The mid-deck bending mode was correlated using data from the axial random vibration test because there was not sufficient energy input in the modal survey to break loose the sliding joints where the upper propellant tank bungs meet the middeck. These joints also caused some problems in one of the payload bending modes due to inconsistent slipping. This problem was solved in a later modal survey by locking the joints in place. Based on the results above, the analytical model was deemed acceptable for use in the coupled loads analysis.

## Axial (X Axis) Vibro-Acoustic Test

### Engineering Model Structure

A combined acoustic and thrust (X) axis random vibration test was performed on the Engineering Model Payload. The acoustic portion of the test simulated the acoustic noise environment seen during launch and Max Q while the mechanical vibration input simulated low frequency structure borne launch vibration. Since below 100 Hz the acoustic chamber is not capable of producing the required sound pressure levels, the mechanical vibration also served to fill in this area of the spectrum. The acoustic spectrum used for this test came from the Titan II users manual while the low frequency random vibration spectrum was an envelope of measured data from several different launch vehicles and had a bandwidth of 20 to 100 hz. The input test levels were 6 dB above the maximum expected flight levels for a two minute duration. These were considered qualification levels. For both structures, the low frequency random vibration input spectrum had to be tailored to prevent major structural components from exceeding design limit loads. The acoustic and random vibration input spectra are shown in figure 5.

The EM Payload was instrumented with accelerometers which were located in component mounting areas. Data from these were analyzed to provide random vibration PSD curves for evaluating and updating preliminary component random vibration specifications.

**Flight Structure**

A similar vibro-acoustic test was performed on the Flight Clementine S/V. The input spectra however, were lowered to 3 dB above maximum expected flight levels for a one minute duration. A subset of the accelerometers from the E/M test (seven) were again measured during this test. After scaling for input level differences and averaging the spectral data from each test, an interesting trend was obvious. Figure 6 compares the averages of the PSD measurements from the EM and the Flight Spacecraft. The Flight Spacecraft had significantly lower response at almost all frequencies above 100 hz. when compared to the E/M data. ( Below 100 hz the response was driven by the electrodynamic shaker input and was not pure acoustic response ) Averaging the Grms values of the same measurement points on the two tests again showed the E/M Grms response to be 4.1 dB higher than the Flight Spacecraft Grms response ( 7.01 vs. 4.35 ). It is likely that this is due to the substitution of flight components for mass simulators and the addition of thermal blanketing. It is assumed that the flight components, being assemblies of a generally complex nature, tend to absorb more energy than solid masses, especially at high frequencies. Also the thermal blankets may have significantly reduced the acoustic sound pressure impingement on the Flight structure. This information will be factored into preliminary vibro-acoustic predictions for future programs.

**Component Random Vibration Testing**

Acoustic sound pressure is generally the most significant driver of component random vibration. Early in the Clementine program a preliminary component random vibration test specification was predicted for component purchasing and early testing. This random vibration specification was estimated by scaling the vibro-acoustic response of similar types of spacecraft structures based on acoustic sound pressure input levels. After the E/M qualification vibro-acoustic test, the PSD responses that were measured were compared to the preliminary component random vibration spectrum. The responses were generally enveloped by the component spectrum, however there were narrow frequency bands where the responses exceeded the specification. Due to the inherent conservatism of shaker random vibration component vibration testing , these areas of exceedance were not deemed significant enough to warrant raising the specification.

## Lateral Random Vibration

This test was originally intended as a system level workmanship / acceptance test for mechanisms and subsystem connections that did not get sufficiently tested during the axial axis combined vibro-acoustic test. However, after reviewing all of the EM test date it was decided that the axial vibro-acoustic test provided a good workmanship for the whole structure without any local over testing. Thus, lateral axis random vibration tests were not performed on the Flight Space Vehicle.

## Quasi-static Loads Testing

During launch, ascent and trans-lunar phases of flight, the spacecraft is exposed to static loads and low frequency vibration (generally less than 50 Hz ) due to rocket thrust, buffeting and other transient events. This is the most severe environment for the primary spacecraft structure and heavy components. These loads were applied to the Clementine Spacecraft using a 35,000 lbf. vibration shaker out putting sinusoidal excitation. The difficult aspect of this test was that the sinusoidal output of the shaker must be low enough in frequency so that minimal structural amplification occurs. Applying relatively high G levels at low frequency requires shaker armature displacements that can easily exceed the capability of the exciter ( One inch Peak to Peak ), so care had to be taken in choosing test parameters.

Quasi-static test loads were defined as 1.05 times design limit loads. Since this is a qualification test, it was performed on the EM S/C but not the Flight S/C Before applying quasi-static loads, the DPA and ISA were removed and the S/C was mounted to the vibration fixture. The S/C was quasi-

statically tested alone because the shaker did not have enough force output to drive the full Space Vehicle Stack to the required loads. This was not a problem since the DPA and ISA were qualified in separate static loads tests.

The methodology for running this test was to use the sine vibration control software to command a sine dwell for one second at the desired amplitude and frequency. In reality, only one full cycle is required at full level but one second was the minimum allowable test time in the controller. Since this test we have modified the technique to set the over test abort limit to full test level. This causes a soft shutdown as soon as the shaker reaches full level and a reduction in the number of full level cycles in a 20 hz. test from 20 to about 3. Another refinement was to include an additional in-axis control accelerometer at the spacecraft center of gravity and use peak limiting control strategy. This provides an additional degree of control in the event of nonlinear structural behavior.

Quasi-static loads were applied in all three axes, the primary overall spacecraft loads were 12.0 Gpk acceleration in the axial direction and 3.5 Gpk in the lateral directions. The 12.0 Gpk axial load was input at 18 hz. The was some local amplification expected on the sensor bench and middeck due to the first bending mode of the middeck and a review of the post test data did show amplification of as much as 2.4 in these areas. However, these areas were designed for higher loads so this was not considered to be a problem.

The 3.5 Gpk lateral loads were input at 10 hz. No failures or significant structural degradation occurred during quasi-static testing. In addition to the quasi-static loads that were generated during launch and ascent, centrifugal loads when generated when the S/V was spinning at 60 RPM during its trans lunar stage of flight. These loads however, were covered during the spin balance test when the Space Vehicle is spun up to 80 RPM.

## Pyroshock Testing

### Engineering Model

A Pyroshock test was performed on the EM to assess the high frequency pyroshock environment and transmissibility. The structure was instrumented with shock accelerometers in component mounting areas. The weight of the SC was off loaded for this test. The Pyrotechnic shock events which occur in flight were initiated two times each during this test.

Data was collected from the accelerometers for each event and pyroshock response spectra were analyzed. These spectra were used for evaluating and updating preliminary component pyroshock specifications.

### Flight Model

A Pyroshock test was performed on the Flight Space Vehicle Payload with Star Motor simulator in place of the Star Motor. This test provided a pyroshock acceptance test for the flight components. Acceleration response data was not recorded during this test. Pyrotechnic shock events which occur in flight were each initiated once.

## Jitter Testing

A preliminary computer analysis indicated that during Clementine mission activities, the operation of certain on board mechanisms and equipment could cause vibration levels sufficient to impair the measurements made by the optical sensors. In order to assess the problem, testing was performed in which the Engineering Model Spacecraft was supported on a soft suspension system, the vibration sources

were activated or simulated and vibration responses were measured on the sensor bench. Two tri-axis accelerometers were mounted on each of the six sensor simulators, oriented so that sensor rotation could be measured. The vibration sources were simulated as follows:

- Solar Array Drive Mechanisms - The solar arrays were installed with bungee cords off loading the gravity force. The arrays were then rotated at all speeds that were feasible for mission operations.

- Reaction Wheels - The four reaction wheels were each run through their full range of operating speed.

- Inertial Measuring Unit (IMU) - One of the IMUs had a dither circuit that caused a 1000 hz. vibration output. The IMU was operated as in flight.

- The Attitude Control Thrusters - The attitude thrusters were a hydrazine mono propellant system that could not be operated in the laboratory. Based on past measurements, the force output of these is a square wave with the amplitude being the rated thruster force output. These forces were simulated using a modal survey type electrodynamic shaker.

- Cryo Cooler Compressor on the LWIR Sensor - The cooler on the LWIR sensor was mounted on the sensor bench with all of the optical sensors. The cooler compressor was operated as in flight.

- Mission scenarios were reviewed to determine which vibration sources might be in operation simultaneously. Two combined cases were identified and simulated. These were Lunar Mapping (cooler, IMU, reaction wheels and solar arrays ) and Asteroid Flyby ( thruster, cooler, IMU and solar arrays ) These source combinations were then operated together.

The accelerometers on each sensor were measured simultaneously in order to maintain the phase relationship for accelerometers on the same sensor. As an example, figure 7 is a plot of the data measured on the UV Vis sensor due to operation of the solar array stepper motor at 200 hz. The top trace is the acceleration time history showing a peak of 50 milli-Gs. The bottom trace is the averaged auto spectrum of the same signal. For analysis purposes a worst case assumption was made, that being that the 50 milli-Gs was all concentrated at the lowest significant frequency of 67.5 hz.

These measured linear accelerations were then converted into angular accelerations based on geometric positions of the accelerometers. Angular velocities were then calculated by integrating the angular accelerations at critical frequencies. The angular velocities were compared directly to the sensor maximum allowable specification which was 1.0 micro-radian per millisecond. Incidentally, based on the data referenced above and shown in figure 7, 200 hz was not an acceptable speed for the solar array stepper motor. The following summarizes the conclusions that were reached:

- The two solar array rotation (stepper motor ) speeds that caused the least jitter were found (100 hz - fast speed and 1 9/16 hz - slow speed ). The mission parameters were modified to accommodate these.

- The responses produced by the reaction wheels were within acceptable limits for sensor operation.

- The IMU vibration was low level and did not cause a problem.

- ACS thruster pulse durations that produced minimum vibration response at the sensor bench were determined. The thrusters were one of the largest jitter sources.

- The Cryo Cooler Compressor operation produced a fundamental frequency of 47 hz but caused large harmonic acceleration responses on the sensor bench at higher frequencies. Integrating the

accelerations into velocities however, reduced the high frequency energy to the point where it was not a problem.

- The combined environment testing also showed acceptable results.

## Summary

The Hybrid Qualification / Protoflight test concept worked well for this program. The Engineering Model testing produced valuable engineering data and insights into Clementine's structural integrity early in the program while cost and time saving were accomplished by only building flight units for many low risk components. Protoflight acceptance testing at 3 dB above flight levels was performed on all flight hardware, both at the component and system level. Some of the higher risk components, had non flight engineering models built which were qualification tested to 6 dB above flight levels early in the program to verify their design.

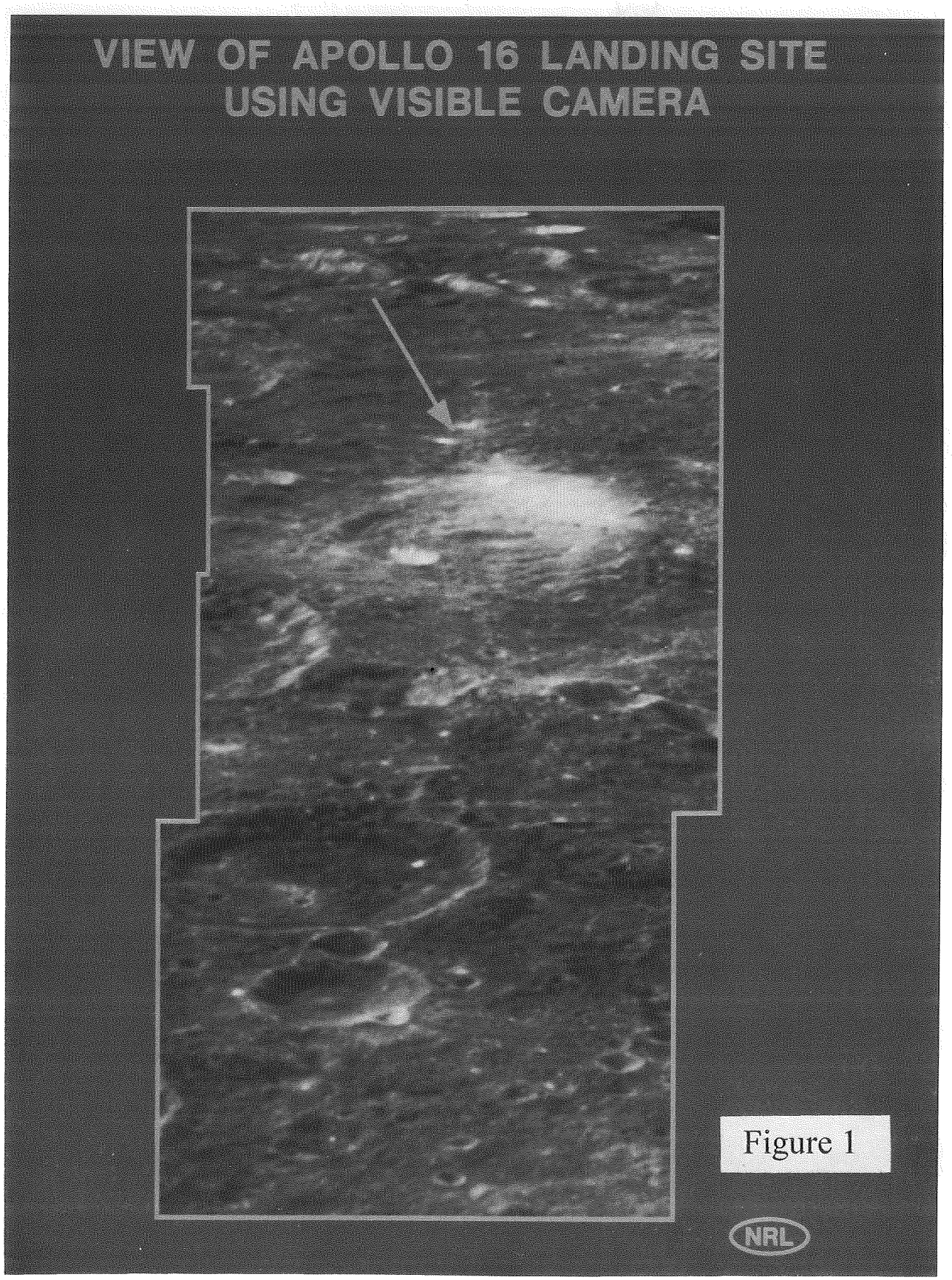


Figure 1

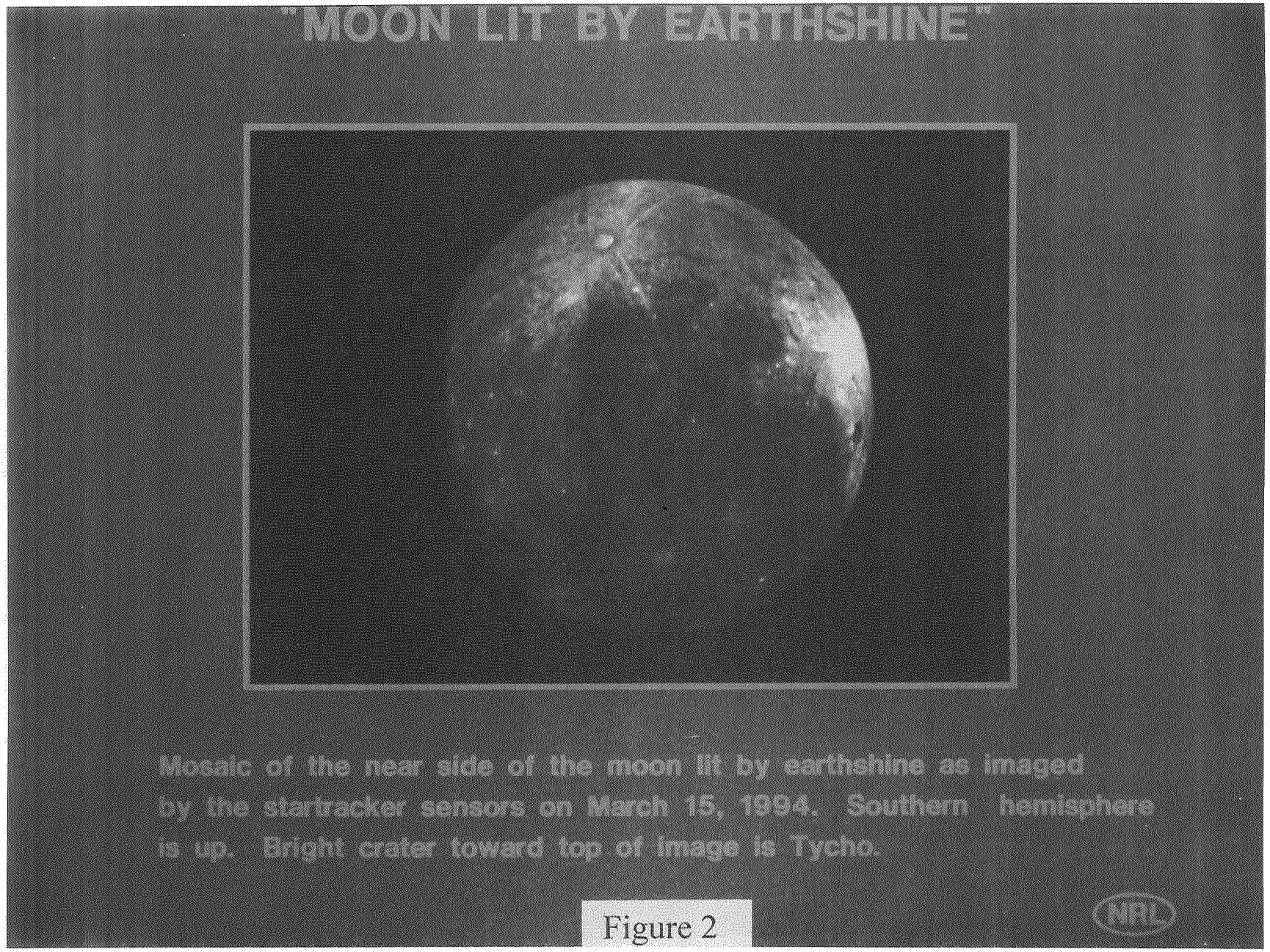
"MOON LIT BY EARTHSHINE"
Mosaic of the near side of the moon lit by earthshine as imaged by the startracker sensors on March 15, 1994. Southern hemisphere is up. Bright crater toward top of image is Tycho.
NRL

Figure 2

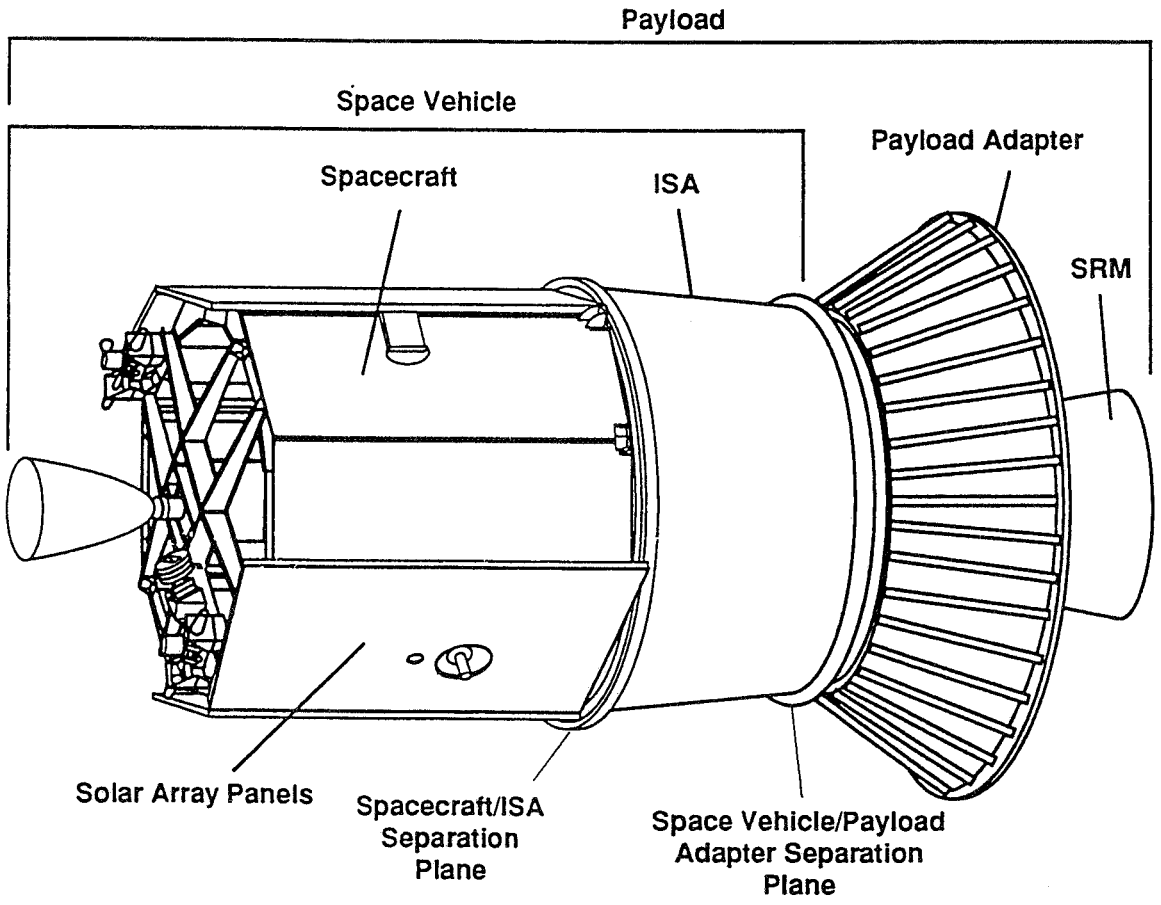
Payload
Space Vehicle
Payload Adapter
Spacecraft
ISA
SRM
Solar Array Panels
Spacecraft/ISA
Separation
Plane
Space Vehicle/Payload
Adapter Separation
Plane

Figure 3

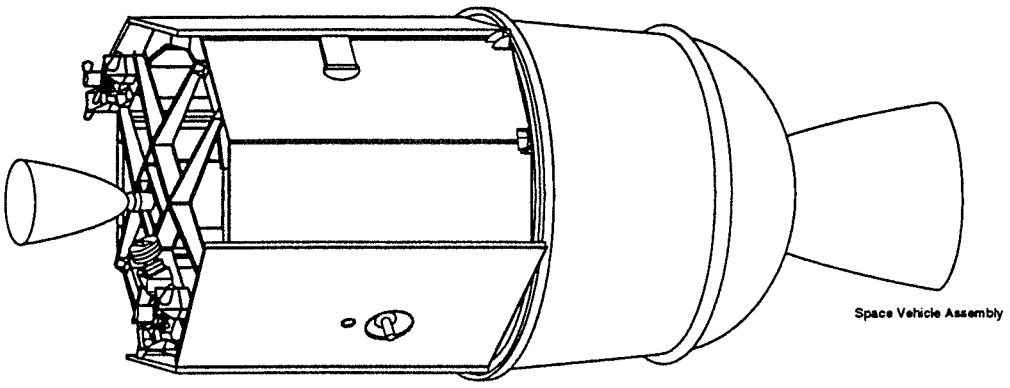


**Configuration After Booster Separation**

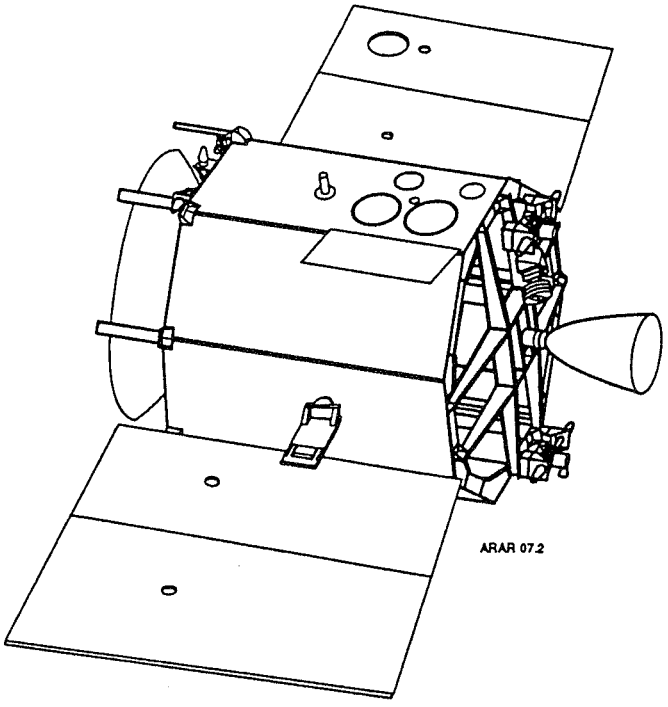


**Configuration After Solid Rocket Motor Separation**

Figure 4

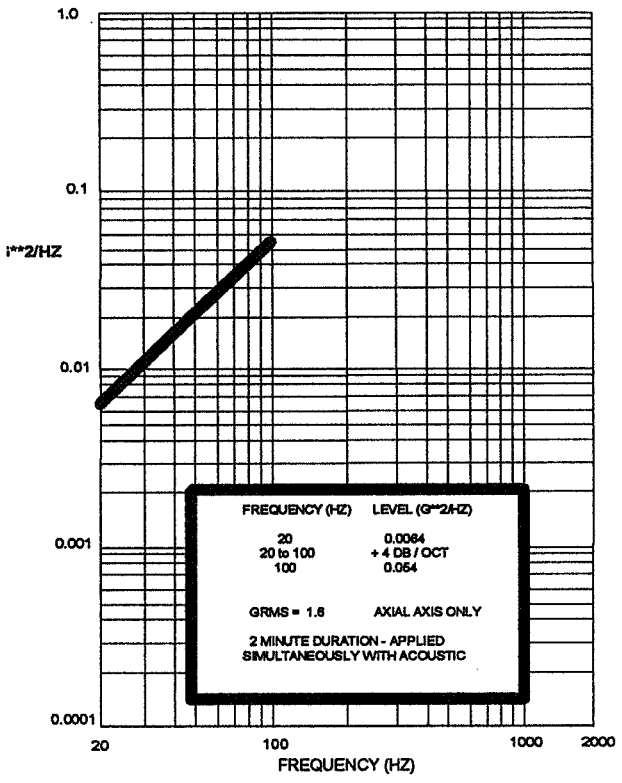


Qualification Random Vibration Spectrum for Engineering Model System Level Axial Vibro-acoustic Test

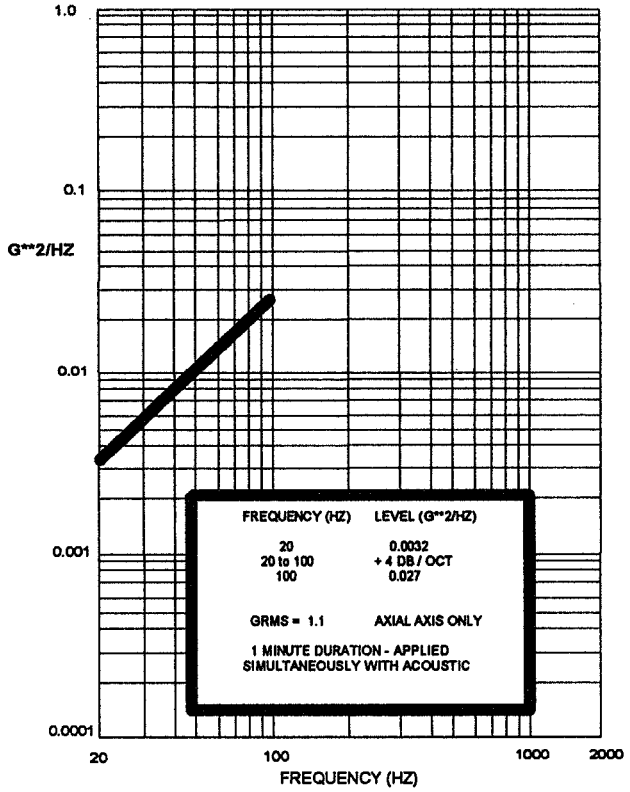


Protoflight Random Vibration Spectrum for Flight Space Vehicle System Level Axial Vibro-acoustic Test

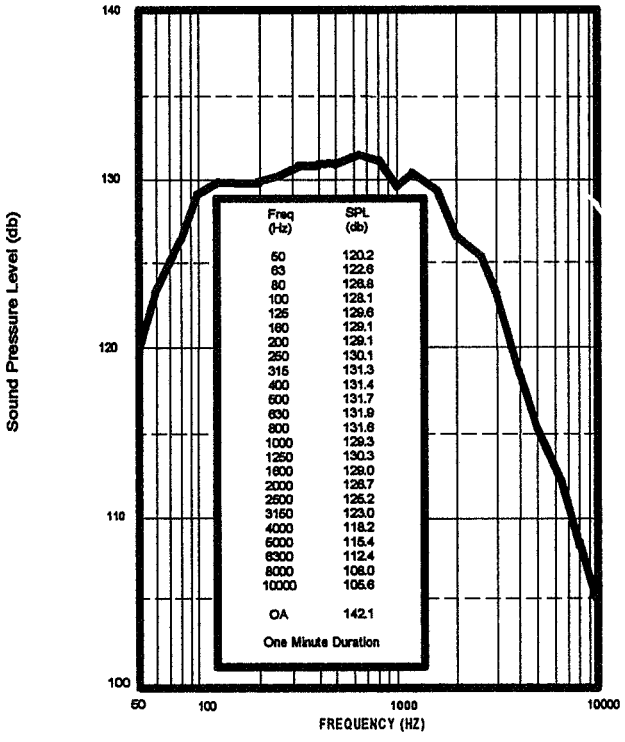


Qualification Acoustic Spectrum for Engineering Model System Level Axial Vibro-acoustic Test

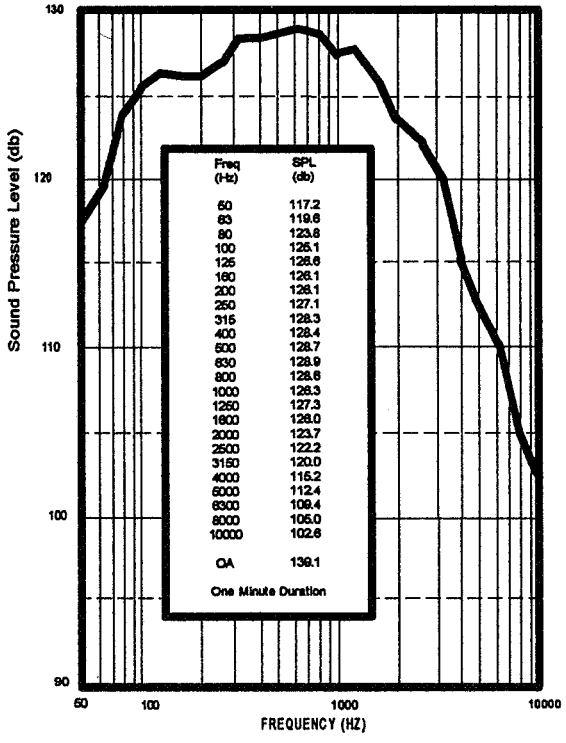


Protoflight Acoustic Spectrum for Flight Space Vehicle for System Level Axial Vibro-acoustic Test

Figure 5

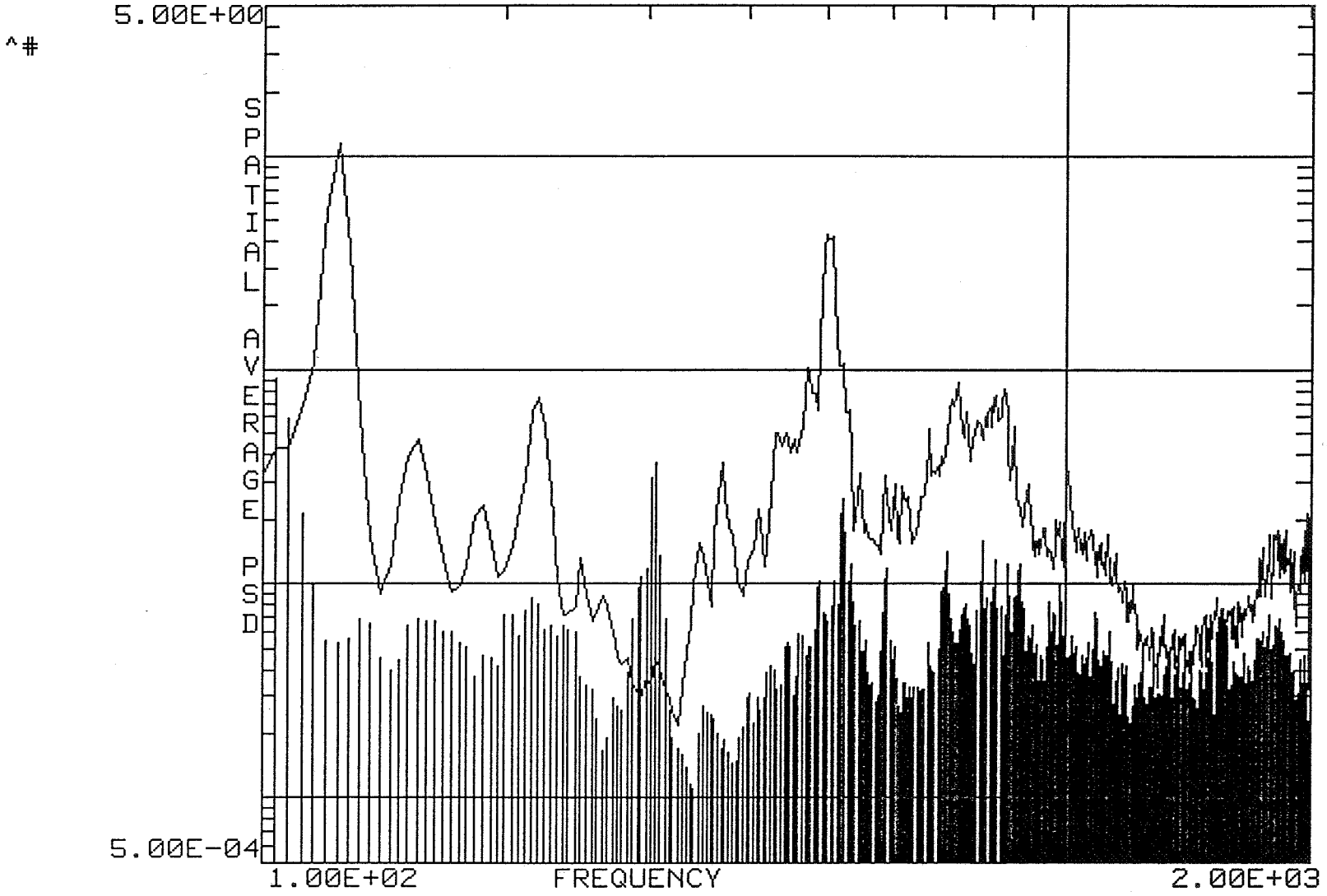
5.00E+00
^#
SPATIAL AVERAGE PSD
5.00E-04
1.00E+02
FREQUENCY
2.00E+03
A2:LINE=E/M DATA
A4:BARS=FLT S/C DATA

Figure 6

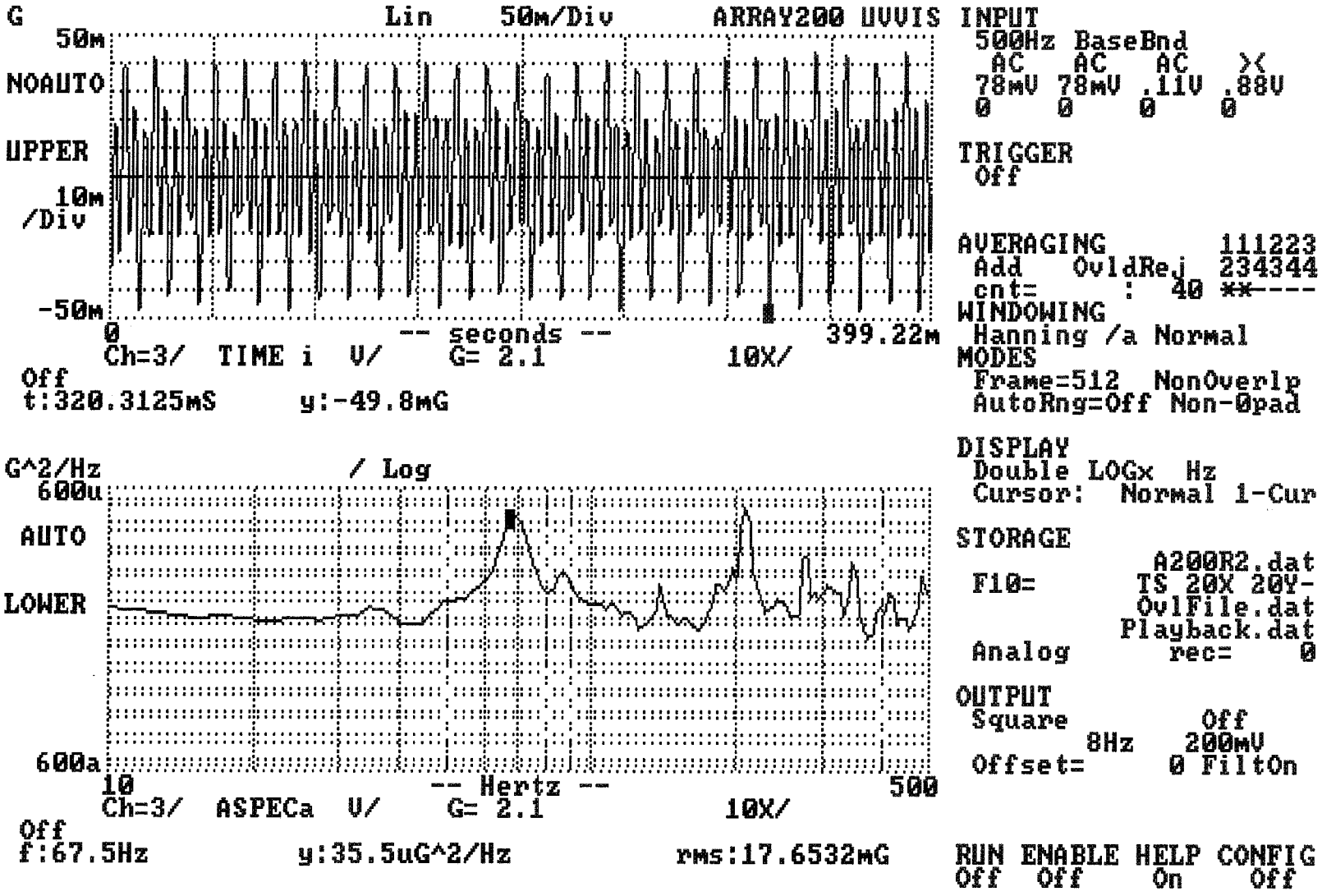
G
Lin
50m/Div
ARRAY200 UUUIS
50m
NOAUTO
UPPER
10m
/Div
-50m
0
-- seconds --
399.22m
Ch=3/ TIME i V/
G= 2.1
10X/
Off
t:320.3125mS
y:-49.8mG
G^2/Hz
/ Log
600u
AUTO
LOWER
600a
10
-- Hertz --
500
Ch=3/ ASPECa V/
G= 2.1
10X/
Off
f:67.5Hz
y:35.5uG^2/Hz
rms:17.6532mG
INPUT
500Hz BaseBnd
AC AC AC X
78mV 78mV .11V .88V
0 0 0 0
TRIGGER
Off
AVERAGING 111223
Add OvldRej 234344
cnt= : 40 **----
WINDOWING
Hanning /a Normal
MODES
Frame=512 NonOverlp
AutoRng=Off Non-0pad
DISPLAY
Double LOGx Hz
Cursor: Normal 1-Cur
STORAGE
A200R2.dat
F10= TS 20X 20Y-
OvlFile.dat
Playback.dat
Analog rec= 0
OUTPUT
Square Off
8Hz 200mV
Offset= 0 FiltOn
RUN ENABLE HELP CONFIG
Off Off On Off

Figure 7

IFD

# EVALUATION OF SENSOR PLACEMENT ALGORITHMS FOR ON-ORBIT IDENTIFICATION OF SPACE PLATFORMS[1]

Robin S. Glassburn
Graduate Student
Department of Mechanical Engineering
University of Kentucky
Lexington, Kentucky 40506-0046

Suzanne Weaver Smith
Assistant Professor
Department of Engineering Mechanics
University of Kentucky
Lexington, Kentucky 40506-0046

## ABSTRACT

Anticipating the construction of the international space station, on-orbit modal identification of space platforms through optimally placed accelerometers is an area of recent activity. Unwanted vibrations in the platform could affect the results of experiments which are planned. Therefore, it is important that sensors (accelerometers) be strategically placed to identify the amount and extent of these unwanted vibrations, and to validate the mathematical models used to predict the loads and dynamic response. Due to cost, installation, and data management issues, only a limited number of sensors wili be available for placement. This work evaluates and compares four representative sensor placement algorithms for modal identification. Most of the sensor placement work to date has employed only numerical simulations for comparison. This work uses experimental data from a fully-instrumented truss structure which was one of a series of structures designed for research in dynamic scale model ground testing of large space structures at NASA Langley Research Center. Results from this comparison show that for this cantilevered structure, the algorithm based on Guyan reduction is rated slightly better than that based on Effective Independence.

## INTRODUCTION

Monitoring the vibration characteristics of orbiting space platforms such as the international space station has received considerable recent attention. Proposed designs of space platforms that use flexible truss structures to connect operating modules and moving elements (i.e., science and habitation modules, solar panels and radiators) require that activities and experiments performed on-orbit not be disturbed by vibrations induced by motors, positioning thrusters, or other activities. Therefore, an accurate and complete understanding of the vibration characteristics is desired. With this in mind, the Modal Identification Experiment (MIE) was proposed for Space Station Freedom (SSF) to provide frequencies, mode shapes, and damping estimates for model verification (Ref. 1,2).

Before any platform is launched, extensive finite element models will anticipate the structure's vibration performance. In order to verify these finite element models, on-orbit modal identification must be performed. Such testing can not be accomplished on the ground, however, due to the platform's size and flexibility. To address this difficulty, testing of hybrid-scale models has been proposed for initial validation efforts (Ref. 3). Even with what verification can be accomplished through these means, on-orbit tests will be required for final verification.

Detecting structural failure due to micrometeroid impact or other failure mechanisms is also a concern. If, for example, a portion of the truss structure that will connect the various parts of the Space Station Freedom were to be damaged,

[1]Supported by a NASA / Kentucky Space Grant Consortium Graduate Fellowship

extensive astronaut Extra Vehicular Activity (EVA) would be required to find and repair the damaged section. Without the ability to locate a damaged section a priori, more risk would be incurred by the EVA astronauts to manually search these large structures. One approach which has shown promise for locating and assessing damage in truss structures is to monitor the vibration characteristics of the truss (Ref. 4).

Modal identification of a structure produces knowledge of its vibration characteristics from time history data. This means that the mode shapes, the damping, and the natural frequencies are determined. Sensor placement for modal identification of large space structures is a relatively recent topic of study with early works presented and published in the late 1980's and early 1990's. To date most of the evaluation and comparison of proposed techniques to date has been accomplished with numerical experiments. One objective of this work is to apply experimental data from a fully-instrumented laboratory truss to evaluate and compare a representative set of sensor placement algorithms. The experimental data involves nonideal conditions and measurement errors that can not be fully simulated in finite-element-model-based numerical experiments.

This work presents four representative sensor placement methods and four criteria to evaluate each method. Frequency response functions (frfs) are used to extract natural frequencies and mode shapes from which displacements were used corresponding to the subset of candidate locations selected by each method. The evaluation criteria applied to these experimental results are compared with those applied to numerical data from only using the finite element model. Conclusions about pretest planning are drawn. Note that this paper presents a portion of a study which provided more detail and also evaluated a fifth method (Ref. 5).

## BACKGROUND

Ideally, a large number of sensors, often accelerometers, would be placed on the platform so mode shape characteristics as well as frequencies could then be extracted from time history measurements. However, because the cost of accelerometers that will survive the dynamic launch forces and temperature changes in the on-orbit environment is high, it is necessary to minimize the number of sensors required to monitor the structure's modal characteristics. This implies an optimization algorithm in which we determine the least number of accelerometers needed and the best places for mounting on the structure to accurately describe these modal characteristics. By definition, the normal mode shapes of distinct modes of an analytical model are linearly independent. Therefore, one goal in sensor placement is to have the mode shapes extracted from the limited number of sensors also be linearly independent. For space platform application, the algorithm must also address the characteristically large number of modes with closely-spaced frequencies that these structures possess.

Sensor number and placement questions arise in other fields. For example, sensor placement applications for HVAC systems to control the work environment in large office buildings could address the possibility of the sick building syndrome (Ref. 6). Sensor placement problems also occur in monitoring various manufacturing processes at all levels from raw materials to finished product (Ref. 7). Sensor placement in buildings is also important for studying the effects of earthquakes. This information helps in the design of new buildings and in the reinforcement of existing buildings to withstand the dynamic forces that earthquakes produce.

In each of the applications above, sensors are placed for one of basically three different goals, state estimation, optimal control, or modal identification. The third of these objectives, system identification, is the focus of this work, specifically the issue of number and placement of sensors to identify specified modes for space platforms.

All algorithms in this work use a finite element model as a starting point for selecting sensor locations. For pretest analysis and test design, this may be the primary available information. Each algorithm attempts a suboptimal approach for placing sensors, an optimal solution often only obtainable through an exhaustive search of every different possible combination of sensors. However, in most practical cases, an exhaustive search is computationally intractable. The number of possible configurations which must be addressed and evaluated in such a search is

$$\eta = \frac{I!}{T![(I-T)!]} \tag{1}$$

where,

$\eta$ = number of possible sensor location configurations,
I = the total number of possible sensor locations,
T = the number of sensors to be placed.

In the small problem of 100 possible locations and given ten sensors to place, $1.7 \times 10^{13}$ possible configurations result.

Therefore in this paper, algorithms which optimize defined cost functions determine the best positions for sensor placement. In what follows, the sensor configurations are then evaluated using selected criteria to determine the acceptability of the results and to compare the merits of various techniques. In ground experiments, sensors are typically mounted triaxially, with three perpendicular sensors mounted as one unit. For the purpose of comparison of algorithms, however, individual sensor placement is used in this study.

Table 1 is a summary of sensor placement literature for modal identification. The methods are listed in chronological order with the authors in the left-hand column. The methods primarily fall into four categories with exceptions listed in the right-hand column. Note that italicized entries indicate where a previously published method was used for comparison with the new method presented in the cited paper. In addition to these works which present new techniques, Larson, et. al. (Ref. 8,9) conducted recent comparative studies for sensor and actuator placement, one using numerical simulations for the same cantilevered truss from which we use experimental data in what follows.

From the methods presented in Table 1, one representative method was chosen from each of the first four columns for this comparison study. These methods are the Guyan Reduction method described by Penny et al. (Ref. 10), the Effective Independence method described by Kammer (Ref. 11), the Driving Point Residue method described by Parker et al. (Ref. 12), and the Kinetic Energy method described by Chung and Moore (Ref. 13). They are each described in detail in the next section. The Effective Independence method has recently become the most widely used method for placing sensors for on-orbit applications and the standard for comparison for new methods for identification of large space structures.

## SENSOR PLACEMENT METHODS

### Effective Independence (EI)

Effective Independence is an iterative method which ranks candidate sensor locations according to their contribution to the linear independence of the target modal partition. The target modal partition, $\phi$, is an m x n column matrix of eigenvectors for all the modes of interest, where m represents the number of candidate sensor locations matching the degrees of freedom (DOFs) of the finite element model and n is the number of "target" modes of interest. The Effective Independence method is usually preceded by calculating the kinetic energy contribution of each DOF. The original candidate set of sensor locations is then decreased by eliminating sensors which contribute little to the kinetic energy of the target modes.

Using Kammer's notation (Ref. 11) the Fisher Information Matrix (FIM), A, is computed as $\phi^T\phi$. The eigenvalues, $\lambda$, and eigenvectors, $\psi$, are determined for the FIM,

$$A\psi = \lambda\psi \tag{2}$$

Since the columns in $\phi$ each represent different modes of the structure, they are linearly independent. Therefore, the eigenvalues of A are real and positive. The eigenvectors are orthogonal and represent n directions in an n-dimensional space which Kammer calls the Absolute Identification Space. Then, an m x n matrix G is formed in which each column is associated with the corresponding eigenvalue of A,

$$G = [\phi\psi] ** [\phi\psi] \tag{3}$$

where "**" indicates term by term multiplication (also called the Hadamard or Schur product). An m x n matrix is constructed to indicate the fractional contribution of the $i^{th}$ sensor location to the $j^{th}$ eigenvalue as

**Table 1. Summary of algorithms found for sensor placement for identification.**
**Note: methods used for comparison are presented in italics.**

| *'Year* Author(s)[Reference #] | Reduction Methods | Effective Independence | Driving Point Residue | Kinetic Energy | Other Methods |
|---|---|---|---|---|---|
| *'78* Shah & Udwadia[Ref. 14] | | | | | Covariance Matrix Norm |
| *'78* Le Pourhiet & Le Letty[Ref. 15] | | | | | Error Sensitivity |
| *'87* Salama, et. al.[Ref. 16] | | | | KE | Simulated Annealing |
| *'90* Parker, et. al.[Ref. 12] | | | DPR | KE | |
| *'91* L.M.S[Ref. 17] | | | Avg. DPR | | |
| *'91* Kammer[Ref. 11] | | EI | | *KE* | |
| *'92* Flanigan & Botos[Ref. 18] | Guyan Red. | | | | |
| *'92* Kammer & Triller[Ref. 19] | | *EI*, EI Derivative | | | |
| *'92* Lim[Ref. 20] | | EI Derivative | | | |
| *'92* Penny, et. al.[Ref. 10] | Guyan Red. | | *Avg. DPR* | | |
| *'93* Lim[Ref. 21] | | EI Derivative | | | |
| *'93* Chung & Moore[Ref. 13] | | | Weighted DPR | Weighted KE | |
| *'93* Yao, et. al.[Ref. 22] | | *EI* | | | Genetic Alg. |
| *'94* Liu & Tasker[Ref. 23] | | *EI* | | | Perturbation Variance & *DV* |
| *'94* Tasker & Liu[Ref. 24] | | *EI* & 3 EI Derivatives | | | |
| *'94* Brillhart & Kammer[Ref. 25] | | *EI* | | 2 KE Methods | |
| *'94* Hemez & Farhat[Ref. 26] | | *EI* & EI Derivative | | | *NRG* |
| *'94* Johnson & Mack[Ref. 27] | A-Set Prioritization | | | KE | |
| *'94* Pape[Ref. 28] | *Guyan Red.* | | | | Chebyshev Interpolation |
| *'94* Larson, et. al.[Ref. 8,9] | | *EI* | | *KE & Avg. KE* | *Eigenvector Product* |

$$F_E=G[\lambda]^{-1} \tag{4}$$

where,

$F_E$ = Fractional Eigenvalue Distribution (m x n).

Finally, a column vector (m x 1) of the effective independence values is calculated as follows,

$$E_D=\left[\sum_{j=1}^{k} F_{E1j} : \sum_{j=1}^{k} F_{E2j} : \ldots : \sum_{j=1}^{k} F_{Esj}\right]^T \tag{5}$$

where,

$E_D$ = Effective Independence Distribution,

in which the $i^{th}$ term in the column vector is the fractional contribution of the $i^{th}$ sensor to the linear independence of the modal partitions.

Values in the vector E range from 0.0 to 1.0. A value of 0.0 indicates that the candidate sensor location does not provide independent information and is not observable from its location. Conversely, a value of 1.0 indicates that sensor location must be retained in order to identify the target modes in the columns of $\phi$. In application, values are between these limits, so a threshold must be established to select those sensors contributing the most to the linear independence. The EI values for all candidate locations are sorted and the location with the lowest value is removed. The process then iterates though these steps beginning with determining the new FIM from the finite element model using only the remaining sensor candidates. At each iteration only one sensor candidate is removed.

**Guyan Reduction (GU)**

The Guyan Reduction sensor placement method came about as a result of the work of Guyan (Ref. 29), who devised a method in 1965 which is used to reduce the size of finite element models, namely stiffness and mass matrices. This placement method works by eliminating those DOF for which the inertia forces are negligible compared with the elastic forces. This is an iterative process where during each iteration one "slave" DOF is defined as the DOF with the largest ratio of stiffness to inertia and the remaining DOFs are termed "master" DOFs. The stiffness and mass matrices for the structure's matrix eigenproblem are reordered and partitioned,

$$\left\{\begin{bmatrix} S_{mm} & S_{ms} \\ S_{sm} & S_{ss} \end{bmatrix} - \omega^2 \begin{bmatrix} M_{mm} & M_{ms} \\ M_{sm} & M_{ss} \end{bmatrix}\right\}\begin{Bmatrix} \delta_m \\ \delta_s \end{Bmatrix} = \begin{Bmatrix} 0 \\ 0 \end{Bmatrix} \tag{6}$$

where,

[δ] = reordered and partitioned eigenvector,
[S] = stiffness matrix,
[M] = mass matrix,
mm = matrix partition corresponding to master DOFs (m x m),
ss = matrix partition corresponding to slave DOF (s x s),
ms,sm = vectors m x s and s x m, respectively,
s = number of slave DOFs = 1,
$\omega^2$ = eigenvalue.

Henshell and Ong (Ref. 30) present the constraint equation from the slave partition,

$$\{\delta_s\}=-[S_{ss}]^{-1}[S_{sm}]\{\delta_m\} \tag{7}$$

which is used in the strain and kinetic energy equations for the structure to produce the reduced stiffness and mass

$$[S*]=[S_{mm}]-[S_{ms}][S_{ss}]^{-1}[S_{sm}] \tag{8}$$

$$[M*]=[M_{mm}]-[S_{ms}][S_{ss}]^{-1}[M_{sm}]-[M_{ms}][S_{ss}]^{-1}[S_{sm}]+[S_{ms}][S_{ss}]^{-1}[M_{ss}][S_{ss}]^{-1}[S_{sm}] \tag{9}$$

where,

[S*] = the reduced stiffness matrix, and
[M*] = the reduced mass matrix.

The new reduced model is ready for the next iteration and the iterations continue until the number of master DOFs remaining equals the number of allowed sensor locations. Henshell and Ong (Ref. 30) suggest only the diagonals of the stiffness and mass matrices be used to determine which DOFs are slave and master from the assumption that off-diagonal terms in the stiffness/inertia ratio matrix can be neglected.

Penny, Friswell, and Garvey (Ref. 10) investigated three different structures using the Guyan Reduction algorithm and concluded that this method selected an appropriate subset when the structure was grounded or had no rigid body modes. They also noted that for structures with one or more rigid body modes, the method works adequately but not as well as the Driving Point Residue method which they used for comparison purposes. We are generally interested in free/free structures with rigid body modes, so we expect this method to perform less adequately on-orbit than our experimental results indicate.

**Driving Point Residue (DPR)**

Another method used to place sensors is by calculating the Driving Point Residue of each DOF. From Parker, Rose, and Brown's paper (Ref. 12), Driving Point Residues are equivalent to modal participation factors, and are a measure of the degree of excitation or participation of each mode in the overall response. Driving Point Residues are proportional to the magnitudes of the resonance peaks in a driving point frequency response function. The Driving Point Residue is calculated for a structure from the following:

$$[DPR]=[\phi]**[\phi][\omega] \tag{10}$$

where,

[DPR] = Driving Point Residue values for the structure,
[ω] = matrix of eigenvalues of target modes.

Each element of the DPR matrix represents the Driving Point Residue contribution of that DOF in a particular target mode. Therefore the $i^{th}$ row represents the contributions of the $i^{th}$ DOF to each of the target modes. Since some of these elements can be small or even zero (if at a node of the target mode), the row is averaged and multiplied by the smallest element in that row to produce a "weighted" measure of the Driving Point Residue contribution of each DOF. Since a sensor placed at a node of a mode would not yield useful information, this biases the method against small or zero elements in the DPR matrix.

**Kinetic Energy (KE)**

The Kinetic Energy approach may be considered the most common approach used to place sensors, since a majority of "Engineering Judgement" in placing sensors is based on it. Typically, those experienced in experimental procedures will look for, among other things, areas of the structure where there is large displacement. These areas would be the best positions for the sensors to observe the behavior of the structure with the largest signal to noise ratios.

Generally, the Kinetic Energy method works by calculating the kinetic energy of each DOF for each mode and then using the DOFs with the largest values as positions for sensor placement. The form used herein takes the equation for the m x n modal kinetic energy (MKE),

$$[MKE]=[\phi]**[M][\phi] \tag{11}$$

and produces a weighted form once again with the weighted average equal to the average value for the row times the minimum value in that row.

## EVALUATION CRITERIA

In order to compare the selected methods, four evaluation criteria are presented. The criteria were designed to judge the ability of a sensor set to accurately determine the mode shapes and natural frequencies of the structure.

### Modal Assurance Criteria

The first two criteria involve the Modal Assurance Criterion (MAC). The MAC is used to present a measure of orthogonality between two eigenvectors (or extracted mode shapes), as,

$$MAC_{ij}=\frac{\phi^T{}_i\phi_j}{\sqrt{\phi^T{}_i\phi_i}\sqrt{\phi^T{}_j\phi_j}} \tag{12}$$

where,

$\phi_i,\phi_j$ = $i^{th}$,$j^{th}$ mode shape vector,

MAC values range from 0 to 1 with 0 indicating that the two vectors are independent. Generally the MACs are presented in a matrix for i,j = 1,...,n. From this matrix, two criteria are derived. First, the maximum off-diagonal MAC value is determined. Second, the root-mean-square (RMS) of the off-diagonal elements is computed.

### Determinant of the Fisher Information Matrix

The determinant of the Fisher Information Matrix (FIM) was selected as a criteria because it is used as an objective function in one method (Ref. 22) and is the inverse of the Covariance Matrix of the estimate error. The estimate error is the difference between the real target mode response and the estimated response (Ref. 11,22). The goal is to minimize the estimate error by maximizing the determinant of the FIM. The FIM is given by,

$$Q=\frac{1}{\chi^2}\phi^T\phi \tag{13}$$

Where,

$\chi^2$ = variance of stationary Gaussian white noise.

The same effect is achieved by maximizing the determinant of the numerator of the MAC described above,

$$A=\phi^T\phi \tag{14}$$

### SVD Ratio

A singular value decomposition of the eigenvector matrix, $\phi$, is determined and the ratio of the largest to smallest value is computed. The SVD ratio takes into account three quantities: mode orthogonality, the condition of the mode expansion problem, and the observability of the modes (Ref. 10). If a singular value is close to zero, the indication is that one mode shape is not independent of the others. With increasing independence, the SVD ratio of highest to lowest is lowered.

## NASA 8-BAY TRUSS EXPERIMENTS

Experimental data from an 8-bay cantilevered laboratory truss was intended to provide a large database for use in validation of proposed methods for on-orbit model verification and damage detection in flexible truss structures (Ref. 31). The truss was part of the hybrid-scaled structure designed for the Dynamic Scale Model Technology research program at NASA Langley Research Center (Ref. 3) and exhibits desired response characteristics of closely-spaced frequencies and light damping. Each bay is 0.5 m (19.685 in.) on a side. The truss was mounted to a rigid backstop plate.

The finite element model for this structure consisted of 32 nodes and 96 DOFs as illustrated in Figure 1. The truss was modeled with rod elements that carry only axial load and concentrated masses for the nodes and instrumentation. Node numbering starts at the free end.

Acceleration time history data was collected at each node in each of the three orthogonal reference-axes directions using accelerometers and two driving points which were excited with a burst random pattern as detailed in NASA TM-107626 (Ref. 31). In the peaks of the sample frequency response function (frf) shown in Figure 2, representing the response at node 30 (near the fixed end) in the -Z direction to the excitation at node 4 (at the free end) in the +X direction, the first five mode frequencies of the structure are seen. The first five mode shapes, extracted using the polyreference method and all 96 sensors, and are depicted in Figure 3 with the fixed end of the truss at the top in each case. Table 2 compares the first five natural frequencies from the analytical model and experimental results.

**Table 2. Frequency values for the analytical model and experimental data.**

| Mode # | Analytical Freq.(Hz) | Experimental Freq.(Hz) | Description |
|---|---|---|---|
| 1 | 13.925 | 13.876 | 1st X-Y Bending |
| 2 | 14.441 | 14.480 | 1st Y-Z Bending |
| 3 | 46.745 | 48.411 | 1st Torsional |
| 4 | 66.007 | 64.035 | 2nd X-Y Bending |
| 5 | 71.142 | 67.465 | 2nd Y-Z Bending |

Figure 4 shows a representation of the FEA analytical and experimental mode shapes for mode 1. Observe that in the analytical model the X and Z DOFs are equal in magnitude, while in the experimental results the X and Z DOFs are unequal. This is because the principle bending axes between the two models are not aligned. Also note that the data from sensors at DOFs 45 and 84 are suspect. Here 45 can be seen. Small values are predicted by the analytical model in the Y direction and these values therefore show the largest percent differences between analytical and experimental results.

The mode shapes and natural frequencies were first extracted using the full set of frf data. Subsets of these mode displacements were used to evaluate each sensor placement method. In response to the question of how the mode extraction might vary with the sensor set selected, only the frfs corresponding to a chosen sensor set were also used to extract mode shapes and natural frequencies. In general, the percent differences between the modes extracted from the full frf set and those from the selected frf set were less than 1 percent for the X and Z DOFs. Because values in the axial direction of the truss (Y) are small, larger differences (typically under 6 percent though) were noted between the mode shapes extracted from the full set of frfs and the mode shapes extracted from the reduced set. DOF 23 showed a percent difference, however, exceeding 200 percent, due to a sign difference between the extractions. The natural frequencies extracted using each method were identical to two decimal places.

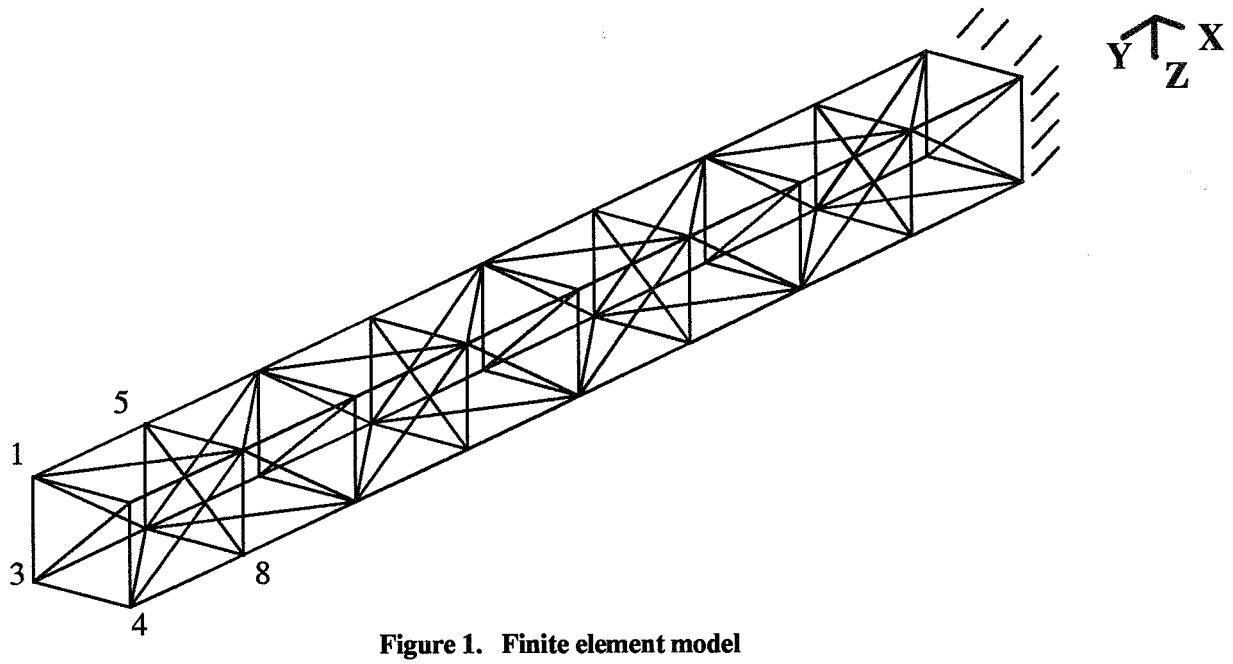


**Figure 1. Finite element model**

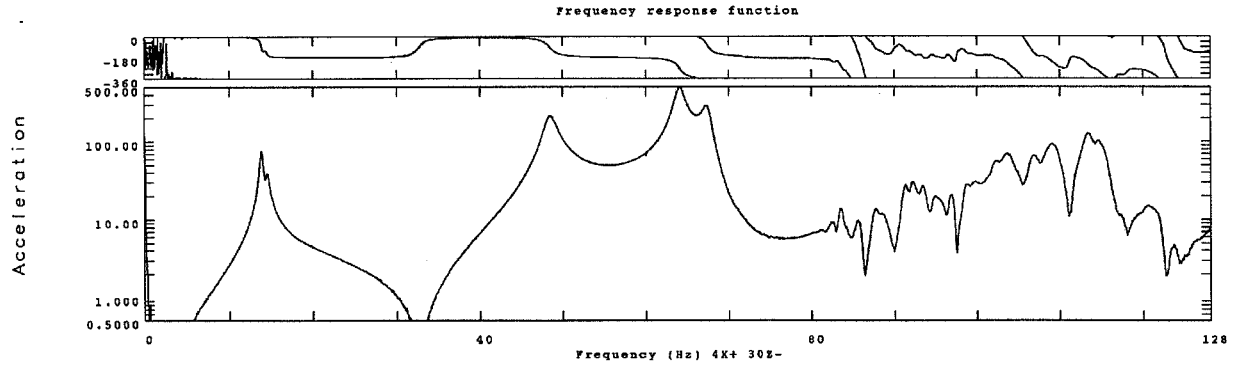


**Figure 2. Sample frequency response function**

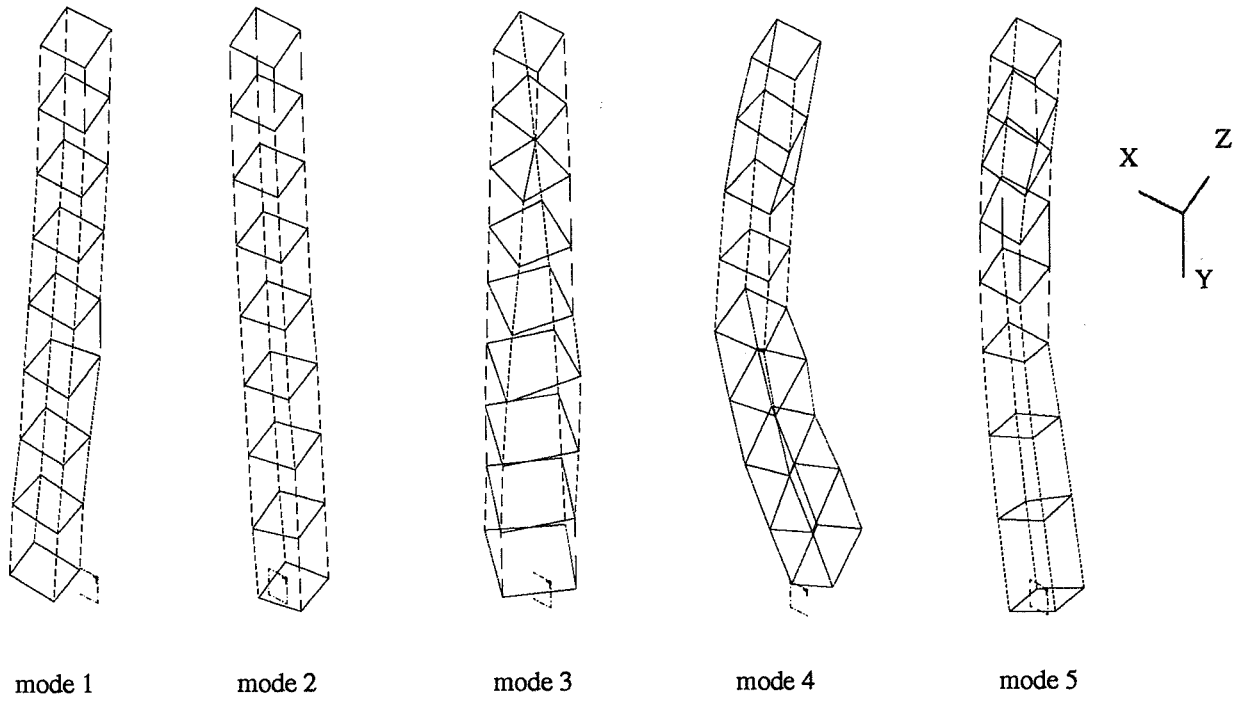


**Figure 3. First five mode shapes extracted from test data**

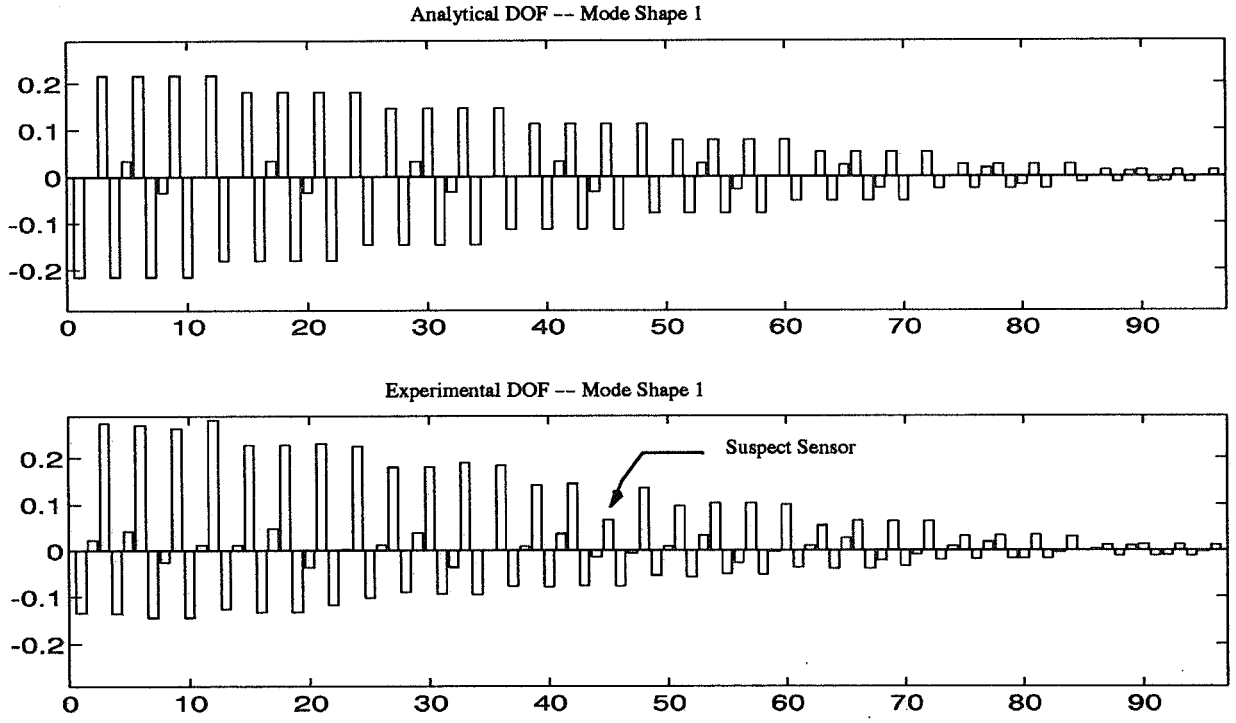


**Figure 4. Analytical vs. Experimental mode shape 1**

## SENSOR PLACEMENT EVALUATIONS

Each of the four methods presented previously were used to select a subset of sensor locations from the full 96-DOF finite element model. Subsets included 5% (5 sensor locations), 10% (10 sensor locations), and 15% (14 sensor locations) of the available DOFs. Ten percent has been suggested as a reasonable number for on-orbit instrumentation (Ref. 32). The 5% and 15% subsets were presented to show the trends of each method. "One sensor minus 10%" (9 sensor locations) and a "one sensor plus 10%" (11 sensor locations) subsets were also evaluated but are not presented here due to the generally small change in evaluation values. It is important to note, however, that between the 10% and the "one plus 10%" subsets for this truss, the SVD ratio and FIM determinant results improved greatly. Figures 5-7 illustrate the sensor locations picked by each method for each case grouped by number of sensor locations. For presentation clarity the diagonal members of the truss are not shown in these figures.

Note that those sensors appearing in the 5% subset are in the 10% subset also and similarly in the 15% subset. So, as iterations or reductions proceed for these four methods, the next iteration or reduction always yields a subset of the previous candidate sensor location set.

In Figures 5-7 placement patterns can be seen for each method. The patterns of sensor locations chosen by the EI and the KE methods are similar. They tend to locate sensors at the mid-section and free-end of the truss, which tends to maximize the observability of the first five modes. In other words, from the mode shapes presented in Figure 2 the maximum displacements are located in these areas. The EI method places more importance on the mid-section of the truss than the KE method as can be seen by comparing Figures 5 and 6.

The GU method distributes the sensor locations over the structure more than the first two methods. Note, however that it also locates sensors at the mid-section and free-end, just not as closely spaced as those from the first two methods. The GU method is also the only method to pick a subset sensor location in the axial (Y) direction from the four methods presented. With the differences between the axial displacements from the analytical model and those from the experimental results, no adverse effect was noticed in the GU subset evaluation results.

The DPR method places sensors at the free-end only. This makes the first mode pair indistinguishable from the second mode pair. As a result, this method performs poorly.

To evaluate each selected sensor subset's performance, the criteria presented above were applied. High values for the FIM determinant and low values for the MAC criteria and the SVD ratio produce a better sensor set. An evaluation was first performed using all of the DOFs to provide a relative measure of the effect of experimental imperfections for the fully instrumented case. These evaluation results are presented in Table 3. Note that the analytical results are slightly better than the experimental results due to modeling error and measurement imperfections. Table 3 is presented to demonstrate experimental effects in the criteria and to give a standard for results which follow.

**Table 3 Experimental and Analytical evaluation results using all finite element DOFs.**

| Evaluation Criteria | Experimental Evaluation Results | Analytical Evaluation Results | Percent Difference |
|---|---|---|---|
| Max MAC | $6.455 \times 10^{-3}$ | $4.982 \times 10^{-3}$ | 30% |
| RMS MAC | $2.769 \times 10^{-3}$ | $2.157 \times 10^{-3}$ | 28% |
| SVD Ratio | 1.120 | 1.073 | 4% |
| FIM Determinant | 0.985 | 0.990 | 5% |

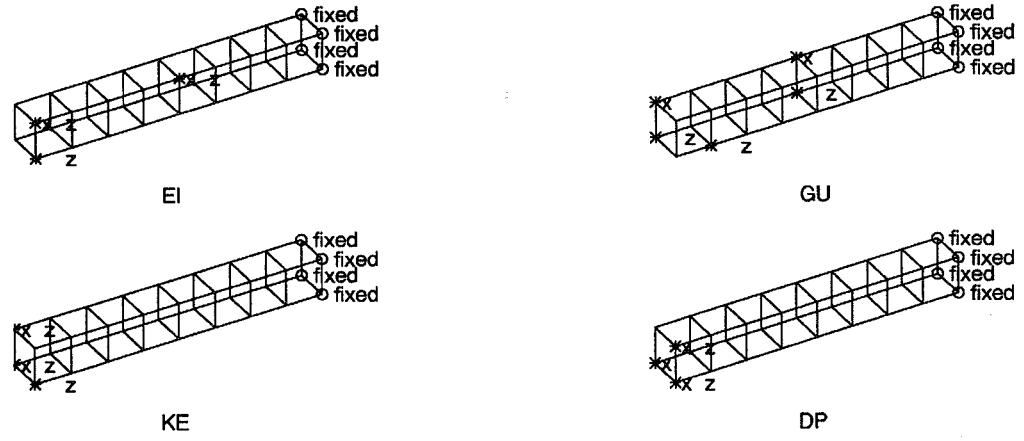


**Figure 5. Truss with 5% instrumentation**

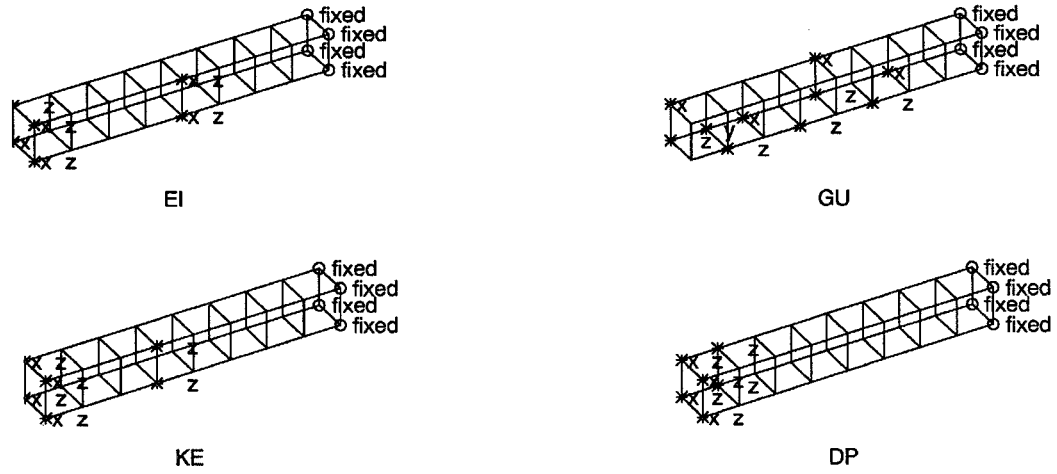


**Figure 6. Truss with 10% instrumentation**

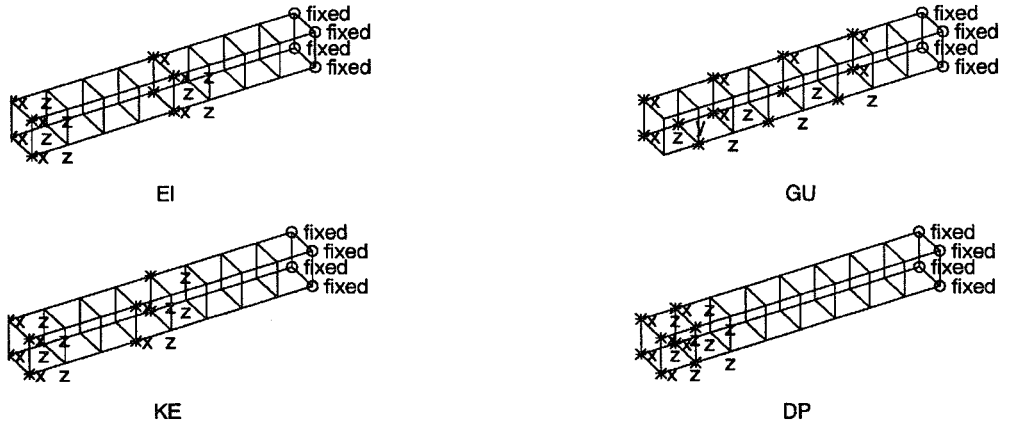


**Figure 7. Truss with 15% instrumentation**

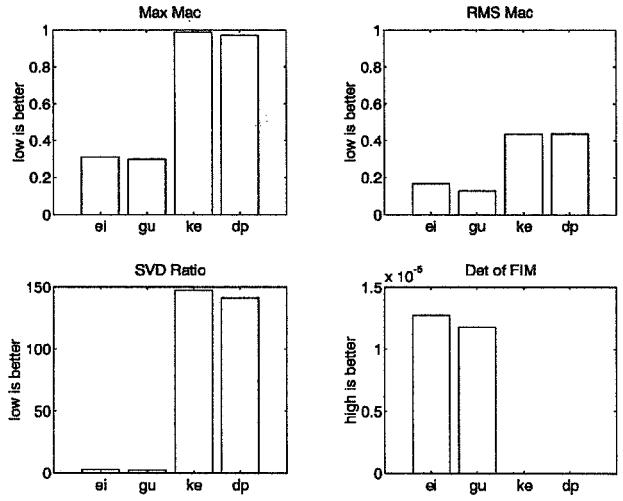


**Figure 8. Evaluation results for 5% instrumentation**

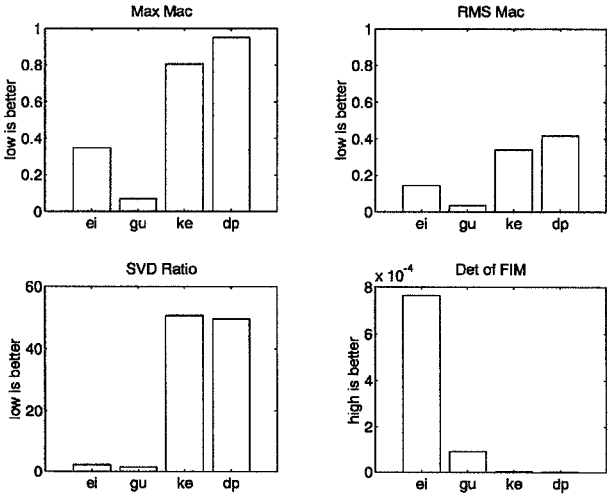


**Figure 9. Evaluation results for 10% instrumentation**

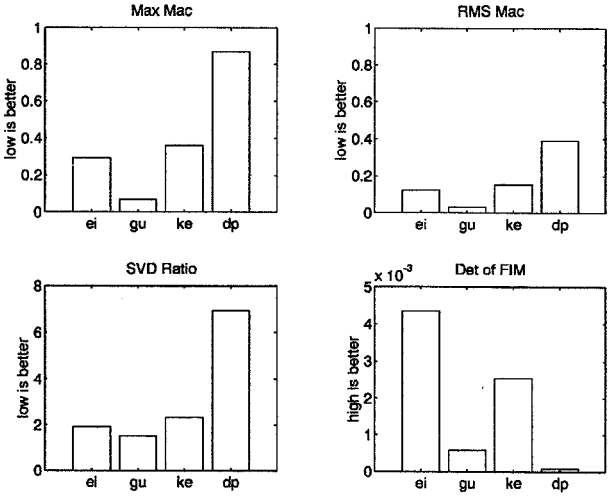


**Figure 10. Evaluation results for 15% instrumentation**

The evaluation results for the 5%, 10%, and 15% instrumentation cases are presented in Figures 8-10, respectively. The MAC evaluation criteria show the GU subset to have the most efficient sensor placement followed by the EI subset. The KE and the DPR subsets ranked much lower than the first two. It was found in Reference 5 that for grounded structures the GU method picks a subset which is generally better than the others and for free structures the DPR method tends to perform better. Penny et. al. found similar results with the GU method (Ref. 10). Larson (Ref. 9) found that the EI method performed better than the KE methods studied.

The SVD ratio changes dramatically between each of the presented subsets. This is partially due to the discrete nature of optimization which is employed by each of these methods. Adding or subtracting one or more sensors a large change in the identifiability could result. The SVD criteria also selects the GU subset as the best set followed by the EI method.

The FIM determinant, however, shows the EI method performing better for all subsets. The GU method is shown as the next best for the 5% and the 10% instrumentation. The KE subset becomes the second best method in this criteria for sensor sets above 10% (beginning at the "10% plus one" subset). A similar result was found in Reference 5 and it was noted that generally the best methods picked by the MAC criteria and SVD ratio were also picked as top methods by the FIM determinant criteria, but not always in the same order).

These four criteria were also applied to evaluate sensor placements using a numerical free/free and fixed/free square plate (no experimental data available). Results were similar and, as expected, the DPR method was superior to the GU method in the free/free case (Ref. 5).

## SUMMARY

Four representative sensor placement methods for modal identification were evaluated using four evaluation criteria. An 8-bay cantilevered laboratory truss was employed to test each method with the evaluation criteria.

The four methods presented were representative of nineteen found in the literature. From these, the GU method produced the most favorable results. The EI method performed second best for this structure. It should be noted, that for free structures the DPR method does generally better than GU as was found in References 5 and 10. Also the EI method performed better than the KE method as was found in Reference 9. The KE and DPR produced evaluation results that were similar for 5% and 10% instrumentation. Above 10% instrumentation, the KE method performs better than both the GU and DPR methods considering the FIM determinant criteria.

All methods were designed for modal identification and evaluated for this purpose as well. However, for damage detection, different placement approaches and evaluation criteria may be needed. In particular, more axial measurements may be required. The axial sensor locations for this truss structure were found to produce relatively large differences between the analytical and experimental results. More sensitive instrumentation should be used for these measurements if required for damage detection.

## REFERENCES


1. Kim, H.M. and Doiron, H.H., "On-Orbit Modal Identification of Large Space Structures," *Sound and Vibration*, Vol. 26, No. 6, June 1992, pp. 24-30.

2. Kim, H.M. and Doiron, H.H., "Modal Identification Experiment Design for Large Space Structures," *AIAA/ASME/ASCE/AHS/ASC 32nd Structures, Structural Dynamics, and Materials Conference*, Baltimore, MD., April 1991, pp. 2968-2976.

3. McGowan, P.E., Javeed, M., and Edighoffer, H.H., "Status of Dynamic Scale Model Technology Research Program," *NASA Technical Memorandum 102764*, Jan. 1991.

4. Smith, S.W. and Hendricks, S.L., "Damage Detection and Location in Large Space Trusses," *AIAA SDM Issues of the International Space Station, A Collection of Technical Papers*, Williamsburg, Va., April 21-22, 1988, pp. 56-63.

5. Glassburn, R.S., "Evaluation of Sensor Placement Algorithms for On-Orbit Identification of Space Platforms," Masters Thesis - University of Kentucky, Lexington, Kentucky 1994.

6. Triplett, T., "Is There Trouble in The Air?," *Safety and Health*, Vol. 145, No. 5, May 1992, pp. 38-44.

7. "MRP II Software Provides Flexibility for Manufacturer," *Industrial Engineering*, Vol. 24, No. 11, Nov. 1992, pp. 25.

8. Larson, C.B., Zimmerman, D.C., and Marek, E.L., "A Comparative Study of Pre-Test Techniques using the NASA 8-bay Truss," *Proceedings of the 12th International Modal Analysis Conference*, Honolulu, Hawaii, Jan.-Feb. 1994, pp. 205-211.

9. Larson, C.B., Zimmerman, D.C., and Marek, E.L., "A Comparative Study of Metrics for Modal Pre-Test Sensor and Actuator Selection Using the JPL/MPI Testbed Truss," *Proceedings of the AIAA Dynamics Specialists Conference*, Hilton Head, S.C., April 21-22 1994, pp. 150-162.

10. Penny, J.E.T., Friswell, M.I., and Garvey, S.D., "The Automatic Choice of Measurement Locations for Dynamic Testing," *Proceedings of the 10th International Modal Analysis Conference*, San Diego, Ca., Feb. 1992, pp. 30-36.

11. Kammer, D.C., "Sensor Placement for On-Orbit Modal Identification and Correlation of Large Space Structures," *Journal of Guidance, Control, and Dynamics*, Vol. 14, No. 2, March-April 1991, pp. 251-259.

12. Parker, G.R., Rose, T.L., and Brown, J.J., "Kinetic Energy Calculation as an Aid to Instrumentation Location in Modal Testing," *Proceedings of the 1990 MacNeal-Schwendler Corporation World Users Conference*, Los Angeles, Ca., March 28-30, 1990.

13. Chung, Y. and Moore, J.D., "On-Orbit Sensor Placement and System Identification of Space Station with Limited Instrumentation," *Proceedings of the 11th International Modal Analysis Conference*, Kissimee, Florida, Feb. 1993, pp. 41-46.

14. Shah, P.C. and Udwadia, F.E., "A Methodology for Optimal Sensor Locations for Identification of Dynamic Systems," *Journal of Applied Mechanics*, Vol. 45, No. 3,March 1978, pp. 188-196.

15. Le Pourhiet, A. and Le Letty, L., "Optimization of Sensor Locations in Distributed Parameter System Identification," Identification and System Parameter Estimation, Rajbman (ed.), North-Holland Co., 1978, pp. 1581-1592.

16. Salama, M., Rose, T., and Garba, J., "Optimal Placement of Excitations and Sensors for Verification of Large Dynamical Systems," *Proceedings of the AIAA/ASME/ASCE/AHS 28th Structures, Structural Dynamics and Materials Conference*, Monterey, Ca., April 1987, pp. 1024-1031.

17. LMS International, "Large-Scale Modal Testing of a Space Frame Structure - from Pretest Analysis to FEA Model Validation," *Sound and Vibration*, Vol. 25, No. 3, March 1991, pp. 6-16.

18. Flanigan, C.C. and Botos, C.D., "Automated Selection of Accelerometer Locations for Modal Survey Tests," *Proceedings of 10th International Modal Analysis Conference*, San Diego, California, Feb. 1992, pp. 1205-1208.

19. Kammer, D.C. and Triller, M.J., "Efficient Sensor Placement for On-Orbit Modal Identification of Sequentially Assembled Large Space Structures," *Proceedings of the 10th International Modal Analysis Conference*, San Diego, Ca., Feb. 1992, pp. 954-964.

20. Lim, T.W., "Sensor Placement for On-Orbit Modal Testing," *Journal of Spacecraft and Rockets*, Vol. 29, No. 2, March-April 1992, pp. 239-246.

21. Lim, T.W., "Actuator/Sensor Placement for Modal Parameter Identification of Flexible Structures," *International Journal of Analytical and Experimental Modal Analysis*, Vol. 8, No. 1, Jan. 1993, pp. 1-13.

22. Yao, L., Sethares, W.A., and Kammer, D.C., "Sensor Placement for On-Orbit Modal Identification via a Genetic Algorithm," *AIAA Journal*, Vol. 31, No. 10, Oct. 1993, pp. 1922-1928.

23. Liu, C. and Tasker, F.A., "Sensor Placement Using Time Domain Perturbation Approach," *Proceedings of the AIAA Dynamics Specialists Conference*, Hilton Head, S.C., April 21-22 1994, pp. 163-172.

24. Tasker, F.A. and Liu, C., "Extended Variance-Based Techniques for Sensor Placement in Modal Identification," *Proceedings of the AIAA Dynamics Specialists Conference*, Hilton Head, S.C., April 21-22 1994, pp. 173-181.

25. Brillhart, R.D. and Kammer, D.C., "Evaluation of Optimal Modal Sensor Placement Using a System Realization Method," *Proceedings of the 12th International Modal Analysis Conference*, Honolulu, Hawaii, Jan.-Feb.1994, pp. 1401-1407.

26. Hemez, F.M. and Farhat, C., "An Energy Based Optimum Sensor Placement Criterion and Its Application to Structural Damage Detection," *Proceedings of the 12th International Modal Analysis Conference*, Honolulu, Hawaii, Jan.-Feb. 1994, pp. 1568-1575.

27. Johnson, C.L. and Mack, N., "Accelerometer Selection for the Modal Survey of the Space Station Combined Cargo Element," *Proceedings of the 12th International Modal Assurance Conference*, Honolulu, Hawaii, Jan.-Feb. 1994, pp. 1230-1236.

28. Pape, D.A., "Selection of Measurement Locations for Experimental Modal Analysis," *Proceedings of the 12th International Modal Analysis Conference*, Honolulu, Hawaii, Jan.-Feb. 1994, pp. 34-41.

29. Guyan, R.J., "Reduction of Stiffness and Mass Matrices," *AIAA Journal*, Vol. 3, No. 2, Feb. 1965, pp. 380.

30. Henshell, R.D. and Ong, J.H., "Automatic Masters for Eigenvalue Economization," *International Journal of Earthquake Structural Dynamics*, Vol. 3, 1975, pp. 375-383.

31. Kashangaki, T., "Ground Vibration Tests of a High Fidelity Truss for Verification of On-Orbit Damage Location Techniques," *NASA Technical Memorandum 107626*, May 1992.

32. Pappa, R.S., "Some Instrumentation Requirement Issues for the Space Station Structural Characterization Experiment," *Presented at the USAF/NASA Workshop on Model Determination for Large Space Systems*, Pasadena, Ca., March 22-24 1988.

# SIMULATION OF SHUTTLE LAUNCH G FORCES AND ACOUSTIC LOADS USING THE NASA AMES RESEARCH CENTER 20G CENTRIFUGE

T. L. Shaw, J. M. Corliss, D. P. Gundo, G. M. Mulenburg

NASA Ames Research Center

G. A. Breit and J. B. Griffith

Bionetics Corporation

## INTRODUCTION

The high cost and long times required to develop research packages for space flight can often be offset by using ground test techniques. This paper describes a space shuttle launch and reentry simulation using the NASA Ames Research Center's 20G centrifuge facility. The combined G-forces and acoustic environment during shuttle launch and landing were simulated to evaluate the effect on a payload of laboratory rats. The launch G force and acoustic profiles are matched to actual shuttle launch data to produce the required G-forces and acoustic spectrum in the centrifuge test cab where the rats were caged on a free-swinging platform. For reentry, only G force is simulated as the aero-acoustic noise is insignificant compared to that during launch.

The shuttle G-force profiles of launch and landing are achieved by programming the centrifuge drive computer to continuously adjust centrifuge rotational speed to obtain the correct launch and landing G forces. The shuttle launch acoustic environment is simulated using a high-power, low-frequency audio system. Accelerometer data from STS-56 and microphone data from STS-1 through STS-5 are used as baselines for the simulations. This paper provides a description of the test setup and the results of the simulation with recommendations for follow-on simulations.

## REQUIREMENTS

The two major simulation requirements were to subject a group of laboratory rats to an accurate re-creation of: 1) the principal acceleration component at a given location on the payload; and 2) the matching acoustic environment of the shuttle mid-deck, simultaneously. In addition, video tape recordings and temperature data were required. The rats were housed in simulated shuttle Animal Enclosure Modules (AEMsim). Reentry simulation occurred 9 days after launch. During the 9 day interim period the animals were housed in an animal holding room.

### G Force Requirements

The orientation and coordinate system for the shuttle and the AEMsims carried in the middeck is shown in Figure 1. The principal acceleration component is in the nose to tail ($G_x$) direction during launch and in the floor to ceiling ( $G_Z$) direction during reentry. The G forces to be simulated were from crew cabin accelerometer data taken during the STS-56 mission (Figures 2 and 3). Within a cab of the 20G Centrifuge, two simulated AEMsims were mounted on the swing platform as show in Figure 4. It was desired to develop a centrifuge rotation rate profile which accurately (±1%) simulated the principal acceleration at a fixed point on the AEMsims.

### Acoustic Requirements

The objective of the acoustic testing was to provide a sound environment representative of the space shuttle mid-deck during launch. Microphone data from shuttle missions STS-1 through STS-5 were used to develop sound pressure level spectra for the lift-off and aeronoise portions of launch. The graphs represent the maximum sound pressure level experienced during these three portions of launch.

## METHODS

The NASA Ames Research Center's 20G centrifuge consists of a truss work arm approximately 56 feet long, supported on a vertical shaft at the center. Cab enclosures are situated at both ends of the rotating arm, each centered 25 feet from the rotational axis. In addition a short radius cab is located near

the center. Two AEMsims were mounted side-by-side on a balanced free-swinging platform (arm length 14 in) positioned at the center of one end cab.

The resultant G force, $G_R$, provided by the centrifuge is the vector sum of the centripetal force due to centrifuge rotation about its central axis ($G_C$), and Earth's gravity (g). This is the acceleration acting on the swing platform. Because  is assumed perpendicular to the floor of the swing platform, the orientation of the AEMsims on the platform was changed from launch ($G_R = G_X$) to reentry ($G_R = -G_Z$) to account for the difference in principal acceleration direction between the two shuttle profiles.

**Centrifuge G Profile Development**

To provide the correct G profile to the animals in the AEMsims, a computer-generated rotational velocity profile for the centrifuge was created based upon STS-56 crew cabin accelerometer data (Figures 2 and 3). All profile development was performed using routines developed in the C language on a 33 MHz i486-based microcomputer. The data were spline interpolated to 10 Hz required for the drive command software. Accelerations less than one g were truncated at 1.01g for the simulation. The desired resultant g data was then translated to centrifuge velocity command voltages and the drive computer software data file generated.

A mathematical model was developed to predict the rpm/resultant g relationship, taking into account the pitch angle of the swing platform. As an approximation, the top surface of the swing platform is assumed to align itself perpendicular to the direction of the local resultant acceleration vector $G_R$. A numerical root finding algorithm was employed to determine a hypothetical set of angle data for each rate for a range of rotation rates. Given the radial position on the swing platform assembly at which the acceleration was to be modeled, a hypothetical resultant acceleration versus rotation rate data set was generated. To create a simple expression for rotation rate as a function of desired acceleration, this data set was fit to a two parameter model. The model is based on the relationship between rotation rate and the resultant acceleration present at a fixed radius on the centrifuge. This approximation expression allowed calculation of the centrifuge rotation rate necessary to generate a desired resultant acceleration at the measurement site on the swing platform.

**Instrumentation**

The resultant acceleration was measured using ±5g Systron Donner 4855 accelerometers which have voltage outputs proportional to acceleration. The voltage signals were passed through an L&M Electronics optical isolation amplifier with unity gain. The signals were then routed through the Centrifuge slip rings and through a patch panel to the data acquisition computer, a video panel meter and a digital voltmeter display. The temperature inside the AEM simulation unit was also recorded via the same routing scheme using a Newport RTD-805/N gas and air temperature probe. The RTD signal was sent through a Newport INFCR Infinity C Programmable Digital RTD Controller and converted to a voltage before being sent through the Centrifuge slip rings. The data acquisition computer was a Hewlett Packard 486/66 with a National Instruments AT-MIO-64F-5 Multifunction I/O board. A data logger program written in National Instruments LabWindows software was used to acquire the acceleration and temperature signals. The data logger provided user selection of the required number of channels, sampling rate, and averaging.

The video camera was mounted to provide a view of one of the cages throughout each run of the Centrifuge. The video signal was routed through slip rings to a video panel meter. The video panel meter combined digital displays of the accelerometer and temperature signals along with the video signal. From the video panel meter these signals were then sent through a video cassette recorder (VCR) and displayed on a video monitor to allow for viewing and recording. This information was saved on 1/2 inch VHS tape using the VCR. A block diagram representation of the accelerometer, temperature and video signal pathways is shown in Figure 5.

**Development of Acoustic Timeline for Launch**

Since no two shuttle launches are identical, the data from missions STS-1 through STS-5 were averaged to provide a representative acoustic spectrum. Figures 6 and 7 show plots of the microphone data for the lift-off and aeronoise portions for the five launches, as well as the average spectra used for the simulation. The lift-off portion of launch has the higher overall level, 107.6 dB, as compared to the aeronoise portion of launch at 102.6 dB. While both spectra have strong low-frequency components, the

aeronoise spectrum has stronger components in the high-frequency regime indicative of aerodynamic noise during high-velocity flight.

After developing the representative acoustic spectra for lift-off and aeronoise, it was necessary to determine how these spectra should be allocated along the launch timeline. For the simulation, the duration of a shuttle launch was defined to be 524 seconds. The launch timeline follows the basic sequence of events listed below (times are approximate).

Table 1: Launch Timeline

| TIME (secs) | EVENT |
|---|---|
| 0 | Lift-off start |
| 100 | Solid Rocket Booster Burnout |
| 120 | Solid Rocket Booster Separation |
| 450 | 3-g Throttle back |
| 514 | First Main Engine Shut-down |
| 524 | End of launch |

The basic philosophy for the simulation is to apply the lift-off acoustic spectrum from Lift-off Start to SRB Burnout (t=0 secs to 100 secs), and to apply the aeronoise spectrum from SRB Separation to the First SSME Shut-down (t=120 secs to 514 secs). Throughout an actual launch the overall sound pressure level varies with throttle changes, velocity changes, and other variable conditions. For the 20G Centrifuge simulation, the maximum 107.6 dB lift-off level and 102.6 dB aeronoise level is held constant throughout the respective portions of the launch. This is primarily because the supplied microphone data does not contain any time history data applicable to the shuttle mid-deck. Taking all of these factors into account, an acoustic timeline for launch was developed for the simulation and is shown in Figure 8.

**Acoustic Equipment**

A high power, low frequency sound system was designed and installed to reproduce the lift-off and aeronoise acoustic spectrums. The primary components of the acoustic system are shown in Table 2. The Hewlett-Packard analyzer, Rane equalizers, and QSC amplifier were located in the control room of

the 20G centrifuge facility. The Electro-Voice speaker and B&K microphone were located in the centrifuge test cab in close proximity to the AEMsims.

Table 2: Primary Acoustic Equipment

| |
|---|
| Hewlett-Packard 35665A Dual-Channel Dynamic Signal Analyzer |
| Rane GE30 Interpolating Constant-Q Graphic Equalizer (1/3 Octave) |
| Rane MPE-28 Programmable Equalizer |
| QSC 1700 Power Amplifier (325 Watts/channel) |
| Electro-Voice TL3512 Very-Low-Frequency Speaker System |
| B&K 1/2" Microphone with Power Supply and Pre-Amp |
| University Sound DWS-100 Wireless Microphone System |

The Hewlett-Packard analyzer generated a pink noise signal which was conditioned by the two Rane equalizers and QSC amplifier to produced the required acoustic spectrum inside the centrifuge test cab. The programmable equalizer was pre-programmed with seven spectra which were designed and timed throughout the launch simulation to compensate for changes in the acoustic response of the test cab. These changes in the test cab's acoustic response were due to the varying angle of the swing platform as the G-forces changed. The acoustic spectra inside the test cab was monitored in real time with the Hewlett-Packard signal analyzer. The set-up of the acoustic system is diagrammed in Figure 9.

## RESULTS

### G Force Results

Representative plots of acceleration data for launch and reentry simulations are shown in Figures 10 and 11 respectively with corresponding STS-56 profiles overlaid. The greatest percentage error occurred at the peaks of acceleration, particularly at the higher levels of acceleration - end of launch, and at where the rate of change of acceleration is greatest - beginning of launch (Figure 10). The average percentage error for the last plateau of the launch profile was calculated to be 0.77%. Error present in the reentry simulations were less than for launch (Figure 11).

**Acoustic Results**

The acoustic data recorded during the test included: 1) the overall dB level inside the centrifuge test cab; and 2) the acoustic spectrum for the lift-off and aeronoise portions of launch.

Overall dB Levels

The overall dB level inside the centrifuge test cab during each test was continuously recorded from the display of the HP 35665A signal analyzer by video camera. This data was later recorded from the video tape into spreadsheet format and is plotted in Figure 12. The overall dB level for each test was held very closely to the test requirements. For the lift-off portion of launch the maximum difference between the as-tested sound pressure level and the test requirement was 1.3 dB t=10 seconds. For the aeronoise portion of launch the maximum difference between the as-tested sound pressure level and the test requirement was 1.0 dB from t=185 seconds to t=190 seconds.

Frequency Spectra

Traces of the acoustic frequency spectra were recorded from the HP 35665A signal analyzer. For each test group, the data from individual time intervals was averaged for both the lift-off and aeronoise portions of launch. The resultant averaged spectra for lift-off and aeronoise are shown in Figures 13 and 14 respectively. The as-tested acoustic spectra closely matched the test requirements and repeated very well between test groups. For both the lift-off and aeronoise spectra the largest deviation from the test requirements occurred at a frequency of 63 Hz. For lift-off the maximum deviation was 4.0 dB and for aeronoise the maximum deviation was 3.2 dB. Note that these deviations are only at one specific frequency band, and that the overall sound pressure level in the centrifuge test cab was consistent with the test requirements.

RECOMMENDATIONS

Development of the centrifuge rotation profiles required mathematical modeling of the relationship between rotation rate and resultant acceleration at a fixed point on the swing platform.

Although this approach yielded satisfactory results, it was nevertheless subject to assumptions about the underlying mechanics. A closed-loop control system utilizing feedback from an accelerometer mounted on the swing platform would bypass the necessity to rely on such approximations, allowing for direct simulation of a desired acceleration profile.

Adding vibration to the simulation would significantly increase the realism. This was investigated for this study, but due to schedule and budget constraints, it was not feasible to include. Single axis vibration, especially during launch simulation, could provide important additional information.

LIST OF FIGURES

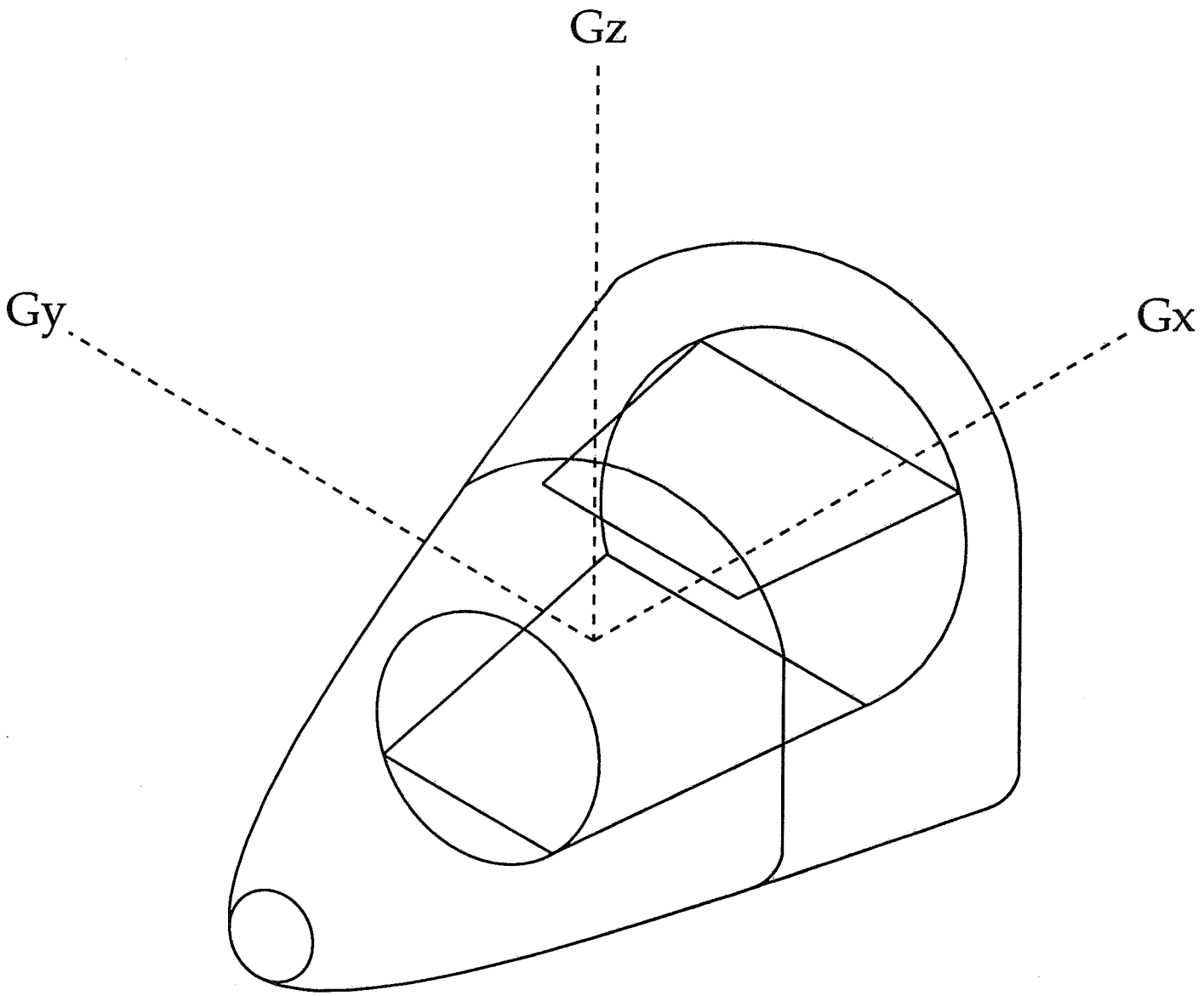


Figure 1: STS Axes Orientation

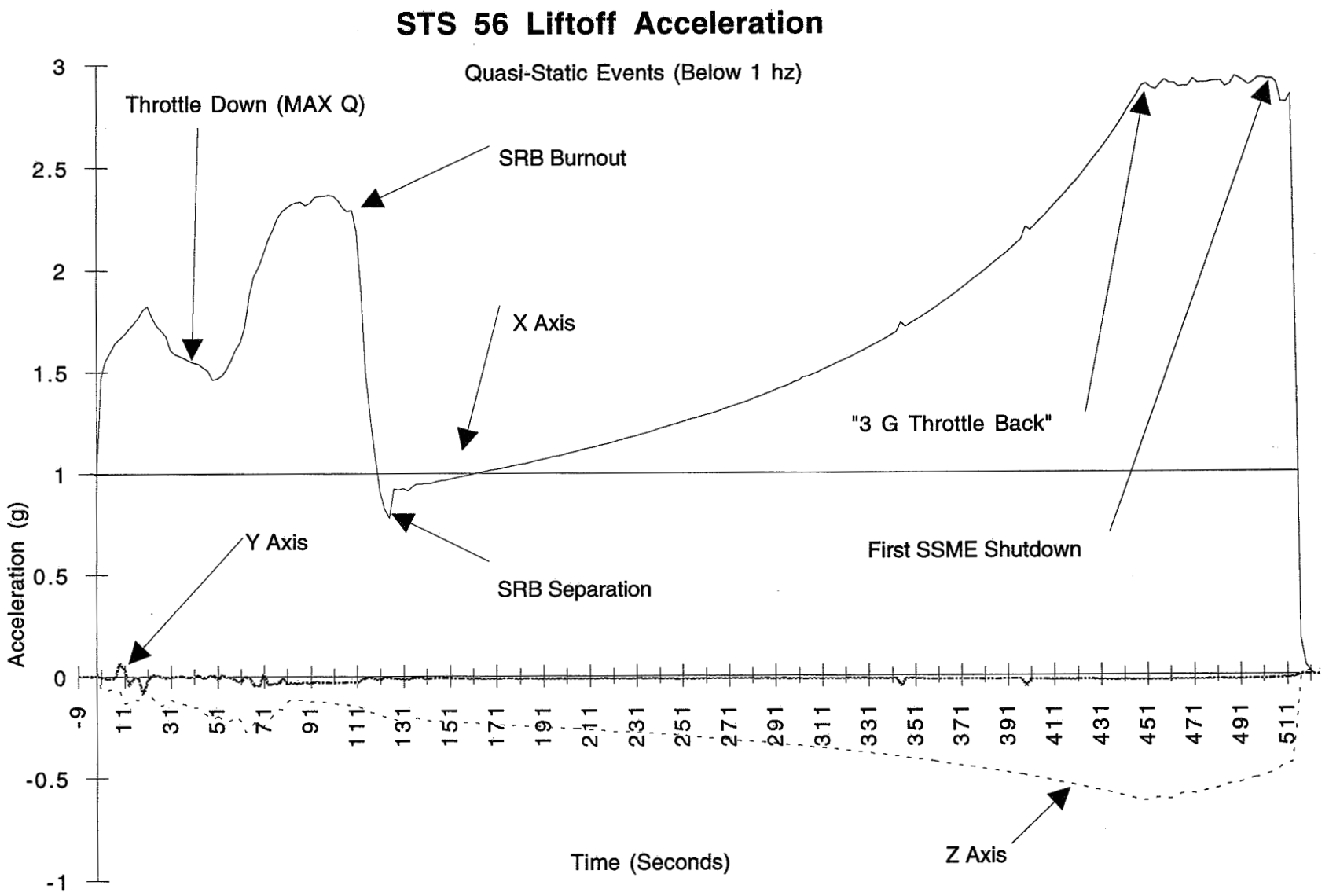


**Figure 2: STS-56 Crew Cabin Acceleration During Launch**

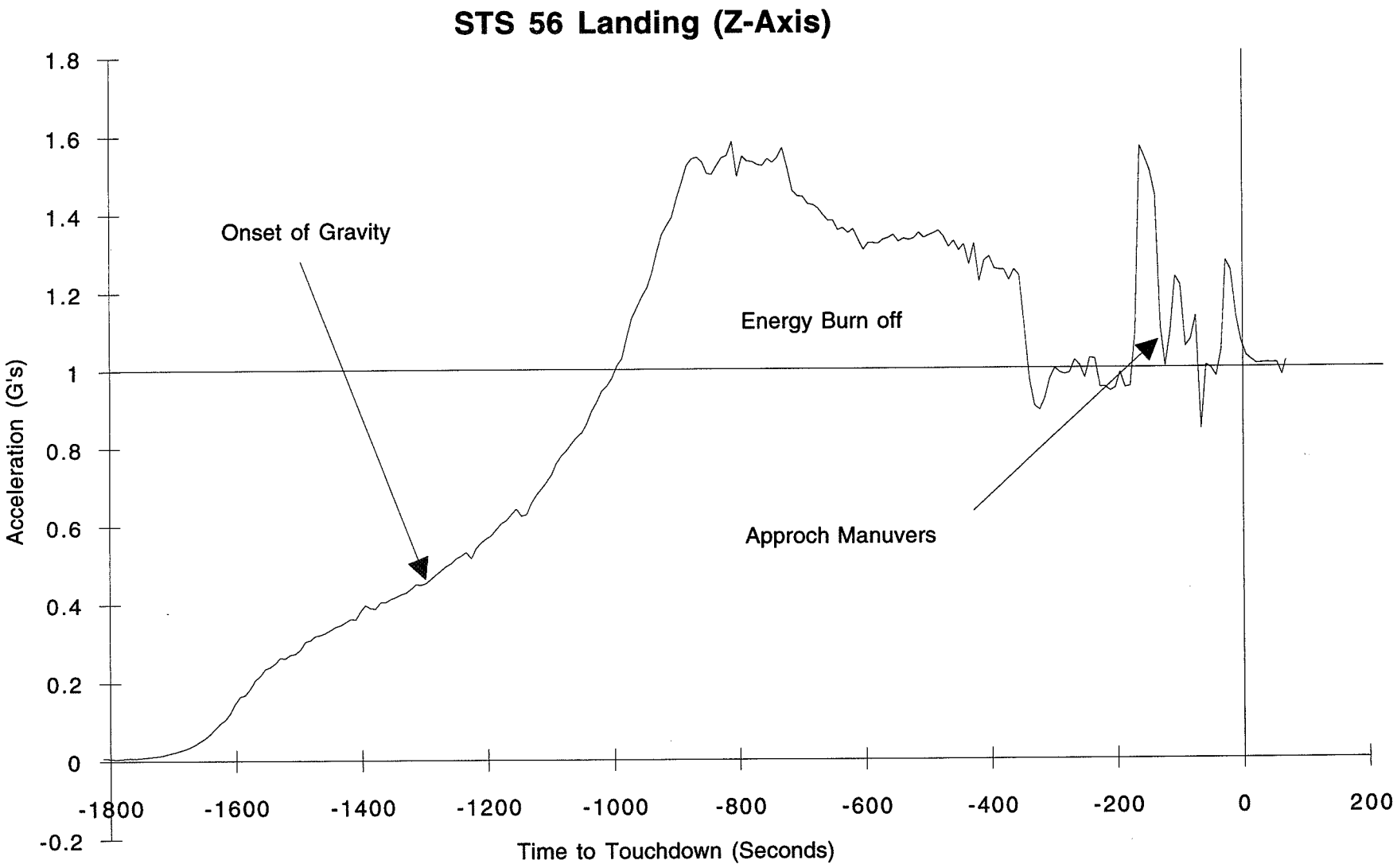


**Figure 3: STS-56 Crew Cabin Acceleration During Reentry**

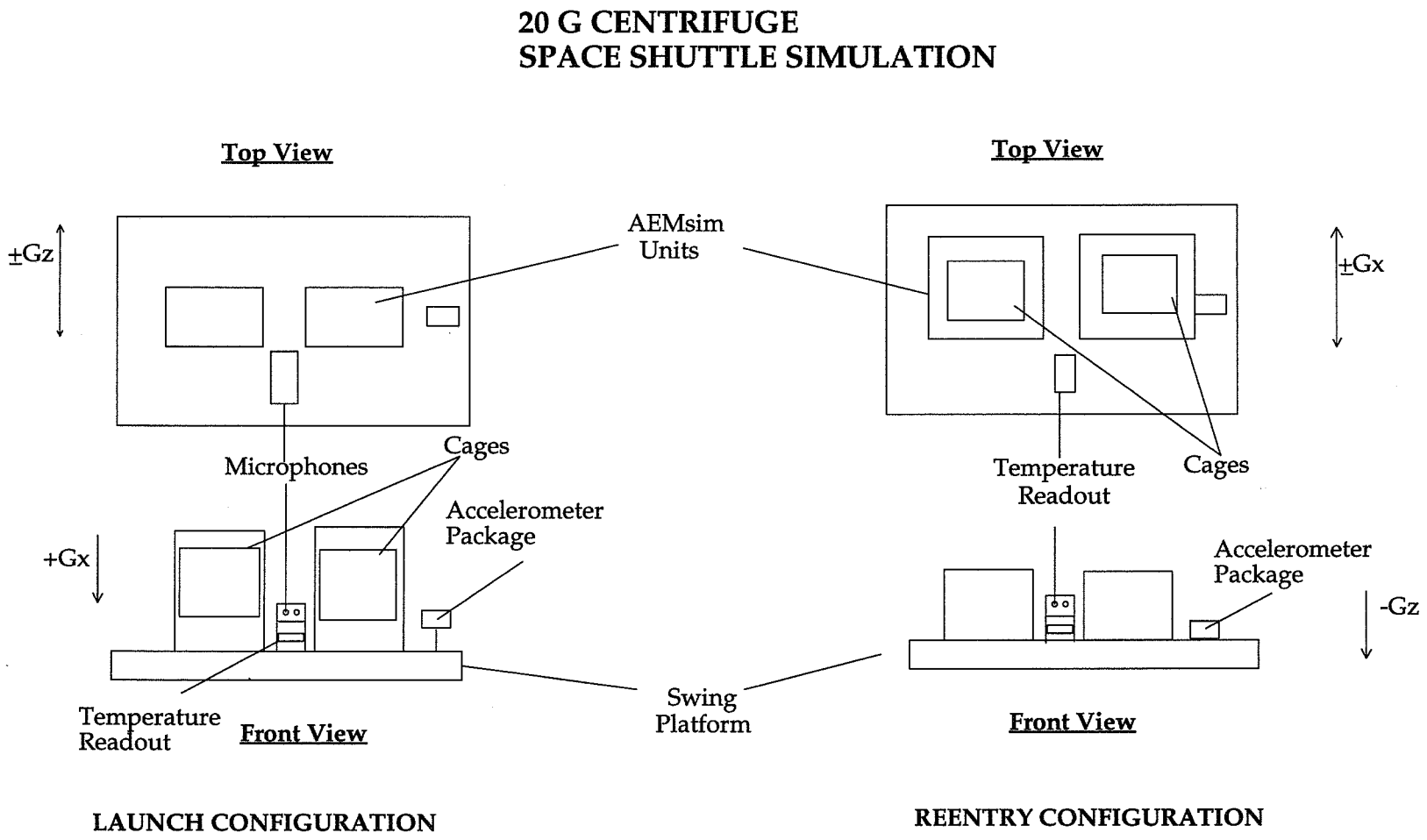


**Figure 4: Simulated Animal Enclosure Modules Launch and Reentry Configurations**

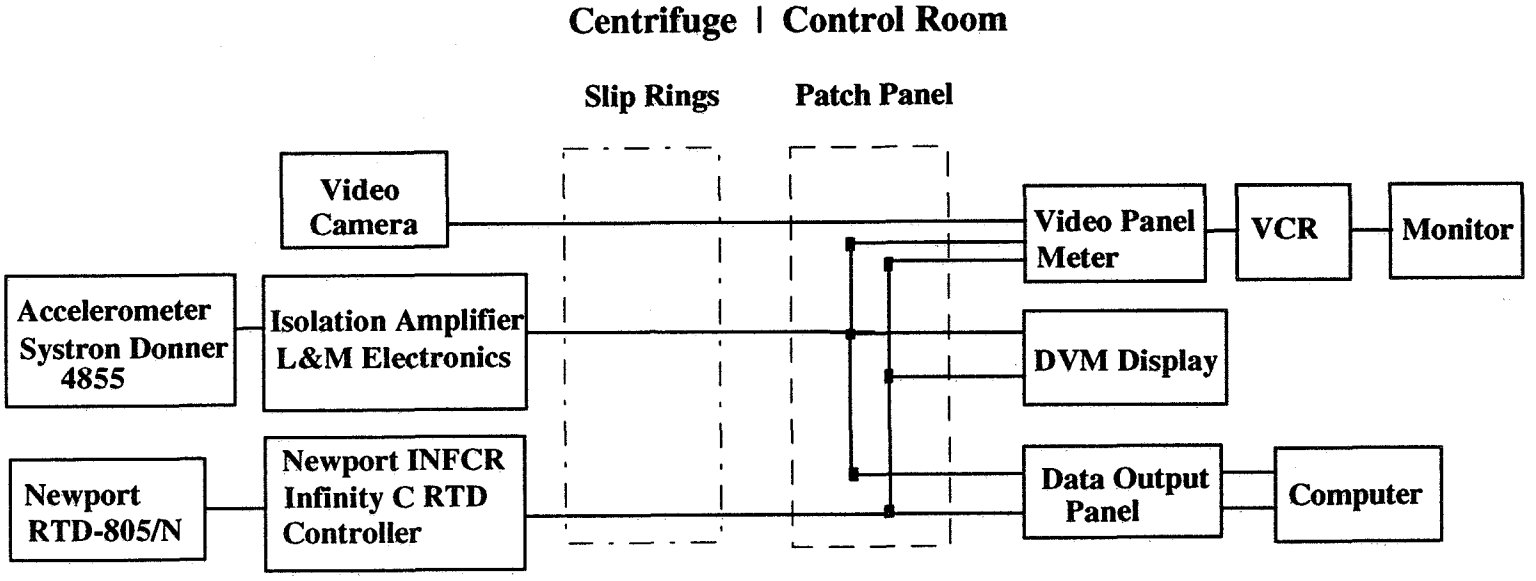


**Figure 5: Block Diagram of Data Acquisition System**

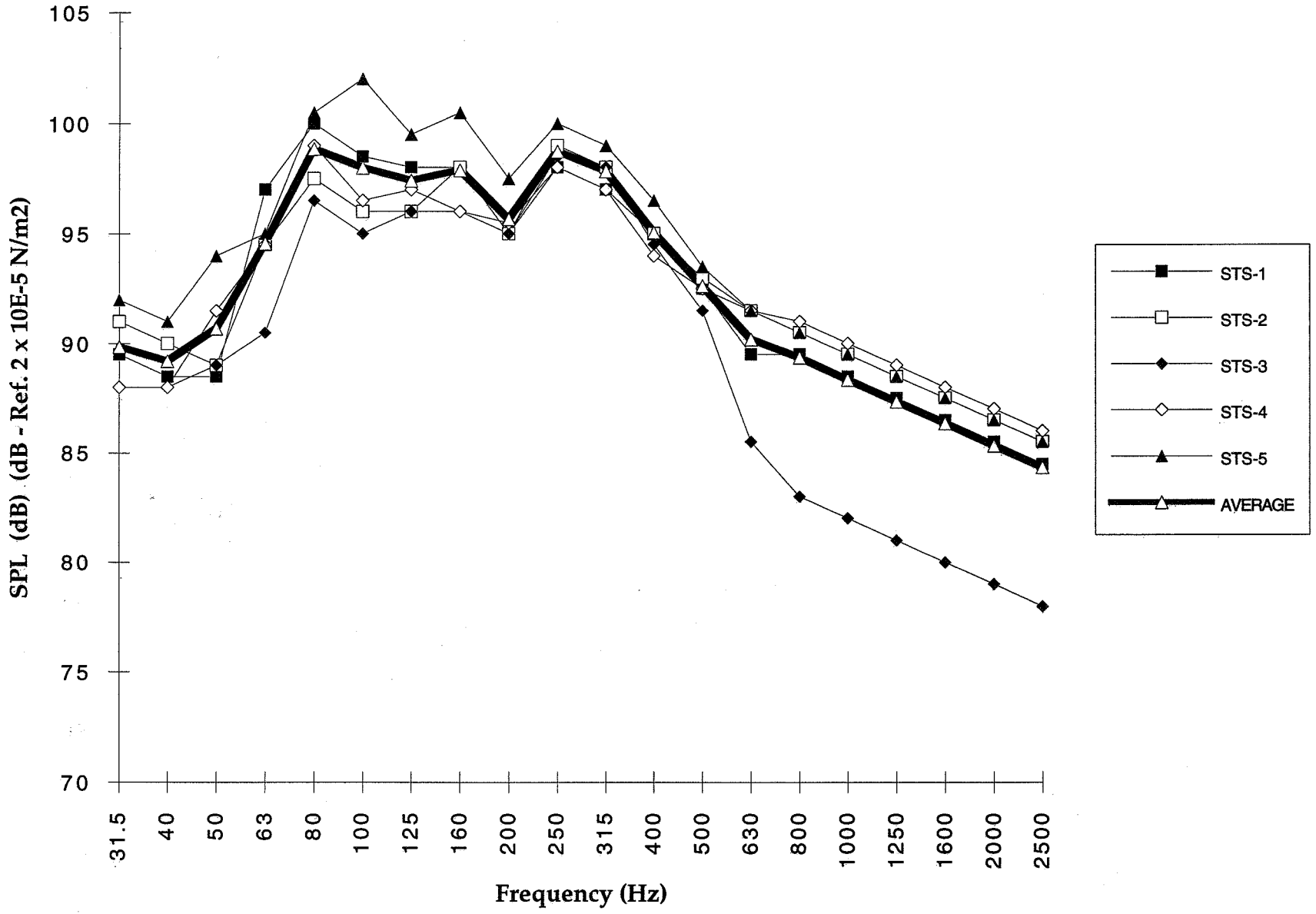


**Figure 6: Lift-Off Acoustic Spectra**

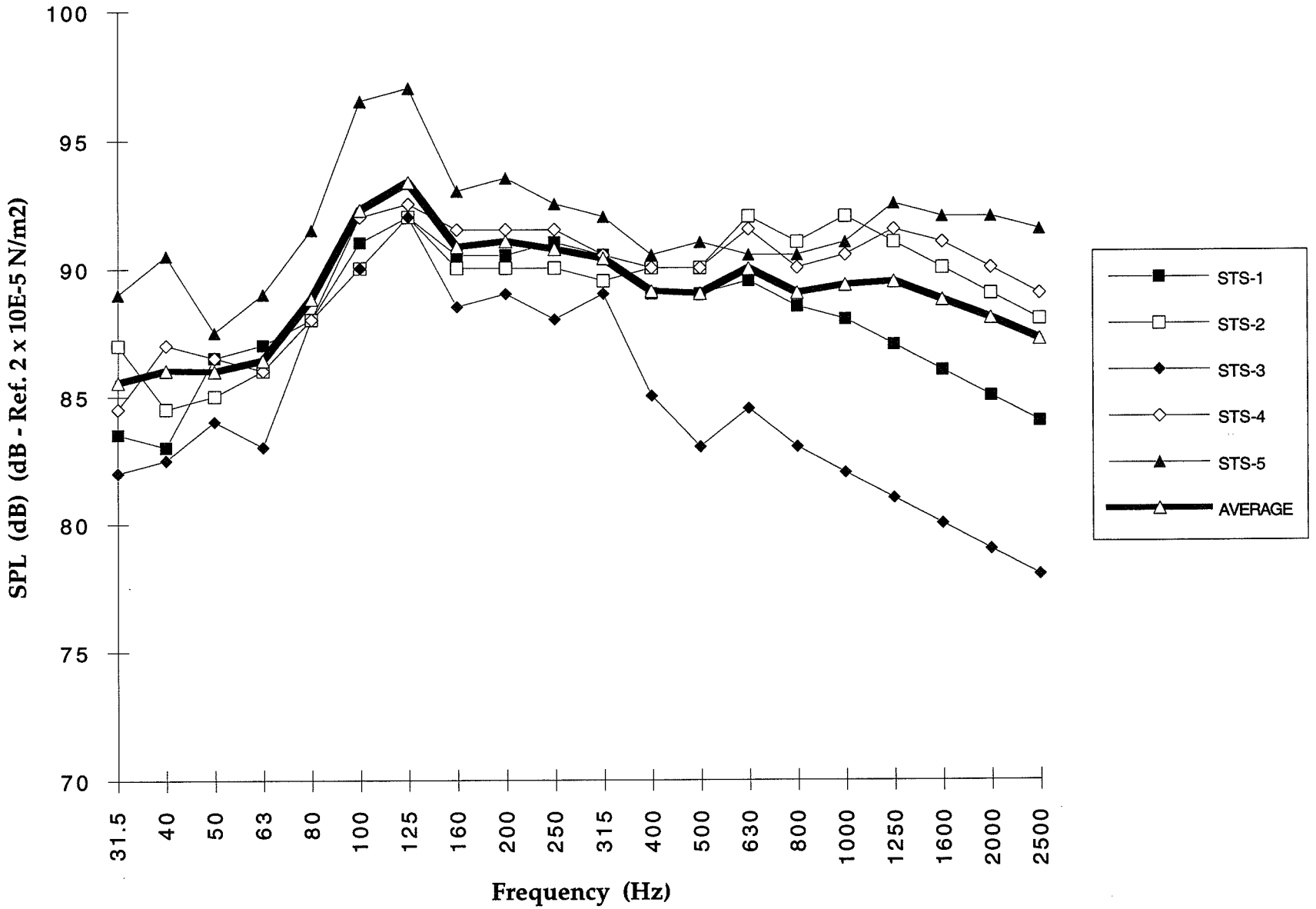


**Figure 7: Aeronoise Acoustic Spectra**

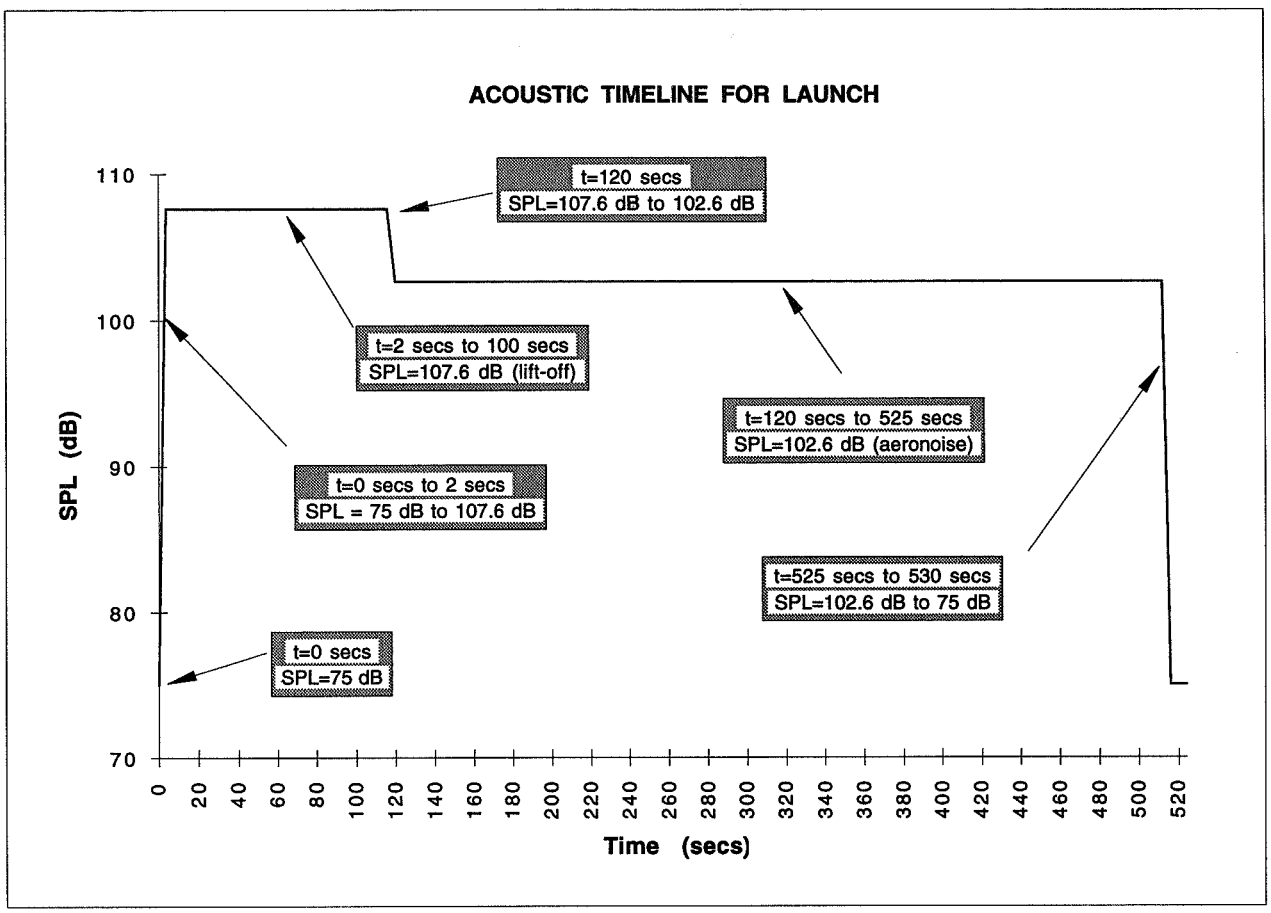


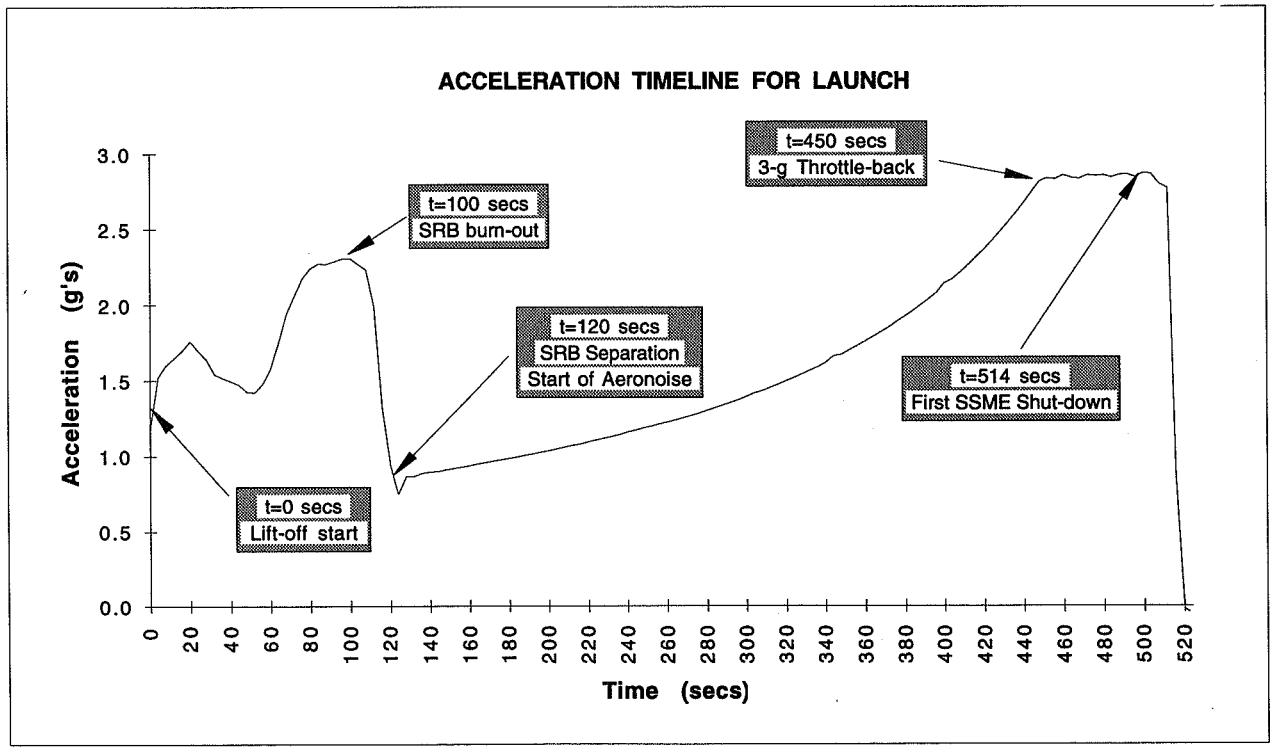


**Figure 8: Acoustic Timeline for Launch**

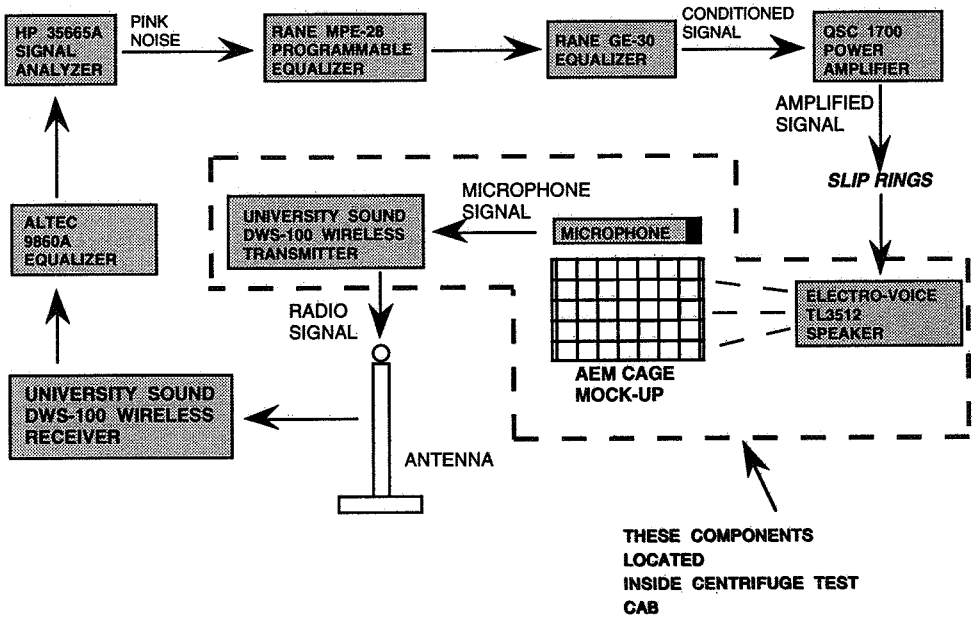


**Figure 9: Acoustic System Set-up**

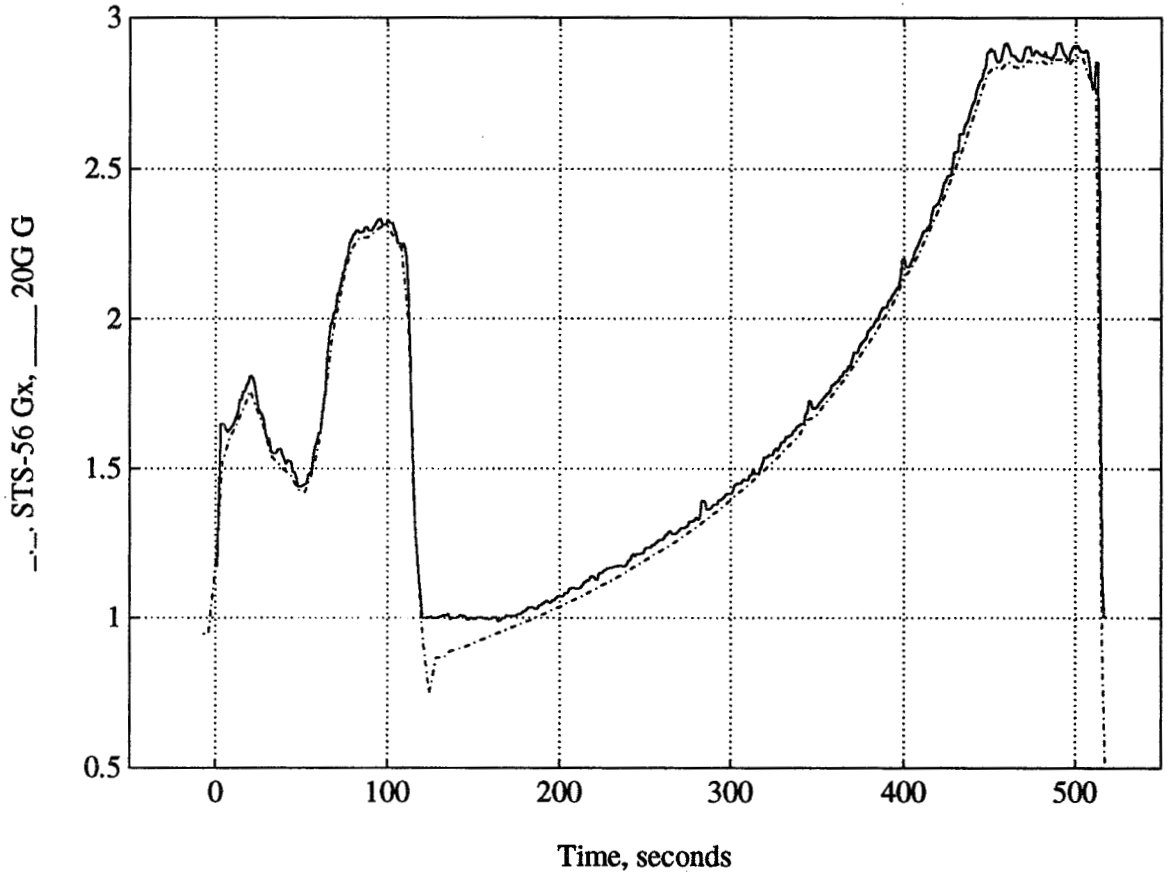


Figure 10: Launch Simulation Acceleration and STS-56 Launch Profiles

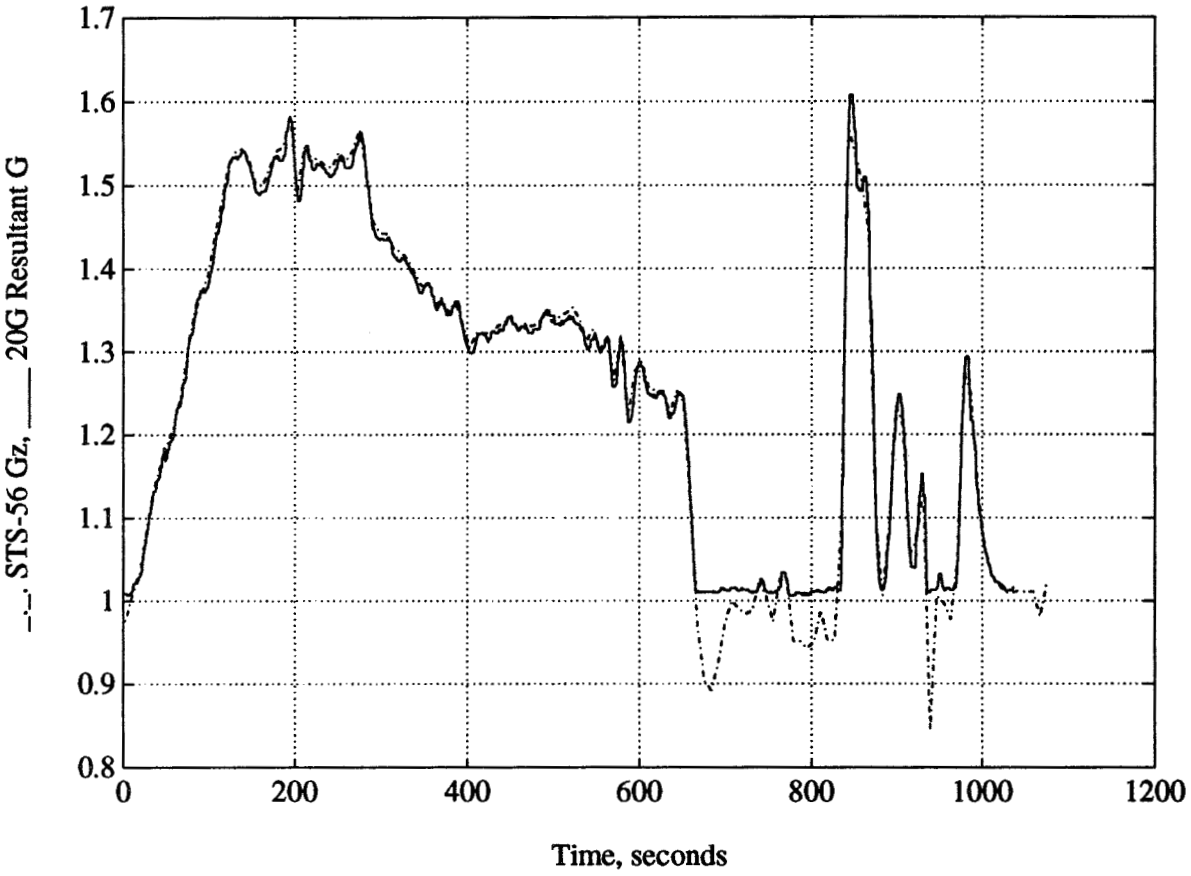


Figure 11: Reentry Simulation Acceleration and STS-56 Reentry Profiles

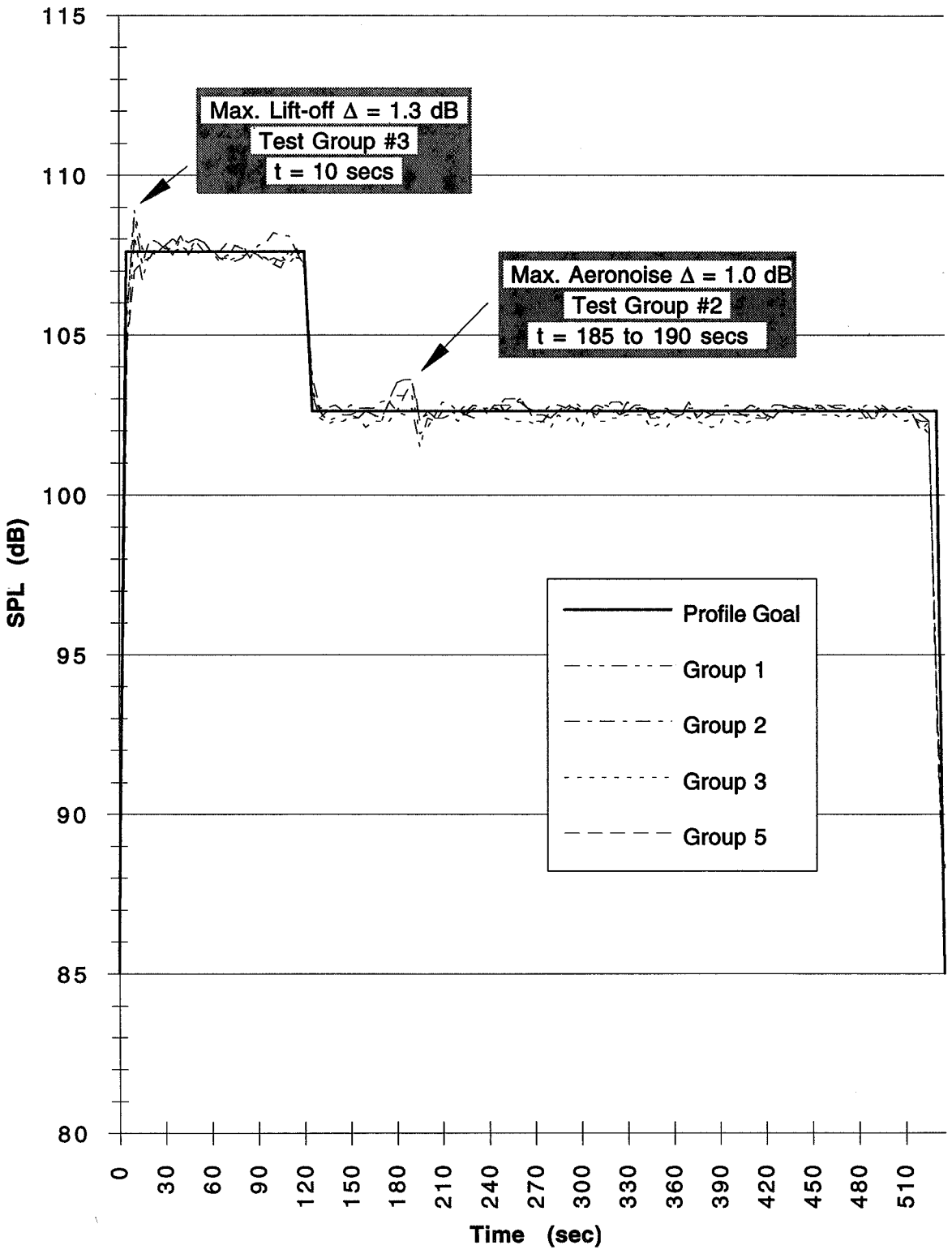


**Figure 12: As-tested Overall dB Levels**



C-5.

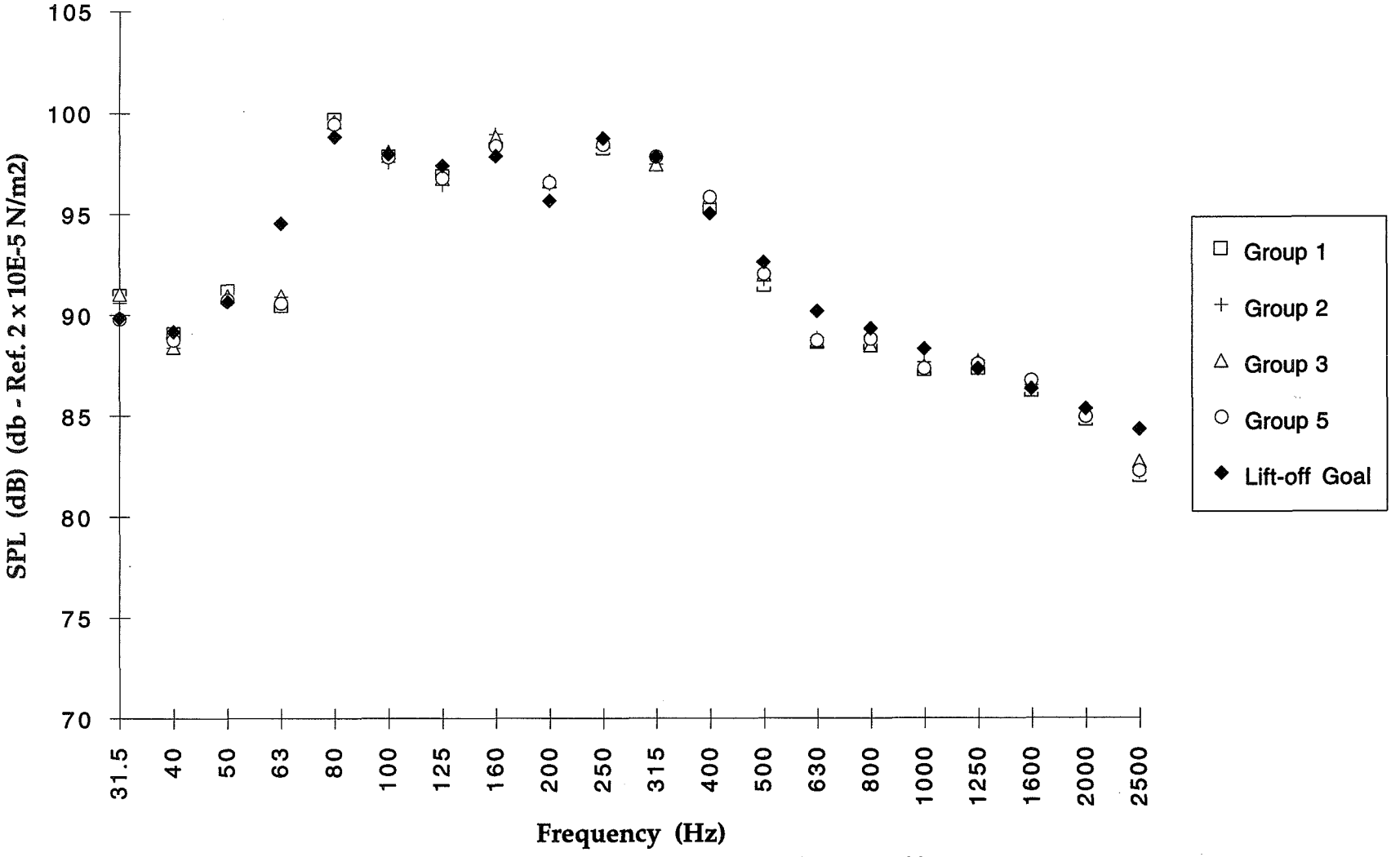


**Figure 13: Summary of As-Tested Lift-Off Spectra**

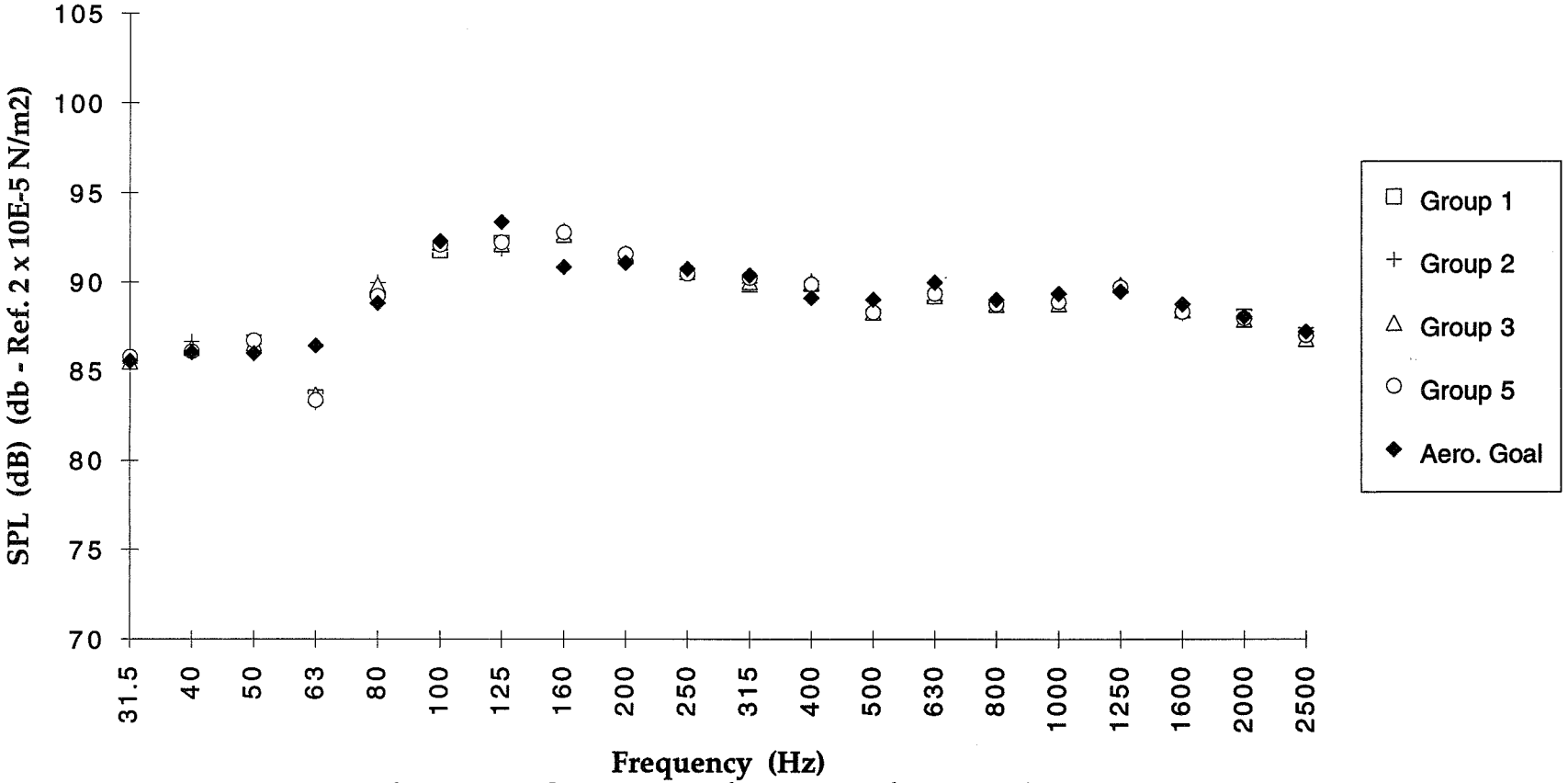


**Figure 14: Summary of As-Tested Aeronoise Spectra**

# DEVELOPMENT OF LIFE SCIENCES EQUIPMENT FOR MICROGRAVITY AND HYPERGRAVITY SIMULATION

G.M. Mulenburg, J. Evans, M. Vasques, D.P. Gundo

NASA Ames Research Center

J.B. Griffith, J. Harper, T. Skundberg

Bionetics Corporation

## INTRODUCTION

The mission of the Life Science Division at the NASA Ames Research Center is to investigate the effects of gravity on living systems in the spectrum from cells to humans. The range of these investigations is from microgravity, as experienced in space, to Earth's gravity, and hypergravity.

Exposure to microgravity causes many physiological changes in humans and other mammals including a headward shift of body fluids, atrophy of muscles - especially the large muscles of the legs -and changes in bone and mineral metabolism. The high cost and limited opportunity for research experiments in space create a need to perform ground based simulation experiments on Earth. Models that simulate microgravity are used to help identify and quantify these changes, to investigate the mechanisms causing these changes and, in some cases, to develop countermeasures.

Hypergravity likewise creates physiological changes of fluids, muscle, and bone. Hypergravity experiments can therefore add substantially to the knowledge of how gravity, in this case greater than 1G, affects living systems. It has been hypothesized that on a long space voyage, exposure to hypergravity for short periods, rather than to 1G for longer periods, may beneficially counteract the deleterious effects of microgravity. Hypergravity experiments, using centrifugation in ground based facilities adds to the knowledge base of gravitational effects on living systems.

This paper describes two unique pieces of research equipment developed by the Life Science Division of NASA's Ames Research Center to study the effects of simulated microgravity and hypergravity: 1) a new metabolic cage for use in simulated microgravity studies in rats, and 2) a paste feeder that was used recently in a two week continuous 2G hypergravity study.

## DEVELOPMENT OF A METABOLIC CAGE TO SIMULATE MICROGRAVITY IN A LABORATORY ENVIRONMENT

Hindlimb suspension of rats is a well established model used to simulate the effects of microgravity. The suspension apparatus includes a light weight foam tape that is attached to the length of the rat's tail and to a pulley system. The hind limbs are raised off of the ground and the rat can move about the cage freely on its forepaws. The animal can eat, drink and groom normally. This model is widely used and has been shown to cause no undue stress to the animal. This suspension model, developed by Wronski & Morey-Holton (1), simulates the effects of microgravity during spaceflight by unloading the hindlimbs and simultaneously producing a headward shift of fluids similar to that seen in a weightlessness environment, For most systems studied, this model accurately mimics microgravity. However, obtaining quantative data on the metabolic status of suspended rats for nutritional, metabolic and renal function studies has not been possible until now.

Using Holton's tail suspension cage as a starting point, a new metabolic suspension cage, Figure 1, was developed. This new cage, effectively collects and separates urine and fecal samples for quantative analysis. The added information from these samples, when coupled with food and water intake data, gives investigators an opportunity to examine the effects of microgravity on many complex body systems.

**Requirements**

The requirements to provide the Holton cage with this new capability and how the new metabolic suspension cage was developed follows:

1) Make the new cage interchangeable with standard Holton cage parts. This requirement was based on results using Holton's cage (a large amount of documented research exists using this cage) and the large floor space available to the animal (144 in. sq.). Clear plastic allows the animal to be observed easily.

2) Provide a means to easily and efficiently separate and collect urine and feces with minimal cross contamination. This requirement is essential to perform accurate analyses of the samples collected.

3) Ensure the ability to efficiently remove samples daily for measurement, storage, and analysis.

4) Ensure the ability to easily and quickly replace the collection equipment with clean units daily, to easily clean the removed equipment, and also, to easily remove animals for daily weighing, inspection or manipulation.

5) Ensure the ability to prevent contamination of the urine and fecal collections with food spilled by the animal.

6) Ensure the ability to easily and efficiently remove remaining food for accurate weighing and consumption determination, and replenish with a new, measured, quantity of food.

**Development**

Figure 2 shows the original Holton suspension cage as the shaded portions with the new metabolic additions as clear. From the figure, it can be seen that the Holton cage design was basically left intact. Letters in parentheses refer to matching numbers in the figure.

Requirement 1) was met by developing a raised base (H) with two solid side walls and an open front and back to support a standard Holton cage as shown in the figure.

Requirement 2) and 3) were met by combining a commercial separator-diffuser (J,K) with a newly designed vacuum formed rectangular funnel (I) to catch and guide the urine and feces to the separator-diffuser. Screw on collection tubes (L), can easily be removed and capped for transportation and storage of samples for later analysis. Installation of new, clean tubes is also quickly accomplished. An open cage top allows easy access to the animal.

Requirement 4) was met by providing for frontal insertion of both the cage floor and the funnel in rails located on the sides of the base walls. A tab was added to the spout of the funnel to insert and support the separator-diffuser. The funnel is made of vacuumed formed ABS plastic and can be easily removed from its supporting rails and cleaned.

Requirement 5) was met through the development of a food cup system (8/217909, patent pending) external to the cage, which allows access to the food by the animal in an area that is not above the collection funnel. This includes a tunnel with an open floor (E) to allow spillage through the floor and not into the funnel. Food is provided to the animal in powdered form to prevent it carrying the food cup back into the cage (and spilling it into the collection funnel). An adjustable metal gate with a rounded cutout on the bottom slides up and down on the food cup itself. The height can be adjusted to limit accessibility to the food for different sized animals.

This is especially important for smaller animals that tend to enter the food cup and scatter the food. Adding this system required shifting the water bottle from its original centered location on the wall to a position slightly off center.

Requirement 6) was met by providing a removable food cup and a spill tray (F) under the access tunnel to collect any spilled food for accurate food consumption measurement.

**Discussion**

The new cage provided satisfactory collections in both ground based and post-spaceflight studies (2).

## DEVELOPMENT OF A PASTE FOOD FEEDER FOR UNINTERRUPTED CENTRIFUGATION STUDIES

Centrifugation has long been used to provide hypergravity for research purposes. Although a complete discussion is beyond the scope of this paper, acceleration due to rotation provides a force that can be substituted for the normal attraction of two masses, such as the Earth and a body on it.

One of the basic questions of gravitational physiology is whether there is a continuum of physiological responses from 0G to 1G and into hyper G. The effects of microgravity (spaceflight) and hypergravity (centrifugation) on living systems have been investigated extensively in independent studies. However, differing experimental conditions (type of rat, diet, etc.) have precluded direct comparison of prior 0G and hyper G studies.

To compare the effects of hypergravity exposure with those of exposure to microgravity in animals flown on the Russian Cosmos 2044 flight, it was critical to continuously centrifuge the animals for 14 days without stopping in order to duplicate the Cosmos 2044 flight length and other environmental parameters.

To duplicate an experiment at hyper G that initially occurred in microgravity all other conditions must be as similar as possible. This included using a paste diet and feeding schedule similar to that used in the Cosmos flight. Stopping the centrifuge for even short periods can create unacceptable changes in research results. Therefore, the feeder must work without stopping the centrifuge for the entire 14 day experimental period.

A specialized paste feeder, Figure 3, was developed to support a hypergravity centrifuge study on the Ames Life Science Division 24 foot diameter centrifuge. The results from this 14 day hypergravity study were compared to the previously flown Russian Cosmos 2044 spaceflight.

**Requirements**

To accomplish this project, the established requirements were as follows:

1) Provide for 14 day continuous 2G centrifugation with no stops.

2) Provide for feeding the animals the same paste diet (which has the consistency of thick oatmeal) as on the Cosmos 2044 mission. The same amount of food must be dispensed (140g) at the same interval (every 6 hours).

3) Provide on demand water delivery to the rats and a waste collection system to operate throughout the 14 day period.

**Development**

Unique features that had to be overcome for this experiment included changes in the consistency of the food over time from a thin paste at the start of the experiment to a much thicker consistency toward the end of the 14 day period. Centrifuge and stationary control cages, each containing 10 rats, were fitted with feeders calibrated to provide 140 $\pm$ 2g of paste diet every 6 hours.

Requirement 1) was met by the inherent capability of the Ames 24 foot diameter animal centrifuge which has a 3 G maximum capability for extended periods of up to a month or more of continuous operation.

Requirement 2) was the greatest challenge. After attempts to find adequate off the shelf food delivery equipment failed, a new feeder design was developed. Numbers in parentheses refer to matching numbers in Figure 4.

The essence of the design included:

a) Food reservoir (1). A stainless steel funnel was welded to an open bottom 7.6 liter stainless cooking stock pot. A 2.5 cm fitting was welded onto the funnel spout to accept a 2.5 cm diameter threaded valve (2). A sealed cover on the reservoir allowed pressurization of the space above the food to 5 psi with nitrogen (7) to help the food flow through the funnel and into the tubing system. A plate slightly smaller than the inside diameter of the reservoir was placed on top of the food to provide a uniform pressure surface.

b) Tubing system. Stainless steel 2.5cm diameter tubing (8) provides a path for food to flow from the reservoir to the food tray inside the cage.

c) Electromechanical valves. Two electromechanical valves are electrically sequenced to control the food flow. The first valve (2) at the base of the funnel opens to allow food to flow from the reservoir. When food is ready to be expelled from the delivery tube, the first valve closes and the second valve opens.

d) Piston. A positive displacement piston (9) in the straight section of the tubing is retracted by a dual motor system (4). The stroke length of the piston is controlled by limit switches (10) at each end of its travel.

e) Electrical relay sequencing system and programmable timer. The sequencing and timing system (5) controls valve opening and closing, and motor operation for piston retraction and extension. The piston retracts with valve (2) open and valve (3) closed. This allows food to flow from the reservoir through the curved tube and into the straight tube (8) behind the retracting piston. When valve (2) closes and valve (3) opens the motors reverse and the piston extends to push food down the straight tube and into the food tray. The programmable timer (18) initiates two sequences of operation every 6 hours, delivering 70g each time for a total of 140g per feeding.

Requirement 3). The water supply requirement was met using a 12 liter water storage bottle mounted near the center of the centrifuge about one meter above the cage. Gravity feed, enhanced by centrifugal force, caused the water to flow through plastic tubing from the bottle to two lixits mounted in the side of the cage.

A stainless steel tray with a hole in the center allows animal waste to flow into a waste collection container (14) mounted under the cage.

## OPERATION

Operation of the feeder system during the 14 day Cosmos comparison study met all specifications for the experiment.

## DISCUSSION

The high cost and rare opportunity for space flight experiments limit accessibility to space. Gravitational research can be conducted utilizing ground based research techniques and specialized equipment. Microgravity simulation using the metabolic suspension cage now offers the capability to gather metabolic data allowing investigators to study the physiological effects of microgravity. Additional details of the metabolic cage design are available in NASA Technical Memorandum 108830.

Hypergravity studies with paste food diets are now possible for continuous periods of centrifugation of up to 14 days. Adaptation of the paste feeder design for longer studies, or more animals, is a straight forward next step. Additional details of the paste feeder design are available in NASA Technical Memorandum 108804.

References

1. Wronski, T.J. and E.R. Morey-Holton. "Skeletal Response to Simulated; Weightlessness: A Comparison of Suspension Techniques",Aviat. Space Environ. Med. 58, 1992, pp63-68.

2. Harper J.S., Mulenburg G.M., Evans J., Navidi M., Wolinsky I., Arnaud S.B., "Metabolic Cages for a Space Flight Model in the Rat", Laboratory Animal Science (Accepted for Publication), 1994.

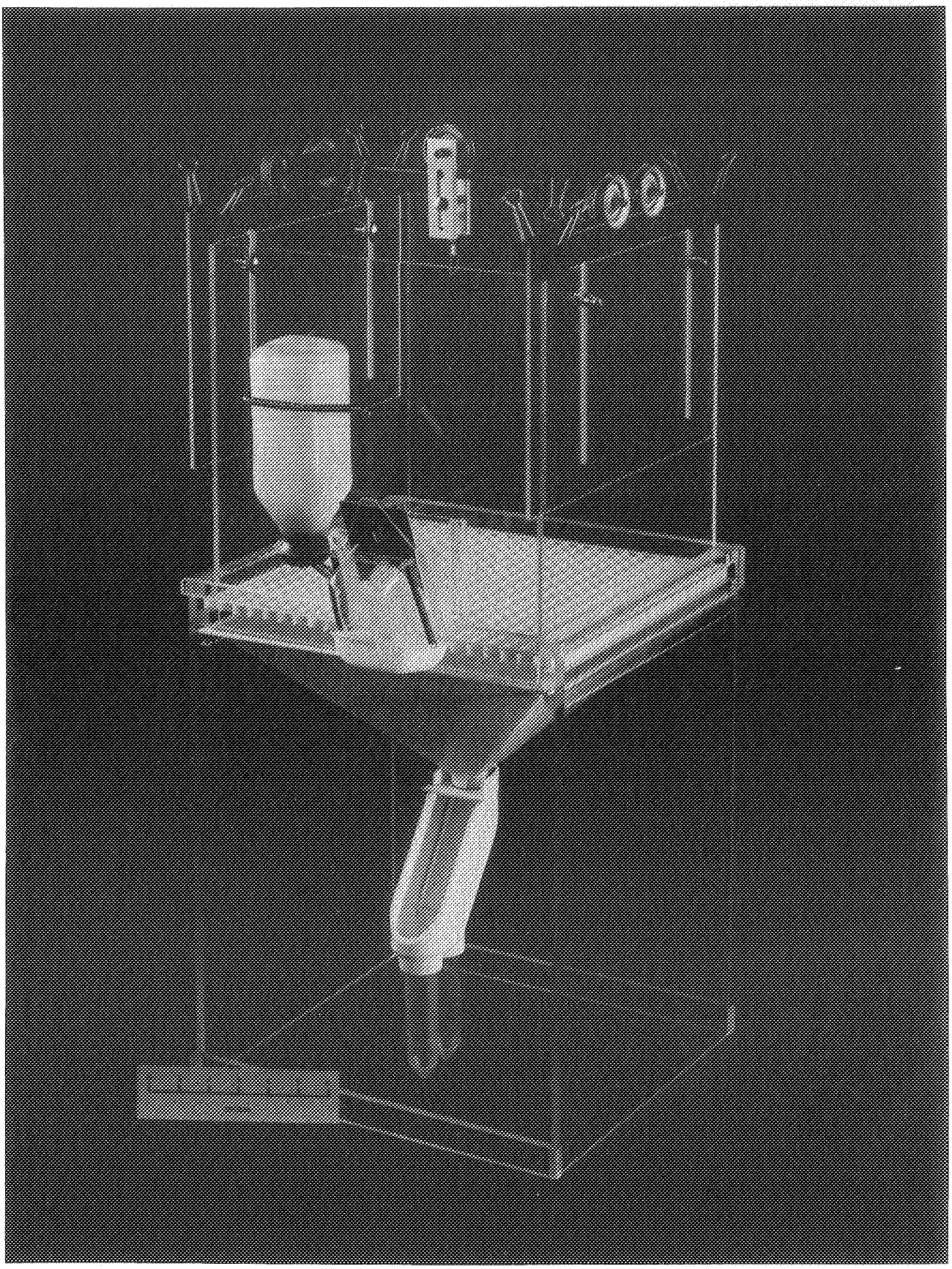

FIGURE 1 ASSEMBLED METABOLIC CAGE

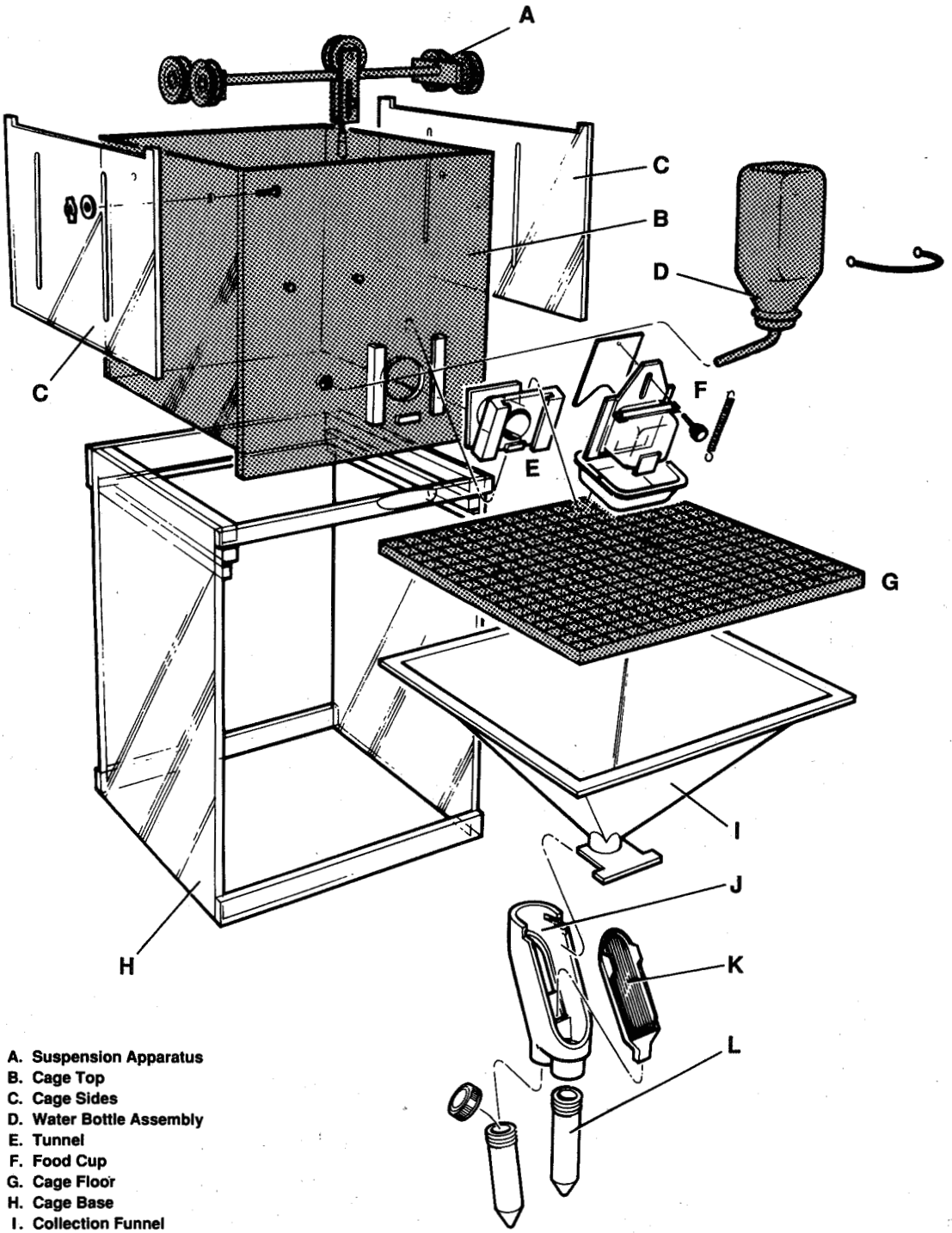


A. Suspension Apparatus
B. Cage Top
C. Cage Sides
D. Water Bottle Assembly
E. Tunnel
F. Food Cup
G. Cage Floor
H. Cage Base
I. Collection Funnel
J. Separator Housing
K. Linear Diffuser
L. Collection Tubes

FIGURE 2 METABOLIC CAGE PARTS IDENTIFICATION

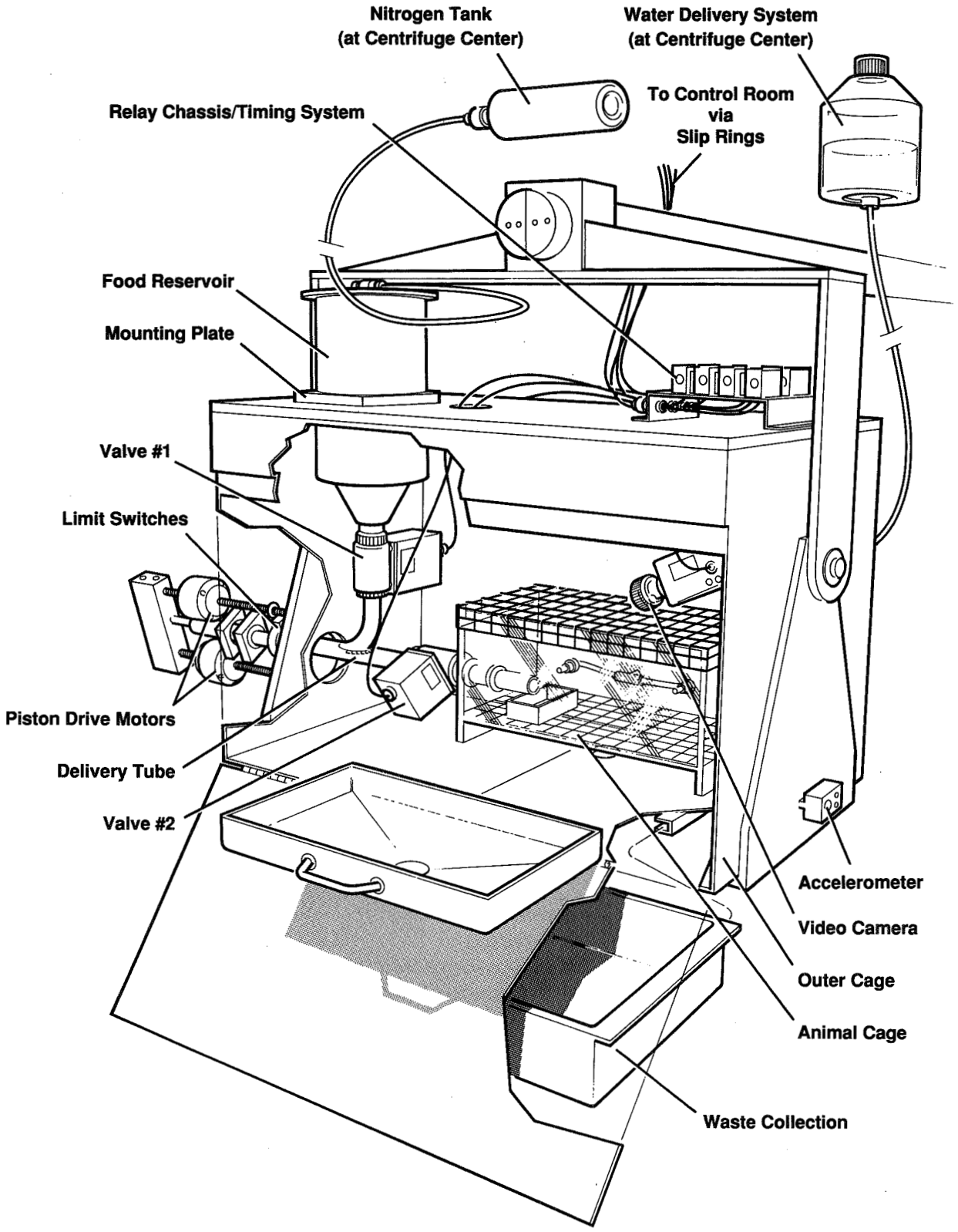


FIGURE 3 PASTE FEEDER AND CENTRIFUGE ARRANGEMENT

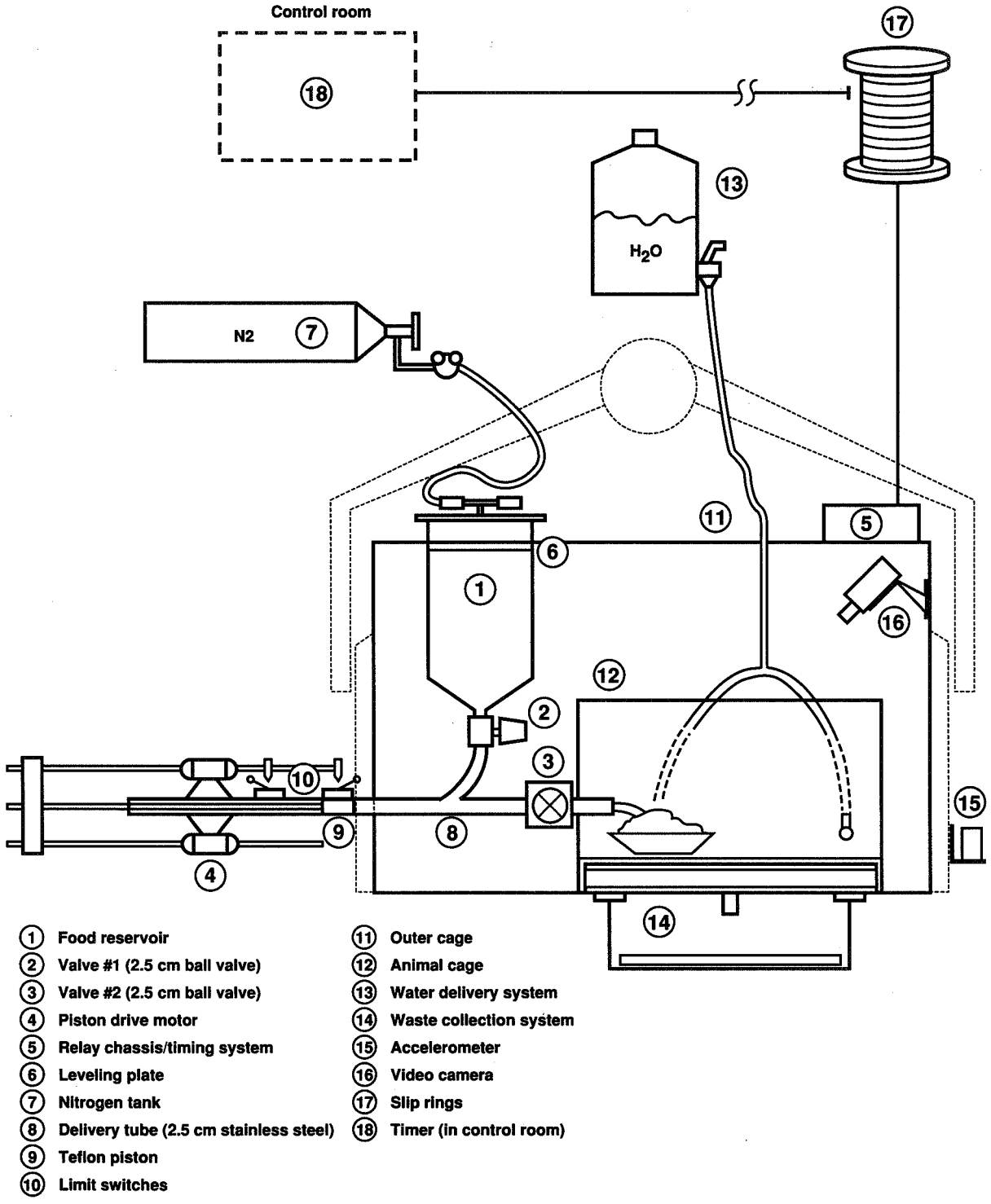


FIGURE 4 PASTE FEEDER PARTS IDENTIFICATION

# UNIQUE LIFE SCIENCES RESEARCH FACILITIES AT NASA AMES RESEARCH CENTER

G.M. Mulenburg, M Vasques, W.F. Caldwell, J. Tucker
NASA Ames Research Center

## INTRODUCTION

The Life Science Division at NASA's Ames Research Center has a suite of specialized facilities that enable scientists to study the effects of gravity on living systems. This paper describes some of these facilities and their use in research. Seven centrifuges, each with its own unique abilities, allow testing of a variety of parameters on test subjects ranging from single cells through hardware to humans. The Vestibular Research Facility allows the study of both centrifugation and linear acceleration on animals and humans. The Biocomputation Center uses computers for 3D reconstruction of physiological systems, and interactive research tools for virtual reality modeling. Psycophysiological, cardiovascular, exercise physiology, and biomechanical studies are conducted in the 12 bed Human Research Facility and samples are analyzed in the certified Central Clinical Laboratory and other laboratories at Ames. Human bedrest, water immersion and lower body negative pressure equipment are also available to study physiological changes associated with weightlessness. These and other weightlessness models are used in specialized laboratories for the study of basic physiological mechanisms, metabolism and cell biology. Visual-motor performance, perception, and adaptation are studied using ground-based models as well as short term weightlessness experiments (parabolic flights). The unique combination of Life Science research facilities, laboratories, and equipment at Ames Research Center are described in detail in relation to their research contributions.

## BACKGROUND

Everything on Earth is exposed to gravity and living things are exposed to varying gravitational forces in their environment. Thus the mission of NASA's Ames Research Center

Life Science Division is to study the effects of gravity on living systems. When physiological changes in response to altered gravity are observed, scientists in the Ames Life Science Division are not just focused on how to develop countermeasures to these changes, but why the changes happen in the first place, i.e. the fundamental mechanisms of gravity on biological systems. From a better understanding of the fundamental physiology will come knowledge useful in both Earth research and space countermeasures. Therefore, a range of gravitational fields (hypergravity, normal gravity and microgravity) and its effects on living systems are studied. Hypergravity is studied using centrifuges and microgravity can be studied in space or through any of a number of microgravity-like models here on earth.

## HYPERGRAVITY

### Centrifuges

Several facilities are available at the NASA Ames Research Center to provide scientists with unique research opportunities at greater than Earth's gravity. In addition to their use for basic research, these facilities can also help to provide answers to many of the questions posed by proponents of rotating human space vehicles.

Extensive hypergravity studies can be performed on the seven centrifuges. A list of the centrifuges and their capabilities is provided in Table 1. Studies done at Ames investigate both behavioral and morphological changes and how they are associated with altered gravity. Using the 24 and 8 foot centrifuges, animals are exposed to hypergravity and their responses studied. Animals exposed to 2 weeks of 2 G will have altered behavior (i.e. unable to right, swimming abnormally, walking abnormally). These behavioral changes may find their cause in alterations in neural, vestibular or muscular systems.

These centrifuges are also used for muscle and bone studies. In microgravity, not only is muscle fiber size reduced in the antigravity muscles but some of the fibers change from the slow, postural type to a faster locomotion type. This could be of critical importance for humans when returning to a gravity environment. Bone is also not a static system but is constantly changing in size and dimension to fit the environment and is particularly sensitive to changes in load. Biomechanical forces, metabolic changes and hormonal changes can be studied using many of the Ames facilities. A better understanding of bone and mineral metabolism may lead to answers regarding diseases such as osteoporosis.

Adaptations of other species provide insight into how basic physiology functions. For example, one study using the 8 Foot Centrifuge (Figure 1) is comparing aquatic and arboreal

(tree climbing) snakes. The aquatic snakes have evolved in a weightless like environment whereas arboreal snakes climb trees head first and climb down head first. They therefore have different cardiovascular adaptations to prevent blood pooling and maintain proper circulation. A comparison of their reponses to hypergravity is underway .

One of the more unique centrifuges that is still being developed is the Spaceflight Environmental Simulator. Using an existing 52-foot diameter cylindrical rotating platform design centrifuge, the revised facility design includes the provision of two human habitats (Figure 2) for long duration studies of the effects of chronic hypergravity on humans. Up to four humans per habitat will be able to live at up to 2 G for as long as one month without stopping the centrifuge. Each habitat, constructed of lightweight honeycomb sandwich panels, is nominally 9 ft high x 11 ft wide x 25 1/2 ft long. A habitat-positioning system provides for radial positioning of each habitat at a distance of 15 to 21 feet from the centrifuge's axis of rotation and adjusts floor angle so the resultant acceleration vector is perpendicular to the midpoint of the habitat's interior floor.

The Man Carrying Rotation Device (MCRD) is another unique hypergravity research tool. The MCRD has a 0-3 meter variable radius and one cab for human or animal research. The center of the cab can be positioned at variable distances from the center of rotation and provides variable gravity levels up to 4.5 G. Hydrostatic bearings allow for precise angular accelerations. Designed primarily for human research, the MCRD can also support research on rodents and primates. It can also be modified for specific needs. For example, it has been recently fitted with a swing platform incubator for hypergravity cell studies (Figure 3).

The human powered centrifuge was developed as a research tool to provide exercise and gravitational forces simultaneously using only human effort (Figure 4). Currently configured with a pedal mechanism, a variety of exercise methods (stair stepper, rowing, etc.) can be incorporated into the drive system to evaluate the benefits of different types of exercise and G levels.

Visual and vestibular systems give the body it's sense of position and direction. The inside of the inner ear is lined with hair cells. Small crystals, otoconia, sit on top of these hairs. As a person turns their head the crystals move due to gravity, stimulating other hair cells. The brain processes this information and that of vision and touch (proprioception) to give the body a sense of position. When entering an altered gravity environment the subject experiences perceptual illusions caused by miscues from the vestibular and visual-motor systems. Perceptual illusions can cause reduced performance which can be disruptive but can also be dangerous for pilots and crew. These miscues from the vestibular and visual-motor systems must be compensated for and adapted in order to function in an altered gravity

environment. The centrifuge suite also includes a 20G human-rated centrifuge often used for these studies (Figure 5).

### Vestibular Research Facility

Scientists also study the differences and similarities in how the brain processes and uses information from vertical and horizontal head movement and vestibular responses to linear acceleration, to better understand how linear acceleration and gravity receptor stimulations control eye movements. The VRF centrifuge and linear sleds enable the study of reponses to smooth, linear motion or to combinations of linear and angular motion over the frequency range of natural head movement (Figure 6) . The facility permits the study of how complex linear and/or rotational accelerations are processed by the brain.

## MICROGRAVITY MODELS

### Parabolic Flights

Since actual flight opportunities are limited, much of the microgravity research is done using models that mimic the effects of microgravity. One of the methods used to test microgravity issues without going into space is parabolic flights. The Lear Jet & the larger KC-135 aircraft are used for these tests. A brief exposure to weightlessness is achieved by flying the plane up following a parabolic pattern at a 45°angle at over 400 mph and then down much the same way. The subjects and equipment in the plane are exposed to 30 seconds of zero gravity from the top to the bottom of each parabola. This allows scientists to conduct experiments as well as test spaceflight hardware prior to a Shuttle mission. The Lear Jet completes approximately 20 parabolas in one flight (40 parabolas for the KC 135).

### Cell Culture Facility

Scientists are looking at individual cells in response to microgravity and physical forces to determine how cellular communication changes under these conditions. The Cell Culture Facility is equipped with basic cell culture equipment as well as a cell spinner. The cell spinner continuously reorients the cells with respect to the direction of the gravity vector. This continuous rotation-reorientation has been shown to nullify the effect of gravity and allows studies in a microgravity-like environment.

### Human Research Facility

When a person lying down suddenly stands up, there is a multitude of force and pressure changes that the body quickly compensates for in order to insure that plenty of blood continues to the brain. When exposed to microgravity, body fluids do not have gravity pulling them down and are redistributed with much of the fluid pooling in the head and chest. The body interprets this as excess fluid, so these extra fluids are excreted. When an astronaut returns to 1 g, gravity forces the fluids footward reducing blood flow to the brain and can cause the person to pass out. This is referred to as orthostatic intolerance.

One of the facilities used to study the effects of fluid redistribution is NASA Ames Research Center's Human Research Facility (HRF). It is designed specifically for conducting ground-simulation studies of the physiological responses of humans to spaceflight. It provides a highly controlled environment with temperature, light intensity, and light cycle automatically controlled, and is suitable for research on both ambulatory and bed-rested subjects. Gurneys and beds are available either supine or 6° head down tilt. Up to 12 subjects can live comfortably in a non-hospital environment, on either an 8 hour or 24 hour basis, for weeks or months, with all their living requirements provided.

Lower body negative pressure (LBNP) is used to challenge the cardiovascular system. A person is placed in the chamber that seals at the waist and negative pressure is applied to the lower half of the body. Ground based studies using LBNP examine the cardiovascular system and in space, LBNP is used to produce cardiovascular and musculoskeletal loads similar to those normally received on earth. The LBNP devices and other test equipment available at ARC that can be used in conjunction with the HRF include the seven centrifuges, a water-immersion tank, a 30 foot linear sled (for conducting human perceptual studies) and the certified Central Clinical Laboratory.

## SCIENCE APPLICATIONS

### Biocomputation Center

The Biocomputation Center at Ames Research Center is dedicated to computer-based three-dimensional (3-D) visualization of cells, tissues and organs, mathematically based modeling, and 3-D simulations of the functioning of living systems from the subcellular and molecular to the organismal level. The emphasis is on teams of broadly based,

interdisciplinary investigators and on a union between computational, theoretical and experimental research.

Cells of the inner ear are gravity sensing receptors that are sensitive to both gravitational and linear acceleration. The Biocomputation Center is used to study the structures and function of these cells. Also examined is the cell circuitry (synapses). A significant increase occurs in the number of synapses in animals exposed to microgravity and a significant decrease after exposure to hypergravity.

## SUMMARY

Basic scientific questions can be investigated with the use of Ames Research Center's unique facilities. The individual facilities themselves offer great opportunities for study, and in combination provide truly unique capabilites for research in the fundamental mechanisms of gravity on living systems.

# TABLE 1 CENTRIFUGE FACILITIES

| FACILITY | DIAMETER (M) | PAYLOAD (KG) | MAX G | MAX RPM (RAD/SEC) | ONSET RATE | TIME AT G | USE |
|---|---|---|---|---|---|---|---|
| 20G CENTRIFUGE | 17.7 | 544.3 | 20 | 5.2 | 1 G/Sec | MIN-HOURS | 3 CABS-HUMANS, ANIMALS, EQUIP. |
| SPACE FLIGHT ENVIRON-SIMULATOR | 15.9 | 2268 | 3 | 2.4 | NOMINAL | WK-MONTHS | 2 CABS-HUMANS, 4 CAGES |
| MAN CARRYING ROTATION DEVICE | VARIABLE 0-3.1 | 226.8 | 4.5 | 4.7 | 0.007-0.52 RAD/SEC SQ. | MIN-WEEKS | 1 CAB-HUMANS, INCUBATOR |
| HUMAN POWERED CENTRIFUGE | 3.8 | 226.8 | 5 | | NOMINAL | MIN-HOURS | HUMANS |
| 24 FOOT CENTRIFUGE | 7.3 | 20 LG CAGES | 4 | 3.1 | NOMINAL | DAYS-WEEKS | SMALL PRIMATES, RODENTS |
| 8 FOOT CENTRIFUGE | 2.4 | 20 SM CAGES | 10 | 8.9 | NOMINAL | DAYS-WEEKS | RODENTS, SNAKES |
| VRF-MULTI AXIS CENTRIFUGE | 1.2 | 2 CANISTERS | 1.75 | 4.2 | 8.7 RAD/SEC SQ. | MIN-HOURS | SMALL PRIMATES, RODENTS |

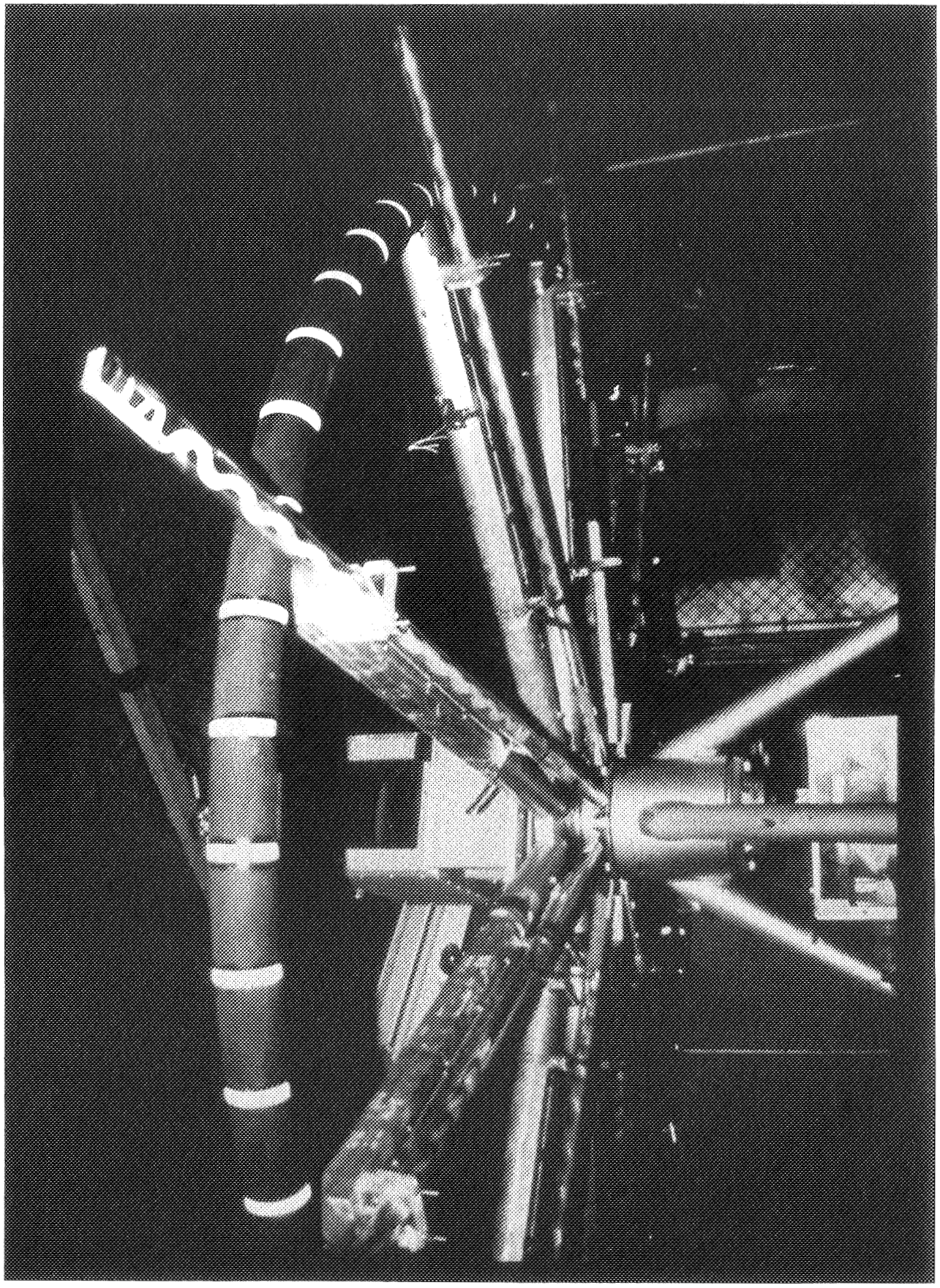

FIGURE 1 8-FOOT DIAMETER ANIMAL CENTRIFUGE

FIGURE 2 SPACE FLIGHT ENVIRONMENTAL SIMULATOR HUMAN HABITAT

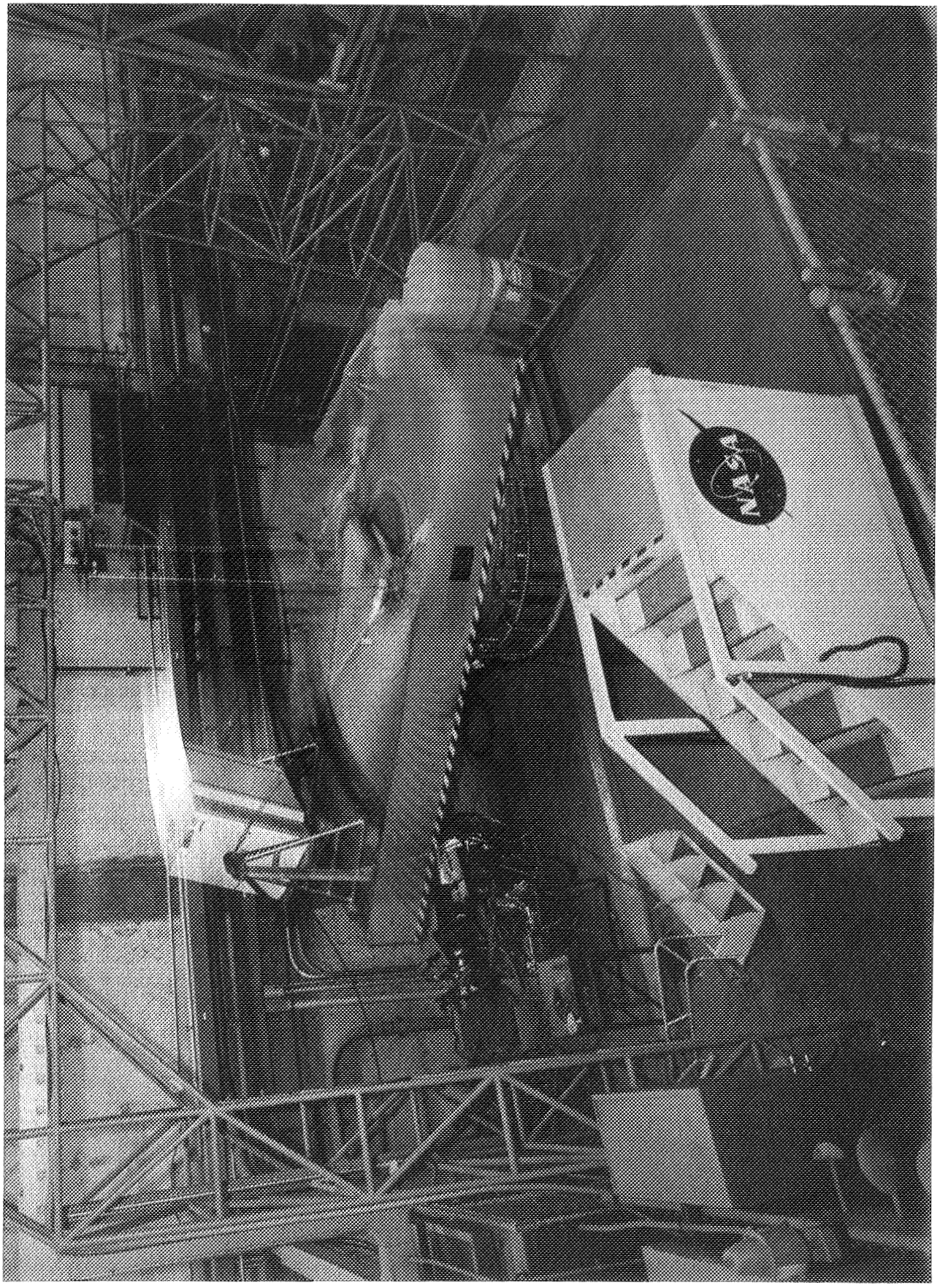

FIGURE 3 MAN-CARRYING ROTATION DEVICE WITH A CELL INCUBATOR

FIGURE 4 HUMAN-POWERED CENTRIFUGE

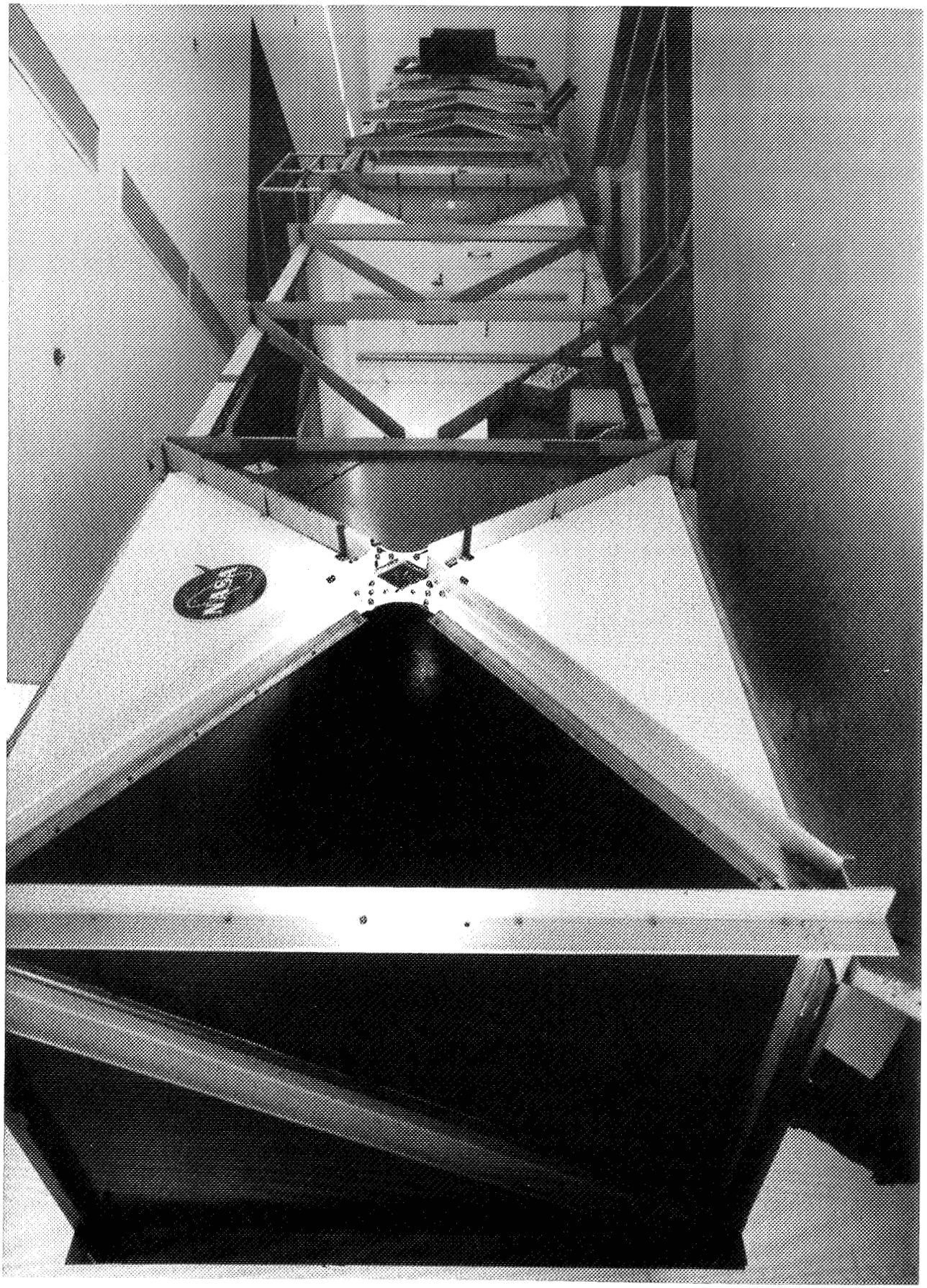

FIGURE 5 20G HUMAN-RATED CENTRIFUGE

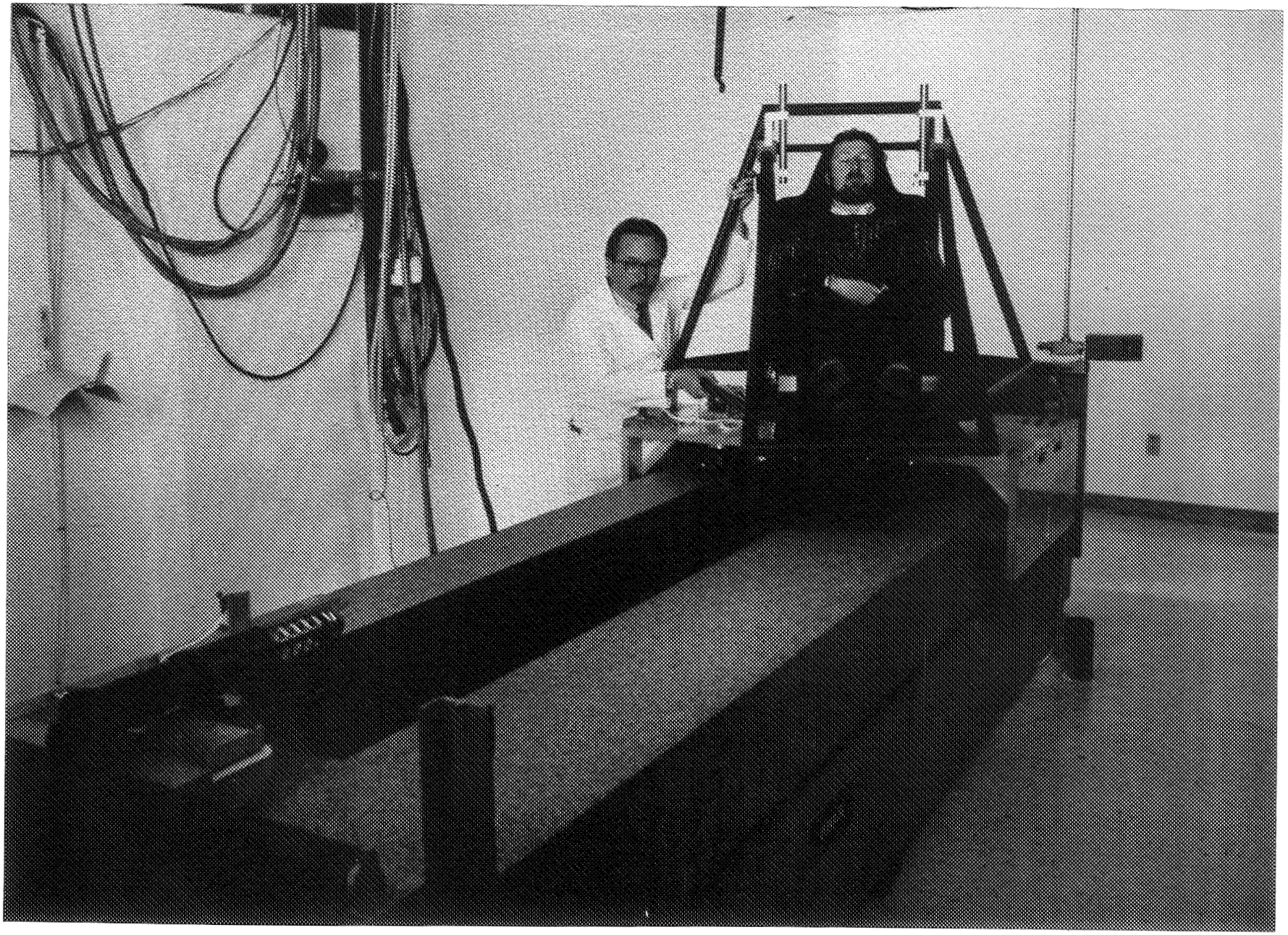

FIGURE 6 30-FOOT LINEAR SLED

# INVESTIGATING AND IMPLEMENTING ENHANCEMENTS TO THE SIMULATION OF SHORT-TERM COLLISION HAZARDS

Jeffrey S. Huth, Dawne E. LeKang, and Darren S. McKnight
Kaman Sciences Corporation

## ABSTRACT

A software tool, the Relative Collision Matrix[1] (RCM), has been developed to provide a quick-look representation of the shortterm collision hazard to space systems from a fragmentation event in Earth orbit. The software performs multiple fragmentation simulations of space objects to quantify the probability of collision for a satellite or a constellation of satellites nearby. Previously, the results were displayed in a color matrix format which showed the relative hazard of each constellation. The RCM can be used for scientific research and operational assessments even though it was designed for test and evaluation applications.

Because of its successful use as an analytical tool, the capabilities of RCM are being extended by enhancing the orbital hazard analysis routines, developing ballistic trajectory hazard analysis routines, and expanding the breakup modeling. Improvements are also being made to the RCM's useability and presentation quality by developing a graphical user interface and by providing graphical animated and nonanimated output.

## INTRODUCTION

The US Space Command maintains a catalog of approximately 7,500 objects in orbit around the Earth. The orbital paths of many of these objects continually cross randomly in time and space. If one of these objects breaks up, debris is produced that could affect many of the nearby satellites. The velocities imparted to the debris as a result of the breakup produces a "cloud" of debris that spans a range of altitudes, inclinations and right ascensions and grows over time. The expanding cloud of debris is characterized by its spatial density, or number of fragments per unit volume, which also changes with time as the debris cloud and each fragment are acted on by atmospheric drag and the gravitational forces of the oblate Earth. Over a period of months to years the cloud of debris disperses and the remaining fragments become part of the background orbital population.

Due to the high velocities on-orbit (around 7 km/s) and wide range of possible encounter angles in space, a collision between a small piece of debris on-orbit and a space system can result in severe consequences. Most likely, a collision with debris roughly 10 cm in size and larger will result in complete destruction of the space system. Collisions with debris approximately 1 cm up to 10 cm in size can, depending upon the size of debris and the encounter conditions, completely destroy the system or, at a minimum, the debris can penetrate the satellite bus and disrupt or destroy a portion of the spacecraft. Debris less than 1 cm in size impacting a space system results, at a minimum, in spacecraft exterior surface erosion and possibly penetration of components. A good example of the effects of impacts by small debris is the Space Shuttle windows that have been replaced due to impacts with small particulates. There have been over 110 "impacts" on shuttle windows leaving features large enough to be recorded by ground inspection crews. About 38 of these features exceeded NASA safety specifications and the windows were replaced.

The combination of the time varying spatial density of a debris cloud and the potentially hazardous results from collisions with debris create the need to estimate the hazard associated with a fragmentation event. The RCM program is a computer simulation tool which was designed to analyze the hazard posed to particular space systems when another satellite nearby fragments. The original version of the RCM provides a first order representation of the hazard to space systems from a satellite fragmentation. The next version of RCM is in the developmental stages and will include the "quick-look" capabilities of the original RCM, but will have additional capabilities for higher order calculations, improved inputs and outputs, and will include a time-dependent analysis capability.

---

[1]The Relative Collision Matrix (RCM) project is sponsored by the Air Force Operational Test & Evaluation Center, AFOTEC.

## ORBITAL DEBRIS FROM A SATELLITE BREAKUP

There have been over 120 satellite breakups in Earth orbit. They range in cause from antisatellite experiments, deliberate detonations, and accidental explosions. Depending on the mass of the fragmenting body, complete (highly energetic) breakups produce a large amount of debris in each of the size regimes previously mentioned. Ground based hypervelocity impact tests are performed to gauge the amount of debris produced. Results from these tests have shown hundreds of fragments are expected greater than 10 cm, several tens of thousands are expected between 1 cm and 10 cm, and millions are expected between 1 mm and 1 cm. Accurately determining the number of pieces generated smaller than 10 cm from an actual on-orbit fragmentation is impossible. Typically, the Space Surveillance Center (SSC), which is responsible for tracking and cataloging objects in space, cannot detect objects smaller than 10 cm in low Earth orbit on a normal operational basis.

Over time, the cloud of debris that results from a fragmentation event expands and eventually encompasses the Earth. Figure 1 depicts the various evolutionary stages of an expanding debris cloud. Immediately after a satellite fragments, the cloud of debris is spherical shaped. After a few minutes the cloud is shaped more like an ellipsoid than a sphere. However, due to the distribution of orbital periods and inclinations resulting from the velocity imparted to the debris, the cloud continues to expand in size and elongate along the orbital path of the original satellite. Eventually the leading edge of the cloud catches up with the trailing edge of the cloud and the cloud begins to take the general shape of a torus. Over a period of months to years, secular orbit changes from the Earth's equatorial bulge will dismantle the torus into a band about the Earth. Depending on the ballistic characteristics of each piece of debris and the altitude of the event, many fragments may reenter the Earth's atmosphere and disintegrate before the cloud reaches a band.

## TYPES OF PROBLEMS RCM ADDRESSES

As we described earlier, the hazard debris in a debris cloud can pose to a satellite can be severe. The effects of the transfer of kinetic energy and momentum from an impact with even small debris can be undesirable. There are basically two categories of debris problems the RCM can address; 1) on-orbit fragmentation events, and 2) ballistic intercept tests. The next section will discuss these two categories and describe the RCM simulation of each.

### On-orbit Fragmentation Events

Normally the exact time a satellite is destroyed is not known. Likewise, the exact position of all collateral satellites will not be known. Only the description of the orbit (apogee, perigee, and inclination) of the breakup object and objects at risk may be available. How then can one do an *a priori* analysis of the hazard a debris cloud can pose?

The RCM addresses these "time-independent" problems by simulating the maximum hazard the fragmentation of a nearby object can pose and then estimating the average hazard the fragmentation can pose. The maximum (e.g., worst case) simulations are performed by iteratively fragmenting each satellite in the list and evaluating the hazard to the remaining satellites treating each remaining satellite as if it were penetrating the debris cloud through the worst possible dimension (given the general orbit parameters) at the worst possible time. The average hazard is then based on the probability that the satellite(s) at risk will ever come into contact with the debris cloud assuming a random distribution of right ascensions. The results are summarized in a matrix form as shown in Figure 2. The columns of the matrix represent the fragmenting space object and the rows represent the objects at risk. The elements of the matrix represent the worst case or average probability of collision between the two pairs listed depending on which matrix is displayed. In the RCM, the simulations are performed and the output matrix is color coded to allow for quick and easy identification and evaluation of the object pairs who pose the greatest risk to each other.

In some cases, the time that a fragmentation can occur may be known. For example, an on-orbit test or operation of some type may be performed at a predetermined time that might result in a fragmentation. In such "time-dependent" cases, the actual probability of collision between a space object and the debris cloud is determined in the RCM. RCM simulates the fragmentation, the growth and evolution of the debris cloud, and the orbital motion of the nearby satellites. In these cases, the nearby objects may never be at risk from the debris cloud until the cloud has dispersed to the point in which it poses a small threat. On the other hand, it is possible to conceive of a situation in which the satellite at risk penetrates the debris cloud very soon after it was generated. If such a

situation were to happen, there would be a non-insignificant probability that the satellite would be struck by debris. The RCM simulating in a "time-dependent" mode can address these situations.

The RCM can be used to determine the "time-independent" probability of collision using the "time-dependent" simulations. This is a Monte Carlo analysis for the average probability of collision for the satellites chosen to be at risk. The orbital parameters (right ascension of the ascending node, argument of perigee, and true anomaly) of the breakup object and objects at risk are allowed to vary uniformly between 0 and $360^{o}$. The probability of collision is evaluated during each simulation and can be statistically combined to calculate the average probability of collision. This capability is useful to determine the best estimate of the average probability of collision.

The fragmentation of a space object either by explosion or collision is simulated using the widely used and documented Fragmentation Algorithms for Strategic and Theater Targets (FASTT) semi-empirical breakup model. FASTT conserves mass, momentum, and energy when simulating a breakup. The impact simulations have been derived from and compared to many ground based hypervelocity impact tests but are still heavily rooted in basic physics. The explosion simulations are derived from the Gurney explosion model. The cumulative number of debris above a given size is estimated. Also, the mass and ballistic characteristics of discrete fragments can be simulated using the statistical distributions within FASTT.

### Ballistic Intercept Tests

Depending on the particulars of the scenario, debris resulting from an intercept between a projectile and a target during a ballistic missile intercept test may pose a hazard to low Earth orbiting satellites. Debris from the event may be given a sufficient velocity impulse such that at or near the apex of the flight the object would be at low Earth orbital altitudes. When a large amount of debris is dispersed, the resulting cloud could expand and pose a risk to operational satellites. This type of analysis will be useful when test programs for the Theater High Altitude Air Defense (THAAD) begin.

The simulation and analysis of this type of problem is analogous to the on-orbit events. Since, in fact, a ballistic trajectory can be considered an orbit with a periapsis below the Earth, the calculational aspects are similar to the on-orbit events with the major difference being the much shorter time frame. (Most of the debris in a ballistic trajectory will not last for more than one revolution, while on-orbit, most of the debris will last for many revolutions.) The RCM simulates this type of problem by breaking up the target vehicle due to the collision using the FASTT breakup model, simulating the motion and evolution of the debris cloud, and determining the hazard to nearby satellites.

The second simulation that RCM performs related to ballistic intercept tests is the ground footprint of the debris fragments as a result of the intercept. Generally speaking this a very difficult problem and is subject to varying aerodynamic and meteorological uncertainties. The footprint simulated by the RCM is intended to provide the analyst with a reasonable order approximation of the ground footprint so that sensitivities of the engagement parameters can be assessed and the location of the footprint to nearby population centers can be determined.

## RELATIVE COLLISION MATRIX

### General Description

The RCM system software operates on a Sun SPARCstation II in the Open Windows Version 3.0 and SunOS 4.1.X software environment. A color monitor and adequate internal RAM is necessary to support the simulation requirements. Hard disk space is also required for storing the RCM data elements — scenarios, constellations, and satellites. When the RCM user interface is used to create the parameters, the RCM software automatically generates the necessary files to store the information.

The ability for the user to specify scenarios (i.e., collection of satellites, satellite constellations, and fragmentation descriptions) is an enhanced feature of the RCM software. This procedure is explained in more detail in the following section. Note that this feature is available to the user, even during simulations, because the software was designed using separate processes. Communication between the software which controls scenario processing, probability and trajectory calculations, and the software which updates the simulation displays, occurs via a RCM system control software package. This system control software package is also responsible for

displaying the main RCM menu, which allows the user to select/define scenarios, control a simulation, and request certain displays. All of the communications within RCM utilize the UNIX system Transport Interface mechanisms.

### Setting Up Simulations

Once the RCM software is started, the user is presented with a main menu. The main menu has three operations which are associated with the definition of scenarios: *Open, Save, and Close*. The *Open* option allows the user to either create a new scenario or open an existent, pre-saved scenario. A scenario must be opened in order to actually execute a simulation, since this is how the RCM software knows which scenario to execute. Once a scenario is opened the user can make changes to a scenario, or execute one of three types of simulations. The three types of simulations are explained in the next section.

A scenario consists of all the satellites or satellite constellations involved in a simulation. Please note that satellite and constellation are not intended to be used interchangeably. The RCM simulates individual satellites or a system of satellites (constellation). In this paper, a constellation refers to a system of *one or more* satellites. The first screen shown to the user is the Scenario Definition screen (see Figure 3). This screen displays the scenario name, the number of satellite constellations in the scenario and a list of all the constellations. Constellations may be added, edited, deleted or viewed.

The next screen associated with the definition of a scenario is the Constellation Definition screen (see Figure 4). This screen allows the user to specify information about the satellite(s); type (two line element set, Satellite Catalog entry, or user-defined), debris dispersion type, and fragmentation type (collision or explosion). When the user wishes to use a satellite defined by either a two line element set or a Satellite Catalog, RCM displays the available file listings. The user can then specify the file (which contains the needed orbital data), a satellite number (which is actually an index into the file) and the mass of the satellite. The User's Manual provides typical satellite masses if actual masses are not known. There are two RCM user-defined satellite options which allow the user to define a constellation; 1) entering a complete set of classical orbital elements or 2) entering only "time-independent" (slowly time varying) orbital parameters which are needed at a minimum to perform a "time-independent" simulation. The third user-defined option allows the user to define the parameters of an object in a ballistic trajectory. Upon hitting *Continue*, screens are presented to the user for entering additional information depending on the data and options selected on this screen.

### Simulation Processing

Once the user has fully defined the scenario and saved the scenario information, one of three simulations are available via the *Execution* menu option. These three simulations or modes of execution are: 1) first-order analytical hazard modeling, 2) "time-independent" higher order, or 3) "time-dependent" simulations. The first-order analytical simulation simulates the debris cloud and calculates probabilities of collision using simple, first-order expressions. This is essentially the original or prototype RCM. The higher-order "time-independent" simulation will simulate the debris cloud and calculate probabilities of collision using higher fidelity (also more time consuming) calculations. The "time-dependent" simulations are for those situations when a breakup time is known and the locations of nearby satellites are also known. The probabilities of collision determined in this mode are completely dependent on the phasings between the satellites at risk in their orbit and the debris cloud.

### Displays

During and after a simulation, the user is provided with displays which animate the hazard calculations. Pictorial displays, which make identification of potential problems easier to recognize, is a major part of the RCM project. There are two basic types of displays available to the user: animated displays which track the satellites and debris from two different view angles and static displays which are available at the end of a simulation.

One of the dynamic displays shows the satellites and debris on a Mercator map projection. Figure 5 is a drawing of this display. The user selects which satellites are shown on this display, the breakup satellite, and associated parameters prior to the start of a simulation. The satellites change colors (green, yellow, red) to represent the associated hazard. Colors were chosen for visualization purposes as opposed to displaying only numerical values (i.e., probabilities). The color green represents no immediate hazard, yellow indicates the satellite is within the altitude boundaries of the debris cloud, and red indicates the satellite is currently passing through the simulated debris cloud.

The second animated view shows the same information from a side view. Figure 6 is a drawing of this display. This display maps altitude along the horizontal axis and longitude along the vertical axis. This view adds a dimensionality (altitude) which is not pictorially represented in the normal Mercator map display.

The available static (non-animated) displays are *PC vs. Time, Ground Footprint* and *Color Matrix.* Which displays are available at the end of a simulation depend on the type of simulation selected by the user. The *Color Matrix* display was the basis for the original RCM and consists of color coded versions of Figure 2 for worst case and average probability of collision. The *Ground Footprint* display shows the location of several debris fragments once they have reached the ground. The ground footprint locations are shown on a Mercator map projection. This display is available if the breakup object was on a ballistic trajectory. The *PC vs. Time* display is available following any high-order simulation. The display shows the cumulative probability of collision (for the user indicated satellite at risk) over time.

In addition to the graphical displays, data from the simulation is written to an output file. This data is available for analysis and post-processing after a session with the RCM is over.

## SUMMARY

As a result of space object fragmenting, a large number of debris will be contained in a relatively small volume of space that changes with time. Because of the high velocities on-orbit, a space system interacting with this debris has a good chance of sustaining damage if not being complete destroyed. The RCM is used to analyze the relative hazards created to a list of space systems if one of these space systems fragments. The current version of the RCM has shown its usefulness in providing an understanding of the relative safety of space systems from a nearby fragmentation. The first version of the RCM has sufficient accuracy to provide an understanding of the parameters and the sensitivity of the parameters involved in a probability of collision analysis. Because of its usefulness as a hazard analysis and instructional tool, RCM is currently undergoing updates to improve the accuracy of the calculations, provide a time-dependent analysis capability, and create new inputs and outputs to expand the type of applications and the output representation of the simulation. The end result of the RCM project is a planning, testing, and educational tool for evaluating spacecraft orbital safety. The unique collision matrix representation and the animated satellite and debris cloud displays provide easily understood results to users of all ability levels.

## REFERENCES


1. McKnight, D.S., "A Phased Approach to Collision Hazard Analysis", ADVANCES. IN SPACE RESEARCH, Vol. 10, No. 3-4, pp. 385-388, 1990.

2. McKnight , D.S. and Lorezen, G., "Collision Matrix For Low Earth Orbit Satellites", JOURNAL OF SPACECRAFT AND ROCKETS, Vol. 26, No. 2, pp. 90-94, March-April 1989.

3. Rubio, R., *et al,* "Satellite Constellation Safety After a Collateral Satellite Fragmentation", presented and the 12th Annual System Safety Society Conference, New Orleans, Louisiana, July, 1994.

4. Maher, R., *et al,* "Fragmentation Algorithms for Strategic and Theater Targets (FASTT) Empirical Breakup Model, Version 3.0", prepared for Defense Nuclear Agency (DNA), February 1994.

5. Chobotov, V.A., "Dynamics of Orbiting Debris Clouds and the Resulting Collision Hazard to Spacecraft", Presented at the 38th international Astronautical Federation Congress, Brighton, England, Oct. 1987, IAA-87-571.

6. Johnson, N.L., McKnight, D.S., ARTIFICIAL SPACE DEBRIS, Orbit Book Company, Malabar, Florida, 1991.

7. Nauer, D.J., "History of On-Orbit Satellite Fragmentations," Seventh Edition, Prepared by Teledyne Engineering for Lockheed Engineering and Sciences Company, July 1993.

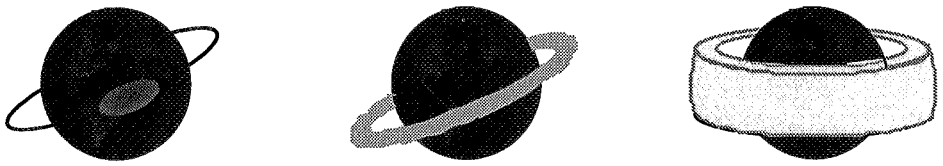

Figure 1: Over time, the cloud of debris that results from a fragmentation event will expand and eventually encompass the Earth.

**Fragmenting System**

| System at risk | System 1 | System 2 | System 3 | System 4 | · · · · · | System n |
|---|---|---|---|---|---|---|
| System 1 | $P_{11}$ | $P_{12}$ | $P_{13}$ | $P_{14}$ | · · · · · · · · | $P_{1n}$ |
| System 2 | $P_{21}$ | $P_{22}$ | $P_{23}$ | $P_{24}$ | | |
| System 3 | $P_{31}$ | $P_{32}$ | $P_{33}$ | $P_{34}$ | | |
| System 4 | $P_{41}$ | $P_{42}$ | $P_{43}$ | $P_{44}$ | | |
| ⋮ | ⋮ | | | | | |
| System n | $P_{n1}$ | | | | | $P_{nn}$ |

$P_{ij}$ = probability of collision for satellite $i$ as a result of satellite $j$ fragmenting

Figure 2: The results from "time-independent" simulations are summarized in a matrix form. The columns of the matrix represent the fragmenting space object and the rows represent the objects at risk. The elements of the matrix represent the worst case or the average probability of collision between the two pairs listed depending upon which matrix is displayed.

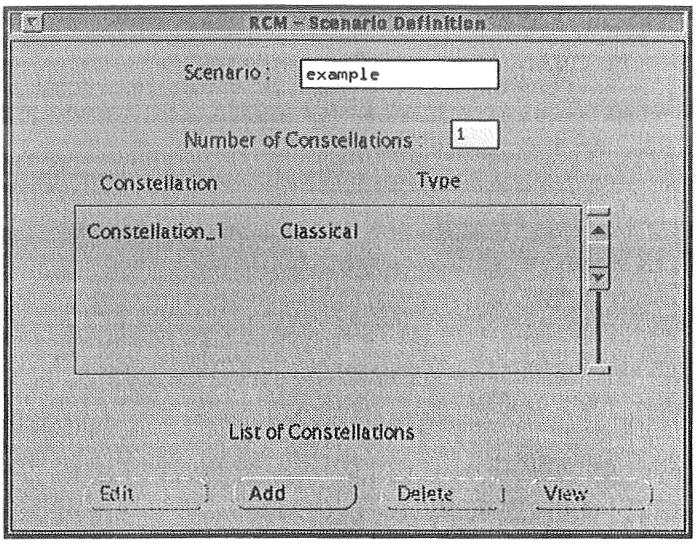


Figure 3: The *Scenario Definition* screen of the RCM. This screen displays the scenario name, the number of constellations, and the list of constellations in the scenario.

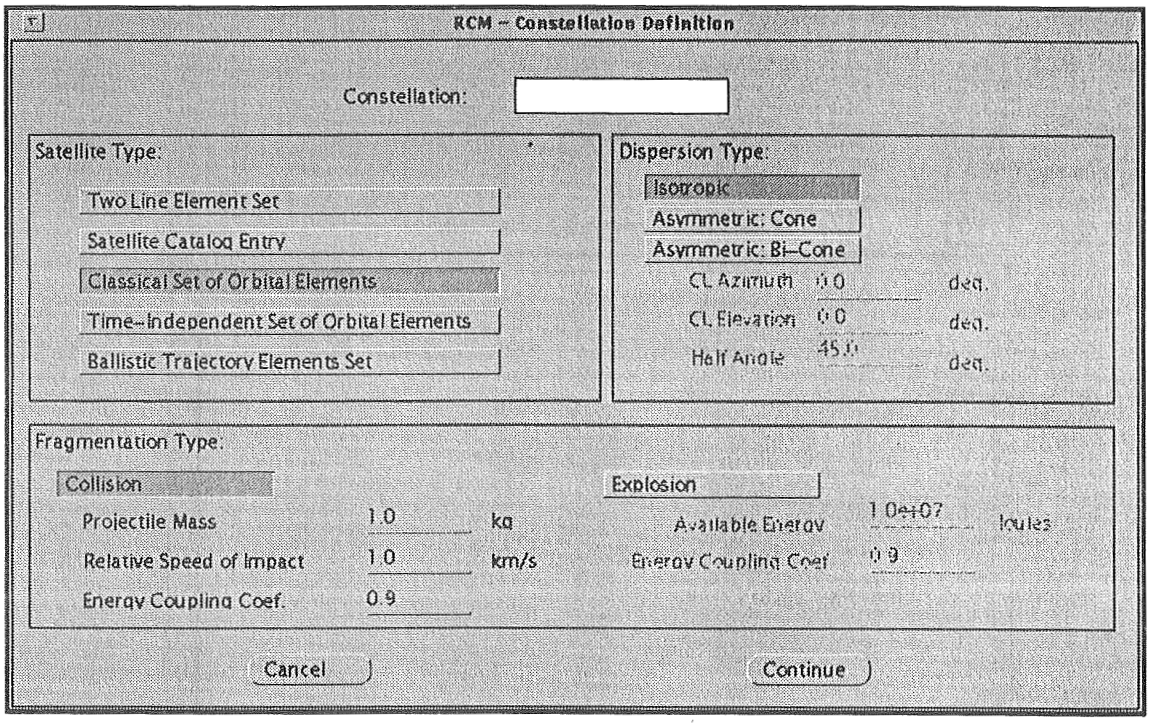


Figure 4: The *Constellation Definition* screen of the RCM. This window allows the user to specify information about the satellite(s) in each constellation.

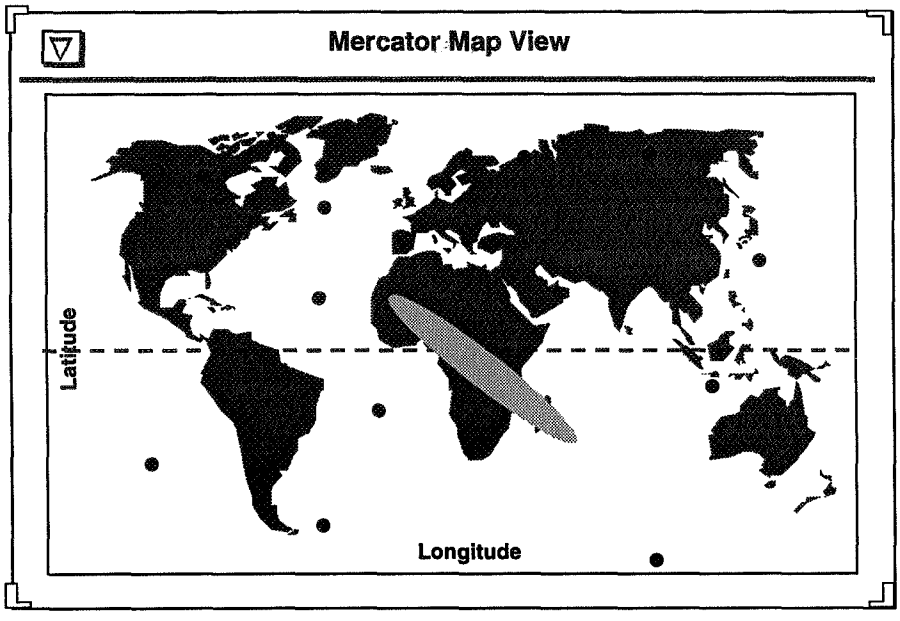


Figure 5: Drawing of the animated Mercator map projection in the RCM. The user selects which satellites are shown on this display, the breakup satellite, and associated parameters prior to the start of a simulation.

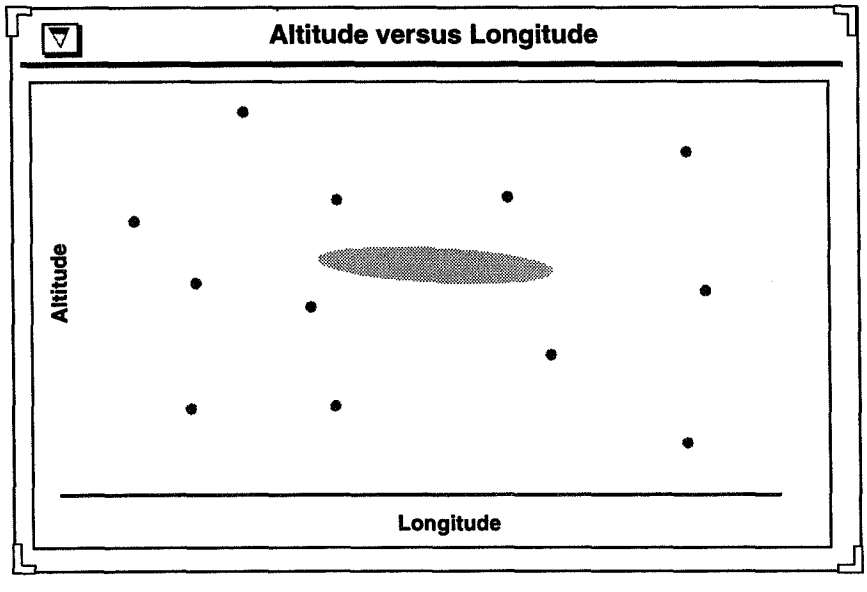


Figure 6: Drawing of the Altitude versus longitude view in the RCM. This display maps altitude along the horizontal axis and longitude along the vertical axis to add dimensionality to the Mercator Map view.

# APPLICATIONS OF A FAST AND EFFICIENT METHOD FOR SIMULATING ORBITAL MISSION SAFETY

Jeffrey Huth and Dr. Darren McKnight
Kaman Sciences Corporation

Dr. Zachari Khutorovsky and Sergei Kamensky
Vympel Corporation

## ABSTRACT

A fast and efficient method for simulating potential interactions between space objects is presented. The specialized hazard analysis simulation is run at the Russian Space Surveillance Center. It simulates the motion of objects in space and determines close encounters between these objects. First, ephemerides are predicted for all space objects over the time interval of concern. Second, using the predicted ephemerides, pairs of satellites that would likely collide are grouped together. Throughout the process, the pairs initially chosen are refined until all pairs of satellites are found which come within a certain miss distance of each other. In addition to the miss distance, other characteristics of the encounter including angle of incidence, relative velocity, type of approaching object, and probability of collision come out of the simulation.

There are many potential applications of this simulation and its results to mission planning and mission safety. Artificial objects can be introduced to the simulation to examine potential encounters between the new objects and current objects for mission design applications. The simultion can be run many times to create data for statistical analysis of encounter parameters. These as well as many other potential applications are presented and discussed.

# Alpha LAMP Integration Facility

Performed Under
BMDO Prime Contract No. SDIO84-89-C-0003
Zenith Star Program

Richard Oshiro
Dennis Sowers
TRW Space and Electronics Group

Joe Gargiulo
Martin Marietta Technologies, Inc.

Mark McGahey
Pitt-Des Moines, Inc.

## Abstract

This paper describes the activity recently completed to meet the simulated space environment requirements for the ground-based testing of an integrated Space Based Laser (SBL) system experiment. The need to maintain optical alignment in the challenging dynamic environment of the pressure recovery system required to simulate space dominated the design requirements. A robust system design was established which minimized the total program costs, most notably by reducing the cost of integrating the components of the experiment. The components of the experiment are integrated on an optical bench in a clean area adjacent to the vacuum chamber and moved on air bearings into the chamber for testing.

## Introduction

The Space Based Laser system experiment consists of the megawatt class Alpha hydrogen-fluoride chemical laser, the four meter (13 foot) diameter Large Aperture Mirror Program (LAMP) beam director, and an outgoing wavefront sensor based beam control system containing adaptive optical elements, as illustrated in Figure 1. The Alpha laser must be maintained at less than 5-10 torr pressure while generating approximately 90 Kg/sec (200 lb/sec) of Free Dry Air Equivalent (FDAE) exhaust gasses. The experiment also contains a diagnostic system incorporating a 1.5 meter (4.9 foot) telescope.

Although ground testing is much less expensive and more flexible than testing in space, the fidelity of space environment simulation is limited by physical constraints and the experiment budget. Management methods similar to the "Integrated Product Team" concept, Design-to-Cost, and "Concurrent Engineering" techniques were used to complete this project on-time and within budget. The design activity through acquisition of the building permit required 12 months. Construction was completed in approximately 24 additional months.

The requirement to pump the laser exhaust gasses up to atmospheric pressure in ground testing and to maintain precise optical bench positioning dominated the design of the space simulation facility. The seismic and acoustic

environment produced by the laser pressure recovery system during testing required optical bench isolation from both the ground as well as the vacuum vessel. Integrated components of the space based laser system were mounted on an optical bench surrounded by a vacuum chamber. Isolators tailored to attenuate the seismic disturbance supported the optical bench from a seismic mass with supporting pilings below the vacuum vessel. Tuned mass dampeners and other passive techniques were also used to further attenuate frequencies near the resonate frequencies of the bench and the components on the bench. Damping of transmission of vibrations from the chamber to the bench was further improved by incorporating use of flex sections in fluid lines, "angel-hairing" of wiring bundles, and rubber seals where the isolators pass through the vacuum chamber floor.

The integration and checkout of precision optical hardware requires personnel to wear cleanroom apparel. This activity, performed in a confined area, can require excessive efforts in time and energy. The lessons-learned during the previous integration of the Alpha Laser in its vacuum vessel was the basis for the requirement for a Class 100,000 "Pre-Integration Area" outside the testing vessel for integration of the experiment components. Once the integration is sufficiently completed, the optical bench with the installed experiment hardware can be transported on air bearings into the minimum size vacuum vessel for testing.

**Configuration**

The experiment, as shown in Figure 1, is housed in two separate vacuum chambers joined by a 19.5 m (64 foot) long, 60 cm (two foot) diameter vacuum beam duct for the transmission of the high power laser beam. One chamber houses the Alpha laser, first tested in 1991. The second chamber, the Alpha/LAMP Integration (ALI) Test Chamber Assembly (TCA), is a 1206 cubic meter (42,600 cubic foot) "D" shaped, flat bottom chamber containing the experiment optical components mounted on a dynamically isolated 90,700 Kg (100 ton) steel optical bench. Adjacent to the TCA is a 3850 cubic meter (136,000 cubic foot) Class 100,000 clean room used for pre-integration of the experiment prior to its installation in the vacuum chamber. Air bearings are used to move the optical bench from the pre-integration area into the vacuum chamber as shown in Figure 2. Once inside the vacuum chamber, the optical bench

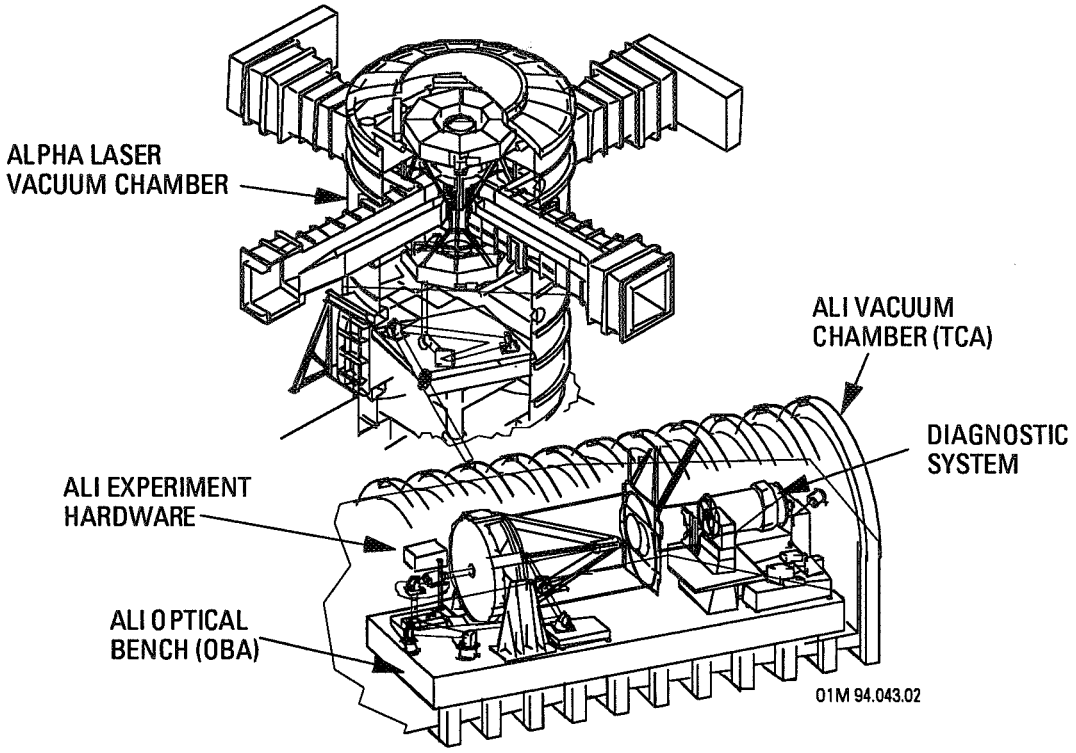


Figure 1. Space Based Laser Experiment Configuration

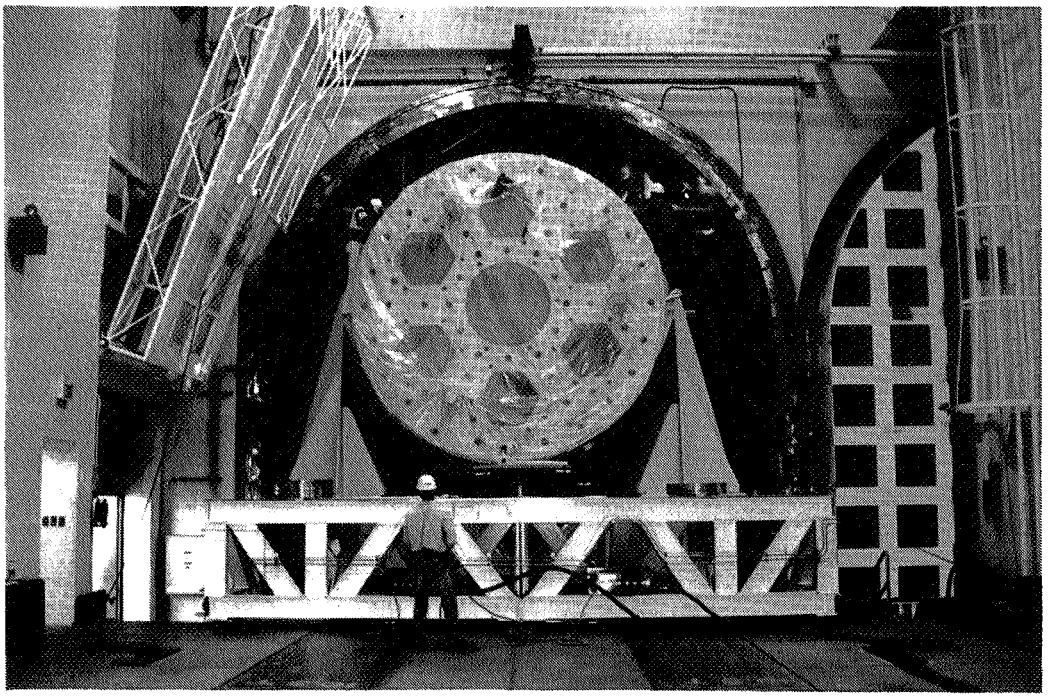

Figure 2. Air Bearing Fit-Check of Optical Bench Into TCA

and experiment components weighing a total of 136,100 Kg (150 tons) are supported on isolators to provide vibration isolation from the surrounding pressure recovery system and maintain precise optical bench positioning during the experiment.

Gate valves and expansion bellows at each end of the vacuum beam duct are used to provide the capability for testing in each chamber independently and to decouple them dynamically. When the laser is operating and the gate valves are open on the vacuum beam duct, the pressure is always maintained higher in the TCA than in the MSA with a positive flow of helium to insure no combustion products from the laser enter from the laser vacuum chamber. This approach saved the cost and complexity of explosion proofing the contents of the TCA.

Support pallets for the TCA vacuum pumps, liquid nitrogen, pneumatics, dry air, and deionized water were fabricated from existing Alpha designs wherever possible to save overall costs. Changes to the designs based on test site experience with Alpha were incorporated to reduce operational and maintenance costs.

**Vacuum Chamber**

In general, the space simulating environment required for this experiment is not particularly difficult to achieve by conventional space simulation standards. No extremely hard vacuum, solar simulation, or cold plates were needed. However, the level of cleanliness, control of the water vapor and contaminant outgassing, and isolation from the seismic environment, were stressing requirements on the chamber design. Design loads for the vessel are full vacuum (external), 5.6 mm of mercury (3 inch water) (internal), seismic conditions, and testing hardware loads associated with the moving of the OBA from the integration area into the vessel.

The basic dimensions of the TCA are 8m (26 ft.) wide at the bottom, 4 m (13 ft.) high vertical walls, and a 4m (13 ft.) radius cylindrical top cap section. Overall length of the chamber is 21.3 m (70 ft.) A patented flex seal design allowed for inclusion of an extremely large closure (8 m x 8 m or 26 ft x 26 ft) without costly field machining and acceptable life cycle costs.

Temperature control and Class 100,000 level cleanliness inside the vacuum vessel is maintained during nontesting periods by a Heating, Ventilation and Air Conditioning (HVAC) system with HEPA filters and a continuous cleaning design. Vacuum cleaner ports are also provided at the level of the optical bench surface inside the vacuum vessel with a central HEPA filter system to facilitate cleaning prior to test. Booty/garment rooms typical of clean room facilities were located as required to transition personnel and equipment into the cleanliness controlled areas.

Chamber environment requirements for water and other contaminants had a major effect on material selection and cost tradeoffs. Stainless steel was selected for the 1.6 cm (5/8 inch) shell and 2.5 cm (1 inch) sidewalls of the vacuum chamber which are exposed to the test environment. However, epoxy painted carbon steel was used for the outside stiffeners, supports, and other ancillary parts to reduce costs. Similarly, stainless steel was used for the top of the optical bench near the optical components, while an epoxy painted carbon steel structure was used below the bench surface which is isolated from the test environment by a designed purge flow/vacuum pump arrangement. Since the vacuum pumps draw the air from below the bench surface (diagonally at two corners), the outgassing of the epoxy painted carbon steel surfaces below the top of the bench is controllable. Careful material selection combined with long periods of soak-out prior to testing were required to control outgassing to meet the requirement for a water content of less than 1000 ppm for the experiment environment. Any polymeric materials including coatings, lubricants and sealants are vacuum stable, low outgassing and non-shedding. The TCA enclosure, including all vacuum seals, are designed so that total leakage of the TCA shall not exceed 100 millitorr per hour when the start-test pressure is 500 millitorr or less.

Three general configurations were considered for the shape of the vacuum vessel: spherical, cylindrical, and "D" shaped. The spherical shape for example had the thinnest wall (lowest weight) but the poorest volumetric efficiency and was not adaptable to the existing site constraints. The cylindrical shape also has similar limitations. The "D" shape was selected for its combined benefits of volumetric efficiency, lifecycle costs, compatibility with the seismic isolation, adaptability with the existing site and the planned hardware integration

approach. The flat bottom chamber design with operable end closure was very compatible with the air bearing system for moving the optical bench between the integration area and the vacuum vessel. A large seismic mass with supporting pilings was conveniently positioned below the isolators of the optical bench. The weight of the vacuum vessel was independently supported around the periphery with its own foundation and supporting pilings. This concept proved to be quite effective in providing vibration isolation between the optical bench and the vacuum vessel, and was compatible with the available space adjacent to the existing Alpha laser facility. The existing building was also modified to provide thermal as well as acoustical protection for the vacuum vessel.

Three levels of electro-optical support rooms with computer floors, conditioned power and fire suppression systems were constructed adjacent to the TCA. Judicious location of mandoors into the vacuum chamber, an emergency shutdown system and combustible gas detection system were included in the chamber design to insure a non-confined work space. This significantly reduced the cost of operation by improving integration efficiency.

**Equipment Handling Provisions**

A 18,000 Kg (20-ton) bridge crane is provided to assemble the parts of the vacuum chamber during construction and also to integrate components in the Pre-Integration Area, as shown in Figure 3. A monorail enabled the hoist of the overhead crane to pick components from the roadway below the PIA, pass through the 4.9 m x 12.2 m (16 foot x 40 foot) bifold doors, and precisely position it within the support boundaries as shown in Figure 4. The crane requirements were driven by the optical bench sections to be delivered. A continuous 1,000 Kg (1-ton ) monorail/bridge system is also provided inside the vacuum chamber as illustrated in Figure 5. The system provides for safe installation of smaller components and optics after the optical bench has been inserted into the chamber.

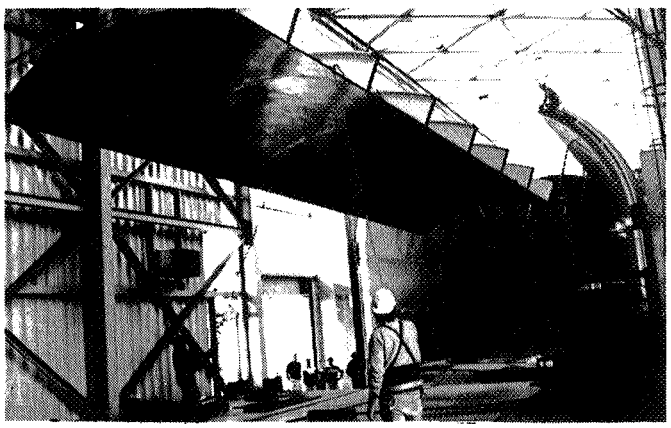

Figure 3a. Bridge Crane - Assembly of TCA

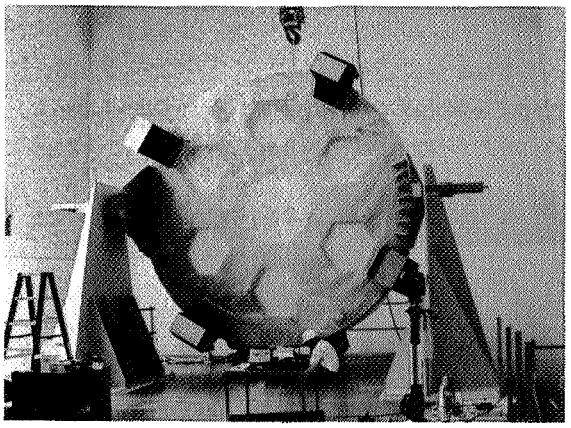

Figure 3B. Bridge Crane - Components Integration In PIA

Figure 4. Optical Bench Segment Lifted Into PIA

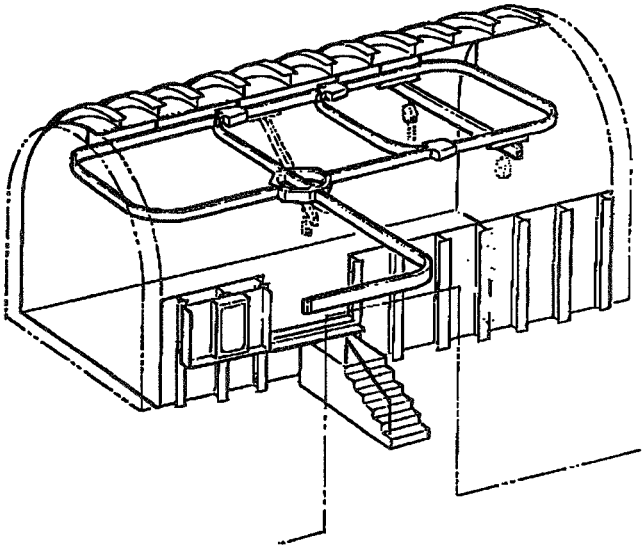

Figure 5. Equipment Handling System inside TCA

A stowable cleanroom was provided to support cleanliness control for hardware transition in and out of the Pre-Integration Area. Each time a component is processed into the clean environment of the PIA for integration, the transition enclosure must be cleaned, the entrapped air cleaned, the component unbagged, and the component transported from the transition area onto the optical bench. Numerous large cleaned and bagged components will be required

to complete the integration of the subsystems so the transition enclosure was made as small as possible since the inside surfaces had to be cleaned each time.

The integration sequence plan also requires a barrier between the PIA and the TCA when the end door of the TCA is opened. A remotely operated roller mechanism was designed to deploy a soft polished vinyl curtain (clean screen) between the sealing surfaces before the door was moved to the stowed position. The stowable clean room and clean screen are depicted in Figure 6.

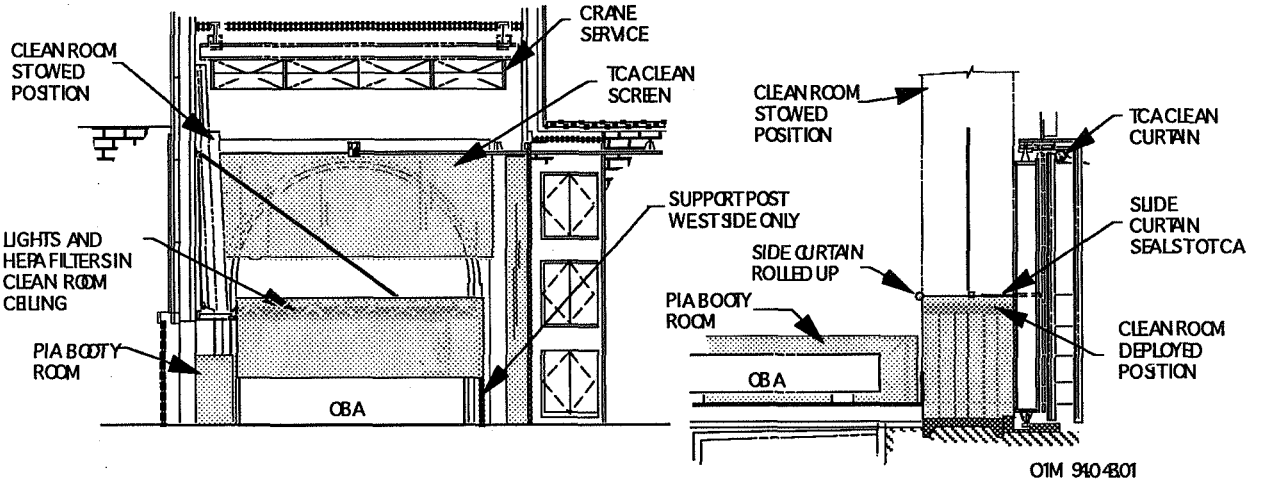


Figure 6. Stowable Clean Room and Clean Screen

## Optical Bench Configuration

The Optical Bench Assembly (OBA) consists of the 7.3 m wide by 19.5 m long by 137 cm high (24-ft x 64-ft x 54-inch) optical bench and its isolation system which provides a stable, level, non-deflecting platform for the ALI experiment. The optical bench was constructed from structural steel shapes and plates welded into a truss or space frame configuration and was fabricated in six

separate subassemblies to facilitate manufacturing and transportation limits. Final assembly of the OBA is shown in Figure 7. The four end segments are 3.6 m wide by 6.2 m long (12-ft x 20-ft 4-in) and weigh 9525 Kg (21,000-lbs) each. The two center bench segments are 3.6 m wide by 7.1 m long (12-ft x 23-ft-4-in) and weigh 19,050 Kg (42,000-lbs) each. The weight difference is a result of optimization of the bench masses to provide an efficient structure at the lowest possible total weight.

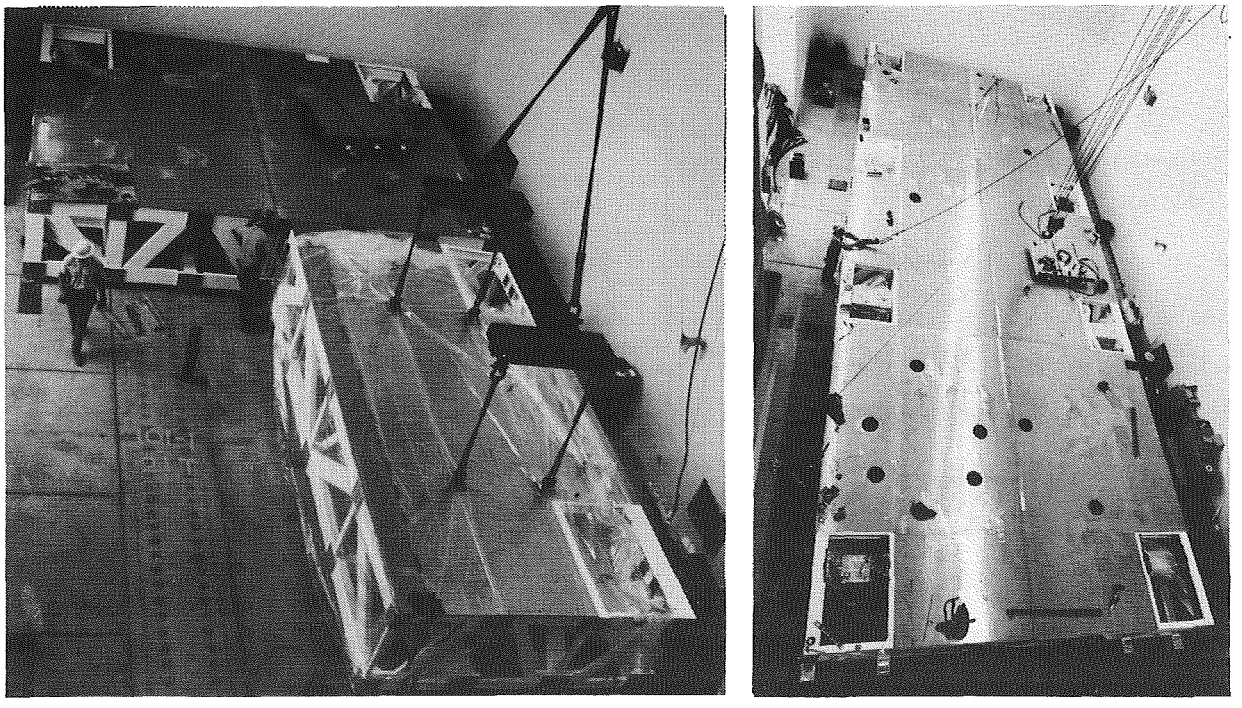

Figure 7. Optical Bench Assembly in PIA

To prevent rusting and a contamination problem within the TCA clean room environment, a white epoxy paint was applied. A spacecraft qualified paint system was utilized with low outgassing properties; i.e., the Collected Volatile Condensable Material (CVCM) is not greater than 0.1% and the Total Mass Loss (TML) is not greater than 1.0%. The top plates were a nominal 1.6 cm (0.625-inch) thick 304L stainless steel plate. These bench segments were bolted at primary beam intersections to maximize local bench stiffness; in addition, tapered pins were installed for joint stiffness and accurate assembly of the optical bench within the PIA prior to final installation into the TCA.

The most challenging requirement for the OBA was to isolate the experiment from the seismic environment created by the rocket driven steam ejection system required to simulate a space environment for the laser system operation. The isolation of the LAMP was critical since its primary mirror modes are in the 2.5 through 9 Hz range. Therefore, the isolators were required to be ≤ 1 Hz with the goal for the lowest possible isolation frequency without developing new isolation technology.

A design goal was to minimize the weight of OBA while maintaining a minimum of 16 Hz frequency for the fundamental bending mode. Considerations for manufacturing, assembly and installation were included in the design process. The 16 Hz minimum frequency chosen met the requirement of being an order of magnitude above the natural frequency of the OBA/LAMP combination. Other design goals were to provide structural damping 2% (Q=50%) in the fundamental mode and minimizing the end-to-end deflection under 10 urad peak-to-peak between 5 to 300 Hz. The structural model of the optical bench was performed on NASTRAN and optimized on a proprietary optimization code which uses design variable sensitivities to minimize the mathematical objective function and satisfy constraint functions. Each truss member was optimized to a minimum cross section which produced the minimum weight.

**OBA Isolation System**

Pneumatic isolators provide one of the best methods for vibration isolation since they are able to accommodate large loads, varying center-of-gravity, and provide fast roll off of the vibration frequencies above the resonance frequency. The OBA is isolated and supported by pneumatic isolators which form a three-point determining system. Eight isolators are interconnected to form three master/slave sets with each master containing the movement sensing servo-valve hardware. The isolator selected uses a laminar flow damping orifice which contains thousands of tiny orifices instead of the single conventional damping orifice. In addition, a hybrid-chamber design enhances the damping efficiency by minimizing the air volume between the piston and damper. This new orifice

design is responsible for the lower natural frequency, faster settling time, better high center of mass stability due to a smaller volume in the spring chamber, and less amplification at resonance due to the smaller volume.

The OBA isolators are designed to perform under 0.8-Hz for the given load of 145,000 Kg (320,000-lbs) for the disturbance PSD shown on Figure 8. Each isolator has a maximum load carrying capacity of 18,000 Kg (40,000-lbs.) The isolators are 91 cm (36-in) high by 91 cm (36-in) diameter supported by a similar sized pedestal. This compact isolator height simplified both the integration task and the vacuum seal design with the TCA floor, as shown in Figure 9. Therefore, the pedestal required only to be a structural base with adjustment capabilities and a vacuum seal interface with the TCA.

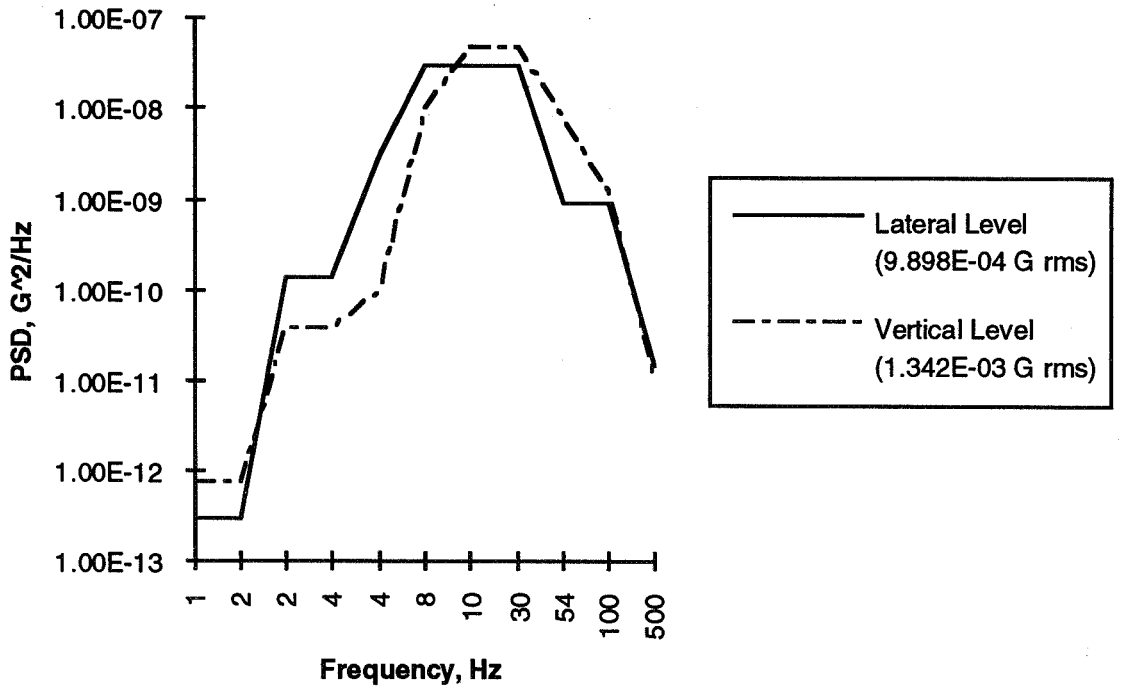


Figure 8. Seismic Disturbance Input

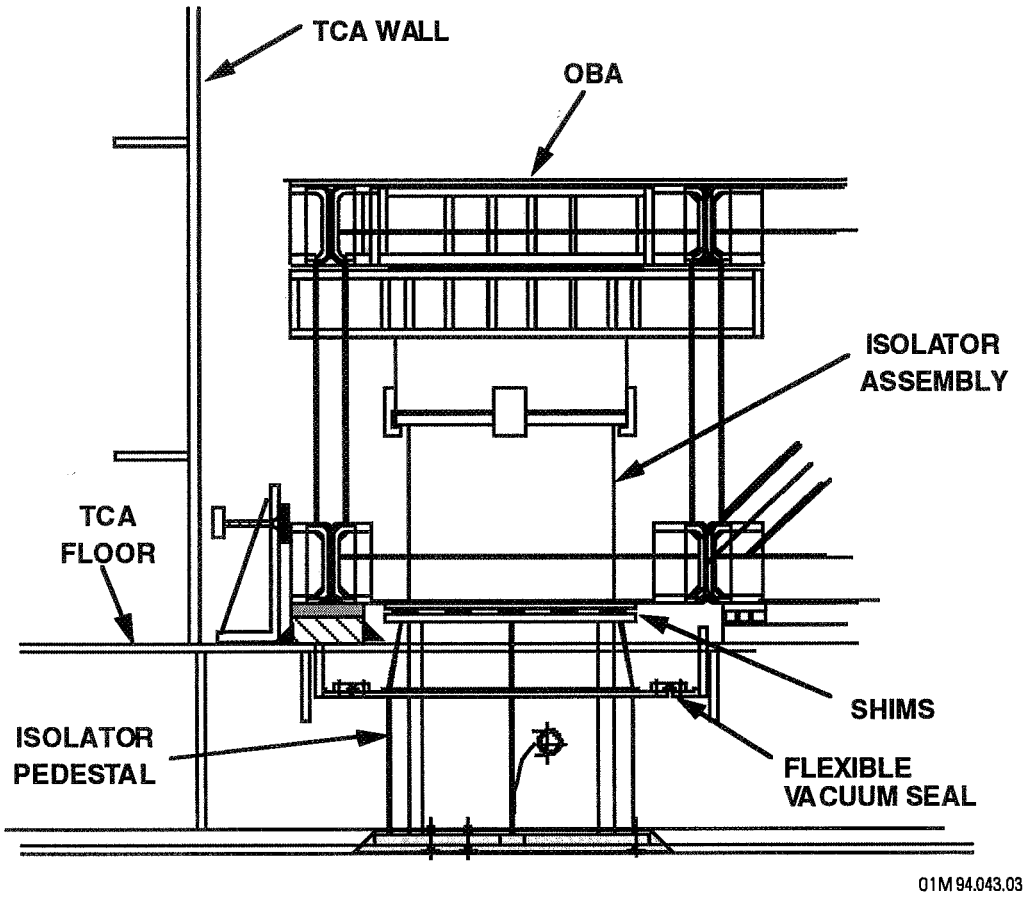


Figure 9. OBA Isolator Assembly Final Installation

The pneumatic isolators/servo-valve system can be bleeding or non-bleeding. The pneumatic supply gasses are vented external to the TCA. When disturbed, the OBA returns to its nominal position +/- the steady state error in less than 0.5 seconds. Leakage into the TCA as measured by a helium leak detector is less than $10^{-5}$ atm/cc/sec. The OBA is capable of movement in six degrees of freedom and is limited to ± 1.0 cm (± 0.38 inches) maximum translational movement in each direction. In addition, the OBA rotation is limited to a maximum of 1.0 milliradian rotation about each axis.

## Optical Bench Damping

The structural passive damping was accomplished with a tuned mass damper. A tuned-mass damper (TMD), also known as an auxiliary mass damper, is a vibration damping device consisting of a mass and a damped "spring" attached to a structure at or near an antinode of a troublesome mode of vibration. The basic theory is that by adding an oscillator whose own natural frequency is close to that of a troublesome mode, it can impart a force (due to its own resonance) back on the base structure that counteracts the base structure's motion. Since another degree of freedom has been added, another system mode is added, and it is very near the frequency of the target mode. The TMD essentially splits the target mode into two coupled modes of the TMD and base structure, each with high damping. This effect and a schematic spring-mass TMD are shown in Figure 10.

The TMD physical mass was determined from an empirical relationship to be 35.6 Kg (78.5 lbs.). Knowing the mass of the TMD, the spring stiffness was determined by calculating the desired tuning ratio. The TMD frequency at 16.65 Hz results in a lower mode of 16.48 Hz with a damping coefficient of 2.23 and an upper mode of 16.96 Hz with a damping coefficient of 2.37.

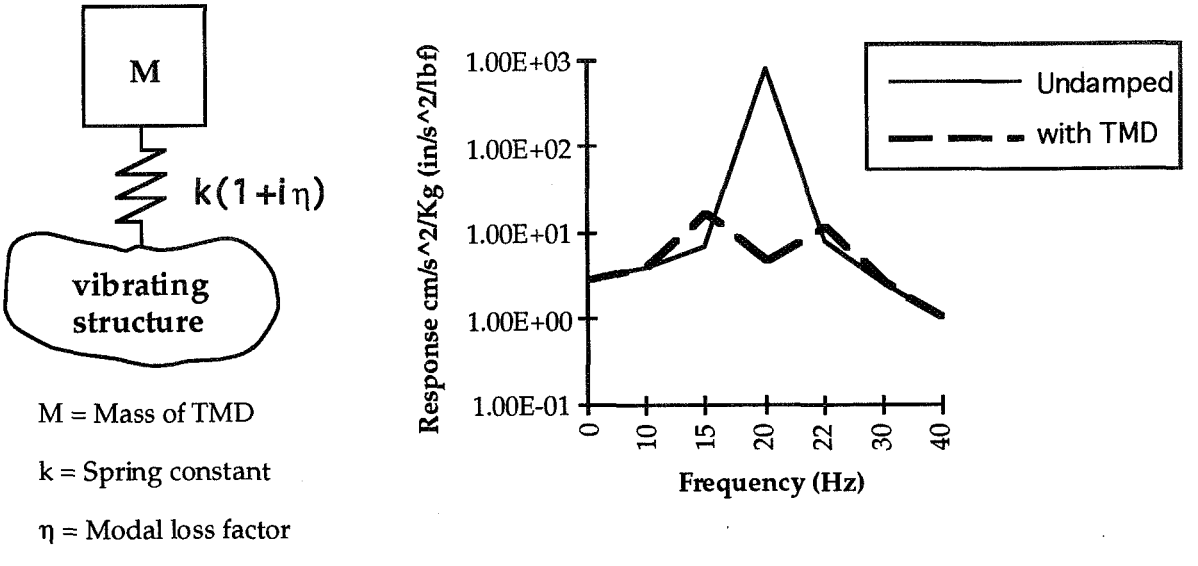


Figure 10. TMD Effects

## Conclusion

This space simulation facility provides a cost effective, practical means to demonstrate a Space Based Laser in a realistic ground test environment. It significantly reduces overall program cost as well as minimizes the technical risk before conducting a flight experiment. The facility design provides for upgrades to the experiment hardware configuration and enables the facility to act as a test bed for future developments. Embodied in the space simulation facility design is a mixture of existing facility engineering practices with innovation in certain areas to meet unique requirements, all implemented in a cost and schedule conscious environment.

# SIMULATION OF A SPATIAL SERVO-HYDRAULIC TEST FACILITY FOR SPACE STRUCTURES

K.-D. Leimbach, H. Hahn

Control Engineering and System Theory Group,
Department of Mechanical Engineering,
University of Kassel, Germany

## ABSTRACT

In this paper different control concepts for servo-hydraulic test facilities are derived using exact linearization techniques. Based on different linear and nonlinear models of the test table and the actuator dynamics several nonlinear controllers of different complexity are derived. The closed loop system performance of the controlled servo-hydraulic test facility is tested in various computer simulations using both, standard test signals and large test signals as system inputs. The simulation results turn out, that in case of standard input signals the test facility controller must include a linear test table mechanics model and a nonlinear servohydraulic actuator model. Additional simulations demonstrate the robustness of the control concept selected for standard test signals with respect to variations of plant parameters.

## INTRODUCTION (1)

Multi-axis servohydraulic test facilities are widely used for vibration testing of critical components of industrial equipment and of future spacecraft. First theoretical investigations of multi-axis test facility control concepts based on modern nonlinear control theory (exact linearization techniques) are (ref. 1) and (ref. 2). The control algorithms derived in (ref. 1, 2) are based on complex nonlinear component models of the test table mechanics and on linear component models of the hydraulic actuators. This paper extends the mathematical models of the servohydraulic actuators in (ref. 1, 2) from linear equations to highly nonlinear relations. Based on the different combinations of linear and nonlinear plant component models (Section 2) different control algorithms have been derived (Section 3). Using the different control algorithms of Section 3 various computer simulations have been made (Section 4) to find a trade-off between the controller complexity needed and the closed loop system behaviour desired. Additional computer simulations proof the robustness of the control concept selected with respect to plant parameter variations. The control algorithm selected provides an excellent system performance and turns out to be amazingly insensitive with respect to plant parameter variations.

## NONLINEAR PLANT MODELING (2)

The test facility considered includes the following components (cf. 1):

- a rigid six degree of freedom test table with a rigid payload rigidly attached to it,
- $l$=6 or $l$=8 servohydraulic actuators and
- an integrated control system.

### Test table and payload mechanics

The **nonlinear model equations** of the test table mechanics are (ref. 1)

$$\begin{aligned} \dot{x}_1 &= T(x_1)\cdot x_2 \\ M\left(J, r_{CP}^L, x_1\right)\cdot \dot{x}_2 &= J_{x1}^T(x_1)\cdot A_k \cdot p - J_{x1}^T(x_1)\cdot D_k \cdot J_{x1}(x_1)\cdot x_2 - n\left(J, r_{CP}^L, x_1, x_2\right) - q_G\left(r_{CP}^L, x_1\right) \end{aligned} \tag{1a}$$

where the first equation of (1a) includes the Poisson equations and the matrix $T(x_1)$ has been chosen as matrix of Bryant angles; $M$ is the inertia matrix of the test facility, $D_K$ and $A_K$ are the diagonal matrices of the actuator damping coefficients and of the actuator piston areas, respectively; $x_1=\left[(r_P^R)^T, \eta^T\right]^T=\left[x_P^R, y_P^R, z_P^R, \varphi, \theta, \psi\right]^T \in \mathbb{R}^6$ is the position

and orientation vector of the spatial test facility, where the position vector $r_P^R=\left[x_P^R, y_P^R, z_P^R\right]^T$ is represented in inertial frame $R$ and the orientations $\eta=[\varphi,\theta,\psi]^T$ are the Bryant angles; $x_2=\left[(\dot{r}_P^R)^T, (\omega_{LR}^L)\right]^T=\left[\dot{x}_P^R, \dot{y}_P^R, \dot{z}_P^R, p^L, q^L, r^L\right]^T \in \mathbb{R}^6$ is the velocity vector, where $\omega_{LR}^L=\left[p^L, q^L, r^L\right]^T$ is the angular velocity vector represented in body fixed frame L; $\dot{x}_2$ is the acceleration vector; $n$ is the vector of the centrifugal forces and of the gyroscopic terms; $q_G$ is the nonlinear vector of the gravitational force and the associated torque and $p:=[p_1,\cdots,p_l]^T \in \mathbb{R}^l$ is the vector of the actuator pressure differences. The nonlinear transformation matrix $J_{x1}^T(x_1)$ maps the actuator forces from joint fixed frames $K_i$ into forces and torques represented in inertial frame $R$ and in body fixed frame $L$, respectively (compare the representation of $x_2$). The associated **linear model equations** are

$$M\left(J, r_{CP}^L\right)\cdot\ddot{x}_1+T_d^T\cdot D_K\cdot T_d\cdot\dot{x}_1=T_d^T\cdot A_K\cdot p \tag{1b}$$

where $T_d^T$ is the linearized transformation matrix $J_{x1}^T$, $J\in\mathbb{R}^{3,3}$ is the inertia tensor and $r_{CP}^L\in\mathbb{R}^3$ is the vector of the common center of gravity.

**Servohydraulic actuators**

The servohydraulic actuators are modeled by the **nonlinear equations** (ref. 3)

$$\dot{p}= B_2(p,x_V)\cdot x_u-C_H^{-1}\cdot Q_{BP}(p)-C_H^{-1}\cdot A_K\cdot J_{x_1}(x_1)\cdot x_2+B_1(p,x_V)\cdot x_V \quad \in\mathbb{R}^l \tag{2a}$$

where (for i=1,..., $l$, ($l$=6 in case of 6 actuators and $l$=8 in case 8 actuators acting onto the test table))

$$\begin{aligned} B_1(p,x_V)&:=C_H^{-1}\cdot K_\alpha\cdot\left\{Q_I(p,x_V)+Q_{II}(p,x_V)\right\} \in\mathbb{R}^{l,l}\\ B_2(p,x_V)&:=C_H^{-1}\cdot K_\alpha\cdot\left\{Q_{II}(p,x_V)-Q_I(p,x_V)\right\} \in\mathbb{R}^{l,l}\end{aligned} \tag{3}$$

and

$$\begin{aligned} K_\alpha &:=diag\left(\alpha_{Di}\cdot\pi\cdot d_i\cdot\sqrt{2/\rho}\right) \in\mathbb{R}^{l,l}\\ Q_I &:=diag\left(\sqrt{|p_0-p_i|/2}\cdot sign(p_0-p_i)\cdot\sigma(x_{vi}-x_{ui})\right) \in\mathbb{R}^{l,l}\\ Q_{II} &:=diag\left(\sqrt{|p_0+p_i|/2}\cdot sign(p_0+p_i)\cdot\sigma(-x_{vi}-x_{ui})\right) \in\mathbb{R}^{l,l}\\ Q_{BP} &:=\left(\alpha_{Di}\cdot A_{BPi}\sqrt{2/\rho\cdot|p_i|}\cdot sign(p_i)\right)_{i=1,\cdots,l}^T \in\mathbb{R}^l\\ C_H &:=\frac{L}{4\cdot B}\cdot A_K \quad (L \text{ actuator length}, B \text{ bulk modulus}).\end{aligned}$$

The associated **linear model equations** are

$$\dot{p}=C_H^{-1}\cdot\left[Q_x\cdot x_V+Q_P\cdot p-A_k\cdot J_{x1}(x_1)\cdot x_2\right] \in\mathbb{R}^l \tag{2b}$$

where $x_V$ is the vector of servovalve piston positions $x_V=[x_{v1},\cdots,x_{vl}]^T \in\mathbb{R}^l$ and $C_H, Q_P, Q_x\in\mathbb{R}^{l,l}$ are the diagonal matrices of the actuator hydraulic capacities, servovalve pressure coefficients and servovalve displacement coefficients, respectively. The plant simulation includes the following model equations of the servovalve mechanics

$$\ddot{x}_{vi}+2\cdot\zeta_{vi}\cdot\omega_{vi}\cdot\dot{x}_{vi}+\omega_{vi}^2\cdot x_{vi}=k_{vi}\cdot\omega_{vi}^2\cdot u_i \in\mathbb{R}^1, \text{ (i=1, ..., } l) \tag{4a}$$

with $\zeta_{vi}$=0.7 and $f_V=\omega_V/2\pi$. In (4a) $u=[u_1,\cdots,u_l]^T\in\mathbb{R}^l$ is the system input. The control laws will be derived taking into account the following simplified servovalve model

$$x_{vi}=k_{vi}\cdot u_i \in\mathbb{R}^1, \text{ (i=1,..., } l). \tag{4b}$$

## NONLINEAR CONTROLLER DESIGN (3)

The subsequent nonlinear controller design is based on the trivial servovalve dynamics of (4b), where the servovalve dynamics included in (4a) has been neglected (ref. 1). This tremendously simplifies the controller design. This simplification will be justified by the subsequent simulation results. Then the choice of the system output $y=h(x_1):=x_1$ leads to a well defined vector relative degree of $[3,3,3,3,3,3]$ (in case of $l$=6 servo-hydraulic actuators). Using in addition the system output $y=x_1$ yields the normal form representation (5) of the simplified plant which provides the basis for the subsequent controller designs.

$$\begin{aligned} \dot{z}_1 &:= \dot{y} = \dot{x}_1 = z_2 \\ \dot{z}_2 &:= \ddot{y} = \ddot{x}_1 = z_3 \\ \dot{z}_3 &:= \alpha_j + \beta_j \cdot u \,. \end{aligned} \tag{5}$$

where $\dot{z}_1=z_2$, $\dot{z}_2=z_3$ and $\dot{z}_3$ are the spatial test table velocity, acceleration and jerk, respectively, and $\alpha_j$, $\beta_j$ (j= I, II, III, IV) are the different normal form plant relations (7a), (7b), (7c), (7d) associated to the plant models collected in Table 1, respectively.

Based on the system equations (5) the nonlinear controller design is straight forward (ref. 1):

$$u=\beta_j^{-1}\cdot\left(v-\alpha_j\right) \tag{6a}$$

where for $l$=6 $\beta_j^{-1}$ is the inverse of $\beta_j$, and for $l$=8 $\beta_j^{-1}$ is defined as the right inverse of $\beta_j$.

A suitable choice of $K_0$, $K_1$, $K_2 \in \mathbb{R}^{6,6}$ in

$$v := \dot{z}_{3d} - K_2\cdot(z_3 - z_{3d}) - K_1\cdot(z_2 - z_{2d}) - K_0\cdot(z_1 - z_{1d}) \tag{6b}$$

guarantees a stable error dynamics of the closed loop system, where $\dot{z}_{3d}$, $z_{3d}$, $z_{2d}$, $z_{1d}$ are the desired jerk, acceleration, velocity and position set point signals, respectively. The measurements required in (6) are the test table degree of freedom positions/orientations $z_1$, velocities $z_2$ and accelerations $z_3$. The plant nonlinearities are compensated by $\alpha_j$ and $\beta_j^{-1}$ (compare (6a)) where, the different representations of the controller relations $\alpha_j$ and $\beta_j^{-1}$ depend on the plant component model equations of Table 1. The different controllers investigated are (comp. Table 1):

**Case j=I** (using (1b) and (2b)):

$$\begin{aligned} \alpha_I &= M^{-1}\cdot T_d^T\cdot A_K\cdot\left\{C_H^{-1}\cdot Q_P\cdot p - C_H^{-1}\cdot A_K\cdot T_d\cdot\dot{x}_1\right\} - M^{-1}\cdot T_d^T\cdot D_K\cdot T_d\cdot\ddot{x}_1 \\ \beta_I &= M^{-1}\cdot T_d^T\cdot A_K\cdot C_H^{-1}\cdot Q_P\cdot K_V, \end{aligned} \tag{7a}$$

**Case j=II** (using (1b) and (2a)):

$$\begin{aligned} \alpha_{II} &= M^{-1}\cdot T_d^T\cdot A_K\cdot\left\{B_2\cdot x_u - C_H^{-1}\cdot Q_{BP} - C_H^{-1}\cdot A_K\cdot T_d\cdot\dot{x}_1\right\} - M^{-1}\cdot T_d^T\cdot D_K\cdot T_d\cdot\ddot{x}_1 \\ \beta_{II} &= M^{-1}\cdot T_d^T\cdot A_K\cdot C_H^{-1}\cdot K_\alpha\cdot\{Q_I + Q_{II}\}\cdot K_V, \end{aligned} \tag{7b}$$

**Case j=III** (using (1a) and (2b)):

$$\begin{aligned} \alpha_{III} &= \frac{d^3 x_1(p, x_1, x_2)}{dt^3} = \left[\frac{\partial\ddot{x}_1}{\partial p}\cdot\dot{p} + \frac{\partial\ddot{x}_1}{\partial x_1}\cdot\dot{x}_1 + \frac{\partial\ddot{x}_1}{\partial x_2}\cdot\dot{x}_2\right] \\ \beta_{III} &= T\cdot M^{-1}\cdot T_d^T\cdot A_K\cdot C_H^{-1}\cdot Q_P\cdot K_V, \end{aligned} \tag{7c}$$

**Case j=IV** (using (1a) and (2a)):

$$\begin{aligned} \alpha_{IV} &= \frac{d^3 x_1(p, x_1, x_2)}{dt^3} = \left[\frac{\partial\ddot{x}_1}{\partial p}\cdot\dot{p} + \frac{\partial\ddot{x}_1}{\partial x_1}\cdot\dot{x}_1 + \frac{\partial\ddot{x}_1}{\partial x_2}\cdot\dot{x}_2\right] \\ \beta_{IV} &= T\cdot M^{-1}\cdot T_d^T\cdot A_K\cdot C_H^{-1}\cdot K_\alpha\{Q_I + Q_{II}\}\cdot K_V \end{aligned} \tag{7d}$$

where

$$\ddot{x}_1 = \frac{\partial}{\partial x_1}\left(T(x_1)\cdot x_2\right)\cdot\dot{x}_1 + T(x_1)\cdot\left\{M^{-1}(x_1)\cdot\left[J_{x1}^T(x_1)\cdot A_K\cdot p - J_{x1}^T(x_1)\cdot D_K\cdot J_{x1}(x_1)\cdot x_2 - n(x_1, x_2) - q_G(x_1)\right]\right\}. \tag{8}$$

Both, the controller complexity and the closed loop system behaviour severely depend on the plant models included in the control law design. Control laws based on **nonlinear test table equations** of motion (1a) (Case III and Case IV) are extreme complex and lengthy (more than one hundred DIN A4 pages of length, ref. 1). This is due to the partial derivatives of $\ddot{x}_1$ with respect to $p$, $x_1$ and $x_2$ in (7c) and (7d), where $\ddot{x}_1$ is defined in (8). Control laws based on **linear test table mechanics** (1b) are much less complex (less than 5 pages of length (Cases I and II)). The simulation results of Section 4 show which component models must be included in the control law design in order to achieve a satisfactory control loop behaviour using different test signal levels.

## SIMULATION RESULTS (4)

### Variation of control concepts (test facility with $l$=6 servo-hydraulic actuators)

The subsequent simulations tend to find a trade-off between the closed loop system behaviour and the complexity of the controller to be implemented. Apart from Simulation No. 5b and 5c (comp. Table 2) all simulations are based on the ideal servovalve model (4a) with an upper limit frequency of $f_v$=1000 *Hz*. As discussed in Section 3 the controller complexity severely depends on the plant model equations taken into account in the controller design. The nonlinear plant (1a), (2a) and (4a) together with the different control laws of Table 1 have been investigated in computer simulations using both, standard transient test signals for vibration testing of space structures used in industry (as shown in Figures 2a and 4a) and large test signals (as shown in Figures 3a and 5a) derived from the standard test signals in order to simulate large spatial motions. A control law based on **linear plant models** of both, the test table mechanics and the actuator dynamics (comp. Table 1, Case I and Equation (7a)) provides in case of standard test signals (cf. 2a) large couplings among the test facility degrees of freedom and a poor tracking behaviour in the y- and z-degrees of freedom (cf. 2b and Simulation No. 1a of Table 2). A control law based on **linear actuator dynamics** and on **nonlinear test table mechanics** (comp. Table 1, Case III and Equation (7c)) provides in case of standard test signals the same poor tracking behaviour in the y- and z-degrees of freedom and large couplings among the test facility degrees of freedom (cf. 2c and Simulation No. 1b of Table 2). Even less quality results hold for simulations using large test signals (cf. 3a) in case of a control concept based on **linear plant models** (cf. 3b and Simulation No. 2a of Table 2) and in case of a control concept based on **linear actuator dynamics** and on **nonlinear test table mechanics** (cf. 3c and Simulation No. 2b of Table 2). The unwanted couplings among all test table degrees of freedom may destroy the payloads to be tested. Both, the tracking and the decoupling behaviour of the test facility have been improved by taking into account **linear test table mechanics** and **nonlinear actuator dynamics** in the control law design (comp. Table 1, Case II and Equation (7b)) using standard test signals (cf. 4b and Simulation No. 3a of Table 2). A control concept based on **nonlinear test table mechanics** and on **nonlinear actuator dynamics** (comp. Table 1, Case IV and Equation (7d)) provides the same excellent tracking and decoupling behaviour using standard test signals (cf. 4c and Simulation No. 3b of Table 2). In case of large test signals the control concept based on **linear test table mechanics** and on **nonlinear actuator dynamics** provides both, a poor tracking behaviour in the y- and z-degrees of freedom and large couplings among all degrees of freedom (cf. 5b and Simulation No. 4a of Table 2). A control concept based on **nonlinear test table mechanics** and on **nonlinear actuator dynamics** provides an ideal tracking and decoupling behaviour even in case of large test signals (cf. 5c and Simulation No. 4b of table 2). From the previous computer simulations the following conclusions have been drawn:

- Using **standard test signals** (cf. 2a) a controller design based on **linear test table mechanics** and on **nonlinear hydraulic actuator models** provides a satisfactory transient and decoupling behaviour of the controlled test facility.

- In case of **large test signals** (cf. 3a) both, the **nonlinear test table mechanics** and the **nonlinear actuator dynamics** must be included in the controller design. This, however, generates controllers of extreme high complexity (comp. Table 1, Case IV).

Additional computer simulation results with **unstructured uncertainties** are shown in Figure 6. The plant simulation still includes the nonlinear test table mechanics (1a), the nonlinear servo-hydraulic actuator dynamics (2a) and the servovalve mechanics model (4a). The control concept selected is based on linear test table mechanics (1b), on nonlinear actuator dynamics (2a) and on the simplified servovalve model (4b) which doesn't take into account any servovalve dynamics. In the simulations the **upper servovalve limit frequency** $f_v$ of the plant model is varied from $f_v$=100 *Hz* to $f_v$=1000 *Hz*. In case of an unrealistic upper limit frequency of $f_v$=1000 *Hz* the transmission behaviour of

the test facility is nearly ideal (cf. 6a). As a consequence the valve dynamics (4a) can be omitted from the controller design in this case. For $f_v$=300 *Hz* the transmission behaviour is of reduced quality but still acceptable (cf. 6b). For $f_v$=100 *Hz* the transmission behaviour is further reduced in comparison to Figure 6b and no longer acceptable (cf. 6c). On the other hand, Figure 6b shows, that an exact linearization controller design for a test facility including high response valves with an upper limit frequency $f_v$ of about 300 Hz may be drastically simplified by omitting the servovalve dynamics in the control law design. The resulting control errors are of minor practical importance.

**Robustness with respect to plant parameter variations (test facility with *l*=8 servo-hydraulic actuators)**

In industrial practice usually not all plant parameters to be implemented in the control algorithms are known exactly. As a consequence, the plant parameter values used in the control law may deviate from the actual parameter values of the plant. The influence of those parametric discrepancies between associated plant and controller parameters is investigated subsequently by the second set of computer simulations (comp. Table 3). The **control concept** selected for these investigations is based on **linear test table mechanics** (1b), on **nonlinear servohydraulic actuator dynamics** (2a) and on the servovalve model (4b). Standard transient test signals used in industry for vibration testing of space structures are used throughout these investigations and the valve limit frequency of the plant is set to $f_v$=1000 *Hz*. Each of the following variations of a controller parameter is counted with respect to the associated nominal value of this controller parameter which is identical to the associated plant parameter. Variations of the **servovalve amplification factor** $k_{vi}$ by 10 % in Figure 7b produce only slight modifications in the tracking behaviour of the system. Only variations of $k_{vi}$ of about 50 % or more have significant influence on the tracking behaviour (cf. 7c). The decoupling of the test table degrees of freedom is insensitive even with respect to large variations of $k_{vi}$. A variation of $k_{vi}$ simultaneously stands for a variation of various other **controller amplifications factors**. Variations of the **bulk modulus B** which stand for variations of the compressibility due to temperature variations and due to oil contaminations caused by air bubbles are shown in Figure 8. The tracking behaviour is only influenced slightly by variations of B of 50% (cf. 8b). Unrealistic variations of B by a factor four or more modify the tracking behaviour significantly according to Figure 8c. In Figure 9b the common **mass *m* of the test table and payload** is modified by a factor 1/2. This drastic mass variation again does not severely influence both, the tracking and the coupling behaviour of the system. Only unrealistic variations of $m$ by a factor four or more have significant influence on the system behaviour (cf. 9c). Variations of all **moments and products of inertia** by a factor 1/2 or 4 have no significant effect on the system behaviour (cf. 10b and cf. 10c). Variations of the **common center of gravity** $r_{CP}^L$ of the test facility and payload are shown in Figure 11. Simultaneous huge modifications of all components of the vector $r_{CP}^L$ from reference point P to center of gravity C (for fixed P) by a factor of 1/2 are shown in Figure 11b. They don't affect the tracking behaviour and only provide slight couplings among the test table degrees of freedom. Only unrealistic variations of $r_{CP}^L$ by a factor four or more show significant modifications of the transmission behaviour of the system (cf. 11c). The nominal plant model equations (5) did not include nonlinear **friction forces** due to dry friction in the hydraulic actuators and in the joints attached to those. As a consequence those friction forces have not been taken into account in the nonlinear control law design. Figure 12 shows simulation results including nonlinear friction forces of different absolute values in the plant model. Friction forces $F_R$ smaller than 1 kN don't provide relevant influences upon the system behaviour (cf. 12b). Friction forces of the order of $F_R$=3 kN don't affect the tracking behaviour. They introduce coupling effects of some test facility degrees of freedom (cf. 12c). Extreme high friction forces in the servo-hydraulic actuators are avoided in practice by using actuators with hydrostatic bearings. The above numerical sensitivity analysis of the control system demonstrates that the exact linearization approach is much less sensitive to plant parameter variations and to controller parameter variations than often predicted.

## CONCLUSION (5)

This paper presents different control designs for spatial multi-axis test facilities with six or eight servo-hydraulic actuators. The various control designs investigated are based on exact linearization techniques taking into account different combinations of linear and nonlinear plant component models. The system performance of the multi-axis test facility controlled by different control concepts has been tested in various computer simulations. In case of standard transient input signals a nonlinear controller design based on nonlinear servo-hydraulic actuator models and on linear test table mechanics is sufficient to achieve an excellent tracking and decoupling behaviour. The amount of the associated controller implementation is kept within acceptable limits. In case of large spatial transient motions of the test table with high velocities and accelerations, the control concept must take into account both, the nonlinear actuator dynamics and the nonlinear test table mechanics. This yields control algorithms of several hundred pages of length which require an enormous amount of hardware implementation work. Additional simulation results demonstrate considerable robustness of the closed loop system with respect to plant parameter variations and with respect to unmodeled servovalve dynamics in the controller.

## REFERENCES (6)


1. Hahn, H., Leimbach, K.-D.:. Nonlinear Control and Sensitivity Analysis of a Spatial Multi-Axis Servohydraulic Test Facility. Proceedings of the 32nd IEEE CDC, San Antonio 1993.

2. Hahn, H., Leimbach, K.-D. and Zhang, X.: Nonlinear Control of a Spatial Multi-Axis Servo-Hydraulic Test Facility. IFAC World Congress, Sydney 1993.

3. Hahn, H.: Theoretische Modellbildung Elektro-Servohydraulischer Antriebe, Lecture Notes, IMAT-Report 2, University of Kassel (ISSN 0939-8678), 1991.


**Table 1. Plant models included in the controller design.**

| *Test Signal Level* | models of mechanical components included in the control law design: linear (1b) | nonlinear (1a) |
|---|---|---|
| models of hydraulic components included in the control law design: linear (2b) | **Case I** ($\alpha_I$, $\beta_I$) *(low controller complexity)* | **Case III** ($\alpha_{III}$, $\beta_{III}$) *(high controller complexity)* |
| models of hydraulic components included in the control law design: nonlinear (2a) | **Case II** ($\alpha_{II}$, $\beta_{II}$) *(low controller complexity)* | **Case IV** ($\alpha_{IV}$, $\beta_{IV}$) *(extreme high controller complexity)* |

**Table 2. Computer simulation runs of the controlled servo-hydraulic test facility (with 6 servo-hydraulic actuators) using different control algorithms. The control algorithms are based on different plant component models and nominal test facility model data.**

| Simulation No. | Test signal | Control concepts | | | | Grading of the closed loop system performance | |
|---|---|---|---|---|---|---|---|
| | | Case I lin mech / lin hyd | Case II lin mech / nl hyd | Case III nl mech / lin hyd | Case IV nl mech / nl hyd | tracking | decoupling |
| 1a) | standard (Figure 2a) | Figure 2b | | | | - | - - |
| 1b) | | | | Figure 2c | | - | - - |
| 2a) | large (Figure 3a) | Figure 3b | | | | - - | - - |
| 2b) | | | | Figure 3c | | - - | - - |
| 3a) | standard (Figure 4a) | | Figure 4b | | | + + | + + |
| 3b) | | | | | Figure 4c | + + | + + |
| 4a) | large (Figure 5a) | | Figure 5b | | | - | - - |
| 4b) | | | | | Figure 5c | + + | + + |
| 5a) | standard (Figure 4a) | | Figure 6a $f_y$=1000 Hz | | | + + | + + |
| 5b) | | | Figure 6b $f_y$=300 Hz | | | + + | + + |
| 5c) | | | Figure 6c $f_y$=100 Hz | | | + | - |

lin mech (nl mech) : linear (nonlinear) model of the test table mechanics
lin hyd (nl hyd) : linear (nonlinear) model of the servo-hydraulic actuators

++: excellent tracking / decoupling behaviour
+: good tracking / decoupling behaviour
-: poor tracking / decoupling behaviour
- -: very poor tracking / decoupling behaviour

**Table 3. Computer simulation runs of the controlled servo-hydraulic test facility (with 8 servo-hydraulic actuators) for plant parameter variations using the control law (7b) and standard test signals.**

| Simulation No. | Test signal | Control concept | Variation | Variation factor | Figure | Grading of the closed loop system performance | |
|---|---|---|---|---|---|---|---|
| | | | | | | tracking | decoupling |
| 6a) | ↑ standard (Figure 2a) ↓ | ↑ Case II lin mech / nl hyd ↓ | servo valve gain factor $k_v$ | 1 (nominal value) | 7a | ++ | ++ |
| 6b) | | | | 0.9 | 7b | + | ++ |
| 6c) | | | | 1.5 | 7c | + | + |
| 7a) | | | bulk modulus $B$ | 1 (nominal value) | 8a | ++ | ++ |
| 7b) | | | | 0.5 | 8b | + | + |
| 7c) | | | | 4 | 8c | - | + |
| 8a) | | | common mass of test table and payload $m$ | 1 (nominal value) | 9a | ++ | ++ |
| 8b) | | | | 0.5 | 9b | + | + |
| 8c) | | | | 4 | 9c | -- | -- |
| 9a) | | | inertia tensor $J$ | 1 (nominal value) | 10a | ++ | ++ |
| 9b) | | | | 0.5 | 10b | ++ | ++ |
| 9c) | | | | 4 | 10c | ++ | ++ |
| 10a) | | | center of gravity of test table and payload $r_{CP}^L$ | 1 (nominal value) | 11a | ++ | ++ |
| 10b) | | | | 0.5 | 11b | ++ | + |
| 10c) | | | | 4 | 11c | - | -- |
| 11a) | | | dry friction force within the actuators $F_R$ | $F_R$=0 kN | 12a | ++ | ++ |
| 11b) | | | | $F_R$=1 kN | 12b | ++ | + |
| 11c) | | | | $F_R$=3 kN | 12c | ++ | - |

lin mech : linear model of the test table mechanics
nl hyd : nonlinear model of the servo-hydraulic actuators

++ : excellent tracking / decoupling behaviour
+ : good tracking / decoupling behaviour
- : poor tracking / decoupling behaviour
-- : very poor tracking / decoupling behaviour

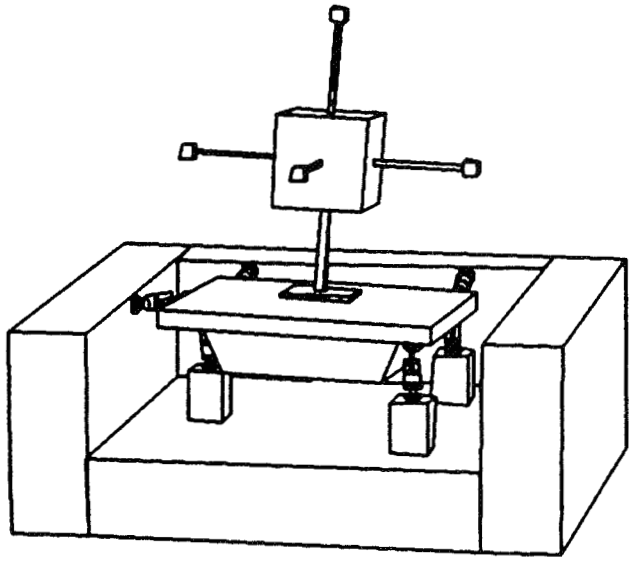

**Figure 1: Computer drawing of a multi-axis servo-hydraulic test facility.**

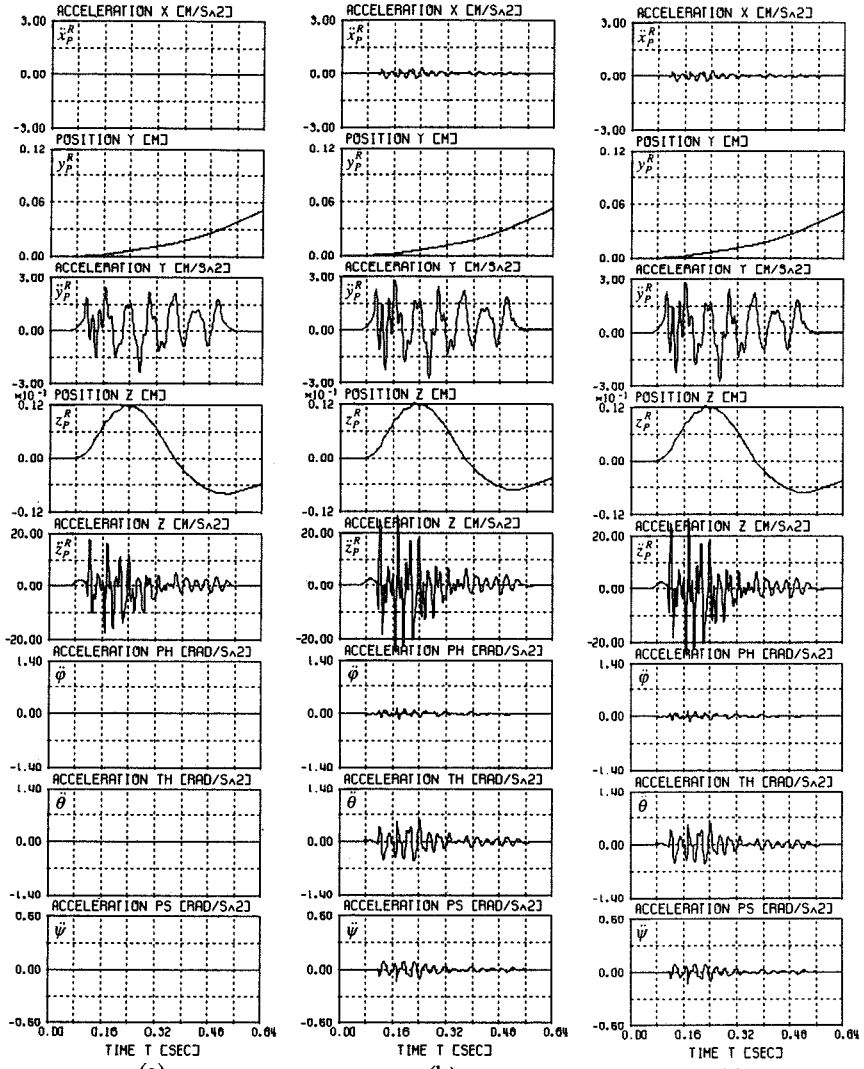


(a) (b) (c)

Figure 2: Computer simulation results of the test facility degrees of freedom using different control concepts of Table 1:

(a) standard set point signals used in industry,
(b) control concept based on Case I (comp. Table 1 and Table 2),
(c) control concept based on Case III (comp. Table 1 and Table 2).

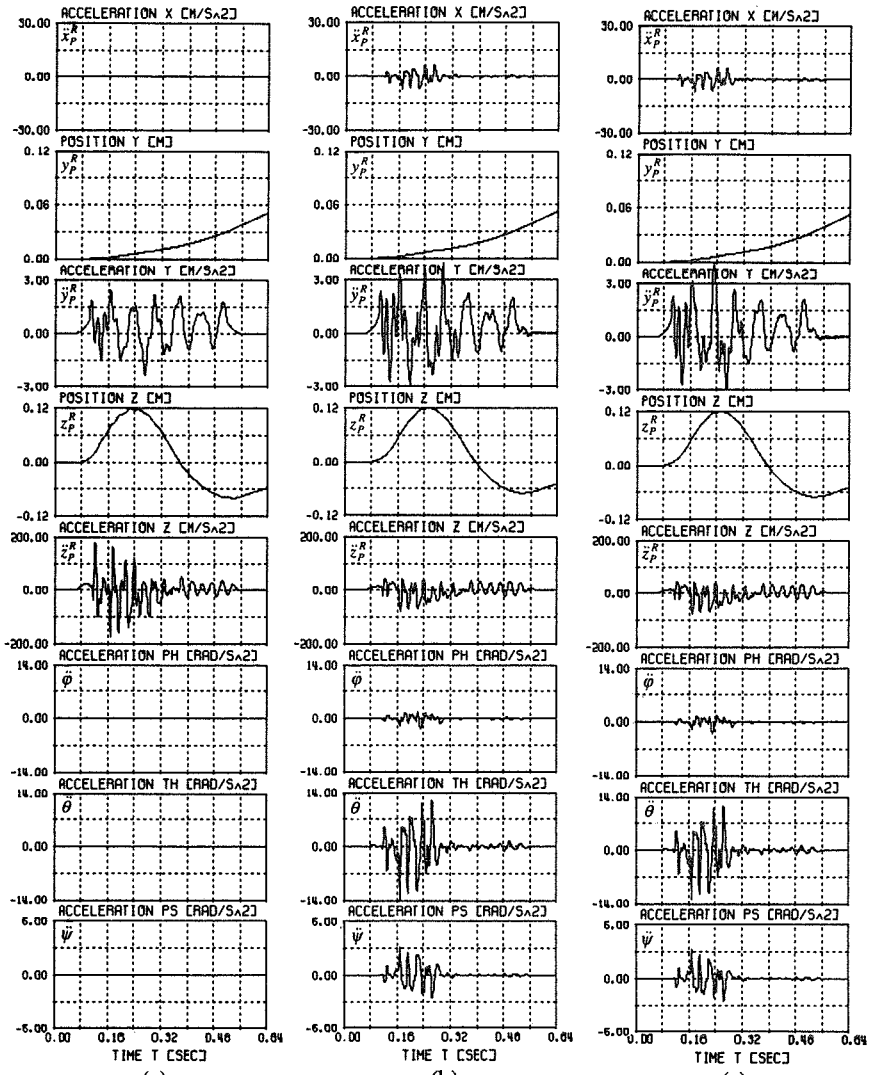


(a) (b) (c)

Figure 3: Computer simulation results of the test facility degrees of freedom using different control concepts of Table 1:

(a) large set point signals,
(b) control concept based on Case I (comp. Table 1 and Table 2),
(c) control concept based on Case III (comp. Table 1 and Table 2).

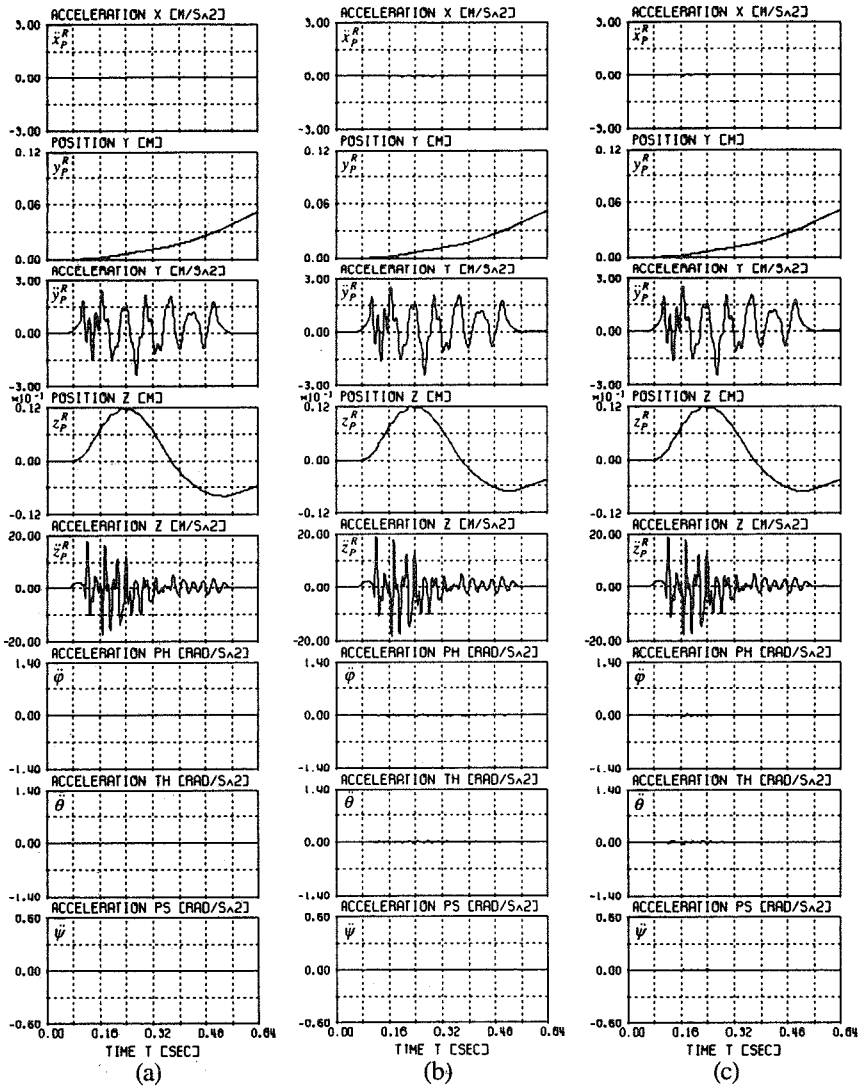


Figure 4: Computer simulation results of the test facility degrees of freedom using different control concepts of Table 1:

(a) standard set point signals used in industry,
(b) control concept based on Case II (comp. Table 1 and Table 2),
(c) control concept based on Case IV (comp. Table 1 and Table 2).

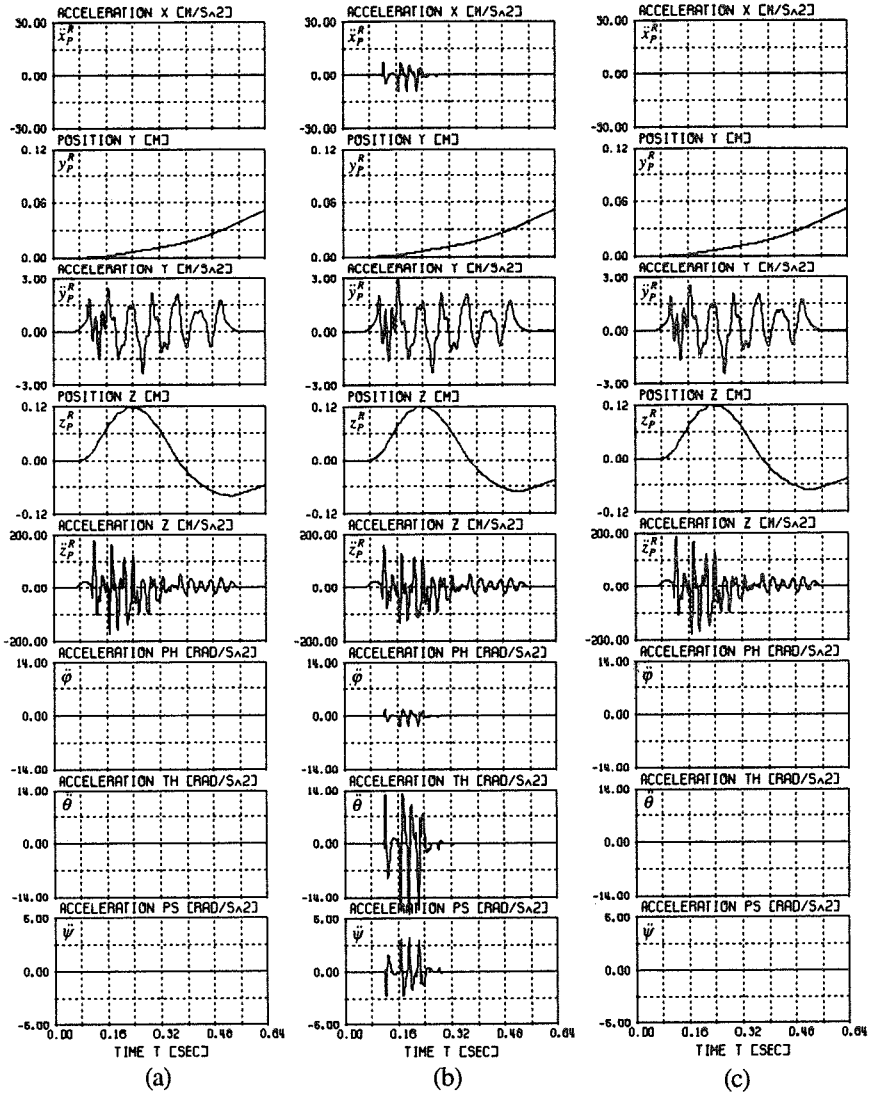


Figure 5: Computer simulation results of the test facility degrees of freedom using different control concepts of Table 1:

(a) large set point signals,
(b) control concept based on Case II (comp. Table 1 and Table 2),
(c) control concept based on Case IV (comp. Table 1 and Table 2).

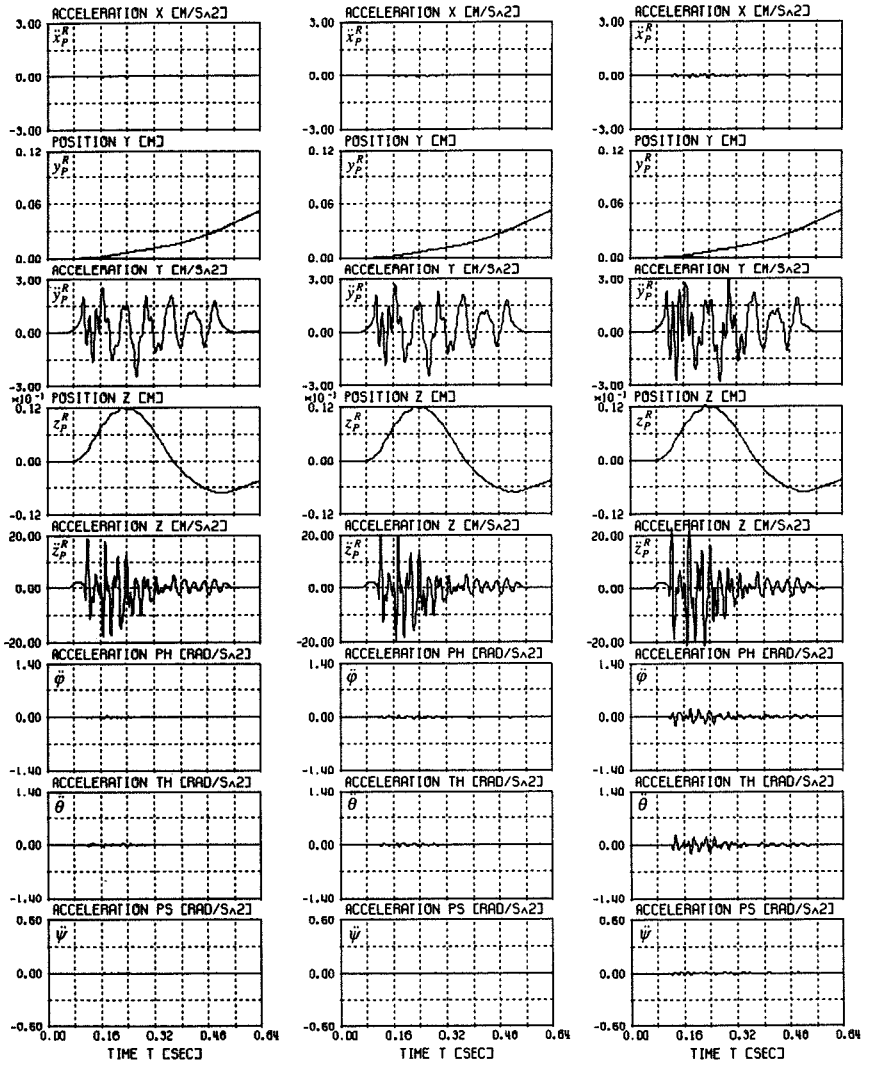


(a) (b) (c)

Figure 6: Computer simulation results of the test facility degrees of freedom taking into account unmodeled valve dynamics $f_v$:

(a) $f_v$ =1000 Hz (control concept of Case II, Table 1),
(b) $f_v$ =300 Hz (control concept of Case II, Table 1),
(c) $f_v$ =100 Hz (control concept of Case II, Table 1).

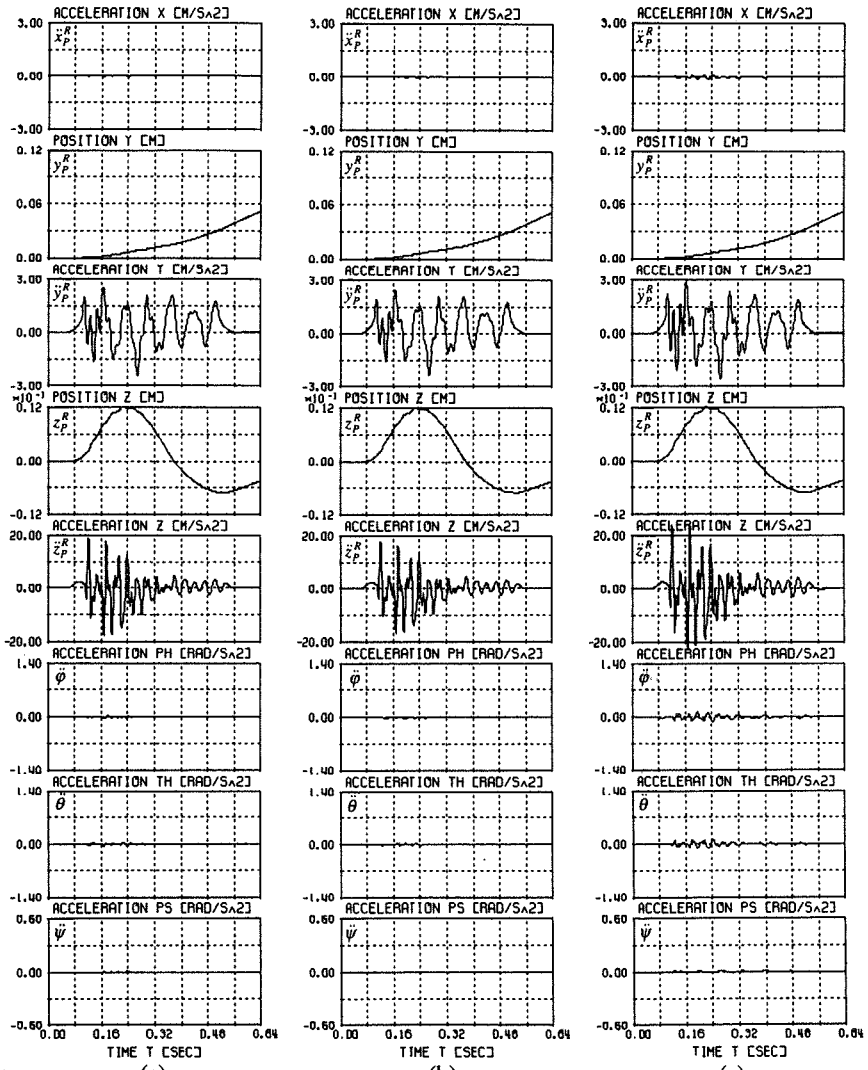


(a) (b) (c)

Figure 7: Computer simulation results of the test facility degrees of freedom taking into account plant parameter variations of the servovalve gains $k_{vi}$ (control concept of Case II, Table 1):

(a) nominal values of $k_{vi}$ (comp.Table 3),
(b) variation of $k_{vi}$ by a factor of 0.9 (comp.Table 3),
(c) variation of $k_{vi}$ by a factor of 1.5 (comp. Table 3).

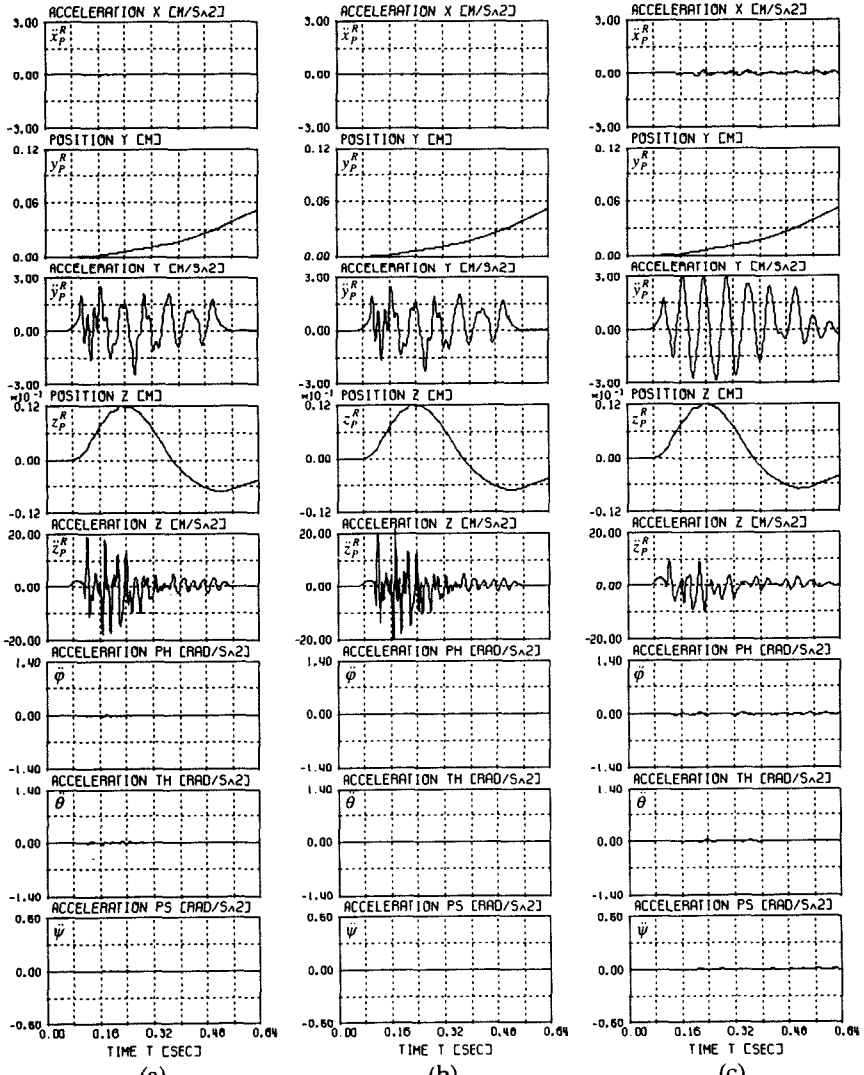


Figure 8: Computer simulation results of the test facility degrees of freedom taking into account plant parameter variations of the bulk modulus B (control concept of Case II, Table 1):

(a) nominal value of B (comp. Table 3),
(b) variation of B by a factor of 0.5 (comp.Table 3),
(c) variation of B by a factor of 4 (comp. Table 3).

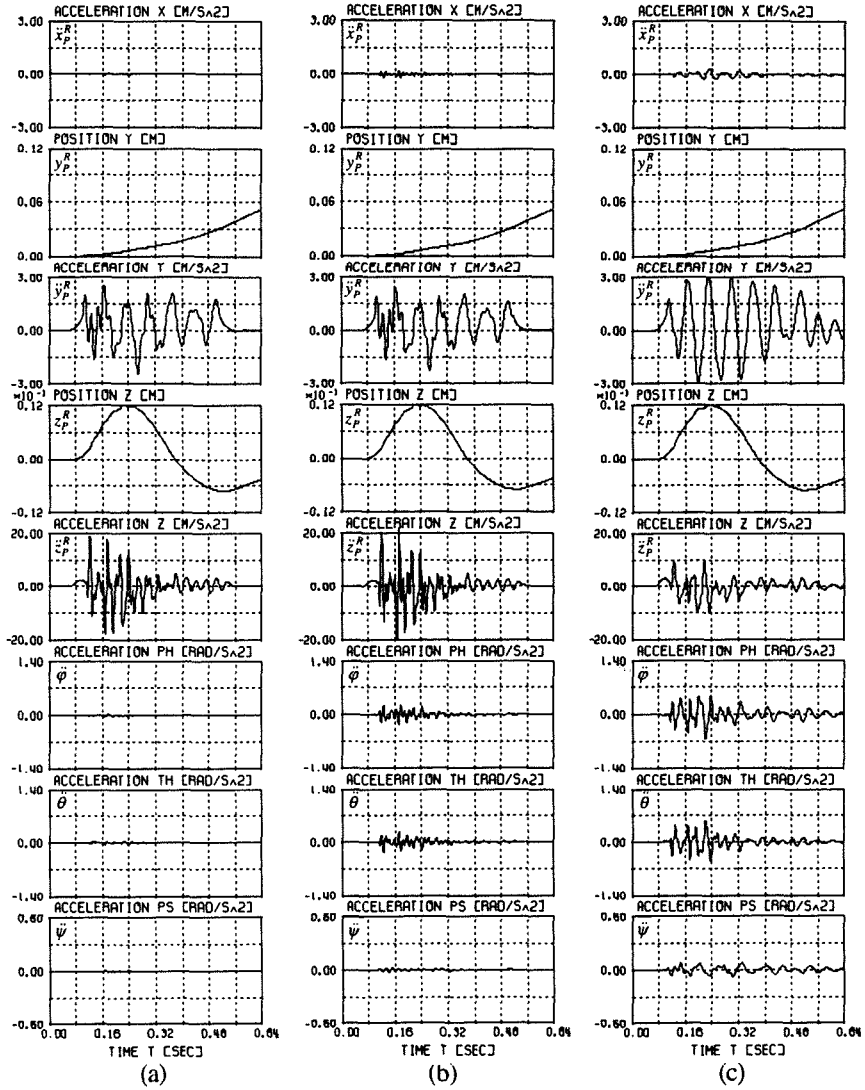


Figure 9: Computer simulation results of the test facility degrees of freedom taking into account plant parameter variations of the common mass m of the test table and payload (control concept of Case II, Table 1):

(a) nominal value of m (comp. Table 3),
(b) variation of m by a factor of 0.5 (comp.Table 3),
(c) variation of m by a factor of 4 (comp. Table 3).

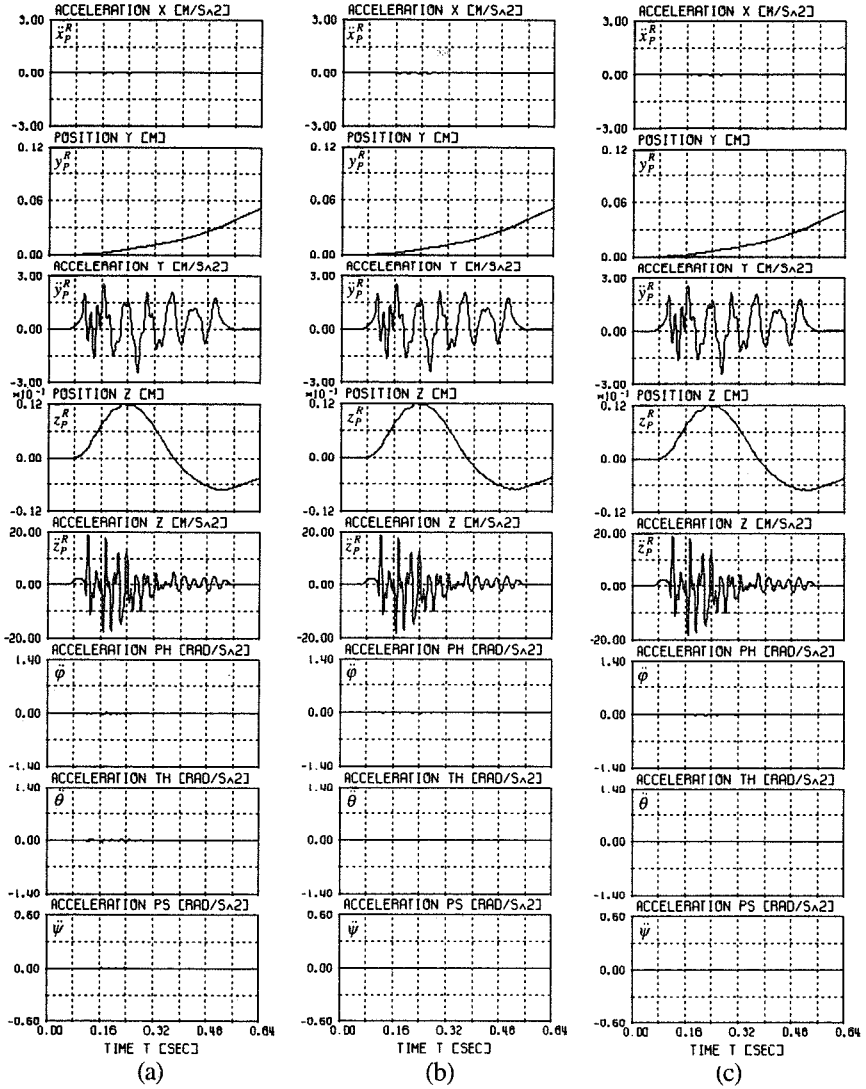


(a) (b) (c)

Figure 10: Computer simulation results of the test facility degrees of freedom taking into account plant parameter variations of the elements of the inertia tensor J (control concept of Case II, Table 1):

(a) nominal values in J (comp. Table 3),
(b) variation of the elements in J by a factor of 0.5 (comp. Table 3),
(c) variation of the elements in J by a factor of 4 (comp. Table 3).

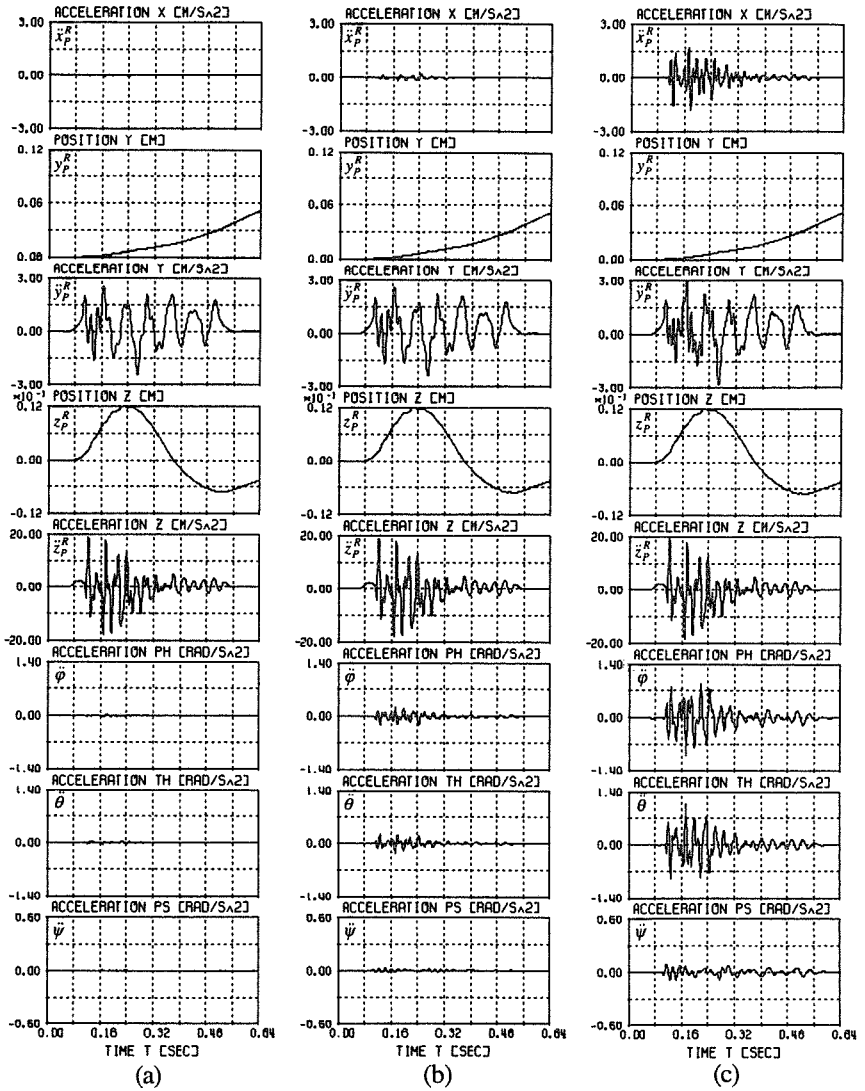


(a) (b) (c)

Figure 11: Computer simulation results of the test facility degrees of freedom taking into account plant parameter variations of the common center of gravity $r_{CP}^{L}$ (control concept of Case II, Table 1):

(a) nominal value of $r_{CP}^{L}$ (comp. Table 3),
(b) variation of $r_{CP}^{L}$ by a factor of 0.5 (comp. Table 3),
(c) variation of $r_{CP}^{L}$ by a factor of 4 (comp. Table 3).

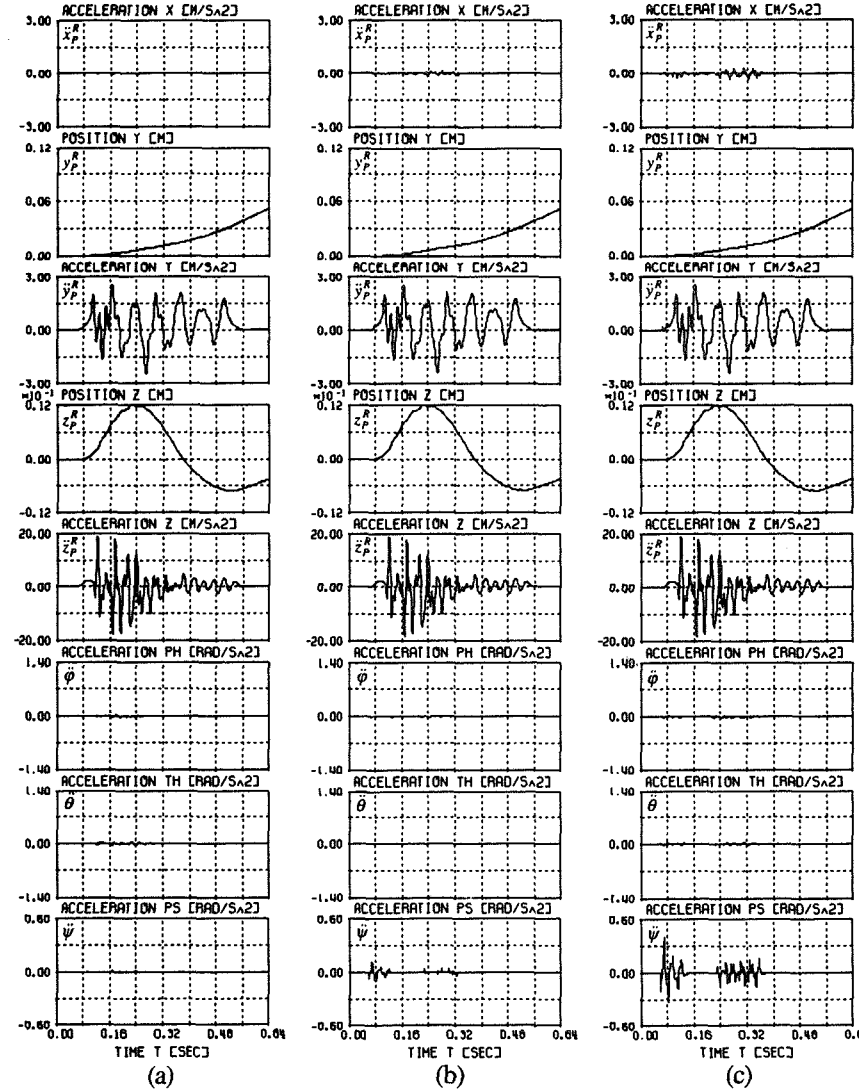


Figure 12: Computer simulation results of the test facility degrees of freedom taking into account dry friction forces $F_R$ within the actuators and the joints attached to those (control concept of Case II, Table 1):

(a) dry friction force $F_R$= 0 kN (comp. Table 3),
(b) dry friction force $F_R$= 1 kN (comp. Table 3),
(c) dry friction force $F_R$= 3 kN (comp. Table 3).

# THERMOACOUSTIC ENVIRONMENTS TO SIMULATE REENTRY CONDITIONS *

Gerhard Bayerdörfer

Industrieanlagen-Betriebsgesellschaft mbH
85521 Ottobrunn/Germany

## ABSTRACT

Aerothermal environments as encountered during the reentry of spaceplanes or during the cruise of hypersonic aircrafts represent complex loading conditions for the external structures of those vehicles. In order to shield against the aerodynamic heating a special Thermal Protection System (TPS) is required which is designed as a light weight structure to reduce the weight penalty.TPS is therefore vulnerable to vibroacoustic fatigue caused by the pressure fluctuations of the environment (1), (2).

Because of the complex interactions between the loading forces and the resulting structural response which make an analytical treatment difficult and in order to provide means for fatigue testing IABG has designed and built a thermoacoustic facility which recently became operational. The facility is capable to produce surface temperatures up to 1.300 °C at sound pressure levels up to 160 dB. This paper describes the design of the facility, some operational test work it also deals with problems associated with the facility instrumentation.

## INTRODUCTION

Thermoacoustic environments are composed of vibroacoustic and thermal loadings of varying severity. Depending on the mission of the vehicle the nature of these environments may be different. A general survey is as follows

| MISSION PHASE | ORIGIN | SEVERITY |
|---|---|---|
| LIFT-OFF LAUNCHER | PROPULSION SYSTEM | |
| | Radiated Noise | severe |
| | Radiated Heat | moderate |
| TRANSONIC LAUNCHER | AERODYNAMIC EFFECTS | |
| | Separated Flows | severe |
| | Aerodynamic Heating | moderate |
| CRUISE OF HYPERSONIC VEHICLES | AERODYNAMIC EFFECTS | |
| | Boundary Layer Noise | remarkable |
| | Aerodynamic Heating | severe |
| REENTRY OF SPACE-PLANES | AERODYNAMIC EFFECTS | |
| | Boundary L./Separated Fl. | remarkable |
| | Aerodynamic Heating | severe |

The objective was to simulate these environments with respect to their acoustic and thermal components. The approach taken consisted in the use of an excisting Progressive Wave Tube (PWT) to generate the acoustic loading with the addition of a specific heating system.

* *Sponsored by Bundesminister für Forschung und Technologie (BMFT)*

## FACILITY DESIGN

The selection of an appropriate heating system is a crucial point because of the required compatibility with the acoustic environment. A comparison between the often used quartz lamps and a flame system is given below

| | QUARTZ LAMPS | FLAME SYSTEM |
|---|---|---|
| CONTROL | GOOD | MODERATE |
| SURFACE TEMP: | max. 560 °C | > 1.300 °C |
| FATIGUE LIFE | POOR | NO PROBLEMS |
| OPERATION | EXPENSIVE | CHEAP |

Mainly because of the higher surface temperatures and the simpler overall design it was decided to go for the flame system.

Fig. 1 shows an array of nine burners mounted into the PWT. Each burner is clamped on a ball pivot to allow individual adjustment. The burners are driven with Methan ($CH_4$) and Oxygen ($O_2$) whereby each burner has its separate control valves. Flame sensors on top of each row control correct burning, in case of irregularities the relevant valves will shut down the gas supply. Spark plugs for each row allow ignition so that the flame unit can be fully remote controlled.

This flame unit can be built into a reverberation chamber (Fig. 2) or installed into the PWT; the relevant data of the resulting facilities are as follows:

| | REVERBER. CHAMBER | PROGR. WAVE TUBE |
|---|---|---|
| SIZE/TEST SECT. | 206 $m^3$ | 0,8 x 1,2 $m^2$ |
| OASPL at R.T. | max. 155 dB | max. 160 dB |
| FREQUENCY R. | 100 Hz - 10 kHz | 50 Hz - 10 kHz |
| HEAT FLUX | max. 100 $W/cm^2$ | max. 100 $W/cm^2$ |
| SURFACE TEMP: | max. 1.300 °C | max. 1.300 °C |

OASPL Overall Sound Pressure Level
RT Room Temperature

No modifications were necessary when installing the flame system into the reverberation chamber. Due to the extensive air flow from the noise generators the temperature increase inside the reverberation chamber is very moderate. As the flame unit is placed in the middle of the chamber the walls are not effected by the heat.

The PWT, however, had to be substantially modified. Burning a flame system with a heat flux of 100 $W/cm^2$ inside a PWT is only possible if the basic structure is shielded against this heat input.

Fig. 9 shows the cross section of the thermoacoustic PWT. By insertion of an inner tunnel made of stainless steel the basic structure is protected against the heat. The duct which is formed by these two elements is subdivided into various channels. An air distribution system feeds these channels with predetermined massflows to provide the necessary cooling. The area around the test section which naturally has the highest temperatures is intensively cooled by the highest mass flow whereas the rear side with much lower temperatures

obtains only reduced cooling air. The total cooling air is delivered by the same compressor which also feeds the noise generators.

The flame heating system is mounted into a window of the PWT so that the flames impinge directly on the test article which is just opposite. Each burner can be adjusted individually so that the total test section of 0,8 x 1,2 $m^2$ is uniformally heated.

Mounting of the test specimen into the thermoacoustic PWT needs a dedicated design. The specimen shall be supported as for its intended use and care should be taken to allow for thermal expansion. If necessary the mounting frame can be additionally cooled with water.

## OPERATIONAL TESTS

In order to illustrate the operation of the facilities two different tests which have been recently performed are described.

### ARIANE 5 Tank Insulation

The European launcher ARIANE 5 presently in the final development stage is depicted in Fig. 3. The tank marked with an arrow contains Helium and is covered with flexible insulation material to protect it against the heat radiated by the engine of the cryogenic main stage. The insulation is equally exposed to the high noise levels at lift-off and to turbulent flows at transonic speeds. In order to verify that the surface of the tank structure will not be subjected to temperatures above 80 °C as well as to qualify the insulation with respect to the turbulent pressure field a thermoacoustic test was performed.

One half of the tank structure partially covered with a sample of the insulation material and the rest covered with ordinary fire resistant carpets was placed inside the reverberation chamber opposite the flame heating system (Fig. 4). Four control microphones were positioned around this test set-up, their locations being well outside the hot zone. In addition a probe microphone was installed for direct measure of the dynamic pressures on the surface of the insulation material inside the hot zone.

The readings of these microphones are presented in Fig. 5. The upper part contains the spectra as measured under RT. There are certain differences in the frequencies up to 315 Hz and beyond 400 Hz, however, the OASPL-value is the same for the probe microphone and the average out of the four control microphones.

Looking at the lower part it is obvious that the spectra obtained during the flame heating process differ substantially. Whereas the shape of the averaged control microphone spectrum is not very much affected, the probe microphone indicates substantially lower noise levels. Due to the lower density of the hot gas medium the sound pressure levels are considerably reduced leading to an OASPL-value which is 6 dB lower compared with RT.

The temperature curves as monitored by thermocouples are displayed in Fig. 6. The requirement was to achieve 660 °C on the surface of the insulation material over a period of four minutes. The upper part shows that this requirement was reasonable good fulfilled. The lower part gives the temperature rise of the tank shell (below the insulation). In this case the temperature did not exceed 80 °C as specified.

### TPS for Advanced Launcher

In the framework of a study sponsored by ESTEC (3) a multiwall TPS-panel was developed by DASA which was used as a candidate for a thermoacoustic test. The TPS-panel is considered to be taken from a reference vehicle (Fig. 7), the arrow indicating the reference location.

Critical loadings occur during separation of the two stages with 700 °C surface temperature and sound pressure levels up to 165 dB and during reentry of the upper stage with 1.000 °C surface temperature and an OASPL = 140 dB. With the objective to simulate these environments the multiwall panel was installed into the thermoacoustic PWT according to Fig. 8.

Fig. 10 shows the facility with the burners alighted, the test window, however, is still open. In the next step the PWT will be closed and the airflow started. Temperature rise on the panel surface will be observed until the specified values are reached. Finally the noise generators are activated over a predetermined time duration.

## FACILITY INSTRUMENTATION

The instrumentation of the facility as shown in Fig.9 is required to monitor the environmental loading conditions as well as the response of the test specimen. However, there are some limitations of current instrumentation which needs to take special provisions.

In order to control the characteristics of the exciting pressure field acting on the surface of the test specimen microphones should be placed in the vicinity of the test article. Apart from very exotic devices no transducers are known which are capable to work in a temperature environment beyond 1.000 °C.

With condensor microphones commonly used the temperature environment is limited to about 60 °C. The approach therefore is to design a probe capable to withstand the high temperatures at the hot end which leeds the dynamic pressures to the sensing capsule where the temperatures are reduced to a level which allows the application of the usual microphone equipment. Such a probe needs extensive calibration testing to take care of the transfer functions. This is a field where current investigations are under way.

Apart from the probe microphones reference microphones are located upstream of the hot section to control the noise output of the generators. Taking into account the change of density of the medium and also the change in speed of sound a first order estimate is possible between the readings of the reference microphones and the characteristics of the dynamic pressures inside the hot zone.

Temperature measurements are presently taken by thermocouples which are directly applied to the exposed surface of the test article. This method is still more reliable and accurate compared with radiation measurements because the latter are heavily disturbed by the open flames. Development tests are directed towards the isolation of the specimen radiated IR-part against the flame radiation.

As far as the dynamic response of the test article is concerned a laser vibrometer can deliver complete mode patterns even under the extrem conditions of flame heating. Direct strain measurements, however, are not feasable in such a hostile environment.

For the purpose of overall control a TV-camera is employed which checks not only the correct flame burning but also provides information about possible desintegration of the test article during noise exposure.

## References

1. Rucker, C.E., Grandle, R.E., "Testing of Space Shuttle Thermal Protection System Panels under simulated Reentry Thermoacoustic Conditions", Seventh Space Simulation Conference, Los Angeles 1973

2. Bayerdörfer, G., "Development of a Thermoacoustic Test Facility", ESA-Conference „Spacecraft Structures and Mechanical Testing", October 1988

3. *Study on Thermal Protection for Advanced Launchers,* ESA/ESTEC-Presentation prepared by DASA, ALENIA, ARCS and IABG, February 1994

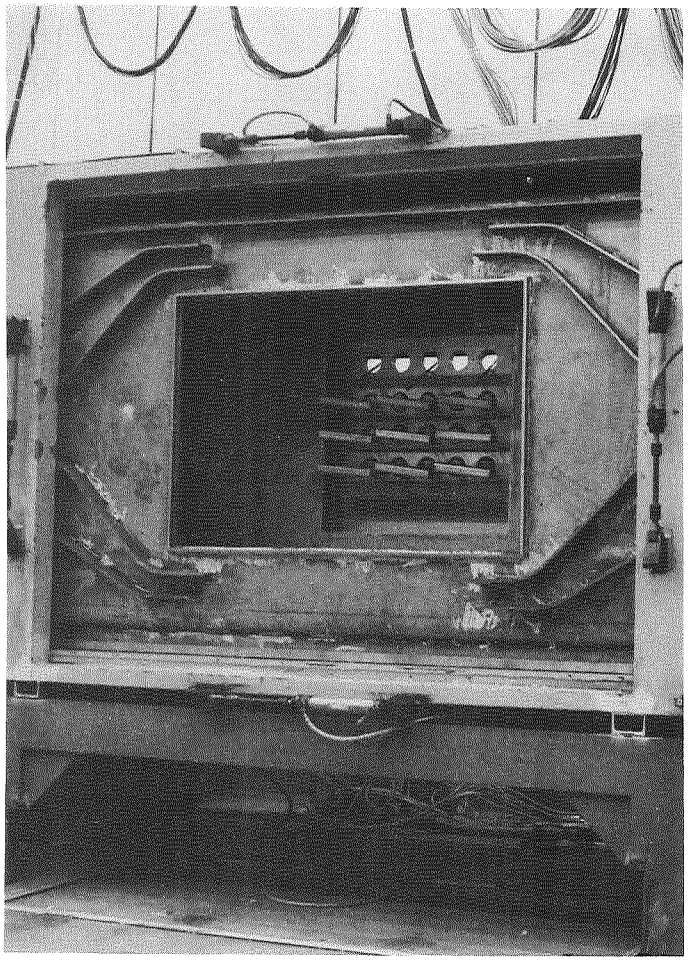

Fig. 1: Burners mounted in PWT

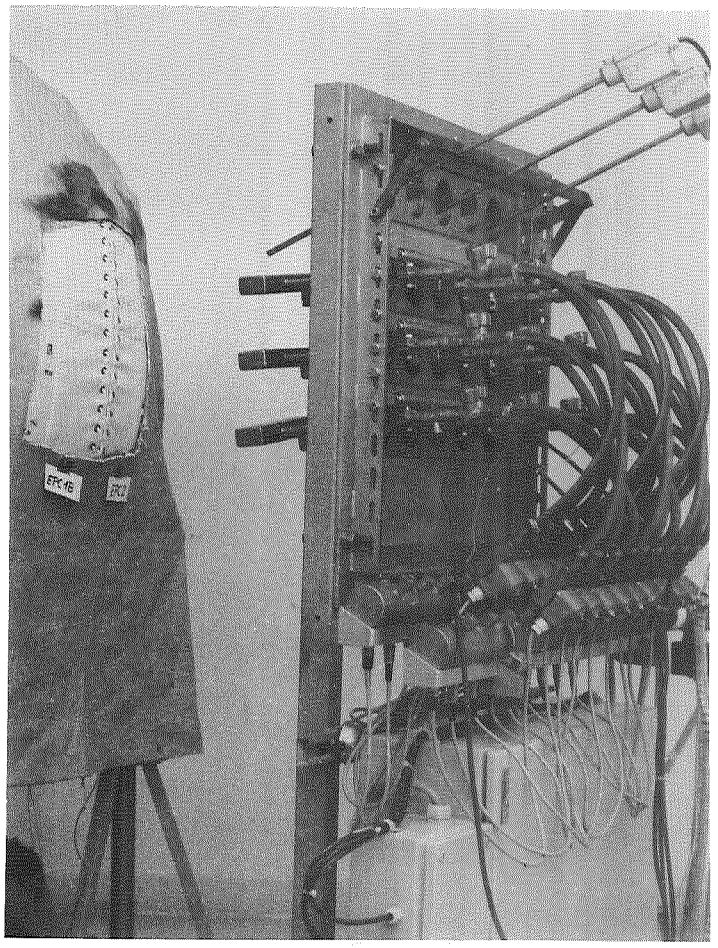

Fig. 2: Burners mounted in Reverberation Chamber

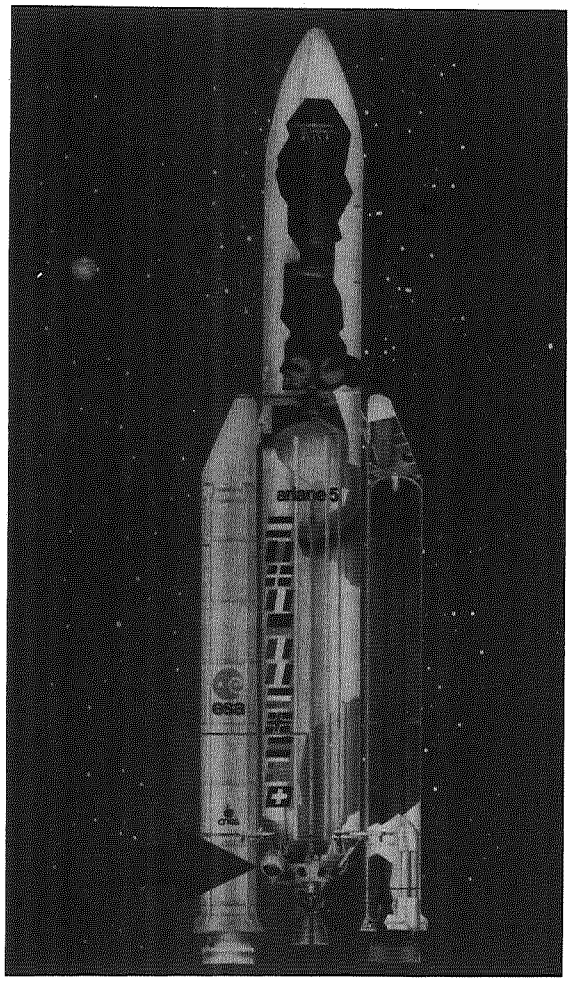


Fig. 3: ARIANE 5-Launcher

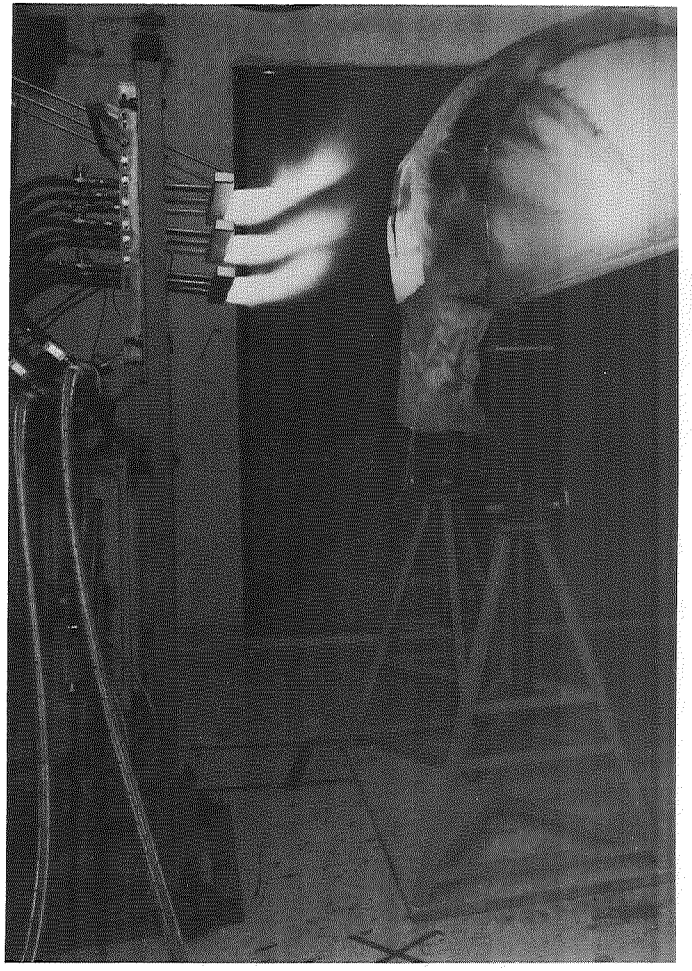

Fig. 4: Thermoacoustic Test
inside Reverberation Chamber

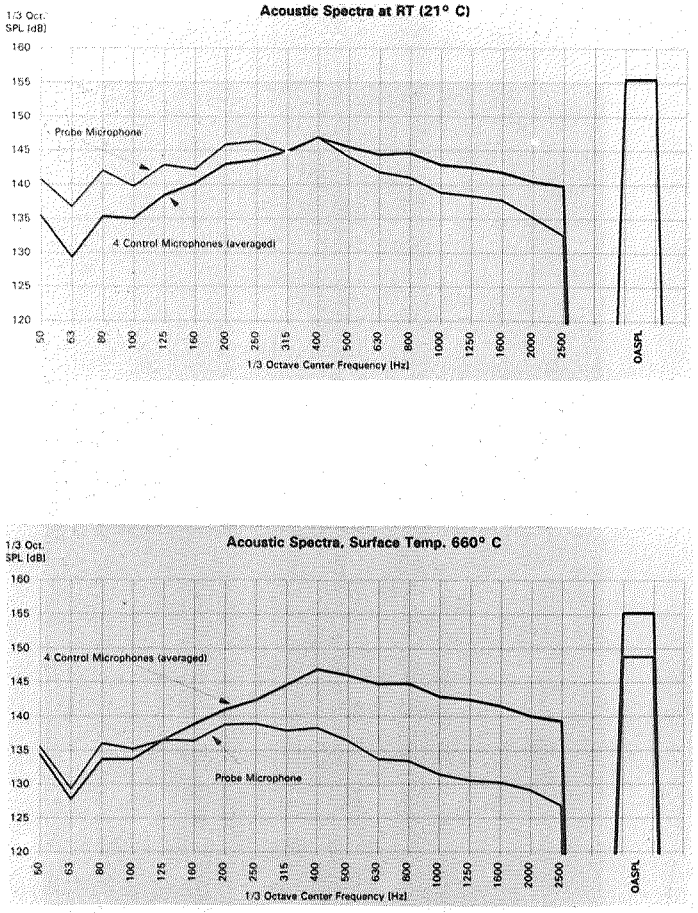


Fig. 5: Acoustic Spectra

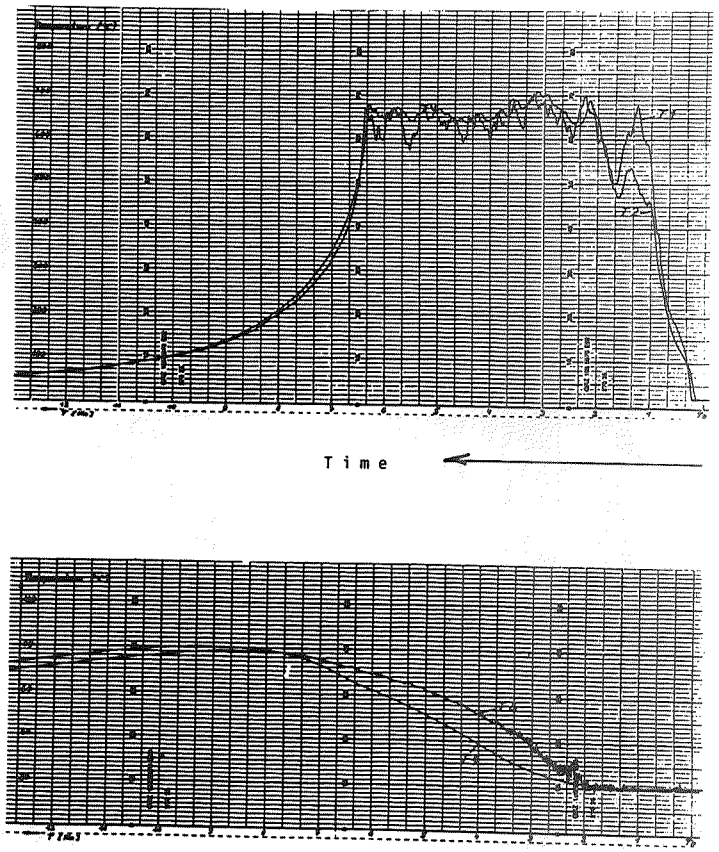


Fig. 6: Temperature Curves

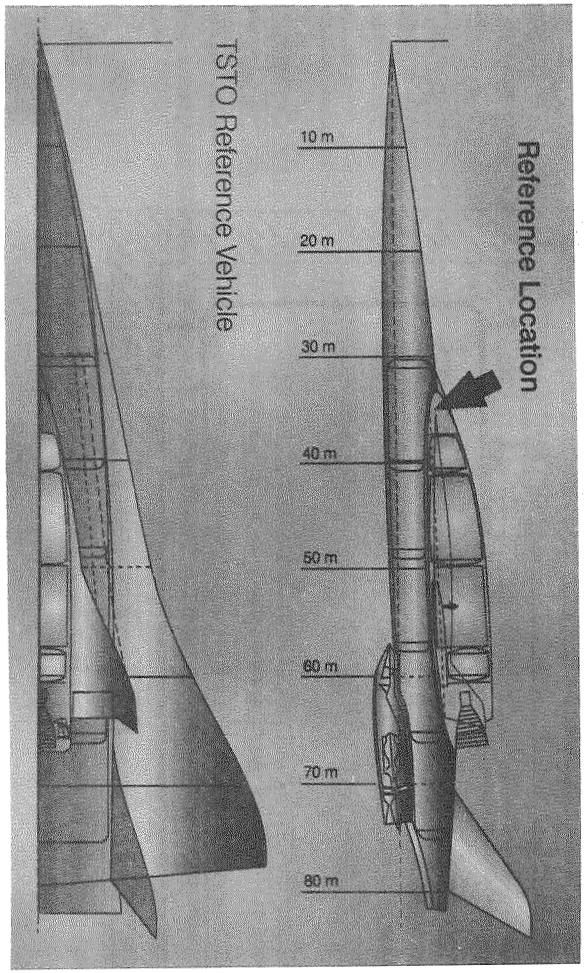


Fig. 7: Reference Vehicle

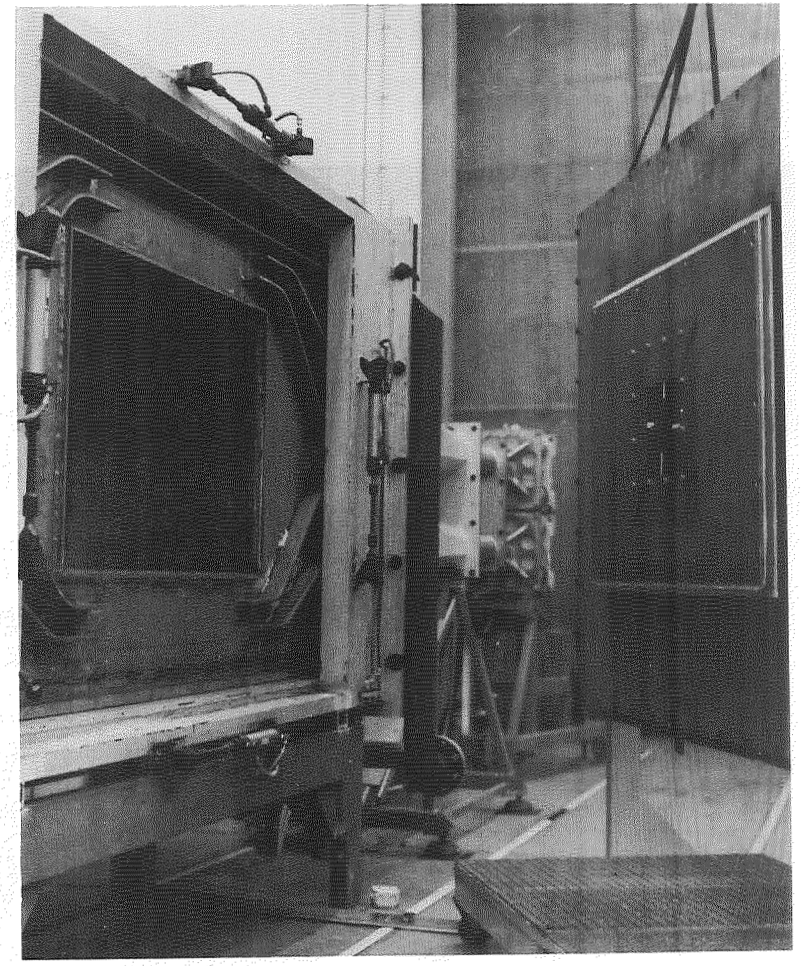

Fig. 8: TPS-Panel built into PWT

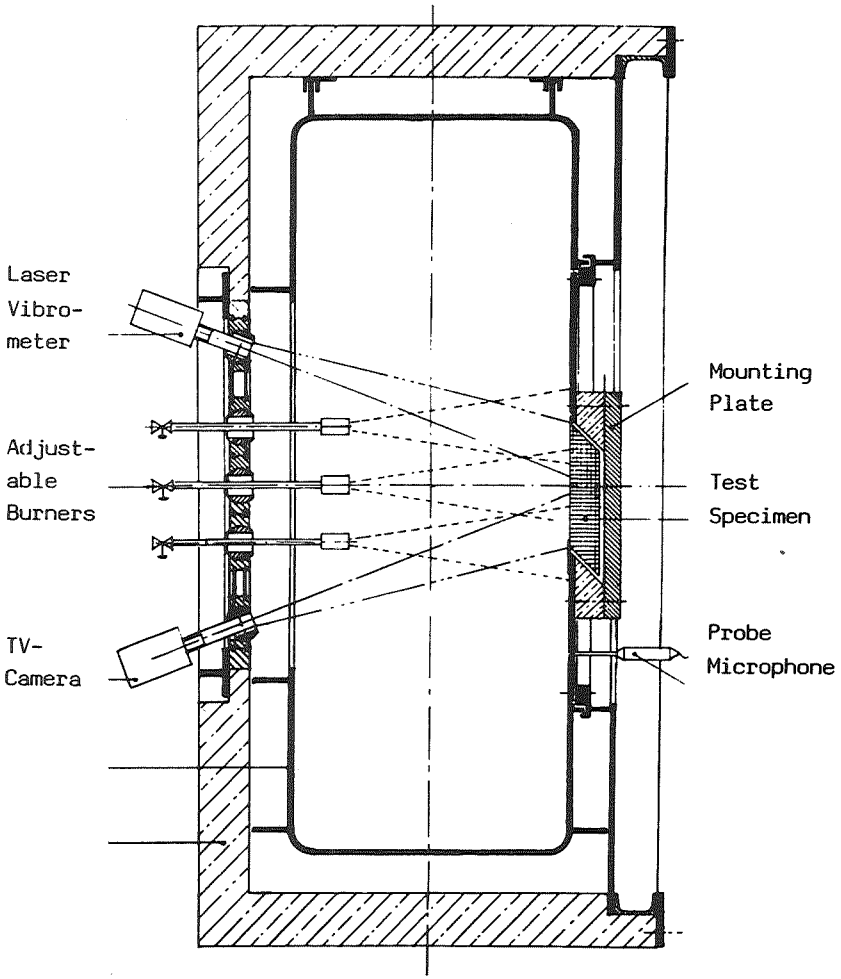


Fig. 9: Thermoacoustic PWT, Instrumentation

Fig. 10: Burners alighted in PWT

# THE AEDC AEROSPACE CHAMBER 7V
## An Advanced Test Capability for Infrared Surveillance and Seeker Sensors*

W. R. Simpson
Calspan Corporation/AEDC Division
Arnold Engineering Development Center
Arnold AFB, TN 37389-6501

## ABSTRACT

An advanced sensor test capability is now operational at the Air Force Arnold Engineering Development Center (AEDC) for calibration and performance characterization of infrared sensors. This facility, known as the 7V, is part of a broad range of test capabilities under development at AEDC to provide complete ground test support to the sensor community for large-aperture surveillance sensors and kinetic kill interceptors. The 7V is a state-of-the-art cryo/vacuum facility providing calibration and mission simulation against space backgrounds. Key features of the facility include high-fidelity scene simulation with precision track accuracy and *in-situ* target monitoring, diffraction limited optical system, NIST traceable broadband and spectral radiometric calibration, outstanding jitter control, environmental systems for 20 K, high-vacuum, low-background simulation, and an advanced data acquisition system.

## INTRODUCTION

AEDC, located on the Arnold Air Force Base, TN, offers a wide range of advanced aerospace ground test capabilities for the DoD and civilian community. The Space Test Complex, shown in Fig. 1, provides a number of space simulation facilities, including a low-background infrared sensor test capability in the 7V Chamber.

### Developing a Strategy for Ground Testing Infrared Sensors

To keep up with advances in the design of surveillance sensors and kinetic energy weapon (KEW) interceptors, new test capability must be developed which utilizes the many advantages of ground testing. Some of these advantages include:

- Shortened system development time and lowered risk with flight tests;
- Cheaper development and test costs;
- Simulation of some test conditions on the ground that are impractical or impossible on orbit;
- Easy separation of test parameters which can be varied quickly, reproduced accurately, and repeated as many times as necessary to establish good statistics on test data; and
- Good access to the sensor or test equipment to diagnose problems rapidly and resume testing in a timely and cost-effective manner.

Despite these advantages, ground testing is limited by programmatic constraints and available technology to fully simulate real-world conditions. Limitations include number of objects and complexity of backgrounds, availability of optics to cover large aperture/large field of view sensors, and ability to simulate zero gravity. Compromises must be made and conflicting requirements of the real world with the limitations of the test world must be resolved. The strategy to accomplish this difficult job is defined as test methodology. Its goal is to design the test capability to meet mission needs with innovative test techniques which simulate the real world with high fidelity, but within the constraints of available technology, cost, schedule, and risk.

### Test Capability at AEDC to Support Sensor Development

Since the late 1960's, 35 IR sensor tests have been conducted in the 7V (ref. 1). However, the increasing complexity in mission needs made it necessary to upgrade this facility and augment it with other test capabilities to support advanced sensor development. Seven years ago AEDC initiated a comprehensive plan (ref. 2) to improve its sensor test capabilities to support development of surveillance and KEW systems. This plan, outlined in Fig. 2, is designed to address test needs during all phases of sensor development. In the initial stages, component testing at the focal plane detector chip or module level is essential to

*The research reported herein was performed by the Arnold Engineering Development Center (AEDC), Air Force Materiel Command. Work and analysis for this research were done by personnel of Calspan Corporation/AEDC Division, technical services contractor for the AEDC aerospace flight dynamics facilities. Further reproduction is authorized to satisfy needs of the U. S. Government.

understanding basic detector performance and evaluating producibility issues. This capability is provided in AEDC's Focal Plane Characterization Chamber, which has been involved over the last 5 years in a number of detector development programs. Once the basic module design is proven, the next step in developing a sensor system is integration of the modules into a complete focal plane assembly with data processors and high-level algorithms. Test issues at this step are addressed in the Focal Plane Array Test Chamber, which uses a laser-based scene generation system to "paint" complex scenes directly on the focal plane. The final step in sensor development integrates the focal plane with its complete mission-level processors and algorithms with the sensor telescope, scan gimbals, and other interfacing systems. Two facilities are available at AEDC to meet system-level test needs: the 7V Chamber, operational since February 1994 for basic sensor calibration and characterization; and the 10V Chamber, scheduled for completion in 1996 for advanced mission simulation. This paper describes the 7V Facility which is shown in Fig. 3.

## TEST METHODOLOGY AND REQUIREMENTS

Requirements for the 7V flow out of a test methodology developed at AEDC to meet test demands for advanced sensor systems based on four premises:

- Test facility requirements must be based on a thorough understanding of mission needs, performance issues, threat definition, and sensor operational environments. Simulations must address critical issues which drive sensor designs, stress their performance, and ultimately dictate mission success. Furthermore, the facility must be versatile considering a range of test articles designed for a number of mission objectives.
- To evaluate critical test issues in the most timely and practical manner, it is necessary to test early and often through the sensor development process. Evaluation of specific issues are more cost effective at the component level than at higher system levels. An example might be access to analog signals from a focal plane which might be impossible at the sensor level unless the designer considered system level testability. This approach simplifies requirements for a given facility by limiting its objectives to what is practical and necessary. However, it requires program involvement early in the development process to include testability in the sensor design and ground testing in the overall program schedule.
- The test facility must be designed such that individual simulation systems are modular. This allows test needs to be satisfied in the most timely and economical manner by choosing equipment for given test objectives without major modification to the test configuration.
- At the full sensor system level, it is critical to maintain fidelity of the simulations while recognizing the practical constraints outlined above. This is accomplished in the 7V by breaking the overall mission into testable phases where parameters are separated for the test objective under consideration. The simulations are set up in a piecewise real time for the particular phase under test with sufficient overlap for continuity in reconstructing mission timelines.

The methodology described above defines test needs necessary to evaluate sensor performance against projected mission issues; matches the test facility capability to critical sensor design parameters; and identifies the simulations, phases, and timing necessary for good fidelity to the real world. Functional requirements for the 7V are defined from this methodology in five key capabilities defined in Table 1. The technical capabilities of the 7V Facility which fulfill these high-level functional requirements are outlined in Table 2. As indicated, most of these were verified during the cooldown of the facility in February 1994. The remaining capabilities await delivery of the Complex Target Simulator and the Sensor Positioner in 1995. All of these capabilities will be discussed in the sections following a brief description of the overall facility.

## FACILITY OVERVIEW

The role for 7V is to provide advanced calibration and performance characterization for both surveillance sensors and KEW seekers. Calibration includes not only the traditional role of radiometric calibration, but also goniometric calibration to evaluate accuracy of sensor target tracking and seeker guidance commands. However, the key to evaluation of sensor mission performance is thorough understanding of its operational characteristics. This includes establishing performance envelopes, defining interrelationships of key variables, identifying nonlinear behavior, and measuring timing and sequencing.

The implementation of these test objectives in 7V is illustrated by a functional diagram shown in Fig. 4. All of the simulation equipment is mounted on a rigid optical bench within the vacuum chamber. For low-infrared background, all equipment along with the bench is cryogenically cooled and totally enclosed inside a light-tight cryogenic liner. The scene is projected into the sensor under test by reflective collimation optics to simulate the target range, and a scan mirror to simulate scene movement for scanning sensors. The sensor is mounted in a separate antechamber on a three-axis gimbal support system for alignment. This

allows the sensor to operate in an ambient vacuum environment interfacing to the low-background test volume through a cryogenically cooled labyrinth baffle. The chamber, antechamber, and optical bench provide a rigid monolithic structure to control relative line-of-sight motions between the scene and the sensor. Jitter is controlled by mounting the entire facility on pneumatic vibration isolators to attenuate seismic inputs and equipment vibrations. Other support systems provide environmental conditions, utilities, cleanrooms, and data acquisition, control, and monitoring functions for the chamber and test equipment, and the sensor under test. The remaining sections describe each of these systems.

## FACILITY SYSTEMS

Figure 5 gives an overview of the 7V Facility providing photographs of the vacuum chamber, cryo/vacuum systems, and the modernized cleanrooms and control room.

### Chamber Systems

The Chamber Systems, extensively modified from the original 7V Facility, include the Vacuum Chamber, Sensor Antechamber, the Vibration Isolation System, the 7 ft in diameter by 23 ft long a with 7-ft-diam by 7-ft-long antechamber on one end. The antechamber has a separate vacuum pumping system and a gate valve to isolate the test article from the main chamber during pumpdown/cooldown to protect it from contamination. The entire chamber shell is supported from building structure on eight pairs of pneumatic vibration isolators to control jitter from ground vibrations. Relative movement between key optical elements such as target sources, mirrors, and the sensor is minimized by stiffness of the vacuum shell structure and the internal helium-cooled optical bench. As shown in Fig. 5, the bench is semi-cylindrical in cross section, about 20 ft long, and weighs 5,000 pounds. It is fabricated from welded aluminum plate and cooled through continuous aluminum extrusions welded to the internal surfaces. To remove weld stresses and stabilize the structure, the entire bench was stress relieved to near annealed conditions prior to final machining. The bench is supported from the vacuum shell by a fixed stainless pedestal in the center. Flexure supports at each end accommodate axial and lateral thermal contraction during cooldown. These supports offer thermal isolation of the cryogenic equipment and provide a rigid structural tie between the technical equipment mounted on the bench and the vacuum shell. For ease of access to the equipment, the bench can be removed quickly from the chamber by lowering it onto rails mounted on the bottom of the shell. The cryogenic, low-background test volume is enclosed by a cold liner which covers the top of the bench and each end. It is constructed from aluminum, cooled with welded extrusions, and coated internally with a flat black, low reflectance paint to absorb stray light. All external surfaces of the bench and liner are wrapped with 30 layers of perforated aluminized Mylar® to control radiation heat loads. Total steady-state refrigeration requirement to maintain the entire 6,500 pounds of equipment at 16 K is about 900 watts.

### Environmental Systems

The Environmental Systems provide vacuum and cryogenic conditioning, contamination monitoring, and utilities for the facility. The Vacuum System consists of a conventional oil-sealed roughing pump and oil-free high-vacuum pumps. The initial evacuation is accomplished by the 140 CFM roughing pump down to 10 torr. This relatively high vacuum level prevents oil backstreaming from free molecular flow. Other oil contamination safeguards include three separate liquid nitrogen traps and an in-line absorbent filter. At 10 torr, the roughing pump is shut down, and three dry, oil-free molecular drag pumps backed by individual membrane pumps are brought on to evacuate the chamber to 0.1 torr. At this point, two 1,100 l/sec turbomolecular high-vacuum pumps backed by the drag pumps bring the chamber to $10^{-5}$ torr range. Cryogenic cooling is then started cryopumping the chamber to the low $10^{-7}$ torr range.

Cooldown of the facility to low background conditions is accomplished by a 3.4-kW closed cycle gaseous helium refrigerator. This system provides low -pressure, cryogenic helium gas at 10 K to four parallel circuits used to cool the optical bench, liner, and the test equipment. Each circuit is independently controlled with supply and return valves and in-line heaters for automated flow and temperature control. The vacuum and cryogenic systems bring the chamber to stable test conditions of 16 K in about three days. This refrigeration system is capable of controlling the chamber at higher temperature levels, if necessary, for higher background sensors. This would save time in getting to test conditions and offer better mission simulation.

Contamination control is critical to protecting the sensor and the test equipment from chemical and particulate contamination. This control is maintained by careful design and selection of materials, the use of cleanrooms, and careful pumpdown/cooldown procedures to cryopump contamination on noncritical surfaces. To ensure a contamination-free environment, the vacuum volume is monitored by several active and passive systems. For *in-situ* monitoring of cryo-condensable contaminants, the

internal cryogenic test volume is equipped with two quartz crystal microbalances for a continuous record of any cryopumped contamination on the optics. These are attached to each main mirror mount tracking the same thermal history. For specie identification, the external vacuum outside the liner and within the antechamber is monitored by two mass spectrometers which continuously sample gases being pumped by both vacuum systems. For identification of non-condensable contaminants, the entire chamber within and without the cryogenic test volume is monitored with witness plates which are measured in a transmission spectrometer after every test.

### Building Modifications

The cleanrooms and control room shown in Fig. 5, were modernized and enlarged to support the increased test capability. The cleanrooms provide a controlled temperature and humidity environment for the sensor during installation with excellent protection from particulate contamination down to Federal Standard 209 - Class 100 (air filtration to limit exposure of critical optics and electronics to a maximum of 100 particles/cubic meter of 0.5 microns or less). Controlled access to the test article is also provided with cipher-locked doors for fully classified testing to the Secret level or higher if necessary. The Control Room is TEMPEST shielded for classified operations providing environmental control for all chamber and user data systems.

## SCENE SIMULATION

The typical mission scenes for exo-atmospheric surveillance and interceptor sensors are illustrated in Fig. 6 showing threat scenarios overlaid on natural space or earth-limb backgrounds. Since the objective of the 7V chamber is to provide sensor calibration and characterization, simulation requirements are simplified in comparison to the more complex scenes provided in other AEDC facilities. The primary objective of the 7V scene simulation is high fidelity to target radiometrics and precise location of individual targets or high-density target clusters. Background simulation is presently limited to variable intensity uniform space, a possible star pattern or a simple spatial gradient to simulate an earth limb. (The earth limb is not presently available but planned as a future upgrade.) Three target simulations shown in Fig. 6 can be tracked across the sensor's field of view: Closely Space Object (CSO) simulation of two or more targets separating into fully resolved targets, a complex cluster of targets expanding from a clump to fully resolved cluster, and a blooming triangular or circular target.

### Closely Spaced Object Simulation

Resolving closely spaced objects into discrete targets is an important task for both surveillance and interceptor sensors. The ability to accomplish this as soon as possible in the mission increases the time available to discriminate decoys and identify targets, establish trajectories and hand over track files to interceptors, centroid targets through penetration aids and establish aim points, and identify hit point for kill assessment. The 7V target system provides CSO simulation using two integrating sphere graybody sources overlaid by a CdTe beam combiner. The beam combiner is cut with a 0.5-deg wedge to reflect ghost images out of the field of view of the collimator. One source moves relative to the other while both are tracked across the field of view of the sensor on a precision X-Y translator. Either source has independent control of temperature and radiometric output. The source intensity can also be dynamically varied to simulate coning targets. For multiple CSO patterns or variable source size, both sources are equipped with output aperture wheels providing up to 30-user selectable patterns. A schematic and photograph of the CSO System is shown in Fig. 7 along with capabilities for this source.

### Complex Target Simulation

Simulation of complex target scenarios is provided an advanced scene generator, called CRISP for Cryo/vacuum Resistor Array Infrared Scene Projector. Honeywell Corporation is developing this capability for AEDC with delivery in 1995. Based on etched silicon micromachining technology, the CRISP generates dynamic patterns of 1 to 400 independent targets using an array of 512 by 512 heated resistor pixels. Each 30-μrad point target is generated by a subarray of 6 by 6 pixels. By sequentially heating and cooling adjacent pixels, the target appears to move in 5-μrad steps. The microphotograph in Fig. 8 shows several individual 90-micron-square pixels. Each is individually addressable over a temperature range of 20 to 400 K controlled within 1 K with response of 10 Hz over the full range. Because any of the 36 pixels per target will image as a diffraction limited point target, the target intensity can be varied over a dynamic range of 36 at constant temperature. The resistor is supported on top of the addressing and control electronics by a thin silicon bridge which isolates the heat and prevents crosstalk. The two-layered structure also increases the fill factor of each pixel to 90 percent. The combination of an optical reflector under the pixel and titanium nitride black emitter surface increases the emittance to about 70 percent with spectral characteristics of a graybody. Presently the CRISP array chip and control electronics are complete and were successfully tested at 20 K. Funding limitations have stretched completion of the controls and software into FY95, but the technology to produce high-resolution, complex scenes is in hand and offers the 7V a unique test capability unmatched anywhere else.

### Expandable Target System

The third scene scenario shown in Fig. 6 is an expandable target for seeker target centroid testing. As shown in Fig. 9, both circular and triangular targets of various aspect ratios can be simulated by using a dynamic cryogenic iris in conjunction with an aperture wheel. To simulate target intensity increase due to range closing, the source also has a linearly variable circular attenuator to dynamically change source intensity over two orders of magnitude. In conjunction with the Scan Mirror, the expandable target can be swept across the seeker field of view at high speed to simulate the effect of miss distance. This is a valuable feature to test seeker centroiding ability at high closure speeds.

### Background Simulation

Simulation of uniform space backgrounds is accomplished by direct projection of a blackbody radiator into the sensor under test. As shown in Fig. 10, this source is located out of the sensor's field of view next to the primary mirror. It illuminates the entrance aperture of the sensor, overfilling its focal plane with uniform illumination. The source is a conical blackbody fitted with a 16-position aperture wheel to vary background intensity at constant source temperature. It is mounted on a translator stage so it can be parked outside the field of view for background or moved on axis when used by itself for sensor focal plane flood source testing.

A conceptual design and prototype of an earth limb simulator is complete but is not implemented in the 7V. This design utilizes an array of individually heated wires located out of focus to provide an intensity gradient simulating earth limb.

## RADIOMETRIC AND GONIOMETRIC CALIBRATION

Calibration of the 7V simulations is divided into two functions - radiometric calibration traceable to the broadband standards of the National Institute of Standards and Technology (NIST) and goniometric calibration for measurement of target position and track accuracy. As shown in Fig. 3 and schematically in Fig. 11, the Radiometric Calibration System (RCS) consists of the Calibration Source for broadband and spectral input to the sensor under test and the Calibration Monitor for *in-situ* measurement of all the source outputs over broadband and spectral regions. The goniometric function is provided by the Alignment Monitor System (AMS), which incorporates an infrared camera to image the scene projected into the sensor. Both monitors are located in an antechamber just in front of the sensor. Either monitor can be used by deploying a gimballed flat mirror into the collimated beam to direct radiation into focusing optics which image the scene onto IR detectors.

### Radiometric Calibration

The RCS Calibration Sources provide several operational modes as point or extended sources with either broadband or spectral output. Low-level, broadband output is provided from an integrating sphere illuminated by a blackbody through a 16-position aperture wheel. This technique provides wide dynamic range of 3.5 orders of magnitude at any temperature over an operating range of 150 to 500 K. The unisphere source is supplemented by a bare cavity blackbody with variable output aperture for an additional order of magnitude at the upper end of the dynamic range. Either source can be attenuated by three neutral density filters to lower the dynamic range by an additional one to three orders of magnitude to a minimum intensity of $10^{-18}$ W/cm$^2$. Including temperature variation, the total dynamic range is almost eight orders of magnitude. Spectral output is provided by the cavity blackbody dispersed by a three-segment Circular Variable Filter (CVF). This provides narrowband energy over 2.5 to 14.5 microns with bandwidth varying from 1.0 percent at the lower end to 1.8 percent at the upper end.

The Radiometric Calibration Monitor System samples the output from any source for radiometric intensity and uniformity. To measure radiometric output, the selector mirror reflects part of the collimated radiation into a 10-cm imaging mirror which focuses the source onto a 2-mrad-square Gallium-doped Silicon detector. The detector operating at 16 K responds over a band of 3 to 18 microns. It is calibrated *in-situ* by a secondary standard blackbody, previously calibrated at NIST to 1-percent accuracy. Spectral calibration of any source uses an identical CVF inserted in front of the Si:Ga detector. All of the sources were calibrated by this approach during the February, 1994 test. Results show overall radiometric uncertainty for the system to be less than 5 percent, with repeatability of 2.8 percent for 17 separate measurements made throughout the 12-day test. This performance is outstanding and is believed to be the best radiometric calibration capability available today.

### Goniometric Calibration

Calibration of target position is accomplished by the Alignment Monitor System (ref. 3) shown in Fig. 12. This device, built for AEDC by Mission Research Corporation, is an infrared sensor equipped with a 256 by 256 Indium Antimonide (InSb)

focal plane which covers a 0.75-deg square portion of the Collimator field of view. (The system can be upgraded to 1-deg square field coverage using 512 by 512 focal plane technology when it becomes available.) The imaging optics cover a circular field of view of 1.5 deg with an all-reflective, highly corrected anastigmatic design using nickel-plated aluminum mirrors. The complete system is actively cooled by the 7V gaseous helium system to 20 K, while the focal plane is independently controlled within a range from 30 to 50 K depending on sensitivity needed. The AMS and its image analysis electronics and sub-pixel centroid algorithm provide absolute target position to an angular accuracy of 2.5 μrad. The AMS, with special surface mapping software developed at AEDC, calibrated target track during the February pumpdown to position uncertainty within the core field of view (FOV) of less than 7 μrad (1 σ). This calibration was "bootstrapped" over the entire 1.2-deg FOV to less than 9-μrad uncertainty. The radiometric sensitivity with the focal plane cooled below 50 K is sufficient to see all of the targets in the chamber. With the ability to vary integration times, AMS proved to be a very versatile diagnostic. Using about several seconds to integrate faint signals, stray light problems were found in two sources and corrected. A ghost image in the CSO source was also corrected by inverting the wedged beam combiner. Using millisecond integration times, the AMS was used to calibrate high-speed performance of the Scan Mirror and to demonstrate that the chamber meets its 5-μrad jitter budget. In summary, the AMS provides a unique capability in a low-background test chamber and will serve as an invaluable tool for future sensor testing.

## OPTICAL SIMULATION

The Chamber Optical System shown in Fig. 3, provides collimation of the Calibration or Scene output, target selection, and single axis azimuth scanning for high-speed target movement and alignment.

### Collimation Optical System

The 7V Collimator is a two-mirror off-axis Cassegrain constructed from nickel plated aluminum for cryogenic operation and low scatter performance. The focal length is 1,650 cm, providing a collimated beam of greater than 50 cm diameter with a circular field of view (FOV) of 1.4 deg. The mirrors are coated with enhanced silver and a protective overcoat, providing reflectance of greater than 98 percent from 0.5 to at least 30 microns. Both the primary and secondary mirrors mount independently to the 7V optical bench on actively cooled, massive aluminum structures. Optical quality of the collimator was measured in the 7V during the cryogenic acceptance test in December, 1993. Typical results are illustrated in Fig. 13, showing a HeNe interferogram over the full 50-cm beam at the center field point. The performance at 20 K is excellent, with peak-to-valley wavefront error of about 2 waves at 0.6328 microns, which is equivalent to diffraction-limited performance at 5.2 microns. Over the entire field of view, the full aperture diffraction-limited performance ranges from 4.5 to 6.5 microns. Smaller areas of the beam around 20 cm diameter are diffraction-limited in the SWIR near visible wavelengths. Based on this performance, this optical system is believed to be the finest cryo-mirror system of its size ever built.

### Scan Mirror System

The Scan Mirror, mounted between the sources and the collimator secondary, provides high-speed azimuth sweep of the targets across the sensor under test. The light-weighted aluminum mirror rotates about a vertical axis on two stainless flexure pivots driven by a brushless DC servo motor with closed-loop position control from a brushless Inductosyn® rotor encoder. In collimated space, this system provides angular position knowledge and resolution of 0.5 μrad over a speed range of 0 to 6 deg/sec.

## SENSOR SUPPORT AND INTERFACING

Services provided in the 7V for the sensor under test include mechanical support, optical alignment, scanning, thermal control for the focal plane and sensor optics, and electrical interface for power and data transfer. With many years of experience in handling flight-qualified hardware and conducting sensor tests, AEDC can provide any support necessary to accommodate user needs.

### Sensor Positioner System

Present capabilities are provided by an existing three-axis gimbal system for pitch, yaw. and roll alignment. This will be replaced by a new Sensor Positioner presently under procurement providing more accurate position control and higher speed scanning with a bandwidth of DC to 5 Hz. Some of the capabilities for both systems are outlined in Table 2.

### Sensor Thermal Control System

Thermal control of the sensor under test can be provided for the focal plane, optics, and ambient housing and electronics, if necessary. A dedicated Helium Refrigerator is available for closed-loop cooling of the sensor over a wide range of temperatures

using gaseous helium. This refrigerator can also liquify helium into portable dewars at 75 l/hr, if required. Liquid nitrogen is also available in large quantities, if needed.

## DATA ACQUISITION AND CONTROL

The 7V Data Acquisition and Control System, shown in Fig. 14, supports the entire operation of the chamber and execution of the test matrix. Five PCs make up the Test Equipment Control System (TECS) to control and monitor the individual sources and other special test equipment. Two major computer systems, the Chamber Monitoring and Control System (CMACS) and Facility Computer, oversee and supervise test operation and acquire, store, and manipulate data.

### Technical Equipment Control System

All of the test simulation equipment discussed above is calibrated, controlled, and monitored by five identical 486 -66 MHz personal computers (Ref. 4). Each PC controls up to 8 stepper motors, 2 chopper motors, and 2 blackbodies or 2 IR detectors in a manual mode for initial checkout or in a fully automated mode for sensor testing. Control parameters for each test scenario, such as temperature, position, and velocity, are downloaded from the CMACS and automatically set up and verified before making a test run. During the run, the TECS monitors and controls test conditions and flags any parameter outside control limits. A user-friendly graphical interface is provided to the operator for monitoring test setup and overall test control.

### Chamber Monitor and Control System

The CMACS, based on a Digital 3400 MicroVAX computer, downloads test parameters, sets up, controls, and monitors performance of all chamber simulation and environmental equipment. It provides 256 channels of analog input, multiplexed for chamber control with 16-bit A/D conversion. The CMACS also provides the operator interface to the facility operation through interactive screens. The CMACS MicroVAX computer is installed in the Control Room, along with the analog/digital I/O equipment.

### Facility Computer System

The existing Facility Computer, based on a VAX 8650, services the entire AEDC Space Test Complex. It is linked to the 7V over a classified Ethernet to provide overall control of testing through its test parameter database. This database approach provides an efficient technique to run a sensor test by setting and verifying the entire test matrix before the chamber is cooled down. By pre-defining all test conditions for individual data runs, information can be quickly downloaded to the CMACS computer to automatically set up test equipment and monitor performance during the run. Once a test run is complete, sensor measurements and facility information can be uploaded back to the Facility Computer for off-line data analysis, plotting, or archiving while the next data point is being run in 7V. If necessary, the extensive computer facilities available at AEDC are readily accessible from the VAX to an AMDAHL 5860 or a CONVEX 3840 over a classified hyperchannel.

## SUMMARY

The 7V Facility provides an advanced test capability for seekers and surveillance sensors up to 50-cm diameter. Its optical system, calibration accuracy, and scene simulation are state of the art. With modern control rooms, environmental systems and data systems, the 7V offers a capability unmatched anywhere for the next generation of infrared sensors.

## REFERENCES

1. Pipes, J. G. and Watson, D. J. "Synopsis of LWIR Sensor Tests in the AEDC Aerospace Chamber (7V) between 1969 and 1985." AEDC-TR-85-18 (AD-B099 302), January 1986.

2. Dawbarn, R. "Development of Ground Test Facilities at AEDC to Conduct DTE and OTE for Space Surveillance Sensors." 15th Aerospace Testing Siminar, Manhattan Beach, CA, Oct. 11-13, 1994.

3. Crosswy, F.L and Bird, C.M. "Alignment Monitor System for Sensor Testing at AEDC, SPIE International Symposium on Optics, Imaging and Instrumentation." San Diego, CA, July 24-29, 1994.

4. McCann, B.E., Russell, M.A., and Smotherman, M.N. "PC-Based Data Acquisition and Control of a Cryogenic Infrared Scene Generation System." Instrument Society of America 94 Technical Conference, Anaheim CA, Oct. 24, 1994.

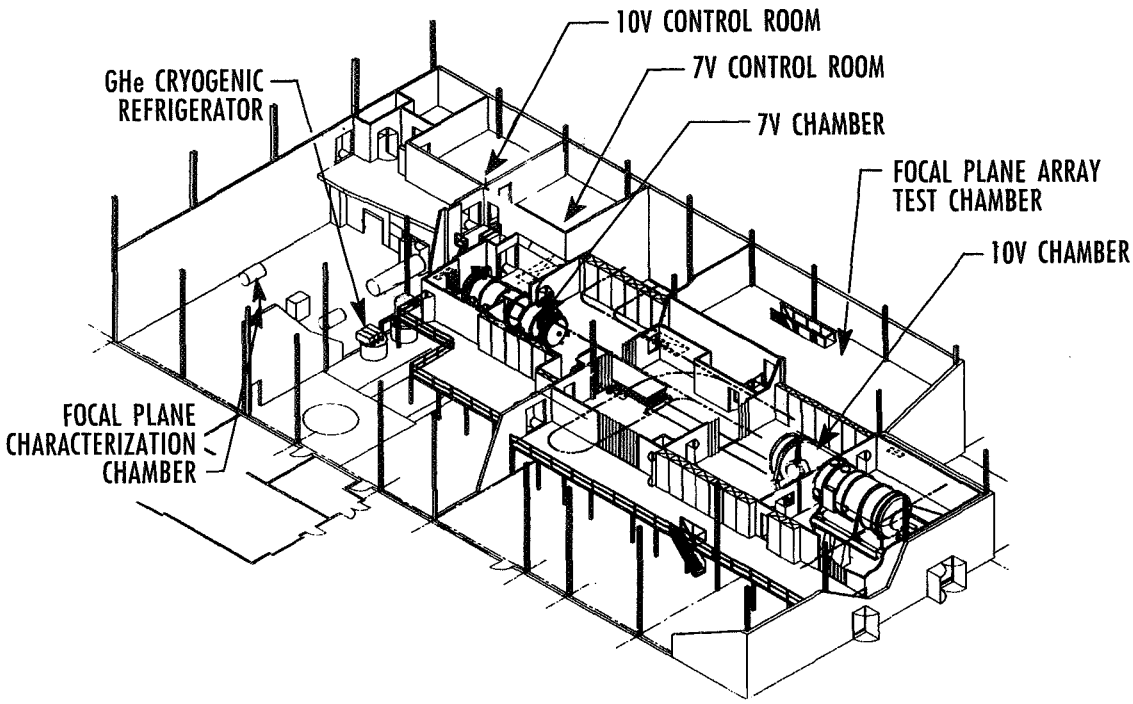


Figure 1. AEDC space test complex.

| AEDC TEST ASSETS \ TEST LEVELS | DT&E: Component/Sensor Calibration Characterization | DT&E: Sensor Mission Performance (Open Loop) | OT&E: Sensor / Platform Performance (Closed Loop) | OT&E: Deployed System (Integration & Operability) |
|---|---|---|---|---|
| Focal Plane Characterization Chamber | Chips | | | |
| Direct Write Scene Generator Chamber | FPA's & Algorithms | | | |
| 7V Sensor Test Chamber | ATH Surveillance & Interceptor Sensors | | | |
| 10V Sensor Test Chamber | | BTH Surveillance Interceptor Sensors | | |
| Focal Plane Array Test Capability | | | Sensor Focal Plane, Emulators & Algorithms | |
| Advanced Sensor Test Capability | | | | Multiple Interactive Focal Planes |

OPERATIONAL | IN BUILDUP | UNDER DEVELOPMENT

Figure 2. AEDC sensor test plan.

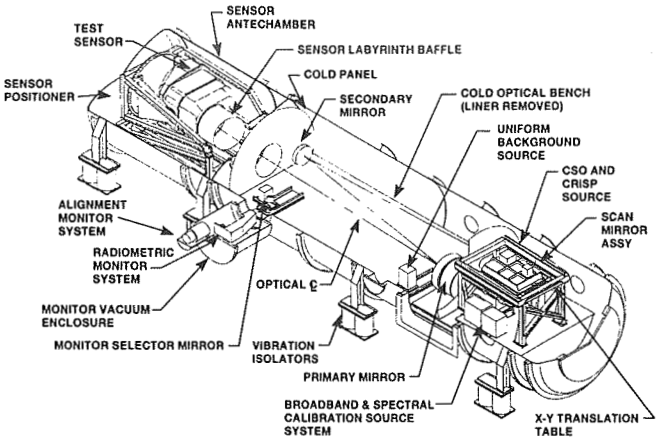


a. Chamber test equipment configuration

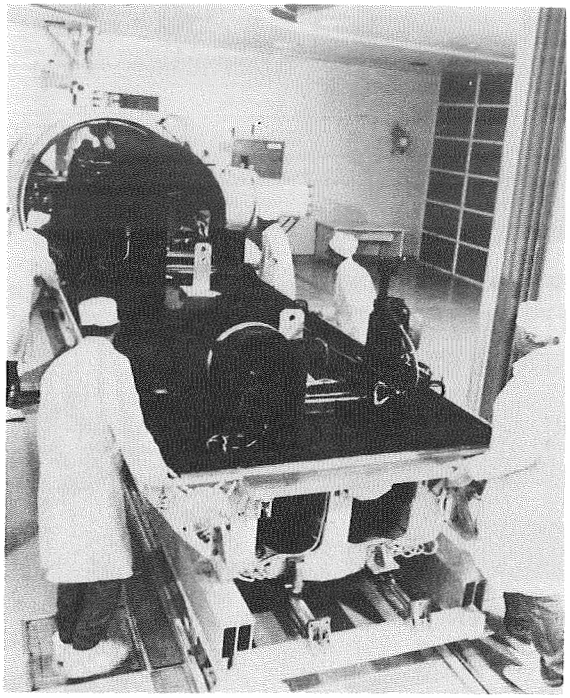

b. Optical bench being installed into 7V vacuum chamber

Figure 3. 7V sensor test facility.

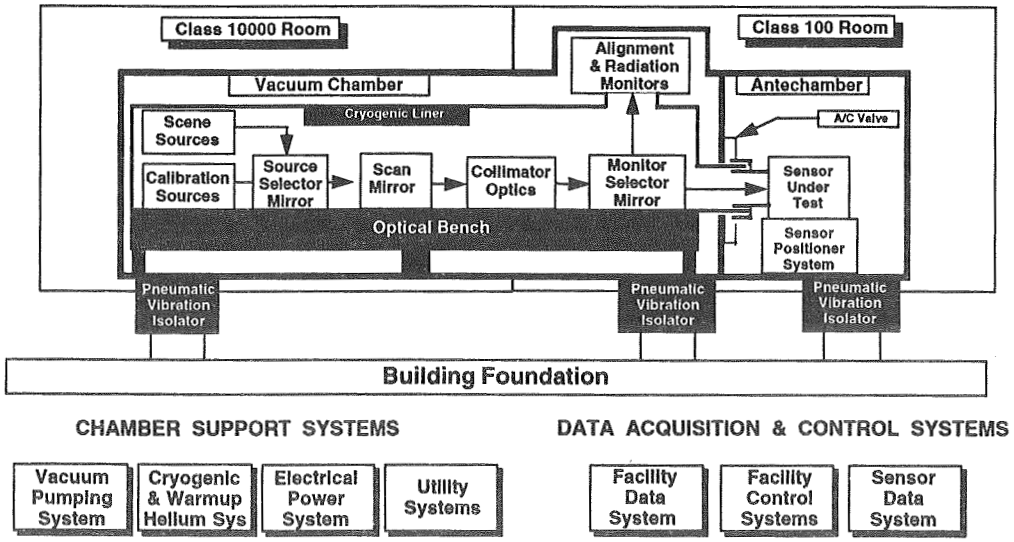


Figure 4. 7V functional layout.

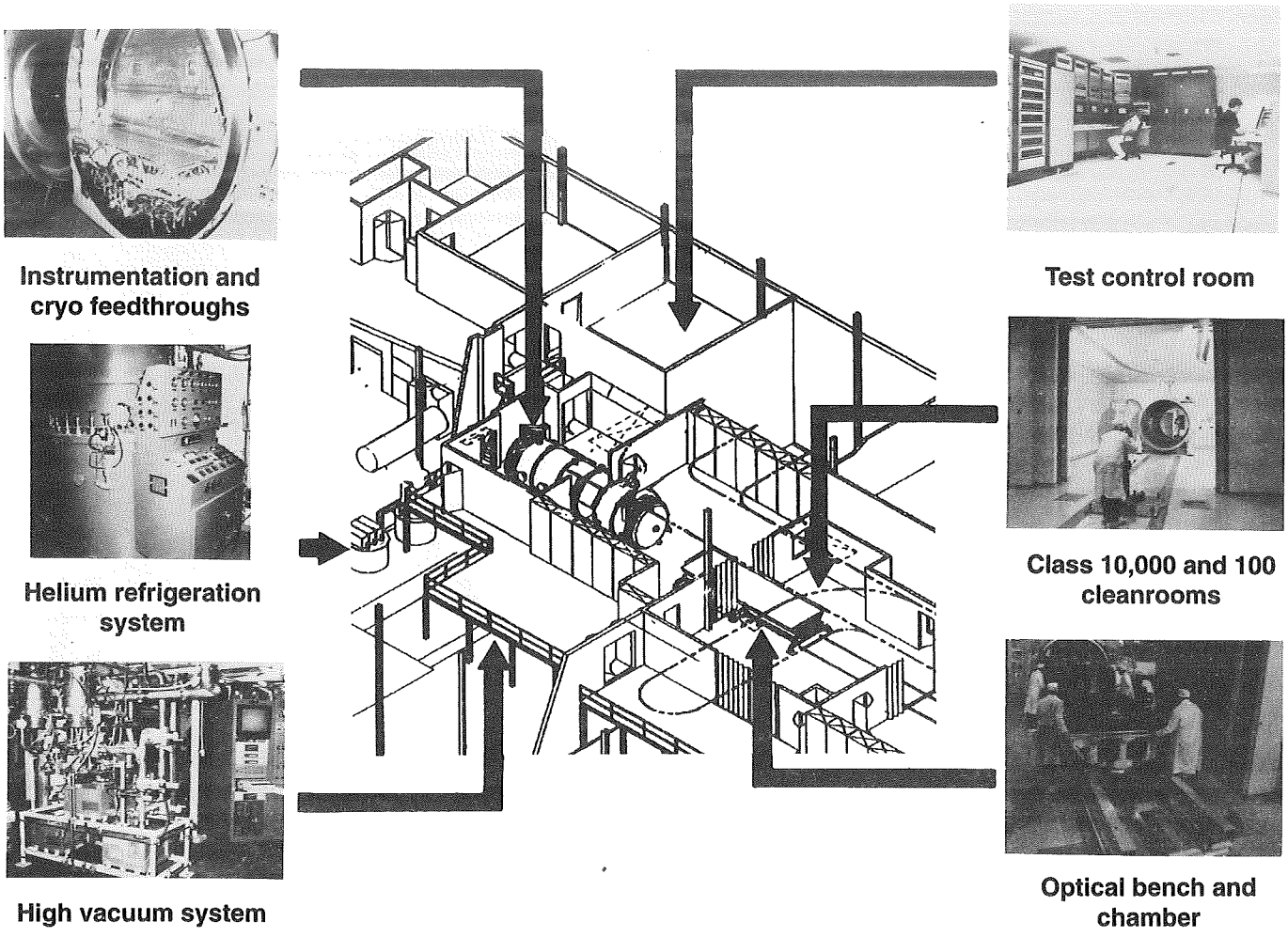


Figure 5. 7V facility systems.

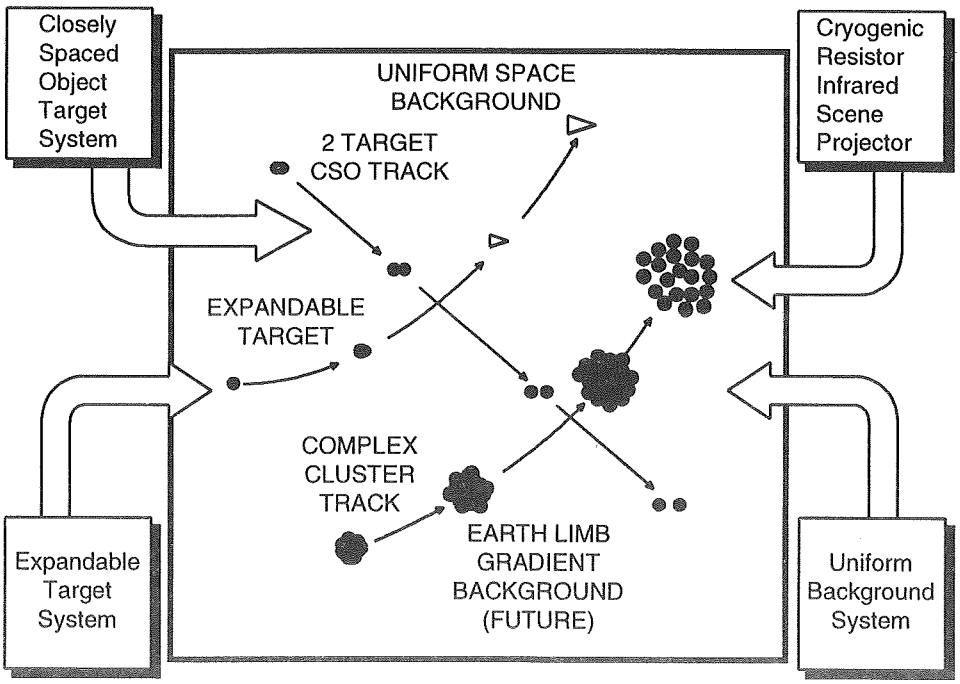


Figure 6. 7V scene simulation.

## CSO SYSTEM FEATURES

- Provides Two Gray - body Targets or Cluster Patterns
  - *One fixed, one movable in 2-dimensions from 0 to 1000 mrad separation*
  - *Separation rate controllable from 0 to 200 mrad / sec*
  - *30 pinhole selections available in each source for various target sizes & patterns*
- Controls Irradiance and Blackbody Temperature Independently
  - *Conical bare blackbody settable from 150 to 500 K unisphere attenuator*
  - *Variable Radiance @ constant Temperature over 2 orders of magnitude*
  - *Temporal variation of irradiance to simulate closing targets*
- Tracks Target Complex over Entire Field of View
  - *Two-dimensional target tracks with speeds from 0 to 1 deg / sec*
  - *Target position knowledge of 5 μrad with minimum step resolution of 0.05 μrad*

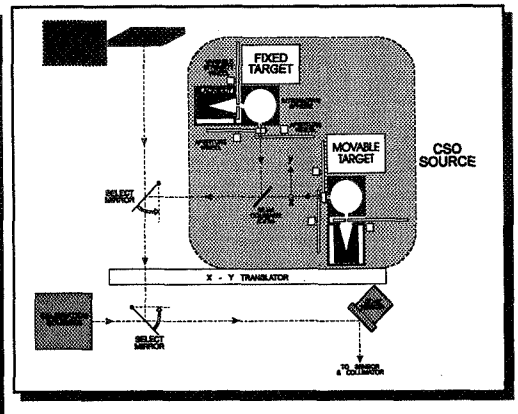


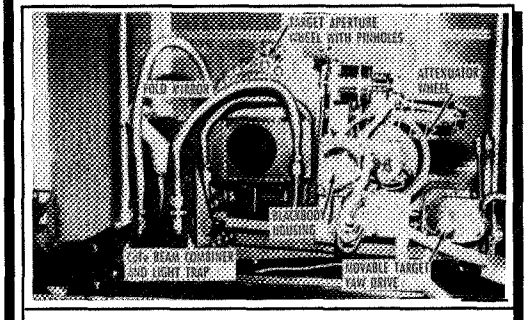


CSO Source Assembly

Figure 7. Closely spaced object system.

## CRISP FEATURES

- 512 x 512 Array of Micro-Resistors covering 2.8 mrad square Field of View
- 0.0035 inch Pixel Size (5.3 μrad) with 90 % Fill Factor
- 1 - 400 Point Targets (6 x 6 pixels)
- Low Power < 20 watts to drive 400 Targets to 400 K
- Temperature Range 20 - 400 K with 1 K Accuracy @ 10 Hz
- 70 % Emittance using Ti-Nx resistor with Optical Cavity
- Variable Frame Rate 0 - 10 hertz
- Integrated CMOS Array, Drive & Control Electronics etched under Emitter Array on 4 inch Silicon wafer certified at 20 K

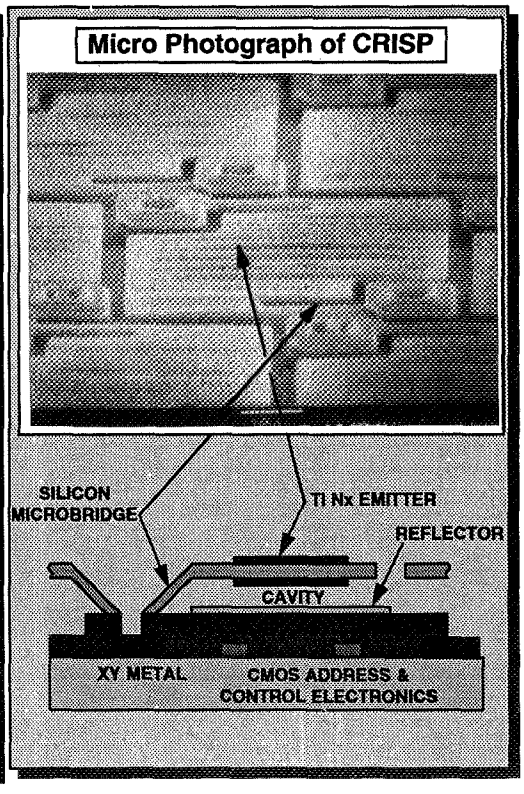


Figure 8. CRISP cluster target system.

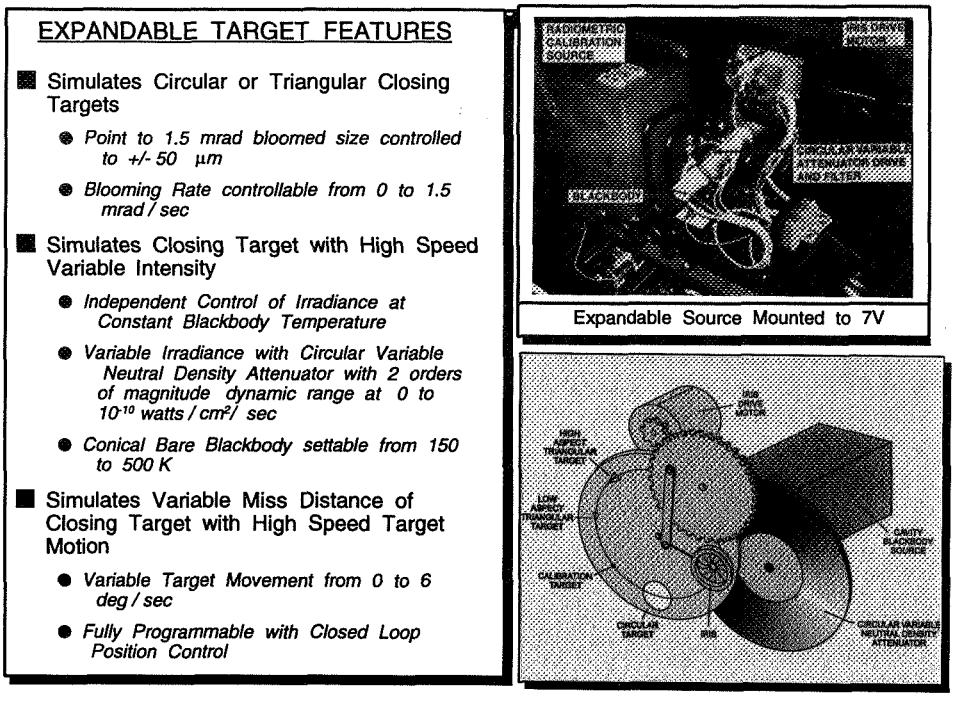


Figure 9. Expandable target system.

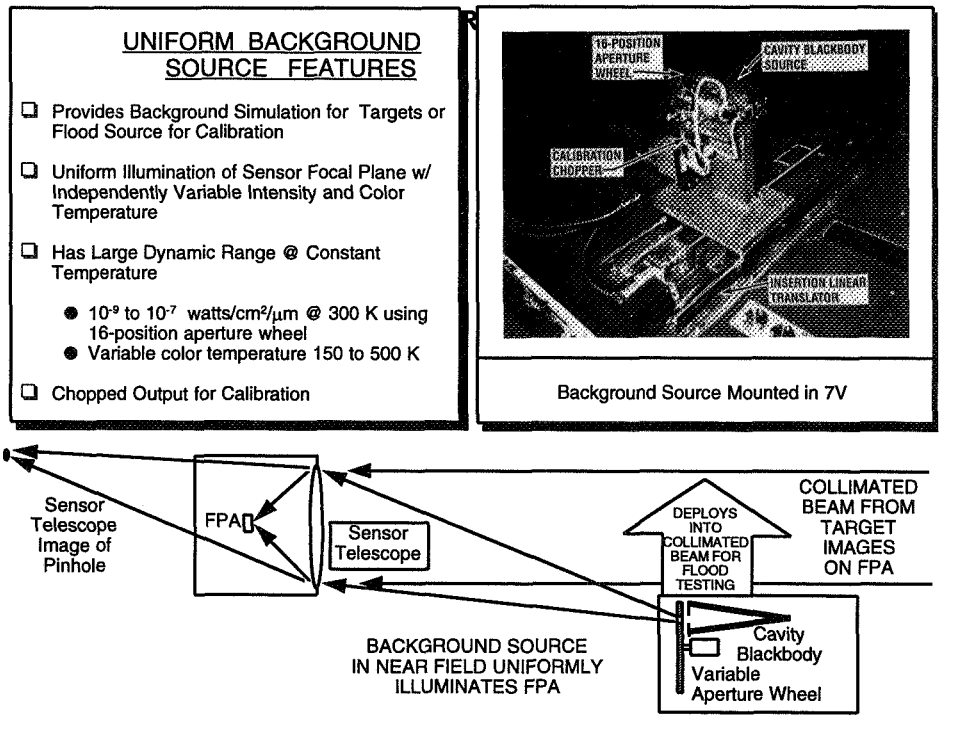


Figure 10. Uniform background system.



C-6.

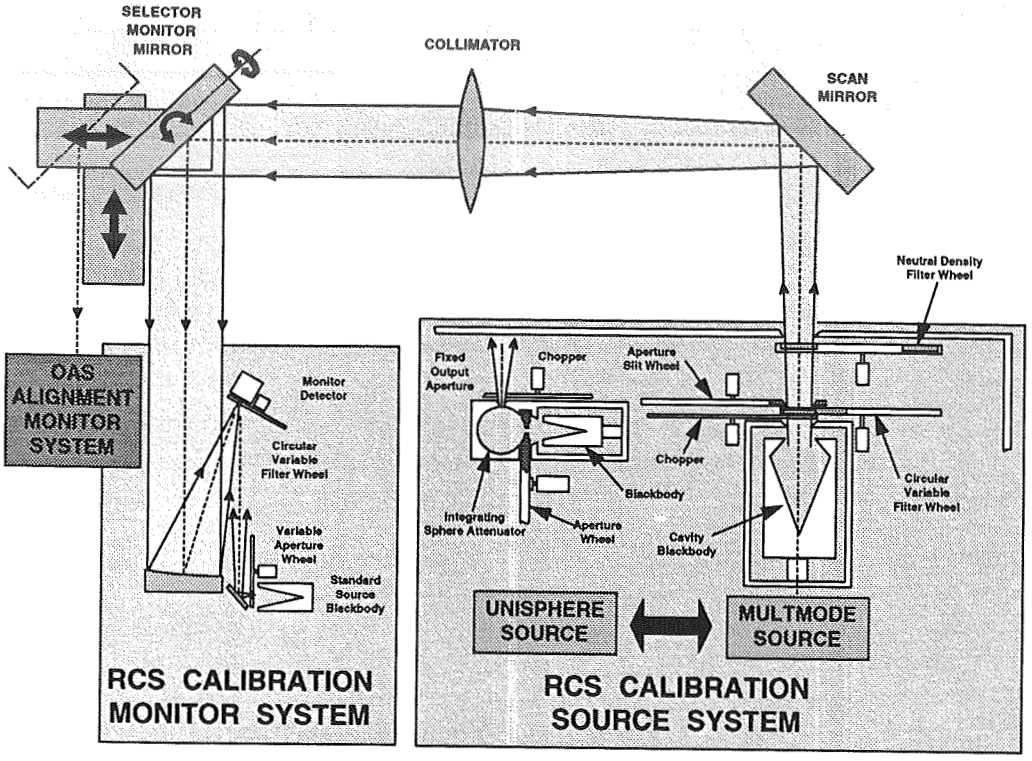


Figure 11. Radiometric calibration system.

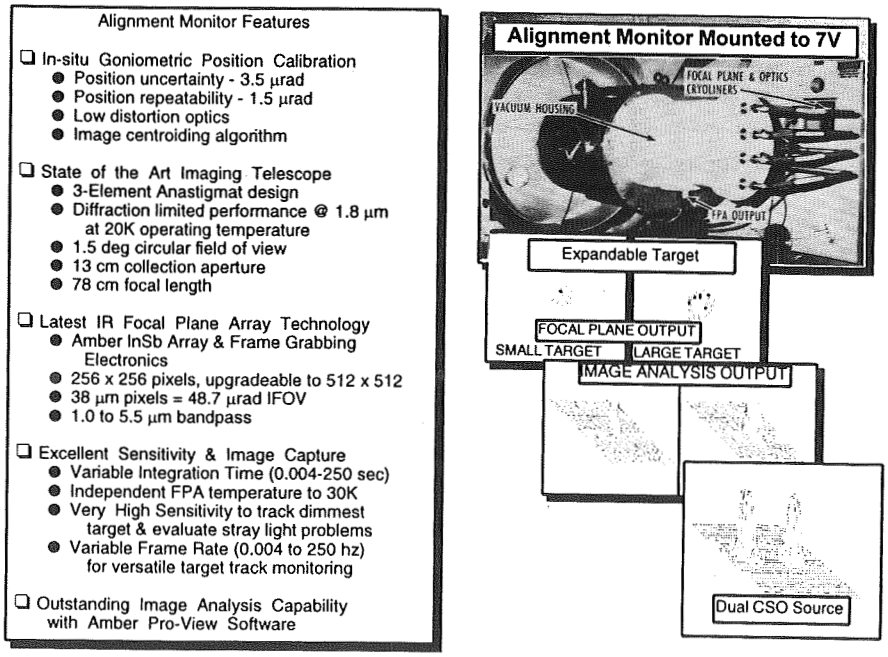


Figure 12. Alignment monitor goniometric calibration system.

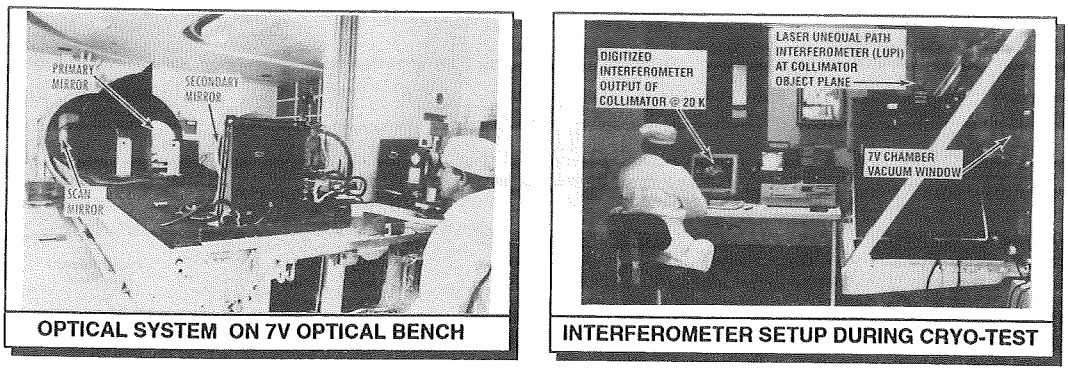


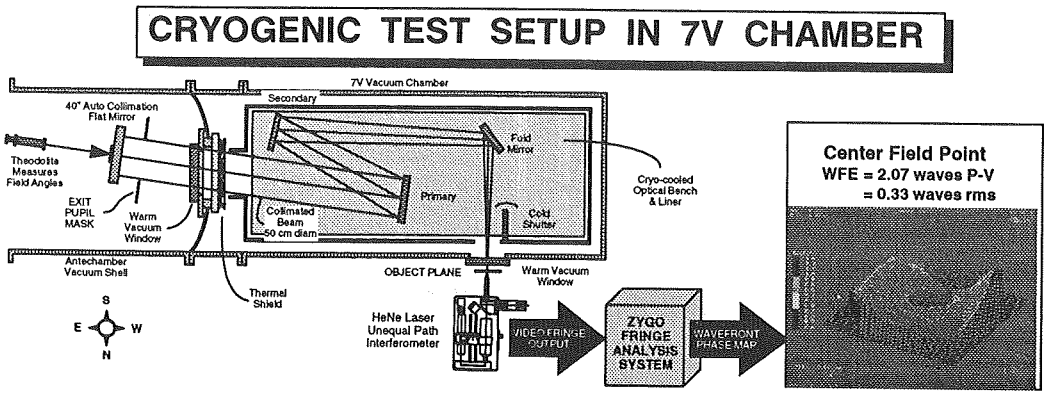


Figure 13. 7V collimator and cryogenic test results.

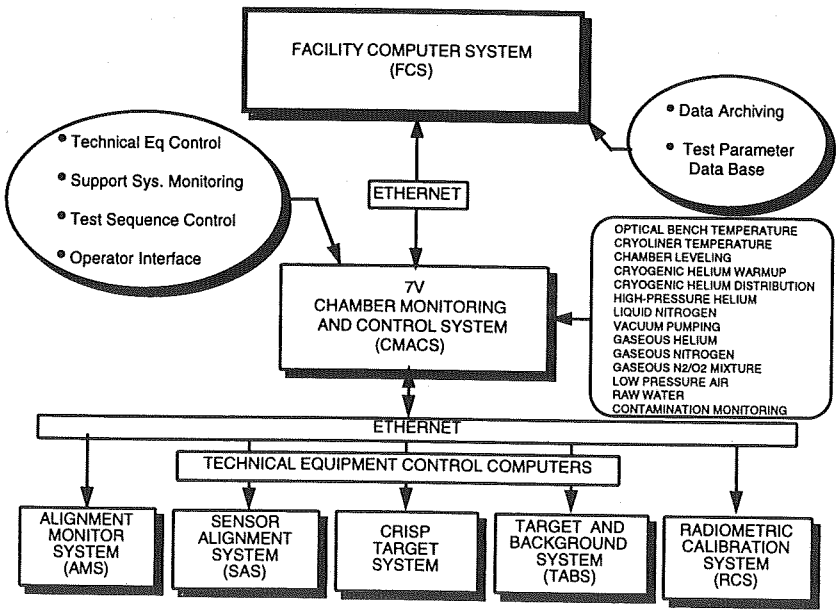


Figure 14. Data acquisition and control system.

Table 1. 7V Chamber Functional Requirements

| CAPABILITY | FUNCTIONAL REQUIREMENT |
|---|---|
| **Target & Background Simulation** | ■ *Simulate Point Targets, Closely Spaced Objects & Clusters*<br>■ *Match Spectral Fidelity of Real Targets*<br>■ *Match Target Motion (Keplerian & Relative)*<br>■ *Simulate Target Blooming*<br>■ *Provide Above the Horizon Backgrounds* |
| **Optical Simulation** | ■ *Collimate Scenes to Simulate Sensor to Target Range*<br>■ *Transfer Scene to Sensor under Test & Match Pupils*<br>■ *Overfill Sensor Aperture & Field of View*<br>■ *Provide Scan function for Scanning Sensors* |
| **Optical Alignment & Goniometric Calibration** | ■ *Provide Reference Alignment of Sources / Optics / Sensor*<br>■ *Calibrate Target Position & Track*<br>■ *Certify Target to Sensor Line of Sight Alignment & Jitter*<br>■ *Certify Optical System Focus* |
| **Radiometric Calibration** | ■ *Provide Broadband & Spectral Calibration*<br>■ *Provide Point & Extended Calibration Sources*<br>■ *Verify Calibration & Scene Irradiance Traceable to NIST*<br>■ *Measure Uniformity of Irradiance onto Sensor* |
| **Sensor Support & Interfacing** | ■ *Mount & Interface Sensor to Cryo Chamber*<br>■ *Provide Sensor Static Alignment & Positioning*<br>■ *Control Sensor Thermal Conditions ( FPA / Optics / Shell )*<br>■ *Provide 3 - Axis Sensor Movement* |

Table 2. 7V Chamber Test Capabilities

| 7V Test Capability | Value Demonstrated [✔] |
|---|---|
| **Optical Performance** | **Decentered Cassegrain all-reflective Aluminum design** |
| ■ Collimated Test Beam Diameter (cm) | 50 ✔ |
| ■ Field of View (deg) | 1.2 x 1.2 ✔ |
| ■ Transmission (5 surfaces) & Waveband (μm) | 88% over 0.5 to 30 ✔ |
| ■ Optical Quality (Wavefron Error) | 1/4 wave @ 6 mm over 50 cm diam ✔ |
| ■ Line of Sight Stability (mrad rms) | < 5 ✔ |
| ■ Optical Scanning Range / Rate | +/- 2 deg Azimuth @ 0 to 6 deg/sec ✔ |
| **Radiometric Calibration** | **Spectral & Broadband traceable to NIST** |
| ■ Blackbody Temperature Range | 150 to 500 K ✔ |
| ■ Irradiance Range (w/cm$^2$) | $10^{-18}$ to $10^{-12}$ ✔ |
| ■ Irradiance Precision/Repeat/Accuracy (%) | < 2 / < 4 / < 10 ✔ |
| ■ Spectral Range (μm) | 2.5 - 14.5 w/ CVF ✔ |
| **CSO Simulation** | **RVs / Decoys / Fixed Clusters** |
| ■ Number & Spacing | 2 @ 0 - 1000 μrad continuous in any direction ✔ |
| ■ Irradiance Range (w/cm$^2$) & Temp | $1e^{-15}$ - $1e^{-13}$ @ 300K (150 to 500 K available) ✔ |
| ■ Target Track Range / Accuracy | 2-D Track over complete FOV @ +/- 10 μrad ✔ |
| **Complex Target Simulation (FY95)** | **1 to 400 Programmable Point Targets** |
| ■ Target Temperature Range ( K ) | 200 to 400 |
| ■ Position Accuracy / Resolution (μrad) | 2 / 5 |
| **Expandable Target Simulation** | **Bloomable Triangular or Circular** |
| ■ Size (μrad) & Blooming Rate (mrad/sec) | 30 to 1600 @ 0 to 1.5 ✔ |
| ■ Irradiance Change (w/cm$^2$) @ Constant Temp | $2e^{-13}$ - $2e^{-11}$ @ 300 K ✔ |
| ■ Rate of Change of Irradiance (w/cm$^2$/sec) | 0 to $6e^{-11}$ ✔ |
| **Background Simulation** | **Uniform Space w/ Earth Limb for Future Growth** |
| ■ Uniform Radiance (w/cm$^2$/sr) | $1e^{-10}$ to $1e^{-6}$ ✔ |
| ■ Earth Limb Gradient (w/cm$^2$/sr/deg) (Future) | $1e^{-6}$ |
| **Sensor Alignment / Positioning** | **Existing** / **On Procurement (FY95)** |
| ■ Range (+/- Pitch/Roll/Yaw degree) | ✔ 4 / 5/20/60 |
| ■ Velocity ( deg/sec) | ✔ 0.0002 to 0.04 / 0.0001 to 25 |
| ■ Position Accuracy / Resolution (μrad) | ✔ +/- 150 @ 5 / +/- 5 @ 1.7 |
| ■ Frequency Response (Hz all axes) | N/A / 5 |

# NEW POTENTIALS OF NIICHIMMASH'S THERMAL VACUUM FACILITIES

N.A. Afanassiev, A.A. Makarov and V.L. Galjaev
NIICHIMMASH, Sergiev Posad, Moscow Region
Russia

## ABSTRACT

• Key words: thermal vacuum facility, environmental simulation, spacecraft

The potentialities of existing test facilities as to simulating space environment governing factors for spacecraft successful development thermal vacuum testing are analyzed, ways of modernizing existing test facilities and specific proposals on their redesign are considered.

The problem of spacecraft (S/C) ground development in simulated external environments, the solution of which started more than 30 years ago, has not lost its urgency today. Stringent requirements on S/C active lifetime under space conditions, module large dimensions, great number of extension elements and complicated mode of their interaction in long mission do not allow S/C designers to abandon ground tests.

S/C thermal modes development is a combination of calculations, thermal vacuum tests and actions on improving S/C design and its thermal control system. Traditionally, tests are carried out by stages from component and end unit level verifications to complex tests of modules and S/C as a whole. In our opinion, sufficient correctness of calculated models and experience gained in organizations designing space systems allow to reduce cost and time of autonomous tests.

Unfortunately, this is not true for complex (integrated) thermal vacuum tests. More than that, their recent programs include tasks of verifying other (than thermal control system) systems of S/C for operation under space simulated conditions. The outlined circumstances are the main reason for critical review of the potentialities of the existing test base, and of NIICHIMMASH's two large thermal vacuum chambers, first of all. The reasons for and ways of enlargement of these facilities potentially are analyzed and the results attained are described.

# UPGRADE OF 8-FOOT-DIAMTER SPACE SIMULATION CHAMBER: JUST IN TIME FOR CLEMENTINE

Robert Baldauff
Naval Center for Space Technology, Naval Research Laboratory
Washington, D.C.

## ABSTRACT

To insure on-schedule, reliable, and accurate thermal design verification and thermal vacuum testing of the Clementine spacecraft in an ultra-clean chamber environment, it was necessary to upgrade the 8-foot-diameter space simulation chamber at the Naval Research Laboratory. What was roughing-pumped and limited temperature range shrouds was transformed to an ultra-clean high-vacuum facility with shroud capability from liquid nitrogen to 120°C. A detailed summary is given of removed hardware and the newly installed pumps, valves, gauging and shrouds, including specifications, schematics and chamber testing performance.

# FROM ANTARCTICA TO SPACE: USE OF TELEPRESENCE AND VIRTUAL REALITY IN CONTROL OF REMOTE VEHICLES

Carol Stoker, Butler P. Hine III, Michael Sims, Daryl Rasmussen, and Phil Hontalas
NASA Ames Research Center

Terrence W. Fong, Jay Steele, and Don Barch
Recom Technologies, Inc.

Dale Andersen, SETI Institute

Eric Miles, Stanford University

Erik Nygren, Massachuettes Institute of Technology

## ABSTRACT

In the Fall of 1993, NASA Ames deployed a modified Phantom S2 Remotely-Operated underwater Vehicle (ROV) into an ice-covered sea environment near McMurdo Science Station, Antarctica. This deployment was part of the Antarctic Space Analog Program, a joint program between NASA and the National Science Foundation to demonstrate technologies relevant for space exploration in realistic field settings in the Antarctic. The goal of the mission was to operationally test the use of telepresence and virtual reality technology in the operator interface to a remote vehicle, while performing a benthic ecology study. The vehicle was operated both locally, from above a dive hole in the ice through which it was launched, and remotely over a satellite communications link from a control room at NASA's Ames Research Center. Local control of the vehicle was accomplished using the standard Phantom control box containing joysticks and switches, with the operator viewing stereo video camera images on a stereo display monitor. Remote control of the vehicle over the satellite link was accomplished using the Virtual Environment Vehicle Interface (VEVI) control software developed at NASA Ames. The remote operator interface included either a stereo display monitor similar to that used locally or a stereo head-mounted head-tracked display. The compressed video signal from the vehicle was transmitted to NASA Ames over a 768 Kbps satellite channel. Another channel was used to provide a bi-directional Internet link to the vehicle control computer through which the command and telemetry signals traveled, along with a bi-directional telephone service. In addition to the live stereo video from the satellite link, the operator could view a computer-generated graphic representation of the underwater terrain, modeled from the vehicle's sensors. The virtual environment contained an animate graphic model of the vehicle which reflected the state of the actual vehicle, along with ancillary information such as the vehicle track, science markers, and locations of video snapshots. The actual vehicle was driven either from within the virtual environment or through a telepresence interface. All vehicle functions could be controlled remotely over the satellite link.

# REPORT DOCUMENTATION PAGE

Form Approved
OMB No. 0704-0188



| 1. AGENCY USE ONLY *(Leave blank)* | 2. REPORT DATE | 3. REPORT TYPE AND DATES COVERED |
|---|---|---|
| | November 1994 | Conference Publication |

**4. TITLE AND SUBTITLE**

Eighteenth Space Simulation Conference
Space Mission Success Through Testing

**5. FUNDING NUMBERS**

750

**6. AUTHOR(S)**

Compiled by Joseph L. Stecher, III

**7. PERFORMING ORGANIZATION NAME(S) AND ADDRESS(ES)**

Goddard Space Flight Center
Greenbelt, Maryland 20771

**8. PERFORMING ORGANIZATION REPORT NUMBER**

94B00132

**9. SPONSORING/MONITORING AGENCY NAME(S) AND ADDRESS(ES)**

National Aeronautics and Space Administration
Washington, D.C. 20546–0001

**10. SPONSORING/MONITORING AGENCY REPORT NUMBER**

CP-3280

**11. SUPPLEMENTARY NOTES**

**12a. DISTRIBUTION/AVAILABILITY STATEMENT**

Unclassified–Unlimited
Subject Category 18
Report is available from the NASA Center for AeroSpace Information, 800 Elkridge Landing Road, Linthicum Heights, MD 21090; (301) 621-0390.

**12b. DISTRIBUTION CODE**

**13. ABSTRACT** *(Maximum 200 words)*

The Institute of Environmental Sciences' Eighteenth Space Simulation Conference, "Space Mission Success Through Testing" provided participants with a forum to acquire and exchange information on the state-of-the-art in space simulation, test technology, atomic oxygen, program/system testing, dynamics testing, contamination, and materials. The papers presented at this conference and the resulting discussions carried out the conference theme "Space Mission Success Through Testing."

**14. SUBJECT TERMS**

Space Simulation, Thermal Simulation, Contamination Control, Dynamic Testing, Spacecraft Materials, New Approaches and Facilities

**15. NUMBER OF PAGES**

473

**16. PRICE CODE**

| 17. SECURITY CLASSIFICATION OF REPORT | 18. SECURITY CLASSIFICATION OF THIS PAGE | 19. SECURITY CLASSIFICATION OF ABSTRACT | 20. LIMITATION OF ABSTRACT |
|---|---|---|---|
| Unclassified | Unclassified | Unclassified | Unlimited |